Sustainable Civil Infrastructures

Guangliang Feng
Ping Xiang
Xiao-Yong Wang
Ana Almerich-Chulia *Editors*

Advances in Computational Modeling and Structural Performance Evaluation for Civil Engineering Systems

ICCE 2025

Springer

Sustainable Civil Infrastructures

Editor-in-Chief

Hany Farouk Shehata : In Memoriam, *SSIGE, Soil-Interaction Group in Egypt SSIGE, Cairo, Egypt*

Series Editor

Mourad Amer, *IEREK—International Experts for Research Enrichment and Knowledge Exchange, Cairo, Egypt*

Editorial Board Members

Hüseyin Bilgin, *Professor in the Civil Engineering Department at Epoka University, Tirana, Albania*
Sherif Mohamed Hafez Ahmed, *Professor at Department of Structural Engineering, Alexandria University, Alexandria, Egypt*
Helder I. Chaminé, *Geologist and Professor of engineering geosciences at the School of Engineering (ISEP) of the Polytechnic of Porto, Porto, Portugal*
Giama Effrosyni A, *Laboratory Teaching Staff, Department of Mechanical Engineering, Aristotle University of Thessaloniki (AUTh), Greece, Thessaloniki, Greece*
Hamad Al Jassmi, *Civil Engineering from the University of New South Wales (UNSW) in Australia, Sydney, NSW, Australia*
Nusrat Jung, *Lyles School of Civil and Construction Engineering at Purdue University., West Lafayette, IN, USA*
Corrado Rindone, *Professor, Department of Information Engineering, Infrastructure and Sustainable Energy, Mediterranean University of Reggio Calabria, Italy, Reggio Calabria, Italy*
Seyed Mohammadreza, *Civil and Transportation Engineering, Logistics, Business, and Management, Enschede, The Netherlands*
Gobinath Ravindran, *Environmental Management and GeoTechmology – College of Engineering, Guindy, Chennai, Tamil Nadu, India*
Hugo Rodrigues, *Professor in the Civil Eng. Department, University of Aveiro, Aveiro, Portugal*
Nadeem Ahmad Khan, *Civil Engineering Department, Mewat Engineering College Nuh, Haryana, Nuh, Haryana, India*
Fabio Fatiguso, *Full Professor of Architectural Engineering (SSD ICAR/10) Polytechnic University of Bari POLIBA, Department of Civil, Environmental, Land, Building Engineering and Chemistry (DICATECh), Bari, Italy*
Muhammad Nawaz Tunio, *University of Sufism and Modern Sciences, Bhit Shah, Pakistan*
Federico Camerin, *Universidad de Valladolid, Valladolid, Spain*
Linchuan Yang, *Professor and Deputy Head of the Department of Urban and Rural Planning at the School of Architecture, Southwest Jiaotong University, Chengdu, China*

Sustainable Civil Infrastructures (SUCI) is a series of peer-reviewed books and proceedings based on the best studies on emerging research from all fields related to sustainable infrastructures and aiming at improving our well-being and day-to-day lives. The infrastructures we are building today will shape our lives tomorrow. The complex and diverse nature of the impacts due to weather extremes on transportation and civil infrastructures can be seen in our roadways, bridges, and buildings. Extreme summer temperatures, droughts, flash floods, and rising numbers of freeze-thaw cycles pose challenges for civil infrastructure and can endanger public safety.

We constantly hear how civil infrastructures need constant attention, preservation, and upgrading. Such improvements and developments would obviously benefit from our desired book series that provides sustainable engineering materials and designs. The economic impact is huge, and much research has been conducted worldwide. The future holds many opportunities, not only for researchers in a given country, but also for the worldwide field engineers who apply and implement these technologies. We believe that no approach can succeed if it does not unite the efforts of various engineering disciplines from all over the world under one umbrella to offer a beacon of modern solutions to the global infrastructure. Experts from the various engineering disciplines around the globe participate in this series, including: Geotechnical, Geological, Geoscience, Petroleum, Structural, Transportation, Bridge, Infrastructure, Energy, Architectural, Chemical and Materials, and other related Engineering disciplines.

The SUCI series publishes the best research papers from various IEREK international conferences, while external conference proceedings proposals are no longer accepted as direct publications. The series does invite significant expansions of selected papers previously submitted to conferences. The Editors' role should be evident in the reviews through an intensive **double-blind peer review** process, helping authors with edits, and collaborating with them to demonstrate **great academic significance** through clear research findings and innovative solutions that go well beyond a typical conference submission.

With the commitment to the above instructions, the SUCI series welcomes external proposals and requests to publish **edited books, contributed volumes, monographs, and textbooks** that align with the series' scope and fit with its policy.

SUCI series is now indexed in SCOPUS and EI Compendex.

Editor-in-ChiefSeries Editor Hany Farouk Shehata Mourad Amer SUCI.series@ierek.com

Guangliang Feng · Ping Xiang ·
Xiao-Yong Wang · Ana Almerich-Chulia
Editors

Advances in Computational Modeling and Structural Performance Evaluation for Civil Engineering Systems

ICCE 2025

Springer

Editors
Guangliang Feng
Chinese Academy of Sciences
Institute of Rock and Soil Mechanics
Wuhan, China

Ping Xiang
School of Civil Engineering
Central South University
Changsha, China

Xiao-Yong Wang
Department of Architectural Engineering
Kangwon National University
Chuncheon-si, Korea (Republic of)

Ana Almerich-Chulia
Department of Mecanica Medios
Polytechnic University
Valencia, Valencia, Spain

ISSN 2366-3405 ISSN 2366-3413 (electronic)
Sustainable Civil Infrastructures
ISBN 978-3-032-32236-4 ISBN 978-3-032-32237-1 (eBook)
https://doi.org/10.1007/978-3-032-32237-1

© The Editor(s) (if applicable) and The Author(s), under exclusive license
to Springer Nature Switzerland AG 2027

This work is subject to copyright. All rights are solely and exclusively licensed by the Publisher, whether the whole or part of the material is concerned, specifically the rights of translation, reprinting, reuse of illustrations, recitation, broadcasting, reproduction on microfilms or in any other physical way, and transmission or information storage and retrieval, electronic adaptation, computer software, or by similar or dissimilar methodology now known or hereafter developed.
Unless otherwise expressly agreed by the Publisher in writing, the Publisher does not authorize use or reproduction of all or any part of this work in any manner for the purpose of training, fine-tuning, evaluating, or developing artificial intelligence models, technologies, or systems. In accordance with Article 4(3) of the EU Directive 2019/790 on copyright and related rights in the Digital Single Market, the Publisher expressly reserves all rights with respect to this work under the text and data mining exception of the directive.
The use of general descriptive names, registered names, trademarks, service marks, etc. in this publication does not imply, even in the absence of a specific statement, that such names are exempt from the relevant protective laws and regulations and therefore free for general use.
The publisher, the authors and the editors are safe to assume that the advice and information in this book are believed to be true and accurate at the date of publication. Neither the publisher nor the authors or the editors give a warranty, expressed or implied, with respect to the material contained herein or for any errors or omissions that may have been made. The publisher remains neutral with regard to jurisdictional claims in published maps and institutional affiliations.

This Springer imprint is published by the registered company Springer Nature Switzerland AG
The registered company address is: Gewerbestrasse 11, 6330 Cham, Switzerland

If disposing of this product, please recycle the paper.

Preface

Civil engineering is intricately linked to people's lives, and the quality of civil engineering projects directly impacts individuals' well-being, personal safety, and significantly influences societal development. Consequently, it is imperative to scrutinize the current state of civil engineering development in order to address and rectify the issues that hinder its progress.

We had the honor of inviting Professor Bin Xu, Jiangxi University of Water Resources and Electric Power, China, to serve as our Conference Chairman, and the conference was attended by 150 individuals and enterprises from all over the world. Divided into three parts, the conference agenda covered keynote speeches, oral presentations, and online Q&A discussion. Firstly, keynote speakers (Professor Prof Ruguo Fan, Wuhan University; Prof Qiuhong Zhao, Beihang University, China; Prof. Ping Xiang, Central South University; Prof, Md. Mahbub Alam, Harbin Institute of Technology (Shenzhen); Prof. Jianwei Yan, East China Jiaotong University) were each allocated 30–35 minutes to deliver their speeches. Then, in the oral presentations, the excellent papers selected were each presented by their authors for 10–15 minutes. During the oral presentation sessions, participants from various universities and research institutions, including Universiti Tunku Abdul Rahman, Tsinghua University, Southeast University, Tongji University, Chang'an University, Beijing University of Technology, Chengdu University of Technology, and Anhui University of Science and Technology, delivered their presentations. Finally, in the poster presentations, the papers selected were presented by their authors for 3–5 minutes each.

This book compiles the proceedings of the 12th International Conference on Civil Engineering (ICCE 2025), held on December 26–27, 2025, at Jiangxi University of Water Resources and Electric Power, China. The conference was proudly hosted by Jiangxi University of Water Resources and Electric Power in collaboration with the Civil Engineering Academy of Jiangxi Province and co-organized by esteemed entities such as the Journal of Rock and Soil Mechanics, the Key Laboratory for Safety of Water Conservancy and Civil Engineering Infrastructure in Jiangxi Province, and the Key Laboratory of Sichuan Province for Road Engineering at Southwest Jiaotong University. Over 250 participants gathered to share insights and engage in discussions on the latest advancements in the field. The book encompasses 43 meticulously peer-reviewed papers, carefully selected from over 230 submissions, spanning a diverse range from theoretical and conceptual frameworks to highly practical applications and industry best practices.

The book shares practical experiences and enlightening ideas from civil engineering and will be of interest to researchers in and practitioners of civil engineering everywhere.

Committee

Chair:

Bin Xu	Nanchang Institute of technology, China

Co-chair:

Bo Zhang	Shandong University, China.
WANG Xiao-Yong	Kangwon National University, Korea
Junxian Zhao	The South China University of Technology, China.
Kaihua Zeng	Nanchang Institute of technology, China
Almerich-Chulia	Polytechnic University of Valencia, Spain.

Committee member:

Brahim Benmokrane	Fellow of the Royal Society of Canada (Academy of Science), Canada.
Chikhotkin Victor	Russian Academy of Natural Sciences, Russia
Jiming Xie	Zhejiang University, China
Hongnan Li	Dalian University of Technology, China.
Xiao Yu	Wuhan University of science and technology, China
Qiuxin Liu	Wuhan University of science and technology, China
Lei Zeng	Changjiang University, China
Jie Sun	Wuhan University of science and technology, China
Mehmet Gesoglu	Gaziantep University, Turkey.
Fang Xu	China University of Geosciences, Wuhan, China
Junqing Lei	Beijing Jiaotong University, China
He Chen	Hebei University of Technology, China
Yifeng Zhong	Chongqing University, China
Libiao Bai	Chang'an University, China
Zongwu Chen	China University of Geosciences, Wuhan, China
Xiaohua Li	Chongqing University, China

Guannan Liu	China University of mining and technology, China
Tiequan Ni	Huanggang Normal University, China
Hongtao Zhang	North China University of technology, China
Yongjun Ni	Beijing Jiaotong University, China
Ali Kaveh	Iran University of Science and Technology, Iran
Abdulqader Said Ali Al-Najmi	The University of Jordan, Jordan
Harvinder Singh	Guru Nanak Dev Engineering College, India
Abdul Rahman M. Sam	Universiti Teknologi Malaysia, Malaysia
Evangelos J. Sapountzakis	National Technical University of Athens, Greece
Mohamed Elgawady	Missouri University of Science and Technology, Switzerland
Shu-Lung Kuo	Open University of Kaohsiung, China
Azer Kasimzade	Ondokuz Mayis University, Samsun, Turkey
Youngjin Cha	University of Manitoba, Canada.
Jamal Khatib	University of Wolverhampton, UK
Awrejcewicz Jan	Lodz University of Technology, Poland
Belkacem Adim	Tissemsilt University, Algeria.
Krzysztof Schabowicz	Wroclaw University of Technology, Poland
Muhammad Hadi	University of Wollongong, Australia
Sadek Deboucha	University Mohamed El Bachir El Ibrahimi of Bordj Bou Arreridj, Algeria
Cristiano Poleto	Federal University of Rio Grande do Sul, Brazil
Qian Wang	Manhattan College, USA
Associate Professor Lei Wang	Changsha University of Science & Technology, China
Chung Bang Yun	Zhejiang University, China
Francisco Agüera-Vega	Universidad de Almería, Spain
G M Tarekul Islam	Bangladesh University of Engineering and Technology, Bangladesh
R Ajith Kumar	Deemed University, India
Eduardo Rojas	Universidad Autónoma de Querétaro, Mexico
Boukhattem Lahcen	University Cadi Ayyad, Morocco.
Guofeng Du	Yangtze University, China
Pawel K. Zarzycki	Koszalin University of Technology, Poland
Francesco Pellicano	University of Modena and Reggio Emilia, Italy
A P Shashikala	National Institute of Technology Calicut, India
Antonio Panico	Pegaso Online University, Italy
Claudia Vitone	Politecnico di Bari, Italy
Masoud Ghodsian	Tarbiat Modares University, Iran.
Yi Bao	Stevens Institute of Technology, USA
Bingxiang Yuan	Guangdong University of Technology, China
Belén González-Fonteboa	University of A Coruña, Spain

Paritosh Srivastava	Galgotias University Greater Noida, INDIA
Mohammad Arif Kamal	Aligarh Muslim University, INDIA
Ehsan Seyedi Hosseininia	Ferdowsi University of Mashhad, Iran
Mohammad Khishe	Imam Khomeini Maritime Sciences University, Iran
Yuncheng HE	Guangzhou University, China
Xingzheng Wu	Hebei University, China.
Ahmed Benamar	Université Le Havre-Normandie, France.
Zengfu Wang	Northwestern Polytechnical University, China
Ali Zaidi	University of Sherbrooke, Canada

Contents

Analysis of Key Technical Points of Hongpu6 Wreck Salvage Project 1
Wei Deng, Qingpeng Wang, Shenghang Fu, and Chuantong Wang

Optimization Analysis of the Mix Proportion of Semi-Flexible Pavement Grouting Materials Based on the Response Surface Methodology 16
Yaping Wang, Yu Mao, Junjie Lin, Haihong Zhang, Wenjing Zhang, and Xiaopeng Zhang

The Co-application of Nitrogen and Zinc Influenced Maize Yield and Quality on the Sanjiang Plain 31
Haoyuan Feng, Xinyi Wang, Jianpeng Zhang, Baoguo Zhu, Xingjie Zhong, Miao Wang, and Nannan Wang

Large-Scale Object Recognition Dataset Construction and Detection Analysis of Construction Scene Based on Video Surveillance 44
Jun Zhang, Yiming Han, Hai Lin, Kaite Shi, Zhe Li, Lizhi Xu, Ende Lin, and Kaiyuan Zheng

Unbalanced Remote Sensing Data Classification Based on NSGA-III and Cost-Sensitive Random Forest 64
Xiang Liu, Yan Xiao, Bin Wang, Moxuan Yang, Xubo Liu, and Jun Pan

Investigation on the Hydro-Mechanical Coupling Evolution in the Near-Wellbore Region during Marine Natural Gas Hydrate Drilling 79
Pan Han and Ken Qin

Energy-Efficient Facade Retrofit for Xi'an Campus Buildings: A Optical Daylighting Approach – A Case Study of the Affiliated Middle School of Xi'an University of Architecture and Technology 92
Ruixin Li and Xianglong Tang

Corner Effect-Driven Spatiotemporal Deformation Mechanisms of Retaining Structures in Soft Soil Deep Excavations 106
Ying Liu and Binhui Xiang

Application of the Xinanjiang Model in Flood Forecasting of Yanjingkou Reservoir 120
Shilei Chen and Qingying Qiu

Improvement of Fatigue Performance at U-Rib Weld by Rigid Deck Pavement 132
Zhiqing Chen, Zhengkai Li, Zheshi Wang, Dengyu Rao, and Jingyuan Chang

Research on Crack Control Technology System of Mass Concrete Side Wall of Open-Cut Tunnel under Water-Rich Environment of Soft Foundation Based on Comprehensive Evaluation 147
Wei Deng, Huan-yong Chen, Jin-liang Wang, Yuan-xi Chen, and Feng Jiang

Research on the Stress Wave Characteristic Curves Method for Detecting Pile Length in Precast Concrete Piles of Multiple Segments 159
Shun Zhai, Haifeng Liu, Yang Mo, Qilin Wang, Ru Qu, Ruilin Du, Wei Li, and Huaijian He

Design and Performance Verification of Burst Pipe Safety Valve for Water Supply Pipeline in Hydro-Power Station 172
Peng Li, Yong Sun, Tongke Shen, Xuefeng Wei, Junze Gao, Yanliang Qiu, and Wei Duan

Research on the Current Development Status and Application Schemes of Low-Altitude Economy During the Construction Period of Railway Engineering 186
Yulong Lu, Hongfei Cao, Lingling Yang, Fei Li, Fangbo Qiao, and Wenhui Feng

Blasting Vibration Analysis of Existing Surface Buildings Induced by Drill and Blast Excavation of Large-Section Tunnels 203
Peng Guo, Shaohua Ji, Jun Wang, and Guowen Xu

Data Integration Framework for Multi-Disciplinary 2D Drawings and 3D BIM through Adjustable Rendering and Lightweight Data Processing 222
Qiao Zheng, Xiaoqiang Liu, Minjin Fang, and Rui Jin

Effect of Water Level and Steel Reinforcement on Seismic Performance of High Concrete Arch Dam-Foundation Systems 234
Xuecong Liu, Jinhui Ouyang, Dawen Tan, Chunyao Hou, and Hui Liang

Sympathetic Detonation Characteristics of Bare Cylindrical TNT Charges 251
Heming Huang, Xinjie Wang, Ruilong Ma, Ziyan Shu, and Fenglei Huang

A Practical Calibration Method for MCC and UH Model Parameters Solely Based on CD Triaxial Tests 266
Binglong Zhu

Early-Age Performance and Hydration Temperature Evolution of an OPC–CSA Composite Binder System 280
Yin Xu, Jing Yang, and Haoran Guo

Analysis of Key Technical Paths for Nearly Zero Carbon Building in the Beijing Area—Taking a Hotel in Tongzhou District as an Example 295
Haoyu Wang, Yingqi Wang, Hongbo Guo, Haifeng Guo, Wen Ding, and Xiaoyu Wang

Automated Evaluation Methods for Open-Ended Question in Hydropower Domain Based on Large Language Models 309
Yubin He, Lizhi Wang, Wei Luo, Xinpeng Yu, Yingjia Li, Dingxiao Liu, Minghui Guo, Shiruo Hu, and Jianshi Zhao

Numerical Simulation of Regular Wave Transmission over a Trapezoidal Breakwater Using CIP Model with Adaptive Mesh 323
Yiyang Zong, Ruian Tie, Shengming Cheng, Shuangcheng Zhang, Hongtao Xu, Lingfeng Wang, and Shuhao Si

Numerical Simulation of Simultaneous Closure Scheme for a High-Pier Long-Span Curved Continuous Rigid Frame Bridge 340
Zhen Fang, Jinyu Ma, and Zhibao Cheng

Fire Risk Assessment for a Subway Station Platform Based on Fuzzy Analytic Hierarchy Process 350
Jin Zhang, Baoqian Dai, Xiushan Lin, Dongxue Li, and Rui Zhou

Impact of Basal Surrounding Rock Deterioration on the Mechanical Properties of the Invert in Mudstone Tunnels 366
Qidong Wu, Sheng Li, Lifang Pai, Bin Li, Jianyong Zhu, and Jianyun Zhu

A Method for Key Structural Design and Multi-Case Safety Assessment of Long-Span Asymmetric Cable Cranes 378
Qinglan Ye and Ning Hong

The Development of Electro-Hydraulic Shaking Table 393
Zilong Zhao, Xiaofei Ma, Juke Wang, Guili Liu, and Lei Lv

Optimization of Main Temporary Pier Location for Small-Radius Curved Steel Box Girder during Incremental Launching Construction 407
Kunfeng Zhang, Ping Zhao, Xi Ding, Jia Mi, Feilong Fan, Yingfu Guo, and Xueming Li

Research on Settlement Prediction Methods for Earth-Rock Dams Based on Multi-source Data Fusion and Deep Learning 421
Chuanqi Shen, Jiangrong Pei, Zhongjun Deng, and Zongqi Li

Experimental Study on Shear Strength of Modified Phosphogypsum Subgrade Materials 438
Zhiwei Nian, Wenguang Guo, Xueqi Wang, Xintong Song, Yuke Li, and Jun Shen

A Novel Integrated Framework for Seismic Analysis of Ultra-High Arch Dams in Construction-Initial Impoundment: Multi-field Coupling and Staged Evolution 451
Jin Yuan, Yanpian Mao, Heng Cheng, Zhiyong Qi, You Mou, and Chenfang Jiang

Migration and Plugging for Temporary Plugging Balls in Multi-cluster Fractured Horizontal Well 464
Aiguo Hu, Hao Chen, Fan Wang, Yanfang Jiang, Yangyang Li, Jinpeng Yan, Huaizhou Wei, Chao Gao, and Can Cai

Slot Width of Plunger Model Valve with Slot Cage Structure Influence on Cavitation Resistance Performance 478
Xuepan Wang, A. Dili, Zhengbai Chang, Ronghui Wang, and Jin Jang

Study on the Temperature Field Change of Frozen Soil Subgrade Treated with Foamed Mixture Soil 491
Qiang Tang, Xintong Song, Yuanxiang Wang, Qindong Li, and Yin Cheng

Dynamic Assessment and Optimization of Daily Operational Resilience for the Urban Roadway Tunnel System 504
Deyi Liu, Jiang Liu, Weiyu Jiang, Yachao Li, Yuehui Wang, Huijun Lan, and Xiaodong Pan

Research on the Impact of Unfavorable Topography on the Seismic Safety of Gravity Dams with Deep Anti-sliding Stability 527
Dudu Su, Chunli Yan, Songtao Zhao, Jin Tu, and Hui Liang

Application of Composite Reinforcement Technology with High-Precision Large-Diameter Pipe Roof and Sleeve Valve Pipe in Urban Ultra-Shallow Buried Backfill Soil Tunneling by Underground Excavation 540
Bo Deng, Wentao Liu, Yunhao Gou, Longquan Zhao, and Rui Su

Application of Integrated Grouting at Tunnel Arch Foot and Face in Ultra-Shallow Buried Backfill Tunneling 556
Wentao Liu, Yunpeng Han, Wenjing Duan, Yuxuan He, and Rui Su

Research on Optimization of Tunnel Rock Mass Support Parameters and Deformation Control Based on Orthogonal Experiments 566
Zhenguo Liu, Fangjie Jiang, Wei Li, Jinhui Duan, and Rui Su

Parameter Analysis of Mechanical Performance of UHPC Continuous Bridge Deck Structure for Concrete Beam Bridge 578
Chaomin Chu, Lvshan Huang, Qiaosha Chen, Liang Xiao, and Runchuan Xu

Performance Analysis of Steel-Concrete Composite Bridge with Thin Steel Bottom Formwork Deck 589
Yangfu Xu, Qing Zhang, Yuhan Liu, and Liang Xiao

Innovative Tool-Type Single-Sided Formwork System for in-Situ Construction of Underground Concrete Walls: Finite Element Analysis and Experimental Validation 601
Wei Liu, Lin He, Jikai Liu, Guanjie Li, Hui Zhang, Chengqiang Zhao, and Xiangle Kong

Author Index 615

Analysis of Key Technical Points of Hongpu6 Wreck Salvage Project

Wei Deng, Qingpeng Wang, Shenghang Fu, and Chuantong Wang(✉)

China Yantai Salvage, NO.100, Zhifudaodong Road, 264000 Yantai, Shandong Province, People's Republic of China
17660103959@163.com

Abstract. Hongpu6 is a wreck that exploded in the middle of the ship and sank into the water. After analyzing the state of the wreck detailly, then the salvage work was completed through the grab of the middle of the ship and the salvage of the fore-and-aft sections respectively. Several key technical points should to be considered during salvage, include ship station location, attack of wire hole, calculation of lifting force, analysis of the key points of lifting, wreck lashing. During the salvage process, take into full consideration of flexible arrangement of ship position according to ship characteristics, use the "bathyeel III" underwater mud penetrator to attack the wire hole, the lifting force is calculated based on theoretical analysis and GHS software, check lashing with reference to towing guidelines. In this paper, the above contents will be elaborated and studied. At the same time, hope to provide ideas for similar salvage projects in the future.

Keywords: Raising integrally · Attack the wire hole · Calculation of lifting force · Analysis of flotation key points

1 Introduction

The Hongpu6 is a 10,000-deadweight-tonnage oil tanker with principal dimensions of 128 m × 19.8 m × 10.8 m and a lightship weight of approximately 3,900 t. On January 10, 2023, the vessel suffered an explosion in the waters off Rizhao, subsequently sank, and came to rest on the seabed at a depth of 30 m. The explosion originated in the compartments between the midship section and the deckhouse. Although the vessel was in ballast condition, approximately 320 t of residual fuel oil remained in the engine room tanks to support the vessel's operational systems, which posed a significant threat of ecological damage to the local marine environment in the event of a leak. Furthermore, the explosion resulted in severe hull damage. While the fore and aft sections remained connected, they settled on the seabed at different attitudes. The stern section is tilted approximately 30° to starboard, with a maximum burial depth of up to 8 m. This complex wreck posture presents substantial challenges for the salvage operation.

The China Yantai Salvage commenced the salvage operation on April 16, 2023. The process encompassed critical phases including underwater oil recovery, removal of the explosively damaged midship section, as well as the attack of wire hole and

© The Author(s), under exclusive license to Springer Nature Switzerland AG 2027
G. Feng et al. (Eds.): ICCE 2025, SUCI, pp. 1–15, 2027.
https://doi.org/10.1007/978-3-032-32237-1_1

the subsequent raising of both the bow and stern sections. The entire operation was successfully concluded on July 3, 2023.

Several innovative techniques were pivotal to the project's success. For the first time in China, a submersible barge was utilized as the primary salvage platform. This approach significantly mitigated the impact of swells on crane operations and reduced the downtime associated with the vessel repeatedly moving off-site for weather avoidance, thereby substantially extending the operational window. Another national first was the deployment of the third-generation underwater mud-pusher, " bathyeel III," for attack of wire hole. This advanced equipment overcame challenges such as significant water depth, hard seabed geology, and deep sediment burial, greatly enhancing operational precision and efficiency. Furthermore, engineering software packages including GHS, Rhino, and Abaqus were employed for static equilibrium analysis, 3D procedural simulation, and structural component strength calculations, which improved the overall accuracy of the salvage plan.

This paper will focus on the key technical aspects of the operation, specifically addressing five critical areas: ship station location, attack of wire hole, lifting force calculation, analysis of the key points of lifting, and wreck lashing.

2 Ship Station Location

Different phases of the salvage operation required specific ship station location [1]. Key positioning scenarios included the stations for attack of wire hole, for wreck lifting operations, and the layout for oil spill prevention and control, which was closely integrated with vessel arrangements.

2.1 Ship Station Location for Attack of Wire Hole

The attack of wire hole [2, 3] was conducted sequentially along the length of the wreck. The primary salvage vessel, De Fu 3, operated in a submerged-bottom mode. Once settled on the seabed, its position became fixed. The underwater mud-pusher [4, 5] is a self-contained unit that, aside from being deployed by the vessel's crane, does not require direct support from the vessel hull. Therefore, to optimize operational efficiency and remain within the crane's operating radius, De Fu 3 was positioned parallel to either the bow or stern section of the wreck. This configuration also ensured that the vessel's anchor wires did not interfere with the wreck. Given that the length of each section (bow or stern) was between 50 and 60 m, a single positioning and settling operation of De Fu 3 was sufficient to cover all required wire hole locations on that section.

While the primary salvage vessel, De Fu 3, conducted attack of wire hole from one side of the wreck, a second vessel was required on the opposite side to retrieve drill rods and bits and to thread guide wires. To maximize operational efficiency, an auxiliary crane vessel was selected for this role and positioned accordingly. To ensure optimal crane performance, the auxiliary vessel needed to continuously adjust its position in sync with the progressing wire hole locations. Consequently, it was decided to position the auxiliary vessel directly alongside the wreck. A schematic diagram of the vessel configuration during the attack of wire hole operation is presented in Fig. 1.

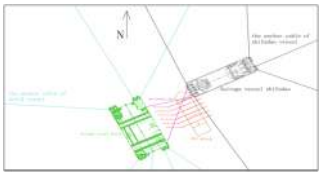

Fig. 1. Schematic of vessel configuration for the attack of wire hole operations.

2.2 Ship Station Location for Wreck Raising Operations

The bow and stern sections were raised separately. Due to differences in the weight of each section and the distinct lifting vessels deployed, their respective ship station location differed.

The bow section, approximately 60 m in length, was rigged with six pairs of underwater lifting wires, resulting in 12 wire ends above water. The raising vessel, De Fu 3600, is equipped with four hooks arranged with a spacing of 24 m (across the vessel's beam) by 9 m (along the vessel's length, varying slightly with boom reach). Consequently, each hook was connected to three wire ends. Specifically, the wire ends from the first, second, and third pairs of lifting wires on the same side of the wreck were grouped onto a single hook, with the remaining wires grouped similarly on the other hooks. The distance between the second and fifth pairs of wires was 24 m, and the wreck's width was 19.8 m. This resulted in the connection points on the hooks being spaced in a 24 m by 19.8 m layout. To minimize the hook offset angle, the crane vessel was positioned directly alongside the wreck. Simultaneously, the transport barge, which would later receive the wreck section, was positioned parallel to the wreck and broadside to the crane vessel's bow.

The stern section, approximately 50 m long, was shorter than the bow section. However, due to the complex structure of the engine room, it was heavier. Consequently, it was rigged with eight pairs of underwater lifting wires, yielding 16 wire ends above water. The initial lifting plan involved two vessels: De Fu 3600 and De Ying. The lifting of the stern section was distributed as follows: De Fu 3600 was designated for the heavier aft segment, and De Ying was deployed for the forward segment. In this setup, the four hooks of De Fu 3600 were rigged to twelve wire ends, leaving the remaining four ends for the hooks of De Ying. This arrangement was designed to adhere to the guideline of maintaining minimal hook inclination angles. The analytical procedure, being identical to that employed for the bow section, is not repeated. The final positioning involved De Fu 3600 stationed parallel to the wreck's stern, De Ying positioned parallel to one side of the wreck, and the transport barge located parallel to the opposite side. The ship station location for raising the bow and stern sections are illustrated in the Fig. 2.

During the actual raising of the stern section, the De Fu 3 vessel was urgently deployed to assist the operation due to an unexpected crane malfunction on the primary vessel. This contingency measure introduced additional complexity to the vessel configuration. The final positioning arrangement for the stern section raising is illustrated in the Fig. 3.

(a) (b)

Fig. 2. Vessel configuration for raising the (a) bow and (b) stern sections of the wreck.

(a) (b)

Fig. 3. (a) indicated and (b) actual wreck stern segment positions upon surfacing.

3 Attack of Wire Hole

The attack of wire hole refers to the process of creating wire hole beneath a wreck's hull to facilitate the threading of lifting slings. In the overall wreck salvage process, this procedure is a critical phase, as its progress directly dictates the timeline of the entire operation.

The most traditional method employs divers using high-pressure water jets to create wire hole, which is inefficient and poses safety risks. Subsequently, a technology adapted from land-based trenchless techniques was developed [6]. This method involves mounting a drilling rig on a support vessel to guide drill rods to the target location beneath the hull via a guiding apparatus (see in Fig. 4(a)). However, the effectiveness of the guiding apparatus is significantly constrained by water depth and sea conditions, generally limiting this technique to waters shallower than 25 m.

At the project site, with a water depth of approximately 30 m and exposure to open-sea swells, the conventional guided drilling method was unsuitable. To optimize operational efficiency and capitalize on the specialized equipment capabilities of China Yantai Salvage, the third-generation underwater mud-pusher, " bathyeel III," (see in Fig. 4(b)) was deployed for the first time. This represents the most advanced tool of its type in China, with a maximum operational depth of 200 m and maximum thrust and pull forces of 22.5 t and 45 t, respectively.

The "bathyeel III" underwater guided mud-pusher system comprises six main components: the underwater tool, an integrated umbilical cable winch, a deck-mounted hydraulic power unit, a mud pumping station, a surface control room, and a screw-type air compressor. The working principle is as follows: The tool is lowered to the seabed by the support vessel's crane and secured using four spiral anchors that penetrate the sediment. After system commissioning, the mud pump is activated, delivering high-pressure mud slurry through an internal pipeline to the jetting bit and steering plate

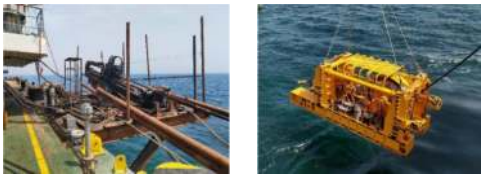

(a) (b)

Fig. 4. Equipment for attack of wire hole: (a) land-based trenchless system and (b) the "bathyeel III" underwater mud-pusher.

assembly at the leading end of the drill string. This high-pressure slurry excavates the wire hole. An injection unit at the front of the tool then advances the drill string via a hydraulic chain drive system. The drill string consists of high-strength, flexible coiled pipe stored on a reel located in the mid-rear section of the tool. As the jetting assembly continues to excavate with the high-pressure slurry, the injection unit pushes the drill string forward while the coiled pipe reel feeds the pipe, enabling continuous wire hole. Simultaneously, the steering plate can be remotely controlled to adjust the drilling direction. This slow, precise rotation enables maneuvers such as diving, turning, maintaining level, or ascending, as required by the trajectory. Upon wire hole completion, the drill bit is steered upward to break the seabed surface on the opposite side of the wreck from the support vessel. The internal flow is then switched from mud slurry to compressed air. By observing the resulting bubble plume at the surface, divers can locate the bit, attach a pilot wire, and then retrieve the drill string. This process pulls the pilot wire back through the wire hole, establishing a connection across the wreck for subsequent standard wire-rope threading operations.

During operation, critical parameters such as the tool's attitude, heading, penetration rate, injection unit thrust, and steering plate orientation were dynamically monitored and controlled from the control room.

The longitudinal arrangement of the wire hole was determined based on the weight distribution of the wreck. However, because the hull's cross-sectional profile varies along its length and the wreck's list and trim cause differential settlement at each position, the drilling path for each individual wire hole1 had to be custom-designed according to the local hull geometry. Vertically, a safety margin was incorporated by designing the wire hole path to be 2–3 m below the lowest point of the wreck. Horizontally, to accommodate the minimum turning radius of the drill string, the entry point into the seabed was typically set approximately 15 m away from the wreck. In this project, the stern section had a maximum settlement of 8 m. For the corresponding wire hole, the drill string reached a depth of at least 10 m below the mudline, with the total length of the drill string embedded in the seabed reaching 60 m. Therefore, the accuracy of the attack of wire hole path design is highly dependent on comprehensive data regarding the wreck's attitude, settlement, and other relevant parameters.

During the actual drilling process, any deviation of the wire hole position from the planned path was monitored in real-time via the control room display. This deviation, representing the discrepancy between the actual and designed paths, was measured by an inertial navigation system integrated into the leading section of the drill string. As

illustrated in the Fig. 5, a rectangle schematic represents the wreck's cross-section. The planned and actual drilling paths are shown by the yellow and red lines, respectively. The upper part of the display provides a profile view indicating vertical deviation, while the lower part offers a plan view showing lateral deviation. This real-time feedback was used to steer the guiding plate and correct the path.

Fig. 5. Real-time monitoring interface displaying the drilling path of the underwater mud-pusher.

3.1 Positioning of the Underwater Mud-Pusher

The underwater mud-pusher is equipped with an internal compass for orientation, but determining its absolute position requires external methods. The traditional positioning method involves divers deploying surface marker buoys on both sides of the wreck at the intended drilling location. The alignment of these two buoys indicates the desired wire hole direction. During deployment, the mud-pusher's lifting sling is aligned with this buoy line to achieve positioning along the wreck's longitudinal axis. However, this method cannot determine the lateral distance from the wreck, which must be estimated visually, leading to significant errors. Furthermore, buoy drift due to currents means their surface position may not accurately reflect the submerged attachment points.

To address the need for precise underwater positioning, an Ultra-Short Baseline (USBL) positioning system was employed [7]. The system hardware primarily consists of a display terminal, a transducer, and transponders. Multiple transponders were installed on the mud-pusher itself and at reference points on both sides of the wreck. The transducer was mounted on the vessel's side, below the waterline. The transducer communicates acoustically with the transponders, and the positions of both are displayed in real-time on the vessel's terminal, enabling accurate positioning of the mud-pusher.

A schematic diagram of the USBL system components and their relative positions is shown in Fig. 6.

Fig. 6. Display interface of the USBL positioning system. (The label 'Ship1' indicates the transducer position, while the yellow markers represent transponder locations)

However, when using the USBL system, signal instability occurred due to interference from the hull of the support vessel, De Fu 3, which was grounded on the seabed. To resolve this issue, a novel positioning method leveraging the crane's radius and slew angle was developed, capitalizing on the fixed position of the grounded vessel. The procedure was as follows: After the vessel was grounded, the precise coordinates of the crane's center of rotation were determined using the vessel's positioning system and remained fixed. The required crane radius and slew angle to lower the mud-pusher to its target location were then calculated based on the geometric relationship between this fixed point and the pre-designed deployment position. The mud-pusher was subsequently deployed using these parameters. A limitation of this method is that its accuracy is affected by errors in the vessel's positioning system and in the measurement of the crane radius and slew angle. Therefore, it was advisable to perform iterative adjustments and verification against other reference data during operation.

3.2 Efficiency of the Attack of Wire Hole Operation

The significant subsidence of the hull section, combined with the hard gravel-sand seabed substrate, presented major challenges for the process of drilling messenger holes. Data compiled from drilling the six wire hole in the bow section and the eight wire hole in the stern section showed that the drilling time per wire hole ranged from 3 to 5 h, and the retrieval time ranged from 1 to 2 h. Including the time for handling and positioning the mud-pusher, the complete cycle for a single wire hole averaged approximately 7 h.

4 Lifting Force Calculation

Compared to the bow section, the stern section presented greater challenges for estimating the required lifting force due to its more complex internal compartmentation and uncertain underwater condition. Therefore, the stern section is used as the primary example for the lifting force analysis. The wreck's lifting weight primarily comprises its lightship weight, the weight of residual oil, water, and silt onboard, and the additional weight of the superstructure [8].

4.1 Lightship Weight

The lightship weight of the stern section was primarily determined from the weight and center of gravity distribution table (see in Fig. 7) in the wreck's loading manual. This table provides the weight of each small segment along the vessel's length. Based on this data, combined with the known length and position of the stern section, the total weight and center of gravity for the section were calculated by summing the contributions of the relevant segments. The calculated lightship weight was approximately 1,983 t, with the center of gravity located 23.5 m forward of the stern tube.

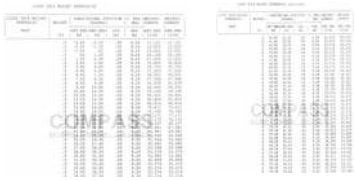

(a) (b)

Fig. 7. Weight and center of gravity distribution table for the stern section of the wreck.

4.2 Weight of Residual Fluids and Silt

The calculation process began by obtaining the location and dimensions of each compartment from the tank capacity diagram. The tank capacity table was then used to determine the volume of residual water or oil based on the fluid height in each compartment. Knowing these fluid heights allows for the calculation of the corresponding weights. The primary challenge, however, lies in estimating the actual fluid height in each compartment, which depends on the effectiveness of the dewatering operation. This requires a detailed analysis to classify compartments based on drain efficiency: those that can be completely emptied, those that will retain a certain residual amount, and those that are difficult to drain (e.g., small or remotely located compartments) and must therefore be assigned a higher estimated volume.

Following the above principles and considering practical construction feasibility, the residual volume for each compartment was analyzed as shown in the Table 1. The calculated weight of the residual water in the stern section was approximately793 t.

The silt load consisted of two components: (1) silt accumulated within flooded and breached compartments, and (2) silt adhered to the hull surface in contact with the seabed. The volume was estimated primarily based on diver inspections and empirical judgment. Using data on the estimated volume and density of the sediment, the total silt weight was calculated to be approximately 130 t. Additionally, the stern section included the superstructure accommodation. Compared to the lightship weight, this area contained various furnishings which absorbed significant amounts of water (e.g., wooden furniture, quilts), leading to a substantial weight increase. Furthermore, given the numerous compartments in the accommodation area and the impracticality of complete dewatering, the additional weight attributed to the superstructure was estimated to be 190 t. Finally, the total weight of the lifting rigging was approximately 105 t.

4.3 Lifting Force Analysis and Hook Configuration

Based on the weight components analyzed above, the total calculated weight of the stern section for lifting was approximately $1{,}983 + 793 + 130 + 190 + 105 = 3{,}201$ t. Applying a dynamic load factor of 1.1 resulted in a required total lifting force of about 3,521 t. To meet this demand, the salvage plan utilized the 3,600-t capacity crane vessel De Fu 3600 and the 1,700-t capacity crane vessel De Ying in a tandem lifting arrangement.

The weight distribution necessitated a detailed analysis to verify the load share borne by each vessel and the force on individual hooks. The forces on the hooks of both

Table 1. Analysis of residual water and oil in compartments of the stern section of Hongpu6.

Category	No.	Compartment Name	Total Capacity (m^3)	Status / Planned Mitigation	Assumed Residual Volume (m^3)	Remarks
Larger Compartments	1	No.1 Fresh Water Tank	78.89	Breach hull or drain to engine room	2	1 m water level assumed
	2	No.2 Fresh Water Tank	55.17	Remove manhole cover and drain to engine room	2	1 m water level assumed
	3	Slop Tank (Port)	288.68	Pump out	22	1 m water level assumed
	4	Slop Tank (Starboard)	288.68	Pump out	22	1 m water level assumed
	5	Aft Peak Ballast Tank (Port)	117.47	Breach outer hull	1.5	1 m water level assumed
	6	Aft Peak Ballast Tank (Starboard)	117.47	Breach outer hull	1.5	1 m water level assumed
	7	Fuel Oil Tank (Port)	188.89	Pump out	16.5	1 m water level assumed
	8	Fuel Oil Tank (Starboard)	192.04	Pump out	18.8	1 m water level assumed
	9	No.5 Ballast Tank (Port)	386	Breached	34.6	0.5 m water level assumed
	10	No.5 Ballast Tank (Starboard)	386	Breached	34.6	0.5 m water level assumed
	11	No.6 Ballast Tank (Port)	106.77	Breached	39.5	0.5 m water level assumed

(*continued*)

Table 1. (*continued*)

Category	No.	Compartment Name	Total Capacity (m^3)	Status / Planned Mitigation	Assumed Residual Volume (m^3)	Remarks
	12	No.6 Ballast Tank (Starboard)	126.27	Breached	46.7	0.5 m water level assumed
Small Engine Room Tanks	13	Boiler Feed Water Tank	23.72		23.72	100% volume assumed
	14	Domestic Sewage Overflow Tank	14.8		14.8	100% volume assumed
	15	Stern Tube Cooling Water Tank	8.47		8.47	100% volume assumed
	16	Diesel Oil Tank (Port)	28.71		28.71	100% volume assumed
	17	Diesel Oil Tank (Starboard)	28.46		28.46	100% volume assumed
	18	Diesel Oil Settling Tank	14.7		14.7	100% volume assumed
	19	No.1 Diesel Oil Daily Tank	8.52		8.52	100% volume assumed
	20	No.2 Diesel Oil Daily Tank	7.71		7.71	100% volume assumed
	21	Fuel Oil Settling Tank	45.35		45.35	100% volume assumed
	22	Fuel Oil Drain Tank	4.62		4.62	100% volume assumed
	23	No.1 Fuel Oil Daily Tank	13.88		13.88	100% volume assumed

(*continued*)

Table 1. (*continued*)

Category	No.	Compartment Name	Total Capacity (m^3)	Status / Planned Mitigation	Assumed Residual Volume (m^3)	Remarks
	24	No.2 Fuel Oil Daily Tank	13.88		13.88	100% volume assumed
	25	Fuel Oil Overflow Tank	10.47		10.47	100% volume assumed
	26	Main Engine Lube Oil Storage Tank	11.05		11.05	100% volume assumed
	27	Stern Tube Lube Oil Tank	1.64		1.64	100% volume assumed
	28	Main Engine Lube Oil Circulating Tank	4.39		4.39	100% volume assumed
	29	Lube Oil Sludge Tank	3.57		3.57	100% volume assumed
	30	Main Engine Lube Oil Settling Tank	8.67		8.67	100% volume assumed
	31	Waste Lube Oil Tank	9.11		9.11	100% volume assumed
	32	Thermal Oil Storage Tank	5.88		5.88	100% volume assumed
	33	Thermal Oil Collecting Tank (Port)	5.25		5.25	100% volume assumed
	34	Thermal Oil Collecting Tank (Starboard)	5.25		5.25	100% volume assumed

(*continued*)

Table 1. (*continued*)

Category	No.	Compartment Name	Total Capacity (m^3)	Status / Planned Mitigation	Assumed Residual Volume (m^3)	Remarks
	35	Fuel Oil Sludge Tank	7.76		7.76	100% volume assumed
	36	Bilge Water Tank	10.78		10.78	100% volume assumed
Void Spaces	37	Engine Room	1737		200	Estimated via modeling
	38	Pump Room	203		55	Estimated via modeling
Total					793.3	

Note: For simplified analysis, the residual volume in oil tanks is calculated using the density of water (1 t/m^3).

crane vessels were determined based on the calculated weight, center of gravity of the stern section, and the positions of the underwater lifting wires, applying the principle of moment equilibrium. Due to the large number of hooks involved, the system was statically indeterminate, meaning that the force on each individual hook did not have a unique solution. However, the total load supported by each crane vessel was a determinate value.

To resolve the statically indeterminate problem, a principle of balanced hook loading was adopted. The forces on a subset of hooks were specified, and the remaining hook forces were solved accordingly. The commercial software GHS was employed for verification. The software was used to calculate the weight for a given ballast condition, providing a reference against the theoretical calculations. Furthermore, within the GHS model, the lifting forces from the crane vessels, the superstructure's additional weight, and the silt load were applied as external forces to the wreck model (with the lifting forces defined as negative, indicating an upward direction). The adequacy of the lifting forces was then assessed by evaluating the wreck's stability and final attitude during the lifting simulation [9].

Considering the dynamic load factor and adjustments for the wreck's transverse inclination, the estimated lifting forces for each vessel during the raising operation are shown in the Fig. 8. Specifically, for the De Fu 3600, two of its four hooks bore a load of 700 t each, while the other two bore 600 t each. For the De Ying, all four hooks carried an equal load of 230 t each. Consequently, the total load share was 2,600 t for the De Fu 3600 and 920 t for the De Ying.

The total measured lifting force during the actual raising of the stern section was approximately 3,300 t after the wreck was completely clear of the water. This value

(a) (b)

Fig. 8. Estimated lifting force distribution for (a) De Fu 3600 and (b) De Ying

shows good agreement with the pre-lift estimated weight of 3,201 t, which excluded the dynamic load factor. Given the inherent uncertainties in assessing the wreck's precise underwater attitude, the lifting force analysis inevitably involved estimations, which presented significant challenges. Therefore, the key to accurately calculating the required salvage lifting force lies in a rational and scientific analysis of all weight components, based on the most reliable information regarding the wreck's actual condition and the practical constraints of the field operation.

5 Analysis of Critical Points during the Raising Operation

The stern section of the Hongpu6 was successfully raised and loaded onto the transport barge. However, several critical issues encountered during the lifting process warrant attention for future projects:

(1) Tightening the underwater lifting wires must be completed thoroughly in a single operation after their installation. If any wire is not sufficiently tightened prior to lifting, its deep penetration into the seabed during hoisting will impose a significant additional load on the corresponding hook, adversely affecting the entire operation. Attempting to tighten individual wires separately just before lifting can also lead to subsea entanglement of the wire system.
(2) Ensure the hook connection to the wire ends is correct and allows for smooth load transfer. Proper initial connection is crucial to avoid the need for repeated diver inspections and adjustments.
(3) Adjust the wreck's attitude during lifting based on its hull form to prevent the underwater wires from slipping. Slippage can lead to a redistribution of moments and forces, posing a risk of overloading individual hooks or even one of the crane vessels. For the stern section, which tapers noticeably towards the aft, maintaining a level or bow-down trim would likely cause the wires to slip aft. To mitigate this risk, a deliberate stern-down trim was actively maintained during the operation.
(4) For enhanced anti-slip measures, securely lash the underwater wires to adjacent strong points on the wreck's structure. This secondary securing was implemented in addition to the optimal attitude control.
(5) During the initial break-out phase from the seabed, consider lifting one end or one corner of the wreck first to break the suction force. The successful break-out can be confirmed by monitoring changes in the crane load indicators and observing the plume of air bubbles released at the water's surface [10].

6 Securing the Wreck for Transport

Successfully raising the wreck and positioning it on the transport barge's deck is a major milestone in the salvage operation, which can sometimes lead to less attention being paid to the subsequent task of securing the wreck. To ensure transport safety during the Hongpu6 project, the strength of the securing arrangements was verified according to the relevant standards of the Guidelines for Marine Towage [11].

The verification process was as follows: First, the vessel's GM value (metacentric height) during the tow was determined, either from the transport vessel's loading manual for a typical condition or via stability calculations based on the wreck's loading information. Next, parameters were selected as stipulated by the Guidelines to calculate the transverse and longitudinal sliding forces, as well as the transverse overturning moment, expected to act on the wreck during transport. These values were then compared against the resisting forces and moments provided by the designed securing structures. The number or size of the securing points was optimized as necessary to ensure safety. Although the wreck is an irregular cargo item, introducing some deviation between the theoretical model and the actual forces on the lashings, applying the standardized calculation methodology from the Guidelines significantly enhanced the scientific basis and engineering reliability of the salvage plan.

When designing the location of the securing points, care was taken to weld them to strong structural members on both the wreck and the transport vessel's deck. Welding positions were avoided near the engine room and fuel tank areas. Practical feasibility during implementation was also a key consideration. Additionally, steel plates used in conjunction with sandbags were employed to protect the transport vessel's deck.

7 Conclusion

This paper presented a technical analysis of typical challenges encountered during the integrated wreck removal project of the Hongpu6 Key aspects of the operation were examined:

(1) Ship station location: The design rationale for ship station location was explained, based on the requirements of the attack of wire hole process and the hook configuration of the crane vessels during the lifting phase.
(2) Attack of Wire Hole: The evolution of attack of wire hole technology was reviewed, with a detailed description of the working principles of the China Yantai Salvage's third-generation underwater mud-pusher, the "bathyeel III".
(3) Lifting Force Calculation: A targeted analysis was conducted on the composition of the wreck's lifting weight, the methodology for determining individual weight components, and the configuration of the crane vessels' lifting forces.
(4) Critical Lifting Factors: Key factors influencing the raising operation were identified, and corresponding risk mitigation measures were proposed.
(5) Wreck Securing: The strength of the securing arrangements was calculated in accordance with the Guidelines for Marine Towage, ensuring transport safety through a scientific and precise methodology.

The insights presented herein, derived from practical field experience, provide valuable guidance for future salvage projects and contribute to the enhancement of our professional salvage capabilities.

References

1. Bi, Y.: Optimization on engineering ship positioning process in wind and/or flow J. Navigation of China. **43**(02), 31–34+45 (2020). https://doi.org/10.3969/j.issn.1000-4653.2020.02.006
2. Pan, D., Lin, C., Sun, D., et al.: Research status of shipwreck salvage technology in China C. In Proceedings of the 8th China International Salvage Forum, pp. 160–164. (2014)
3. Wang, Z.: Current development of rescue and salvage equipment J. J. Mech. Eng. **49**(20), 91–100 (2013). https://doi.org/10.3901/JME.2013.20.091
4. Xu, Y.: Applied research and improvement scheme of underwater guided mud-penetrating devices. J. China Water Transport. **11**, 142–146 (2020). https://doi.org/10.13646/j.cnki.42-1395/u.2020.11.054
5. Yan, H., Ge, T., Yang, K., et al.: Research on attitude measuring method of bit in underwater mud-penetrator J. J. Shanghai Jiaotong Univ. **46**(03), 446–450 (2012). https://doi.org/10.16183/j.cnki.jsjtu.2012.03.020
6. Bi, Y., Hu, W., Wang, D.: Technical study on stern section salvage of M/V "Chang Tong" C., 2009. In: Annual Rescue & Salvage Proceedings, pp. 113–121. China Institute of Navigation, Wuhan (2009)
7. Wang, K., Zhou, X., Tang, Q., et al.: Application of underwater navigation and positioning technology in ocean scientific investigation J. Hydrographic Surveying and Charting. **41**(04), 65–69 (2021). https://doi.org/10.3969/j.issn.1671-3044.2021.04.014
8. Gong, Y.: Salvage Engineering M., pp. 103–116. Dalian Maritime University Press, Dalian (2012)
9. Pan, D., Sun, D., Lin, C., et al.: Analysis and computation for salvaging wrecked ship by hoisting machinery J. J. Dalian Maritime Univ. **40**(04), 7–12 (2014). https://doi.org/10.16411/j.cnki.issn1006-7736.2014.04.016
10. JT/T 1536–2024: Safety Code of Practice for Salvage Lifting Operation of Floating Crane. Ministry of Transport of the Peoples Republic of China, p. 5
11. GD 02–2012: Guidelines for Towage at Sea. China Classification Society, pp. 16–18

Optimization Analysis of the Mix Proportion of Semi-Flexible Pavement Grouting Materials Based on the Response Surface Methodology

Yaping Wang[1], Yu Mao[2(✉)], Junjie Lin[3], Haihong Zhang[2], Wenjing Zhang[2], and Xiaopeng Zhang[2]

[1] Gansu Communication Investment Management Co., Ltd., Lanzhou 730030, China
[2] Gansu Provincial Transportation Research Institute Group Co., Ltd., Lanzhou 730030, China
137436909@qq.com
[3] Lanzhou University of Technology School of Civil Engineering, Lanzhou 730050, China

Abstract. The optimized mix design serves as an essential prerequisite for semi-flexible pavements to exhibit outstanding mechanical performance. In this study, the volume method was employed to conduct the optimized mix design of the matrix asphalt mixture. Subsequently, based on the response surface methodology, with the mechanical indices of the grouting material as response variables, the interactive effects between the water-binder ratio and sand-binder ratio were systematically explored, and the mix design optimization of the grouting material was carried out. Additionally, the semi-flexible pavement was fabricated using self-developed grouting equipment. Finally, the rutting test and small beam bending test were utilized to assess its pavement performance. The results demonstrate that the volume method is highly effective. The optimal asphalt-aggregate ratio of the matrix asphalt mixture was determined to be 4.3%, with the porosity and interconnected porosity reaching 26.77 and 24.33 respectively, fully meeting the grouting requirements. By taking the initial fluidity, 30-min fluidity, bleeding rate, 7-day flexural strength, and 7-day compressive strength as response values, the impacts of the water-binder ratio and sand-binder ratio on the mechanical properties of the grouting material were analyzed in detail. It was concluded that the optimal water-binder ratio and sand-binder ratio of the grouting material were 0.46 and 0.15 respectively. The self-developed grouting equipment enabled efficient grouting of the grouting material, achieving a grouting rate of 93%, which complies with the grouting criteria. The pavement structure exhibited excellent high-temperature stability and low-temperature crack resistance, thus fulfilling the application requirements under heavy traffic conditions on typical road sections.

Keywords: Semi-flexible pavement · Response surface method · Grouting material · Volume method · Road performance

1 Introduction

In recent decades, asphalt pavements have faced escalating challenges due to prolonged exposure to harsh environmental conditions and the cumulative effects of heavy traffic loads. Rutting has emerged as a particularly prevalent and persistent issue, especially

© The Author(s), under exclusive license to Springer Nature Switzerland AG 2027
G. Feng et al. (Eds.): ICCE 2025, SUCI, pp. 16–30, 2027.
https://doi.org/10.1007/978-3-032-32237-1_2

in critical road segments such as intersections, extended steep slopes, and dedicated bus lanes [1]. This degradation not only undermines road safety and ride quality but also incurs substantial maintenance costs. Extensive research has demonstrated that semi-flexible pavements represent a highly promising solution to combat rutting. By integrating the flexibility of asphalt with the rigidity of cementitious materials, semi-flexible pavements offer a durable and sustainable alternative for long-term highway infrastructure, thereby playing a pivotal role in facilitating seamless transportation, driving economic progress, and ensuring social stability [2]. Semi-flexible pavements are engineered by injecting a custom-designed rigid cement-based grouting material into the voids of a high-porosity, open-graded flexible asphalt mixture matrix (typically with a void content ranging from 20% to 30%). This unique construction results in a composite material that combines the aesthetic appeal and riding comfort of asphalt with the high-strength and stability characteristics of cement concrete. The resultant pavement exhibits exceptional resistance to rutting and water-induced damage, making it an ideal choice for high-traffic areas [3, 4], its preparation process is shown in Fig. 1.

The structural integrity of semi-flexible pavement materials relies on a complex multi-level, dual-network architecture formed through the intricate interaction between the cementitious matrix of asphalt mortar and the crystalline structure of cement mortar. This intricate microstructure underscores the critical importance of optimizing the mix proportion during the design phase. Currently, the lack of standardized guidelines for semi-flexible pavement mix design means that most researchers adopt methodologies originally developed for open-graded friction courses (OGFC). Additionally, the orthogonal experimental design, a commonly used approach for grouting material mix design, while capable of generating viable results, often requires an extensive number of experimental trials. This limitation not only increases the time and cost of research but also poses significant practical challenges for many researchers [5, 6]. To address these limitations, this study presents a comprehensive approach to mix proportion optimization. It takes into account the profound influence of the matrix asphalt mixture's volumetric properties on asphalt performance, integrating the interlocking mechanism of the primary aggregate skeleton with the filling properties of fine aggregates. By merging these principles, a volume-based design method is employed to optimize the matrix asphalt mixture. Furthermore, to ensure that the grouting material possesses optimal workability and mechanical performance, the response surface methodology (RSM) is applied for mix proportion optimization. Through a series of mechanical property evaluations, this study aims to provide valuable technical insights and practical guidance for the design and construction of semi-flexible pavements.

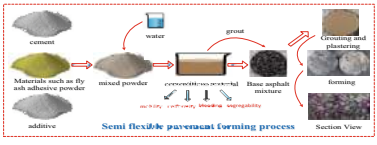

Fig. 1. Preparation process diagram of semi flexible pavement.

2 Material Performance Testing and Specimen Molding Methods

2.1 Selection and Performance Testing of Raw Materials for Matrix Asphalt Mixtures

Asphalt. The matrix asphalt mixture of semi-flexible pavement is a typical open-graded mixture, with the content of coarse aggregates exceeding 70%. Moreover, the skeleton of coarse aggregates lacks the filling of fine aggregates. As a result, ordinary base asphalt has a relatively low viscosity and is difficult to restrict and restrain the coarse aggregate skeleton. Therefore, in this study, SBS modified asphalt with high viscosity is adopted [7]. According to the Test Procedures for Asphalt and Asphalt Mixtures of Highway Engineering (JTG E20–2011), the technical indicators of SBS modified asphalt were tested. The results are shown in Table 1. The results indicate that all indicators of this asphalt meet the requirements of the specifications.

Table 1. Test results of technical indicators for SBS modified asphalt.

Test Parameters		Test results	Technical Requirements
Penetration (25 °C,100 g,5 s)/ 0.1 mm		71	60 ~ 80
Softening Point TR&B/°C		81	≥75
5 °C Ductility,5 cm/min/cm		37	≥35
135 °C Kinematic Viscosity / Pa·s		2.12	1.8 ~ 3
Elastic Recovery (25 °C)/%		95.3	≥85
Solubility/%		99.80	≥99
Flash Point/°C		297.5	≥230
Density (g/cm^3)	15 °C	1.024	/
	25 °C	1.016	/
Storage Stability (Segregation, 48 h Softening Point Difference)/°C		1.5	≤2.5

Aggregates. Both the coarse and fine aggregates are sourced from the stone material factory of Gansu Yuanda Highway Materials Co., Ltd. The main component of the aggregates is tuff. The aggregate has distinct edges and corners, good surface texture, and have excellent adhesion with asphalt. The results of the mechanical index tests indicate that all the indicators meet the requirements of the Test Procedures for Aggregates in Highway Engineering (JTG3432–2024) in China, and the results are shown in Tables 2 and 3.

Table 2. Test results of technical indicators for coarse aggregate.

Test Parameters	Unit	Test results	Technical Requirements
Flat and elongated index content	%	12	≤15
Los Angeles abrasion rate	%	15.9	≤30
Water absorption rate	%	0.55	≤2.0
Crushing Value	%	15.8	≤28
Apparent Relative Density	/	2.98	≥2.5
Soundness	%	11.5	≤12

Table 3. Test results of technical indicators for fine aggregate.

Test Parameters	Unit	Test results	Technical Requirements
Apparent relative density	/	2.93	>2.5
Soundness	%	8.6	≤12
Clay content	%	2.2	≤3
Sand equivalent	%	86.2	≥60

2.2 Selection and Performance Testing of Raw Materials in Grouting Materials

The grouting material for semi-flexible pavements is mainly composed of cementitious binders, fine aggregates, admixtures, and water. To ensure the grouting rate and pavement performance, the grouting material must possess the following properties: (1) Sufficient compressive strength and flexural strength; (2) Good fluidity; (3) Small volume change characteristics; (4) Small dry shrinkage and thermal shrinkage characteristics; (5) Good bonding characteristics with asphalt mixtures [8].

Sand. Sand is an important factor affecting the mechanical properties and grouting effect of the grouting material. When the sand particle size is relatively large, it is likely to cause the blockage of the voids in the matrix asphalt mixture. When the sand particle size is relatively small, the specific surface area increases, leading to an increase in the water consumption, which in turn affects the mechanical properties of the structure. Therefore, in this study, sand with a particle size smaller than 0.6 mm is selected as the research object, and its particle size parameters are shown in Table 4.

Table 4. Grading of sand.

Sieve size/mm	Passing percentage of sieve/%
1.18	100
0.6	100
0.075	≤2

Cement. Cement is an important component of the grouting material. The cement paste solidifies and hardens in the connected voids of the matrix asphalt mixture, transforming from a plastic body into a three-dimensional "condensation-crystallization" network structure of cement stone, thereby ensuring that the structural strength meets the requirements [9]**.** In this study, P.O.42.5 Portland cement is used, and the test results are shown in Table 5. All its indicators meet the requirements of the specifications. In addition, in order to ensure that the grouting characteristics and mechanical strength of the grouting material meet the requirements, fly ash, silica fume, rubber powder, water reducing agent and early strength agent are respectively selected as the admixtures of the grouting material.

Table 5. P.O.42.5 Technical index test results of Portland cement.

Test Parameters	Apparent Density/(g·cm^{-3})	Standard Consistency/%	Initial Setting Time/min	Final Setting Time/min	Soundness
Test results	3.095	28	190	372	Qualified
Technical Requirements	/	/	≥400	≤600	/

2.3 Test Method

Mix Proportion Design of Matrix Asphalt Mixture. In this study, the volume method is adopted for mix proportion design based on the ion interference theory. The calculation is as follows [10]:

$$V_{VC} = \left(1 - \frac{\rho_{sc}}{\rho_{tc}}\right) \times 100 \tag{1}$$

$$q_c + q_f + q_p = 100\% \tag{2}$$

$$\frac{q_c}{100\rho_{sc}}(V_{VC} - V_{VS}) = \frac{q_f}{\rho_{tf}} + \frac{q_\rho}{\rho_{tp}} + \frac{q_a}{\rho_a} \tag{3}$$

In the formula, V_{VC} (%) is the void ratio of the main aggregate; V_{VS} (%) is the percentage of the designed porosity of the asphalt mixture; ρ_{sc} (g/cm^3) is the compacted

density of the main aggregate; ρ_{tc} (g/cm^3)is the apparent density of the main aggregate; q_c (%) is the mass percentage of the coarse aggregate; q_f (%) is the mass percentage of the fine aggregate; q_p (%) is the mass percentage of the mineral powder; ρ_{tf} (g/cm^3)is the apparent density of the fine aggregate; ρ_{tp} (g/cm^3) is the apparent density of the mineral powder; ρ_a (g/cm^3) is the apparent density of the coarse aggregate.

According to the above method, the mineral aggregate gradation is synthesized and Marshall specimens are formed. Then, the stability and flow value of the specimens are measured. After they meet the requirements, the Cantabro loss test and the Scheiben flow test are respectively adopted to determine the optimal asphalt content [11].

Mix Proportion Design of Grouting Materials. (1) in this study, influencing factors such as the water-binder ratio and sand-binder ratio are fully considered. Taking fluidity, bleeding rate, 7d flexural strength and 7d compressive strength, etc. as the indexes, test measurements are carried out through the factor analysis method. And the response surface method is used to compare and analyze the test results respectively, so as to screen out the optimal water-binder ratio and sand-binder ratio under the coupled action of multiple factors.

(2) On the basis of the above research, fly ash, silica fume, rubber powder and early strength agent are respectively used as admixtures to optimize the performance of the grouting materials. With fluidity, bleeding rate, 7d flexural strength and 7d compressive strength, etc. as the evaluation indexes, test analysis is carried out to determine the optimal dosage of the admixtures. In addition, in order to reduce the influence of the hydration heat of the grouting materials, an appropriate amount of water reducing agent is added, and the optimal dosage of it is determined according to the performance test results of the grouting materials.

Specimen Molding. (1) According to the Test Procedures for Asphalt and Asphalt Mixtures in Highway Engineering (JTG E20—2011) in China, standard Marshall specimens and rutting specimens are prepared in accordance with the mix proportion design results of the matrix asphalt mixture. After demoulding, the specimens are placed at room temperature for future use [12]**.**

(2) After demoulding, the specimens were carefully retrieved. Their lateral surfaces and bottoms were sealed with waterproof adhesive tape. Subsequently, the specimens were horizontally positioned on the platform of a self-developed grouting apparatus, as illustrated in Fig. 2. The vibration frequency was set at 50 Hz, with a vibration duration of 5 min. During the vibration process, the grouting material was prepared according to the mix-proportion design results obtained in this study. The prepared grouting material was then poured onto the upper surfaces of the asphalt mixture specimens. The grouting process was deemed complete when no more bubbles emerged from the surface slurry and the bottom of the specimens was fully grouted. Finally, a spatula was employed to level the surface until the aggregate surface was exposed, as shown in Fig. 3.

(3) Place the specimens in a curing chamber with a temperature of 20 °C ± 3 °C and a humidity greater than 90%. After curing for 7d, take out the specimens, and then measure various mechanical indexes as required.

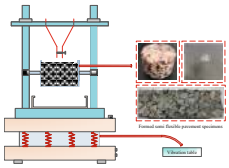

Fig. 2. Experimental diagram of semi flexible pavement grouting material injection molding.

Fig. 3. Semi flexible pavement specimen.

3 Results and Discussion

3.1 Mix Proportion Design Results of Matrix Asphalt Mixture

According to the test method in 1.3, the mix proportion of the matrix asphalt mixture for semi-flexible pavement was designed, and the results are shown in Table 6. Then, various basic indexes of the mixture were tested respectively, and the results are shown in Table 7.

Table 6. Design results of mix proportion for base asphalt mixture.

Type	Aggregate ratio/%				Mineral powder ratio/%	Asphalt-aggregate ratio/%	Wood fibe ratio/%
	10-15 mm	5-10 mm	3-5 mm	0-3 mm			
SFP-13	77	12	2	6	3	4.3	0.3

Table 7. Asphalt mixture testing indicators.

Void ratio/%	Connected void ratio/%	Stability/kN	Bleeding loss/%	Scattering loss/%
26.77	24.33	4.59	0.14	24.77
16–28	15–25	≥3	≤0.5	≤30

From the above mix proportion design results, it can be known that the optimal asphalt-aggregate ratio of this asphalt mixture is 4.3%, and the void ratio and connected void ratio are 26.77 and 24.33 respectively, which meet the grouting requirements. In addition, after measurement, its stability is 4.59 kN, which meets the requirements of the specification. Based on this, it can be considered that the mix proportion design results of the matrix asphalt mixture obtained in this study meet the application requirements.

3.2 Results of the Mix Proportion Design of Grouting Materials

Based on the previous research results, in this study, the range of the water-binder ratio is set as 0.42 to 0.5, and the range of the sand-binder ratio is set as 0.1 to 0.2. Tests are carried out on the initial fluidity, fluidity after 30 min, bleeding rate after 3 h, 7d flexural strength, and 7d compressive strength. The test results are shown in Table 8 below [13].

Table 8. Test results of mechanical indicators of grouting materials.

Water-binder ratio	Sand-binder ratio	Initial fluidity(mm)	30 min fluidity(mm)	Bleeding rate (%)	7d flexural strength (MPa)	7d compressive (MPa)
0.42	0.1	45.18	50.22	0.001	7.95	36.90
0.46	0.15	11.36	16.38	0.008	5.60	35.30
0.42	0.2	38.15	42.55	0.060	7.70	45.83
0.50	0.1	15.36	21.22	0.014	6.20	25.60
0.46	0.15	15.53	20.35	0.001	5.45	30.58
0.46	0.15	11.57	17.43	0.001	4.90	35.90
0.46	0.15	13.32	19.64	0.003	5.83	35.05
0.50	0.2	11.44	17.74	0.024	4.85	34.50
0.40	0.15	60.80	69.96	0.001	7.80	45.40
0.46	0.22	12.18	22.11	0.001	6.00	29.91
0.46	0.08	32.00	39.33	0.017	6.90	32.53
0.46	0.15	10.88	14.58	0.006	4.90	37.00
0.52	0.15	19.78	26.35	0.059	5.36	24.93

$$Y_1 = 1967.97917 - 7870.91263x_1 - 740.02928x_2 + 388.75000x_1x_2 + 8102.89063x_{12} + 1545.85000x_2 \quad (4)$$

$$Y_2 = 2041.41164 - 8188.50579x_1 - 676.24689x_2 + 8508.28125{x_1}^2 + 1958.30000{x_2}^2 \quad (5)$$

$$Y_3 = -0.933697 + 6.35318x_1 - 59.41053x_1x_2 - 9.32340{x_1}^2 + 51.41679{x_2}^2 + 102.74193{x_1}^2x_2 - 112.43597x_1{x_2}^2 \quad (6)$$

$$Y_4 = 101.42115 - 385.18338x_1 - 15.57198x_2 - 137.50000x_1x_2 + 413.75000{x_1}^2 + 238.80000{x_2}^2 \quad (7)$$

$$Y_5 = -1592.67034 + 7131.45657x_1 + 11975.68594x_2 - 50917.56366x_1x_2 - 7858.23728{x_1}^2 - 557.70000{x_2}^2 + 54797.62354{x_1}^2x_2 \quad (8)$$

3.3 Analysis of Variance

Using the response surface method, the test results in Table 8 above are analyzed through Design-Expert. Taking the water-binder ratio (x_1) and the sand-binder ratio (x_2) as the independent variable factors, and taking the initial fluidity (Y_1), the fluidity after 30 min (Y_2), the bleeding rate (Y_3), the 7-day flexural strength (Y_4), and the 7d compressive strength (Y_5) as the response values, the calculation and analysis are carried out. The fitting analysis of variance is shown in Eqs. (4), (5), (6), (7), and (8), and the fitting analysis of variance for the 5 groups is shown in Tables 9 and 10.

In the analysis of variance of the response surface, the P (P-value) and F (F-statistic) values represent the significance of the established model. The larger the F value, the more significant the model. Generally speaking, when the P value is less than 0.05, the model or the corresponding coefficient is usually considered statistically significant. By

analyzing the F value and the P value, the reliability and effectiveness of the response surface model can be determined, as well as the influence degree of each independent variable on the response value. In addition, the P value of the lack-of-fit term reflects the degree of difference between the predicted value and the actual value [13]. From the calculation results in Tables 9 and 10, it can be seen that the F values of Y_1 to Y_5 are all relatively large, indicating that the model as a whole is significant, which shows that the water-binder ratio, the sand-binder ratio are closely related to the values of the initial fluidity, the fluidity after 30 min, the bleeding rate, the 7d flexural strength, and the 7d compressive strength. Moreover, since the P values are all less than 0.005, it further proves the significance of the model. In addition, according to the P values of the lack-of-fit terms, all these values are greater than 0.05, indicating that the lack-of-fit terms are not significant, which reflects that the fitting results of this model are good and there is no obvious lack-of-fit situation.

Table 9. Fit analysis P-value.

	Y_1	Y_2	Y_3	Y_4	Y_5
Model	<0.0001	<0.0001	0.02227	0.0004	0.0020
x_1	<0.0001	<0.0001	0.0030	0.0001	0.0001
x_2	0.0044	0.0173	0.1968	0.0274	0.4349
x_1x_2	0.6557		0.4999	0.1764	0.3980
x_1^2	<0.0001	<0.0001	0.0197	0.0020	0.5168
x_2^2	0.0186	0.0152	0.8027	0.0035	0.1479
$x_1^2x_2$			0.1868		0.0312
$x_1x_2^2$			0.0907		
Lack-of-fit term	0.0615	0.0674	0.0643	0.7411	0.6743

Table 10. Fit analysis of F-value

	Y_1	Y_2	Y_3	Y_4	Y_5
Model	54.38	45.19	7.17	21.42	15.60
x_1	146.93	94.67	29.11	60.55	78.73
x_2	17.02	8.95	2.22	7.71	0.6998
x_1x_2	0.2166		0.5282	2.26	0.8278
x_1^2	104.76	73.21	11.42	22.78	0.4743
x_2^2	9.31	9.47	0.0694	18.53	2.76
$x_1^2x_2$			2.34		7.84
$x_1x_2^2$			4.38		
Lack-of-fit term	5.78	5.31	6.43	0.4332	

3.4 Analysis of Mechanical Properties under the Interaction of x_1 and x_2

Taking the initial fluidity (Y_1), the fluidity after 30 min (Y_2), the bleeding rate (Y_3), the 7-day flexural strength (Y_4), and the 7-day compressive strength (Y_5) as the evaluation indexes, the influence of the water-binder ratio (x_1) and the sand-binder ratio (x_2) on the mechanical properties of the grouting material is explored. The interaction surfaces of the two factors are shown in Figs. 4, 5, 6, 7, and 8.

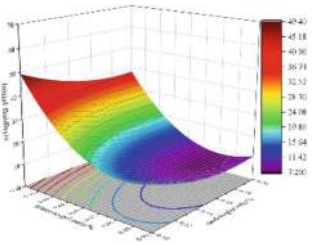

Fig. 4. Relationship diagram between x_1, x_2 and Y_1.

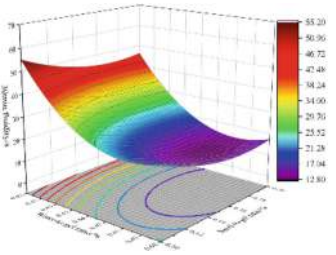

Fig. 5. Relationship diagram between x_1, x_2, and Y_2.

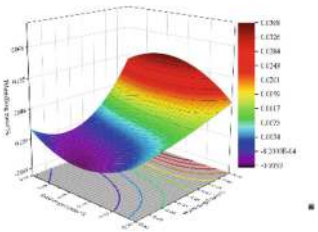

Fig. 6. Relationship diagram between x_1, x_2, and Y_3.

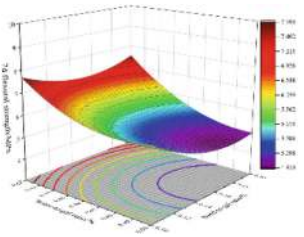

Fig. 7. Relationship diagram between x_1, x_2 and Y_4.

As can be seen from Figs. 4 and 5, both the initial fluidity and the fluidity after 30 min increase with the increase of the water-binder ratio and the sand-binder ratio. In addition, from Fig. 6, it can be known that the bleeding rate increases with the increase of the water-binder ratio; however, it shows a trend of increasing first and then decreasing with the increase of the sand-binder ratio. From Fig. 7, it can be seen that as the water-binder ratio and the sand-binder ratio continue to increase, the 7d flexural strength gradually decreases. From Fig. 8, it can be observed that during the process of the continuous decrease of the water-binder ratio and the continuous increase of the sand-binder ratio, the 7d compressive strength keeps increasing. From the above, it can be concluded that the water-binder ratio and the sand-binder ratio are important factors affecting the various mechanical properties of the grouting material. Therefore, when obtaining the optimal water-binder ratio and sand-binder ratio of the grouting material, the changes in various mechanical properties should be comprehensively considered. In view of this situation,

according to the above analysis results, this study determines the optimal water-binder ratio and sand-binder ratio, and the obtained optimal water-binder ratio and sand-binder ratio are 0.46 and 0.15 respectively.

In order to verify the reliability of the theoretical analysis results, the grouting material was prepared according to the above-mentioned optimal water-binder ratio and sand-binder ratio, and various mechanical indexes of the grouting material were measured respectively. At the same time, a comparative analysis under the same conditions was carried out according to the above-mentioned theoretical analysis method, and the results are shown in Table 11.

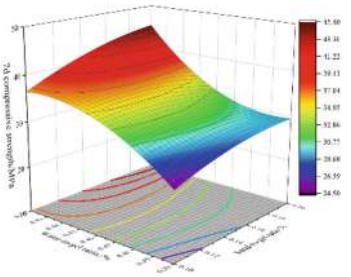

Fig. 8. Relationship diagram between x_1, x_2 and Y_5.

Table 11. Predicted values, actual values, and technical requirements

	Initial fluidity/s	30 min fluidity/s	3 h Bleeding rate/%	7d flexural strength/MPa	7d compressive strength/MPa
Predicted value	12.532	17.676	0.0038	5.366	34.766
Actual value	11.570	17.430	0.0010	4.900	35.900
Technical requirements	10–14	<18	<0.01	≥2	≥15

As can be seen from Table 11, under the same conditions, the predicted values of various mechanical indexes of the grouting material are basically close to the measured values, indicating that the theoretical analysis has a certain degree of reliability. At the same time, it also shows that it is feasible to determine the optimal water-binder ratio and sand-binder ratio of the grouting material by using the response surface method [14].

3.5 Evaluation of Grouting Effect and Pavement Performance

In this study, the grouting material was synthesized in strict accordance with the aforementioned analytical outcomes. Through a series of meticulous experimental investigations, the optimal dosages of fly ash, silica fume, rubber powder, water-reducing agent, and coupling agent were precisely determined to be 9%, 6%, 3%, 0.8%, and 0.2% by mass, respectively. To comprehensively evaluate the workability during construction and

the pavement performance of the developed grouting material, in line with real-world engineering applications, the matrix asphalt mixture was grouted using this custom-formulated material, as vividly illustrated in Fig. 8. Upon completion of the grouting process, the grout infusion rate was carefully measured and analyzed, and the obtained value of 93% indicated full compliance with the established grouting requirements.

To conduct an in-depth assessment of the pavement performance of this novel structural system, a battery of advanced testing procedures was employed. The rutting test, a well-established method for evaluating high-temperature stability, and the small-beam bending test, which is widely recognized for assessing low-temperature crack resistance, were executed with stringent adherence to relevant standards. For a more comprehensive and scientifically robust comparative analysis of its mechanical properties, the AC-16 conventional asphalt mixture was selected as a reference material, and parallel performance tests were carried out under precisely controlled and identical conditions [15–18]. The detailed test results are meticulously presented in Figs. 9 and 10. Additionally, a representative field site was carefully chosen for the construction of a test pavement section. The construction process and its subsequent status are comprehensively documented in Figs. 11 and 12. Post-construction, a series of elaborate mechanical property tests were performed, and the resulting data are illustrated in Figs. 13 and 14.

The test results presented in Figs. 9 and 10 demonstrate that the semi-flexible pavement exhibits satisfactory high-temperature stability and low-temperature crack resistance that meet the specification requirements, with performance values significantly superior to those of conventional asphalt pavement under identical conditions. This indicates excellent pavement performance of this structural system. The superior performance is primarily attributed to the following mechanism: When the grouting material permeates into the matrix asphalt mixture, the hydration and hardening of cementitious components lead to the formation of crystals and cementitious gels. This process creates a three-dimensional lattice framework within the voids. The cohesive force generated by the hardened cement paste synergistically combines with the adhesive properties of the asphalt mixture, forming a robust composite bonding system. Consequently, the semi-flexible pavement develops a dense skeletal structure that delivers outstanding mechanical performance [19, 20].

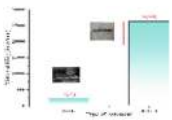

Fig. 9. Results of rutting test.

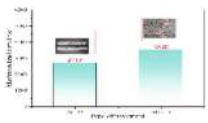

Fig. 10. Small beam bending test results.

According to the test results shown in Figs. 13 and 14, the water stability and mechanical performance of the semi-flexible anti-rutting pavement meet the required standards, with the values significantly higher than those of conventional asphalt pavement. This indicates that the pavement structure exhibits excellent high-temperature stability and deformation resistance, as well as remarkable durability and water stability under freeze-thaw cycles [21, 22]. The primary reasons for these advantages are as follows: After the

Fig. 11. Semi flexible pavement test section paving.

Fig. 12. Extraction of semi flexible pavement core samples.

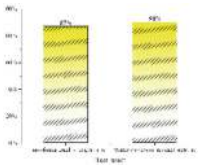

Fig. 13. Results of freeze-thaw splitting strength ratio and immersion residual stability test.

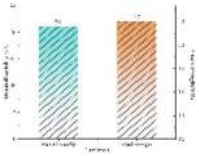

Fig. 14. Marshall stability and splitting strength test results.

cement-based grouting material fills the voids in the matrix asphalt mixture, it gradually undergoes hydration and hardening over time, transforming from a plastic state into a networked structure. This process continuously fills the structural voids, forming a dense structure that prevents water infiltration. Furthermore, the infusion of cement-based grouting material results in partial encapsulation of its particles by asphalt, forming a layer of structural asphalt on the particle surfaces. Consequently, the amount of free asphalt in the mixture is significantly reduced, while the proportion of structural asphalt increases progressively. This enhances the cohesive strength of the semi-flexible pavement material, thereby fundamentally improving its overall strength and water stability [15].

4 Conclusion

(1) The mix proportion of the matrix asphalt mixture for semi-flexible pavement was optimized using the volume method. The optimal asphalt-aggregate ratio of this asphalt mixture was determined to be 4.3%, with a void ratio of 26.77% and a connected void ratio of 24.33%, both of which meet the grouting requirements.
(2) Taking the initial fluidity, 30 min fluidity, bleeding rate, 7d flexural strength, and 7d compressive strength as response values, the response surface method was employed to analyze the influence of the water-binder ratio and sand-binder ratio on the mechanical properties of the grouting material. The optimal water-binder ratio and sand-binder ratio of the grouting material were determined to be 0.46 and 0.15, respectively.
(3) During the formation process of the semi-flexible pavement, the self-developed grouting equipment enabled effective grouting of the grouting material, achieving a grouting rate of 93%, which meets the grouting requirements.

(4) Through mechanical property tests, it was found that the semi-flexible pavement exhibits excellent high-temperature stability and low-temperature crack resistance, meeting the application requirements for heavy-traffic conditions on typical road sections.

Acknowledgements. This study was supported by the Gansu Provincial Department of Transportation Fund Project (2023-25). This study was supported by the Lanzhou Science and Technology Bureau Plan Project (2022-5-47). This study was supported by the Science and Technology Project of Gansu Highway Traffic Construction Group Co., Ltd. (GJJ-ZH-2023-062). We thank LetPub (www.letpub.com) for language assistance in the preparation of this manuscript.

References

1. Editorial Department of China Journal of Highway and Transport: Review on China's pavement engineering research: J. China J. Highw. Transp. **37**(3), 1–81 (2024). https://doi.org/10.19721/j.cnki.1001-7372.2024.03.001
2. Cheng, P.F., Wang, Y.H.L., Li, Y.M., et al.: Study on low temperature performance of semi-flexible pavement materials based on response surface method. J. Functional Materials. **55**(6), 6118–6127 (2024). https://doi.org/10.3969/j.issn.1001-9731.2024.06.015
3. Wang, T., Gao, Y., Zhu, Z.G., Ji, Z.P., et al.: Influence of slope rate on perfusion rate and pavement performance of semi-flexible pavement materials J. J. Shenyang Univ. (Nat. Sci.). **36**(3), 246–254 (2024). https://doi.org/10.16103/j.cnki.21-1583/n.2024.03.002
4. Xiong, Z.J., Gong, M.H., Deng, C., et al.: Influence of different maintenance conditions on performance of semi-flexible pavement materials J. Journal of Highway and Transportation Research and Development. **40**(9), 37–44 (2023). https://doi.org/10.3969/j.issn.1002-0268.2023.09.005
5. Cheng, P.F., Ma, G.T., Zhang, Z.M.: Performance enhancement mechanism of silane coupling agent on semi-flexible pavement material J. J. Chongqing Jiaotong Univ. (Nat. Sci.). **42**(7), 37–44 (2023). https://doi.org/10.3969/j.issn.1674-0696.2023.07.06
6. Wu, Z.G., Dong, H., Wu, B.W., et al.: Effect of geopolymer grouting material on performance of semi-flexible pavement. J. Concrete. **1**, 188–192 (2023)
7. Liu, J.Q., Tian, Q.W., He, Y.Q., et al.: Application of semi-flexible pavements with red mud-based cementitious J. J. China Univ. Min. Technol. (Nat. Sci.). **42**(5), 21–32 (2022)
8. Zheng, X.G., Wu, L.B., Shui, L.L.: Road performance of high performance pouring semi-flexible pavement material J. J. Build. Mater. **26**(6), 638–643+652 (2023). https://doi.org/10.3969/j.issn.1007-9629.2023.06.009
9. Chen, Z.H., Liang, X.Y., Yu, L.B.: Impact analysis of cement mortar admixture on the cracking resistance of semi-flexible pavement J. J. Wuhan Univ. Technol. **44**(6), 32–38 (2022). https://doi.org/10.3963/j.issn.1671-4431.2022.06.006
10. Zhang, H.G., Jiang, Y.W., Chen, J., et al.: Regulation and control of admixtures on working performance of early strength cement based grouting material for semi-flexible pavement J. Bull. Chin. Ceramic Soc. **41**(4), 1308–1317+1335 (2022). https://doi.org/10.16552/j.cnki.issn1001-1625.2022.04.010
11. Shen, W.G., Zheng, X.P., Wang, Q., Xu, J.W., et al.: Service investigation of flexible and semi-flexible road base J. J. Wuhan Univ. Technol. **43**(12), 1–6 (2021). https://doi.org/10.3963/j.issn.1671-4431.2021.12.001

12. Bao, H.M., Tang, M.F., Chi, E.T., et al.: Mix proportion design of geopolymer mortar for semi-flexible pavement J. J. Huaqiao Univ. (Nat. Sci.). **41**(6), 744–751 (2020). https://doi.org/10.11830/ISSN.1000-5013.202004024
13. Imran, M.K., Hartadi, M.S., Bin, M.N., et al.: Irradiated polyethylene terephthalate and fly ash based grouts for semi-flexible pavement: design and optimisation using response surface methodology J. Int. J. Pavement Eng. **23**(8), 2515–2530 (2022). https://doi.org/10.1080/10298436.2020.1861446
14. Yao, Z., Ye, W., Wu, Z.G., et al.: Optimal design of geopolymer grouting material for semi-flexible pavement based on response surface methodology. J. Constr. Building Mater. **306** (2021). https://doi.org/10.1016/j.conbuildmat.2021.124779
15. Khan, I.M., Sutanto, H.M., Napiah, B.M., et al.: Optimization of cementitious grouts for semi-flexible pavement surfaces using response surface methodology J. IOP Conf. Ser. Earth Environ. Sci. **498**(1), 012004 (2020). https://doi.org/10.1088/1755-1315/498/1/012004
16. Tang, M.C.J., Cai, K., Li, R., et al.: Study on the synergistic optimization of mineral admixtures for cementitious grouting materials in semi-flexible pavement J. J. Silicate. **41**(3), 1102–1112 (2022)
17. Gao, X.Y., Liu, L.J., Chen, Z.Q.: Study on the flowability of cementitious grouting materials for semi-flexible pavement J. Highway. **62**(7), 280–285 (2017)
18. Song, Y.Z., Chen, Y.Y., et al.: Design and performance of semi-flexible pavement material mix design. J. Concr. **9**, 124–131 (2019). (in Chinese)
19. Li, Z.H., You, H., Yang, S.Q., et al.: Composite rigid-flexible pavement structure and materials and development trend. J. China Foreign Highway. **44**(2), 27–53 (2024). https://doi.org/10.14048/j.issn.1671-2579.2024.02.004
20. Nouman, M.K., Imran, M.K., Habib, J.K., et al.: Exploring waste marble dust as an additive in cementitious grouts for semi-flexible pavement applications: analysis and optimization using RSM. J. Constr. Building Mater. **411**, 134554 (2024). https://doi.org/10.1016/j.conbuildmat.2023.134554
21. Li, X.J., Yang, X.Y., Cui, C., et al.: Preparation and performance study of semi-flexible pavement modified emulsified asphalt grouting material J. Highway Eng. **49**(6), 127–133 (2024). https://doi.org/10.19782/j.cnki.1674-0610.2024.06.19
22. Yu, J.J., Mi, X.S.: Optimization of semi-flexible pavement cement grouting based on response surface method. J. Constr. Mach. **11**, 93–97 (2021). https://doi.org/10.14189/j.cnki.cm1981.2021.11.013

The Co-application of Nitrogen and Zinc Influenced Maize Yield and Quality on the Sanjiang Plain

Haoyuan Feng[1,2,3], Xinyi Wang[1,2,3], Jianpeng Zhang[1,2,3], Baoguo Zhu[1], Xingjie Zhong[1], Miao Wang[1], and Nannan Wang[1,2,3](✉)

[1] Jiamusi Branch of Heilongjiang Academy of Agricultural Sciences, Jiamusi, China
fhy2375@163.com, wangnannan_1787@163.com
[2] Key Laboratory of Breeding and Cultivation of Main Crops in the Sanjiang Plain, Jiamusi, China
[3] Albic Soil Machinery Improvement Engineering Technology Research Center, Jiamusi, Heilongjiang Province, China

Abstract. A nitrogen and zinc co-application experiment was conducted as a split-plot design in the Sanjiang Plain. Yield, seed starch, seed protein, and seed fat were analyzed. The nitrogen fertilizer application is divided into four levels: 0 kg/ha (N0), 180 kg/ha (N1), 240 kg/ha (N2), and 300 kg/ha (N3). The zinc fertilizer application is classified into four distinct levels: 0 kg/ha (Zn0), 12 kg/ha (Zn1), 15 kg/ha (Zn2), and 18 kg/ha (Zn3). The results indicated that the primary factor, nitrogen, notably increased yield and seed protein, with no substantial effect on seed starch or seed fat. The secondary factor, zinc, increased yield and seed protein, decreased seed starch, and didn't significantly influence seed fat. The interaction of nitrogen and zinc resulted in a significant increase in yield and seed protein, a notable decrease in seed starch, and no significant effect on seed fat. The N3Zn1 treatment yielded the highest at 12,946.71 kg/ha, and the N3Zn2 treatment resulted in the highest seed protein of 8.22%. Therefore, nitrogen-zinc co-application could not only increase maize yield but also increase seed protein content in the Sanjiang Plain.

Keywords: Maize · Nitrogen · Zinc · Co-application · Yield · Seed starch · Seed protein

1 Introduction

As an essential food, forage, and industrial crop, maize (Zea mays L.) plays a critical role in global agricultural development. In 2023, China's maize yield reached 288.84 million tons, representing 41.5% of the total annual cereal yield. The maize sowing area in Heilongjiang Province, China's major grain-producing area, is approximately 6,451.7 thousand hectares, including the Sanjiang Plain [1]. Therefore, it is crucial to increase maize production in the Sanjiang Plain. Zinc is a vital trace element for the growth and development of humans, animals, and plants. Insufficient zinc intake can lead to

© The Author(s), under exclusive license to Springer Nature Switzerland AG 2027
G. Feng et al. (Eds.): ICCE 2025, SUCI, pp. 31–43, 2027.
https://doi.org/10.1007/978-3-032-32237-1_3

a blockage in DNA synthesis and a decline in human immunity [2]. Zinc also plays a significant role in the metabolism of carbohydrates, proteins, and auxin in plants [3]. Maize is sensitive to zinc. Zinc deficiency can lead to growth retardation, delays in the maturation period, and other issues that result in reduced maize yield [4]. Applying zinc fertilizer through foliar or soil methods can significantly enhance maize growth and improve seed quality. For instance, early-stage soil zinc application increased maize seedling height by 7% to 41% across various soil types [5]. Zhang et al.'s research indicated that maize plants treated with foliar zinc application exhibited higher zinc levels in seeds across different maize varieties than the control group [6].

Nitrogen is an essential element for plant growth and development. Nitrogen is the most vital structural component for plants and the most active substance in physiological metabolism, serving as the principal constituent of enzymes [7]. Studies have shown that nitrogen can enhance zinc's efficacy, increasing zinc absorption and transport to the seed [8]. Zinc application can also improve Nitrogen absorption and utilization by promoting Nitrogen metabolism [9]. Mahadev et al. reported that the combined application of nitrogen and zinc sulfate resulted in the highest recorded plant height of 182.4 cm and the maximum plant dry weight of 98.81 g in maize grown in sandy loam [10]. Aher et al. reported that the cob length in the Nitrogen-zinc co-application treatment exceeded that of the control by a range of 18.4% to 85.7%, while the yield was noted to be 1.4% to 50.4% higher than that of the control [11].

Numerous studies regarding the co-application of nitrogen and zinc for maize cultivation have focused on growth and yield. However, the effects of nitrogen on starch, protein, and fat in seeds have received comparatively less attention. This article analyzes these elements and makes a preliminary investigation for the maize planting on the Sanjiang Plain.

2 Materials and Experimental Methodology

2.1 Experimental Site Condition

The experimental site is located within the agricultural land of the Jiamusi Branch of the Heilongjiang Academy of Agricultural Sciences, China (46°47′29.9328"N, 130° 24 ′ 29.5056″E), in the inner area of the Sanjiang Plain. The climate classification is categorized as a medium-temperate continental monsoon climate. The mean annual temperature is 3 °C, and the average yearly precipitation is 527 mm, with an extended winter and a brief summer. Rainfall occurs in conjunction with heat during the summer months. The experimental block's fundamental physical and chemical properties are as follows: pH 6.35, alkaline Nitrogen 125.60 mg/kg, available phosphate 76.43 mg/kg, rapidly available potassium 182.46 mg/kg, and soil organic matter 24.2 g/kg.

2.2 Experiment Design

A split-plot design is employed for the experiment with three repetitions. The primary factor is nitrogen, while the secondary factor is zinc. Urea is utilized as the topdressing nitrogen fertilizer, while zinc sulfate (ZnSO4) is used as the zinc fertilizer.

The nitrogen fertilizer application is divided into four levels: 0 kg/ha (N0), 180 kg/ha (N1), 240 kg/ha (N2), and 300 kg/ha (N3). Similarly, the zinc fertilizer application is classified into four levels: 0 kg/ha (Zn0), 12 kg/ha (Zn1), 15 kg/ha (Zn2), and 18 kg/ha (Zn3). The total number of treatment blocks is 48, with each individual block measuring 5 m in length and about 2.72 m in width (4 ridges). Nitrogen and zinc are scheduled to be applied at half the amount in the jointing and tasseling stages. Zinc sulfate (ZnSO4) is uniformly mixed into fine soil and scattered across the ridges. According to the specified nitrogen for soil testing formula, the recommended fertilizers are diammonium phosphate (125 kg/ha), urea (50 kg/ha), and potassium chloride (60 kg/ha). The maize variety for the experiment is Heyu236.

The experiment was conducted in 2024. Maize was sown on April 27, 2024, and harvested on October 8, 2024. Each experimental block sampled ten successive cobs from the middle two ridges (20 cobs). The cobs near the walkway were not considered due to superior ventilation and illumination. Following the harvest, the yield composition was measured. The starch, protein, and fat data from the seeds were collected by the DA7200 Near Infrared Spectroscope (Perten).

2.3 Data Analysis

The experimental data were analyzed using Excel 2016 and R version 4.4.0 for statistical computation. The least significant difference (LSD) method ($\alpha = 0.05$) was used to conduct multiple comparisons.

3 Yield Results

3.1 The Two-Factor ANOVA Results for the Yield

The yield is analyzed utilizing the two-factor ANOVA with the split-plot design. According to the two-factor ANOVA, the data are divided into two parts: the primary and secondary plots. The primary plot includes the primary factor, nitrogen. The secondary plot involves the secondary factor, zinc, and the interaction of the primary factor and the secondary factor. The F values for these three items are supposed to be calculated and compared with the standard values at the specified degrees of freedom. The result shows that the F-value for nitrogen, the primary factor, is 73.96, exceeding the F0.01 value of 9.78, indicating that Nitrogen has a highly significant impact on maize yield. The F-value for zinc, the secondary factor, is 10.59, exceeding the F0.01 value of 4.72, indicating that zinc exerts a highly significant influence on maize yield. The F-value for the interaction of nitrogen and zinc is 10.64, surpassing the F0.01 value of 3.26, indicating that this interaction significantly influences maize yield in Table 1.

Table 1. Multiple comparisons of yield, seed protein, and seed starch across various treatments

Treatment	Yield(kg/ha)	Seed starch (%)	Seed Protein (%)
N3Zn3	12791.63 ± 362.84a	73.16 ± 1.40ab	7.94 ± 0.01ab
N3Zn2	12454.12 ± 372.82a	71.87 ± 0.77b	8.22 ± 0.23a
N3Zn1	12946.94 ± 222.71a	73.03 ± 1.26ab	7.96 ± 0.08ab
N3Zn0	11397.93 ± 253.72b	74.57 ± 0.39ab	7.76 ± 0.03b
N2Zn3	11475.52 ± 314.39b	73.51 ± 0.66ab	7.86 ± 0.03b
N2Zn2	12483.93 ± 800.15ab	71.92 ± 1.23b	7.67 ± 0.07b
N2Zn1	12195.40 ± 452.66ab	73.71 ± 0.38ab	7.74 ± 0.10b
N2Zn0	11756.77 ± 525.99b	73.31 ± 0.56ab	7.68 ± 0.20b
N1Zn3	12297.83 ± 389.75ab	73.97 ± 0.83ab	7.71 ± 0.22ab
N1Zn2	11652.06 ± 230.64b	72.51 ± 1.21b	7.90 ± 0.30ab
N1Zn1	12118.42 ± 161.99b	74.21 ± 0.54ab	7.96 ± 0.19ab
N1Zn0	11669.73 ± 171.03b	73.74 ± 0.18ab	7.59 ± 0.05b
N0Zn3	11222.73 ± 368.65bc	73.54 ± 0.47ab	6.90 ± 0.16c
N0Zn2	10571.33 ± 441.35c	75.08 ± 0.69a	6.78 ± 0.08c
N0Zn1	8419.91 ± 712.23d	74.85 ± 0.59a	6.46 ± 0.10d
N0Zn0	8479.39 ± 414.82d	74.32 ± 0.11ab	6.57 ± 0.03d

3.2 Multiple Comparisons of Nitrogen on the Yield

The multiple comparisons of the primary factor, nitrogen, are shown in Fig. 1. It is observed that maize yields increase as the amount of nitrogen fertilizer applied rises. The N3 treatments achieve the highest average yield of 12,397.65 kg/ha. The N0 treatments have the lowest average yield at 9,673.34 kg/ha. There is no significant difference ($p < 0.05$) among the yields of the N1, N2, and N3 treatments; however, all these yields are significantly higher than that of N0.

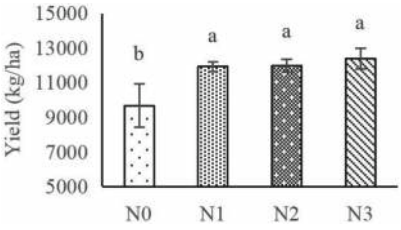

Fig. 1. Multiple comparisons of nitrogen's effect on yield

3.3 Multiple Comparisons of Zinc on the Yield

The multiple comparisons of the secondary factor, zinc, are shown in Fig. 2. Likewise, maize yields increase with the amount of zinc fertilizer applied. No significant difference ($p < 0.05$) is found between the yields of the Zn3 and Zn2 treatments. The yield of Zn2 treatment is markedly superior ($p < 0.05$) to that of N1. The yield of Zn1 treatment is markedly superior ($p < 0.05$) to that of N0. Zn3 treatment achieves the highest yield of 11,946.93 kg/ha, while Zn0 treatments yield the lowest amount, at 10,811.09 kg/ha.

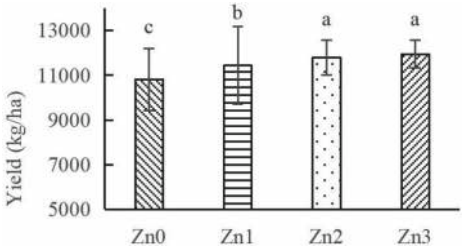

Fig. 2. Multiple comparisons of zinc's effect on yield.

3.4 Multiple Comparisons on the Yield across Various Zinc Levels within the Same Nitrogen Level

The yield' s multiple comparisons across varying levels of secondary factor (zinc) within the same primary factor (nitrogen) are demonstrated in Table 2. Yields increase significantly with zinc without nitrogen fertilizer application (N0). Applying a low level of zinc (Zn1) does not affect yield significantly ($p < 0.05$) compared to not applying zinc (Zn0) when nitrogen fertilizer is not used (N0). No significant difference ($p < 0.05$) is observed among the various zinc application treatments when compared to the N1 treatment. Yields initially increase with zinc application but then decrease under N2 treatment. The highest zinc application (Zn3) receives the lowest yield in this situation. The yields associated with zinc application (including Zn1, Zn2, and Zn3) are significantly higher ($p < 0.05$) than those without zinc application (Zn0) under the N3 treatment. Nevertheless, no significant differences ($p < 0.05$) are identified among the Zn1, Zn2, and Zn3 treatments within this context.

Table 2. Multiple comparisons on the yield across different zinc levels within the same nitrogen level

N0		N1			
Zn	Yield (kg/ha)	Significance 0.05	Zn	Yield (kg/ha)	Significance 0.05
Zn3	11222.73	a	Zn3	12297.83	a
Zn2	10571.33	a	Zn1	12118.42	a
Zn1	8479.39	b	Zn0	11669.73	a
Zn0	8419.91	b	Zn2	11652.06	a
N2		N3			
Zn	Yield (kg/ha)	Significance 0.05	Zn	Yield (kg/ha)	Significance 0.05
Zn2	12483.93	a	Zn1	12946.94	a
Zn1	12195.40	a	Zn3	12791.63	a
Zn0	11756.77	ab	Zn2	12454.12	a
Zn3	11475.52	b	Zn0	11397.93	b

3.5 Multiple Comparisons on the Yield across Various Treatments

Table 1 presents the results of multiple comparisons on yield across various treatments. It is observed that the N3Zn1 treatment yields the highest at 12,946.71 kg/ha, which is 52.7% higher than that of the N0Zn0 treatment. The highest nitrogen and zinc applications (the N3Zn3 treatment) do not yield the highest results. No significant differences are found among the mid-nitrogen (N2Zn0, N2Zn1, N2Zn2, and N2Zn3) and the low-nitrogen treatment group (N1Zn0, N1Zn1, N1Zn2, and N1Zn3). Applying higher zinc levels alone (N0Zn2 and N0Zn3) can significantly increase yield ($p < 0.05$).

4 Seed Starch Results

4.1 The Two-Factor ANOVA Results on the Seed Starch

The starch is analyzed using the two-factor ANOVA with the split-plot design. The result shows that the F-value for nitrogen, the primary factor, is 2.26, which is lower than the F0.05 value of 4.67, indicating that nitrogen does not have a significant impact on seed starch. The F-value for zinc, the secondary factor, is 4.67, greater than the F0.05 value of 3.01, indicating that zinc significantly influences seed starch. The F value for the interaction of nitrogen and zinc is 2.51, surpassing the F0.05 value of 2.30, indicating that this interaction significantly influences seed starch. According to the ANOVA results on the seed starch, multiple comparisons of nitrogen would not be debated.

4.2 Multiple Comparisons of Zinc on the Seed Starch

Figure 3 shows the multiple comparisons of zinc on seed starch. It is noted that seed starch does not increase with zinc application. Low zinc applications (Zn0 and Zn1) yield a significantly higher seed starch than high zinc applications. (Zn2 and Zn3).

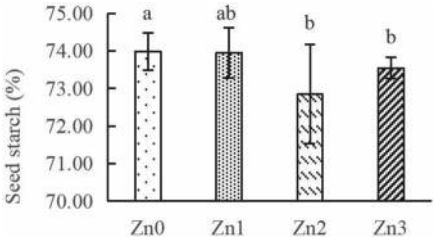

Fig. 3. Multiple comparisons of zinc for seed starch.

4.3 Multiple Comparisons on the Seed Starch across Various Zinc Levels within the Same Nitrogen Level

Table 3 presents the multiple comparisons on seed starch across various zinc levels within the same nitrogen level. Both the highest (Zn3) and the lowest (Zn0) zinc applications result in significantly lower ($p < 0.05$) starch without nitrogen application (N0). Zn1 and Zn3 treatments show significantly higher starch levels ($p < 0.05$), while Zn2 exhibits the lowest levels ($p < 0.05$) under the N1 and N2 conditions. Zn0 and Zn3 treatments yield higher starch than the other two treatments under the N3 condition.

Table 3. Multiple comparisons on the seed starch across various zinc levels within the same nitrogen level

N0			N1		
Zn	Starch (%)	Significance 0.05	Zn	Starch (%)	Significance 0.05
Zn2	75.08	a	Zn1	74.21	a
Zn1	74.85	ab	Zn3	73.97	a
Zn0	74.32	b	Zn0	73.74	ab
Zn3	73.54	b	Zn2	72.51	b
N2			N3		
Zn	Starch (%)	Significance 0.05	Zn	Starch (%)	Significance 0.05
Zn1	73.71	a	Zn0	74.57	a
Zn3	73.51	a	Zn3	73.16	ab
Zn0	73.31	a	Zn1	73.03	b
Zn2	71.91	b	Zn2	71.87	b

5 Seed Protein Results

5.1 The Two-Factor ANOVA Results on the Seed Protein

Seed protein is analyzed using the two-factor ANOVA with the split-plot design. The result shows that the F value for nitrogen, the primary factor, is 95.49, which is higher than the F0.01 value of 9.78, indicating that nitrogen has a highly significant impact on seed protein nitrogen. The F-value for the zinc, secondary factor, is 5.13, greater than the F0.01 value of 4.72, indicating that zinc exerts a highly significant influence on seed protein nitrogen. The F value for the interaction of nitrogen and zinc is 2.46, surpassing the F0.05 value of 2.30, which shows that the interaction of nitrogen and zinc also significantly influences the seed protein nitrogen.

5.2 Multiple Comparisons of Nitrogen on the Seed Protein

Figure 4 illustrates the multiple comparisons of seed protein nitrogen of the primary factor, nitrogen. It is observed that the seed protein nitrogen significantly increases ($p < 0.05$) with the application of nitrogen fertilizer. No nitrogen application (N0) results in the lowest seed protein nitrogen content. No significant difference ($p < 0.05$) is found between the N1 and N2 treatments. The N3 treatment shows the highest seed protein nitrogen.

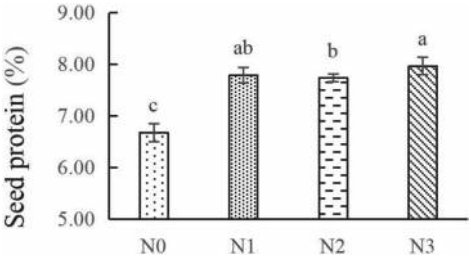

Fig. 4. Multiple comparisons of nitrogen on the seed protein

5.3 Multiple Comparisons of Zinc on the Seed Protein

Figure 5 illustrates the multiple comparisons of the seed protein nitrogen for the secondary factor, zinc. It is noted that seed protein nitrogen significantly increases ($p < 0.05$) with zinc supplementation. No zinc application (N0) results in lower seed protein nitrogen levels compared to other treatments. No significant difference ($p < 0.05$) is found among the Zn1, Zn2, and Zn3 treatments.

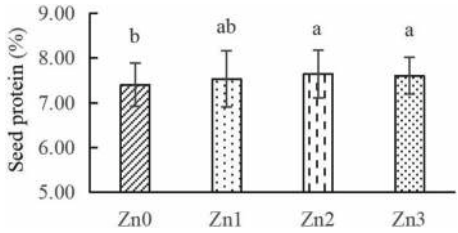

Fig. 5. Multiple comparisons of zinc on the seed protein.

5.4 Multiple Comparisons on the Seed Protein Nitrogen across Various Zinc Levels within the Same Nitrogen Level.

Table 4 shows multiple comparisons of seed protein nitrogen across different secondary factor levels of zinc within the same primary factor, nitrogen. Higher zinc application (Zn3 and Zn2) results in higher protein nitrogen compared to no nitrogen application (N0). The seed protein nitrogen of zinc-treated groups (Zn1, Zn2, and Zn3) is all significantly higher than that of the no zinc treatment (Zn0) under N1 conditions. However, there are no significant differences among these three zinc treatments (Zn1, Zn2, and Zn3). No significant differences ($p < 0.05$) are found among zinc application treatments under N2 conditions. The seed protein nitrogen of Zn2 is significantly higher ($p < 0.05$) than Zn0 under N3 treatment, but there are no significant differences ($p < 0.05$) among Zn1, Zn2, and Zn3.

Table 4. Multiple comparisons of nitrogen on the seed protein across various zinc levels within the same nitrogen level

N0			N1		
Zn	Protein (%)	Significance 0.05	Zn	Protein (%)	Significance 0.05
Zn3	6.9	a	Zn1	7.96	a
Zn2	6.78	ab	Zn2	7.9	a
Zn0	6.57	b	Zn3	7.71	ab
Zn1	6.46	b	Zn0	7.59	b
N2			N3		
Zn	Protein (%)	Significance 0.05	Zn	Protein (%)	Significance 0.05
Zn3	7.86	a	Zn2	8.22	a
Zn1	7.74	a	Zn1	7.96	ab
Zn0	7.68	a	Zn3	7.94	ab
Zn2	7.67	a	Zn0	7.76	b

5.5 Multiple Comparisons on the Seed Protein across Various Treatments

Table 1 presents the multiple comparisons of seed protein across various treatments. N3Zn2 treatment yields the highest seed protein content of 8.22%, which is 25.1% higher than the lowest treatment, N0Zn0. No significant differences are observed among the mid-nitrogen treatment group (N2Zn0, N2Zn1, N2Zn2, and N2Zn3) and the low-nitrogen treatment group (N1Zn0, N1Zn1, N1Zn2, and N1Zn3). Zinc can significantly increase seed protein when nitrogen is not applied.

6 Seed Fat Results

The nitrogen of fat is analyzed using a two-factor ANOVA with a split-plot design. The results indicate that the F-value for nitrogen, the primary factor, is 2.67, which is below the F0.05 value of 4.67, suggesting that nitrogen does not have a statistically significant impact on the seed fat nitrogen. Similarly, the F-value for zinc, the secondary factor, is 0.31, also lower than the F0.05 value of 3.01, indicating that zinc does not exert a statistically significant influence on seed fat nitrogen. Furthermore, the F-value for the interaction of nitrogen and zinc is 0.97, which is below the F0.05 value of 2.30, demonstrating that the interaction of nitrogen and zinc does not significantly affect the seed fat nitrogen. According to the ANOVA results for seed fat, the multiple comparisons would not be implemented.

7 Discussion

7.1 Yield

The co-application of nitrogen and zinc could raise maize yield. In this study, the yields of N3Zn3, N3Zn2, and N3Zn1 were significantly higher than that of N3Zn0, the treatment without zinc application, indicating that the co-application of nitrogen and zinc resulted in a better yield than nitrogen application alone. This outcome aligned with Song's findings [12].

Nitrogen plays a vital role in plant growth. As a key component of proteins, nitrogen application enhances plant development. In this study, maize yield increased significantly with nitrogen addition, consistent with previous findings [13, 14]. However, there was no significant difference in yields between the N2 and N3 treatments. The possible reason is that the nitrogen application in the N2 treatment was already sufficient for maize's requirements, and additional nitrogen would not increase yield.

Zinc is an essential nutrient for crop growth and development. It participates in the metabolism of carbohydrates, proteins, and the growth hormone IAA within plants [15]. The effect of zinc on carbohydrate metabolism primarily results from its influence on photosynthesis. As a C4 plant, maize requires Carbonic Anhydrase (CA), which zinc is a necessary component of [16]. CA catalyzes the conversion of CO2 to HCO- 3, which is ultimately assimilated via NADP-malic enzyme [17]. In this study, maize yield increased with zinc application, especially when nitrogen was not applied (N0). The Zn2 and Zn3 treatments yielded significantly higher yields than the lower zinc treatments (Zn0 and Zn1) under the N0 condition, aligning with the research of Zhang et al. [18]. No significant differences were observed among the Zn1, Zn2, and Zn3 treatments under the N3 condition; however, their yields all surpassed that of Zn0. This situation may be attributed to an ample supply of nitrogen. Abundant nitrogen enhances the utilization efficiency of zinc by synthesizing greater quantities of transfer proteins in the root system.

7.2 Seed Starch

This study indicated that nitrogen application did not significantly affect seed starch content. However, many previous studies have shown that nitrogen application increases maize starch content [19–21]. Starch synthesis involves a series of enzyme-catalyzed reactions, and adequate nitrogen application can enhance starch production. Some studies also reported that low nitrogen application may enhance partial gene expression, thereby increasing starch synthesis [22]. The minimal impact of nitrogen on starch may be due to the soil conditions of the experimental blocks. These blocks are part of a yearly soybean-maize rotation system. The maize for the experiment was cultivated in an area previously cultivated with soybeans, thereby leaving adequate root nodules in the soil. The nitrogen from the root nodules may mitigate the effect of additional nitrogen on seed starch in the experimental treatments.

Research indicates that co-application of nitrogen and zinc can enhance starch accumulation in maize seeds [12]. However, in this study, seed starch content decreased with zinc application, contrary to expectations. Further experiments are necessary to explore the influence of zinc on seed starch to understand the reasons for this decline.

7.3 Seed Protein

Co-application of nitrogen and zinc increased protein content in maize seeds in this study. The protein content of the co-application treatments was significantly higher than that of both single nitrogen and single zinc application treatments. The protein in N3Zn3 was 15.1% higher than in N0Zn3. Similarly, the protein in N3Zn3 was 2.3% higher than in N3Zn0. Zinc is a component of RNA polymerase, involved in protein synthesis, and proteases that influence nitrogen metabolism. Additionally, it is a component of glutamate dehydrogenase, which produces glutamic acid. It is closely connected to plant nitrogen metabolism [8]. Nie et al. also discovered that the co-application of nitrogen and zinc increased the transport of these elements to the seed, thereby enhancing protein synthesis [23].

8 Conclusion

An experiment was conducted to examine the effects of co-applying nitrogen and zinc on maize yields and on seed starch, protein, and fat content. The findings demonstrated that nitrogen, the primary factor, notably enhanced yield and seed protein, with no substantial effect on seed starch or seed fat. The secondary factor, zinc, increased yield and seed protein, reduced seed starch, and had no significant impact on seed fat. Additionally, the interaction of nitrogen and zinc resulted in a significant increase in yield and seed protein, a notable decrease in seed starch, and no significant effect on seed fat. The N3Zn1 treatment yielded the highest at 12,946.71 kg/ha, and the N3Zn2 treatment resulted in the highest seed protein of 8.22%. Therefore, nitrogen-zinc co-application could not only increase maize yield but also increase seed protein content. This is expected to be used as a high-yield and high-quality technology for maize cultivation in the Sanjiang Plain.

Acknowledgments. This work is supported by Research projects of scientific research institutes in Heilongjiang province (CZKYF2024-1-B003, CZKYF2025-1-B009), and Jiamusi City's Municipal Science and Technology Planning Project of Innovation Incentive Category (NY2025JL0021).

References

1. National Bureau of Statistics: China Statistical Yearbook 2023. China Statistics Press, Beijing (2023)
2. Mcclung, J.P.: Iron, zinc, and physical performance. Biol. Trace Elem. Res. **188**(1), 135–139 (2019). https://doi.org/10.1007/s12011-018-1479-7
3. Alloway, B.J.: Zinc in Soils and Crop Nutrition. (2008)
4. Suganya, A., Saravanan, A., Manivannan, N.: Role of zinc nutrition for increasing zinc availability, uptake, yield, and quality of maize (Zea mays L.) grains: an overview. Commun. Soil Sci. Plant Anal. **51**(15), 2001–2021 (2020). https://doi.org/10.1080/00103624.2020.1820030
5. Capo, L., Battisti, M., Blandino, M.: The role of zinc fertilization and its interaction with nitrogen and phosphorus starter fertilization on early maize development and grain yield. Field Crop Res. **307**, 109245 (2024). https://doi.org/10.1016/j.fcr.2023.109245

6. Zhang, P.P., Shao, Y.H., Liu, J.B., et al.: Effect of nitrogen and zinc application on the accumulation and distribution of dry matter and nitrogen and zinc of different summer maize varieties. Acta Agric. Boreali-Sinica. **37**(02), 96–103 (2022). https://doi.org/10.7668/hbnxb.20192579
7. Zhao, P., Sun, G.C., Peng, S.L.: Ecophysiological research on nitrogen nutrition of plant. Ecol. Sci. **17**(02), 37–42 (1998). https://doi.org/CNKI:SUN:STKX.0.1998-02-006
8. Zhao, L.F., Yuan, L., Zhang, S.Q., et al.: Effects of combined application of zinc and nitrogen fertilizers on crop yield, quality and nutrient utilization: a review. Soil Fertil. Sci. China. **6**, 346–352 (2021). https://doi.org/10.11838/sfsc.1673-6257.20507
9. Khan, A.M., Hussain, S., Rengel, Z., et al.: Zinc bioavailability and nitrogen concentration in grains of wheat crop sprayed with zinc sulfate, ammonium sulfate, ammonium chloride, and urea[J]. J. Plant Nutr. **41**(15), 1926–1936 (2018). https://doi.org/10.1080/01904167.2018.1484472
10. Aher, A., Umesha, C.: Effect of nano urea and zinc on growth and yield of baby corn (Zea mays L.) under Prayagraj condition. Int. J. Environ. Clim. Chang. **13**(6), 285–291 (2023). https://doi.org/10.9734/ijecc/2023/v13i61825
11. Mahadev, P.R., Singh, V., George, S.G.: Determining the effect of nitrogen and zinc on growth and yield of maize (Zea mays L.). J. Exp. Agric. Int. **46**(8), 143–147 (2024). https://doi.org/10.9734/jeai/2024/v46i82687
12. Song, X.L.: Effects of Zinc and Nitrogen Interaction on Growth Characteristics, Yield and Quality of Waxy Maize. Shanxi Agric. Univ. (2024)
13. Kang, Y.L., Ma, Z.H., Li, H.Y., et al.: Effect of application of nitrogen and zinc fertilizers on dry material accumulation and yield in maize. Soil Fertil. Sci. China. **01**, 34–38 (2011). https://doi.org/10.3969/j.issn.1673-6257.2011.01.008
14. Tharaka, M., Ravi Chandra, K., Singh, V.: Influence of nitrogen and zinc on growth and yield of baby corn (Zea mays L.). Int. J. Plant Soil Sci. **33**(23), 64–70 (2021). https://doi.org/10.9734/ijpss/2021/v33i2330719
15. Broadley, M.R., White, P.J., Hammond, J.P., et al.: Zinc in plants. New Phytol. **173**(4), 677–702 (2007). https://doi.org/10.1111/j.1469-8137.2007.01996.x
16. Tobin, A.J.: Carbonic anhydrase from parsley leaves. J. Biol. Chem. **245**(10), 2656–2666 (1970). https://doi.org/10.1016/S0021-9258(18)63120-5
17. Hatch, M.D., Burnell, J.N.: Carbonic anhydrase activity in leaves and its role in the first step ofC4 photosynthesis. Plant Physiol. **93**(2), 825–828 (1990). https://doi.org/10.1104/pp.93.2.825
18. Zhang, P.P., Qiao, J.F., Hou, C.W., et al.: Effect of foliar zinc application on the grain yield and quality of different genotypes of summer maize. J. Maize Sci. **33**(02), 94–102 (2025). https://doi.org/10.13597/j.cnki.maize.science.20250211
19. Xu, C.: Effect of Different Nitrogen Application on the Formation of Starch and Yield of Maize with Drip Irrigation and Fertilization Integration. Ningxia University (2018)
20. Liu, W.X.: Effect Mechanism of Reduced Nitrogen Application on Grain Quality of Spring Maize with Different Nitrogen Efficiency. Inner Mongolia Agricultural University (2023)
21. Omar, S., Abd Ghani, R., Khaeim, H., et al.: The effect of nitrogen fertilisation on yield and quality of maize (Zea mays L.). Acta Aliment. **51**(2), 249–258 (2022). https://doi.org/10.1556/066.2022.00022
22. Doehlert, D.C., Duke, E.R., Smith, L.J.: Effect of nitrogen supply on expression of some genes controlling storage proteins and carbohydrate synthesis in cultured maize kernels. Plant Cell Tissue Organ Cult. **47**(2), 195–198 (1997). https://doi.org/10.1007/BF02318958
23. Nie, Z., Wang, J., Rengel, Z., et al.: Effects of nitrogen combined with zinc application on glutamate, glutamine, aspartate and asparagine accumulation in two winter wheat cultivars. Plant Physiol. Biochem. **127**, 485–495 (2018). https://doi.org/10.1016/j.plaphy.2018.04.022

Large-Scale Object Recognition Dataset Construction and Detection Analysis of Construction Scene Based on Video Surveillance

Jun Zhang[1(✉)], Yiming Han[1], Hai Lin[1], Kaite Shi[1], Zhe Li[1], Lizhi Xu[2], Ende Lin[1], and Kaiyuan Zheng[1]

[1] Institute of Science and Technology, China Three Gorges Corporation, Beijing 100038, China
zhang_jun39@ctg.com.cn

[2] School of Mechanical, Electronic and Control Engineering, Beijing Jiaotong University, Beijing 100044, China

Abstract. Construction sites of pumped-storage power stations are characterized by complex environments, diverse object categories, and strong scene dynamics. However, existing construction-related visual datasets generally suffer from limited scale, single-class representation, and insufficient scene diversity, making them inadequate for intelligent construction monitoring and object recognition. To address this, this study proposed a method for constructing large-scale object recognition dataset based on the video surveillance system, and further proposes a multi-object detection method that integrates multi-scale feature modeling with global context awareness. A systematic pipeline involving data collection, filtering, and semi-automatic annotation is established to make full use of the video surveillance system data. Meanwhile, a high-quality dataset covering various construction machinery, workers, and typical working areas is built. Based on the YOLOv8 framework, the proposed method improves feature extraction and multi-scale fusion structures to tackle challenges such as large scale variations, frequent occlusions, and severe background interference, while incorporating a global attention mechanism to enhance modeling of spatial relationships and contextual information among objects. The dataset constructed in this paper covers 21 typical construction scene categories, covering a rich sample distribution under multi-scale, multi-pose, multi-occlusion, and multi-meteorological conditions. Experimental results show that on the self-constructed dataset, the improvements reach 3.20% and 8.19% in mAP@0.5 and mAP@0.5:0.95. The detection algorithm significantly enhances recognition accuracy in complex construction environments. The proposed method can provide feasible data construction technology path and key technical support for intelligent video monitoring, construction behavior analysis and application of visual foundation model in engineering scene.

Keywords: The pumped-storage power station · Large-scale image datasets of construction scenes · Construction scenario multi-object recognition · The improved YOLOv8 model · Intelligent video surveillance system

© The Author(s), under exclusive license to Springer Nature Switzerland AG 2027
G. Feng et al. (Eds.): ICCE 2025, SUCI, pp. 44–63, 2027.
https://doi.org/10.1007/978-3-032-32237-1_4

1 Introduction

To enhance safety management in engineering construction, extensive video surveillance systems have been deployed across hydropower projects, particularly pumped-storage power stations, to enable continuous, efficient monitoring of dispersed and complex work areas. We use many video cameras to watch work areas in hydropower projects. Watching videos by hand is slow and tiring. It also misses some parts. So, we need computers to find important things in videos fast and well. AI and big models help us. Now, good data is very important to make these models work well. We must make data sets faster to use AI in building projects. Object recognition helps us find machines, workers, and if they wear helmets. This helps us warn about dangers. Object detection changed from two-step methods like Faster R-CNN [1], Mask R-CNN [2] to one-step methods like YOLO [3–5]. Now, we use new models like DETR [7], DINO [8]. Big pre-trained models like SwinV2 [9], Florence [10] make these better.

Among these, the YOLO series is widely adopted in industrial settings due to its high efficiency and practicality. Shi Xingyong et al. [11] incorporated the Bidirectional Feature Pyramid Network (BiFPN) and the DIoU loss function into YOLOv3 to improve the accuracy of multi-scale localisation for machinery and personnel. Meanwhile, Wang Renchao et al. [12] constructed the lightweight M1-DSC-YOLOv4 + ECA model by replacing backbone convolutions with Deep Separable Convolutions, achieving real-time detection of roller. Xiang Yuanzhi [13] integrated a RepVGG module and a BiFPN structure with learnable weights into YOLOv5 to enhance robustness against complex backgrounds. Song Xiaogang et al. [14] and Zhang Sherong et al. [15] both significantly improved the detection rate of critical objects, such as workers and concrete mixer, in construction scenarios by adding small object detection layers and introducing attention mechanisms (e.g. ECA and NAM) and optimising loss functions. Chen Yun et al. [16] proposed the YOLOv5-SS algorithm, which integrates CBAM attention with a weighted feature fusion structure to effectively identify slender objects, such as scaffolding and wires. Hu Hao et al. [17] improved the YOLOX-S model by introducing a Large Kernel Attention (LKA) module and an AdamW optimiser to further enhance detection stability in complex working conditions.

Although the aforementioned algorithms have produced results in certain scenarios, they are largely based on general natural image datasets (e.g. COCO, PASCAL VOC). The data distribution, object scale, background texture and other characteristics of these datasets differ significantly from those of real construction environments. When directly transferred to hydropower construction sites characterized by uneven lighting, frequent occlusions, dense targets, and a wide range of scales, issues such as high false negative rates, severe false positives, and insufficient generalization capabilities often arise. This is primarily due to the current lack of large-scale, specialised object recognition datasets tailored for complex construction scenarios to serve as foundational support for model training and evaluation.

Existing construction-related datasets commonly suffer from limitations such as small scale, narrow categorization, and insufficient scene representativeness. For instance, datasets constructed by Humaira T et al. [18] and Xiao B et al. [19] only include 5 to 10 categories of construction machinery, with a total image count under 20,000. Kim H et al. [20] selected construction machinery images from ImageNet, but these

lacked contextual information about construction sites. Roberts D et al. [21] focused on action recognition tasks with limited samples, while Wu et al. [22] and Natha N D et al. [23] primarily addressed safety equipment detection with restricted object coverage. Although some studies have proposed larger datasets, such as the MOCS dataset [24] (with 42,000 images and 13 object categories) and the SODA dataset [25] (with 19,800 images and 15 categories), it is difficult to fully reflect the unique complex construction patterns of pumped-storage power station, such as large-scale machinery clusters operating, frequent occlusions, coexisting near and distant objects, and interactions among multiple equipment types during excavation and filling of the upper and lower basins. Furthermore, existing datasets predominantly rely on drone aerial photography or handheld device capture, with annotation processes that are heavily labour-intensive. This approach is costly, inefficient, and lacks end-to-end automated construction methods tailored for video surveillance systems. Consequently, vast surveillance video resources remain underutilised and are not efficiently converted into high-quality annotated data suitable for deep learning training.

To address the aforementioned challenges, this paper proposes an automated method for constructing large-scale object recognition datasets tailored to construction scenarios of pumped-storage power station, and proposes an improved object detection model for construction scenarios.

2 Dataset Construction Method

2.1 Image Acquisition

Regional Division and Multi-Source Data Strategy. According to the construction general layout of the pumped storage power station and densely distributed variability of construction objects, key acquisition areas for construction scene images are defined first. The key acquisition areas include dam filling area, reservoir base excavation area of the upper/lower reservoir, construction area of inlet/outlet, entrance area of access tunnels, ventilation tunnels, diversion and discharge tunnels, construction area of underground powerhouse, and construction areas related to the transportation and processing of construction materials such as material yards, waste slag yards, sand and gravel mixing systems. These zones feature diverse machinery types, high personnel activity, dense spatial arrangements, and dynamic operations, making them representative of real construction scenes. The primary image data were obtained from on-site video surveillance systems through continuous video stream capture. To address the limited field of view of fixed cameras, high-resolution digital cameras and UAV-based imaging systems were used as supplementary sources. This combination expanded spatial coverage, enhanced local detail resolution, and captured multi-view imagery, thereby improving the spatial diversity and geometric completeness of the collected data.

Multi-View and Variable Focus Imaging Mechanism. To enrich the dataset in terms of scale, posture, and spatial distribution, a dynamic view control mechanism was employed. Using PTZ (Pan-Tilt-Zoom) cameras, the horizontal angle, vertical tilt, and optical zoom were adjusted to capture the same object from multiple distances and angles. This approach simulated the scale variations and posture differences of construction machinery during real operations, reducing overfitting caused by homogeneous samples.

In large open areas such as the upper and lower dam zones, a hierarchical sampling method combining near-range (<50 m), mid-range (50–200 m), and far-range (>200 m) imaging was adopted. This strategy ensured effective capture of multi-scale objects, providing solid data support for subsequent multi-scale detection network design.

Coverage of Complex Visual Scenarios. Data collection places particular emphasis on covering complex visual scenes. These included structural occlusions (e.g., trees, safety nets), object occlusions caused by dense mechanical operations, densely distributed objects and small objects. Although such conditions are rarely represented in public datasets, they are critical for assessing model robustness. By actively collecting these challenging scenarios, the performance of models in tasks such as small object recognition, and scale adaptation can be effectively enhanced.

Data Acquisition Under Multiple Meteorological Conditions. Given the long construction period of pumped-storage power station, the dataset also encompasses various weather conditions, such as sunny, cloudy, rainy, snowy, and foggy days. Changes in illumination, contrast, and color under different weather introduce real-world variability that challenges recognition algorithms. By including samples under low-light, low-contrast, and reduced-visibility conditions, the dataset enables models to learn from natural degradation factors, improving stability and robustness in adverse environments.

Filtering Invalid and Redundant Data. To ensure data quality and efficiency, a strict filtering mechanism was applied. Video frames captured during non-working hours (e.g. 23:00–6:00), extreme weather conditions that halted construction, and during specific procedures (such as pre-blasting clearance periods) were excluded. By integrating motion detection algorithms such as optical flow, segments that remain static for extended periods or lack sufficient semantic information are removed, thereby preventing model bias caused by learning from large volumes of invalid samples.

The final dataset was generated by combining fixed-interval frame extraction with event-triggered sampling, supplemented with manually captured high-resolution images. The resulting large-scale dataset includes five main object categories: heavy machinery (e.g., excavators, bulldozers, dump trucks), small equipment (e.g., buckets, crushing hammers), construction workers, safety equipment (e.g., helmets, vests), and safety signage, totaling several hundred thousand images.

2.2 Image Filtering

The initial image dataset established through video frame extraction at a specified time interval tends to be large. For example, at a fixed frame rate, using 15-s interval and with 6:00 a.m. to 11:00 p.m. as the valid time period, 4080 images can be captured from just one day's video at a acquisition area. Under the fixed acquisition area and adjacent acquisition time conditions, the extracted construction scene images may have a high degree of similarity. Additionally, due to factors such as network transmission issues, environmental interference, video frame rate instability, or variations in video decoding formats, some data loss may occur in the acquired video images. This can result in abnormal color blocks in some areas of the image, leading to what is commonly referred to as "flickering image". To improve the effectiveness of dataset and reduce the manual effort required for image filtering, it is essential to develop specific methods for detecting duplicates and identifying screen artefacts.

Duplicate Image Detection. To eliminate redundant samples, the evaluation model of image similarity based on the structural similarity (SSIM) index is built. The SSIM index measures the similarity between two images by comparing their luminance, contrast, and structural information. The SSIM value ranges from [0, 1], where a higher value indicates greater similarity between the two images. Images exceeding a similarity threshold were removed. The calculation formula of the SSIM is given as follows:

$$SSIM\,(x, y) = \frac{\left(2\mu_x\mu_y + c_1\right)\left(2\sigma_{xy} + c_2\right)}{\left(\mu_x^2 + \mu_y^2 + c_1\right)\left(\sigma_x^2 + \sigma_y^2 + c_2\right)} \tag{1}$$

Where, μ_x and μ_y represent the mean pixel values of the two images, respectively, which reflect the luminance information; σ_x and $\sigma_y$denote the standard deviations of pixels of the two images, respectively, which reflect the contrast information; σ_{xy}stands for the covariance of pixels of the two images, which reflects the structural similarity information; andc_1 andc_2 are constants introduced to avoid instability when the luminance or contrast is close to zero.

As shown in Fig. 1, comparative analysis across multiple thresholds (0.7 ~ 0.9) showed that an SSIM value of 0.8 provided the best balance between data retention and diversity, effectively eliminating duplicates while maintaining representativeness.

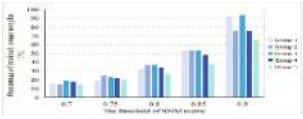

(a) proportion of retained image samples under different SSIM threshold conditions

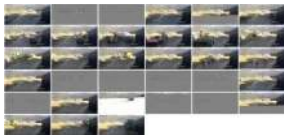

(b) detection results when the SSIM threshold is set to 0.8

Fig. 1. Results of similarity evaluation performed in the construction scenario of tunnel entrance area.

Flickering Image Detection. Since both the type and the proportion of abnormal color blocks in flickering images affects whether the image sample can be used for subsequent computer vision tasks, this paper classifies flickering images into five types: large-area solid color flickering image, small-area solid color flickering image, large-area striped flickering image, small-area striped flickering image, and color distortion flickering image, as shown in Fig. 2. Here, "large-area" refers to the proportion of abnormal color blocks in the image, such as solid color or striped artifacts, exceeding one-third of the entire image.

If an image sample is identified as a large-area solid color flickering image or a large-area striped flickering image, it is assumed that the construction objects are obscured or affected by abnormal color blocks, and thus, this image sample will be removed from the initial dataset. Image samples of other flickering types will be retained, as they can enhance the robustness of computer vision models applied in real-world scenarios without hindering the feature learning of the construction objects.

Given the uneven distribution of sample quantities across different flickering types (with color distortion samples being notably scarce), this paper introduces the Remix

(a) large-area solid-color flickering image

(b) small-area solid-color flickering image

(c) large-area striped flickering image

(d) small-area striped flickering image

(f) color distortion flickering image

Fig. 2. Types of filtering images.

strategy [26] for the offline augmentation of training data. By weighting samples at both the feature and label levels, it assigns higher weights to minority classes during the generation of synthetic samples, enabling the automatic recognition of image flickering types while accounting for long-tail distribution characteristics. The experimental dataset included 1,170 samples equally divided between normal and distorted images, with an 6:2:2 split for training, validation, and testing. ResNet18 and ResNet50 were selected as baseline models, with three data strategies implemented: original, Remix ($\times$1.0), and Remix ($\times$2.0). Results showed that ResNet18 with moderate Remix augmentation ($\times$ 1.0) achieved the best classification performance, reaching 98.29% accuracy on the test set (Table 1).

Table 1. Comparison of recognition performance of filtering images under different models and data strategies.

Model	Training Data Strategy	Accuracy	Macro Avg F1
ResNet18	Original Data	97.44%	93.74%
ResNet18	Remix-augmented Data (×1.0)	98.29%	95.40%
ResNet18	Remix-augmented Data (×2.0)	97.44%	92.15%
ResNet50	Original Data	97.86%	93.09%
ResNet50	Remix-augmented Data (×1.0)	94.87%	87.61%
ResNet50	Remix-augmented Data (×2.0)	97.86%	94.07%

2.3 Semi-Automatic Annotation of Construction Scene Images

Manual frame-by-frame annotation of construction surveillance images is both labor-intensive and time-consuming, particularly given the scale and complexity of pumped-storage construction sites. To address this issue, a semi-automatic annotation workflow was developed to enhance labeling efficiency and accuracy. The proposed process combines automated open-set object detection with human verification, effectively balancing automation and precision.

As shown in Fig. 3, the overall workflow consists of four main stages: (a) Open-Set Detection, (b) Filtering, followed by a decision step—Is a machinery parking area included? If yes, the process continues to (c) Annotation of Machinery Parking Areas; if no, it proceeds to (d) Manual Correction.

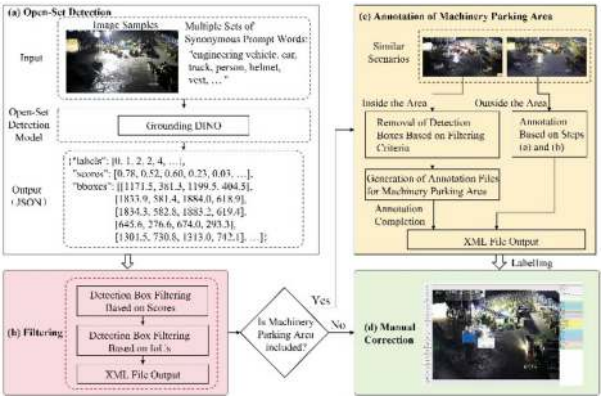

Fig. 3. Semi-automatic labeling process of object categories in Construction Scene Images.

Open-Set Detection. A pretrained Grounding DINO model [27], which integrates visual and language understanding within an open-set detection framework, was used

to automatically generate object annotations. Natural language prompts such as "engineering vehicle" "truck" "car" "helmet" and "vest" were input to guide detection. To improve category coverage, multiple synonymous prompts were used in parallel (e.g., "engineering vehicle" and "truck"), enhancing the recognition of diverse machinery types. Some detection results are presented in Fig. 4, where green dashed boxes indicate missed objects and red dashed boxes represent boundary deviations.

(a) Image of dam filling area

(b) Image of upper reservoir basin excavation area

(c) Image of sand and gravel mixing system area

(d) Image of lower reservoir dam material transportation area

Fig. 4. Open-set object detection results based on the Grounding DINO model.

Filtering. The initial detection results were filtered to retain only bounding boxes with confidence scores above a preset threshold (e.g., 0.3). Redundant boxes were removed using the Intersection-over-Union (IoU) metric to ensure that each object was uniquely represented. The filtered detection results were then exported as XML files for further processing.

Annotation of Machinery Parking Areas. In the construction site of the pumped storage power station, certain areas are occasionally designated as temporary zones for the transfer or storage of construction machinery. Take the construction area at sand and gravel mixing system as examples, as shown in Fig. 5, static construction machinery is temporarily parked within the red dashed boxes. Direct object-level annotation for these areas would generate a great deal of redundant work. To handle efficiently, bounding box filtering rules were introduced. By setting spatial thresholds (e.g., minimum Xmin and maximum Xmax values), all bounding boxes located within defined parking zones were removed. Corrected bounding box information was saved in separate annotation files and automatically integrated into the corresponding construction scene images. This procedure enabled batch completion of annotations in static areas, greatly reducing manual effort.

(a) Sand and gravel mixing system area-comparison 1

(b) Sand and gravel mixing system area-comparison 2

Fig. 5. Temporary parking area of static construction machinery.

Manual Correction. After merging the bounding boxes from the previous step, the filtered annotations are manually inspected and refined using LabelImg to correct for boundary deviations and missed detections. While open-set detection occasionally exhibited reduced accuracy in densely distributed or occluded regions, it significantly improved annotation efficiency for large-scale and sparsely distributed targets.

This unified semi-automatic annotation strategy ensures both efficiency and precision, making it adaptable to the dynamic characteristics of large construction sites while maintaining scalability for dataset expansion.

3 Dataset Introduction

Based on the dataset construction methodology described in Sect. 2, a large-scale, diverse image dataset was developed using the video surveillance system deployed during the construction of a pumped-storage power station. The dataset has been designed to reflect the unique characteristics of large-scale civil construction projects, with a particular focus on the complexity and variability of construction scene, operation conditions, and object types. It serves as a unified foundation for subsequent intelligent vision tasks such as object detection, recognition, and scene understanding in construction environments.

The dataset contains 22,540 images and 192,505 annotated instances, with image resolutions primarily at 2560×1440, and supplementary resolutions including 1080×1920, 2916×5184, 3888×5184, 4096×3072, and 5520×2400. It encompasses 21 representative object categories frequently encountered in hydraulic construction, including truck, tanker, excavator, concrete mixer, loader, bulldozer, excavator with crushing hammer, roller, concrete pump truck, rock drilling rig, air compressor, crane, drilling machinery, bucket, crushing hammer, vehicle, worker, helmet, vest, safety signage, and other vehicle. Figure 6 presents examples of images from the dataset captured under complex construction environments.

Fig. 6. Sample images from the large-scale construction scene dataset under complex conditions at the pumped-storage power station.

Further comprehensive statistical analyses demonstrate the representativeness of the dataset. As shown in Fig. 7(a), all 21 categories are well-covered, with "truck" appearing most frequently, reflecting its prevalence in real construction operations. The overall data distribution exhibits a long-tail characteristic, ensuring inclusion of both common and rare object types. Figure 7(b) shows that over 65% of images contain at least five objects, and approximately 34% contain ten or more, with an average of 8.56 objects per image. This density distribution effectively captures scenes of multi-machine collaboration and dense personnel environment, providing a multi-scale learning environment for model training. Additionally, as indicated in Fig. 7(c), most object bounding boxes occupy relatively small proportions of the total image area, except for concrete pump trucks. This confirms that the dataset spans wide field-of-view scenes, posing realistic challenges for small-object detection. Compared with publicly available datasets, such as MOCS and SODA, the dataset constructed in this paper better reflects the open, large-scale construction scenarios encountered in actual engineering projects. It encompasses a rich distribution of samples across multiple scales, orientations, occlusions, and weather conditions. This supports the development of robust, generalisable vision models for construction monitoring and management in hydraulic engineering projects.

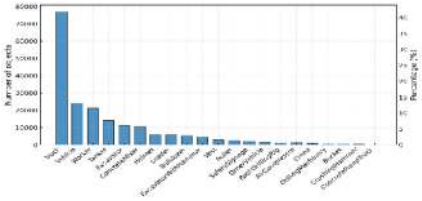

(a) Category distribution

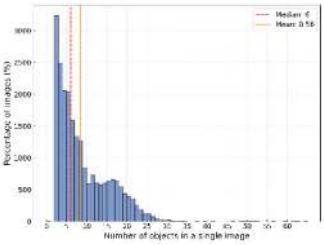

(b) Number of objects per image

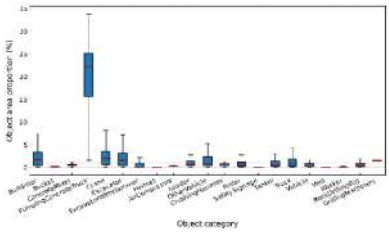

(c) Bounding box area ratios across categories

Fig. 7. Statistical overview of the dataset.

4 Feasibility Verification of the Bulit Dataset and the Proposed Object Detection Model

4.1 Model Design for Construction Scene Detection

Construction sites are characterized by a wide range of object scales, dense distribution of machinery, frequent occlusions, and complex background textures. General object detection models often struggle to fully learn data in such highly complex environments. To address this, this paper improves the YOLOv8 framework by enhancing three aspects: the backbone network, feature fusion architecture, and bounding box regression mechanism. These enhancements aim to boost the feature representation and detection robustness of model in complex construction scenarios. The overall model architecture is shown in Fig. 8.

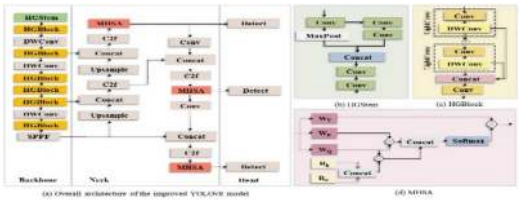

Fig. 8. Overall architecture of the improved construction scene multi-object recognition model.

(a) Backbone Enhancement. The original convolutional layer is replaced with an HGStem module, and the standard C2f block is substituted with the HGBlock module. HGStem performs efficient down sampling through parallel pooling and convolution branches, preserving shallow feature fidelity and edge detail. The HGBlock, composed of cascaded lightweight convolution units (LightConv), incorporating multiple 1×1 convolution and depth wise separable convolutions (DWConv) modules to achieve joint optimization of channel compression and spatial feature extraction. Multi-branch outputs are concatenated and fused through compression convolution, mitigating gradient vanishing and improving sensitivity to small and low-texture objects.

(b) Feature Fusion Enhancement. To strengthen global context modeling, a multi-head self-attention (MHSA) module [28] is embedded after the multi-scale fusion layers in the neck network. MHSA captures long-range dependencies across spatial locations through multiple attention heads and refines attention distribution with relative position encoding. This improves discrimination of densely arranged or partially occluded objects.

(c) Bounding Box Optimization. In the bounding box regression stage, this study adopts the Generalized Intersection over Union (GIoU) loss function [29] instead of the original CIoU loss to improve localization accuracy and stability under complex working conditions. On the basis of the traditional IoU metric, GIoU introduces the smallest enclosing rectangle C of the ground-truth box and the predicted box, while considering the spatial relationship between overlapping and non-overlapping regions. By introducing the enclosing rectangle constraint into gradient propagation, GIoU can provide more continuous and stable optimization signals when the object is partially occluded or has an irregular shape.

By integrating the aforementioned improvements, the model significantly enhances detection robustness for multi-scale, low-contrast, and partially occluded objects while maintaining the high inference efficiency. This better aligns with the complex and diverse visual feature distribution in complex construction scenarios, providing better support for engineering monitoring and intelligent scheduling.

4.2 Experimental Setup

A total of 12,000 annotated images were randomly selected and divided into training and testing sets at a 7:3 ratio. All images were resized to 640×640 before input to ensure stable training and fair comparison.

Training was conducted on an NVIDIA A100 GPU using the stochastic gradient descent (SGD) optimizer with an initial learning rate of 0.01, decaying to 0.0001. The momentum coefficient was set to 0.937, and other hyperparameters followed the YOLOv8 defaults. Training continued for a maximum of 300 epochs, with early stopping once validation loss stabilized.

Model performance was evaluated using precision (P), recall (R), and mean average precision (mAP) under two Intersection over Union (IoU) thresholds: 0.5 (mAP@0.5) and 0.5:0.95 (mAP@0.5:0.95). These metrics comprehensively assess localization accuracy, coverage, and overall detection capability. Each metric is defined as follows:

$$P = \frac{N_{TP}}{N_{TP} + N_{FP}} \tag{2}$$

$$R = \frac{N_{TP}}{N_{TP} + N_{FN}} \tag{3}$$

$$AP = \int_0^1 P(R)dR \tag{4}$$

$$mAP = \frac{\sum_{i=1}^{n} AP(i)}{n} \tag{5}$$

Where *NTP* (True Positives) denotes the number of correctly detected objects in construction scenarios; *NFP* (False Positives) represents the number of incorrectly detected objects in construction scenarios; *NFN* (False Negatives) stands for the number of missed objects in construction scenarios; and n is the total number of object categories in construction scenarios.

4.3 Detection Results and Analysis

To assess both generalization and domain-specific performance, experiments were conducted on the public MOCS dataset and the proposed construction scene dataset. Comparative evaluation included several mainstream detectors: DNN-EFocalL1-SEIOU, EMS Faster R-CNN, YOLOv4-EFNB0, improved YOLOX-S, Faster R-CNN, RetinaNet, and YOLOv8. Results are summarized in Tables 2 and 3.

Table 2. Comparative experiments on the MOCS dataset.

Model	Metrics			
	P	R	mAP@0.5/%	mAP@0.5:0.95/%
DNN-EFocalL1-SEIOU	–	–	0.482	–
EMS Faster R-CNN	–	–	0.547	–
YOLOv4-EFNB0	–	–	0.523	–
Refined YOLOX-S	–	–	0.514	
YOLOv8	0.815	0.588	0.674	0.491
Ours	0.846	0.673	0.755	0.568

Note: The calculation results of the DNN-EFocalL1-SEIOU [30], EMS Faster R-CNN, YOLOv4-EFNB0, and improved YOLOX-S17 models on the MOCS dataset are cited from the respective papers.

Table 3. Comparative experiments on our built dataset.

Model	Metrics			
	P	R	mAP@0.5/%	mAP@0.5:0.95/%
Faster R-CNN	0.326	0.701	0.544	–
Retinanet	0.729	0.482	0.531	–
YOLOv8	0.881	0.724	0.782	0.623
Ours	0.893	0.764	0.807	0.674

On the MOCS dataset (see Table 2), the proposed model achieved superior detection accuracy across all metrics. Compared to the original YOLOv8, the improved model achieves 3.80%, 14.46%, 12.02%, and 15.68% gains in P, R, mAP@0.5, and mAP@0.5:0.95 metrics, respectively. This demonstrates that the model enhancements proposed in this paper exhibit significant generalization capabilities across diverse construction scenarios.

On our custom dataset (see Table 3), the model again outperformed other approaches. Compared with Faster R-CNN (ResNet-50 backbone) and RetinaNet, mAP@0.5 increased by 48.35% and 51.98%, respectively. Relative to YOLOv8, precision improved by 1.36%, recall by 5.52%, and mAP@0.5:0.95 by 8.19%. These results confirm that the proposed model maintains high robustness and localization accuracy under dense occlusion, low contrast, and significant scale variation conditions.

To further visually validate the model performance, Figs. 9, 10, 11, 12, 13, and 14 present detection results across various construction scenes, including tunnel entrances, slag yards, dam filling and excavating sites, and material transport areas. From the visualization results, it can be observed that the Faster R-CNN and Retinanet models exhibit relatively weak overall detection performance, with obvious missed detection and false detection phenomena. YOLOv8 can recognize most mechanical equipment in regular construction scenarios, but it still suffers from duplicate detection (e.g., the dump truck group in the upper right of Fig. 12(c)) and missed detection (e.g., the left excavator in Fig. 11(c)) under complex conditions. In scenarios where objects are occluded by vegetation or mountains (Fig. 13), the missed detection issue of YOLOv8 becomes more prominent; in low-contrast environments (Fig. 14), some false detections also appear. By contrast, the improved YOLOv8 model proposed in this study achieves more accurate object recognition under various complex environments. The model not only effectively suppresses duplicate detection and missed detection but also maintains high detection stability and accuracy in complex construction scenarios, such as multi-scale object distribution, dense occlusion of mechanical equipment, and low-contrast backgrounds. This verifies its practicality in the construction monitoring task of pumped-storage power station and also indicates that the large-scale construction scenario image dataset constructed in this study has strong engineering application value.

(a) Faster R-CNN

(b) Retinanet

(c) YOLOv8

(d) The proposed model

Fig. 9. Detection effect of images acquisition in construction tunnel entrance.

(a) Faster R-CNN

(b) Retinanet

(c) YOLOv8

(d) the proposed model

Fig. 10. Detection effect of images acquisition in the construction process of slag yard.

(a) Faster R-CNN

(b) Retinanet

(c) YOLOv8

(d) the proposed model

Fig. 11. Detection effect of images acquisition in the dam filling construction process.

(a) Faster R-CNN

(b) Retinanet

(c) YOLOv8

(d) the proposed model

Fig. 12. Detection effect of images acquisition in the excavating construction process.

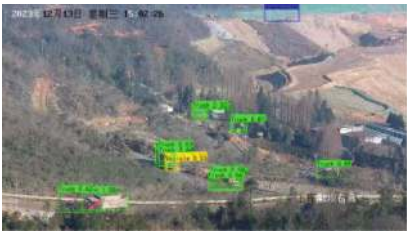

(a) Faster R-CNN

(b) Retinanet

(c) YOLOv8

(d) the proposed model

Fig. 13. Detection effect of images acquisition in the vehicle transportation process.

(a) Faster R-CNN

(b) Retinanet

(c) YOLOv8

(d) the proposed model

Fig. 14. Detection effect of images acquisition in the transportation process of dam material.

5 Conclusion

This study addresses the challenges of visual perception in the complex and dynamic environment of pumped-storage power station construction. To overcome the limitations of existing datasets, particularly with regard to their restricted scale, limited category coverage and poor scene representativeness, an automated workflow for constructing image datasets based on video surveillance was developed. Using this approach, we built the first large-scale image dataset specifically tailored for pumped-storage construction scenes. By integrating image acquisition, filtering, and semi-automatic annotation, the proposed method significantly improves data collection and labeling efficiency, filling a critical gap in visual data resources for such engineering projects. The dataset provides a scalable foundation for intelligent monitoring in hydropower construction and offers a feasible technical route for future applications. Building upon this dataset, an improved multi-object detection framework was proposed to enhance recognition performance for small, occluded, and background-interfered objects commonly present in construction environments. The developed algorithm demonstrates strong potential for supporting intelligent supervision, equipment scheduling, and safety management in pumped-storage and other hydropower engineering projects.

In future work, the dataset will be further expanded to support downstream visual analysis tasks such as object tracking, equipment operation recognition, and construction quantity evaluation. Moreover, it will facilitate the application and optimization of large models in engineering vision scenarios, building a more intelligent and robust visual understanding framework for construction scenarios.

Acknowledgments. This work was supported by the research project (No. NBZZ202300718) of China Three Gorges Corporation.

References

1. Ren, S.Q., He, K.M., Girshick, R., et al.: Faster R-CNN: towards real-time object detection with region proposal networks J. IEEE Trans. Pattern. Anal. Mach. Intell. **39**, 1137–1149 (2017). https://doi.org/10.1109/TPAMI.2016.2577031
2. He, K.M., Gkioxari, G., Dollar, P., et al.: Mask R-CNN J. Proc. IEEE Int. Conf. Comput. Vis. Venice. (2017). https://doi.org/10.1109/ICCV.2017.322
3. Redmon J, Divvala S, Girshick R, et al.: You only look once: Unified, real-time object detection J. Proc. IEEE Conf. Comput. Vis. Pattern. Recognit. Las Vegas: 779–788 (2016). DOI: 10.1109/CVPR.2016.91.
4. Redmon, J., Farhadi, A.: YOLO9000: Better, faster, stronger J. Proc. IEEE Conf. Comput. Vis. Pattern. Recognit. Honolulu, 7263–7271 (2017). https://doi.org/10.1109/CVPR.2017.690
5. Redmon, J., Farhadi, A.: YOLOv3: An incremental improvement J. Preprint https://arxiv.org/abs/1804.02767 (2018)
6. Vaswani, A., Shazeer, N., Parmar, N., et al.: Attention is all you need J. Proc. 31st Int. Conf. Neural. Inf. Process. Syst., 6000–6010 (2017). https://doi.org/10.5555/3295222.3295349
7. Carion, N., Massa, F., Synnaeve, G., et al.: End-to-end object detection with transformers J. Proc. Eur. Conf. Comput. Vis., 213–229 (2020). https://doi.org/10.1007/978-3-030-58452-8_13

8. Zhang, H., Li, F., Liu, S., et al.: DINO: DETR with improved denoising anchor boxes for end-to-end object detection J. Preprint https://arxiv.org/abs/2203.03605 (2022)
9. Liu, Z., Hu, H., Lin, Y., et al.: Swin transformer v2: scaling up capacity and resolution J. Proc. IEEE/CVF Conf. Comput. Vis. Pattern. Recognit., 11999–12009 (2022). https://doi.org/10.1109/CVPR52688.2022.01170
10. Yuan, L., Chen, D.D., & Chen, Y.L.: Florence: a new foundation model for computer vision. Preprint https://arxiv.org/abs/2111.11432 (2021)
11. Shi, X.Y., Li, Z.M., Feng, D.Y., et al.: Research on object detection method for construction equipment of waterway engineering J. Port. Waterway Offshore Eng. **60**, 76–81 (2023)
12. Wang, R.C., Xie, J.K., Mao, S.J.: A construction machinery detection method based on improved YOLOv4 J. J. Civil Eng. Manag. **40**, 16–23 (2023)
13. Xiang, Y.Z.: Research on Construction Machinery Target Detection and Recognition Based on Improved YOLOv5 Master Thesis. Sichuan Agricultural University, Sichuan (2023)
14. Song, X.G., Zhang, D.D., Zhang, P.F., et al.: Real-time object detection algorithm for complex construction environments J. J. Comput. Appl. **44**, 1605–1612 (2024)
15. Zhang, S.R., Liang, B.J., Ma, Z.G., et al.: Unsafe behavior recognition method of construction workers in water conservancy project J. J. Hydroelect. Eng. **42**, 98–109 (2023). https://doi.org/10.11660/slfdxb.20230811
16. Chen, Y., Tu, Y.X., Chen, S., et al.: Recognition method for multi-elements in human-machine-environment scenarios of concrete dam construction J. J. Hydroelect. Eng. **43**, 13–22 (2024). https://doi.org/10.11660/slfdxb.20241202
17. Hu H, Guo F and Liu Z: Object detection based on improved yolox-s model in construction sites J. J. Front. Comput. Sci. Technol., 56: 11–24 (2020). DOI: https://doi.org/10.3778/j.issn.1673-9418.2205012.
18. Humaira, T., Zhu, Z.: Image dataset development for measuring construction equipment recognition performance. J. Autom. Constr. **48**, 1–10 (2014). https://doi.org/10.1016/j.autcon.2014.07.006
19. Xiao B and Kang S C: Development of an image data set of construction machines for deep learning object detection J. J. Comput. Civ. Eng., 35: 05020005 (2020). DOI: https://doi.org/10.1061/(ASCE)CP.1943-5487.0000945.
20. Kim, H., Kim, H.K., Hong, Y.W., et al.: Detecting construction equipment using a region-based fully convolutional network and transfer learning J. J. Comput. Civ. Eng. **32**, 04017082 (2018). https://doi.org/10.1061/(ASCE)CP.1943-5487.00007
21. Roberts, D., Golparvarfard, M.: End-to-end vision-based detection, tracking and activity analysis of earthmoving equipment filmed at ground level. J. Autom. Constr. **105**, 1–15 (2019). https://doi.org/10.1016/j.autcon.2019.04.006
22. Wu, J.X., Cai, N., Chen, W.J., et al.: Automatic detection of hardhats worn by construction personnel: a deep learning approach and benchmark dataset. J. Autom. Constr. **106**, 102894 (2019). https://doi.org/10.1016/j.autcon.2019.102894
23. Nath, N.D., Behzadan, A.H., Paal, S.G.: Deep learning for site safety: real-time detection of personal protective equipment. J. Autom. Constr. **112**, 103085 (2020). https://doi.org/10.1016/j.autcon.2020.103085
24. An, X.H., Zhou, L., Liu, Z., et al.: Dataset and benchmark for detecting moving objects in construction sites. J. Autom. Constr. **122**, 103482 (2021). https://doi.org/10.1016/j.autcon.2020.103482
25. Duan, R., Deng, H., Tian, M., et al.: SODA: a large-scale open site object detection dataset for deep learning in construction. J. Autom. Constr. **142**, 104499 (2022). https://doi.org/10.1016/j.autcon.2022.104499
26. Chou, H.P., Chang, S.C., Pan, J.Y., et al.: Remix: rebalanced mixup. Preprint https://arxiv.org/abs/2007.03943 (2020)

27. Liu, S.L., Zeng, Z.Y., Ren, T., et al.: Grounding dino: marrying dino with grounded pre-training for open-set object detection. Preprint https://arxiv.org/abs/2007.03943 (2024)
28. Cordonnier, J.B., Loukas, A., Jaggi, M.: On the relationship between self-attention and convolutional layers. J. Proc. Int. Conf. Learn. Representations, Addis Ababa. (2020). https://doi.org/10.48550/arXiv.1911.03584
29. Rezatofighi, H., Tsoi, N., Gwak, J.Y., et al.: Generalized intersection over union: a metric and a loss for bounding box regression J. Proc. IEEE/CVF Conf. Comput. Vis. Pattern Recognition. (2019). https://doi.org/10.1109/CVPR.2019.00075
30. Wang, X.Y., Wang, H.Y., Zhang C, L., et al.: A sample balance-based regression module for object detection in construction sites. J. Appl. Sci. **12, 6752** (2022). https://doi.org/10.3390/app12136752

Unbalanced Remote Sensing Data Classification Based on NSGA-III and Cost-Sensitive Random Forest

Xiang Liu[1], Yan Xiao[1(✉)], Bin Wang[2], Moxuan Yang[1], Xubo Liu[1], and Jun Pan[1]

[1] Changchun Institute of Technology, School of Prospecting & Surveying Engineering, Changchun 130012, China
0215062@ccit.edu.cn

[2] Changchun Surveying and Mapping Institute, Changchun 130012, China

Abstract. This paper addresses the issues of class imbalance and feature dimension disaster in hyperspectral remote sensing image classification. It proposes a fusion model (S-N-CSRF) that integrates SMOTE oversampling, NSGA-III multi-objective feature selection, and a cost-sensitive random forest. The method first utilizes the SMOTE algorithm to generate synthetic samples, thereby balancing the class distribution while preserving the original data characteristics. It then employs the NSGA-III algorithm for multi-objective feature se-lection to ensure the model's classification accuracy while reducing feature dimensionality. Finally, a cost-sensitive mechanism is incorporated to construct a random forest classifier, enhancing recognition performance for minority class samples. Experiments conducted on three benchmark datasets (Indian Pines, Salinas, and Pavia University) show that this method outperforms four comparative models in terms of overall accuracy, AUC, and G-mean, achieving the highest accuracies of 93.78%, 95.74%, and 93.21%, respectively. These results significantly improve the classification performance for imbalanced hyper-spectral remote sensing data. The findings demonstrate that this method provides clear classification advantages and offers a feasible solution for hyperspectral remote sensing image classification.

Keywords: Imbalanced Classification · Cost-Sensitive · Oversampling · NSGA-III · Feature Selection

1 Introduction

Remote sensing image classification has long been an important research direction in the field of remote sensing [1]. Although existing machine learning methods have been widely applied to remote sensing classification tasks, most algorithms assume balanced training data [2]. However, the distribution of land cover categories in actual remote sensing images is often highly unbalanced. Specifically, a few categories (such as built-up land and water bodies) occupy small spatial areas and have limited samples, whereas major categories (such as farmland and forest land) are widely distributed and have abundant samples. Moreover, remote sensing data are constrained by imaging conditions and

© The Author(s), under exclusive license to Springer Nature Switzerland AG 2027
G. Feng et al. (Eds.): ICCE 2025, SUCI, pp. 64–78, 2027.
https://doi.org/10.1007/978-3-032-32237-1_5

geo-graphical factors, which further exacerbate the difficulty of obtaining balanced category samples. This imbalance leads to degraded performance in traditional classification methods that focus on overall accuracy, making it difficult to accurately identify minority categories and meet the requirements of practical applications [3].

At present, research on the classification of imbalanced data in the field of remote sensing is relatively limited; however, it has been extensively studied in other domains such as biomedicine, finance, and information security. Regarding the issue of imbalanced data classification, the academic community primarily conducts research at the data level and the algorithm level [4]. At the data level, resampling methods adjust the distribution of training samples to alleviate imbalance [5], and typical methods include SMOTE (Synthetic Minority Oversampling Technique) [6]. SMOTE interpolates by randomly selecting samples of the same class from the neighborhood and generating new, non-repetitive minority-class samples, which can, to some extent, mitigate the problem of overfitting [7, 8]. At the algorithm level, ensemble learning and cost-sensitive learning are widely applied to imbalanced classification tasks [9]. The former improves overall performance by integrating multiple classifiers and resampling strategies. For example, Chen Shengling et al. [10] combined Bagging, Boosting, and SMOTE algorithms and proposed the Rotation SMOTE algorithm, while Zhang Jiawei et al. [11] proposed the weighted random forest algorithm. However, accurately estimating classification costs poses a significant challenge in practical applications [8]. Cost-sensitive learning enhances the recognition performance for minority classes by introducing different classification costs for different classes. For instance, Li et al. [12] proposed a cost-sensitive hybrid attribute measure multi-decision tree method. Currently, increasing research focuses on incorporating cost sensitivity into ensemble algorithms. For example, Sun et al. [13] introduced a cost adjustment function into the weight formula of AdaBoost based on the cost-sensitive AdaBoost ensemble algorithm, enabling the algorithm to pay more attention to minority classes and improving the effectiveness of imbalanced data classification. Similarly, Yang Jieming et al. [14] adjusted weight voting in a cost-sensitive random forest algorithm to improve classification accuracy.

Current research on the imbalanced classification of hyperspectral remote sensing images often focuses solely on the issue of sample quantity imbalance, with insufficient attention to feature space optimization. However, the inherently high-dimensional nature of hyperspectral data makes feature selection a key step in improving classification performance. Traditional single-objective feature selection algorithms usually take classification accuracy as the sole optimization objective, making it difficult to balance the number of features and model complexity. They are also highly dependent on weight parameter definitions and prone to falling into local optima, as seen in Genetic Algorithm (GA) and Particle Swarm Optimization (PSO). Wang Jinjie et al. used mutual information as an evaluation index for feature contribution and combined it with PSO for redundant feature elimination, but did not consider the relationships among other feature combinations and prediction results [15]. In contrast, multi-objective feature selection treats classification accuracy and the number of features as two independent objectives, balancing them during the search process and ultimately providing multiple solutions that better align with practical application needs. Zhang Guiyu et al. combined NSGA-III

with band selection methods to identify optimal features for target classification, thereby reducing redundant information in the model and improving prediction accuracy [16].

In hyperspectral remote sensing image classification research, the issue of data im-balance is particularly prominent. Hyperspectral data contain hundreds of consecutive spectral bands, which not only enrich spectral information but also introduce a large number of redundant features [17]. These redundant features increase computational complexity and can easily lead to model overfitting, further amplifying the impact of class imbalance on classification performance. To address these problems, this paper proposes a cost-sensitive random forest classification method based on the non-dominated sorting genetic algorithm (NSGA-III) combined with SMOTE and an elitist strategy. SMOTE helps preserve the distribution characteristics of the original data and reduces the risk of overfit-ting. NSGA-III significantly reduces feature dimensionality in a multi-dimensional space. On this basis, integrating a cost-sensitive random forest can effectively enhance the classification performance for imbalanced data.

2 Materials and Methods

2.1 Correlation Technique

SMOTE Sampling. SMOTE, proposed by Chawla et al. in 2002, is a synthetic oversampling method that generates new samples through linear interpolation among minority-class samples and adds them to the dataset, thereby reducing the risk of overfitting [18]. The basic idea is to select k samples from the nearest neighbors of each sample in the minority class, randomly choose n samples from these k neighbors for linear interpolation, and finally com-bine the newly synthesized samples with the original data to form an augmented dataset. The interpolation formula is:

$$x_{new} = x + \text{rand}(0, 1) \times \left(\widetilde{x} - x\right) \tag{1}$$

In this formula, x represents the current minority-class sample; $\widetilde{x}$ denotes a randomly selected neighbor from the k nearest neighbors of x; and rand(0,1) is a random number between 0 and 1 used to control the interpolation position. The schematic diagram of SMOTE is shown in Fig. 1.

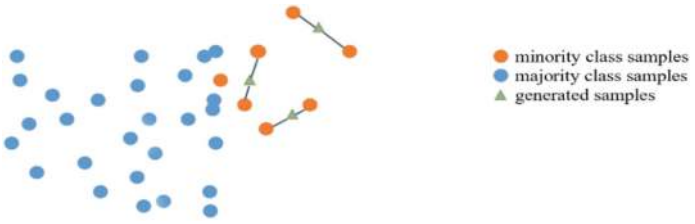

Fig. 1. Schematic diagram of SMOTE.

Non-dominated Genetic Algorithm (NSGA-III). Multi-objective optimization problems are widespread in real-world applications, and the Evolutionary Multi-Objective Optimization (EMO) algorithm is an effective tool for solving them. The NSGA-II algorithm proposed by Deb et al. is a classic approach in this field [19]. It adopts an elitist retention strategy and a selection mechanism based on crowding distance, which significantly improves algorithm performance while reducing computational complexity. However, the selection mechanism of NSGA-II substantially degrades its performance when handling high-dimensional optimization problems with more than three objectives. To overcome the limitations of NSGA-II in high-dimensional objective spaces, Deb proposed the NSGA-III algorithm in 2013 [20]. This algorithm represents a significant improvement to the NSGA-II framework, with its core innovation lying in the introduction of a selection mechanism based on reference points, which replaces the original crowding-distance sorting method.

The basic process of the NSGA-III algorithm can be divided into three stages:

(1) Population crossover and mutation: Using genetic operators (such as simulated binary crossover and polynomial mutation), a new offspring population is generated.
(2) Fast non-dominated sorting: The merged population is divided into multiple non-dominated levels (Pareto fronts).
(3) Selection based on reference points: When selecting individuals for the next generation, those with higher non-dominated ranks are prioritized. If individuals must be chosen from the same rank, the algorithm uses a set of predefined reference points to guide the selection, preferentially retaining individuals associated with these reference points and having a sparse distribution. This approach better maintains population diversity and convergence in high-dimensional objective spaces [21].

NSGA-III effectively addresses the high-dimensional selection challenges faced by NSGA-II in multi-objective optimization and demonstrates superior performance in problems with three or more objectives [22]. The algorithm flow is shown in Fig. 2.

Cost-sensitive Classification. Due to the substantial differences in the distribution of various categories, the results of the fusion model often favor the majority class, leading to poor classification performance for the minority class. Cost-sensitive classification is a method that considers the error costs of different categories. In traditional classification models, algorithms typically assume that all classification errors incur the same cost; however, in practical applications, the costs associated with different types of errors can vary greatly. Cost-sensitive classification aims to minimize the overall classification cost [14]. The cost of misclassification by the classifier is usually represented by a cost matrix (see Table 1). Here, $\boldsymbol{c_0}$represents the minority class, $\boldsymbol{c_1}$represents the majority class, and $\boldsymbol{C(i,j)}$ denotes the cost of misclassifying category i as j.

After the cost matrix is determined, the risk function can be constructed based on Bayes' theorem, as shown in Eq. (2):

$$R(c_i|x) = \sum P(c_j|x)C(c_j, c_i) \tag{2}$$

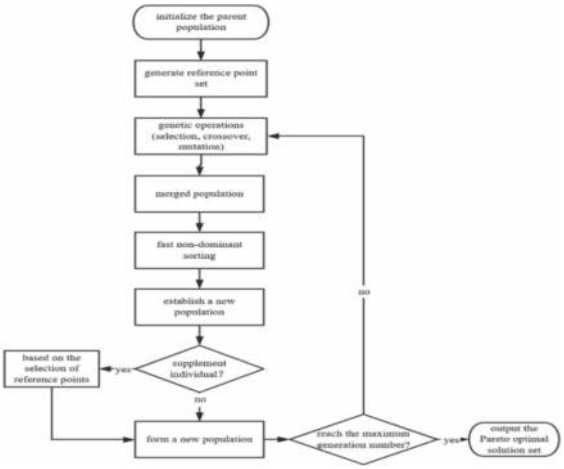

Fig. 2. Flowchart of the NSGA-III algorithm.

Table 1. Cost Matrix.

	c_0	c_1
c_0	$C(c_0, c_0)$	$C(c_0, c_1)$
c_1	$C(c_1, c_0)$	$C(c_1, c_1)$

In Eq. (2), $P(c_j| x)$ represents the posterior probability of assigning the sample xto class c_j. The minimum misclassification cost function is expressed as:

$$Cost = C(c_0, c_1)FN + C(c_1, c_0)FP \tag{3}$$

In Eq. (3), FN represents the number of minority-class samples misclassified as majority-class samples, while FPrepresents the number of majority-class samples misclassified as minority-class samples:

2.2 A Cost-Sensitive Random Forest Classification Model Driven by the Fusion of SMOTE and NSGA-III

Multi-objective The Random Forest (RF) algorithm is an improved version of the bagging algorithm. The base classifiers in a Random Forest are decision trees that use the ensemble learning method to combine multiple trees. These trees form a forest to train and predict samples, and the final classification decision is determined through a voting mechanism. Due to the introduction of randomness in the feature subspace selection process, the performance differences among the base classifiers when handling imbalanced data can be substantial, thereby affecting the overall ensemble performance. The Cost-Sensitive Random Forest (CSRF) enhances the focus on minority classes by introducing

a misclassification cost mechanism, thereby mitigating the class imbalance problem [23].

Incorporating a cost-sensitive learning mechanism into the Random Forest algorithm is typically achieved by embedding the misclassification cost into the node-splitting criterion of each decision tree. Traditional algorithms often use indicators such as the Gini index or information gain, which assume equal misclassification costs, as the basis for attribute selection, whereas cost-sensitive methods use the reduction in misclassification cost as the splitting criterion [14]. This reduction value is defined as the difference between the misclassification cost after using attribute A_i as the splitting attribute and the mis-classification cost of the node before splitting. The algorithm prioritizes the attribute that maximizes this reduction value for splitting, thereby guiding the model to minimize high-cost errors and improve recognition performance for high-cost categories [24]. The cost reduction value is expressed in Eq. (4):

$$Rec = Mc - \sum_{i=0}^{n} Mc(A_i) \tag{4}$$

Introducing In Eq. (4), Mc represents the pre-splitting value.

The experiment employs the SMOTE algorithm to synthesize minority-class samples. By interpolating between minority-class samples and their neighboring samples, new samples are generated to optimize the data distribution, providing a preliminarily balanced and information-rich training foundation for CSRF. Simultaneously, NSGA-III multi-objective optimization is applied for feature selection, aiming to minimize feature dimensionality and classification cost. The Pareto-optimal feature subset is then obtained, effectively compensating for the randomness inherent in Random Forest feature selection and enhancing the model's adaptability to complex remote sensing scenarios.

The classification model developed in this study consists of the following steps:

Step 1: Count the number of majority- and minority-class samples (N_0 and N_1, respectively). Use SMOTE linear interpolation sampling to augment the minority-class samples. After removing noisy samples, a balanced dataset is obtained.
Step 2: Apply NSGA-III multi-objective optimization to identify the most representative feature subset. With the minimization of feature dimensionality and classification cost as the objectives, the optimal Pareto feature subset is obtained through binary encoding, genetic operations (selection, crossover, and mutation), and reference-point selection.
Step 3: Based on the optimal feature subset, calculate the cost reduction value Rec for each candidate feature, defined as: Rec = total cost of the node before splitting - weighted total cost of the child nodes after feature splitting. Select the feature with the highest Rec value to split the node and generate a non-pruned cost-sensitive decision tree.
Step 4: Each decision tree of the CSRF model evaluates the OOB (Out-of-Bag) samples and computes the AUC value.
Step 5: Assign weights to each decision tree based on its AUC value.
Step 6: Each weighted decision tree makes a category prediction for the test sample.

2.3 Results

Experimental Data Set and Evaluation Criteria. To verify the effectiveness of the algorithm proposed in this study on imbalanced datasets, three publicly available benchmark hyperspectral datasets were selected for testing: Indian Pines, Salinas, and Pavia University. Among them, the Indian Pines dataset has a spatial resolution of approximately 20 m and a wavelength range of 0.4–2.5 μm. Twenty water absorption bands (104–108, 150–163, and 220) were removed, resulting in 200 valid spectral bands and a total of 16 vegetation classes. The Salinas dataset has a spatial resolution of approximately 3.7 m and contains 224 consecutive bands. Twenty water absorption bands (108–112, 154–167, and 224) were removed, leaving 204 effective spectral bands and 16 vegetation classes. The Pavia University dataset has a spatial resolution of approximately 1.3 m and a wavelength range of 0.43–0.86 μm. Twelve noise-affected bands were removed, resulting in 103 valid spectral bands and 9 ground-object categories. The parameters of the datasets are summarized in Table 2, and the pseudo-color and label images of the three datasets are shown in Fig. 3.

Table 2. Experimental data set.

Data Set	Indian Pines	Salinas	Pavia University
pixel	145 * 145	512 * 217	610 * 340
characteristic number	200	204	103
Class number	16	16	9
Sample size	10249	54129	42776

In traditional classification evaluation, only the overall accuracy of classification is considered. However, in the field of imbalanced classification, greater emphasis is placed on the minority class. To more meaningfully evaluate the performance of classification models, the confusion matrix method is commonly adopted, as shown in Table 3. In this experiment, Accuracy, G-mean, and AUC were selected as evaluation metrics for measuring the performance of the algorithm. Specifically, Accuracy refers to the number of correctly classified samples divided by the total number of samples; G-mean represents the geometric mean of the accuracies of the minority and majority classes; and AUC is a widely used indicator for assessing the classification performance of imbalanced datasets. Generally, higher values of these three indicators indicate better model performance, and all three range between 0 and 1.

Design of Experiment. In traditional classification evaluation, only the overall accuracy of classification is considered. However, in the field of imbalanced classification, greater attention is given to the minority class. To more effectively evaluate the performance of classification models, the confusion matrix method is typically used, as shown in Table 3. In this experiment, Accuracy, G-mean, and AUC were selected as evaluation metrics to measure the algorithm's performance. Specifically, Accuracy refers to the number of correctly classified samples divided by the total number of samples; G-mean represents the geometric mean of the accuracies of the minority and majority classes; and

a. Pavia University pseudo-color image

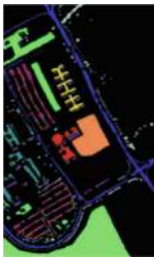

b. Pavia University label image

c. Salinas pseudo-color image

d. Salinas label image

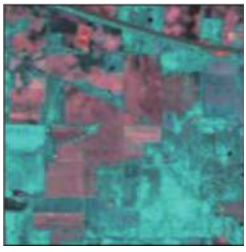

e. Indian Pines pseudo-color image

f. Indian Pines label image

Fig. 3. Pseudo-color image and label image of the dataset.

Table 3. Hybrid matrix.

Class	Classified as a minority category	Divided into the Majority category
Actually classified as the minority category	TP	FP
Actually classified as the majority category	FN	TN

AUC is a widely used indicator for assessing the classification performance of imbalanced datasets. Generally, higher values of these three metrics indicate better model performance, and all three range be-tween 0 and 1.

3 Results and Discussion

3.1 The Experimental Results on the Indian Pines Dataset

Authors The Indian Pines dataset was randomly divided, with 5% used for training and 95% for testing. Table 4 presents the average classification accuracy of five algorithms after 20 independent runs. The first 16 rows correspond to the classification results of each class, while the last three rows show the AUC, G-mean, and Accuracy across all

Table 4. Classification results of the Indian Pines dataset.

Class	S-P-CSRF	S-G-CSRF	S-N-RF	S-CSRF	S-N -CSRF
1	84.30	19.12	91.87	71.46	90.17
2	68.29	63.51	65.43	86.15	87.75
3	63.26	72.41	53.16	65.03	97.53
4	65.69	32.75	78.23	80.51	74.66
5	83.86	88.23	81.08	82.34	92.87
6	92.61	97.54	95.12	92.98	98.32
7	75.48	98.83	92.86	88.55	98.45
8	98.70	94.97	91.77	96.15	97.13
9	57.43	68.68	98.00	16.74	100.00
10	67.92	73.23	55.73	77.95	88.68
11	85.85	87.99	48.35	55.92	87.05
12	62.73	59.34	86.98	81.43	94.88
13	91.53	97.51	99.16	96.32	99.37
14	93.65	98.12	83.82	92.77	96.93
15	74.48	66.88	79.43	65.88	90.26
16	94.08	92.59	89.74	96.17	98.59
AUC/%	85.64	83.54	84.67	66.12	90.75
G-mean/%	89.58	85.76	82.64	78.97	92.45
Accuracy/%	88.85	86.31	86.75	72.67	93.78

classes. The highest accuracy for each class is highlighted in bold. As shown in Table 4, the S-N-CSRF model proposed in this study achieves the best results across all three comprehensive evaluation metrics. Its AUC reaches 90.75%, G-mean is 92.45%, and Accuracy is 93.78%, outperforming the other comparative methods in all aspects. S-N-CSRF exhibits superior overall performance compared with S-P-CSRF and S-G-CSRF. Particularly in difficult-to-classify categories, S-N-CSRF achieves a precision of 97.53% in category 3, which is 25.12 percentage points higher than that of S-G-CSRF, and it achieves perfect classification accuracy (100%) in category 9, which is 83.26 percentage points higher than that of S-CSRF. In terms of addressing class imbalance, the G-mean index of S-N-CSRF reaches 92.45%, significantly higher than that of other models. S-CSRF performs poorly in terms of AUC (66.12%) and Accuracy (72.67%), verifying the importance of collaborative optimization. Furthermore, the results indicate that the proposed model not only mitigates the class imbalance problem through SMOTE but also enhances feature representation through NSGA-III-based feature selection, thereby improving the classification accuracy of minority classes while maintaining balance across all categories in Fig. 4.

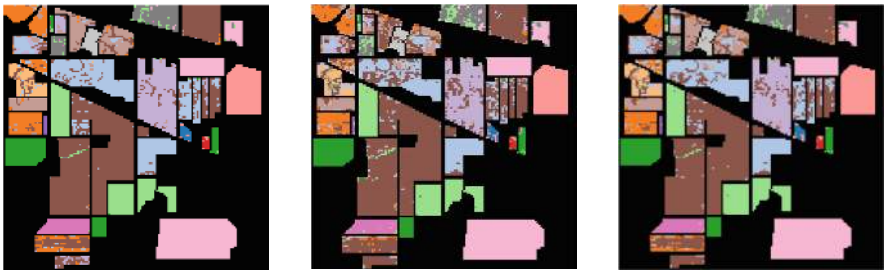

a. S-P-CSRF b. S-G-CSRF c. S-N-RF

d. S-CSRF e. S-N-CSRF

Fig. 4. Classification effect diagrams of different models on the Indian Pines dataset.

3.2 The Experimental Results on the Salinas Dataset

The Salinas dataset was randomly divided, with 1% used for training and 99% for testing. Table 5 presents the classification results of five algorithms. It can be observed that the classification accuracy of these algorithms exceeds 90% in most classes. As shown in Table 5, the S-N-CSRF model achieved the best results across all three core indicators: AUC was 92.78%, G-mean was 94.95%, and Accuracy reached 95.74%, significantly out-performing the other comparative models. S-N-CSRF improved classification accuracy by 5.39 percentage points compared with S-P-CSRF and by 2.96 percentage points compared with S-G-CSRF, demonstrating the advantage of NSGA-III in multi-objective feature selection.

Analyzing the classification accuracy for each category, S-N-CSRF achieved excellent results of 99.97%, 99.36%, 99.12%, and 99.18% in key crop categories 4, 6, 7, and 12, respectively. In terms of handling class imbalance, the G-mean index of S-N-CSRF reached 94.95%, which is significantly higher than that of other models. Compared with the S-CSRF model without feature selection, all variant models incorporating feature selection exhibited substantial performance improvements, confirming the importance of feature selection for hyperspectral data classification. Particularly in the AUC metric, S-N-CSRF showed an improvement of 12.25 percentage points compared with S-CSRF, highlighting the enhancement effect of feature selection on the model's discriminative capability in Fig. 5.

Table 5. Classification results of the Salinas dataset.

Class	S-P-CSRF	S-G-CSRF	S-N-RF	S-CSRF	S-N -CSRF
1	99.75	99.15	99.06	92.55	99.51
2	95.63	99.79	98.99	96.73	94.78
3	95.18	95.80	97.52	86.27	96.88
4	97.07	98.44	98.54	91.04	99.97
5	99.81	93.32	93.66	95.61	98.51
6	95.51	97.78	98.87	89.63	99.36
7	96.88	98.46	95.56	96.88	99.12
8	86.15	90.08	87.31	81.21	88.34
9	90.70	91.33	98.19	93.50	95.38
10	92.47	95.45	95.61	90.08	96.49
11	90.86	97.94	94.57	88.36	98.72
12	96.76	95.66	95.84	92.79	99.18
13	96.84	99.01	98.75	96.21	97.36
14	95.09	82.56	94.63	87.70	95.88
15	88.97	92.15	88.73	83.47	95.16
16	96.46	92.19	94.60	97.84	92.31
AUC/%	87.56	90.77	85.92	80.53	92.78
G-mean/%	89.81	90.11	89.32	83.44	94.95
Accuracy/%	90.35	92.78	91.37	85.61	95.74

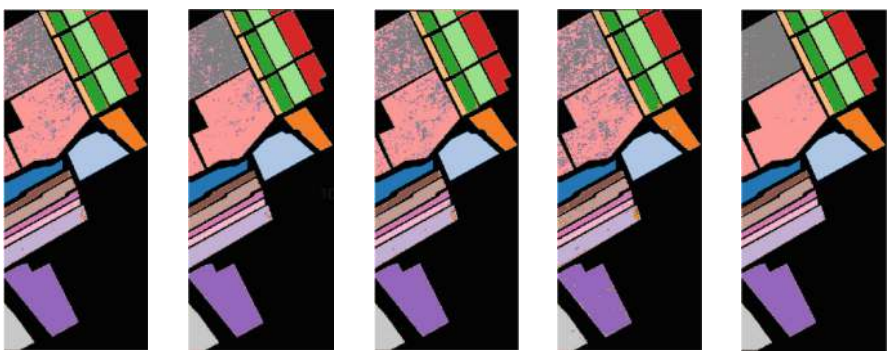

a. S-P-CSRF b. S-G-CSRF c. S-N-RF d. S-CSRF e. S-N-CSRF

Fig. 5. Classification effect of different models on Pavia University dataset.

3.3 The Experimental Results on the Pavia University Dataset

The Pavia University dataset was randomly divided, with 5% used for training and 95% for testing. Table 6 presents the classification results of five algorithms. As shown in Table 6, the S-N-CSRF model achieved the best results across all three core indicators: AUC was 92.37%, G-mean was 91.94%, and Accuracy reached 93.21%. It comprehensively outperformed the other four models. S-N-CSRF improved classification accuracy by 5.46 percentage points compared with S-P-CSRF and by 2.37 percentage points compared with S-G-CSRF. In category 2, it achieved a precision of 99.91%, which was nearly a perfect classification. In categories 4 and 6, it reached high precisions of 98.36% and 99.76%, respectively. In terms of addressing class imbalance, the G-mean index of S-N-CSRF reached 91.94%, significantly higher than that of the other models in Fig. 6.

Table 6. Classification results of the Pavia University dataset.

Class	S-P-CSRF	S-G-CSRF	S-N-RF	S-CSRF	S-N -CSRF
1	80.45	89.71	92.14	72.48	93.47
2	90.16	95.87	98.08	85.97	99.91
3	82.33	63.55	85.17	82.74	83.45
4	86.08	90.84	93.86	95.78	98.36
5	93.54	98.01	99.12	96.85	98.14
6	73.65	70.49	87.93	90.68	99.76
7	86.99	85.29	83.25	88.95	84.29
8	90.93	90.19	86.99	82.74	73.51
9	98.44	99.84	93.62	98.86	99.07
AUC/%	85.43	89.96	89.45	85.76	92.37
G-mean/%	86.28	88.63	89.87	86.76	91.94
Accuracy/%	87.57	90.84	91.76	88.11	93.21

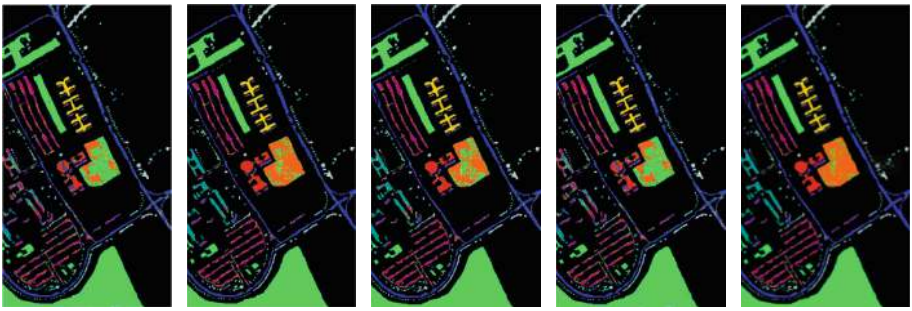

a. S-P-CSRF b. S-G-CSRF c. S-N-RF d. S-CSRF e. S-N -CSRF

Fig. 6. Classification effect of different models on Pavia University dataset.

4 Conclusions

This study addresses the problem of class imbalance and the curse of dimensionality in hyperspectral images and proposes a fusion model, S-N-CSRF, based on SMOTE, NSGA-III, and a cost-sensitive random forest. Experimental results on three benchmark datasets (Indian Pines, Salinas, and Pavia University) demonstrate that the proposed model significantly outperforms the comparative models in terms of overall classification accuracy, AUC, and G-mean metrics, achieving the highest accuracies of 93.78%, 95.74%, and 93.21%, respectively.

The main contributions of this study are as follows:

(1) By employing the NSGA-III multi-objective optimization algorithm, an effective balance between the number of features and classification accuracy was achieved for high-dimensional hyperspectral data, overcoming the limitations of traditional feature selection methods.
(2) By integrating SMOTE with feature selection and classifier design, a comprehensive classification framework was established, effectively reducing the risk of overfitting.
(3) The proposed S-N-CSRF model demonstrated strong generalization ability and stability across different hyperspectral datasets, providing an innovative and effective solution for hyperspectral image classification.

Future work will focus on lightweight model development and extending applications to multi-source remote sensing data.

Acknowledgments. This research was funded by Foundation of Jilin Provincial Science & Technology De-partment (Grant No.YDZJ202201ZYTS499).

References

1. Wang, F., Du, X., Zhang, W., et al.: Remote sensing LiDAR and hyperspectral classification with multi-scale graph encoder-decoder network. J. Remote Sens. **16**(20), 3912 (2024). https://doi.org/10.3390/rs16203912

2. Liu, Q., Yue, J., Kuang, Y., et al.: SemiRS-COC: semi-supervised classification for complex remote sensing scenes with cross-object consistency. J. IEEE Trans. Image Process. **33**, 3855–3870 (2024). https://doi.org/10.1109/TIP.2024.3414122
3. Zheng, X., Jia, J., Chen, J., et al.: Hyperspectral image classification with imbalanced data based on semi-supervised learning. J. Appl. Sci. **12**(8), 3943 (2022). https://doi.org/10.3390/app12083943
4. Leng, Q.K., Sun, X.Z., Meng, X.F.: An oversampling method for imbalanced data based on sample potential and noise evolution J. J. Comput. Appl. **44**(8), 2466–2475 (2024). https://link.cnki.net/urlid/51.1307.TP.20231120.1707.006
5. Wang, X., Zhang, R., Zhang, Z.: A novel hybrid sampling method ESMOTE+SSLM for handling the problem of class imbalance with overlap in financial distress detection. J. Neural Process. Lett. **55**(3), 3081–3105 (2022). https://doi.org/10.1007/s11063-022-10998-0
6. Chawla, N.V., Bowyer, K.W., Hall, L.O., et al.: SMOTE: synthetic minority over-sampling technique J. J. Artif. Intell. Res. **16**(1), 321–357 (2002). https://doi.org/10.1613/jair.953
7. Tong, Y., Feng, W., Song, Y., et al.: Dynamic ensemble algorithm of SMOTE and rotation forest for imbalanced hyperspectral remote sensing classification. J. Natl. Remote Sens. Bull. **26**(11), 2369–2381 (2022). https://doi.org/10.11834/jrs.20210216
8. Li, Y.X., Chai, Y., Hu, Y.Q., et al.: Review on classification methods for imbalanced data. J. Control Decis. **34**(4), 673–688 (2019). https://doi.org/10.13195/j.kzyjc.2018.0865
9. Lu, C., Ke, H., Zhang, G., et al.: An improved weighted extreme learning machine for imbalanced data classification. J. Memet. Comput. **11**(1), 27–34 (2019). https://doi.org/10.1007/s12293-017-0236-3
10. Chen, S.L., Shen, S.Q., Li, D.S.: Ensemble learning method for imbalanced data based on sample weight updating. J. Comput. Sci. **45**(7), 31–37 (2018). https://doi.org/10.11896/j.issn.1002-137X.2018.07.005
11. Zhang, J.W., Guo, L.M., Yang, X.M.: An improved algorithm for oversampling and random forest for imbalanced data J. Comput. Eng. Appl. **56**(11), 39–45 (2020). https://link.cnki.net/urlid/11.2127.tp.20200120.1652.012
12. Li, F., Zhang, X., Zhang, X., et al.: Cost-sensitive and hybrid-attribute measure multi-decision tree over imbalanced data sets. J. Inf. Sci. **422**, 242–256 (2018). https://doi.org/10.1016/j.ins.2017.09.013
13. Sun, Y.M., Kamel M, S., Wong, A.K.C., et al.: Cost-sensitive boosting for classification of imbalanced data. J. Pattern Recognit. **40**(12), 3358–3378 (2007). https://doi.org/10.1016/j.patcog.2007.04.009
14. Yang, J., Gao, C., Qu, Z.Y., et al.: Random forest classification algorithm based on cost-sensitive for imbalanced data. J. Sci. Technol. Eng. **18**(6), 285–290 (2018)
15. Wang, J.M., Li, W.: A multi-objective feature selection method combining mutual information and particle swarm algorithm J. J. Front. Comput. Sci. Technol. **14**(1), 83–95 (2020)
16. Zhang, G.Y., Xiang, X.R., Zhang, L., et al.: A combined feature selection method of iPLS-iNSGA-III for determining the acidity of yellow water using near-infrared spectroscopy. J. Food Sci. **46**(17), 283–291 (2025). https://doi.org/10.7506/spkx1002-6630-20250214-046
17. Cheng, Y.K., Zhang, B.H., Lv, X.Q., et al.: Spectral adaptive enhancement method for class imbalance hyperspectral image classification. J. Sci. Surv. Mapp. **49**(2), 143–152 (2024). https://doi.org/10.16251/j.cnki.1009-2307.2024.02.015
18. Chawla N, V., Bowyer K, W., Hall, L.O., et al.: SMOTE: synthetic minority over-sampling technique J. J. Artif. Intell. Res. **16**, 321–357 (2002). https://doi.org/10.1613/jair.953
19. Deb, K., Pratap, A., Agarwal, S., et al.: A fast and elitist multiobjective genetic algorithm: NSGA-II J. IEEE Trans. Evol. Comput. **6**(2), 182–197 (2002). https://doi.org/10.1109/4235.996017

20. Deb, K., Jain, H.: An evolutionary many-objective optimization algorithm using reference-point-based nondominated sorting approach, part I: solving problems with box constraints. J. IEEE Trans. Evol. Comput. **18**(4), 577–601 (2013). https://doi.org/10.1109/TEVC.2013.2281535
21. Zhang, M., Wang, J.S., Liu, Y., et al.: Multi-objective optimization algorithm based on clustering guided binary equilibrium optimizer and NSGA-III to solve high-dimensional feature selection problem. J. Inf. Sci. **648**, 119638 (2023). https://doi.org/10.1016/j.ins.2023.119638
22. Zhu, Y., Liang, J., Chen, J., et al.: An improved NSGA-III algorithm for feature selection used in intrusion detection. J. Knowl. Based Syst. **116**, 74–85 (2017). https://doi.org/10.1016/j.knosys.2016.10.030
23. Ping, R., Zhou, Y.S., Li, D.: Cost-sensitive random forest classification algorithm for highly imbalanced data. J. Pattern Recognit. Artif. Intell. **33**(3), 249–257 (2020). https://doi.org/10.16451/j.cnki.issn1003-6059.202003006
24. Wang, J.H., Yan, J.R.: Classification algorithm based on undersampling and cost-sensitiveness for unbalanced data J. J. Comput. Appl. **41**(1), 48–52 (2021). https://doi.org/10.11772/j.issn.1001-9081.2020060878

Investigation on the Hydro-Mechanical Coupling Evolution in the Near-Wellbore Region during Marine Natural Gas Hydrate Drilling

Pan Han[1(✉)] and Ken Qin[2]

[1] School of Petroleum Engineering, China University of Petroleum (East China), Qingdao 266580, China
hanpan013727@163.com

[2] Energy Storage Technology Co., Ltd, PipeChina, Shanghai 200011, China

Abstract. To address the wellbore instability problem caused by thermo-hydro-mechanical coupling during marine natural gas hydrate drilling, this study establishes a comprehensive mathematical model that fully couples heat and mass transfer induced by drilling fluid circulation, hydrate phase change, multiphase seepage, and geomechanical deformation. The reliability of the model is verified through numerical simulation. Based on this model, the multi-field evolution and the instability mechanisms in the near-wellbore formation during drilling are systematically revealed. The results indicate that the temperature of the drilling fluid exceeding the in-situ phase equilibrium temperature of the hydrate is the direct cause of hydrate dissociation. The radius of thermal disturbance gradually expands with circulation time. Concurrently, hydrate dissociation leads to increased permeability and reduced seepage resistance near the wellbore, which promotes the continuous expansion of the pore pressure disturbance zone. The hydrate saturation around the well decreases significantly, with hydrate being nearly completely dissociated within 0.5 m of the wellbore after 2000 min. Under the combined effects of hydrate dissociation, increased pore pressure, and decreased effective stress, the near-wellbore formation progressively undergoes plastic yielding, and the yielded zone continuously expands, reaching a wellbore yield enlargement rate of 91.68% after 20 h.

Keywords: Wellbore instability · Thermo-hydro-mechanical coupling · Hydrate dissociation · Multiphase seepage · Plastic yielding

1 Introduction

Natural gas hydrate (hereinafter referred to as hydrate) is a clathrate ice-like crystalline compound formed by natural gas and water under specific high-pressure and low-temperature conditions. Globally, marine gas hydrate resources are abundant and are considered a strategic alternative to conventional oil and gas resources [1]. However, their commercial development faces severe technical challenges, among which wellbore stability control during drilling is a critical bottleneck [2]. The dissociation

© The Author(s), under exclusive license to Springer Nature Switzerland AG 2027
G. Feng et al. (Eds.): ICCE 2025, SUCI, pp. 79–91, 2027.
https://doi.org/10.1007/978-3-032-32237-1_6

of hydrates, triggered by changes in pressure and temperature during drilling operations, can fundamentally alter the physical and mechanical properties of the sediment matrix, leading to serious geo-mechanical risks such as severe formation weakening, sand production, or even wellbore collapse. This intrinsic instability is exacerbated by the shallow, unconsolidated nature of typical marine hydrate-bearing sediments (HBS). Consequently, deeply revealing the evolution laws of hydro-mechanical coupling in the near-wellbore formation under drilling disturbance is a fundamental core issue that must be resolved to overcome the technical barriers for safe hydrate drilling and promote their resource utilization. A precise understanding of this coupling is crucial for designing effective drilling strategies, optimizing drilling fluid parameters, and ultimately ensuring operational safety.

Focusing on the hydro-mechanical coupling problem in the near-wellbore formation during marine natural gas hydrate drilling, domestic and international scholars have conducted a series of studies ranging from reservoir characterization and constitutive modeling to multi-physics field coupling simulation, with a clear developmental trajectory and identifiable major contributions. Early research primarily focused on revealing the fundamental physical properties of reservoirs. For instance, regarding the Shenhu area in the South China Sea, scholars systematically described the characteristics of its silt and silty sandstone reservoirs, such as shallow burial, under-compaction, and weak cementation [3], which are directly linked to the engineering challenges of a narrow safe drilling fluid density window and susceptibility to wellbore instability [2]. These intrinsic geological features imply a low inherent strength and high sensitivity to external perturbations. At the mechanistic level, Lei and Santamarina [4] conducted a comparative analysis of the occurrence patterns between silty and sandy hydrate reservoirs, highlighting how differences in sediment fabric influence hydrate morphology and, consequently, macroscopic behavior. Li et al. [5] specifically investigated the mechanical properties of hydrate-bearing sediments in the South China Sea through triaxial tests, providing essential data on strength and deformation parameters. These works laid the foundation for understanding material behavior. As research deepened, the focus shifted to multi-physics field coupling modeling to simulate more complex interactive processes. Freij-Ayoub et al. [6] made an early attempt to introduce a simplified multiphase flow model induced by hydrate dissociation into a wellbore stability model, establishing a temperature-pressure-mechanics coupling framework. Cheng et al. [7] developed a hydro-mechanical coupling model for hydrate formation drilling, focusing on the influence of drilling fluid density and temperature on stability. Wang et al. [8] further derived an analytical solution for the coupling of temperature, seepage, and mechanics during drilling, analyzing the wellbore degradation mechanism from a theoretical perspective, which offered valuable insights into parameter interactions. Recently, the study by Ning, Sun et al. [9] is more engineering-oriented. Using the actual reservoir in the South China Sea Shenhu area as an example and employing the TOUGH+FLAC3D coupling platform while considering factors like drilling fluid salinity, they simulated the wellbore response under drilling fluid invasion, bridging numerical simulation closer to field conditions. These studies have progressively built a research framework from characterization to multi-field coupling simulation.

However, significant knowledge gaps persist, hindering the development of predictive and universally applicable models. Current experimental research often focuses primarily on heat transfer and dissociation itself, with insufficient direct correlation to mechanical responses under the complex, transient conditions of drilling, where loading paths and drainage conditions are constantly evolving. Numerical studies frequently lack comprehensive consideration of the full thermo-hydro-mechanical-chemical (THMC) coupling process, either by simplifying seepage as a single-phase steady-state flow or failing to deeply couple dynamic phase change, non-equilibrium multiphase seepage with the constitutive relationship for rock deformation [10]. This disconnect often leads to models that cannot accurately capture the positive or negative feedback loops between different physical processes. In summary, most existing models are either established under idealized boundary conditions or focus on a limited number of coupled processes, which restricts their applicability to realistic drilling scenarios. In particular, the dynamic disturbance induced by drilling fluid circulation, including continuous heat exchange, filtrate invasion, and non-equilibrium hydrate dissociation, has not been sufficiently incorporated into a unified modelling framework. The evolution characteristics of multi-field coupling and their combined impact on near-wellbore mechanical instability remain inadequately understood. There is a lack of a refined mathematical model that deeply integrates the coupled mechanisms of dynamic thermal-seepage invasion by drilling fluid, hydrate phase change kinetics, and their full coupling with formation seepage and deformation.

Therefore, to address these identified gaps, this paper incorporates the thermal-flow coupling effects induced by drilling fluid circulation into the research framework. It deeply couples the heat and mass transfer between drilling fluid and the formation with the hydrate phase change process and establishes a seepage-deformation constitutive relationship precisely linked to these processes, aiming to reflect the continuous evolution of formation properties. Consequently, a fully coupled mathematical model for wellbore stability in natural gas hydrate formations, capable of characterizing dynamic drilling disturbances, is constructed. Based on this model, the multi-field evolution and instability mechanisms in the near-wellbore formation during drilling are systematically analysed, aiming to provide a more reliable theoretical tool for predicting and mitigating wellbore instability risks in hydrate drilling operations. The simulations will specifically elucidate how the coupled processes evolve spatially and temporally, leading to a clearer identification of instability triggers and critical periods during drilling.

2 Model Formulation

2.1 Porous Media Flow Model

Multiphase Seepage Model. Since hydrate in marine sediments mainly exists in pore-filling or cementing forms and does not migrate independently during short-term drilling operations, it is reasonable to assume that hydrate particles remain immobile within the porous medium. Under drilling disturbance, the dominant transport mechanisms of mass within the formation are fluid seepage and phase change between hydrate, gas, and water, rather than the physical movement of hydrate particles themselves. Therefore, treating hydrate as an immobile solid phase allows the essential features of multiphase

flow induced by hydrate dissociation to be captured without introducing unnecessary complexity. The continuity equations for free gas, water, and hydrate, based on the principle of mass conservation, can be expressed as:

$$\frac{\partial(\phi\rho_w S_w)}{\partial t} + \nabla\cdot\left(-\rho_w\left(\frac{kk_{rw}}{\mu_w}\right)(\nabla p_w + \rho_w g)\right) = m_w \tag{1}$$

$$\frac{\partial\left(\phi_{wg}\rho_g S_g\right)}{\partial t} + \nabla\cdot\left(-\rho_g\left(k\frac{k_{rg}}{\mu_g}\right)(\nabla p_g + \rho_g g)\right) = m_g \tag{2}$$

$$\frac{\partial(\phi\ \rho_h S_h)}{\partial t} = m_h \tag{3}$$

Where: k is the effective permeability of the hydrate-bearing formation (m^2), which has an exponential relationship with hydrate saturation, $\boldsymbol{k} = \boldsymbol{k_0}(1 - S_h)^N$, where N is the permeability reduction index related to the pore scale and structure of hydrate-bearing sediments, typically ranging from 7 to 15, this exponential relationship reflects the strong sensitivity of pore connectivity to hydrate saturation in fine-grained marine sediments. Even a moderate decrease in hydrate saturation can lead to a pronounced increase in effective permeability, especially in reservoirs characterized by small pore throats and weak cementation. Such permeability evolution plays a critical role in controlling the subsequent pressure redistribution and fluid migration in the near-wellbore zone during drilling; k_{rw} and k_{rg} represent the relative permeabilities of the water and gas phases, respectively; μ_w and μ_g are the viscosities of the water and gas phases (Pa·s), respectively; p_g and p_w are the pressures of the gas and water phases within the pores (Pa); m_w, m_g, and m_h denote the mass change rates of water, gas, and hydrate, respectively (kg/(m^3•s)).

$$m_w = \left(\frac{N_h M_w}{N_h M_w + M_g}\right) * m_h,\ m_g = \left(\frac{M_g}{N_h M_w + M_g}\right) * m_h \tag{4}$$

Taking the average pressure of the gas and liquid phases within the porous medium as the pore pressure, and according to the relationship between gas/liquid phase pressures and capillary pressure (pc), we have: $p_w = p - 0.5p_c$, $p_g = p + 0.5p_c$. p_c is the capillary pressure (Pa).

Assuming the density of water is constant within the range of reservoir pressure variation, the water phase continuity equation can be simplified to:

$$\frac{\phi(1 - S_h)\partial S_w}{\partial t} - \frac{\phi S_{w\partial S_h}}{\partial t} + \nabla\cdot\left(-\frac{kk_{rw}}{\mu_w\left(\nabla p - \frac{\nabla p_c}{2} + \rho_w g\right)}\right) = \frac{m_w}{\rho_w} \tag{5}$$

Changes in gas density must be considered throughout the flow domain, and the effective pore volume of the porous medium is saturated with gas and water. The following relationship can be obtained:

$$\frac{\partial\rho_g}{\partial p} = \frac{M_g}{Z\,R\,T} \tag{6}$$

$$\frac{\partial S_w}{\partial t} + \frac{\partial S_g}{\partial t} \tag{7}$$

Where: M_g is the molar mass of gas (kg/mol); Z is the gas compressibility factor. Substituting the above equations into the gas phase continuity equation yields:

$$-\frac{\phi(1-S_h)\partial S_w}{\partial t} + \phi(1-S_h)S_g * \left(\frac{1}{\rho_g}\right) * \frac{\left(\frac{M_g}{ZRT}\right)\partial p}{\partial t} - \frac{\phi S_g \partial S_h}{\partial t} + \nabla\cdot\left(-\frac{kk_{rg}}{\mu_g\left(\nabla p + \frac{\nabla P_c}{2} + \rho g g\right)}\right) = \frac{m_g}{\rho_g} \tag{8}$$

Heat Transfer Model for the Reservoir. Given that the pore-scale characteristic length in hydrate-bearing sediments is small and that heat exchange among the solid skeleton, pore fluids, and hydrate occurs much faster than the timescale of drilling operations, This allows the complex heat transfer process to be represented by a single effective temperature field while still providing sufficient accuracy for engineering analysis. The assumption of local thermal equilibrium remains reasonable under drilling conditions. Assuming local thermal equilibrium, i.e., the temperatures of the gas phase, liquid phase, hydrate, and rock matrix are equal within a representative elementary volume, the heat transfer equation for the hydrate-bearing formation is:

$$\frac{(\rho C)_{eff}\partial T_e}{\partial t} + \nabla\cdot\left[\left(\phi S_g C_{g\rho_{gv_g}} + \phi S_w C_{w\rho_{wv_w}}\right)T_e\right] - \nabla\cdot\left(k_{eff}\nabla T_e\right) = -Q_h \tag{9}$$

Where: T_e is the temperature of the hydrate-bearing formation (K); $(\rho C)_{eff}$ is the effective heat storage capacity of the hydrate-bearing formation J/(m^3•K); K_{eff} is the effective thermal conductivity of the hydrate-bearing formation W/(m•K); Q_h is the heat sink/source term due to hydrate dissociation/formation (J/s).

2.2 Wellbore Stability Model for Hydrate-Bearing Formations

Formation Mechanical Properties Model. Considering the continuously changing mechanical properties of the hydrate-bearing formation, an elastic-plastic constitutive framework is particularly suitable for hydrate-bearing sediments, as their mechanical response under drilling disturbance typically involves an initial elastic deformation stage followed by progressive yielding as hydrate dissociates. This approach enables the model to capture not only stress redistribution around the wellbore but also the irreversible deformation and plastic strain accumulation associated with mechanical degradation of the formation. An elastic-plastic constitutive equation to describe the incremental relationship between stress and strain:

$$d\sigma_{ij} = D_{ijkl}d\varepsilon_{kl} \tag{10}$$

Where: $d\sigma_{ij}$ is the incremental effective stress tensor; D_{ijkl} is the elastic-plastic constitutive matrix tensor of the hydrate-bearing formation; $d\varepsilon_{kl}$ is the incremental strain tensor of the formation skeleton.

The static equilibrium equation is expressed in terms of the effective stress tensor as:

$$\sigma_{ij},j - \left(\alpha_B\delta_{ij}p\right),j + F_i = 0 \tag{11}$$

Where: σ_{ij} is the total stress tensor of the formation skeleton; α_B is the Biot coefficient; δ_{ij} is the Kronecker delta; F_i is the body force vector.

The relationship between displacement and strain is expressed in tensor form as:

$$\varepsilon_{ij} = \frac{1}{2}\left(w_i, j + w_j, i\right) \tag{12}$$

Where: ε_{ij} is the strain tensor of the formation skeleton; w represents the displacement components.

In addition to the aforementioned mechanical constitutive model, determining the mechanical parameters of the hydrate-bearing formation is crucial for studying the evolution of formation mechanical properties. Based on triaxial tests on hydrate-bearing silty clay samples, Li et al. [11] reported that the internal friction angle of hydrate-bearing silty clay ranges between 8.4° and 12.4°, which is significantly lower than the approximately 30° for sandy reservoirs. A functional relationship between the internal friction angle (φ) and hydrate saturation (S_h), regressed from their experimental data, is as follows:

$$\varphi = -158.33\, S_h^3 + 117.3\, S_h^2 - 17.05\, S_h + 10.687 \tag{13}$$

Where φ is the internal friction angle of the hydrate reservoir.

Miyazaki et al. [12] established an empirical model relating cohesion (c) to hydrate saturation, as shown below:

$$C(S_h) = C(S_h = 0) + \left(\frac{1 - sin\varphi}{2cos\varphi}\right) * \alpha\, S_h^{\beta} \tag{14}$$

Where: α and β are empirical coefficients characterizing the formation cohesion.

According to hydrate cementation and load-bearing theory, the elastic modulus of the hydrate-bearing formation exhibits an exponential relationship with hydrate saturation. Field and experimental data indicate that when hydrate saturation decreases from 0.63 to complete dissociation, the elastic modulus reduces from 182 MPa to 32 MPa [13]. Therefore, through regression fitting, the relationship between the elastic modulus (E) of the hydrate-bearing formation and hydrate saturation is expressed as:

$$\log E(S_h) = \log E(S_h = 0) + 1.1983\, S_h \tag{15}$$

Where: E is the elastic modulus of the hydrate-bearing formation (MPa).

Wellbore Failure Criterion. Wellbore instability in hydrate-bearing formations is mostly caused by shear failure in the near-wellbore zone. According to the Mohr-Coulomb shear failure model, the criterion is expressed as follows:

$$\sigma^1 = \left(\frac{1 + sin\varphi}{1 - sin\varphi}\right)\sigma^3 + \frac{2Ccos\varphi}{1 - sin\varphi} \tag{16}$$

2.3 Hydro-Thermo-Mechanical Coupling Strategy

In the proposed model, the hydro-thermo-mechanical coupling is achieved through the dynamic interaction among temperature evolution, multiphase seepage, hydrate phase change, and mechanical deformation of the formation. Specifically, heat transfer induced by drilling fluid circulation alters the temperature field of the near-wellbore formation, which directly affects hydrate stability conditions and controls the rate of hydrate dissociation. The dissociation process, in turn, generates free gas and water, leading to changes in pore pressure and phase saturation.

The evolution of pore pressure and hydrate saturation further influences the effective permeability and mechanical parameters of the formation, including elastic modulus, cohesion, and internal friction angle. These parameters are continuously updated according to the local hydrate saturation, allowing the mechanical response of the formation to evolve consistently with thermal and hydraulic disturbances. Meanwhile, changes in stress and deformation affect pore structure and seepage behavior through the effective stress principle. The coupling among thermal, hydraulic, and mechanical processes in hydrate-bearing formations is inherently nonlinear and strongly interdependent. Temperature evolution directly controls hydrate stability and dissociation rate, while hydrate dissociation modifies phase saturation and pore structure, thereby altering permeability and pore pressure distribution. The resulting changes in pore pressure affect effective stress, which governs deformation and yielding of the formation skeleton. Meanwhile, mechanical deformation further influences seepage behavior by modifying pore volume and connectivity. Through continuous iteration of these processes, a positive feedback mechanism may develop, accelerating the degradation of mechanical properties and promoting wellbore instability. Through this iterative exchange of field variables, the model captures the strongly coupled and nonlinear nature of near-wellbore response in hydrate-bearing formations under drilling disturbance.

3 Numerical Solution and Validation of the Model

The hydrate production simulation experiment conducted by Masuda et al. is considered a classic and pioneering study in the field, and it has been widely used to validate the accuracy of mechanistic models for hydrate exploitation [14]. In this experiment, the system comprised water, gas, and hydrate within a porous sandy medium, and the temperature and pressure fields as well as the gas production volume during hydrate dissociation were recorded in real time. A comprehensive comparison between the model developed in this study and the Masuda experimental data was performed to validate the model's accuracy. During the validation process, identical initial and boundary conditions to those reported in the experiment were adopted to ensure consistency between the numerical model and laboratory observations. Key parameters governing hydrate dissociation kinetics, multiphase flow, and heat transfer were calibrated within physically reasonable ranges. The comparison focuses on cumulative gas production, which serves as an integrated indicator reflecting the coupled effects of thermal stimulation, phase change, and fluid flow.

Figure 1 shows a comparison of the cumulative gas production between the simulation results of this study and the experimental data from Masuda. The simulation

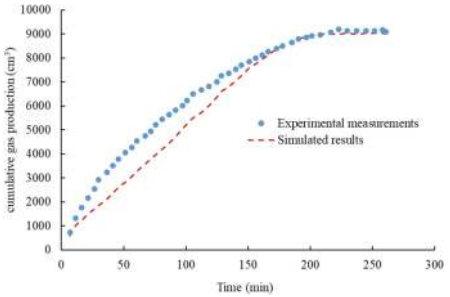

Fig. 1. Comparison of cumulative gas production.

results exhibit a high degree of agreement with the experimental data, with the error controlled within 13.8%. The overall trend and magnitude of gas production are well reproduced, indicating that the proposed model can effectively capture the dominant physical processes governing hydrate dissociation and fluid flow.

4 Results and Discussion

Based on the model established above, a numerical simulation study was conducted using data from a hydrate reservoir in the Shenhu area of the South China Sea. The basic parameters for drilling in the hydrate-bearing formation used in the simulation are listed in Table 1, and the mechanical property parameters of the hydrate reservoir are shown in Table 2.

Table 1. Basic parameters for drilling in the hydrate-bearing formation.

Parameter	Value	Parameter	Value
Porosity	0.373	Hydrate layer pressure (MPa)	14.752
Hydrate saturation	0.31	Hydrate layer temperature (°C)	14.817
Average permeability (mD)	20	Bottomhole pressure (MPa)	16.77
Wellbore radius (m)	0.12	Bottomhole temperature (°C)	15.92

During drilling in the hydrate-bearing formation, the temperature of the drilling fluid exceeding the in-situ phase equilibrium temperature of the hydrate is the direct cause inducing hydrate dissociation in the formation. This thermal disturbance originates primarily from the continuous circulation of drilling fluid, which serves as an effective heat transfer medium between the wellbore and the surrounding formation. As drilling progresses, the cumulative heat input gradually alters the original low-temperature environment required for hydrate stability, thereby triggering localized phase change processes in the near-wellbore zone. Figure 2 shows the temperature field distribution in the near-wellbore region during horizontal well drilling in the hydrate reservoir. As can be seen

Table 2. Mechanical property parameters of the hydrate reservoir.

Parameter	Value
Elastic Modulus (MPa)	32 (Sh = 0), 182 (Sh = 0.63)
Cohesion (MPa)	0.1 (Sh = 0), 2.0 (Sh = 1)
Poisson's Ratio	0.35
Dilation Angle (deg)	10
Thermal Expansion Coefficient	$1e{-}5$

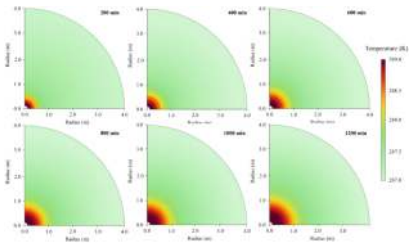

Fig. 2. Variation of temperature distribution around the wellbore during drilling in the hydrate-bearing formation.

from the figure, influenced by both drilling fluid invasion and convective heat exchange with the wellbore, the temperature of the hydrate formation gradually increases, causing progressive hydrate dissociation. The radius of thermal influence reaches approximately 1.23 m after 1200 min. These results indicate that thermal disturbance induced by drilling fluid circulation has a sustained and accumulative effect, providing the primary driving force for subsequent hydrate dissociation and multi-field coupling evolution. It is worth noting that the thermal disturbance exhibits a cumulative effect with drilling time. Unlike transient thermal shocks, continuous drilling fluid circulation maintains a persistent heat flux at the wellbore wall, causing the temperature front to propagate gradually into the formation. This sustained thermal input ensures that hydrate dissociation is not limited to the immediate vicinity of the wellbore, but progressively affects a broader zone, thereby amplifying subsequent hydraulic and mechanical responses.

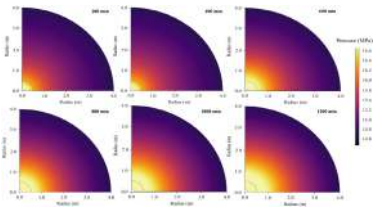

Fig. 3. Variation of pressure distribution around the wellbore.

Figure 3 illustrates the pressure field distribution around the wellbore during drilling in the hydrate reservoir. Over time, the range of pressure disturbance gradually expands. This expansion process reflects the combined effects of drilling fluid filtrate invasion and the evolution of formation permeability caused by hydrate dissociation. With the gradual opening of pore space and flow channels, fluid migration becomes more pronounced, allowing pressure perturbations to propagate deeper into the formation. Concurrently, due to the continuous dissociation of hydrate in the near-wellbore zone, the permeability increases exponentially, leading to a significant reduction in seepage resistance. Consequently, the pressure in the near-wellbore area gradually increases. After 2000 min, the pressure fluctuation can affect the outer boundary of the simulation domain (at a radius of 4 m). This phenomenon indicates that pressure evolution is not solely controlled by drilling fluid overbalance, but is also strongly influenced by hydrate dissociation-induced permeability enhancement. The coupling between pressure and permeability forms an accelerating mechanism: increased permeability facilitates pressure propagation, while pressure redistribution further promotes fluid migration, enlarging the disturbed zone around the wellbore.

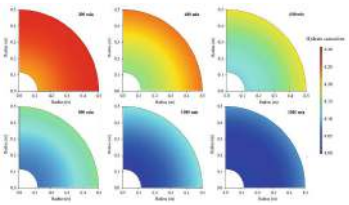

Fig. 4. Variation of hydrate saturation around the wellbore.

Hydrate dissociation in the formation is jointly influenced by in-situ temperature and pressure, and is also the fundamental cause of the degradation of the formation's mechanical properties. The reduction in hydrate saturation not only alters the pore-scale phase distribution but also fundamentally changes the load-bearing structure of the sediment skeleton. As hydrate acts as both a cementing agent and a load-supporting component, its dissociation directly weakens particle bonding and accelerates mechanical degradation in the near-wellbore region. Figure 4 shows the distribution of hydrate saturation in the near-wellbore zone of the hydrate reservoir at different times. On one hand, drilling fluid filtrate invasion increases the reservoir pore pressure to some extent, thereby raising the phase equilibrium temperature of the hydrate. On the other hand, under the influence of the high-temperature drilling fluid in the wellbore, hydrate around the well gradually dissociates, leading to a decrease in saturation. The simulation results show that after 2000 min of drilling, hydrate within 0.5 m of the wellbore is almost completely dissociated.

Drilling fluid circulation alters the physicochemical environment of the near-wellbore formation, triggering dynamic redistribution of the temperature, pressure, and stress fields. This process, accompanied by the migration of formation fluids, phase change dissociation of hydrate, and the response of the sediment skeleton, constitutes complex hydro-mechanical coupling. Figure 5 shows the evolution characteristics of

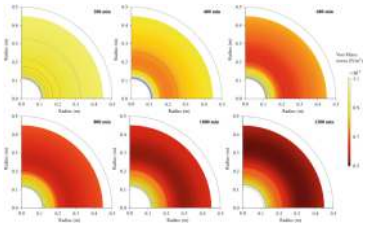

Fig. 5. Stress field distribution in the near-wellbore hydrate formation.

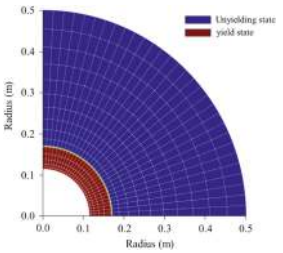

Fig. 6. Stress yield state around the wellbore after 1200 min.

the stress field in the near-wellbore hydrate formation during drilling. Under initial formation conditions, the overburden stress is mainly supported by the rock skeleton and solid hydrate particles. As hydrate dissociates, the cementation between hydrate and the pore matrix gradually weakens, and the shear strength of the formation decreases accordingly. When hydrate saturation decreases from the initial 0.31 to 0, the formation's shear strength drops from 3.24 MPa to 2.09 MPa. Simultaneously, after opening the hydrate reservoir, the release of in-situ stress and the increase in formation pore pressure cause a reduction in effective stress in the near-wellbore zone. All these factors cause the near-wellbore formation to evolve from elastic strain to plastic yield, with the effective plastic strain gradually increasing as hydrate dissociates, exacerbating wellbore instability. This progressive transition from elastic deformation to plastic yielding indicates that the mechanical response of hydrate-bearing sediments is highly sensitive to coupled thermal and hydraulic disturbances. Once yielding initiates, the redistribution of stress around the wellbore further accelerates deformation, forming a positive feedback mechanism that promotes the continuous expansion of the yielded zone. Figure 6 shows the yield zone around the wellbore at the 2000-min mark. As drilling fluid continues to invade, the range of temperature and pressure disturbance in the near-wellbore zone expands, hydrate gradually dissociates, and the mechanical properties of the formation progressively degrade, leading to the onset and continuous expansion of reservoir yielding. After 20 h, the wellbore yield enlargement rate reaches 91.68%.

The above results demonstrate that wellbore instability in hydrate-bearing formations is not governed by a single physical process, but rather by the strong coupling among thermal disturbance, fluid flow, hydrate phase change, and mechanical degradation. Thermal invasion caused by drilling fluid circulation serves as the initial trigger, which destabilizes hydrate and initiates dissociation in the near-wellbore zone. The

generated fluids subsequently alter pore pressure and seepage patterns, while the rapid increase in permeability further amplifies pressure propagation.

These hydraulic and thermal effects jointly accelerate the degradation of mechanical properties by reducing hydrate cementation and effective stress, ultimately leading to plastic yielding of the formation. The simulation results highlight the existence of a positive feedback mechanism, in which hydrate dissociation, permeability enhancement, pressure increase, and mechanical weakening mutually reinforce each other. This coupled evolution explains the rapid expansion of the yielded zone observed during drilling and underscores the necessity of considering fully coupled hydro-thermo-mechanical processes when evaluating wellbore stability in marine hydrate reservoirs.

5 Conclusions

- To address the wellbore stability issue during marine natural gas hydrate drilling, a fully coupled mathematical model integrating dynamic wellbore-reservoir heat and mass transfer, hydrate phase change, multiphase seepage, and geomechanical deformation under drilling fluid circulation conditions was established. The model calculation results were validated.
- Drilling fluid temperature is the key factor inducing hydrate dissociation. When the drilling fluid temperature exceeds the in-situ phase equilibrium temperature of the reservoir, the formation temperature around the wellbore gradually increases, leading to hydrate dissociation. The radius of thermal influence can reach 1.23 m after 1200 min.
- The pore pressure evolution and the seepage field undergo significant changes. Both drilling fluid invasion and gas release from phase change jointly affect the formation pressure field. The permeability in the near-wellbore zone increases markedly due to hydrate dissociation, leading to reduced seepage resistance and rapid expansion of the pressure disturbance range. After 2000 min, pressure fluctuations can reach the outer boundary of the simulation domain.
- Hydrate dissociation causes continuous degradation of the formation's mechanical properties, and the coupled multi-field interactions ultimately lead to wellbore instability. Under the combined effects of hydrate dissociation, increased pore pressure, and decreased effective stress, the near-wellbore formation evolves from elastic deformation to plastic yielding, with gradual accumulation of plastic strain. The simulation indicates a wellbore yield enlargement rate as high as 91.68% after 20 h, signifying a substantial risk of instability.

References

1. Boswell, R.: Is gas hydrate energy within research? J. Sci. **325**, 957 (2009). https://doi.org/10.1126/science.117507
2. Sun, J.X.: Characteristics of reservoir response to drilling and production in gas hydrate-bearing sediments in the South China Sea China University of Geosciences. Ph.D. Thesis (2018)

3. Ye, J.L., Qin, X.W., Xie, W.W., et al.: Main progress of the second gas hydrate trial production in the South China Sea. J. Geol. China. **47**(3), 557–568 (2020). https://doi.org/10.12029/gc20200301
4. Lei, L., Santamarina, J.C.: Physical properties of fine grained sediments with segregated hydrate lenses. J. Mar. Pet. Geol. **109**, 899–911 (2019). https://doi.org/10.1016/j.marpetgeo.2019.08.053
5. Li, Y.L., Liu, C.L., Liao, H.L., et al.: Mechanical properties of the mixed system of clayey-silt sediments and natural gas hydrates. J. Nat. Gas Ind. **40**, 159 (2020). https://doi.org/10.3787/j.issn.1000-0976.2020.08.013
6. Freij-Ayoub, R., Tan, C., Clennell, M.B., et al.: A wellbore stability model for hydrate bearing sediments. J. Pet. Sci. Eng. **57**(1–2), 209–220 (2007). https://doi.org/10.1016/j.petrol.2005.10.011
7. Cheng, Y., Li, L., Mahmood, S., et al.: Fluid-solid coupling model for studying wellbore instability in drilling of gas hydrate bearing sediments. J. Appl. Math. Mech. **34**, 1421–1432 (2013). https://doi.org/10.1007/s10483-013-1756-7
8. Wang, H., Chen, X., Jiang, M., et al.: Analytical investigation of wellbore stability during drilling in marine methane hydrate-bearing sediments. J. Nat. Gas Sci. Eng. **68**, 102885 (2019). https://doi.org/10.1016/j.jngse.2019.04.021
9. Sun, J., Ning, F., Lei, H., et al.: Wellbore stability analysis during drilling through marine gas hydrate-bearing sediments in Shenhu area: a case study. J. Pet. Sci. Eng. **170**, 345–367 (2018). https://doi.org/10.1016/j.petrol.2018.06.032
10. Rutqvist, J., Grover, T., Moridis, G.J.: Coupled hydrological, thermal and geomechanical analysis of wellbore stability in hydrate-bearing sediments. OTC Conf. (Houston, USA, May 2008), OTC, 19572 (2008). https://doi.org/10.4043/19572-MS
11. Li, Y., Liu, C., Liao, H., et al.: Mechanical properties of the clayey-silty sediment-natural gas hydrate mixed system. J. Nat. Gas Ind. B. **8**(2), 154–162 (2021). https://doi.org/10.1016/j.ngib.2020.08.002
12. Miyazaki, K., Yamaguchi, T., Sakamoto, Y., et al.: Effect of confining pressure on mechanical properties of sediment containing synthetic methane hydrate. J. Cryst. Growth. **126**(7), 408–417 (2011). https://doi.org/10.2473/journalofmmij.126.408
13. Rutqvist, J., Moridis, G.J., Grover, T., et al.: Coupled multiphase fluid flow and wellbore stability analysis associated with gas production from oceanic hydrate-bearing sediments. J. Pet. Sci. Eng. **92-93**, 65–81 (2012). https://doi.org/10.1016/j.petrol.2012.06.004
14. Li, X., Wang, Y., Duan, L., et al.: Experimental investigation into methane hydrate production during three-dimensional thermal huff and puff. J. Appl. Energy. **94**, 48–57 (2012). https://doi.org/10.1016/j.apenergy.2012.01.024

Energy-Efficient Facade Retrofit for Xi'an Campus Buildings: A Optical Daylighting Approach – A Case Study of the Affiliated Middle School of Xi'an University of Architecture and Technology

Ruixin Li and Xianglong Tang(✉)

Lanzhou Jiaotong University, Gansu, China 730070
tangxl@mail.lzjtu.cn

Abstract. Urban development is now focused on updating existing resources. In cold regions, campus buildings often have problems with too little daylight in winter and too much glare in summer. This study takes typical campus buildings in Xi'an as an example to construct a research framework of "subjective evaluation, dynamic simulation, and solution verification". The real feelings of teachers and students towards the light environment were collected through questionnaire surveys. Combined with the dynamic lighting simulation of the Rhino-Grasshopper platform the light and thermal environment characteristics of the existing building facades in different seasons were systematically evaluated. The results show that the core demands of teachers and students are glare control and uniform lighting. The research proposed a combined strategy of "window optimization plus dynamic shading", and the results confirm that the adjustable hybrid shading system successfully maintains the summer daylight glare index below 0.35, while increasing the illuminance in the rear zone to above 150 lx during winter, thereby achieving a synergistic optimization of photothermal performance. This study provides an empirical design paradigm that takes into account both energy-saving efficiency and human-oriented needs for the renewal of campus building stock in cold regions by deeply integrating user perception with climate-adaptive design.

Keywords: Daylighting environments · Campus buildings · Energy retrofit · Dynamic shading · User perception

1 Introduction

Urban construction enters the stage of updating existing resources. Campus buildings in cold regions are confronted with the core contradiction of insufficient winter lighting and excessive glare in summer. However, most of the existing research focuses on static simulation and the optimization of individual technologies. They lack systematic analysis based on the real light experience of users, resulting in a disconnection between the renovation strategies and the actual needs [1].

© The Author(s), under exclusive license to Springer Nature Switzerland AG 2027
G. Feng et al. (Eds.): ICCE 2025, SUCI, pp. 92–105, 2027.
https://doi.org/10.1007/978-3-032-32237-1_7

For this reason, this study takes typical campus buildings in Xi'an as an example and proposes a collaborative design method of "window optimization plus dynamic shading" through the combination of subjective evaluation and dynamic simulation. This method aims to achieve humanized regulation and energy-saving improvement of the light environment, and provide a solution that takes into account policy, climate and usage requirements for building renovation in cold regions. By bridging the gap between occupant experience and parametric environmental analysis, this research endeavors to deliver a more responsive and evidence-based retrofit strategy.

2 Case Overview and Research Method

2.1 Site Overview

The research site is located in a cluster of campus buildings in the old urban area of Xi'an. It is dominated by row house style multistory buildings, built in the 1990s and utilitarian in design, and multistory buildings which have occurred since 2010. This represents an age-span of facades and thermal-daylighting design strategies. The climate of the site is temperate semi-humid continental. The winter is cold and dry and the increased smog reduces the natural light due to the haze. The summer is hot, with high solar radiation so that glare and worse reflection on the blackboards and desks occurs.

The first survey found some problems in classrooms. The east side is too dark, and it's too bright in summer. Desks far from the windows don't get enough light. In summer, the rooms are too hot, and in winter, they are dry and cold. The renovation needs to balance the two sides, one is the building's history and the other is light and heat performance. It should solve the small windows and simple shading problems. The preliminary site investigation identified several environmental issues in the classroom: uneven daylight distribution with areas of insufficient illumination away from windows, excessive brightness in summer, and thermal discomfort characterized by overheating in summer and dry cold conditions in winter. Consequently, the retrofitting strategy must balance heritage conservation with synergistic light and thermal optimization, specifically addressing problems such as the reduced window-to-wall ratio and oversimplified shading design, thereby providing a basis for subsequent dynamic design.

2.2 Research Method

This study applies a step-by-step framework, in which we measure the data and simulate real conditions, see Fig. 1. First, a survey is conducted to gather feedback from teachers and students about the lighting and thermal environment. This helps identify the main renovation needs [1]. Secondly, a parametric model was constructed based on the Rhinos-Grasshopper platform. Through the Ladybug and Honeybee plugins, combined with the typical meteorological year data of Xi'an, dynamic daylighting environment simulation was carried out [2], and the daylighting coefficient, glare index and temperature distribution in winter and summer under the original state were quantitatively analyzed. Furthermore, multiple comparison schemes (such as window-to-wall ratio adjustment, low-emissivity glass, vertical and horizontal shading, etc.) [3] were set up to conduct

dynamic simulation verification and evaluate the improvement effects of each strategy on the photothermal performance; Ultimately, by integrating subjective preferences and objective simulation results for multi-objective optimization, a renovation strategy of "adjustable shading + exterior window coordination" that takes into account both energy-saving efficiency and human-oriented needs is proposed, providing systematic methodative support for the renewal of campus buildings in cold regions.

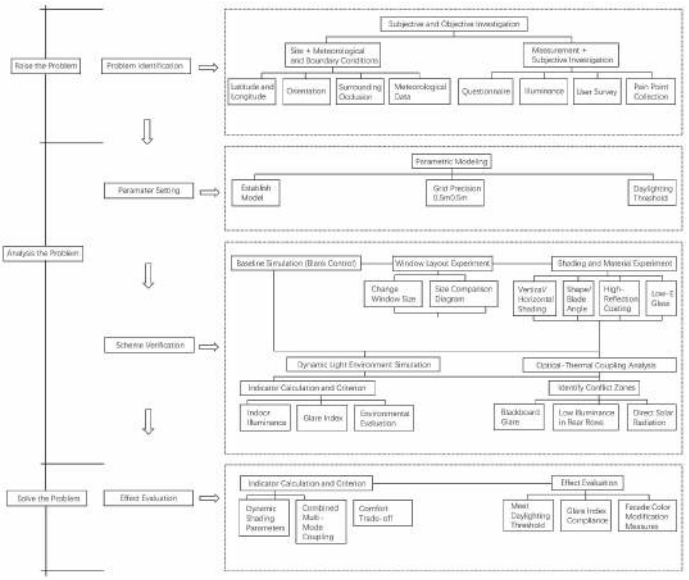

Fig. 1. Technical route of the study.

This mixed-methods approach ensures that the technical solutions are not only performance-driven but also aligned with the occupants' lived experiences and comfort priorities. The parametric model allowed for the iterative testing of a wide range of design variables, moving beyond conventional static analysis to capture the temporal dynamics of environmental conditions.

3 Daylighting Environment Evaluation and Survey Analysis

3.1 Subjective Evaluation Survey on Visual Comfort of the Daylighting Environment

The survey moves from personal feelings to renovation needs. Seeing Table 1, it looks at natural light, glare, and thermal comfort. The analysis of 73 valid questionnaires collected shows that the main problems of satisfaction with natural lighting (average 3.4/5) are glare and insufficient rear illuminance. The issue of temperature comfort is the low temperature in winter mornings and the excessive heat in summer afternoons, with an average of 3.7/5. Teachers pay more attention to whether the light is uniform

or not, while students are more sensitive to glare. This divergence in priorities may stem from their different roles and primary tasks within the classroom; teachers often need to see the entire room clearly to monitor students, whereas students are focused on their desks and reading materials, making them more vulnerable to direct and reflected glare, see Fig. 2. Light-colored reflective materials and adjustable shading systems are currently the mainstream renovation preferences. The preference for adjustable systems highlights a desire for user control over the indoor environment.

Table 1. Scoring standards corresponding to questionnaire evaluation levels.

Statistical Score/ Evaluation Level	2	1	0	−1	−2
Satisfaction with Indoor Daylighting Environment	Very Satisfied	Relatively Satisfied	Neutral	Relatively Dissatisfied	Very Dissatisfied
Uniformity of Indoor Daylighting	Very Uniform	Relatively Uniform	Neutral	Relatively Non-Uniform	Very Non-Uniform
Thermal Comfort Indoors	Very Comfortable	Relatively Comfortable	Neutral	Relatively Uncomfortable	Very Uncomfortable
Satisfaction with the Energy-Saving Effect of the Current Façade Design	Very Satisfied	Relatively Satisfied	Neutral	Relatively Dissatisfied	Very Dissatisfied

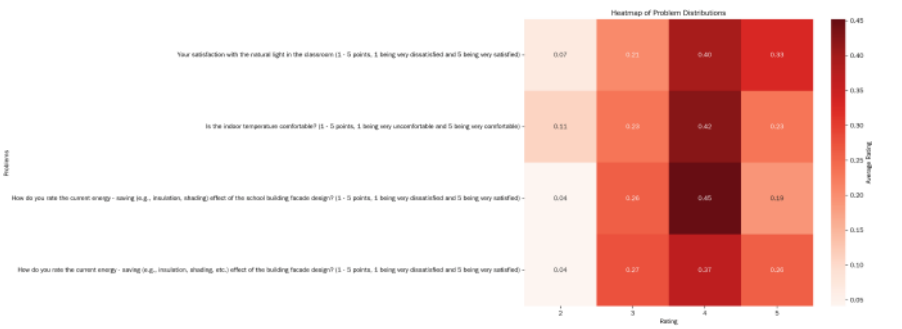

Fig. 2. Heatmap of questionnaire item distribution.

The results suggest break the traditional ways of dealing with lighting and thermal issues. Also, it should go back to what users truly care about. And improve daylighting design to solve the "dark back row" problem. Use dynamic shading to deal with "direct sunlight glare". Consequently, the retrofit strategy must be capable of operating in multiple modes, providing diffuse light penetration for uniformity when needed and sharp cut-offs for glare protection at other times, a flexibility that static shading systems cannot offer. Therefore, the design strategy must be multi-faceted, tackling both the quantitative issue of illuminance levels and the qualitative issue of visual discomfort.

3.2 Reliability and Validity Test

The factor structure in this study shows the core needs of teachers and students for the light-thermal environment. The order is: glare control, lighting uniformity, and temperature comfort. These results confirm the questionnaire's validity, and also clear the renovation priorities.

The test showed that the questionnaire has high reliability, with a Cronbach's α of 0.906, good structural validity, with KMO is 0.78 (a cumulative variance explanation of 75%). The reliability is supported by confirmatory factor analysis (AVE = 0.564, CR = 0.83). It shows the core needs of teachers and students for the light and thermal environment, ranked as glare control, lighting uniformity and temperature comfort. This result helps clarify the renovation priorities. The robust statistical validity of the survey instrument reinforces the credibility of the identified user needs. This data-driven hierarchy of comfort criteria—glare control being paramount, followed by lighting uniformity and thermal comfort—provides a clear and justified sequence for prioritizing intervention measures in the retrofit design. The high internal consistency of the survey results (Cronbach's $\alpha > 0.9$) indicates that the respondents' perceptions of the different environmental factors are coherent and reliable, strengthening the validity of the derived design priorities. The clear factor structure that emerged from the analysis, with items cleanly loading onto the three identified constructs (glare control, uniformity, thermal comfort), indicates that these are distinct yet critical dimensions of the occupants' environmental experience.

3.3 Regression Analysis

The interaction mechanism between the light and heat factors are explained by regression analysis. The result shows that the clear synergy effect between the two, see Fig. 3. This provides a clear systematic design path and shows two key causal chains.

(1) Improvement of sunshade design. The result of regression analysis found that improve the sunshade design can solve both the glare and the radiant heat. The design directly solve the glare pain problem that users are most concerned about. It also prevent the heat from solar radiation in summer. This indicates that the top priority in addressing the summer brightness issue is to improve the shading system. Consequently, shading is not merely a visual comfort element but a crucial component for thermal management. The regression model quantitatively links specific shading design parameters to reductions in both glare index and cooling load,

providing a dual-justification for its implementation. This dual benefit is economically significant, as it means the cost of an improved shading system can be offset by savings from both improved visual comfort (potentially reducing eyestrain and improving productivity) and reduced mechanical cooling energy.

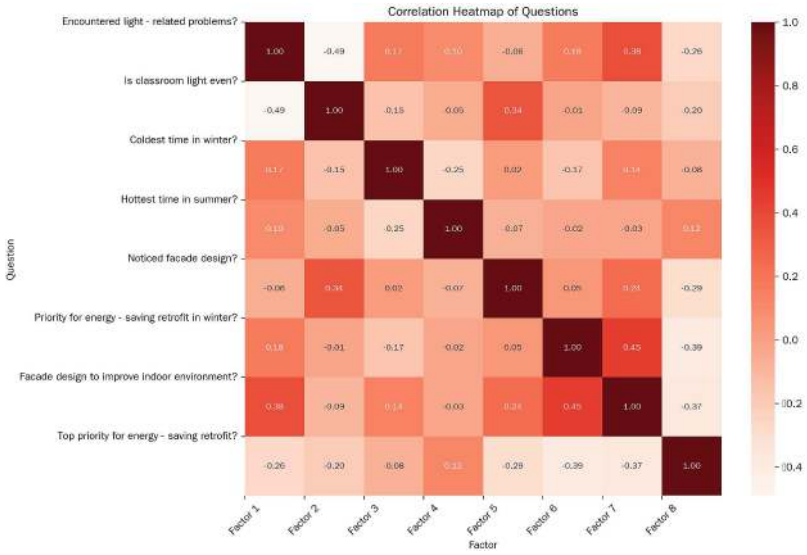

Fig. 3. Heatmap of correlation coefficients of questionnaire items.

(2) Optimization of the lighting layout. The study found that optimizing the lighting layout can reduce lighting energy consumption. It will indirectly enhances thermal comfort. This finding broadens daylighting design. It moves beyond visual comfort to energy management and thermal environment optimization. This aligns well with the study's focus on energy-saving renovation. For instance, a 10% improvement in daylighting autonomy was correlated with a predictable reduction in lighting energy use, which in turn showed a measurable impact on reducing the internal heat gain, particularly during the shoulder seasons. This reveals the interconnected nature of energy efficiency and occupant comfort in building design.

The above analysis indicates that a systematic strategy needs to be adopted, coordinating dynamic shading and lighting design to resolve the contradiction of dark in winter and bright in summer. This synergy suggests that investments in high-performance, adaptive building envelopes can yield compounded benefits across comfort and energy domains, improving the overall return on investment for retrofit projects.

4 Simulation Analysis of the Original Daylighting Environment

To accurately evaluate the light environment performance of campus buildings in Xi'an in their original state, this study, based on the Rhino-Grasshopper platform and combined with Ladybug and Honeybee plugins [4], constructed a complete parametric dynamic daylighting simulation workflow, mainly including the following core links:

Firstly, based on the on-site mapping drawings, an accurate geometric model of a typical classroom is established in Rhino, and optical properties of the materials, such as a transmittance of 0.82 for ordinary glass and a reflectance of 0.7 for white walls, etc. are assigned as the physical basis for the simulation.

Subsequently, the typical meteorological year (TMY) data of Xi'an was imported through the Ladybug plugin, and parameters such as the solar path, direct radiation and scattered radiation intensity were read to provide real climate-driven for dynamic simulation [5]. Based on this, this study establishes a circular framework for calculating the position of the sun and ray tracing on a daily basis. Set the simulation parameters through Honeybee, namely a time step of 1 h and 10,000 ray tracing per square meter. Subsequently, the light environment at three typical moments, namely 10:00, 12:00, and 17:00, was analyzed in detail. The results show that the spatiotemporal heterogeneity of the light environment is significant under the condition of no shading. For example, the illuminance ratio between the area closest to the window and the rear area could exceed 20:1 at certain times, creating a highly uneven visual field and forcing occupants' eyes to constantly readjust. Such extreme contrast ratios are known to cause visual fatigue and reduce reading speed and comprehension, directly impacting the primary function of the classroom as a learning space. The illuminance distribution at 10:00 is extremely uneven, with less than 150 lx in the far window area. At 12:00, the glare was severe, with a DGP > 0.35. At 17:00, the westward sunlight brings excessive illuminance and radiant heat. This temporal variation underscores the need for a responsive, rather than static, shading solution. The simulations made it clear that any fixed shading geometry would be a compromise, necessarily sacrificing performance at one time of day or season to achieve adequacy at another.

This dark in winter and bright in summer problem of light reveals the lack of coordination in the facade's shading and lighting. It also highlights the necessity of performance optimization based on parametric dynamic light simulation [6]. The simulation quantitatively confirmed the "winter-dark, summer-bright" paradox inherent in the existing façade design. This spatiotemporal performance contradiction underscores a fundamental lack of coordination between the building's fenestration and its solar shading mechanisms. The findings powerfully demonstrate the limitations of a static façade and validate the critical need for a dynamic, climate-responsive optimization approach, which can only be thoroughly investigated through parametric and time-series simulation techniques. The simulations thus served as a virtual laboratory, allowing for the precise diagnosis of environmental problems and the testing of potential solutions without the cost and disruption of physical mock-ups.

5 Design Schemes and Simulation Results

5.1 Design Schemes

The hybrid shading system works well, combining the optimization of vertical and horizontal blinds [7].

This study first compared the hybrid shading system with blank group that had no shading. Then, the study clarifies the need for shading. It shows that vertical and horizontal shading help reduce glare, prevent overheating in summer, and address insufficient lighting in winter. The study also quantifies how different shading types optimize the lighting coefficient, glare index, and temperature control [8]. This comparative methodology is crucial for identifying the most effective configuration.

This indoor light adjustment may involve the setting positions, the opening size of door and window, and the positioning of blinds and sun visors [9]. This study used Honeybee to assess the dynamic performance and design of adjustable shading systems. It simulated the light environment of low-emissivity glass vertical blinds and aluminum horizontal blinds. Different angles and times were considered. The glasses' performance in daylighting, glare control, and heat radiation blocking is compared. Material properties, such as the reflectivity of aluminum and the thermal properties of low-e glass, were key parameters in these simulations. The iterative simulation process allowed for the optimization of these parameters; for instance, a balance was found between a high enough reflectivity to enhance daylight penetration and a low enough specularity to avoid creating new, localized glare spots from the louvers themselves. For instance, the specular reflectivity of the aluminum louver surfaces was tuned in the model to explore its impact on redirecting light deep into the room, while the low-e coating's solar heat gain coefficient (SHGC) was critical for assessing its contribution to reducing summer cooling loads.

5.2 Simulation Results

Blank Control Group. Seeing Fig. 4. To clarify the necessity of shading measures, the study compares a control group without any shading to groups using vertical and horizontal shading. The control group shows a clear periodic contradiction in the lighting environment. From 10:00 to 17:00 in summer, the indoor daylighting coefficient remains high. It peaks at 1352.79. This causes severe glare. The glare index exceeds the comfortable threshold of 0.35. As a result, there is strong thermal discomfort. In winter, due to the window design and lack of shading, the daylighting coefficient indoors is low, leading to a reliance on artificial lighting. This reliance not only increases energy consumption but also introduces a qualitatively different light spectrum and distribution, which can affect the atmosphere and visual quality of the classroom. The control group simulation thus established a clear performance baseline and quantified the 'cost of inaction', providing a strong economic and environmental incentive for proceeding with the proposed retrofit measures.

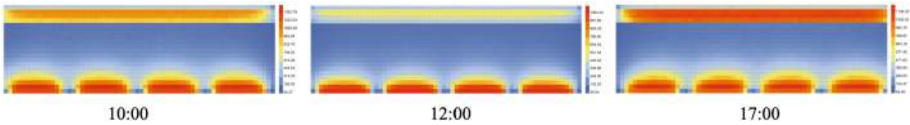

Fig. 4. Indoor daylighting environment at 25° without shading.

Vertical Shading System.

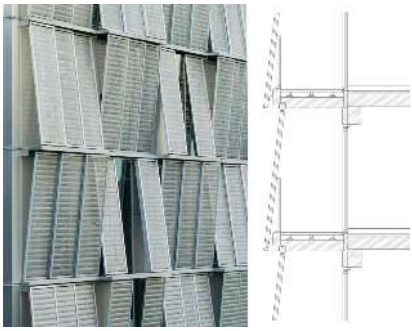

Fig. 5. Vertical shading system design diagram.

(1) Louvers with larger openings at the top and smaller openings at the bottom: Simulation results show that the "large-top, small-bottom" louver design works well with the changing solar angles throughout the day. At 10:00, it provides enough uniform daylight without causing glare. At 12:00, it reduces peak daylight and avoids direct glare. At 17:00, during west-facing exposure, it keeps the daylighting balanced and reduces radiant heat, showing good adaptability all day. Seeing Figs. 5 and 6.
(2) Louvers with smaller openings at the top and larger openings at the bottom: Simulation results show that the "small-top, large-bottom" louver design is most effective at blocking direct sunlight at 12:00, preventing glare. However, it results in medium or low daylight levels throughout the day, including at 10:00 and 17:00. This shows that it sacrifices overall daylight to control glare at midday. Seeing Fig. 7.
(3) Louvers with mixed opening sizes as shown in the combined layout: Simulation results demonstrate that the mixed-opening louver design, through dynamic configuration of blade combinations, exhibits superior control over the daylighting–thermal environment. At 10:00, it balances illuminance and uniformity; at 12:00, it simultaneously ensures glare control and brightness in core areas; and at 17:00 during west-facing exposure, it balances natural light admission with radiant heat blocking. This design keeps the indoor environment within a suitable range at different times of the day, proving its high flexibility and overall performance. Seeing Fig. 8.

Looking at the simulation results for three time periods, vertical shading has the best opening designs for each time. At 10:00, large-top, small-bottom openings are ideal for

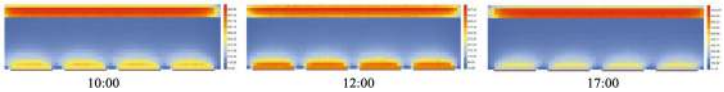

Fig. 6. Indoor daylighting environment with louvers all tilted upwards at 25°.

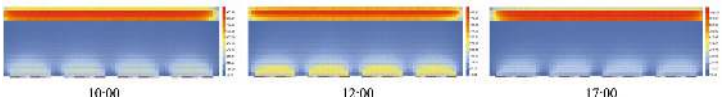

Fig. 7. Indoor daylighting environment with louvers all tilted downwards at 25°.

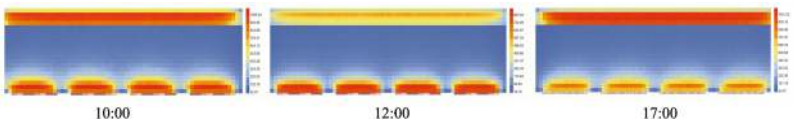

Fig. 8. Indoor daylighting environment with mixed louver angles.

providing enough uniform daylight. At 12:00, small-top, large-bottom openings are better for blocking strong sunlight and preventing glare. At 17:00, mixed openings work best for west-facing exposure. Therefore, designing shading panels with adjustable angles allows them to adapt to the changing solar angles, creating optimized daylighting for all times and meeting campus teaching needs. The optimal angle for vertical louvers was found to vary by over 30° between the morning and afternoon, underscoring the significant performance gain achievable with adjustability compared to a fixed configuration in Fig. 9.

Horizontal Shading.

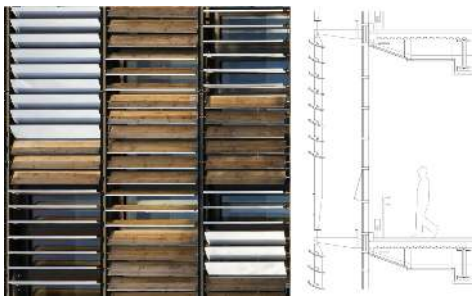

Fig. 9. Horizontal shading system design diagram.

(1) Louvers Tilted Upwards: Simulation results show that horizontal aluminum louvers tilted upward by 25° perform well in regulating daylight. At 10:00, they allow enough

natural light to meet basic illumination needs. At 12:00, they block part of the strong light to prevent glare while maintaining reasonable illuminance. By 17:00, during west-facing exposure, they still block some oblique sunlight, reducing radiant heat gain, and thus maintain a stable light environment throughout the day. Seeing Fig. 10.

(2) Louvers Positioned Horizontally: The horizontal shading at 10:00 has a relatively gentle light incident Angle. The horizontal leaves block less light, allowing more natural light to be introduced, and the light transmission coefficient is at a relatively high level. At 12:00, the horizontal leaves have limited shielding from strong light, which can easily lead to local glare and a relatively high peak of light transmission. At 17:00, the blades can block the oblique light to a certain extent, but the overall heat control effect is not as good as that of the design with adjustable angles. Seeing Fig. 11.

(3) Louvers Tilted Downwards, Opening at Approximately 25° Relative to the Horizontal: At 10:00, the incidence angle of sunlight is small, and the downward-tilted louvers block natural light more significantly, leading to a relatively low daylighting coefficient and possible insufficient illumination indoors. At 12:00, this angle effectively intercepts direct strong sunlight, with good glare control performance, but also results in relatively dim conditions in some areas. At 17:00, the blocking effect against oblique sunlight is significant, reducing radiant heat transmission, but at the expense of overall indoor brightness. Seeing Fig. 12.

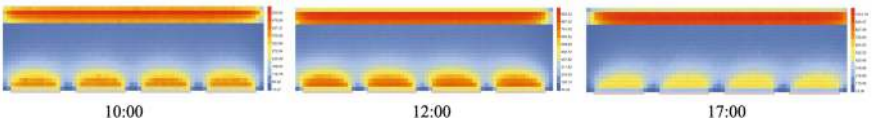

Fig. 10. Indoor daylighting environment with louvers tilted upwards at 25°.

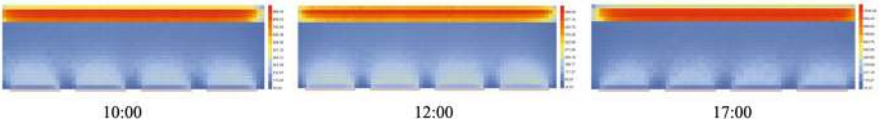

Fig. 11. Indoor daylighting environment with louvers positioned horizontally at 25°.

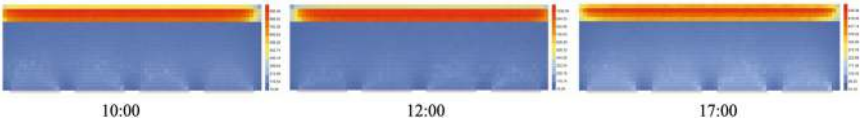

Fig. 12. Indoor daylighting environment with louvers tilted downwards at 25°.

(4) Mixed Louver Arrangement: The simulation results show that the mixed layout of horizontal shading has good dynamic adaptability. It can balance the uniformity of lighting at 10:00, effectively block direct strong light and maintain the illuminance of the core area at 12:00. At 17:00, it manages both light entry and thermal radiation blocking. This helps maintain a stable lighting environment throughout the day. Therefore, the horizontal shading of aluminum alloy louvers has the optimal angles at different times. At 10:00, the blades are tilted upwards by 25° for sufficient lighting. At 12:00, they are tilted downwards by 25° for good anti-glare effect, and at 17:00, they are placed in a mixed manner to balance lighting and heat control. The simulation of horizontal louvers also highlighted their effectiveness in blocking high-angle summer sun while permitting the penetration of lower-angle winter sun, a passive solar design principle that is automatically leveraged through seasonal adjustment. Seeing Fig. 13.

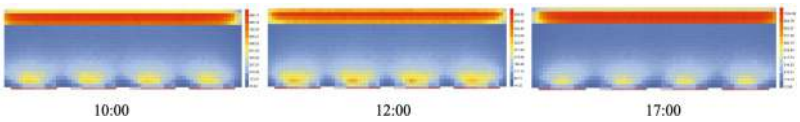

Fig. 13. Indoor daylighting environment with mixed horizontal louver angles.

Seeing Table 2, research shows that the contradiction between light and heat stems from the conservative design of exterior Windows and the extensive shading. The core demands of teachers and students are mainly focused on glare control, uniform lighting and temperature comfort [10]. The simulation verified the effectiveness of the "resize the window plus move the shade" scheme. The adjustable vertical and horizontal sunshades can adapt to changes in the sun's Angle. In winter, the rear row illuminance can reach over 150 lx, and in summer, the glare index can be controlled below 0.35, while reducing energy consumption. Among them, the sunshade form with a hybrid opening and adjustable Angle performs the best and meets users' preferences. This performance alignment with user preferences strengthens the practical relevance and potential acceptance of the proposed retrofit solution. The fact that the best-performing technical solution (hybrid-adjustable) also corresponds to the user-expressed preference for 'adjustable systems' greatly increases the likelihood of successful implementation and long-term user satisfaction, avoiding the common pitfall of post-occupancy tampering or disuse of building technologies.

Table 2. Comparison of simulated data results after assuming the sunshade device.

Before		After						
	Without Shading	Vertical Shading System			Horizontal Shading System			Vertical and Horizontal System
	No Angle	Upwards at 25°	Vertical	Downwards at 25°	Upwards at 25°	Horizontal	Downwards at 25°	Mixed Angles
10:00	55.27–1352.79	23.65–982.99	22.47–1025.24	22.71–985.48	13.27–530.82	16.22–986.45	19.99–985.48	16.32–986.17
12:00	39.54–1064.34	16.98–527.52	16.18–803.42	16.04–527.81	24.22–983.22	14.57–528.59	16.09–1036.58	14.32–528.24
17:00	48.49–1106.32	21.24–1034.97	20.07–1031.22	19.43–1030.17	13.2–1031.16	13.37–1032.33	18.18–529.38	12.89–1024.99

6 Conclusion

In conclusion, this study provides a practicable solution for the energy-saving renovation of campus buildings in cold regions. More importantly, it has initiated a brand-new research paradigm, deeply integrating subjective user perception with objective performance simulation.

This study proposes the "policy - experience - climate" plan, which provides a renovation model for campus buildings in cold regions. It can take into account both energy conservation and humanistic culture [11]. This also practices and deepens the concept of the Green Campus Evaluation Standard [12]. It also provides a technical framework and empirical basis for the optimization of the building light environment in similar climate zones. Future research will build on this foundation, further expand the universality and application potential of this framework through cross-climate zone empirical verification, long-term data monitoring and intelligent control integration, and jointly strive to provide a more sustainable, comfortable and intelligent environment for the next generation of buildings, thereby contributing solid scientific strength to China's green urban renewal.

This study ultimately underscores that the future of building retrofit lies not only in higher-performing materials and components but in smarter, more adaptive systems that are deeply informed by and responsive to the people who use the buildings every day.

Figure 4 (color image): The young lady selling aluminum panels. The beauty of architectural design Curtain wall aluminum veneer sunshade series (2024-05-20).[http://xhslink.com/m/P7Q35pclhg]

Figure 8 (color image): vangough. Curtain wall design and details of the new mechanical building at EPFL in Lausanne (2025-11-18). [http://xhslink.com/m/1UL7VTNaNIQ]

References

1. Wang, L., Wang, Y., Fei, F., et al.: Research hotspots and trend analysis of thermal environment in Chinese campus buildings based on CiteSpace J. Chin. J. Sch. Health. **43**(6), 925–929 (2022). https://doi.org/10.16835/j.cnki.1000-9817.2022.06.030
2. Wang, X., et al.: Study on the relationship between natural daylighting and visual comfort in classrooms J. Build. Sci. **34**(6), 72–79 (2018)
3. Mardaljevic, J., Heschong, L., Lee, E.: Daylight metrics and energy savings J. Light. Res. Technol. **41**(3), 261–283 (2009). https://doi.org/10.1177/1477153509339703
4. Zhang, A., Bokel, R., van den Dobbelsteen, A., et al.: Optimization of thermal and daylight performance of school buildings based on a multi-objective genetic algorithm in the cold climate of China J. Energy Build. **139**, 371–384 (2017). https://doi.org/10.1016/j.enbuild.2017.01.048
5. Chen, Z., Cui, Y., Zheng, H., et al.: A case study on multi-objective optimization design of college teaching building atrium in cold regions based on passive concept J. Buildings. **13**(9), 2391 (2023). https://doi.org/10.3390/buildings13092391
6. Luo, J., Yan, G., Zhao, L., et al.: Evaluation of design parameters for daylighting performance in secondary school classrooms based on field measurements and physical simulations: a case study of secondary school classrooms in Guangzhou J. Buildings. **14**(3), 637 (2024). https://doi.org/10.3390/buildings14030637

7. Tzempelikos, A., Athienitis, A.K.: The impact of shading design and control on building cooling and lighting demand J. Sol. Energy. **81**(3), 369–382 (2007). https://doi.org/10.1016/j.solener.2006.06.015
8. Liu, B., Liu, Y., Xin, Q., et al.: Energy-efficient design of immigrant resettlement housing in Qinghai: solar energy utilization, sunspace temperature control, and envelope optimization J. Buildings. **15**(9), 1434 (2025). https://doi.org/10.3390/buildings15091434
9. Affa, N.Y., Yoon, G., Sato, T.: Energy savings for a junior high school classroom that actively uses daylighting and sensitivity study on the effect of the building envelope thermal performance J. Japan Archit. Rev. **5**(4), 609–620 (2022). https://doi.org/10.1002/2475-8876.12281
10. Gunay, H.B., O'Brien, W., Beausoleil-Morrison, I.: A critical review of observation studies, modeling, and simulation of adaptive occupant behaviors in offices J. Build. Environ. **70**, 31–47 (2013). https://doi.org/10.1016/j.buildenv.2013.07.020
11. Lakhdari, K., Sriti, L., Painter, B.: Parametric optimization of daylight, thermal and energy performance of middle school classrooms, case of hot and dry regions J. Build. Environ. **204**, 108173 (2021). https://doi.org/10.1016/j.buildenv.2021.108173
12. Ministry of Education, Center for School Planning, Construction and Development: Green Campus Evaluation Standard (T/CSUS 04–2020). China Architecture & Building Press, Beijing (2020)

Corner Effect-Driven Spatiotemporal Deformation Mechanisms of Retaining Structures in Soft Soil Deep Excavations

Ying Liu(✉) and Binhui Xiang

School of Civil and Architectural Engineering, Jiangxi University of Water Resources and Electric Power, Nanchang 330099, China
28152680@qq.com

Abstract. Based on a deep excavation project in a densely urban area of Shanghai, this study investigates the spatiotemporal characteristics of deep excavation-induced deformation by analyzing field data concerning the planar features of pit geometry and sensor layout. Special emphasis is placed on examining the influence patterns of convex and concave corners on deformation behavior. The results show that: (1) Soil excavation-induced unloading leads to progressive development of retaining structure deflection and surrounding soil displacement, particularly with intensified deformation observed during the excavation of deep soil layers. This indicates that controlling deformation caused by the excavation of deep soils is crucial for the overall performance of a deep excavation. (2) Significant spatial effects are observed in lateral wall deflection and ground settlement: displacements near the corners are restrained significantly due to enhanced structural stiffness of the areas. The maximum lateral displacement at corner areas reduces by 50% compared to mid-span sections, while ground settlement decreases by 47.75%. (3) Vertical displacement of column piles exhibits distinct spatial distribution patterns, showing significantly greater heave values at central positions compared to peripheral locations. These findings provide valuable references for similar excavation projects in soft soils as well as underground space development in urban environments.

Keywords: Deep foundation pit · Corner · Field measurement · Enclosure structure · Spatiotemporal effect

1 Introduction

With the process of urbanization in China, urban areas expand continuously, leading to diminishing availability of usable land. To alleviate land resource shortage, the development of underground and high-rise spaces has become an effective strategy, resulting in a surge of deep excavation projects [1–7]. However, as urban service infrastructure becomes increasingly sophisticated, complex networks of pipelines and utilities crisscross beneath cities, leaving limited construction space and permissible disturbance

© The Author(s), under exclusive license to Springer Nature Switzerland AG 2027
G. Feng et al. (Eds.): ICCE 2025, SUCI, pp. 106–119, 2027.
https://doi.org/10.1007/978-3-032-32237-1_8

zones for underground projects. Therefore, underground constructions such as deep excavations are often situated within densely built environments, where minor errors during construction may induce instability of retaining structures or severe damage to adjacent infrastructures, leading to substantial economic losses and adverse social impacts [8–12]. Incidents of excavation instability causing catastrophic accidents are not uncommon. On December 29, 2018, a partial soil collapse occurred at a construction site near Xinlong Road in Qibao Town, Minhang District, Shanghai, resulting in three fatalities. On April 10, 2019, a local collapse during excavation at the B2 plot of the Guxinyuan Resettlement Community in Guangling District, Yangzhou, claimed five lives and injured one. On December 30, 2023, a foundation pit collapsed during the renovation of a combined sewer network and urban flood control project in the Daming Lake drainage area of Jinan, causing three deaths. More recently, on June 1, 2024, a collapse at a construction site in Zhangjiang Central District, Pudong New Area, Shanghai, led to one fatality. These incidents underscore that despite decades of development and accumulated engineering experience, deep excavation projects remain high-risk endeavors. Research on deformation behavior and early-warning systems for deep excavations remains a critical challenge requiring urgent resolution.

Deep excavation-related problems worldwide have been studied thoroughly by numerous researchers [13–18], and the corresponding mechanisms have been relatively well developed. In terms of the spatiotemporal effects of deep excavation, Liu Jianhang and Hou Xueyuan have proposed the spatiotemporal effect theory of deep excavations based on extensive practical experience in Shanghai as early as the 1990s. This theory emerged from the unique geological conditions of Shanghai, where excavations are situated in deep sedimentary zones with pronounced soil creep behavior, and thus significant spatiotemporal effects. Based on this theory, Guo et al. [19] assessed the effects of soil creep, emphasizing observational analysis, parametric simulation, displacement control, and measure optimization to mitigate the long-term deformation of deep supported excavations. Subsequently, many scholars and engineers [20–24] further explored the temporal-spatial effects of excavation deformations using different methods. For example, Wu et al. [25] developed a three-dimensional numerical model to systematically analyze the creep behavior of soft soil, the changes in adjacent structures and ground settlement, as well as the spatiotemporal effects during soft soil excavation. Lin et al. [26] employed numerical simulation to analyze the spatiotemporal evolution patterns of deformation in the foundation pit support structures, as well as the changes in ground surface settlement and internal forces within the supports during excavation. Roy et al. [27] conducted an experimental study on time-dependent ground settlement behind supported excavations in soft clay using a geotechnical centrifuge, and utilized the test results to predict the impact of construction delays on several key factors, including the rate of settlement and the evolution of the affected zone behind the retaining wall. He et al. [28] conducted a case study on an ultra-large deep excavation in soft clay, analyzed several possible factors leading to excessive ground movement, and pointed out that excessive lateral wall displacement and ground surface settlement were induced by the excavation. Tan Yong et al. [29] summarized the field data from nine metro-station pits in Shanghai, and investigated the potential corner effects (i.e., the retaining walls near pit corners have stronger capabilities to resist deformation than those distant away as a product of

spatial arching effects across the pit corners) of long and narrow multiproped metro station excavations. Previous studies elucidated temporal-spatial deformation patterns and mechanisms of deep excavations in soft soil [30]. However, contemporary urban developments increasingly involve irregularly shaped excavations with multiple convex and concave corners within dense building clusters. The deformation mechanisms of such excavations exhibit more complex temporal-spatial behaviors, yet systematic analyses of these patterns remain scarce in the literature.

This study investigates a deep excavation project within a densely built urban area in Shanghai. By analyzing field monitoring data, considering pit geometric characteristics and layouts of monitoring points, the temporal-spatial deformation characteristics of the excavation are examined. Furthermore, the influence of convex and concave corners on excavation deformations is quantitatively evaluated. The findings provide valuable insights for understanding and addressing temporal-spatial deformation challenges in soft soil excavations within dense urban environments, offering technical support for deep underground space development in similar geological regions.

2 Project Information

2.1 Site and Structure Description

The project introduced in this paper is located in Pudong New Area, Shanghai, in which a 40.5-m-high commercial building, a 66.7-m-high Apartment Hotel, a 23.5-m-high cultural podium, and a 14.0-m-high kindergarten are built. The engineering foundation pit comprises both an underground first floor and an underground second floor. The foundation pit for the underground first floor covers an area of approximately 1,865 square meters, with a perimeter of approximately 219 linear meters. In contrast, the foundation pit for the underground second floor extends over an area of approximately 9,108 square meters, with a perimeter measuring approximately 471 linear meters. The plan view and a typical cross-section of the project foundation pit are shown in Figs. 1 and 2, respectively. According to Fig. 2, the pit has an excavation depth of 11.3 m with a 700 mm-thick base slab. The enclosure structure of the excavation contains bored piles (φ1100@1300, φ1200@1400) combined with cement soil mixing piles (φ850@600) as a waterproof curtain, which is supported by two-layer concrete supports.

The construction site's surrounding environment is notably complex. The unambiguous surrounding environment significantly impacts the analysis of the spatial deformation behavior of foundation pit retaining structures. To the east of the foundation pit lies Kangshi Road, with the excavation boundary situated approximately 9.3 m from the property line. Beyond this boundary is Kangshi Road, and further east is the Bailian Dongjiao Shopping Center. The southeast corner of the site is adjacent to two factory buildings, which are single-story structures composed of brick and concrete with natural foundations. In contrast, the northeast corner, beyond the property line, is adjacent to the Kangshan 110 kV substation. This substation features a single-story structure above ground and a single-story underground, supported by a pile-raft foundation. The engineering piles are prestressed concrete pipe piles, each with a diameter of 400 mm and a length of 22 m. The substation is located at distances of 58.7 m, 22.8 m, and 13.4 m from the foundation pit, respectively.

On the southern side of the foundation pit, the excavation boundary is approximately 4.6 m from the designated red line of the land. Beyond the red line on the western section lies the eastern boundary river, currently under construction, with a width of approximately 14.5 m. The blue line of the river channel is situated about 10.2 m from the foundation pit. Presently, the river channel is undergoing excavation, and sidewalks and revetments are being constructed, with the revetments supported by pile foundations. During the project's enclosure construction, the river channel was dredged, and the construction of sidewalks and revetments was completed. To the south of the river is the Yisheng Yunjinyuan residential area, with the primary adjacent structure being an 18-floor high-rise residential building, supported by a pile foundation, located approximately 33.8 m from the foundation pit. Beyond the red line on the eastern section is the Dongbao Municipal Plant Office Park, where the adjacent structure is primarily a single-story plant plank house with a natural foundation, situated approximately 19.4 m from the foundation pit.

On the western side of the foundation pit, the excavation boundary is approximately 5 m from the designated red line. Within this red line, prior to the excavation of the foundation pit for the project, a temporary two-story plank house with a natural foundation was constructed, situated approximately 6 m from the foundation pit. Beyond the red line lies Kangshan Road, which is approximately 24 m wide. Beneath this road are pipelines for water supply (φ 300 mm), gas (φ 250 mm), sewage (φ 300 mm), and rainwater (φ 1000 mm), positioned at distances ranging from 16.9 to 29.7 m from the foundation pit.

On the northern side of the foundation pit, the excavation boundary is approximately 2.7 m from the red line. Beyond this red line is Yunan Road, also approximately 24 m wide. To the north of Yunan Road is the established 12a-03 industrial research and development plot. Adjacent to the road are five three-story industrial R&D office buildings with pile foundations, located approximately 31.6 m from the foundation pit boundary. Beneath Yunan Road, there are power lines, street lamps, and pipelines for gas (φ 250 mm), sewage (φ 300 mm), and rainwater (φ 1000 mm), situated at distances ranging from 5.6 to 18.8 m from the foundation pit.

Fig. 1. Plane view of the project.

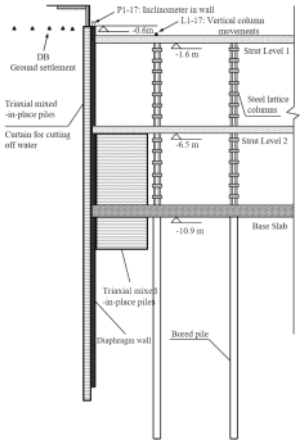

Fig. 2. A typical cross-section of the project.

2.2 Subsurface Conditions

Prior to the construction, subsurface conditions at the site were investigated extensively. The encountered soil layers and corresponding approximate distributions are presented in Table 1.

Table 1. Information of layered soils at the site.

Layer	Layer name	Thickness (m)	Moisture	c (kPa)	Φ (°)	Compressibility
①1	Miscellaneous fill	2.83		–	–	High
①2	Creek fill	4.28	Wet	–	–	High
②	Silty clay	1.72	Saturate d	4–15	23.2–33.1	Medium
③	Muddy silty clay	4.70	Saturated	11–16	14.5–19.5	High
③1	Clayey silt	1.85	Saturated	10–17	24.3–35.2	Medium
④	Muddy clay	5.01	Saturated	12–16	10.5–16.3	High
⑤1	Clay	4.61	Saturated	19–24	14.3–21.9	High
⑤2	Sandy silt and silty clay interbedding	10.19	Saturated	4–8	32–36	Medium
⑤2a	Silty clay with sandy silt	1.82	Saturated	6–8	28.4–31.5	Medium
⑥3–1	Silty clay with clayey silt	7.22	Saturated	28–43	32–36	Medium

The shallow groundwater influencing construction activities at the site is classified as phreatic water, primarily recharged by atmospheric precipitation, with the water table fluctuating seasonally.

Within the site, the semi-confined aquifer is identified in layer ⑤2 at a depth of approximately 21.00 m BGS (i.e., Below Ground Surface), while the confined aquifer is located in layer ⑦ at approximately 51.00 m BGS. Both the semi-confined and confined aquifers exhibit annual cyclic fluctuations in water levels. The water table depth of the semi-confined aquifer varies between 3.0 m and 11.0 m, whereas the confined aquifer ranges from 3.0 m to 12.0 m.

3 Instrumentation

According to Chinese Technical Standards for Foundation Pit Engineering (GB 50497–2019), the monitoring level for this project is classified as Grade I. This study mainly focuses on the two-level excavation zone. In accordance with the construction characteristics, site conditions, and regulatory monitoring requirements, the monitoring program encompasses the following parameters: vertical and horizontal displacements of surrounding underground pipelines, vertical displacements of adjacent buildings and structures, vertical and horizontal displacements at the retaining structure tops, inclinometer measurements of the retaining structures, support axial forces, vertical displacements of column piles, and phreatic water, etc. To specifically investigate the spatiotemporal effects of structure deformation, this analysis selects three critical monitoring datasets, i.e., deflections of retaining structures, ground surface settlements outside the excavation, and vertical displacements of column piles. The spatial distribution of monitoring points is shown in Fig. 3.

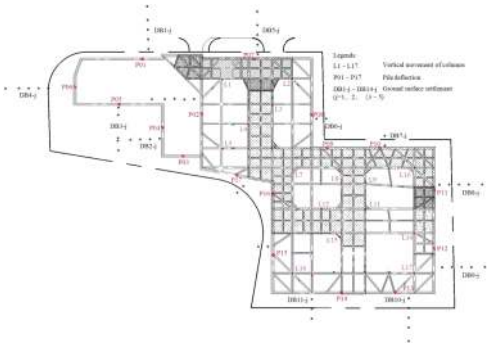

Fig. 3. Layout of several most relevant instrumentation.

The construction of the foundation pit employs a sequential methodology, initiating with the development of the second basement level area. Upon the completion of the primary structure of the second basement level and the subsequent backfilling of the surrounding trenches, the excavation of the first basement level area will commence. The monitoring work for the two-level underground excavation in this project commenced on

December 16, 2022 (i.e., prior to the construction phase), and concluded on November 22, 2023, when the underground structure reached the ground level (±0.000 elevation). Detailed construction schedules of the project are summarized in Table 2.

Table 2. Detailed construction schedules of the project.

Stage	Construction	Duration	
1	Construction of engineering piles, enclosure piles, waterproof curtains, and reinforcement of soils	2022-12-16	2023-04-30
2	Removal of the first layer of soil and setting the	2023-05-03	2023-06-11
3a	Removal of the second layer of soil	2023-06-13	2023-07-07
3b	Construction of the second level of support	2023-07-08	2023-07-20
4a	Excavation of the third layer of soil	2023-07-21	2023-08-15
4b	Construction of the base slab	2023-08-16	2023-08-31

4 Evaluation of the Measurement

4.1 Deflections of the Retaining Wall

According to the database, retaining structures at all monitoring points of the current case developed similar horizontal movement profiles. Therefore, monitored deflections at two typical locations (i.e., P09 near a corner, and P14 at the middle span) are described and compared in Fig. 4.

The figure shows that lateral wall deflections exhibit a bulging pattern along the depth. In other words, the displacement initially increases and subsequently decreases with depth, aligning with conventional observations of excavation retaining wall behavior [11–13]. Such performance is primarily attributed to reduced earth pressure acting on the upper portion of the retaining piles near the ground surface and the restraining effect of the embedded section near the bottom. Further analysis of lateral displacement evolution with time and excavation depth reveals that as excavation progresses, both the magnitude of deflection and the depth of its maximum value gradually increase, and the maximum deflection ultimately stabilizes near the excavation surface.

Comparative analysis of lateral displacements under different construction stages indicates that the lateral deformation of retaining piles during the third-layer soil excavation and the construction of the base slab significantly exceeds that observed during the second-layer soil excavation and installation of the second-level struts. Such a performance highlights the heightened sensitivity of lateral wall displacement to the excavation of deep soils. To avoid excessive displacements, it is suggested to enhance monitoring during the removal of deep soil layers in practice.

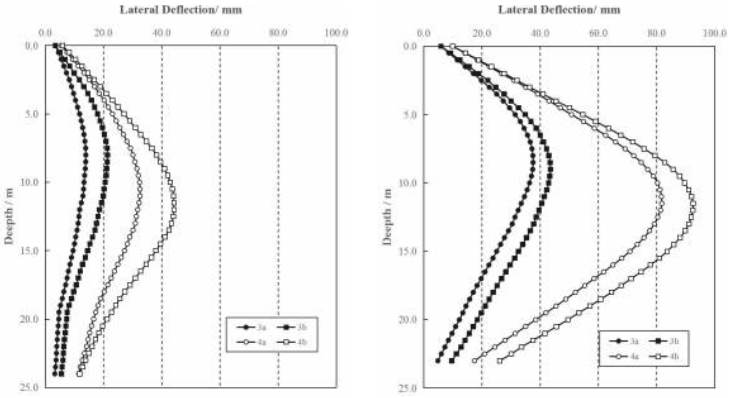

(a) P09 (b) P14

Fig. 4. Wall deflections at two typical locations along the construction process.

Figure 5 summarizes maximum lateral pile displacements at different locations and different construction stages. The results show that monitoring points near the convex corners (e.g., P08, P09, P16) develop substantially smaller maximum lateral displacements (i.e., 30–50 mm) compared to those at mid-span positions (e.g., P12, P14, P13), which exhibit displacements of 80–100 mm. This spatial disparity underscores the pronounced spatial effects in retaining structure deformation, where convex corners effectively constrain lateral displacement development [20]. A further examination shows that displacement increments developed during the installation of struts are generally smaller than those developed during the soil removal stages (i.e., 3a larger than 3b, and 4a larger than 4b shown in the figure). In addition, the temporal analysis also reveals that the corner restraint effect predominantly mitigates displacements induced during soil excavation phases, while the influence on deflection development during the installation of struts is limited.

Owing to the mutual support provided by the two lateral retaining walls, a spatial arch effect is generated, which effectively constrains horizontal displacement and significantly reduces displacement at the external corner, accounting for approximately 30% to 70% of the maximum displacement observed at the midpoint. Concurrently, the soil at the corner of the excavation site is constrained in two directions, resulting in increased soil pressure and enhanced stability within the passive zone. Conversely, the soil in the shaded area is subjected to bidirectional tensile stress, which may precipitate local shear failure, diagonal cracking, or interface separation in the retaining wall, potentially leading to settlement of the soil outside the excavation site. Consequently, during the design process, it is imperative to reinforce the enclosure structure at the inner corner area—such as by increasing the reinforcement ratio, incorporating concealed columns or corner piles—and to meticulously segment and layer the excavation process. Additionally, it is crucial to control the excavation sequence near the inner corner and to enhance waterproofing and joint treatment at this location.

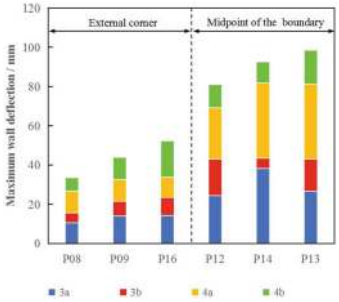

Fig. 5. Summarized maximum lateral deflections at distinct locations.

4.2 Ground Surface Settlements

The monitored ground surface settlements at a typical location outside the excavation are presented in Fig. 6. It can be observed that the settlement exhibits an initial increase followed by a gradual decrease in the direction away from the retaining piles. This phenomenon primarily results from the effects of the deflected retaining structure on the adjacent soil mass near the enclosure structure. As the distance continues to increase, the influence of excavation activities on the distant soil diminishes, leading to correspondingly reduced settlements in these areas. Furthermore, analysis of the impacts from different excavation stages reveals that the excavation of the third soil layer induced the most significant ground settlement. The maximum settlement during this stage accounted for approximately 47.75% of the total maximum settlement, which aligns with the lateral displacement patterns of retaining piles analyzed in Sect. 4.1. This consistency has also been addressed by previous studies [13–15].

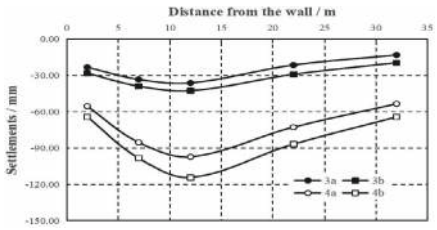

Fig. 6. Monitored ground surface settlements at Point-DB10.

Figure 7 compares the measured surface settlements near the corner and the midpoint of the pit. All the selected monitored points are located 7 m away from the enclosure structure. Combined with the layout of the instrumentation shown in Fig. 3, it can be seen that the surface settlements near the midspan of the long side of the pit (i.e., Ponit-DB10-2 and DB11-2) are significantly larger than those near corners (i.e., Points-DB8-2, DB9-2, DB12-2, and DB12-2), with a minimum amplitude of 44.02%. This displacement distribution trend is consistent with the retaining structure deformation

distribution analyzed in Sect. 4.1, indicating that the enhanced stiffness of the retaining structure near corners enables more effective resistance against the earth pressure due to the excavation-induced stress relief [22].

In contrast to the traditional two-dimensional plane strain hypothesis, which assumes a uniform subsidence trough, the consideration of spatial effects reveals a complex "three-dimensional subsidence basin" configuration. The most notable characteristic of this spatial effect is the uneven distribution observed along the edge of the foundation pit. The settlement is most pronounced behind the middle of the long side, where the settlement trough is widest and the area of influence extends the farthest. At this location, the deformation of the supporting structure is greatest, and the plane strain condition is most evident. As one moves toward the corners, the settlement value gradually decreases, the settlement trough narrows, and the area of influence contracts. The settlement behind the corner is minimal, and the shape of the settlement trough resembles a local depression. This is primarily due to the support provided by corner stiffness, resulting in settlement mainly caused by the uplift of the foundation pit and a minor degree of corner wall deformation. For non-rectangular foundation pits, such as those with L-shaped, circular, or irregular geometries akin to the foundation pit in this project, the configuration of the settlement basin becomes increasingly complex. This complexity is predominantly governed by three-dimensional spatial effects. This holds substantial importance for the enhanced environmental risk assessment of foundation pits. The region directly opposite the midpoint of the long side is identified as the "red area," indicating the highest risk, whereas the area behind the corner is considered the relatively safe "green area." It is advisable for pipelines and significant structures to avoid high-risk zones and instead utilize low-risk areas whenever possible.

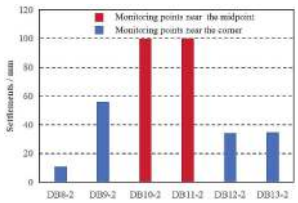

Fig. 7. Spatial distribution of ground surface settlements.

4.3 Vertical Movements of Column Piles

Figure 8 presents the monitored vertical movements of column piles. It can be observed that column piles generally develop progressively upward heaves with increasing magnitude as excavation-induced stress relief progresses. This phenomenon primarily originates from the elastic rebound of basal soils following excavation-induced unloading [23, 24]. In addition, the amplified deformation of supporting structures and the ground settlement outside the pit caused by increasing internal-external pressure differentials further exacerbate basal heave.

Further examination reveals a marked acceleration in vertical displacement rates from August 1 to August 10, 2023. Combined with the construction stages summarized in Table 2, it can be seen that this period coincided with the removal of the third-layer soil, indicating that deep soil removal induces a more pronounced column pile heave. After the construction of the base slab, the movements of piles remained stable, indicating the effective control of the vertical structural movements of base slab casting.

Figure 9 summarizes the maximum vertical column pile movement. The vertical displacement of the column pile at the measurement point situated at the midpoint of the foundation pit edge is substantially greater than that observed at the measurement point positioned at the corner of the foundation pit. The vertical displacement exhibits an increase of approximately 20% to 30%. This observation aligns with the patterns identified in the horizontal displacement of the retaining structure and the surface settlement beyond the perimeter of the foundation pit. This phenomenon is primarily attributed to the fact that the foundation pit does not conform to a uniform two-dimensional cross-section; instead, it constitutes a complex three-dimensional force system. The corner regions demonstrate high stiffness and minimal deformation, whereas the central area exhibits comparatively lower stiffness and greater deformation. Simultaneously, the intrinsic shear strength of the soil mass creates a "soil arch" at the corner of the foundation pit, redistributing a portion of the soil pressure to the more stable regions on either side. This redistribution consequently diminishes the effective load exerted on the supporting structure at the corner, representing an additional contributing factor.

The examination of spatial effects in foundation pits offers valuable insights for optimizing support design. Firstly, a differentiated approach can be applied to the support structure of foundation pits. This involves strengthening the central area by reducing pile spacing, increasing support prestress, and enhancing pile diameter or wall thickness, while allowing for cost-effective reductions in support for corner areas. Secondly, the support system can be strategically configured by reinforcing corner slant supports or installing corner trusses to leverage the inherent stiffness of the corners. Additionally, this analysis can inform the construction plan. The "spatiotemporal effect" theory is especially critical in regions with soft soil, such as Shanghai, where effective control of foundation pit deformation can be achieved by meticulously managing the excavation size and exposure duration of each earthwork layer, and promptly establishing support to capitalize on the soil's slight elasticity over short periods.

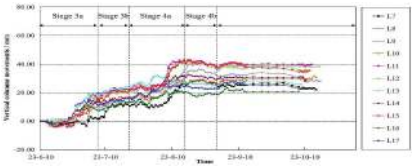

Fig. 8. Developments of the monitored vertical movements of column piles against time.

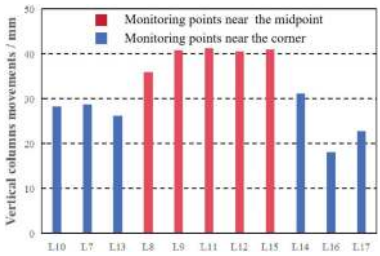

Fig. 9. Summarized maximum vertical column pile movements.

5 Conclusions

This study describes and analyzes the monitored performance of an irregularly shaped deep excavation situated within a densely built urban area. Particular emphasis of the study is put on the spatiotemporal effects of retaining structure deformation concerning the corner effect. The principal conclusions are summarized as follows:

(1) Excavation-induced stress relief led to progressive deformation in both retaining structures and ground outside the pit. Both retaining structure deformations and ground settlements exhibited magnitude escalation with construction advancement. Notably, the excavation of deep soil layers generates disproportionately significant deformations, establishing deformation control during the excavation of deep soils as the key to controlling overall excavation performance.
(2) Retaining structures demonstrate pronounced spatial heterogeneity in lateral displacement and ground surface settlements. The corner regions, benefiting from the enhanced structural stiffness of the support system, effectively constrain deformation development – achieving a 50% reduction in retaining pile lateral displacements and a 47.75% decrease in exterior ground settlements compared to non-corner regions.
(3) Column piles exhibit distinct spatial differentiation in vertical displacements, with interior piles demonstrating substantially greater heave magnitudes (i.e., approximately 2.1 times higher) than peripheral column piles adjacent to pit boundaries. Such uneven settlements may lead to strut instability and should be taken seriously in practice.

References

1. Ren, B.K., Shen, Y., Zhao, T.T., et al.: Deformation monitoring and remote analysis of ultra-deep underground space excavation J. Undergr. Space. **8**, 30–44 (2023). https://doi.org/10.1016/j.undsp.2022.04.005
2. Sekhavatian, A., Choobbasti, A.J.: Application of random set method in a deep excavation: based on a case study in Tehran cemented alluvium J. Front. Struct. Civil Eng. **13**(1), 66–80 (2019). https://doi.org/10.1007/s11709-018-0461-y
3. Bayesteh, H., Sabermahani, M., Ostadhossein, H., et al.: Performance of a large-span deep excavation in saturated fine-grained soil adjacent to a historical building: a case study J. Tunnel. Undergr. Space Technol. **162** (2025). https://doi.org/10.1016/j.tust.2025.106638

4. Tabaroei, A., Sarfarazi, V., Moaveni, M., et al.: Deep excavation–induced stability evaluation of a triple tunnel using discrete and continuum numerical modeling J. Int. J. Geomech. **25**(1), 04024299 (2025). https://doi.org/10.1061/IJGNAI.GMENG-9963
5. Gui, Y., Zhao, Z.X., Qin, X.Q., et al.: Study on deformation law of deep foundation pit with the top-down method and its influence on adjacent subway tunnel J. Adv. Civil Eng., 1–4 (2020). https://doi.org/10.1155/2020/8852336
6. Yao, C., Zhong, H., Zhu, Z.: Development of a large shaking table test for sand liquefaction analysis J. Lithosphere. **137** (2024). https://doi.org/10.2113/2024/lithosphere_2024_137
7. Zhao, J., Zhu, Z., Zhang, X.: Macro-micro mechanism of sand liquefaction under different waveforms via discrete element method J. Soil Dyn. Earthq. Eng. **198**, 109604 (2025). https://doi.org/10.1016/j.soildyn.2025.109604
8. Ray, P.K., Rasagna, D.L.S., Koley, S.K., et al.: Deep excavation by controlled rock blasting considering ground condition and nearby structures in ug metro station—a case study J. Lec. Notes Civil Eng., 67–79 (2024). https://doi.org/10.1007/978-3-031-37256-8_6
9. Cui, J.F., Yang, Z.K., Azzam, R.: Field measurement and numerical study on the effects of under-excavation and over-excavation on ultra-deep foundation pit in coastal area J. J. Mar. Sci. Eng. **11**(1), 219 (2023). https://doi.org/10.3390/jmse11010219
10. Sakuma, K., Ishii, E., Murakami, H.: Predicting the long-term natural decay of inflow from faults or fractures encountered during excavation of deep underground tunnels using the flow dimension J. Environ. Earth Sci. **84**, 663 (2025). https://doi.org/10.1007/s12665-025-12680-9
11. Yang, Z.K., Chen, Y.L., Azzam, R., et al.: Performance of a top-down excavation in shanghai: case study and numerical exploration J. Eur. J. Environ. Civil Eng. **26**(15), 7932–7957. https://doi.org/10.1080/19648189.2021.2013950
12. Park, S., Son, Y., Kim, J.G., et al.: Thermal and mechanical impact of artificial ground-freezing on deep excavation stability in nakdong river deltaic deposits J. Eng. Geol. **343** (2024). https://doi.org/10.1016/j.enggeo.2024.107796
13. Clough, G.W., O'Rourke, T.D.: Construction induced movements of insitu wall, design and performance of earth retaining structure. ASCE. **25**, 439–479 (1990)
14. Ou, C.Y., Hsieh, P.G., Chiou, D.C.: Characteristics of ground surface settlement during excavation J. Can. Geotech. J. **30**(5), 758–767 (1993). https://doi.org/10.1139/t93-068
15. Finno, R.J., Bryson, S., Calvello, M.: Performance of a stiff support system in soft clay. J. Geotech. Geoenviron. Eng. **128**(8), 660–671 (2002). https://doi.org/10.1061/(ASCE)1090-0241(2002)128:8(660)
16. Roboski, J., Finno, R.J.: Distributions of ground movements parallel to deep excavations in clay J. Can. Geotech. J. **43**(1), 43–58 (2006). https://doi.org/10.1139/t05-091
17. Dong, Y.P., Burd, H.J., Houlsby, G.T.: Finite-element analysis of a deep excavation case history J. Géotechnique. **66**(1), 1–15 (2016). https://doi.org/10.1680/jgeot.14.P.234
18. Whittle, A.J., Corral, G., Jen, L.C., et al.: Prediction and performance of deep excavations for courthouse station, Boston J. J. Geotech. Geoenviron. Eng. **141**(4), 04014123 (2015). https://doi.org/10.1061/(ASCE)GT.1943-5606.0001269
19. Guo, P., Lei, G., Luo, L., et al.: Soil creep effect on time - dependent deformation of deep braced excavation J. Adv. Mater. Sci. Eng. **4**, 1–14 (2022). https://doi.org/10.1155/2022/5655592
20. Xiong, Y.F., Ying, H.W., Zhang, J.H., et al.: Analysis method for ground settlement induced by ultra-deep excavation in Hangzhou soft clay considering time-space effect. J. Shanghai Jiaotong Univ., 1–19 (2024). https://doi.org/10.16183/j.cnki.jsjtu.2023.199
21. Zdravkovic, L., Potts, D.M., St John, H.D.: Modelling of a 3d excavation in finite element analysis J. Géotechnique. **55**(7), 497–513 (2005). https://doi.org/10.1680/geot.2005.55.7.497
22. Fuentes, R., Devriendt, M.: Ground movements around corners of excavations: empirical calculation method. J. Geotech. Geoenviron. Eng. **136**(10), 1414–1424 (2010). https://doi.org/10.1061/(ASCE)GT.1943-5606.0000347

23. Szepesházi, A., Mahler, A., Móczár, B.: Three dimensional finite element analysis of deep excavations' concave corners J. Period. Polytech. Civil Eng. **60**(3), 371–378 (2016). https://doi.org/10.3311/PPci.8608
24. Li, Z., Han, M., Liu, L.L., et al.: Corner and partition wall effects on the settlement of a historical building near a supported subway excavation in soft soil J. Comput. Geotech. **128**, 103805 (2020). https://doi.org/10.1016/j.compgeo.2020.103805
25. Wu, Q., Wang, J., Long, Y., et al.: The field monitoring and numerical simulation of spatiotemporal effects during deep excavation in mucky soft soil: a case study J. Appl. Sci. **15**(4), 1992 (2025). https://doi.org/10.3390/app15041992
26. Lin, Z.B., Li, Y.H., Liu, J.Q.: A study on the spatial-temporal evolution regularity of the deformation of a foundation pit in soft soil J. Mod. Tunnel. Technol. **53**(3), 82–90 (2016). https://doi.org/10.13807/j.cnki.mtt.2016.03.012
27. Roy, S., Dan, K., Sahu, R.B.: An experimental study on time dependent ground settlement behind a braced excavation in soft clay using geotechnical centrifuge J. Sādhanā. **48**(3), 181 (2023). https://doi.org/10.1007/s12046-023-02247-4
28. He, P., Xu, Z., Wang, W., et al.: Observed performance of an ultra large deep excavation in shanghai soft clay. In: GeoShanghai International Conference, pp. 161–170. Springer, Singapore (2018). https://doi.org/10.1007/978-981-13-0011-0_18
29. Tan, Y., Wei, B., Diao, Y.P., et al.: Spatial corner effects of long and narrow multipropped deep excavations in shanghai soft clay. J. Perform. Constr. Facil. **28**(4), 04014015 (2014). https://doi.org/10.1061/(ASCE)CF.1943-5509.0000475
30. Chen, K.C., Xu, R.Q., Ying, H.W., et al.: Observed performance of a 30.2 m deep-large basement excavation in Hangzhou soft clay J. Tunnel. Undergr. Space Technol. **111**, 103872 (2021). https://doi.org/10.1016/j.tust.2021.103872

Application of the Xinanjiang Model in Flood Forecasting of Yanjingkou Reservoir

Shilei Chen[1,2] and Qingying Qiu[3](✉)

[1] ChangJiang Schinta Software Technology Co., Ltd., Wuhan 430010, China
[2] Internet+ Intelligent Water Conservancy Key Laboratory of ChangJiang Water Resources Commission, Wuhan 430010, China
[3] College of Civil Engineering and Architecture, Guangxi University, Nanning 530004, China
qiu_qingying@163.com

Abstract. Flood disasters are characterized by high occurrence frequency, wide coverage of impact, and extremely severe losses. As a key hub within the flood control system, the accuracy of reservoir flood forecasting is directly related to the effectiveness of flood control and disaster reduction efforts in the river basin. This study takes Yanjingkou Reservoir, located in Liangping District, Chongqing Municipality, as the study area. Based on the three-source Xinanjiang model, a flood forecasting model is constructed, and simulation verification is conducted using six individual flood events that occurred during the period from 2020 to 2023. The results indicate that the Xinanjiang model performs well in daily-scale flood forecasting for Yanjingkou Reservoir. The average DC value of the simulation results is 0.84, the average RPE is -4.36% with a qualification rate of 100%, and the average RRE is 5.60%, with four out of the six floods meeting the qualification criteria, corresponding to a qualification rate of 66.7%. Combined with the analysis of flood hydrographs, it is concluded that the Xinanjiang model still demonstrates good overall forecasting capability, providing reliable technical support for the flood control operation of Yanjingkou Reservoir.

Keywords: Xinanjiang Model · Flood Forecasting · Yanjingkou Reservoir

1 Introduction

Flood disasters occur with high frequency, affect a wide range of areas, and cause extremely severe losses to both human society and the natural environment. In recent years, with the intensification of global climate change, extreme rainfall events have become more frequent and intense, leading to an increased risk of flood disasters in many regions. This has further highlighted the importance of effective flood forecasting as a key measure for flood control and disaster reduction, given its vital role in promptly providing disaster-related information and mitigating the resulting losses and impacts [1, 2]. By predicting the occurrence time, magnitude, and scope of floods in advance, flood forecasting provides a scientific basis for flood control decision-making, such as the scheduling of reservoirs, the evacuation of people in flood-prone areas, and the deployment of flood control materials.

© The Author(s), under exclusive license to Springer Nature Switzerland AG 2027
G. Feng et al. (Eds.): ICCE 2025, SUCI, pp. 120–131, 2027.
https://doi.org/10.1007/978-3-032-32237-1_9

Reservoirs, as key components of flood control engineering systems, deliver multi-faceted benefits in flood regulation, water resource allocation, ecological protection, and hydropower generation through scientific and optimal operation. During flood seasons, when upstream rainfall leads to increased runoff, reservoirs can store excess floodwaters during peak flow periods, effectively regulating the runoff process and reducing downstream peak discharges. This significantly alleviates the flood control pressure in downstream areas, protecting the lives and property of residents along the river and the normal operation of various economic activities [3, 4]. However, the effectiveness of reservoir operations is inherently dependent on the accuracy of flood forecasting. Only with reliable and timely forecasting results can reservoir managers make informed scheduling decisions, balancing flood control safety with the efficient utilization of water resources. Therefore, the accuracy of reservoir flood forecasting is directly associated with the effectiveness of flood control and disaster reduction work in the entire river basin [5].

The Xinanjiang model is China's first complete conceptual watershed hydrological model. Since its proposal in 1973, it has been extensively and successfully applied in various aspects of hydrological simulation and forecasting across China [6, 7]. The three-source Xinanjiang model calculates runoff yield based on the saturation excess runoff theory, which is particularly suitable for humid and semi-humid regions where soil saturation is the main mechanism of runoff generation. A key feature of this model is that it divides the water sources into three components: surface runoff, interflow, and groundwater runoff. This unique structure enables the model to well simulate the complex runoff generation and confluence processes in watersheds, accurately reflecting the different pathways and characteristics of water movement from the land surface to the river channel [8–10].

The Yanjingkou Reservoir is located in a subtropical humid monsoon climate zone, characterized by significant precipitation during the flood season, which makes it highly susceptible to rainstorm-induced flood disasters. Such floods not only threaten the safe operation of the reservoir but also pose potential risks to agricultural production, industrial activities, and daily life in the downstream areas. Therefore, improving the accuracy of flood forecasting for Yanjingkou Reservoir is crucial for ensuring the reservoir's safe operation and reducing flood risks in the downstream areas. Given the above background, this study takes Yanjingkou Reservoir as the research object and constructs a flood forecasting model based on the three-source Xinanjiang model. Through systematic simulation and validation of typical flood processes that occurred from 2020 to 2023, the applicability and forecasting accuracy of the model in the study area are comprehensively evaluated. This research aims to provide a scientific basis for optimizing flood control operations at Yanjingkou Reservoir, improve the local flood forecasting and early warning system to enhance regional flood disaster prevention and reduction capacity, and offer technical references for flood forecasting in similar watersheds and reservoirs.

2 Study Area and Data

2.1 Study Area

The medium-sized irrigation district of Yanjingkou Reservoir is located in Liangping District, Chongqing Municipality. Situated in the eastern parallel ridge-valley region of the Sichuan Basin and the western edge of the Three Gorges Reservoir area, it spans geographical coordinates of 30°25′N–30°53′N and 107°24′E–108°05′E, with a total area of 1892.13 km^2. Liangping District has an altitude ranging from 221 m to 1221 m, dominated by mountainous and hilly terrain, with six major rivers flowing through it. Belonging to the subtropical humid monsoon climate zone, the district is characterized by uneven annual rainfall distribution, with a multi-year average precipitation of 1252.9 mm and a multi-year average temperature of 16.6°C.

Yanjingkou Reservoir is situated in Longxi Village, Pingjin Town, Liangping District. It is a medium-sized water conservancy project primarily for irrigation and flood control, with comprehensive utilization including water supply, power generation, and tourism. The reservoir's watershed is located in the upper reaches of the Qijian River, a right tributary of the Longxi River within the Yangtze River system, with geographical coordinates of 107°32′E longitude and 30°37′N latitude. The catchment area above the reservoir dam is 54.6 km^2, the main river course length is 22.4 km, and the comprehensive average river slope is 25.9‰, with the river generally flowing from northeast to southwest.

The reservoir project is composed of five main parts: key hub projects, auxiliary water supply projects, interconnection and water transfer projects, irrigation district projects, and power station projects. The total storage capacity of the reservoir is 19.36 million m^3, the checked flood level is 516.12 m (corresponding to a storage capacity of 19.36 million m^3), the normal storage level is 513.10 m (corresponding to a storage capacity of 16.35 million m^3), the dead water level is 480.0 m (corresponding to a storage capacity of 0.30 million m^3), and the effective storage capacity is 16.05 million m^3.According to long-term hydrological data, the average annual discharge of the reservoir is 1.08 m^3/s, corresponding to an average annual runoff of about 3399 million m^3 over the years, indicating relatively abundant water resources. The average annual available water supply of the reservoir reaches 31.79 million m^3, of which 9.43 million m^3 is allocated for urban and rural domestic and production water supply, 4.48 million m^3 for inter-basin ecological environment water transfer, 7.73 million m^3 for agricultural irrigation water supply, and 10.15 million m^3 for hydropower generation (including 3.38 million m^3 of ecological discharge water), which can fully meet the diverse water demand in the downstream areas.

2.2 Data Sources

To ensure the reliability and accuracy of model construction and simulation analysis, a comprehensive set of hydrometeorological observation data for Yanjingkou Reservoir from 2020 to 2023 was collected and processed. These records include daily inflow discharge data, evapotranspiration data, and rainfall data observed within the basin. Six representative flood events were selected from long-term hydrometeorological data

series as research samples for model calibration. The selected flood events must adhere to the criteria of having a strong correlation between rainfall and runoff data, ensuring that the flood events are primarily driven by rainfall inputs. The selection should also cover a range of flood magnitudes (small, medium, and large) to comprehensively evaluate the model's performance under different hydrological conditions. Additionally, the observed data must be complete and of high quality, including continuous rainfall records, complete runoff hydrographs, and reliable evapotranspiration data, to ensure the reliability of the model calibration results.

3 Methodology

3.1 Xinanjiang Model

The three-source Xinanjiang model was adopted as the core tool for flood forecasting in this study due to its mature theoretical system, clear physical meaning of parameters, and proven excellent performance in hydrological simulation and forecasting. This model is a conceptual model which abstracts and simplifies the complex rainfall-runoff process into four interconnected components: evapotranspiration calculation, total runoff yield calculation, water source division, and confluence calculation [11]. The integration of these four components forms a complete hydrological simulation system that can comprehensively simulate the transformation process of rainfall into runoff in the basin and the confluence process of runoff to the outlet of the reservoir.

For the evapotranspiration calculation, the model uses a three-layer evaporation model to simulate the evapotranspiration process, dividing the soil profile into upper, lower, and deep layers based on the vertical distribution of soil moisture and evaporation characteristics. Each layer has different water storage capacities and evaporation characteristics, which can more realistically reflect the actual evapotranspiration process in the basin. The total evaporation is the sum of the evaporation rates of the three layers. The evaporation process follows a specific sequence: the soil water in the upper layer first evaporates according to the potential evapotranspiration capacity; if the water content in the upper layer is insufficient to support the required evapotranspiration, the soil water in the lower layer begins to evaporate at a rate of WL/WLM (where WL refers to the actual water storage in the lower layer and WLM is the maximum water storage capacity of the lower layer); when the soil water in both the upper and lower layers is insufficient to meet the evapotranspiration demand, the soil water in the deep layer evaporates with the help of the deep evapotranspiration coefficient.

The runoff generation module is centered on the saturation excess runoff mechanism, which is well-suited for humid and semi-humid regions where runoff is primarily generated when the soil is saturated. Due to spatial variability in soil texture, topography, vegetation cover, and other factors across different areas within a watershed, the tension water capacity exhibits spatial variability. This leads to uneven runoff generation: during rainfall events, some areas may reach saturation and produce runoff first, while others require additional rainfall before runoff occurs. The model employs an exponential tension water-holding capacity curve to describe the spatial variability of soil tension water-holding capacity within the watershed. When the sum of initial soil moisture storage and net rainfall (i.e., rainfall minus evapotranspiration during the rainfall period)

exceeds the soil tension water storage capacity at a given location, the excess water generates runoff. The total runoff yield of the basin is calculated by integrating the runoff generation processes across the entire watershed, considering the spatial variability of tension water storage capacity. Its expression is shown below, where the exponent B reflects the degree of spatial variability of tension water storage capacity in the entire watershed. A higher B value indicates a more uniform spatial distribution of tension water capacity.

$$\frac{f}{F} = 1 - \left(1 - \frac{WM}{WMM}\right)^{B} \tag{1}$$

where: $\frac{f}{F}$ is the proportion of runoff-generating area; WM is the average tension water storage capacity of the basin; WMM is the maximum value of tension water storage capacity at each point in the basin; and B is the exponent of the tension water storage capacity curve.

To accurately simulate the different runoff components and their confluence characteristics, the model introduces a free water storage reservoir for water source division. The total runoff yield is partitioned into three components: surface runoff, interflow, and groundwater runoff. Different runoff components have distinct confluence speeds and recession characteristics, which have a significant impact on the shape of the flood hydrograph. Similar to the tension water storage capacity curve, a free water storage capacity curve is used to represent the spatial distribution of free water storage capacity, with its expression shown below. The amount of surface runoff (RS) generated is determined by the water volume stored in the reservoir after runoff yield inflows, while interflow (RI) and groundwater runoff (RG) are discharged from the free water reservoir through their respective outflow coefficients: KSS for interflow and KG for groundwater runoff.

$$\frac{f}{F} = 1 - \left(1 - \frac{SM}{MS}\right)^{EX} \tag{2}$$

where: SM is the average free water storage capacity of the basin; MS is the maximum value of free water storage capacity at each point in the basin; and EX is the exponent of the free water storage capacity curve.

The confluence process is divided into two sequential stages: slope confluence and river network confluence. Surface runoff, characterized by fast confluence speed and short travel time, undergoes slope confluence calculation using the Instantaneous Unit Hydrograph (UH), which describes the time distribution of surface runoff arriving at the river network. In the Xinanjiang model, the UH is usually represented by a gamma distribution function, with two main parameters: the unit hydrograph time parameter (K) and the unit hydrograph shape parameter (N). They respectively reflect the average travel time of surface runoff from the farthest point of the basin to the river network, and the concentration degree of surface runoff. A larger K value indicates a longer travel time, and a larger N value indicates a more concentrated runoff. Groundwater runoff and interflow exhibit slower concentration speeds and longer recession periods, and the model employs the linear reservoir method for their simulation. The corresponding recession coefficients are KKG (groundwater recession coefficient) and KKSS (interflow recession coefficient), which respectively regulate the proportion of recession contribution from

the two types of runoff. A larger coefficient indicates stronger continuity of recession from the previous period's flow. This approach effectively captures the gradual release of water from the soil profile and underground aquifers, reproducing the slow recession characteristics of flood hydrographs. The total flow at the reservoir's outlet section is obtained by superimposing the confluence outputs of the three runoff components after their respective confluence processes. By simulating the confluence processes of different runoff components separately, the model can accurately reproduce the different characteristics of the flood hydrograph, which is crucial for accurately simulating the entire flood process, including the peak discharge, the timing of the peak, and the shape of the hydrograph.

The model treats the entire river basin as a single hydrological unit, simplifying the computational complexity while maintaining the physical realism of the hydrological processes. It consists of 15 independent parameters, each with clear physical meanings, including parameters related to soil water storage capacity (upper, lower and deep soil water storage capacity: WUM, WLM, WDM), evaporation characteristics (deep evapotranspiration coefficient C, and evaporation capacity conversion coefficient KC), runoff generation (B, SM), water source division (EX, KSS, KG), and confluence (K, N, KKG, KKSS), as well as the impervious area ratio (IMP). These parameters are closely related to the underlying surface characteristics and hydrological processes of the basin, and their reasonable calibration is crucial for ensuring the model's simulation accuracy [12].

3.2 Parameter Calibration Method

The calibration of model parameters is a critical step in hydrological modeling, as the rationality of parameter values directly determines the accuracy and reliability of forecasting results. In this study, the SCE-UA (Shuffled Complex Evolution) global optimization algorithm was selected for parameter calibration, which was implemented using the runoff data of six flood events in the Yanjingkou Reservoir. Proposed by Duan et al. in 1992, the SCE-UA algorithm is a powerful global optimization method that integrates the simplex method, competitive evolution theory, and complex shuffling strategy [13]. It is widely recognized for its excellent performance in handling high-dimensional, nonconvex, and nonlinear optimization problems, making it particularly suitable for the calibration of hydrological model parameters [14].

The SCE-UA algorithm has several prominent advantages that make it particularly suitable for the calibration of hydrological model parameters. Firstly, it has strong global optimization capabilities. Hydrological model parameters often have complex relationships with simulation results, and the objective function surface may have multiple local optimal solutions. The SCE-UA algorithm can effectively avoid falling into local optimal solutions by means of complex division, independent evolution, and shuffling, thereby finding the global optimal parameter combination. Secondly, the algorithm excels at handling high-dimensional optimization problems. By leveraging the synergistic evolution of multiple complexes, the SCE-UA algorithm efficiently searches high-dimensional spaces, ensuring optimal solutions are found within a reasonable number of iterations. Thirdly, the algorithm exhibits insensitivity to initial parameter values and objective function forms, delivering stable and reliable calibration results for diverse hydrological models and catchments. Finally, its clear structure and minimal control parameters

allow flexible adaptation to specific optimization problem characteristics, optimizing outcomes accordingly [15, 16].

In this study, the deterministic coefficient (DC) was selected as the objective function for parameter calibration. The deterministic coefficient is a widely used indicator for evaluating the degree of agreement between simulated and observed flow processes. A value closer to 1 indicates a higher degree of agreement and better simulation accuracy. The calculation formula of the deterministic coefficient is as follows:

$$DC = 1 - \frac{\sum_{t=1}^{N}\left[Q_{sim}(t) - Q_{obs}(t)\right]^2}{\sum_{t=1}^{N}\left[Q_{obs}(t) - \overline{Q}_{obs}\right]^2} \tag{3}$$

where: N is the total number of statistical periods; $Q_{obs}(t)$ is the observed discharge value at time t; $Q_{sim}(t)$ is the simulated discharge value at time t; and $\overline{Q}_{obs}$ is the average observed discharge value during the statistical period.

3.3 Model Evaluation Indicators

To evaluate the simulation accuracy of the model, in addition to the DC value, absolute error and relative error values are calculated. The permissible error standard is applied to assess the simulated peak discharge, runoff volume, and flood hydrograph. Specifically, according to China's "Hydrological Information and Hydrological Forecasting Standard" (GB/T 22482-2008) [17], the permissible error standard for flood peak discharge and runoff is set at 20% of the observed runoff. When both the absolute values of the relative runoff error value (RRE) and relative peak error value (RPE) are below 20%, the simulation results are deemed acceptable. The formulas for calculating RRE and RPE are as follows:

$$RRE = \frac{\mathrm{R_s} - \mathrm{R_o}}{R_o} \tag{4}$$

$$RPE = \frac{QM_s - QM_o}{QM_o} \tag{5}$$

where: R_s is the simulated runoff; R_o is the observed runoff; QM_s is the simulated peak flow; and QM_o is the observed peak flow.

4 Results and Analysis

The model parameters are calibrated by using the data from each individual flood event, and the calibration results are presented in Table 1. The parameters of the adopted model are basically consistent with the hydrological characteristics of the basin, and their values are reasonably selected, laying a solid foundation for the subsequent simulation and verification. The calculation results of each flood index are shown in Table 2 and the corresponding flood hydrographs are illustrated in Fig. 1 to Fig. 6.

Combining the analysis of the index calculation results and the flood hydrographs, the overall simulation performance of the model are satisfactory. The deterministic coefficients of all six floods are above 0.7, with an average DC value of 0.84. Among these

Table 1. Calibration results of xinanjiang model parameters for yanjingkou reservoir.

Parameters	Parameter Meaning	Parameter Value
IMP	Impervious area ratio	0.002
WUM	Upper soil water storage capacity	177.402
WLM	Lower soil water storage capacity	181.014
WDM	Deep soil water storage capacity	111.968
B	Exponent of tension water storage capacity curve	0.437
C	Deep evapotranspiration coefficient	0.119
EX	Exponent of free water storage capacity curve	0.500
KC	Evaporation capacity conversion coefficient	0.500
SM	Free water storage capacity	22.265
KG	Groundwater runoff outflow coefficient	0.162
KKG	Groundwater runoff recession coefficient	0.601
KSS	Interflow outflow coefficient	0.091
KKSS	Interflow recession coefficient	0.691
K	Unit hydrograph time parameter	19.999
N	Unit hydrograph shape parameter	0.284

Table 2. Evaluation results of simulation effect for yanjingkou reservoir.

Flood Event	Rain fall (mm)	Peak Discharge (m^3/s)				Runoff (10^4 m^3)				DC
		Measured Value	Simulated Value	Absolute Error	RPE (%)	Measured Value	Simulated Value	Absolute Error	RRE (%)	
2020.6.3	47.5	2.31	2.61	0.30	12.99	67.56	75.76	8.20	12.14	0.79
2022.4.25	118.8	14.42	14.06	−0.36	−2.48	259.40	324.66	65.26	25.32	0.94
2022.5.28	80.5	3.93	3.22	−0.71	−18.19	221.96	187.48	−34.48	−15.58	0.78
2023.6.6	70.7	5.28	5.16	−0.08	−2.27	207.02	180.97	−26.05	−12.59	0.72
2023.8.27	126.6	10.52	10.38	−0.14	−1.33	156.52	199.84	43.32	27.67	0.94
2023.11.4	88.9	6.52	5.55	−0.97	−14.88	196.67	190.11	−6.56	−3.34	0.88
Average	88.8	7.16	6.83	−0.33	−4.36	184.86	193.14	8.28	5.60	0.84

floods, the DC values of the two events, namely “20220425” and “20230827”, both reach 0.94. The corresponding flood hydrographs (Fig. 2 and Fig. 5), show that the simulated flood hydrographs are almost overlapping with the observed hydrographs, especially in the rising limb and peak phase of the flood. This indicates that the Xinanjiang model can satisfactorily simulate the flood process shapes of these two flood events and accurately capture the rising and falling trends of the floods. The DC of the remaining four flood events range from 0.72 to 0.88, which also indicates satisfactory consistency between the simulated and observed flood processes. As can be seen from Figs. 3, 4, and 6, the

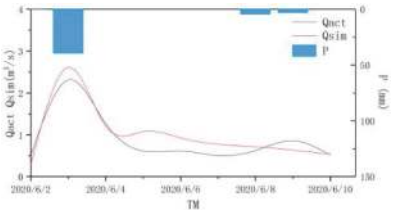

Fig. 1. Flood Event of June 3, 2020.

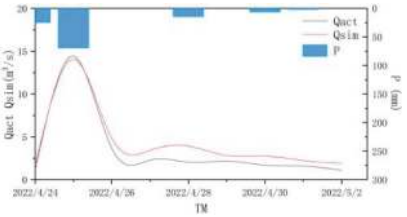

Fig. 2. Flood event of April 25, 2022.

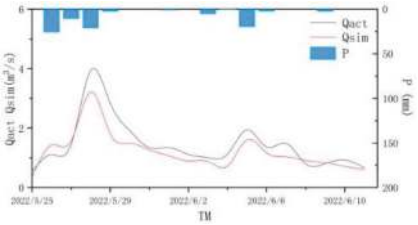

Fig. 3. Flood event of May 28, 2022.

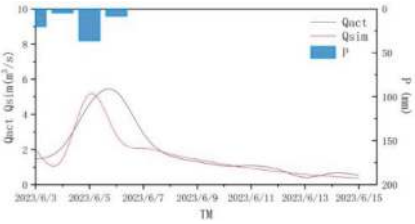

Fig. 4. Flood event of June 6, 2023.

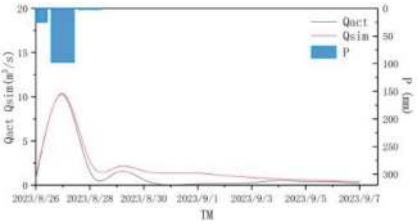

Fig. 5. Flood event of August 27, 2023.

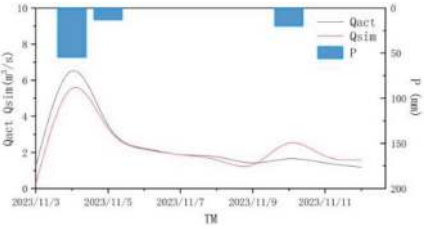

Fig. 6. Flood event of November 4, 2023.

simulation results for these three flood events are generally characterized by the underestimation of observed runoff volume. In contrast, the simulation result corresponding to Fig. 1 mainly overestimates the observed runoff volume. Although the simulated hydrographs deviate from the observed ones to varying extents for these four flood events, the overall trend is consistent. This shows that the Xinanjiang model has strong adaptability to the hydrological conditions of the Yanjingkou Reservoir basin, and can effectively simulate the flood processes under different rainfall conditions.

Peak discharge is one of the most critical indicators in flood forecasting. The average RPE for the six floods is −4.36%, which mainly shows an underestimation of the measured peak discharges. According to the RPE values of individual flood events, only the flood event on June 3, 2020 (20200603) shows an overestimation of the observed peak discharge, while the remaining five flood events all exhibit underestimation. Nevertheless, the RPE values for all six flood events are controlled within 20%, resulting in a qualification rate of 100%. This demonstrates that the model has a certain degree of reliability in simulating peak discharges.

In contrast to the peak discharge simulation, the model exhibits a slight overestimation of runoff volume, with an average RRE of 5.60%. Among the six flood events, four meet the ±20% qualification standard, resulting in a qualification rate of 66.7%. It is found that although the DC values of the two floods "20220425" and "20230827" reach 0.94 and the degree of underestimation of peak discharge is relatively small, the runoff volumes are overestimated by 25.32% and 27.67% respectively. Through the analysis of the flood hydrographs, it is observed that these two floods can well simulate the trend of the measured flood hydrographs, but they significantly overestimate the measured discharge during the low-flow recession period, which leads to a large relative error in the runoff volume. In the other four flood events with lower discharge magnitudes, the accuracy of the simulated runoff hydrographs decreases. This was primarily manifested in insufficient capture of peak discharge and an overly rapid simulation of the recession phase. These typical features of the simulated hydrograph align with the overall fitting level indicated by the DC value.

Overall, the Xinanjiang model can effectively simulate the flood processes in the Yanjingkou Reservoir. It features high simulation accuracy for peak discharge and favorable performance in reproducing the overall trends of flood hydrographs. Nevertheless, certain deficiencies remain in runoff volume simulation, particularly the overestimation of runoff volume during the flood recession period. The simulation discrepancies primarily stem from two aspects: firstly, the lumped structure of the model simplifies the spatial variability of the basin underlying surface, which may lead to deviations in the simulation of runoff generation and confluence processes in local areas; secondly, only daily-scale rainfall and runoff data have been collected, resulting in low temporal resolution that fails to accurately characterize the short-term abrupt changes of individual flood events and the detailed hydrological processes. In future research, targeted optimization and improvement can be conducted to further enhance the simulation accuracy and reliability of the model.

5 Conclusion

In this study, a flood forecasting model for Yanjingkou Reservoir is constructed based on the Xinanjiang model, and the SCE-UA optimization method is applied to determine the parameters of the forecasting scheme model. Simulation verification is conducted by using six typical flood events that occurred from 2020 to 2023, and the main conclusions drawn are as follows:

1) The three-source Xinanjiang model exhibits excellent applicability and adaptability in flood forecasting of Yanjingkou Reservoir. The average DC of the six flood events reaches 0.84, with values ranging from 0.72 to 0.94, indicating that the model can accurately simulate the flood processes in the study area, capturing the rising and falling trends, peak timing, and key characteristics of floods. This confirms the model's reliability in reproducing the hydrological responses of the basin to rainfall inputs.

2) The model demonstrates high accuracy in simulating peak discharge, with an average RPE of −4.36% and a 100% qualification rate (relative error within ±20%). This enables the model to provide reliable early warning information about peak floods for the flood control operation of the reservoir.
3) The model generally shows a slight overestimation in the simulation of runoff volume, with an average RRE of 5.60%. The overall runoff qualification rate stands at 66.7%, indicating that four of the six flood simulations satisfied the comprehensive evaluation standards. The unqualified flood events mainly have the problem of overestimating the low-flow part, which needs to be further optimized in subsequent studies.
4) Based on the comprehensive analysis of the index calculation results and the flood hydrographs, it is concluded that the Xinanjiang model still demonstrates good overall forecasting capability. It can meet the actual needs of flood forecasting for Yanjingkou Reservoir and provide reliable technical support for the flood control operation of the reservoir.

References

1. Ming, X., Liang, Q., Xia, X., et al.: Real-time flood forecasting based on a high-performance 2-D hydrodynamic model and numerical weather predictions J. Water Resour. Res. **56**(7), e2019WR025583 (2020). https://doi.org/10.1029/2019WR025583
2. Byaruhanga, N., Kibirige, D., Gokool, S., et al.: Evolution of flood prediction and forecasting models for flood early warning systems: a scoping review. J. Water **16**(13), 1763 (2024). https://doi.org/10.3390/w16131763
3. Rahimi, H., Ardakani, M.K., Ahmadian, M., et al.: Multi-reservoir utilization planning to optimize hydropower energy and flood control simultaneously. J. Environ. Process. **7**(1), 41–52 (2020). https://doi.org/10.1007/s40710-019-00404-8
4. Sun, J., Chen, W., Hu, B., et al.: Roles of reservoirs in regulating basin flood and droughts risks under climate change: historical assessment and future projection. J. J. Hydrol. Reg. Stud. **48**, 101453 (2023). https://doi.org/10.1016/j.ejrh.2023.101453
5. Ren, M., Zhang, Q., Yang, Y., et al.: Research and application of reservoir flood control optimal operation based on improved genetic algorithm. J. Water **14**(8), 1272 (2022). https://doi.org/10.3390/w14081272
6. Cui, Z., Zhou, Y., Guo, S., et al.: A novel hybrid XAJ-LSTM model for multi-step-ahead flood forecasting. J. Hydrology Res. **52**(6), 1436–1454 (2021). https://doi.org/10.2166/nh.2021.016
7. Liu, P., Zhang, X., Zhao, Y., et al.: Improving efficiencies of flood forecasting during lead times: an operational method and its application in the Baiyunshan Reservoir. J. Hydrol. Res. **50**(2), 709–724 (2019). https://doi.org/10.2166/nh.2018.051
8. Nan, Y., Chen, C., Zhao, Y., et al.: A historical overview of experimental hydrology in China. J. Hydrol. Processes **38**(7), e15233 (2024). https://doi.org/10.1002/hyp.15233
9. Hao, G., Li, J., Song, L., et al.: Comparison between the TOPMODEL and the Xin'anjiang model and their application to rainfall runoff simulation in semi-humid regions. J. Environ. Earth Sci. **77**(7), 1–13 (2018). https://doi.org/10.1007/s12665-018-7477-4
10. Yang, X., Magnusson, J., Huang, S., et al.: Dependence of regionalization methods on the complexity of hydrological models in multiple climatic regions. J. Hydrol. **582**, 124357 (2020). https://doi.org/10.1016/j.jhydrol.2019.124357
11. Zhao, R.: The Xinanjiang model applied in China. J. Hydrol. **135**(1–4), 371–381 (1992). https://doi.org/10.1016/0022-1694(92)90096-E

12. Wang, Z., Zhang, X., Liu, C., et al.: Hydrological simulation and parameter optimization based on the distributed Xin'anjiang model and the particle swarm optimization algorithm: a case study of Xunhe watershed in Shandong. China J. Water **16**(22), 3168 (2024). https://doi.org/10.3390/w16223168
13. Duan, Q., Sorooshian, S., Gupta, V.: Effective and efficient global optimization for conceptual rainfall-runoff models. J. Water Resour. Res. **28**(4), 1015–1031 (1992). https://doi.org/10.1029/91WR02985
14. Jiang, C., Zhang, S., Xie, Y.: Constrained shuffled complex evolution algorithm and its application in the automatic calibration of Xinanjiang model. J. Front. Earth Sci. **10**, 1037173 (2023). https://doi.org/10.3389/feart.2022.1037173
15. Xu, D., Wang, W., Chau, K., et al.: Comparison of three global optimization algorithms for calibration of the Xinanjiang model parameters. J. Hydroinf. **15**(1), 174–193 (2013). https://doi.org/10.2166/hydro.2012.053
16. Naeini, M.R., Analui, B., Gupta, H.V., et al.: Three decades of the shuffled complex evolution (SCE-UA) optimization algorithm: review and applications. Scientia Iranica **26**(4), 2015–2031 (2019). https://doi.org/10.24200/sci.2019.21500
17. Ministry of Water Resources of the People's Republic of China: Standard for Hydrological Information and Hydrological Forecasting GB/T 22482-2008, Standards Press of China: Beijing, China (2008). (In Chinese)

Improvement of Fatigue Performance at U-Rib Weld by Rigid Deck Pavement

Zhiqing Chen[1(✉)], Zhengkai Li[1], Zheshi Wang[1], Dengyu Rao[1], and Jingyuan Chang[2]

[1] Guangzhou Expressway Co., Ltd., Guangzhou 510000, China
1429705033@qq.com
[2] China Railway Design Corporation, Wuhan 300308, China

Abstract. Orthotropic steel decks are widely used in various bridge types due to their high load-bearing capacity and excellent mechanical performance. However, two major issues persist in engineering applications: cracking at structural details and damage to deck pavement. This study investigates a steel cable-stayed bridge with severe pavement damage and minor cracks at the weld between the U-rib and top plate. A ultra-high toughness concrete (UHTC) composite structure was proposed as a new pavement scheme to replace the severely damaged asphalt pavement. The aim was to explore the effect of pavement replacement on the fatigue resistance of structural details and the control of crack propagation at the weld. To accurately evaluate the fatigue resistance, the hot-spot stress method was adopted. The stress history was calculated using the extrapolation formula recommended by the International Institute of Welding (IIW), and the fatigue life was further estimated. The results indicate that the stiffness loss of asphalt pavement significantly impairs the fatigue performance of the U-rib weld detail. The UHTC composite pavement demonstrates effective improvement in the fatigue resistance of this detail.

Keywords: Bridge Engineering · Orthotropic Steel Deck · Hot-Spot Stress Method · Ultra-High Toughness Concrete Composite Structure · Fatigue Life · Fatigue Performance

1 Introduction

Currently, domestic and international codes still widely adopt the nominal stress method for fatigue performance assessment. BS5400 [1] points out that the fatigue strength classification of structural details derived from the nominal stress method is not applicable to orthotropic steel deck (hereinafter referred to as OSD) structures. For this reason, researchers worldwide have drawn on the concept of the traditional nominal stress S–N curve method and further extended it to propose the hot spot stress S–N curve method.

Existing research shows that while the computational process and procedures are generally well-established when applying the hot spot stress S–N curve theory combined with finite element numerical methods to evaluate OSD structures, certain elements still require further discussion and determination based on specific practical issues. For

© The Author(s), under exclusive license to Springer Nature Switzerland AG 2027
G. Feng et al. (Eds.): ICCE 2025, SUCI, pp. 132–146, 2027.
https://doi.org/10.1007/978-3-032-32237-1_10

instance, the determination of the fatigue vehicle load model is significantly influenced by traffic volume statistics and computational efficiency, including the choice between single-axle or double-axle wheel loads, whether to consider lateral wheel path distribution, and the selection of an appropriate lateral probability model [2]. Additionally, the rationality of various hot spot stress extraction methods remains a topic of discussion [3]. Furthermore, regarding the mesh sensitivity inherent in the hot spot stress method, the "sub-model" approach [3, 4] is generally adopted to improve computational efficiency and result accuracy, though this inevitably introduces boundary condition errors. While many meaningful research findings provide valuable references, no unified approach exists for addressing these issues in specific case analyses.

This paper takes a bridge with observed fatigue damage in its orthotropic steel deck as the research prototype. Using the hot spot stress S–N curve method combined with finite element numerical simulations, the fatigue life at the rib-to-deck (hereinafter referred to as RD detail) weld is estimated under two conditions: the original asphalt pavement and the proposed STC pavement to be replaced [5, 6] This allows for an analysis of the improvement in fatigue resistance at this detail resulting from the rigid pavement overlay.

Taking an orthotropic steel deck bridge that has developed fatigue cracks as the research prototype, this study employs the hot spot stress S–N curve approach combined with finite element numerical simulations to estimate the fatigue life at the rib-to-deck (hereinafter referred to as the RD detail) weld under two conditions: the original asphalt pavement and the STC pavement scheduled for replacement. The objective is to evaluate the effectiveness of the rigid pavement system in enhancing the fatigue resistance of this critical structural detail.

2 Engineering Background

This study is based on a single-pylon, two-span cable-stayed bridge exhibiting deck pavement damage and micro-cracks in its orthotropic steel deck. The main girder consists of a composite structure with both steel and prestressed concrete sections. The prestressed concrete box girders are arranged on both sides of the pylon centerline, while the remaining segments of the main girder comprise a thin-walled steel box girder with five single-cell chambers. Figure 1 shows the 1/2 standard cross-section of the steel box girder.

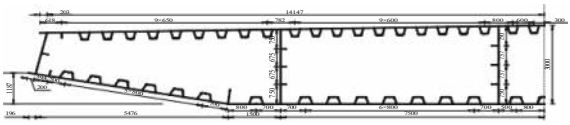

Fig. 1. Details of 1/2 standard cross-size of steel box girder (size unit: mm).

During its service life, the bridge has exhibited multiple defects, including severe deterioration of the asphalt pavement and the appearance of fine cracks at the rib-to-deck (RD) details of the steel deck. Previous studies have confirmed that for the same

structural detail, the fatigue failure mode is not unique—both the crack initiation location and propagation direction may vary, influenced by factors such as initial defects and loading conditions. Taking the U-rib-to-deck (RD) detail as an example, there exist four potential failure modes [7], as illustrated in Fig. 2. Existing research, both domestic and international, indicates that the most prevalent failure mode at this detail corresponds to case 1 in the figure. In alignment with actual bridge inspection findings, this study focuses on failure mode 1 of the RD detail for finite element analysis.

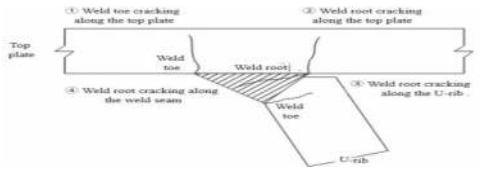

Fig. 2. Weld between u-rib and top plate.

The original deck pavement of the main bridge employed a 7 cm thick epoxy asphalt concrete layer. As shown in Fig. 3, given the presence of micro-cracks at certain rib-to-deck (RD) details, it was decided to replace the existing pavement with a Super-Toughness Concrete (STC) system to mitigate crack propagation. The STC pavement structure is illustrated in Fig. 4.

Fig. 3. Asphalt concrete pavement of original bridge.

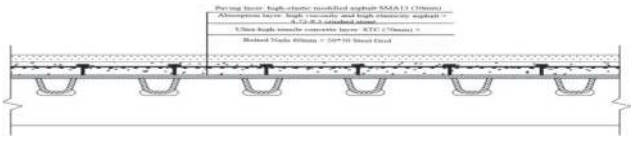

Fig. 4. STC paving diagram.

3 Theory of Fatigue Life Assessment

3.1 Actual Stress Composition at the Weld Toe

The hot-spot stress refers to the maximum structural stress or the critical stress at a hazardous point within a dangerous section of a structure, It is composed of the sum of components σ_{mem} and σ_b at the hot spot on the welded structural surface. As illustrated in Fig. 5, it should be noted that the hot-spot stress does not equal the true stress at the hot spot. The actual stress at the hot spot comprises three components: σ_{mem}, σ_b and σ_{nlp}. Among these, σ_{nlp} represents a self-equilibrating force system, primarily induced by the notch effect at the weld toe.

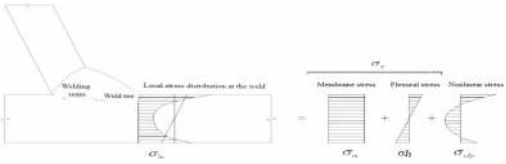

Fig. 5. True stress composition at weld toe.

3.2 Surface Extrapolation Method

The hot-spot stress at critical weld details can be obtained either through experimental measurements or via finite element analysis. The finite element methods for determining hot-spot stress include the direct extraction method, the surface extrapolation method, the linear thickness-dependent method, and Dong's hot-spot stress method.

As illustrated in Fig. 6, the subsequent calculations utilize the three-point quadratic extrapolation formula, which is widely used and recommended by the International Institute of Welding (IIW).The extrapolation procedure utilizes three nodal points, designated as $0.4t$, $0.9t$, $1.4t$ through the following formula (1):

$$\sigma_{hs} = 2.52\sigma_{0.4t} - 2.24\sigma_{0.9t} + 0.72\sigma_{1.4t} \tag{1}$$

Note: t denotes the plate thickness at the weld toe.

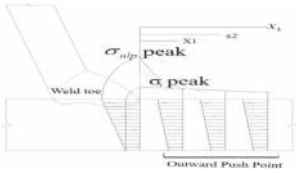

Fig. 6. Three-point twice surface extrapolation diagram [8].

3.3 Hot-Spot Stress S-N Curves

The hot-spot stress method offers advantages over the nominal stress method by accounting for stress concentrations caused by geometric discontinuities in welded details, thereby reducing reliance on multiple S-N curves and decreasing data scatter in fatigue assessment. In contrast to the notch stress method, it avoids considering intense stress concentrations induced by weld geometry, cracks, or notches, making it more straightforward to compute.

As shown in Fig. 7 (extracted from the European Standard 2005), Curves C90, C100, and C112 [9] are adopted for the subsequent fatigue life assessment. The parameters of these curves are summarized in Table 1, with the values in parentheses indicating the abscissa values.

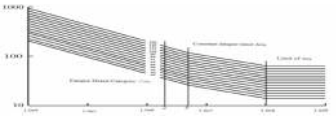

Fig. 7. Fatigue strength grade curve in eurocode3.

Table 1. Partial S-N curve values in eurocode3.

Detail Category	Fatigue Strength (2×10^6)	Constant Amplitude Fatigue Limit $\Delta\sigma_C$ (5×10^6)	Cut-off Limit $\Delta\sigma_L$ (1×10^8)	Negative Inverse Slope m
C112	112	83	45	3
C100	100	74	40	3
C90	90	66	36	3

3.4 Calculation of Equivalent Stress Amplitude and Fatigue Damage Assessment

The fatigue design verification using a two-slope S-N curve can be divided into the following steps:

(1) Determine the equivalent stress amplitude based on the principle of damage equivalence $\Delta\sigma_E$ [10], as given in Eq. (2);
(2) Modify the stress amplitude by incorporating the impact coefficient $\Delta\sigma_{eq}$ as specified in Eqs. (3), (4);
(3) Compare $\Delta\sigma_{eq}$ and $\Delta\sigma_D$, if $\Delta\sigma_{eq} > \Delta\sigma_D$, proceed to calculate the cumulative damage D using Miner's rule, as shown in Eq. (5);
(4) Estimate the service life of the structure $T = 1/D$

$$\Delta\sigma_E = \left[\left(\sum\left[n_i(\Delta\sigma_i)^{m_1}\right] + \Delta\sigma_D^{m_1-m_2}\sum\left[n_i\left(\Delta\sigma_j\right)^{m_2}\right]\right)/\left(\sum n_i + \sum n_j\right)\right]^{1/m_1} \quad (2)$$

$(\Delta\sigma_i, n_i)\left(\Delta\sigma_j, n_j\right)$——The stress spectrum pertaining to the linear segments $m_2 = 5$ and $m_1 = 3$ of the two-slope S-N curve;

$\sum n_i + \sum n_j$——The number of cycles corresponding to each stress amplitude is set at 2 million for the purpose of fatigue verification.

$$\mu = \left(yxmax_{dmax}/y_{xmax}\right) \quad (3)$$

μ denotes the impact factor; y_{dmax} denotes the maximum dynamic effect; y_{xmax} denotes the maximum static effect.

The stress range is modified using Equation:

$$\Delta\sigma_{eq} = \Delta\sigma'_{eq}(1 + \mu) \quad (4)$$

Miner Rule:

$$D_f = \sum_{i=1}^{m} \frac{n_i}{N_i} = \frac{n_1}{N_1} + \frac{n_2}{N_2} + \cdots + \frac{n_m}{N_m} = \frac{1}{C} \sum \left[n_i (\Delta\sigma_i)^m \right] \tag{5}$$

In Eq. (5):

m——total number of stress levels in the variable-amplitude loading spectrum;

n_i——actual number of cycles applied at the σ_i-th stress level;

N_i——constant amplitude fatigue life of the material or detail at the σ_i-th stress level;

D_f——cumulative damage index for the fatigue detail. Fatigue failure is predicted to occur when D_f reaches a critical threshold value.

4 Fatigue Life Estimation Using the Hot-Spot Stress S-N Curve Method

4.1 Multi-scale Finite Element Model

For fatigue-sensitive details in steel bridge deck structures, the stress state is primarily influenced by the secondary and tertiary structural systems, with minimal contribution from the primary system. Thus, the primary system effects may be neglected in the analysis. The extraction of hot-spot stresses via finite element analysis is highly sensitive to mesh size. To balance computational accuracy and efficiency, a half-span bridge segment model was adopted. A multi-scale finite element model was established by connecting local solid elements (refined mesh) with large-scale shell elements using the Multi-Point Constraint (MPC) algorithm. The specific element types used to define the MPC algorithm in ANSYS are illustrated in Fig. 8.

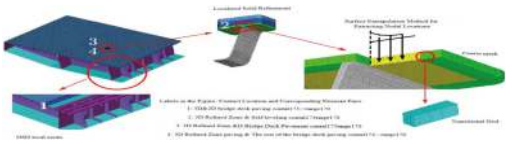

Fig. 8. Multi scale finite element model.

The model focused on a half-structure of six segments within a 9 m longitudinal range centered on the roof plate between two transverse diaphragms. Shell181 elements were employed to model the primary-scale plate components, while Solid186 elements simulated the bridge deck pavement. Simply supported constraints were applied at both longitudinal ends of the model.

To accurately extract the hot-spot stress at the weld toe of the U-rib-to-deck connection, a refined solid-element submodel was developed within a 240 mm × 150 mm region. The local weld geometry between the U-rib and diaphragm was modeled using 20-node Solid186 elements. A 7 mm fillet weld was adopted at the weld foot, with no initial welding defects considered, and the weld material properties were assigned identical to those of the bridge deck.

Refined meshing in the hot-spot stress extrapolation zone is critical for reliable stress extraction. Element sizes must be strictly defined in all directions, ensuring consistency with the selected extrapolation points and maintaining regular element shapes. Following the IIW recommendations [11], a swept mesh with six layers [12] was applied in the refined zone. The farthest extrapolation point in the formula was set at 2.5t from the weld toe. To minimize the influence of element distortion in the transition region, the refined mesh size was controlled within 2.0–2.5 mm, with a maximum extrapolation length of 35 mm.

Asphalt Pavement. Considering the severe deterioration of the original pavement during bridge service, which may amplify the stress response at fatigue details under identical vehicle loads, the finite element analysis incorporated reduced asphalt stiffness values (80%, 60%, and 40% of the original stiffness) to represent varying degrees of pavement damage. The original thickness and material parameters of the asphalt pavement are summarized in Table 2.

Table 2. Material and thickness of asphalt pavement.

Component	Thickness/mm	Material	Elastic Modulus (Mpa)	Poisson's Ratio	Density (t/mm^3)
Top Asphalt Layer	30	AC13	1400	0.35	2.35E-09
Bottom Asphalt Layer	40	AC25	1000	0.35	2.45E-09

STC Pavement. The bridge deck and pavement layer are connected by shear studs, whose shear resistance is typically considered as the primary mechanical contribution in analysis. Modeling the interface as fully bonded may yield overly conservative results. Thus, this study adopts a partially bonded interface for simulation. Common interface modeling techniques include contact elements, interface elements, or spring elements. Contact elements can account for interface friction, bond-slip, and surface roughness, and although they require more computational parameters, they provide more accurate results that better reflect real stress states.

This study investigates both the improvement effect of STC pavement on the fatigue performance of U-rib welds and the influence of STC pavement interface conditions on the fatigue performance at the weld toe of the deck-to-U-rib connection. Four interface bonding states—representing varying degrees of continuity between the steel deck layers—were defined by setting friction coefficients to 0.4, 0.6, 0.8, and 1.0. A total of 16 working conditions were analyzed by combining these friction coefficients with different wheel load magnitudes to obtain longitudinal stress time histories. The analysis of the pavement and orthotropic steel deck interaction is a surface-to-surface contact problem. Thus, contact elements were assigned to the bottom surface of the pavement layer. Compared to the asphalt pavement model, the contact element types (see Fig. 8) and key parameters were modified to simulate interface slip: The MPC algorithm in CONTA173 and CONTA174 elements was replaced with the penalty function method. The contact

behavior was changed from "bonded" to "no separation with sliding."Additionally, the material parameters of the pavement layers were adjusted as summarized in Table 3.

Table 3. Parameters of STC paving materials.

Component	Thickness/mm	Material	Elastic Modulus (MPa)	Poisson's Ratio	Density (t/mm^3)
SMA13 Top Layer	30	SMA13	1400	0.35	2.46E-09
STC Bottom Layer	50	STC	4.00E + 05	0.3	2.80E-08

4.2 Fatigue Vehicle Load

Field investigations indicated that heavily loaded trucks crossing the bridge are primarily four-axle coal transporters, often operating with significant overload. Based on toll station statistics, two typical axle load configurations were identified for fatigue assessment, as illustrated in Fig. 9(a).

Given the highly localized stress distribution characteristics of orthotropic bridge decks, and considering the large axle spacing of the fatigue vehicle model, preliminary calculations confirmed that the interaction effects between axles are negligible. Consequently, only the rear tandem axle group was applied for loading. In accordance with the Chinese specification JTG D64-2015 Code for Design of Steel Highway Bridges, the tire contact area was defined as 600 mm × 200 mm, as shown in Fig. 9(b).

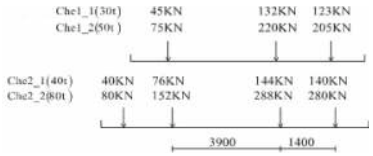

(a) Fatigue load axle weight distribution diagram

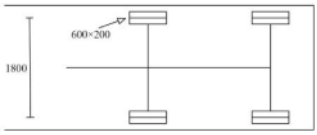

(b) Wheel load layout plan

Fig. 9. Axle load distribution and wheel load plan (size unit: mm).

4.3 Most Unfavorable Transverse Load Position

Based on the defined fatigue vehicle load and established finite element model, seven transverse load cases were determined centered on the critical fatigue detail, as illustrated in Fig. 10. During loading, the longitudinal center of the wheel load was positioned directly above the fatigue detail.

Computational results indicated that the transverse stress at the weld zone between the deck plate underside and the U-rib reached its maximum value when the dual-wheel load was applied at Case 6. Figure 11 shows the deformation contour under Case

6, revealing that the stress distribution was localized around individual wheel loads. Consequently, multiple vehicles in the same or adjacent lanes did not exhibit significant stress superposition effects at specific locations. This finding is consistent with the full-scale test results reported by Wang Chunsheng [13]. Therefore, multi-vehicle effects were neglected in the calculation of longitudinal stress time histories, and only single-vehicle (tandem-axle dual-wheel) loading was applied. Similar conclusions have been drawn in relevant literature analyzing the local mechanical behavior of orthotropic steel bridge decks [14].

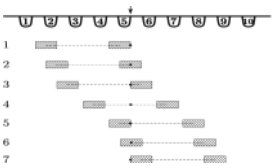

Fig. 10. Transverse load condition.

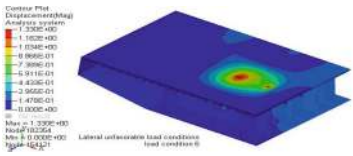

Fig. 11. Deformation plan of condition 6.

4.4 Longitudinal Stress Time History

Calculation Results for Asphalt Pavement. After determining the most unfavorable transverse wheel position, the longitudinal moving load simulation was performed using a tandem-axle dual-wheel configuration to convert the load frequency spectrum into a stress spectrum. The front axle started 4.2 m ahead of the critical detail and moved in 0.3 m increments until fully passing the target deck plate location.

The stress extraction and interpolation methods consistent with the transverse analysis were applied. Figure 12 presents the results of 16 stress time histories corresponding to four vehicle loads and four pavement stiffness conditions.

Calculation Results for STC Pavement. For clarity, the following notations are defined, Symbols $\boldsymbol{\sigma_{s-x}}$ and $\boldsymbol{\sigma_{s-3}}$ represent the hot-spot stresses obtained through interpolation calculations based on three nodal extracts $\boldsymbol{\sigma_x}$ and $\boldsymbol{\sigma_3}$; $\boldsymbol{\Delta\sigma_{s-x}}$ and $\boldsymbol{\Delta\sigma_{s-3}}$ denote the amplitudes derived from the stress time histories of $\boldsymbol{\sigma_{s-x}}$ and $\boldsymbol{\sigma_{s-3}}$, respectively.

The primary distinction between the longitudinal stress time histories of the STC and asphalt pavement models lies in the variation of principal stress directions with wheel positions. Figure 13(a) spatially illustrates the results from Fig. 12: for intact asphalt pavement, the orientations of the three principal stresses at Point 1 (the interpolation point closest to the fatigue detail) and their projections in the longitudinal and transverse directions vary with the Che2_2 vehicle position. Correspondingly, Fig. 13(b) shows the variation in principal stress directions at the same point for the STC pavement model with a friction coefficient U = 1.

To further investigate the characteristics of the stress time histories in the STC model, the direction cosine of each interpolation point σ_3 along the X-axis (transverse direction) was extracted for the Che2_2 case, as plotted in Fig. 14. In each subfigure: (a) shows the hot-spot stress time history σ_3 obtained by interpolating point σ_{s-3}; ; (b) presents the

direction cosine of point σ_3 along the X-axis; (c) displays the projection of σ_{s-3} from (a) onto the x-y plane σ_{s-x}, , mapped via (b).

Analysis of Fig. 12 indicates that reduced pavement stiffness significantly increases the stress amplitude at the rib-deck (RD) detail. Figure 13(a) reveals an abrupt change in principal stress direction when the wheel load is directly above the fatigue detail. In contrast, Fig. 13(b) demonstrates that considering interface contact in the STC model delays and smoothens this directional change, resulting in a more gradual transition.

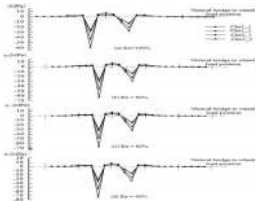

Fig. 12. Longitudinal stress history of asphalt pavement under various stiffnesses.

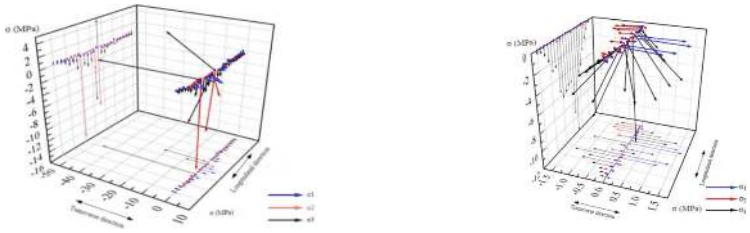

(a) Asphalt Pavement EX=100%, Che2_2 (b) STC Pavement 1.0 , Che2_2

Fig. 13. Comparison of stress direction with load position in two models.

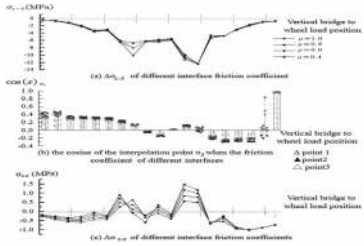

Fig. 14. Che 2–2 longitudinal stress history when acting on STC pavement.

By comparing Figs. 13(a) and (b), the following observations can be drawn:

1) For both models, one of the three principal stresses remains zero at any wheel load position, while the other two lie within the *x-z* plane. The stress directions indicate

that, when neglecting the influence of welding residual stresses, the fatigue detail remains under biaxial compression under wheel loading alone.

2) For the asphalt pavement, when the wheel load acts directly above the fatigue detail, σ_x is entirely governed by σ_3. Further analysis reveals that the difference between $\Delta\sigma_{s-x}$ and $\Delta\sigma_{s-3}$ is approximately 4% for the front axle and 13% for the rear axle. In contrast, the STC model shows differences of about 80% and 85% for the front and rear axles, respectively.
3) Due to the increased stiffness and thickness of the STC pavement, the peak stresses calculated in the STC model are significantly reduced. When the wheel load is far from the fatigue detail, the compressive stress values are negligible ($\leq$5MPa) and thus excluded from analysis. Only the algebraic variations of σ_{s-3} from both models are considered. Compared to the intact asphalt pavement, the STC model with four interface friction coefficients ($\mu = 1.0$, $\mu = 0.8$, $\mu = 0.6$, $\mu = 0.4$) exhibits reductions in B for the front axle of 88.5%, 89.2%, 89.9%, and 90.7%, respectively, and for the rear axle of 55.0%, 57.8%, 60.8%, and 64.4%. These results demonstrate that neglecting stress direction changes and focusing solely on stress amplitude reduction after pavement replacement may lead to an overestimation of stress reduction [15–17].

Further comparison of Figs. 14 (a) and (c) reveals:

1) The influence of interface friction coefficient variation on σ_{s-x} differs between the front and rear axles when directly above the fatigue detail.
2) The shape of the stress time history in the STC model differs significantly from that of the asphalt pavement;
3) The two stress peaks generated by the front and rear axles exhibit superposition effects. The slow decay of the stress peak after the front axle passes the detail in (a) contributes to the three peaks observed in the mapped.

Figure 14(b) demonstrates:

1) The direction of each interpolation point σ_3 remains nearly unchanged across different interface friction coefficients.
2) For a given friction coefficient and vehicle load, the directions of all interpolation points are consistent.
3) When interface slip is considered in the STC model, the interaction between axles leads to superimposed computational results.
4) For any specific load and friction coefficient, although the principal stress direction varies longitudinally, the stress directions at interpolation points remain consistent at fixed wheel positions, validating the feasibility of hot-spot stress extrapolation.

4.5 Calculation of Equivalent Stress Amplitude

The equivalent stress amplitudes for both pavement types were calculated according to the specified formula, as summarized in Table 4 and Table 5.

Table 4. Asphalt pavement equivalent stress amplitude calculation results.

Stiffness	C90(MPa)	C100(MPa)	C112(MPa)
$Ex = 100\%$	99.82	102.13	104.50
$Ex = 80\%$	105.61	108.05	110.56
$Ex = 60\%$	112.61	115.21	117.89
$Ex = 40\%$	121.54	124.35	127.24

Table 5. STC pavement equivalent stress amplitude calculation results.

Stiffness	C90(MPa)	C100(MPa)	C112(MPa)
$\mu = 1.0$	3.51	3.59	3.67
$\mu = 0.8$	2.92	2.98	3.05
$\mu = 0.6$	2.37	2.42	2.47
$\mu = 0.4$	1.86	1.90	1.95

The dynamic impact coefficients for both pavement types were calculated based on the specified formula, yielding values of 1.234 for the asphalt pavement and 1.236 for the STC pavement. With reference to domestic and international standards and literature [18], the calculated impact coefficient may be taken as $\mu = 0.15 \sim 0.75$ (typically not exceeding 0.3). The modified equivalent stress amplitudes, further computed using the formula, are summarized in Table 6 and Table 7.

Table 6. Asphalt pavement equivalent stress amplitude correction results.

Stiffness	C90(Mpa)	C100(Mpa)	C112(Mpa)
$Ex = 100\%$	123.18	126.03	128.95
$Ex = 80\%$	130.32	133.33	136.43
$Ex = 60\%$	138.96	142.17	145.48
$Ex = 40\%$	149.98	153.45	157.01

Table 7. STC pavement equivalent stress amplitude correction results.

Stiffness	C90(MPa)	C100(MPa)	C112(MPa)
$\mu = 1.0$	4.34	4.44	4.54
$\mu = 0.8$	3.61	3.68	3.77
$\mu = 0.6$	2.93	2.99	3.05
$\mu = 0.4$	2.30	2.35	2.41

4.6 Fatigue Damage and Life Assessment

Using the calculated results incorporating the impact coefficient, the damage and service life of the detail under varying pavement stiffness conditions were evaluated according to the European standard fatigue strength category curves (C90, C100, C112) shown in Fig. 7. Figure 15 presents the daily traffic volume for each fatigue vehicle type required for the calculation, and Fig. 16 shows the corresponding fatigue stress amplitudes under each pavement condition. It can be observed that for a fixed stiffness condition, each passage of a wheel load induces two distinct stress peaks, resulting in eight stress amplitudes for the four vehicle types. Further analysis reveals that when the pavement stiffness is reduced to 80%, 60%, and 40%, the increase in damage D caused by the front and rear axles remains proportional across all vehicle types, despite differences in their axle weights. The proportional increases for the front axle under the three reduced stiffness conditions are 5.79%, 6.60%, and 7.78%, respectively, while those for the rear axle are 6.24%, 7.34%, and 9.01%.

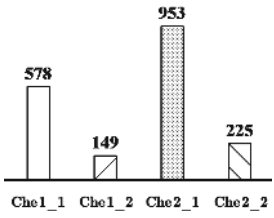

Fig. 15. Daily traffic of different vehicle model.

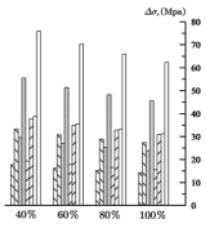

Fig. 16. Stress of different pavement stiffness.

Following the aforementioned formula and referring to the standard curves, the cumulative damage caused by each vehicle type (considering only the overloaded vehicles Che1_2 and Che2_2, whose stress amplitudes contribute to damage) was computed for the three S-N curves under different pavement stiffness conditions. Figure 17 illustrates the cumulative damage values (outside parentheses) and their respective proportions (inside parentheses) contributed by these two vehicle types.

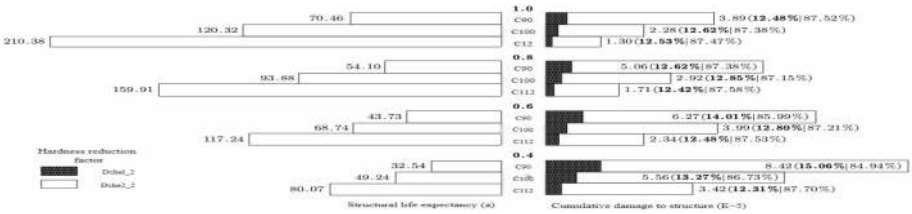

Fig. 17. Damage life for different pavement stiffnesses corresponding to different S-N curves.

The results indicate that the choice of S-N curve significantly influences the calculated fatigue life, and stiffness reduction markedly affects the fatigue performance of the studied detail.

5 Conclusion

1) Asphalt pavement deterioration significantly impacts the fatigue performance of the rib-deck (RD) detail. The stress time history shape of the STC pavement model differs considerably from that of the asphalt pavement. Based on finite element results of the STC pavement, neglecting the influence of stress direction changes and considering only the reduction in stress amplitude after pavement replacement is incomplete, potentially leading to an overestimated stress reduction. Essentially, after STC pavement application, the fatigue behavior of the RD detail transitions from a uniaxial to a biaxial fatigue model.
2) For stress time history results simulated using the STC interface slip model, the vectorial nature of stress should be considered in the analysis.
3) Owing to the increased stiffness and thickness of the STC pavement, the peak stress is significantly reduced to below the constant amplitude fatigue limit, theoretically endowing the detail with infinite fatigue life.

Acknowledgments. This work was supported by the National Key Research and Development Program of China [2022YFC3801100].

References

1. British Standard: Steel, Concrete and Composite Bridges-Part 10: Code of Practice for Fatigue. BS5400 (1999)
2. Yang, S.L: Effect of transverse multi-track loading on fatigue behavior of orthotropic steel bridge deck (Master Dissertation) Southwest Jiaotong University (2015)
3. Wang, Y., Shao, X., Chen, J., et al.: UHPC-based strengthening technique for orthotropic steel decks with significant fatigue cracking issues. J. Constructal Steel Res. **176**, 106393 (2021). https://doi.org/10.1016/j.jcsr.2020.106393
4. Pu, Q.H., Gao, L.Q., Liu, Z.B., et al.: Fatigue assessment of orthotropic steel bridge deck based on hot spot stress method. J. Southwest Jiaotong Univ. **26**(3), 395–401 (2013). https://doi.org/10.3969/j.issn.0258-2724.2013.03.001

5. Fan, L., Yang, W., Zhou, D., et al.: Temperature distribution and mechanical response of orthotropic steel bridge deck during paving of gussasphalt pavement. Int. J. Steel Struct. **21**(2), 315–328 (2021). https://doi.org/10.1007/s13296-020-00440-3
6. Su, Q., Xie, W., Shi, Z., et al.: Cracking behavior of segmented-casting joint in steel-UHPC composite bridge deck system: experiment and numerical simulation. J. Eng. Struct. **315**, 118457 (2024). https://doi.org/10.1016/j.engstruct.2024.118457
7. Li, C., He, L., Pei, B., et al.: Fatigue behavior and damage mechanism of steel plate-UHPC composite bridge deck subjected to negative bending moment. J. Structures **65**, 106754 (2024). https://doi.org/10.1016/j.istruc.2024.106754
8. Huang, Y., Chen, S., Gu, P.: Interface stress analysis and fatigue design method of steel-ultra high performance concrete composite bridge deck. J. Structures **38**(9/11), 1453–1464 (2022). https://doi.org/10.1016/j.istruc.2022.03.005
9. Shi, Z., Su, Q., Kavoura, F., et al.: Behavior of short-headed stud connectors in orthotropic steel-UHPC composite bridge deck under fatigue loading. J. Int. J. Fatigue **160**, 106845 (2022). https://doi.org/10.1016/j.ijfatigue.2022.106845
10. Xiang, H.F.: Higher Bridge Structure Theory (Second Edition) Beijing: China communications press (Book) (2013)
11. Hua, Y., Zhe, Y., Bing, H., et al.: Failure mechanisms governing fatigue strength of steel–SFRC composite bridge deck with U-Ribs. J. Bridge Eng. **26**(4), 04021014 (2021). https://doi.org/10.1061/(ASCE)BE.1943-5592.0001692
12. Ji, B.H., Fu, Z.Q.: Fatigue and maintenance of steel bridges Beijing: China communications press (Book) (2016)
13. Guan, Y., Wu, J., Sun, R., et al.: Shear behavior of short headed studs in Steel-ECC composite structure. J. Eng. Struct. **250**, 113423 (2022). https://doi.org/10.1016/j.engstruct.2021.113423
14. Feng, B.: Hot spot stress analysis and fatigue research on structural details of highway orthotropic steel bridge deck (Master Dissertation) Southwest Jiaotong University (2014)
15. Xu, X.Q., Liu, Y.Q.: Punching shear behavior of steel-concrete composite decks with different shear connectors. J. Adv. Struct. Eng. Mech. **25**(6), 1351–1357 (2024)
16. Cheng, Z.Y., Zhang, Q.H., Bao, Y., et al.: Flexural behavior of corrugated steel-UHPC composite bridge decks. J. Eng. Struct. **246**, 113066 (2021). https://doi.org/10.1016/j.engstruct.2021.113066
17. Zhou, Z.M., Xie, X.Q., Xiao, L.J.: Research and application of new orthotropic steel plate-STC composite bridge deck structure. J. Liaoning Provincial College Commun. **04**, 81 (2013)
18. Jiang, J., Zou, Y., Yang, J., et al.: Study on bending performance of epoxy adhesive prefabricated UHPC-steel composite bridge deck. J. Adv. Civil Eng. **1**, 6658451 (2021). https://doi.org/10.1155/2021/6658451

Research on Crack Control Technology System of Mass Concrete Side Wall of Open-Cut Tunnel under Water-Rich Environment of Soft Foundation Based on Comprehensive Evaluation

Wei Deng[1,2(✉)], Huan-yong Chen[1,2], Jin-liang Wang[3], Yuan-xi Chen[3], and Feng Jiang[4]

[1] Guangdong Bay Area Transportation Construction Investment Co., Ltd., Guangzhou 511455, China
1742333450@qq.com
[2] Guangdong Provincial Highway Construction Co., Ltd., Guangzhou 510699, China
[3] China Communications Road and Bridge Construction Co., Ltd., Beijing 100120, China
[4] School of Transportation Science and Engineering, Harbin Institute of Technology, Harbin 150090, China

Abstract. Aiming at the cracking problem of mass concrete side wall of open-cut tunnel in soft foundation water-rich environment, a composite construction technology system combining active crack resistance and weakening constraint is proposed. Through 11 groups of field tests, the research integrates various measures such as horizontal reinforcement encryption, adding anti-cracking agent and segmented pouring, breaks through the limitations of a single process, selects a better process, and constructs a set of physical indicators and economic indicators. The comprehensive index of crack control evaluation, introducing "unit effect incremental cost" as the core decision-making basis. The results show that the composite process of "horizontal reinforcement encryption + anti-cracking agent" can stably control the maximum crack width within the design limit of 0.15 mm, which is the first choice under the high performance demand, and the comprehensive evaluation further identifies that the segmented pouring is the preferred scheme for zero cost efficiency. The complete technical path from composite technology to comprehensive evaluation formed in this study provides a certain reference from method to decision for the active control of cracks in tunnel engineering.

Keywords: Composite construction technology · Evaluation index system · Crack control · Open-cut tunnel · Cost-effective

1 Introduction

With the rapid development of China's economy and the continuous investment in infrastructure construction, China has gradually become the country with the fastest construction and the largest number of tunnels and underground projects in the world. According

© The Author(s), under exclusive license to Springer Nature Switzerland AG 2027
G. Feng et al. (Eds.): ICCE 2025, SUCI, pp. 147–158, 2027.
https://doi.org/10.1007/978-3-032-32237-1_11

to statistics, by the end of 2023, there have been 18,573 railway tunnels in operation in China, with a length of 23,508 km, including 4,561 high-speed railway tunnels, with a total length of 7735 km [1]. In the traditional open-cut tunnel engineering, cracks in mass concrete structures are common and difficult to completely avoid technical problems [2]. Although there have been many studies on the causes of concrete cracking, anti-cracking materials and temperature change control [3–7], there are relatively few studies on other construction techniques. The existing tunnel mass concrete side wall has limitations in structural safety and durability, and the research on crack control technology of open-cut tunnel side wall needs to be strengthened.

During the construction and operation of water-rich tunnel on soft foundation, it is faced with the safety challenges of tunnel lining cracking and water leakage, especially in poor strata and groundwater-rich areas [8–11]. In addition, the structure of water-rich tunnel on soft foundation adjacent to existing buildings is complex, and the change of groundwater level is easy to cause floating cracking or uneven settlement cracking of tunnel concrete structure. It has the characteristics of long duration, easy repetition of disasters and high degree of harm, which seriously reduces the mechanical properties and durability of lining structure and affects the safe service life of water-rich tunnel on soft foundation.

In order to solve the problem of crack control of mass concrete side wall of open-cut tunnel in water-rich environment of soft foundation, this study proposes an innovative composite construction technology system. Firstly, the causes of cracks are obtained by analyzing the structure and environment of the tunnel side wall. Then, according to the on-site construction progress, the process test is carried out from two aspects: enhancing the anti-cracking ability of the side wall structure (adding polypropylene fiber, encrypting longitudinal structural bars, adding anti-cracking agent, setting prestress) and weakening the constraints and reducing the pouring temperature peak (segmented pouring of side wall), and the cracks are observed. Finally, the evaluation index system of crack control is established, and the comprehensive comparison and selection are carried out in combination with engineering economy to determine the optimal crack control construction technology. The purpose of this study is to provide theoretical basis and practical reference for crack control of mass concrete side wall of open-cut tunnel, which is of positive significance to improve the construction quality of similar projects.

2 Project Profile

The under-crossing tunnel of provincial highway P111 in the Lion Ocean Link Project is located in Miaobei Village, Nansha District, Guangzhou City, and adopts the standard of two-way six-lane first-class highway and urban trunk road. The tunnel adopts a single-layer scheme, with a maximum transverse slope of 2%, a maximum buried depth of 2.3 m, a clearance size (width × height) of 13.25 m × 5.0 m, and a total length of 495 m. The length of the entrance open section is 180 m, which is divided into 6 segments. The length of the buried section of the open cut excavation is 150 m, and the construction is divided into 5 sections. The length of the open section of the exit is 165 m, which is divided into 5 segments. The open section of the entrance and exit of the underpass tunnel adopts an open U-shaped groove frame structure, and the buried section adopts

a rectangular section. The thickness of the structural bottom plate is 80 cm–120 cm, and the side wall is 70 cm–110 cm. All of them are C45 waterproof concrete with impermeability grade P8. The cross section is shown in Fig. 1.

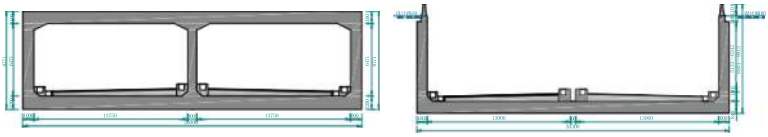

(a) Buried section (b) Open segment

Fig. 1. The main cross-section structure of the underpass tunnel (unit: mm).

2.1 Vehicle Model and Load Conditions

Since the construction of the side wall of the P111 tunnel began, vertical penetration cracks have occurred in the construction of the side wall. Taking MJD16 as an example, under the maintenance measures that meet the requirements of the specification, vertical penetration cracks occurred in the construction of the first section of the side wall MJD16.Cracks began to appear on the 3rd day after the completion of the pouring, and the cracks stopped changing after 5 days: a total of 10 cracks on the left side, with a crack width of 0.10 mm–0.25 mm and an average width of 0.16 mm; there are a total of 18 cracks on the right side, with a crack width of 0.10 mm–0.25 mm and an average width of 0.18 mm.

The main causes of tunnel side wall cracks are construction technology, environmental factors and structural design. In view of the construction technology, there is a age difference between the tunnel floor and the side wall in two times of pouring, which makes the concrete shrinkage of the floor and the side wall inconsistent. The floor is poured first, hardened and relatively stable, and the side wall is poured later. During the shrinkage process, it is constrained by the floor to form a large shrinkage stress. Once the tensile strength of the concrete is exceeded, the side wall will crack. In view of the environmental factors, after the side wall concrete is poured, the hydration heat causes the internal temperature to rise sharply. In autumn and winter in Guangdong, the temperature difference between day and night is large, the temperature is low in the morning and evening, the temperature is high at noon, and the external environment temperature is low. This temperature difference between inside and outside aggravates the shrinkage of concrete. At the same time, the windy environment on site causes the surface of concrete to lose water too fast before initial setting, which further promotes the generation of shrinkage cracks. For the structural design, the horizontal reinforcement spacing of the side wall of the project is 200 mm. The spacing is relatively large, and the restraint ability of the concrete shrinkage is insufficient. It is difficult to effectively resist the tensile stress caused by shrinkage, and to a certain extent, it also creates conditions for cracks. Based on the field situation and mechanism analysis, the cracking of the side wall concrete is mainly shrinkage cracks. The tensile stress caused by the deformation of

the bottom plate under the constraint of the side wall is greater than the crack resistance of the side wall concrete itself, so cracks are generated.

3 Process Test

3.1 Test Scheme

The test object selects the large volume concrete side wall of the tunnel under the provincial road P111 of the Shiziyang channel project. The thickness of the side wall is 1 m, and the length is divided into 30 m or 35 m according to the actual pouring length. One pouring, pouring into the mold temperature is considered to be 28 °C, and the temperature difference between the inside and outside is 30 °C. Before pouring, the aggregate is poured, the concrete is mixed with ice and other measures to ensure that the concrete mold temperature is controlled below 28 °C. The maintenance adopts film + geotextile for spray curing, which is a general process for mass concrete construction and reduces cracking. The specific construction object is shown in Fig. 2.

Fig. 2. Side wall diagram.

Under the above standard construction technology, according to the on-site construction progress, the process test is carried out from two aspects: enhancing the anti-cracking ability of the side wall structure itself and weakening the constraints and reducing the pouring temperature peak. The following four measures are adopted to enhance the anti-cracking ability: (1) Adding polypropylene fiber; (2) The longitudinal structural reinforcement is encrypted to 10 cm (φ16@10 cm) or 20 cm (φ16@20 cm); (3) Adding magnesia high-performance anti-cracking agent (8% content); (4) Set up post-tensioned prestressing, a bundle of three steel strands, a single steel strand diameter of 15.2 mm (3ϕs15.2). Weaken the constraints and reduce the pouring temperature peak using the side wall segment pouring, the specific test plan is shown in Table 1.

After the side wall of the tunnel is poured for 3 days, the strength is up to the standard, and the mold is removed and maintained. At the same time, the development of cracks is observed. At 3–7 days, the development of cracks is observed twice a day. After 7 days, the development of cracks is observed every 2 days until the cracks do not develop. Record the width, length, depth and distribution position of the cracks, as shown in Fig. 3.

3.2 Crack Control Evaluation Indicators

In order to quantitatively evaluate the actual effects of various crack control processes proposed, and to select a better process plan that is technically and economically feasible,

Table 1. Process test plan.

Process number	Length (m)	Width (m)	Height	Crack control measures (m)
P0	30	0.9	3.34	No measures, as a control group according to the original design and construction
P1	30	0.9	3.34	Polypropylene fiber added to concrete
P2	30	0.9	4.53	Horizontal reinforcement encryption (φ16@20 cm) + anti-cracking agent (8%)
P3	30	1	5.74	Segmental pouring (15 m)
P4	30	1	5.74	Post-tensioned prestress (3ϕs15.2)
P5	30	1.1	6.92	The original design of steel bars and densified steel bars are φ16@10 cm
P6	30	1	5.54	Post-tensioned prestress (3ϕs 15.2) + reinforcement encryption (half of the original design reinforcement + φ16@20 cm, half of φ16@10 cm)
P7	30	1	5.54	Post-tensioned prestress (3ϕs 15.2) + horizontal reinforcement encryption (φ16@20 cm)
P8	35	0.9	4.20	Horizontal reinforcement encryption (φ16@20 cm) + anti-crack agent (8%) + segmented pouring (15 m)
P9	35	0.8	2.76	Magnesium high performance anti-cracking agent (8%)
P10	35	0.8	2.76	The middle 12 m horizontal steel bars are encrypted (φ16@20 cm).

Fig. 3. In-situ crack observation map.

a comprehensive crack control evaluation index system was studied and constructed, and a progressive comprehensive evaluation was carried out from three dimensions: physical index (technical effect), economic index (cost) and comprehensive index (cost-effective).

(1) Physical indicators are obtained by on-site observation and data collection of the tunnel side wall after the maintenance period, aiming to directly quantify the morphological characteristics of the cracks. The physical indicators used in this study are as follows: number of cracks, maximum crack width, minimum crack width, average crack width, and total crack width.
(2) Economic indicators, from the cost point of view to assess the feasibility of engineering application of crack control technology, the incremental cost as the core economic indicators. The incremental cost is the additional cost of implementing a certain crack control process compared with the traditional benchmark process, including the material cost (such as polypropylene fiber, anti-cracking agent, additional steel bar), labor cost and mechanical use cost (such as prestressed tension, segmented formwork support, etc.) directly increased by the new process.
(3) Comprehensive indicators. In order to overcome the limitation of single dimension evaluation and realize the unity of technical effect and economic benefit, 'unit effect incremental cost 'is proposed as the core comprehensive index for process comparison and selection. The unit effect incremental cost is defined as the ratio of the improvement degree of physical index to the incremental cost of economic index, and its calculation is shown in the Eq. (1).

$$\lambda = \frac{C_i - C_0}{W_0 - W_i} \tag{1}$$

λ: Incremental cost per unit effect (yuan/m^3/mm);
$W0$: The total crack width (mm) of the reference process (control group);
Wi: The total crack width (mm) of the i-type crack control process;
$C0$: the unit volume cost of the benchmark process (yuan/m^3);
Ci: The unit volume cost (yuan/m^3) of the i-type crack control process.

The economic meaning of this indicator is: for every 1 mm reduction in the total width of the crack, the additional cost per unit volume required to be invested (yuan). The smaller the value of the process, the higher the cost-effectiveness, which is the optimal choice under the balance of technology and economy.

4 Analysis of the Results

4.1 Physical Indicators

In order to systematically evaluate the actual effect of different crack control processes, the tunnel side wall of P0–P10 test party was observed on site, and the quantitative data of physical indexes such as crack number, maximum width, minimum width, average width and total width were obtained. The results are summarized in Table 2, and the total crack width is shown in Fig. 4.

As shown in Table 2 and Fig. 4, compared with the control group (P0), most of the new processes (P2–P9) show a significant reduction in the total width of cracks, which proves the overall effectiveness of crack control measures. However, the effect of P1 and P10 is not ideal. The total crack width of P1 is even 7.0% higher than that of the control group, while P10 is increased by 23.0%, which indicates that the two processes have

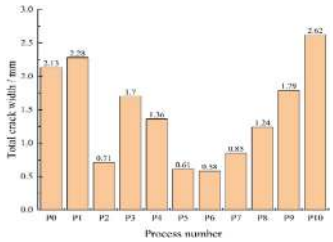

Fig. 4. Comparison of total width of cracks in different processes.

serious problems in the application environment. From the comprehensive index of total crack width, P6 (0.58 mm), P5 (0.61 mm) and P2 (0.71 mm) are the three schemes with the most excellent crack control effect, and the total crack width is reduced by 72.8%, 71.4% and 66.7% respectively compared with P0.

The maximum crack width is directly related to the durability limit of the structure. The best P2 and P6 successfully limit the maximum crack width to 0.12 mm, which is much lower than the 0.25 mm of the control group, which is very important for improving the long-term durability of the structure. The maximum crack width of P9 reaches 0.29 mm, which is the most unfavorable of all schemes and may pose a threat to the waterproof performance of the structure.

Table 2. Observation results of physical indexes of different crack control processes.

Process number	Crack number	Maximum crack width (mm)	Minimum crack width (mm)	Average crack width (mm)	Total crack width (mm)
P0	11	0.25	0.12	0.19	2.13
P1	11	0.25	0.14	0.21	2.28
P2	10	0.12	0.01	0.07	0.71
P3	10	0.2	0.1	0.17	1.7
P4	8	0.2	0.15	0.17	1.36
P5	6	0.15	0.05	0.10	0.61
P6	7	0.12	0.04	0.08	0.58
P7	9	0.15	0.04	0.09	0.85
P8	12	0.14	0.06	0.10	1.24
P9	8	0.29	0.17	0.22	1.79
P10	19	0.24	0.03	0.14	2.62

The average crack width reflects the overall level of crack development. P2 (0.07 mm) and P6 (0.08 mm) also perform best, indicating that the process can not only suppress the widest cracks, but also generally refine all cracks. The difference between the minimum crack width and the maximum and minimum crack width can reflect the uniformity of

crack development. The minimum crack width of P2 is only 0.01 mm, and the difference between the maximum and minimum width (0.11 mm) is small, indicating that the crack morphology is mostly fine and uniform distribution, which is beneficial to the durability of the structure.

Among them, P10 shows an extremely abnormal working condition: the number of cracks (19) is far more than other schemes, but the average crack width (0.14 mm) and the maximum crack width (0.24 mm) are not the highest, which indicates that P10 may greatly increase the brittleness of concrete, resulting in a large number of fine cracks, but it inhibits the development of macroscopic main cracks, and its comprehensive effect (the maximum total crack width) is the worst. The indicators of P1 were almost the same or slightly worse than those of the control group P0, indicating that the measure was basically ineffective under the conditions of this study.

From the perspective of physical indicators, P6, P5 and P2 are the three schemes with the best crack control effect. They can significantly reduce the number, width and total width of cracks, while P1, P9 and P10 should be reviewed or eliminated in the subsequent comprehensive evaluation due to their poor effect or negative impact.

4.2 Economic Indicators

Economic index is the key dimension to judge the feasibility of crack control process engineering. This study takes incremental cost as the core economic index, and calculates the incremental cost per unit volume generated by ten new crack control processes P1–P10 compared with the traditional benchmark process P0, including material cost, labor cost and mechanical use cost. The specific results are summarized in Table 3, and the total cost of process increment is shown in Fig. 5.

Table 3. Incremental cost per unit volume of different fracture control processes.

Process number	Labor costs (yuan/m^3)	Material costs (yuan/m^3)	Mechanical use costs (yuan/m^3)	Total cost (yuan/m^3)
P1	9.53	0.00	0.00	9.53
P2	136.26	0.00	0.00	136.26
P3	0.00	0.00	0.00	0.00
P4	103.07	87.15	0.00	190.21
P5	81.24	0.00	0.00	81.24
P6	167.54	90.28	0.00	257.82
P7	203.18	90.28	0.00	293.46
P8	154.25	0.00	0.00	154.25
P9	38.66	0.00	0.00	38.66
P10	67.54	0.00	0.00	67.54

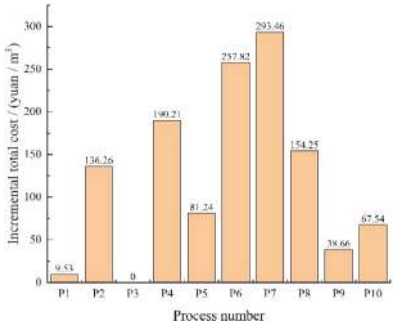

Fig. 5. Incremental cost comparison of different fracturing control processes.

It can be seen from Table 3 and Fig. 5 that the incremental costs of the 10 crack control processes are significantly different, and the distribution range is from 0 yuan/m^3 to 293.46 yuan/m^3.

The incremental cost of single measure process (P1–P5) is distributed in the range of 0 ~ 190.21 yuan/m^3. Among them, the cost of P3 is zero, showing a unique economic advantage, and P4 has become the most expensive solution in a single measure because it involves material costs.

The incremental cost of the composite measure process (P6–P1) is distributed between 38.66 and 293.46 yuan/m^3, which is significantly higher than that of the single measure, which is in line with the general law of "measure superposition and cost superposition" Among them, P7 integrates higher labor and material costs, which is the highest incremental cost (293.46 yuan/m^3) among the 10 schemes.

From the economic point of view, P3 with 0 cost and P1 and P9 with low cost are the first choices. However, the decision must be made in combination with the effect of physical crack control. Some processes with medium cost, such as P5 with excellent effect, may have high application value. P7 with the highest cost, unless it shows excellent performance in physical indicators, its economy will face severe challenges. P10 with the worst effect, although the cost is not high, cannot be adopted due to the failure of the technical route.

From the economic point of view, P3 with 0 cost and P1 and P9 with low cost are the first choices. However, the decision must be made in combination with the effect of physical crack control. Some processes with medium cost, such as P5 with excellent effect, may have high application value. P7 with the highest cost, unless it shows excellent performance in physical indicators, its economy will face severe challenges. P10 with the worst effect, although the cost is not high, cannot be adopted due to the failure of the technical route.

The analysis of economic indicators shows that the effect of crack control is not directly proportional to the cost. Zero-cost or low-cost processes need to verify their effectiveness. High-cost processes need to prove the uniqueness of their technical advantages. The selection of processes needs to be combined with physical indicators for comprehensive evaluation, that is, comprehensive indicators are needed.

4.3 Comprehensive Indicators

According to the measured data, the λ values of each process are calculated and sorted from high to low. The results are summarized in Table 4. The comparison of unit cost crack control is shown in Fig. 6.

The calculation results and analysis of Table 4 and Fig. 6 show that the process P3 and P5 have high cost performance. The total cost of unit effect increment of P3 is 0, which means that the total crack width is reduced by 20.2% at zero additional cost. The total cost of unit effect increment of P5 is higher than that of P3 at 53.45 yuan/m^3/mm.

Table 4. Comprehensive evaluation results of different fracture control processes.

Process number	λa (yuan/m^3/mm)	λb (yuan/m^3/mm)	λc (yuan/m^3/mm)	λt (yuan/m^3/mm)
P1	−63.54	0.00	0.00	−63.54
P2	95.96	0.00	0.00	95.96
P3	0.00	0.00	0.00	0.00
P4	133.85	113.18	0.00	247.03
P5	53.45	0.00	0.00	53.45
P6	108.09	58.24	0.00	166.33
P7	158.73	70.53	0.00	229.26
P8	173.31	0.00	0.00	173.31
P9	113.70	0.00	0.00	113.70
P10	−137.85	0.00	0.00	−137.85

λa: Incremental labor cost per unit effect (yuan/m^3/mm); λb: incremental material cost per unit effect (yuan/m^3/mm); λc: incremental mechanical use cost per unit effect (yuan/m^3/mm); λt: incremental total cost per unit effect (yuan/m^3/mm).

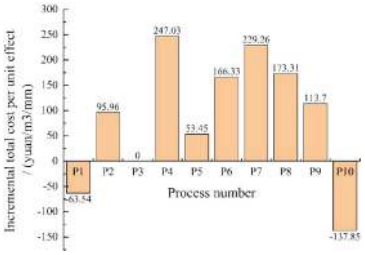

Fig. 6. Comparison of increment total cost per unit effect.

Although the process P4 and P7 have better crack control effect (the total width of cracks is reduced by 36.2% and 60.1% respectively), the total cost of unit effect increment is 247.03 yuan/m^3/mm and 229.26 yuan/m^3/mm respectively, that is, to obtain the crack

control effect per millimeter needs to pay 2–3 times the cost of high quality scheme, especially P7. Although the physical index ranks the top, the extremely high cost restricts its engineering application value. The negative anomaly data of P1 and P10 reflect the problems that have been found in the analysis of physical indicators: P1 deteriorates the crack control effect while increasing the cost, and P10 confirms the failure of its technical route with the total value of-137.85 yuan/m^3/mm.

Through the progressive analysis of physical, economic and comprehensive indicators, this study clearly recommends P3 as the optimal solution, which achieves significant crack control effect at zero cost and has unparalleled economy. P2 and P5 are selected as supplementary solutions, which provides a good cost-effective choice for projects that pursue better crack control effect and provides a cost-effective solution for projects with higher benefit requirements. The recommended scheme system fully considers the budget constraints and effect requirements of different projects, and provides a scientific, reasonable and economical solution for the crack control of the mass concrete side wall of the open-cut tunnel under the water-rich environment of soft foundation.

5 Conclusion

Taking the Lion Ocean Link project as an empirical case, the paper discusses the common problem of crack control in the mass concrete side wall of open-cut tunnel, and systematically constructs a complete solution from cause diagnosis to process test and comprehensive evaluation. The main results and conclusions are as follows.

(1) The test results show that the general process (P0) that simply relies on optimizing materials and temperature control is not enough to solve the problem of constrained cracks, and the composite process system based on the dual path of " enhancing the crack resistance of the structure itself " and " weakening external constraints " shows good results. In particular, P3 (segmented pouring) can achieve a more significant crack control effect at zero incremental cost. In addition, schemes such as P2 (horizontal reinforcement encryption + anti-crack agent) and P5 (high-density double reinforcement encryption) have a high cost performance ratio.
(2) The crack control evaluation indicators that integrates physical indicators and economic indicators is established. The comprehensive index of "unit effect incremental cost" is introduced, and the process optimization is promoted from the simple technical feasibility level to the overall optimization of technology and economy.
(3) Although the research has made some progress in the construction process, it is still the future direction to move towards the intelligent and long-term effect of tunnel engineering. The follow-up work will establish an intelligent prediction and control system for cracks based on real-time monitoring data, and track and verify the long-term durability of the selected process, so as to finally realize the transformation of crack control from passive prevention to active intelligent prevention and control.

References

1. Gong, J.F., Wang, W., Wang, F., et al.: Statistics of China's railway tunnels by the end of 2023 and overview of tunnels of key new projects in 2023 J. Tunnel Constr. **44**(2), 377–392 (2024). https://doi.org/10.3973/j.issn.2096-4498.2024.02.017

2. Liu, D., Xu, W., Xie, B., et al.: Control technology of cracks in mass side wall concrete of Shen Zhong link tunnel J. New Build. Mater. **48**(12), 75–79 (2021). https://doi.org/10.3969/j.issn.1001-702X.2021.12.017
3. Liu, X.H., Zhou, C.B., Chang, X.L., et al.: Simulation of mass concrete temperature cracking propagation process J. Rock Soil Mech. **31**(8), 2666-2670+2676 (2010). https://doi.org/10.16285/j.rsm.2010.08.022
4. Yu, Y.N., Zhang, W., Sheng, Y.G.: Control measures for preventing crack on the surface of mass concrete abutment in early stage J. J. Zhejiang Univ. (Eng. Sci.). **44**(8), 1621–1628 (2010). https://doi.org/10.3785/j.issn.1008-973X.2010.08.033
5. Gao, D.F., Zhou, X., Fei, X.C., et al.: Crack inhibiting technology of mass sidewall concrete in cast-in-situ tunnel J. New Build. Mater. **47**(3), 4-8+32 (2020). https://doi.org/10.3969/j.issn.1001-702X.2020.03.002
6. Chen, Y.Z., Sun, T., Ma, F.K., et al.: Research on the temperature control measure in the winter construction of C20 large volume concrete of Zhijing River bridge. J. Journal of Wuhan University of Technology. **3**, 111–113 (2007). https://doi.org/10.3321/j.issn:1671-4431.2007.03.031
7. Yang, Q.L., Ma, K.S.: Analysis of massive concrete 3-dimensional finite element hydrated heat temperature field J. J. Harbin Institute Technol. **2**, 261–263 (2004). https://doi.org/10.1007/BF02911033
8. Li, Y.X., Hu, J., He, G.Q., et al.: Study on treatment measures and application of crack leakage diseases in expressway tunnels J. Mod. Eng. Technol. **4**(17), 69–72 (2025). https://doi.org/10.26929/j.cnki.issn.2097-1672.2025.17.018
9. Peng, P.: Cause analysis and treatment measures for deffects of qianyang tunnel J. Mod. Eng. Technol. **48**(1), 137–143 (2011). https://doi.org/10.13807/j.cnki.mtt.2011.01.029
10. Liu, W.W., Guo, Y.: Research on the disposal scheme of highway tunnel diseases J. Mod. Eng. Technol. **4**(06), 121–124 (2025). https://doi.org/10.26929/j.cnki.issn.2097-1672.2025.06.031
11. Han, Y.Y., Cui, D.: Experimental study on lining crack repair with geopolymer-cement composite material in highway tunnel J. J. Highway Trans. Res. Dev. **41**(05), 118–124 (2024). https://doi.org/10.3969/j.issn.1002-0268.2024.05.014

Research on the Stress Wave Characteristic Curves Method for Detecting Pile Length in Precast Concrete Piles of Multiple Segments

Shun Zhai[1], Haifeng Liu[2,3(✉)], Yang Mo[2], Qilin Wang[2], Ru Qu[2,3], Ruilin Du[2], Wei Li[1], and Huaijian He[2]

[1] China Railway Siyuan Survey and Design Group Co., Ltd., Wuhan 430063, China
[2] State Key Laboratory of Geomechanics and Geotechnical Engineering Safety, Institute of Rock and Soil Mechanics, Chinese Academy of Sciences, Wuhan 430071, China
hfliu@whrsm.ac.cn
[3] University of Chinese Academy of Sciences, School of Engineering Science, Beijing 100049, China

Abstract. As a foundation project with strong concealment, it is highly necessary to conduct post-construction pile length testing for precast concrete piles. However, due to factors such as attenuation of stress waves in multiple piles, continuous reflection between piles, and soil squeezing effects, conventional low-strain signal analysis techniques are unable to accurately identify the characteristic points of stress waves between pile nodes and pile bottoms in the measured wave forms of pile foundations. This article is based on the low-strain method for dynamic pile testing and develops the stress wave characteristic curves method for pile length detection of precast concrete piles. Additionally, a precast pile length testing and analysis system has been developed. The proposed method for identifying characteristic points in the time-domain signal of stress waves measured on foundation piles has successfully achieved post-construction pile length detection of precast concrete piles, solving the technical problem of difficult and inaccurate detection of pile length for this type of pile. Currently, for concrete precast piles with a total length of less than 40 m and a total number of sections within 3, the pile length detection error is within 5%, meeting the requirements of pile foundation engineering detection.

Keywords: Precast concrete piles · Pile length detection · Stress wave characteristic curves method

1 Introduction

Precast concrete piles include prestressed concrete pipe piles, solid circular piles, hollow square piles, and solid square piles. Due to their advantages such as reliable pile quality, high bearing capacity, and high construction efficiency, they are widely used in foundation pile engineering [1–5].

© The Author(s), under exclusive license to Springer Nature Switzerland AG 2027
G. Feng et al. (Eds.): ICCE 2025, SUCI, pp. 159–171, 2027.
https://doi.org/10.1007/978-3-032-32237-1_12

However, based on actual surveys of pile foundation design and construction, it has been found that the phenomenon of intentionally shortening pile lengths at construction sites occurs frequently. Such malicious "human-induced defects" pose significant engineering risks, directly leading to insufficient bearing capacity of the piles and an imbalance between the vertical load at the pile top and the stratum reaction force. This can cause uneven settlement of the superstructure and generate additional internal stresses. When the cantilevered ends of the foundation are subjected to shear stress from the upper loads, vertical relative displacements or even shear failure may occur in the local structural system, seriously threatening the functionality and safety of the building [6–10].

Currently, neither national nor industry standards provide clear methods, procedures, or requirements for post-construction pile length detection of precast concrete piles. Only a few provincial local standards and association standards propose techniques such as magnetic logging [11, 12], borehole imaging [13], and cross-hole seismic wave methods [14] for detecting the length of engineering piles.

In terms of technical maturity, the magnetic logging method measures the magnetic field intensity inside and around the reinforcement cage within a certain range and evaluates the spatial distribution of the reinforcement cage based on magnetic anomaly characteristics. While this detection technology is relatively mature, in practical applications, other ferromagnetic materials buried underground, such as pipelines, structures, or discarded materials, can easily create interfering magnetic fields. When the intensity of the interfering magnetic field exceeds that of the reinforcement cage, the distribution characteristics of the cage's induced magnetic field may be obscured, preventing effective detection. Therefore, the magnetic logging method imposes high requirements on site conditions around the pile [15–17] and lacks broad applicability.

In terms of detection costs, methods such as magnetic logging, borehole imaging, and cross-hole seismic wave methods require pre-embedded or newly drilled test holes. These approaches are associated with high costs and slow detection speeds in large-scale pile foundation testing [18].

In light of this, this paper adopts the stress wave characteristic curves method to detect the post-construction length of precast concrete piles, with data collection performed at the pile top after pile installation. This method offers advantages in terms of cost, featuring a streamlined sampling process and low data acquisition costs, making it suitable for large-scale pile foundation detection. In terms of technical maturity, this method has undergone extensive testing and validation, with improvements made to the post-processing of low-strain data. Specific regulations and requirements for pile length detection analysis and evaluation of precast piles are also proposed.

2 Technical Principle

The stress wave characteristic curves method for pile length detection has evolved from the low-strain pile integrity testing technology. Currently, the most widely used non-destructive testing method for piles globally is the low-strain reflection wave method. This method uses transient excitation to measure the time-domain and frequency-domain characteristics of acceleration or velocity signals at the pile top. The pile integrity is then analyzed based on one-dimensional elastic wave theory [19, 20].

The principle of detecting pile length using the stress wave reflection method is as follows: A vertical excitation is manually applied at the pile top, causing stress and strain on the pile surface. This results in displacement and vibration of the pile mass particles, which then propagate downward along the pile body, forming stress waves. When the stress wave encounters a difference in wave impedance during propagation, the reflected energy is larger and the transmitted energy is smaller when there is a greater difference in wave impedance between the two media. Conversely, when the reflected energy is smaller, the transmitted energy is larger [21–23].

In the case of a significant wave impedance interface in the pile body (such as the pile toe or joints between sections of a multi-section pile), stress waves generate reflection and transmission at the interface between media [24–26]. Figure 1 illustrates the propagation of stress waves in multi-section piles. During field testing, the signals received by sensors at the pile head form a dynamic response curve of the vertical excitation at the pile top. By analyzing and calculating the reflection information from different sections, the lengths of individual pile segments and the overall pile can be determined.

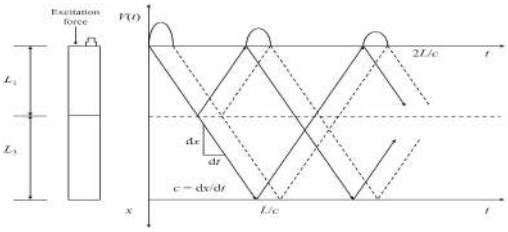

Fig. 1. Schematic diagram of stress wave propagation in multiple segments pile.

During operation, based on the stress wave propagation speed measured on-site for the concrete precast pile shaft, combined with the round-trip time of the incident wave captured by the signal acquisition device, the corresponding total pile length can be calculated using formula (1).

$$L = \frac{1}{2} C \Delta T \tag{1}$$

Where L is the pile length, c is the stress wave velocity, and ΔT is the round-trip travel time of the incident wave.

3 Technical Verification

The prerequisite for applying the stress wave characteristic curves method to detect the length of multi-section precast piles is the presence of a same-direction reflection from the pile toe in the stress wave time-domain curve. To validate the applicability of this detection method for multi-section precast piles, the authors conducted verification tests at the precast facility of Jianhua Building Materials (China) Co., Ltd. As shown in Fig. 2, the tests followed on-site pile foundation construction procedures. Four sections of concrete precast pipe piles and four sections of concrete precast square piles were assembled

and welded section by section. Low-strain tests were successively performed at the pile top. The test results indicate that the stress wave reflections from the joints and the pile toes of both the four-section concrete pipe piles and the four-section concrete square piles were highly distinct. Theoretically, the test results confirm that, without considering the influence of geological layers, the stress wave characteristic line analysis technique can be used to calculate and detect the post-construction length of concrete precast piles with up to four sections. Additionally, this number of construction sections already covers the pile length detection requirements for the vast majority of pile locations.

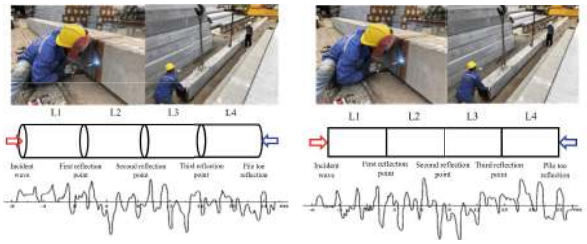

(a) Four-section prestressed concrete pipe pile (b) Four-section prestressed concrete square pile

Fig. 2. Verification test of stress wave characteristic curves method.

4 Engineering Software Development

To promote and facilitate the industrialization, promotion, and application of testing and analysis technology for multi-section pile lengths, the authors have developed the Precast Pile Length Testing and Analysis System V1.0 [27]. This system was built on the Windows platform using an object-oriented design approach, the Visual C++ programming language, and OpenGL technology. The software system architecture is illustrated in Fig. 3. The system takes into consideration the geological information of the pile foundation site and the structural parameters of the pile. It uses the characteristic lines of the dynamic response of stress waves within the precast pile body to perform numerical simulations and generate simulated time-domain signal curves. These simulated signals are then compared and analyzed alongside the stress wave reflection signals measured on-site at the pile foundation. This process identifies characteristic points in the measured stress wave waveform, such as reflections from the pile toe and joints between pile sections, enabling the detection of the length of each section and the total length of the engineering pile. Based on software development principles and a summary of practical measurement results, this software offers the following advantages in the testing and analysis of precast pile lengths.

(1) Database Creation and Engineering Data Query/Retrieval: The system includes functions for creating and editing databases. Operators can input project data and precast pile data to form an engineering database, facilitating timely queries and retrieval of structural parameters, geological information at pile locations, and other project data for specified pile numbers.

(2) Stress Wave Simulation Waveform Generation and Pile Length Determination: The system utilizes the characteristic line method of the wave equation, time-domain analysis, and the stress wave reflection method to generate numerical simulation waveforms of stress waves. Operators can perform comparative analysis between simulated waveforms and measured waveforms to determine the length of each section and the total length of the precast pile.
(3) 3D Visualization and Analysis of Precast Pile Structure: Additionally, based on test results, the system can generate a 3D model reflecting the structural parameters of the precast pile with a single click, allowing for multi-angle stereoscopic display. In practice, operators can rotate the 3D model of the precast pile by clicking and dragging the mouse, enabling intuitive inspection of specific details of the pile structure.

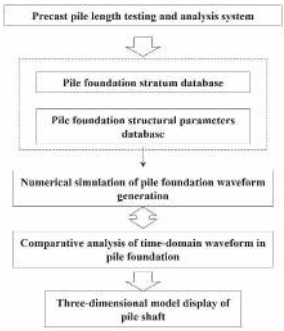

Fig. 3. Basic framework of precast pile length testing and analysis system.

5 Key Technical Points of Pile Length Detection

The stress wave characteristic curves method for detecting pile length relies on obtaining high-quality stress wave reflection signals from the pile foundation and conducting precise analysis and interpretation. Therefore, the research presented in this paper thoroughly incorporates stress wave reflection signal acquisition methods used in low-strain pile integrity testing. The paper proposes specific regulations, recommendations, and requirements for the detection instruments and equipment, pile top pretreatment, sensor installation, signal acquisition, wave velocity measurement, and pile length analysis and determination.

5.1 Instrumentation and Equipment

The equipment used for detecting pile length includes excitation devices, sensors, signal acquisition and processing units, and specialized accessories, typically consisting of low-strain pile integrity testing instruments. The instruments must meet the performance standards outlined in the Technical Code for Testing of Building Foundation Piles (JGJ

106-2014) [28] and should have reliable on-site display, recording, storage, and query functions.

5.2 Pile Top Pretreatment Prior to on-Site Testing

The detection surface at the pile top must be leveled and compacted, ensuring it is perpendicular to the pile axis. The sensor installation point and excitation point should be ground smooth. When the detection surface is an end plate, the plate must be tightly bonded to the pile body concrete without voids or looseness.

5.3 Sensor Installation

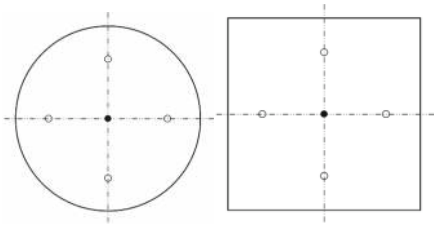

(a)solid circular pile (b) solid square pile

Fig. 4. Schematic diagram of the layout of solid pile excitation points and sensor installation points: *filled circle* represent excitation point, *open circle* represent sensor installation point

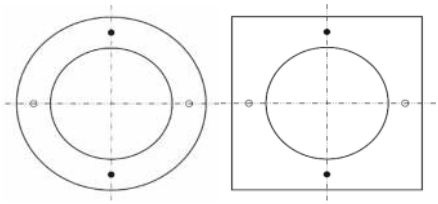

(a)solid circular pile (b) solid square pile

Fig. 5. Schematic diagram of the layout of hollow pile excitation points and sensor installation points: *filled circle* represent excitation point, *open circle* represent sensor installation point.

During the actual testing process, measurement sensors and excitation operations are conducted in groups. It is important that the excitation direction aligns with the pile axis.

The excitation point should be carefully selected and the sensor installation location should be chosen to avoid any interference from the main reinforcement in the reinforcement cage. The sensor should be installed on the top surface of the pile, which must be smooth, and the surrounding area should be free of cracks. It is crucial that the sensor

is kept perpendicular to the pile top surface and securely attached to it. If a couplant is used for bonding, it is essential to ensure sufficient bonding strength to prevent slipping or loosening during signal acquisition. For solid piles, the excitation point should be located at the center of the pile, while the sensor installation point should be positioned at a distance of 2/3 of the radius or 1/3 of the side length from the center, as shown in Fig. 4. In the case of hollow piles, the excitation point and measurement point should be placed at half the wall thickness of the thin-walled section, with an angle of approximately 90° formed between the lines connecting these points to the pile center, as shown in Fig. 5. When the diameter or side length of the precast concrete pile is equal to or less than 600 mm, there should be a minimum of two measurement points. If the diameter or side length exceeds 600 mm, there should be a minimum of three measurement points.

5.4 Signal Acquisition

When using the stress wave characteristic curves method to detect pile length, different energy levels can be obtained by selecting excitation heads made of different materials and excitation equipment of varying masses. This can result in either low-frequency wide pulses or high-frequency narrow pulses. For short piles, it is recommended to select the effective high-frequency component of the impact pulse at around 2 kHz and use manual hammer excitation. For longer piles, equipment such as force rods or force hammers with high excitation energy and low-frequency wide pulses should be chosen. It is important to ensure that the number of valid signal acquisitions at a single measurement point is no fewer than three, and that the collected waveforms exhibit good consistency without distortion or zero drift. In cases of significant signal interference, techniques such as signal enhancement or multiple signal averaging can be employed to improve the signal-to-noise ratio.

5.5 Wave Velocity Measurement

The wave velocity in a precast concrete pile can be measured on-site using the dual-channel method, as illustrated in Fig. 6. Before the precast piles are transported to the site for driving, no fewer than five foundation piles are selected for low-strain testing on the ground. Based on the length of the pile sections and the reflection times at the pile top and bottom, the wave velocity in the pile body is calculated, and the average value is taken. The calculation formula is as follows.

$$c_m = \frac{1}{n}\sum_{i=1}^{n} c_i \tag{2}$$

$$c_i = \frac{\Delta L \times 1000}{\Delta t} \tag{3}$$

In the formula: c_m is the average wave velocity of the pile body (m/s), c_i is the measured wave velocity value of the i pile included in the statistics, in m/s, and it must satisfy the condition $\frac{|c_i - c_m|}{c_m} \leq 5\%$, ΔL is the distance between the two sensors along the pile axis in the dual-channel testing method(m), Δt is the time difference between the

Fig. 6. On site testing of stress wave velocity in piles.

first peaks of the time-domain signals from the two sensors(ms), n is the number of measured wave velocity values used to calculate the average wave velocity, with $n \geq 5$.

When on-site measurement of the pile body wave velocity is not feasible, the wave velocity can be comprehensively determined by referring to the measured stress wave velocities of piles with the same type and construction process in the project area, combined with empirical relationships between concrete strength grade and stress wave velocity [28].

5.6 Pile Length Analysis

The collected time-domain signal waveforms are analyzed to identify the characteristic reflection points of stress waves at individual pile segments (welded joint connections) and the pile toe. Combined with the wave velocity of the pile body, the length of each precast pile segment and the total post-construction pile length are calculated and determined, as illustrated in Fig. 7.

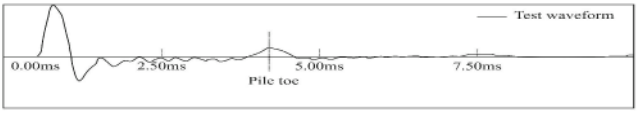

Fig. 7. Judging pile bottom reflection based on analysis of time-domain signals.

When the stress wave signals obtained from foundation pile testing are complex, and the characteristic reflection points at pile joints or the pile toe cannot be identified, characteristic line analysis of stress wave propagation in the precast pile can be performed based on the post-construction structural parameters of the pile foundation. The Precast Pile Length Testing and Analysis System can then be utilized to generate numerical simulation curves of the dynamic response of stress waves propagating through the precast pile body. Building on this, a comparative analysis between the numerically simulated signals and the measured stress wave reflection signals is conducted to identify the characteristic points in the measured stress wave waveform of the pile foundation. This enables the determination of the lengths of individual sections of the engineering pile. The propagation patterns of stress waves in multi-section precast piles are illustrated in Fig. 1.

6 Engineering Testing and Validation

6.1 Practical Operation Steps

In engineering practice, the steps for detecting the length of multi-section precast concrete piles are illustrated in Fig. 8. This process is conducted in conjunction with a software system [27].

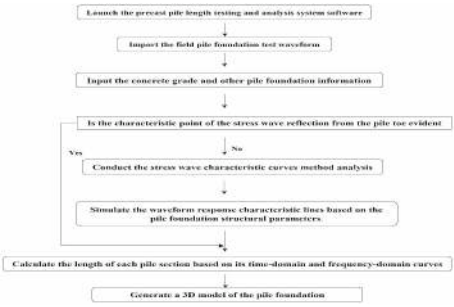

Fig. 8. Analysis process of pile length using stress wave characteristic curves method.

First, standardized low-strain dynamic pile testing is performed in accordance with the Technical Code for Testing of Building Foundation Piles [28] to obtain accurate and complete dynamic test data of the foundation piles. Next, the software's time-domain curve analysis function is activated. This function allows for site-specific detection and analysis of precast concrete pile lengths by identifying significant characteristic reflection points from the pile toe in the time-domain curve. When distinct characteristic reflection points of stress waves from pile joints and the pile toe are evident in the time-domain curve, the lengths of individual precast pile sections and the total pile length can be calculated and determined by combining the time-domain curve with the wave velocity of the pile body.

When distinct characteristic reflection points for stress waves at inter-pile joints or the pile toe are absent in the time-domain curve, the structural parameters of the test pile must be invoked to perform a comprehensive analysis of the stress wave propagation path through each pile section and the entire pile (including incidence and reflection). In practical operation, the analysis software utilizes the characteristic line method of the wave equation, time-domain analysis, and the stress wave reflection method to generate a numerical simulation waveform of the stress wave. By comparing and analyzing the simulated waveform against the measured waveform, operators can assess the consistency between the as-built pile foundation parameters and the actual parameters. Determining the length of each precast pile section and the total length of the pile foundation constitutes verification testing of the concrete precast pile.

This method has been widely used in various engineering fields in China, and has proven to be economically beneficial. The types of soil surrounding the engineering piles at the project site in Wuhan include miscellaneous fill, silt, silty soil, fine sand, gravelly sand, rounded gravel, and various other soil layers. The geological conditions at the

pile toe consist of fine silty sand, gravel-containing fine silty sand, Silurian mudstone, siltstone, and argillaceous sandstone. In the following section, we will use the example of a three-section precast concrete pile at the Wuhan project site to demonstrate the testing procedures and error analysis of the stress wave characteristic curves method for multi-section precast concrete pile length detection.

6.2 Test Case of Three-Section Concrete Precast Pile Length

The test pile is part of a residential reconstruction project in Wuhan and is being used as a foundation pile for a pile cap foundation. It consists of three sections of prestressed concrete pipe piles that have been welded together. The outer diameter of the pipe pile is 600 mm and the concrete strength grade is C80. The total designed length of the pile is 39 m, with each precast pile section measuring 13 m, 12 m, and 14 m from top to bottom.

During on-site low-strain dynamic pile testing, the operator followed the technical guidelines outlined in Chap. 5 of this paper. Petroleum jelly was used to bond the sensor to the cleaned and leveled end plate of the pile top, and a copper-headed hand hammer was used for excitation. The time-domain signal from the on-site dynamic testing is shown in Fig. 9.

However, due to the considerable length of the pile, the reflection from the pile toe was not clearly visible in the time-domain curve of the dynamic testing signal. To address this issue, the testing personnel used the structural parameters of the pile and applied the stress wave characteristic curves method to analyze the pile length. The simulated time-domain waveform generated by the software system [27] was compared to the measured waveform in Fig. 10.

Fig. 9. The time domain signal waveform measured for precast concrete piles.

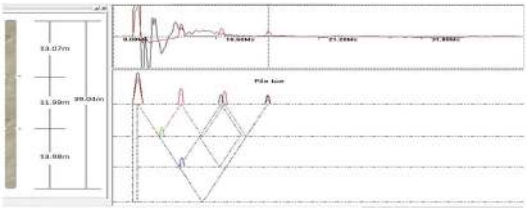

Fig. 10. Measurement results for pile length using the stress wave characteristic curves method for precast concrete piles.

By referencing the schematic diagram of stress wave incidence and reflection within each pile section, the reflection signals from the pile joints and the pile toe were identified in the measured time-domain waveform. The measured lengths of the three sections of the precast concrete pile at this location were determined to be 13.07 m, 11.99 m, and 13.98 m, resulting in a total pile length of 39.04 m. These results demonstrate that the stress wave characteristic curves method can accurately detect the length of three-section precast concrete piles, meeting the requirements for engineering testing. This technology has been successfully applied in over 50 projects in cities such as Wuhan, Xiangyang, and Xiaogan, with over 2,000 concrete precast piles being tested. For concrete precast engineering piles with a total of no more than three sections and a total length of less than 40 m, the detection error is within 5%, satisfying the requirements for pile foundation engineering testing.

7 Conclusions

This paper focuses on precast concrete piles as the subject of research. The aim is to address the challenges in conventional low-strain pile length detection methods for such piles, such as weak reflections from pile joints and the pile toe in stress wave signals. To overcome these challenges, a pile length detection technology based on the stress wave characteristic curves method has been proposed and developed, along with the corresponding Precast Pile Length Testing and Analysis System. Standardized technical specifications for pile length detection using this method have also been established. In engineering practice, the method has been successfully applied in over 50 construction projects in Hubei Province, yielding favorable results. The current research has achieved the following innovative outcomes.

(1) Development of the Precast Pile Length Testing and Analysis System: This system can simulate the response curve of stress wave propagation within the pile foundation, generate numerical simulation waveforms of stress waves, and enable comparative analysis between simulated and measured stress wave waveforms in the time-domain signal, based on the structural parameters of the pile foundation provided during construction.
(2) Proposed Method for Identifying Characteristic Points of Stress Waves at Pile Joints and the pile toe in Measured Waveforms: This method addresses the technical challenges in low-strain pile length detection for multi-section precast concrete piles caused by factors such as stress wave attenuation, continuous reflections at joints, and soil displacement effects. It ensures that the characteristic reflection points of stress waves at the tip of each pile section can be reliably identified.

Engineering practice has shown that the precast pile length testing and analysis system can provide relatively accurate detection results for the length of precast concrete piles. However, further research is needed for piles with more than three combined sections or those with fractured welds at the end plates after construction. This is because the current research primarily targets precast concrete piles with no more than three combined sections and intact welds at the end plates. Additionally, the precision and accuracy of precast concrete pile length testing and analysis can be influenced by the

expertise of the operators. Therefore, future efforts in promoting and applying the Precast Pile Length Testing and Analysis System will involve strengthening training for personnel responsible for signal acquisition and testing analysis to enhance their professional skills.

Acknowledgements. This work was supported by the Key Project of Science and Technology Development Plan of China Railway Siyuan Survey and Design Group Co., Ltd. (2020 K033), the Hubei Province Science and Technology Innovation Talent Plan Project (2025DJB007), the National Natural Science Foundation of China (42107202, 42277185) and the Research Fund of State Key Laboratory of Geomechanics and Geotechnical Engineering Safety (SKLGME02202, SKLGME-JBGS2405).

References

1. Liu, H.L.: Technological innovation methods and practices in geotechnical engineering. J. Chin. J. Geotech. Eng. **35**(1), 34–58 (2013)
2. Zheng, G., Zhang, N., Ba, Z.N., et al.: Seismic performance of PHC pipe piles in layered soft soils. J. Chin. J. Geotech. Eng. **35**(S2), 506–510 (2013)
3. Xu, Q.B., Chen, G., He, J.F., et al.: Experimental study on axial compression behavior of composite reinforced concrete Prefabricated Square piles. J. Build. Struct. **38**(10), 168–174 (2017). https://doi.org/10.14006/j.jzjgxb.2017.10.020
4. Hu, H.S., Tang, M.X., Liu, C.L., et al.: Vertical bearing capacity characteristics of large-diameter DPC pipe piles based on field tests. J. China Civ. Eng. J. **55**(2), 92–99 (2022). https://doi.org/10.15951/j.tmgcxb.2022.02.007
5. Yan, N., Sun, G., Yuan, B.X., et al.: Field test study on bearing behavior of the fourth strata Prestressed concrete pipe pile. J. Cent. South Univ. (Sci. Technol.). **54**(8), 3273–3285 (2023). https://doi.org/10.11817/j.issn.1672-7207.2023.08.029
6. Liu, Y., Xiao, Z.R., Jiang, M.M.: Model test on influence of pile length on pile resistance and bearing capacity characteristics. J. Sci. Technol. Eng. **19**(7), 215–219 (2019)
7. Chen, G.S., Yang, M.L., He, J.B., et al.: Bearing capacity analysis of long short pile composite foundation. Highw. Eng. **43**(1), 114–117 (2018)
8. Tang, H.J., Zhang, H., Jin, L.J.: Problems and treatment of pile sinking in a project of Nanchang. J. Build. Struct. **47**(S1), 1082–1084 (2017). https://doi.org/10.19701/j.jzjg.2017.s1.233
9. Wang, B., Wang, Y.: Discussion about pressed-in piped piles owing to send in soft foundation. J. Build. Struct. **47**(S1), 1085–1087 (2017). https://doi.org/10.19701/j.jzjg.2017.s1.234
10. Gao, W.S., Liu, J.L., Zhao, X.G., et al.: Some understanding of Prestressed concrete pipe pile in engineering application. J. Rock Soil Mech. **36**(S2), 610–616 (2015). https://doi.org/10.16285/j.rsm.2015.S2.086
11. Fujian Provincial Department of Housing and Urban-Rural Development: Technical Specification for Testing of Reinforcement Cage Length of Foundation Piles by Magnetic Logging Building in Fujian: DBJ/T 13-235-2016. Fuzhou. (2016)
12. Jiangsu Provincial Department of Housing and Urban-Rural Development: Technical Code for Testing of Reinforcement Length in Reinforced Concrete Piles: DB32/T 4397-2022. Nanjing. (2022)
13. China Association for Engineering Construction Standardization: Technical Specification for Testing Method with Video Monitor Through the Hole of Foundation Pile: CECS 253:2009. Beijing. (2009)

14. Guangdong Municipal Industry Association: Technical Specification for Inspection of Municipal Bridges Existing Pile Foundation: T/GDSZ 003-2024. Guangzhou. (2024)
15. Hao, Z.P.: Effect analysis of testing conditions for testing of reinforcement length in cast-in-situ piles by magnetic logging method. J. Shanxi Archit. **46**(22), 60–62 (2020). https://doi.org/10.13719/j.cnki.cn14-1279/tu.2020.22.024
16. Xu, L., Zhang, Y.L., Zhou, C.R.: The application of magnetic method to the detecting of the length of Prestressed concrete piles. J. Chin. J. Eng. Geophys. **13**(3), 323–326 (2016). https://doi.org/10.3969/j.issn.1672-7940.2016.03.013
17. Ding, H., Xu, M.H., Zhang, J.H., et al.: The magnetic method application and analysis of reinforcement cage length testing. J. Geotech. Investig. Surv. **39**(4), 90–93 (2011)
18. Ma, C.: Comprehensive application of multiple testing methods in determining pile length and reinforcing cage length. J. Eng. Des. Ground. **23**, 43–45 (2024)
19. Tang, Q.H., Ou, Y.Z., Chen, Y.R., et al.: Case analysis of several typical defective piles with low strain method foundation pile detection. J. Chin. J. Eng. Geophys. **16**(4), 552–558 (2019). https://doi.org/10.3969/j.issn.1672-7940.2019.04.019
20. Chen, H., Dong, C.Q., Zhang, B.Z., et al.: Theoretical model analysis of defect piles in low strain method. J. Chin. J. Eng. Geophys. **9**(3), 342–345 (2012). https://doi.org/10.3969/j.issn.1672-7940.2012.03.018
21. Chai, H.Y.: Application of stress wave theory to quantitative analysis of pile integrity. J. Vib. Eng. **3**, 76–81 (1996)
22. Zhao, Z.D., Sanzo, S., Yoshio, S.: Analytical study on low strain integrity testing for piles. J. Earthq. Eng. Eng. Vib. **4**, 104–112 (1995). https://doi.org/10.1016/s0148-9062(97)87530-4
23. Lei, L.Y., Yang, C.T.: The mathematical models and basic characteristics of transient response for dynamic test of pile. J. Chin. J. Geophys. **4**, 501–509 (1992)
24. Cai, J., Zhang, X.M., Wang, J.H.: Experimental study on pile-soil interaction parameter in pile integrity test. J. Chin. J. Geotech. Eng. **5**, 617–621 (2006)
25. Chai, H.Y.: Effects of soil damping on the propagation of stress-wave in 1-D Bar with varying impedance. J. Civ. Eng. **3**, 41–49 (1994). https://doi.org/10.15951/j.tmgcxb.1994.03.005
26. Xu, T.P., Ke, L.W.: The study of the theory and test about low strain dynamic test of pile with PIT. J. Chin. J. Rock Mech. Eng. **3**, 103–109 (1996)
27. Wuhan Institute of Rock and Soil Mechanics, Chinese Academy of Sciences: Prefabricated Pile Length Test and Analysis System: 2021SR0466249 (2021)
28. Industrial Code of the People's Republic of China: Technical Code for Testing of Building Foundation Piles: JGJ 106–2014. China Architecture & Building Press, Beijing. (2014)

Design and Performance Verification of Burst Pipe Safety Valve for Water Supply Pipeline in Hydro-Power Station

Peng Li[1(✉)], Yong Sun[1], Tongke Shen[2], Xuefeng Wei[3], Junze Gao[1], Yanliang Qiu[1], and Wei Duan[4]

[1] Institute of Science and Technology, China Three Gorges Corporation, Beijing 101100, China
lphhu@163.com
[2] Xiakoutang Plant, Lichuan, Hubei 445400, China
[3] Xiluodu Plant, Yongshan, Yunnan 657300, China
[4] Wudongde Plant, Luquan, Yunnan 651500, China

Abstract. Hydropower station water pipelines feature long length, complex networks, numerous buried pipes, large flow rates, and high pressure. Based on hydraulic control, the pipe burst safety valve achieves rapid automatic closure by using pressure or flow rate before and after the valve as judgment criteria. It suits pipelines with various parameters, solving issues like complex operation and single detection function of existing solutions. A 360 m hydraulic test platform verified the serialized valves' design principle, dynamic response, and water hammer characteristics. The six valve types have adjustable closing set values and speeds, meeting rapid shut-off needs during pipe bursts. Applied in xiakoutang hydropower station, they provide a basis for product design and selection in hydropower water pipeline systems.

Keywords: Hydro-Power Station · Pipe · Burst safety valve · Hydraulic tes

1 Introduction

The clean water supply pipeline system of underground powerhouse in hydropower stations is characterized by long pipeline length, complex pipe network, numerous buried pipes, large water supply flow rate, and high water supply pressure. The clean water storage tank is usually located at the upper part of the mountain, and the main water supply pipeline is arranged on one side of the corridor in the underground powerhouse. In case of uncontrollable factors, a pipe burst accident will discharge a large volume of water instantaneously. The underground powerhouse is low-lying with dense equipment layout, and the emergency drainage capacity of local areas is limited. Once a pipe burst accident occurs, it is prone to cause serious consequences such as powerhouse flooding and loss of production water supply pressure. The causes of pipe burst accidents include accidental collision by vehicles entering and exiting the powerhouse, falling rocks from mountains, and pipeline water hammer caused by improper operation.

© The Author(s), under exclusive license to Springer Nature Switzerland AG 2027
G. Feng et al. (Eds.): ICCE 2025, SUCI, pp. 172–185, 2027.
https://doi.org/10.1007/978-3-032-32237-1_13

1.1 Existing Solutions

To address the above problems, extensive research on water hammer protection for long-distance pressurized water transmission pipeline systems has been carried out in China, but the technical measures for pipe burst protection after water hammer occurrence have not been mentioned. Such risks also exist in various pipelines such as water supply engineering, thermal engineering, and petrochemical transportation. In terms of product development, domestic and foreign manufacturers have developed valve devices that can quickly cut off fluid after pipe burst. The existing product names include pipe burst control valve, pipe burst shut-off valve, pipe burst emergency shut-off valve, or pipe burst protection device [1]. At present, there is no unified naming standard for such functional devices at home and abroad, nor have relevant technical standards for design, manufacture, or selection been issued. Therefore, it is imperative to develop a pipe burst protection device that can quickly close the accident pipeline, maintain the pressure of the upstream main pipeline, prevent powerhouse flooding, and minimize secondary disasters caused by accidents to the greatest extent.

Current pipe burst protection devices mainly adopt two technical routes: one is based on electrical sensor control, and the other is based on mechanical hydraulic control. The pipe burst protection equipment based on electrical control usually consists of a hydraulic device, sensors and control circuits, a driving device, and a main valve. Its operating principle is to real-time monitor the flow state of the medium inside the pipeline through pressure or flow sensors, and close the main valve through the driving mechanism after detecting the flow state change caused by pipe burst. The pipe burst protection equipment based on hydraulic control usually comprises a hydraulic device and a paddle device. It detects the flow velocity inside the pipeline through the paddle; when the flow rate exceeds the standard value, the paddle acts against the preload force to drive the hydraulic system to close the main valve. The former needs to be connected to a power supply, while the latter must be equipped with a small hydraulic station as an energy storage device. From the perspective of on-site application, some pipe burst protection equipment has problems such as long closing time, high procurement cost, frequent false shut-off accidents [2–5], bulky and complex components, difficult operation and use, lack of automatic reset function in most cases, and single-function detection devices, which cannot meet the requirements of independent setting of pipeline flow rate and velocity [6, 7].

Domestic research on pipe burst safety protection theory started relatively late, and current research mainly focuses on theoretical aspects such as performance simulation analysis of safety valves [8, 9]. However, the results of such simulation theoretical research often lack experimental or on-site verification, making it impossible to confirm the valve performance. There is an urgent need to combine theoretical analysis and experimental research methods to develop new pipeline protection equipment with stable performance, good adjustability, simple operation and use, and wide applicability to medium flow rate and pressure ranges.

2 The Solution in this Article

Focusing on the safety protection against accidental pipe burst in the pipeline of hydropower station water supply system, this paper overcomes the difficulties such as complex control and operation of existing pipe burst protection devices, and develops a pipe burst safety valve that automatically and rapidly closes based on the flow state inside the pipeline. In principle, this valve adopts the hydraulic control principle, without the need for external power supply or energy storage device. It only relies on the characteristics such as pressure or flow velocity of the pipeline before and after the valve as judgment conditions, and realizes valve actuation based on the fluid pressure of the pipeline itself. It has the prominent features of standardized design, strong versatility, and high stability, and is suitable for pipeline engineering with high safety requirements, high pipe burst hazards, long pipeline distances, and the need for unattended operation.

Based on the above design principle, this paper designs and manufactures 6 sets of serialized prototypes of pipe burst safety valves with different models, builds a dedicated dynamic hydraulic test platform to verify their basic operation functions, and comprehensively tests their comprehensive performance indicators such as setting value, closing speed, drag coefficient, and water hammer pressure.

3 Principle and Basic Parameters of Pipe Burst Safety Valve

3.1 Principles and Methods

For water supply pipelines drawing water from reservoirs with stable water levels and operating at a constant flow rate, pipe burst is characterized by an excessively high flow velocity and an abrupt pressure drop inside the pipeline. From the perspective of the installation site of the pipe burst safety valve, when a pipe burst occurs in the downstream pipe section, the flow rate or velocity passing through the valve will rise rapidly, leading to an increase in the resistance of the upstream pipeline and a sharp pressure drop at the valve installation point. Therefore, detecting the pressure or flow rate at the valve installation point can serve as a basis for judging whether a pipe burst has occurred.

For instance, when the water consumption of users is constant, pipe burst can be determined by detecting the flow rate/velocity through the valve. When the pressure of the water source is stable (e.g., the water source is a pool or reservoir with a constant water level), pipe burst can be judged by detecting the water pressure at the valve installation point. In cases where the water source pressure is uncertain and the water demand of users changes constantly, pipe burst can be identified by detecting the resistance coefficient of the pipeline downstream of the valve.

In terms of the driving mode, the main valve body of the pipe burst safety valve adopts a hydraulic control valve with a Y-shaped flow channel structure, which is mainly composed of a main valve body, a middle end cover, an upper end cover, a valve shaft, a valve plate, a return spring, and a diaphragm piston. Among them, the

upper end cover and the diaphragm piston form an upper control chamber, while the middle end cover and the diaphragm piston enclose a lower control chamber. The return spring keeps the valve shaft and valve plate in an upward or fully open state. The valve

can be closed by filling water into the upper control chamber and restored to the fully open state by releasing the pressure [10–15].

In terms of the control method, pressure detection can be realized by a pilot valve, referred to as a pressure pilot valve [11]; flow rate or velocity detection is achieved through a pitot tube, referred to as a flow velocity pilot valve [13]; and the detection of the resistance coefficient downstream of the valve is accomplished by a proportional pilot valve [15]. Various types of pilot valves are respectively adapted to constant or variable pressure, different closing speeds, and accuracy classes, meeting the needs of different users.

3.2 Basic Parameters of the Prototype

This paper takes the pressure pipelines of hydropower stations as the application object, explores 6 types of control and drive modes, and designs and manufactures 6 prototypes including pneumatic type, pilot-operated type, differential pressure type, doubly-fed type and proportional type. The basic parameters are shown in Table 1, and the external dimensions are illustrated in Fig. 1.

Table 1. Basic parameters of the prototype burst pipe safety valve.

No.	Name	Actuation Method	Adjustment Form
Prototype 1	Pneumatic Pipe Burst Safety Valve	Compressed Nitrogen	Gas Storage Tank Pressure
Prototype 2	Pilot-Operated Pipe Burst Safety Valve	Pressure Pilot Valve	Pilot Valve Spring
Prototype 3	Differential Pressure Pipe Burst Safety Valve	Direct Control	Main Valve Spring
Prototype 4	Pilot Differential Pressure Pipe Burst Safety Valve	Flow Velocity Pilot	Pilot Valve Spring
Prototype 5	Doubly-Fed Pipe Burst Safety Valve	Dual Pilot Valve (Pressure & Flow Velocity)	Pilot Valve Spring
Prototype 6	Proportional Pipe Burst Safety Valve	Proportional Pilot Valve	Pilot Valve Lever

The main differences in the principles and structures of the 6 prototypes of pipe burst safety valves are as follows:

(1) Prototype 1 adopts pneumatic control and is mainly composed of a main valve and a nitrogen gas storage tank. The valve closing pressure set value is determined by adjusting the pressure of the gas storage tank. When the pipeline pressure drops below the closing pressure set value, the main valve is driven to close. It features a simple structure and fast closing speed [10].

(2) Prototype 2 is controlled by a pressure pilot valve and consists mainly of a main valve and a pilot valve. The pilot valve can detect the upstream pressure of the valve. When the pipeline pressure falls below the closing set value, the pilot valve opens to connect the upstream side of the main valve with the upper control chamber, thereby driving the main valve to close. It is characterized by simple structure, fast closing speed, compact layout and low flow resistance [11].
(3) Prototype 3 employs direct flow velocity control and is mainly made up of a main valve and a pitot tube. Based on Bernoulli's principle, the pipeline flow velocity increases in the event of a pipe burst, leading to a larger pressure difference between the upstream side of the main valve and the pitot tube, which then drives the main valve to close. It has the advantages of simple structure and reliable performance [12].
(4) Prototype 4 is controlled by a flow velocity pilot valve and is composed primarily of a main valve, a pilot valve and a pitot tube. The pilot valve can detect the pressure difference between the upstream pressure of the main valve and the pitot tube. When the flow velocity increases, the pilot valve is activated to connect the upstream water source of the main valve with the upper control chamber, thus driving the main valve to close. It is notable for convenient adjustment and reliable operation [13].
(5) Prototype 5 adopts dual control of a pressure pilot valve and a flow velocity pilot valve, and is mainly composed of a main valve, a pressure pilot valve, a flow velocity pilot valve and a pitot tube. When the two series-connected pilot valves detect that the upstream pressure of the valve is lower than the pressure set value and the flow velocity through the valve exceeds the flow velocity set value, they are activated respectively to connect the upstream water source of the main valve with the upper control chamber, thereby driving the main valve to close. It is characterized by accurate set values and reliable operation [14].
(6) Prototype 6 is controlled by a proportional pilot valve and consists mainly of a main valve, a pilot valve and a pitot tube. The proportional pilot valve detects the ratio of the flow velocity variable to the pressure variable simultaneously. When the ratio exceeds a certain threshold, the pilot valve is triggered to connect the upstream water source of the main valve with the upper control chamber, thus driving the main valve to close. It can adapt to continuously changing water source pressure and pipeline flow velocity, and features strong adaptability and reliable operation [15].

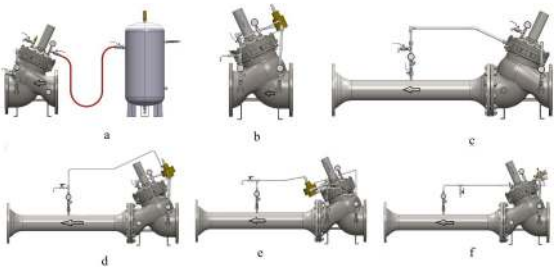

Fig. 1. Outline drawing of the prototype of the burst pipe safety valve, from a to b are Prototype 1 to Prototype 6 respectively.

In addition to the automatic shut-off function, the prototypes of the pipe burst safety valve are also equipped with functions of manual forced shut-off, manual forced opening, and lock-out/operation withdrawal, which meet the needs of manual intervention on the water supply pipeline by users in emergency situations. The manual intervention functions are realized by the ball valves installed on the control pipelines, through filling water into or releasing pressure from the upper and lower control chambers of the main valve [10–15].

4 Prototype Test Scheme

4.1 Brief Introduction to the Test Platform

A hydraulic test platform was built to conduct experimental verification on six prototypes of the pipe burst safety valve respectively. The performance parameters of the valve prototypes were tested under multiple working conditions with varying pipeline pressure and flow rate, including flow coefficient, flow resistance coefficient, actuation pressure, actuation flow velocity and response time. The test platform is mainly composed of a water pump, a surge tank, a pressure pipeline, a pressure gauge, a flowmeter, a pressure sensor, a temperature sensor, a flow control valve, a gate valve, a butterfly valve, an electric butterfly valve, a pneumatic butterfly valve and the tested valve. The system composition is shown in Fig. 2, and the prototype installation platform is presented in Fig. 3.

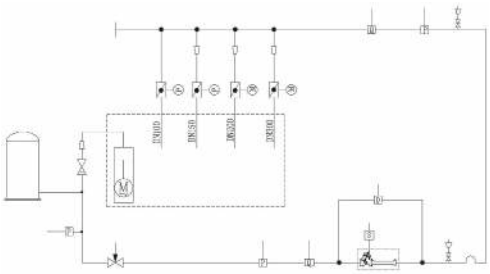

Fig. 2. System diagram of hydraulic test platform.

The test platform is composed of three parts, namely the constant-pressure water supply device, the test pipeline, and the data acquisition unit.

The constant-pressure water supply device consists of a 185 KW water pump, a 200 KW frequency converter and a surge tank, which is used to ensure the flow rate required for the test. The test pipeline adopts a 360-m-long DN300 seamless steel pipe. The data acquisition unit includes pressure sensors, flowmeters, differential pressure sensors and a monitoring platform. By adjusting the pipeline pressure and flow rate, it simulates the pressure fluctuations and flow fluctuations before and after the valve prototype under the pipe burst valve working condition, collects the curves of pressure, flow rate and other data changes before and after the prototype actuation, and records the closing law of the prototype, so as to meet the product design requirements. 2.4Subsection heading.

Fig. 3. Prototype installation platform.

4.2 Test Content and Methods

The test content includes tightness test, manual operation test, flow coefficient/flow resistance coefficient test, and automatic shut-off test, which are conducted to verify the basic performance, resistance characteristics, manual intervention operation performance, and post-activation automatic shut-off characteristics of the valves respectively.

The tightness test is carried out in accordance with GB/T 13927-2022 Industrial Valves—Pressure Tests.

The flow coefficient/flow resistance coefficient test is performed in compliance with the standard GB/T 30832-2014 Valves—Test Methods for Flow Coefficient and Flow Resistance Coefficient.

The manual operation test is conducted as follows: the test pipeline is filled with water to a specified pressure and flow rate to simulate normal operating conditions. The ball valves on the control pipelines of the pipe burst safety valve are operated to forcibly fill water into or release pressure from the upper or lower control chamber of the main valve, thereby controlling the main valve in three states: manual forced shut-off, manual forced opening, and lock-out/operation withdrawal.

The automatic shut-off test is implemented through the following steps: the pipe burst safety valve prototype is installed on the test pipeline, and the pipeline is maintained at a certain pressure and flow rate to simulate the normal water supply condition. Then, the pneumatic valve (with a minimum closing time of 1 s) or electric valve at the outlet of the test pipeline is quickly opened to simulate the pipe burst condition. The variation trends of pressure, flow rate at the measuring points before and after the valve, as well as the valve stem stroke over time are detected, so as to obtain the shut-off characteristics of the prototype.

5 Formatting of Manuscript Components

5.1 Basic Performance Test

The basic performance test includes the tightness test, manual operation test, and flow resistance coefficient & flow coefficient test, which are conducted to verify the valve's shut-off performance, operation performance under manual intervention, and resistance characteristics respectively.

(1) Fill the valve with liquid medium. The shell test pressure shall be at least 1.5 times the cold working pressure of the valve shell, i.e., above 2.4 MPa. Both the upper seal test pressure and the seal test pressure shall be 1.76 times the cold working pressure, i.e., 2.4 MPa, with pressure holding for 120 s. The test results meet the requirements specified in GB/T 13927-2022 Industrial Valves—Pressure Tests.
(2) Manual operation is performed by manually operating the ball valves on the control pipelines to forcibly open and close the valve, and verify the stability of its state retention. The test results show that all 6 prototypes are equipped with three functions including "manual emergency shut-off", "manual emergency opening" and "lock-out/operation withdrawal". Moreover, after operation, the opening/closing or valve position state remains unaffected regardless of the changes in pipeline pressure.
(3) Flow resistance coefficient and flow coefficient test of prototypes. For each of the 6 prototypes, 4 to 5 groups of flow-pressure difference data across the valve were collected to calculate the flow coefficient and flow resistance coefficient. The test results indicate that Prototype 2 has the minimum flow resistance, followed by Prototype 1. Prototypes 4, 5 and 6 equipped with pitot tubes exhibit basically the same flow resistance, which is nearly twice that of the models without pitot tubes (e.g., Prototype 2). The flow resistance of Prototype 1 is higher than that of Prototype 2; the flow resistance of Prototype 3 is higher than that of Prototypes 4, 5 and 6. This indicates that the flow resistance of the models with the main valve installed in the reverse direction is slightly higher than that of the models installed in the forward direction, as shown in Fig. 4.

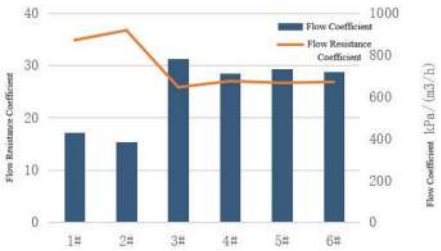

Fig. 4. Comparison of flow resistance coefficient and flow coefficient of prototype.

5.2 Automatic Shut-off Test

The method of the automatic shut-off function test is to simulate a pipe burst in the pipeline downstream of the pipe burst safety valve, record parameters such as the valve shut-off duration, pressure and flow rate at the measuring points before and after the valve during the shut-off process, test its actuation response, shut-off speed and water hammer characteristics during shut-off, and verify the main performance of the prototypes.

As shown in Figs. 5, 6, 7, 8, 9, and 10, during the automatic shut-off process of the six pipe burst safety valve prototypes, the valve position stroke all showed an irreversible downward trend until the valve was fully closed, with the shut-off duration ranging from 4 s to 16 s. The upstream pressure of Prototypes 1 to 4, along with that of other prototypes, exhibited a V-shaped or U-shaped variation trend after the pipe burst, and reached the

maximum value when the valves were completely closed. In contrast, Prototypes 5 and 6, driven by dual pilot valves and proportional pilot valves respectively, showed no water hammer effect. This indicates that the possible water hammer pressure after the shut-off of the pipe burst safety valve is one of the main bases for valve selection. Among them, Prototype 1 is directly driven by compressed air and thus features relatively fast shut-off, with its upstream pressure exceeding the initial value by 40%. Prototype 3 is directly driven by a spring, with its upstream pressure exceeding the initial value by 60%, showing an obvious water hammer effect. This demonstrates that the main valve installed in the reverse direction has a more significant water hammer effect.

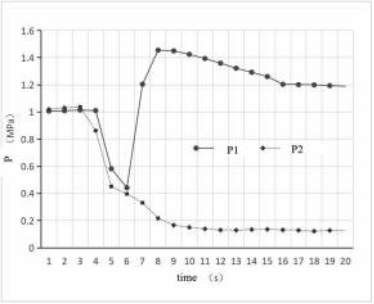

Fig. 5. Pressure characteristics during automatic shutdown of prototype 1, wherein, P1 represents the pressure before the valve, P2 represents the pressure after the valve.

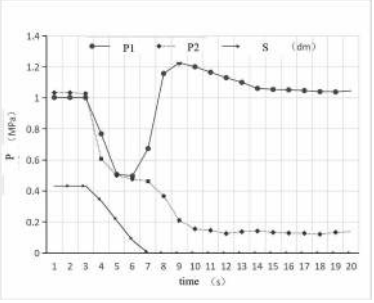

Fig. 6. Pressure characteristics during automatic shutdown of prototype 2, wherein, P1 represents the pressure before the valve, P2 represents the pressure after the valve, and S represents the valve stroke.

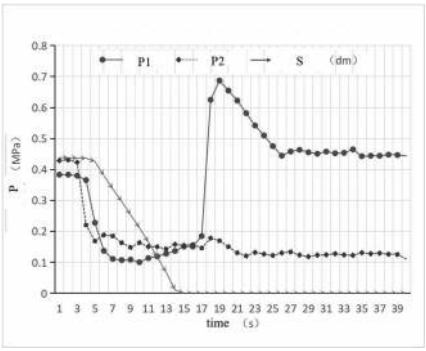

Fig. 7. Pressure characteristics during automatic shutdown of prototype 3, wherein, P1 represents the pressure before the valve, P2 represents the pressure after the valve, and S represents the valve stroke.

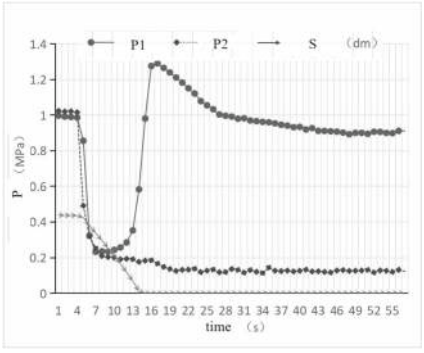

Fig. 8. Pressure characteristics during automatic shutdown of prototype 4, wherein, P1 represents the pressure before the valve, P2 represents the pressure after the valve, and S represents the valve stroke.

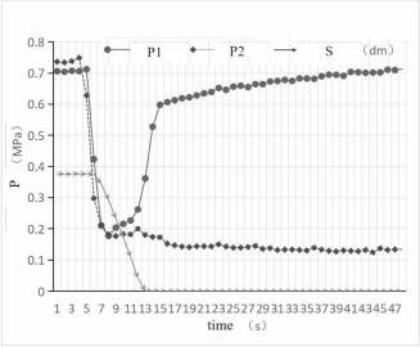

Fig. 9. Pressure characteristics during automatic shutdown of prototype 5, wherein, P1 represents the pressure before the valve, P2 represents the pressure after the valve, and S represents the valve stroke.

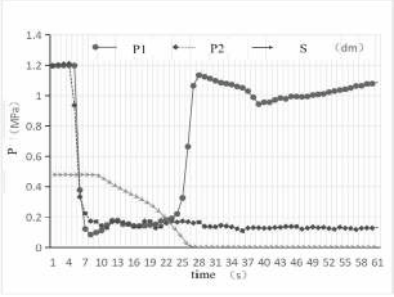

Fig. 10. Pressure characteristics during automatic shutdown of prototype 6, wherein, P1 represents the pressure before the valve, P2 represents the pressure after the valve, and S represents the valve stroke.

5.3 Performance Evaluation

The main valve structures of the six prototypes are identical, and the flow patterns during the shut-off process follow similar variation laws, which are manifested in the following aspects:

(1) Operational StabilityUnder the same boundary conditions—i.e., identical pipeline flow rate, pipeline pressure, outlet valve opening degree, and flow control valve opening degree—the calibrated pipe burst safety valves all maintain a stable open state.
(2) Shut-off CharacteristicsAll six prototypes exhibit consistent flow-dependent shut-off characteristics. When a pipe burst condition occurs, the pressure drops while the flow rate rises, triggering valve actuation until full closure is achieved.

(3) Water Hammer Peak ValueThe upstream pressure of the valve shows a trend of first decreasing and then rising rapidly. When the valve position stroke reaches zero—i.e., at the moment of full closure—the upstream pressure peaks, which is defined as the water hammer peak value. The water hammer pressure is positively correlated with the initial pipeline pressure and negatively correlated with the shut-off duration.

The six prototypes adopt different control modes, including direct control, pressure pilot valve control, flow velocity pilot valve control, and proportional pilot valve control, leading to distinct variation laws of flow patterns during the shut-off process. The specific differences are as follows:

(1) Due to inertia, the increase in pipeline flow rate after a pipe burst is gradual. Therefore, the pressure curves of Prototypes 3, 4, 5, and 6, which adopt flow rate control, show a distinct U-shape, as illustrated in Figs. 5, 6, 7, 8, 9, and 10.
(2) Water Hammer EffectThe upstream water hammer peak occurs at the moment of full valve closure. For Prototypes 1, 2, 3, and 4, the peak water hammer pressure is positively correlated with the initial pressure and negatively correlated with the shut-off duration. In contrast, Prototypes 5 and 6 employ dual detection of pressure and flow rate; the pipeline pressure remains low during actuation, resulting in an insignificant water hammer effect.
(3) AdjustabilityExcept for the direct-controlled differential pressure pipe burst safety valve, the shut-off set values of the other five prototypes can be freely adjusted. The calibration method for the pneumatic pipe burst safety valve (Prototype 1) involves adjusting the compressed nitrogen pressure. For Prototype 2 (pilot-operated safety valve), Prototype 4 (pilot differential pressure pipe burst safety valve), and Prototype 5 (doubly-fed pipe burst safety valve), calibration is achieved by adjusting the pilot valve adjusting bolts. The calibration of Prototype 6 (proportional pipe burst safety valve) is completed by adjusting the lever bolts.
(4) The shut-off pressure of Prototypes 1 and 2 is only related to the pressure set value, and independent of the initial pressure, initial flow rate, and full-opening speed of the pneumatic valve. The shut-off flow rate of Prototypes 3 and 4 is solely dependent on the flow rate set value. The shut-off condition of Prototype 5 is associated with both the pressure set value and flow rate set value. The shut-off set value of Prototype 6 is only related to the downstream opening degree of the valve or the flow resistance coefficient.

5.4 Conclusions and Recommendations

(1) Through theoretical analysis and research, this paper completes the structural design of the pipe burst safety valve. In the design process, principles such as product modularization, serialization, adjustment convenience and operation convenience are fully considered to adapt to pipelines with different pressures and flow rates. After a pipe burst occurs, the pipe burst safety valve can automatically close according to the set value, and can also be manually closed and opened in emergency situations. The valve features a compact overall structure and can be installed at any angle without being restricted by installation space or environment, and its automatic shut-off set value can be easily and arbitrarily adjusted.

(2) Experimental comparison and verification were carried out on six different types of valves, and the dynamic performance indicators of different types of valves were obtained. The conclusions show that the six types of valves meet all performance indicators, which proves the feasibility of the pipe burst safety valve in the protection of water supply pipelines in hydropower stations.
(3) Analysis and verification confirm that the pipe burst safety valve developed in this paper is safe and reliable. As an application demonstration project, Prototype 4, the pilot differential pressure pipe burst safety valve, has been installed in the water supply project of Xiakoutang Power Station. It prevents water source loss, avoids powerhouse flooding, and ensures the intrinsic safety of power production.
(4) Prototypes 4 and 5 have been applied to the water supply systems of Xiakoutang Hydropower Station, Xiluodu Hydropower Station, and Wudongde Hydropower Station respectively. These applications have verified the correctness of the design concept and test process for the serialized pipe burst safety valve products.

Acknowledgments. This work was supported by Independently-developed Scientific Research Projects of China Three Gorges Corporation [WWKY-2021-0187].

References

1. Liu, J.: Localized development of pipe burst protection devices for long-distance natural gas pipelines J. Oil Gas Storage Trans. **36**(8), 948–953 (2017). https://doi.org/10.6047/j.issn.1000-8241.2017.08.013
2. Li, K., Niu, S.: Fault analysis and countermeasures for LineGuard electronic control unit failure J. Instrum. Cust. **19**(6), 81–83 (2012). https://doi.org/10.3969/j.issn.1671-1041.2012.06.029
3. He, D., Zheng, H., Xu, H., et al.: Study on pressure drop rate setting and duration of pneumatic-hydraulic actuators for gas transmission pipelines J. Mod. Chem. Ind. **36**(2), 194–196 (2016). https://doi.org/10.16606/j.cnki.issn0253-4320.2016.02.051
4. Zhu, Z., Sun, L., Xu, H., et al.: Discussion on common faults and handling methods of LineGuard 2200 J. Neijiang Sci. Technol. **36**(5), 38–39 (2015). https://doi.org/10.3969/j.issn.1006-1436.2015.05.027
5. Lu, M., Luo, Y., He, J.: Simulation of pipe burst protection for line block valves in gas transmission pipelines J. Nat. Gas Oil. **33**(5), 14–17 (2015). https://doi.org/10.3969/j.issn.1006-5539.2015.05.004
6. Huang, F.: Study on high-pressure and large-flow safety valves for high-water-based fluids Luoyang: Henan University of Science and Technology. Master's Thesis (2012)
7. Shen, K., Ji, Y.: Classification and fault analysis of safety valves J. Valves. **145**(3), 29–31 (2006). https://doi.org/10.16630/j.cnki.1002-5855.2006.03.010
8. Liang, H.: CFD numerical simulation and experimental study on the flow field at the valve port during the opening process of safety valves Guangzhou: South China University of Technology. Master's Thesis (2010)
9. Chen, D., Liu, D., Dong, H., et al.: Numerical simulation study on the flow field of safety valves J. Fluid Machinery. **36**(10), 24–28 (2008). https://doi.org/10.3969/j.issn.1005-0329.2008.10.007
10. China Three Gorges Corporation: Pneumatic pipe burst safety valve and method, China, ZL202110415599.5, Patent. (2021)

11. China Yangtze Power Co., Ltd.: Pilot-operated pipe burst shut-off valve and control method, China, ZL201810063997.3, Patent. (2018)
12. China Three Gorges Corporation: Differential pressure type pipe burst safety valve and method, China, ZL202110616326.7, Patent. (2021)
13. China Three Gorges Corporation: Pilot-operated differential pressure pipe burst safety valve and method, China, ZL202110615586.2, Patent. (2021)
14. China: Three Gorges Corporation. A pipe burst safety valve, China, ZL202211442642.8, Patent. (2023)
15. China Three Gorges Corporation: A pipe burst safety valve, China, ZL202211462561.4, Patent. (2023)

Research on the Current Development Status and Application Schemes of Low-Altitude Economy During the Construction Period of Railway Engineering

Yulong Lu[1], Hongfei Cao[2], Lingling Yang[1(✉)], Fei Li[1], Fangbo Qiao[2], and Wenhui Feng[1]

[1] Beijing Jingwei Information Technology Co., Ltd., No. 2, Daliushu Road, Beijing 010-51849256, China
315693917@qq.com

[2] Institute of Computing Technology, China Academy of Railway Sciences Co., Ltd., No. 2, Daliushu Road, Beijing 010-51849256, China

Abstract. As a strategic emerging industry, the low-altitude economy has demonstrated enormous application potential in the railway sector of railway- developed countries worldwide. By systematically sorting out the current development status and typical application cases of the railway low-altitude economy at home and abroad, this paper further puts forward the application demands in such business scenarios as survey and design, construction and building, environmental and water conservation management, and emergency management during the construction period of railway engineering, aiming at the pain points of traditional survey and design, construction process control and other work, such as low manual efficiency, insufficient precision and high safety risks. On this basis, it designs and constructs the application architecture of the low-altitude economy during the railway engineering construction period, proposes the engineering UAV adaptation schemes as well as data acquisition and transmission schemes for eight typical application scenarios including route survey and design and terrain modeling, points out the challenges faced by the development of the low-altitude economy during the railway engineering construction period and puts forward development suggestions, providing technical guidance for the high-quality development and transformation of railway engineering construction.

Keywords: Low-Altitude Economy · Railway Engineering Construction · Engineering UAV

1 Introduction

The low-altitude economy refers to a comprehensive economic form that carries out production and service activities through unmanned aerial vehicles (UAVs), low- altitude aircraft and other equipment within the low-altitude airspace, usually the airspace within

© The Author(s), under exclusive license to Springer Nature Switzerland AG 2027
G. Feng et al. (Eds.): ICCE 2025, SUCI, pp. 186–202, 2027.
https://doi.org/10.1007/978-3-032-32237-1_14

1,000 m of vertical height from the ground. It is a strategic emerging industry with broad prospects and a typical representative of new-type productivity [1]. In February 2021, the "National Comprehensive Three-dimensional Transportation Network Planning Outline" incorporated the low-altitude economy into the outline to promote the integrated development of transportation and related industries such as equipment manufacturing. The government work report at the 2024 National People's Congress and the National Committee of the Chinese People's Political Consultative Conference pointed out that "efforts should be made to build new growth engines such as biological manufacturing, commercial aerospace and the low-altitude economy". The issuance of national policy documents has provided policy guidance and guarantee for the development of the low-altitude economy in the railway industry. With the rapid development of China's railways, guided by the construction of the "Six Modern Systems", higher standards and requirements have been put forward for railway engineering construction [2]. The construction period of railway engineering covers multiple links such as survey and design, construction and construction, and safety control. The traditional operation methods or technical means mainly relying on manual measurement and analysis are gradually unable to meet the efficient, accurate and comprehensive management needs of modern railway engineering construction due to the limitations of operation efficiency bottlenecks, data collection limitations and backward analysis methods. Especially under the conditions of complex geological environments, their shortcomings are more obvious. The application of low-altitude economic technologies centered on UAVs has the advantages of flexible flight, wide coverage and high operation efficiency. Integrating technologies such as LiDAR, oblique photography and the Internet of Things, and adopting the mode of "air perception + data fusion + intelligent analysis", it can solve the pain points such as "inaccessible areas, inaccurate measurement and slow response" in the traditional manual mode, and has shown great application potential in survey and design, progress control, safety inspection and other aspects of railway engineering construction.Focusing on the specific stage of the railway engineering construction period, combined with the unique needs of construction project management, this paper systematically sorts out the application requirements of typical business scenarios, conducts in-depth research on the technical schemes supporting these scenario applications, provides an overall solution for the application of the low-altitude economy for all participants in railway engineering construction, and promotes the development of railway engineering construction towards the direction of higher measurement accuracy, higher construction quality and faster project progress.

2 Analysis of the Current Development Status and Application Demands of the Low-Altitude Economy During the Construction Period of Railway Engineering

2.1 Current Development Status at Home and Abroad

In recent years, railway companies in countries and regions such as the United States, Japan, South Korea and Europe have leveraged the advantages of small UAVs, including high maneuverability, ease of operation, capability to capture high-resolution images at

altitude and access to areas unreachable by humans. They have focused on the application of UAVs in such fields as infrastructure inspection and monitoring, accident rescue investigation and disaster assessment, as well as route survey and design and project construction progress inspection [3, 4]. Domestic railway bureaus and depots have adopted UAVs for infrastructure operation and maintenance, covering applications like inspection of linear infrastructures, bridges, tunnels and other facilities, monitoring of geological disasters such as landslides and debris flows along railway lines, prediction of structural damages to infrastructure, and emergency command at accident and disaster sites. However, most of these applications rely on consumer-grade UAV platforms, and there remains room for improvement in terms of automated inspection, data acquisition and intelligent analysis capabilities [4, 5].

The field of railway engineering construction features distinct industry-specific characteristics, forming a unique management model for project construction administration. Schedule management is marked by such traits as the long span of linear projects and tight connection between construction procedures. Quality management is characterized by stringent requirements for structural safety, a high proportion of concealed works, as well as the compliance and diversity of construction materials. Safety management mainly confronts challenges including the concentration of high-risk operation scenarios, prominent risks of geological disasters, and dense distribution of on-site operators. Traditional methods and technical means for schedule, quality, and safety management rely heavily on manual work. With the continuous advancement of projects, these approaches are confronted with limitations such as low efficiency, insufficient precision, and delayed response. These drawbacks have driven the application of low-altitude economy technologies centered on UAVs in railway engineering management.

At present, typical application cases of UAVs during the construction period of railway engineering in China mainly include:

Wang et al. [6] addresses the problems of low efficiency, insufficient precision, and high safety risks in railway surveys in complex regions such as Tibet, Sichuan, and Yunnan. It explores the application of UAV-based 3D imaging technology to identify adverse geological features including dangerous rockfalls, landslides, and debris flows, as well as conduct regional geological surveys such as structural interpretation and karst identification. Compared with traditional manual operations, this technology demonstrates significant advantages in terms of safety, efficiency, and precision, and can be widely applied to railway surveys in complex and rugged mountainous areas.

Zhou et al. [7] focuses on the constraints imposed by harsh environments on railway survey operations in complex plateau mountainous areas, where traditional manual methods are associated with high safety risks and low efficiency. By employing multirotor UAVs equipped with oblique photography cameras and developing low-altitude aerial survey geological interpretation software, this study realizes adverse geological interpretation and quantitative extraction of rock mass information based on 3D oblique photogrammetry models. It transforms the manual qualitative acquisition of rock mass structural information into computer-aided quantitative analysis, thus significantly improving survey efficiency and precision.

Wang [8] targets the characteristics of railway engineering EPC projects, such as complex terrain and high management difficulty. It systematically investigates UAV types

and payload matching, data acquisition, processing, management, and application, and constructs an application system based on the Browser/Server architecture. Leveraging intuitive data provided by UAVs, the system offers technical support for railway EPC project management.

Lv [9] addresses the land acquisition issues during the initial construction phase of the Shijiazhuang-Hengshui-Cangzhou-Huanghua Port Intercity Railway. It proposes a method for managing current ground feature conditions using aerial images and videos captured by lightweight UAVs to obtain high-resolution images and videos. After processing, these data enable rapid general surveys of the landforms and ground features along the railway line. The efficiency is nearly three times higher than that of traditional methods, and the digital results are convenient for management and application.

Zou et al. [10] takes the construction section of the Chengdu-Kunming Railway Double Line as an example. It uses fixed-wing UAVs for surveying, calculates the earthwork volume for construction access road excavation through 3D modeling and cross-section generation, and elaborates on the unique application mechanism of this technology in railway construction with large elevation differences. The technology exhibits remarkable advantages over traditional methods.

Through the analysis of the above typical application cases, the current application of the low-altitude economy in China's railway engineering construction mainly focuses on the route survey and design in the complex and rugged areas of Southwest China. Combined with geological interpretation technology, it reduces the lag time of data updating and improves the accuracy of geological interpretation, so as to minimize major design modifications. However, in the actual process of engineering construction, there are relatively few application scenarios in terms of project schedule, quality, safety, environmental and water conservation management, and disaster prevention. It is still unable to form effective productivity to solve the problems faced by traditional manual methods or means. Therefore, it is necessary to actively carry out research on low-altitude economy technologies in combination with the characteristics of railway engineering and the needs of construction management, and explore the practical application of the low-altitude economy centered on UAVs.

2.2 Analysis of Application Demands

Through the analysis of the development status and typical cases of the low-altitude economy in the railway sector, this paper sorts out and clarifies the technical requirements and functional demands of low-altitude equipment for typical application scenarios in response to the business needs of different stages and different management objects during the construction period. This provides a basis for subsequent scheme design and comprehensively improves the management efficiency and level of railway engineering construction.

Survey and Design Phase. During the railway survey and design phase, the difficulty of survey and design will be greatly increased when the railway line passes through complex terrains such as plateaus, canyons and dense forests. To complete the line survey efficiently, it is necessary to use UAVs equipped with oblique photography cameras, LiDAR and other devices to conduct full-area scanning of the line, generate a

centimeter-level precision 3D real-scene model, and extract micro-topographic features such as gullies, karst caves and dangerous rock masses, so as to solve the deviation problem of traditional discrete-point interpolation modeling. Meanwhile, for the boundary identification of geological risk zones such as landslides, collapses and debris flows as well as the interpretation of structural planes, it is essential to utilize UAVs combined with hyperspectral imaging and time-series interferometric synthetic aperture radar technology. With artificial intelligence algorithms, the automatic identification of landslide boundaries, the interpretation of the occurrence of rock mass structural planes, and the capture and marking of potential risk zones with an annual deformation greater than 1 mm can be realized, which provides data support for line location optimization and reduces subsequent design modifications [11].

Construction Phase. Railway engineering features an extensive linear distribution and requires synchronous construction across multiple sections. Traditional schedule management, which relies on manual reports and sampling measurements, suffers from data acquisition lags of generally over one week, and it is difficult to quantify the actual completion volume of structures such as bridges and tunnels. By conducting weekly regular 3D scanning of construction areas using UAVs, point cloud data models are generated and compared with the construction information models delivered in the design phase. This enables the automatic calculation of construction progress indicators including bridge pier pouring progress, subgrade filling and excavation volumes, and tunnel excavation contour deviations, as well as the generation of schedule delay early warning information to promptly remind construction unit managers to optimize construction organization. For the quality inspection of concealed indicators such as tunnel lining cracks, bridge bearing displacements, and subgrade compaction, traditional manual visual inspection or destructive testing methods are inefficient and prone to missed detections. UAVs equipped with LiDAR and infrared thermal imagers are employed to perform 3D reconstruction of tunnel lining structures and identify internal cracks; they conduct non-contact measurements of bridge bearing displacements, replacing traditional manual climbing inspections and reducing the risks of high-altitude operations; thermal imaging technology is used to monitor the temperature field distribution of subgrade fillers, thereby judging the uniformity of compaction. Regarding safety control for operations in scenarios such as tunnel blasting, bridge hanging basket construction, and high-slope excavation, traditional manual patrols have visual blind spots, which are likely to lead to accidents such as collapses and falls. UAVs fitted with high-definition cameras and monitoring sensors are utilized to conduct real-time monitoring of safety risks including unauthorized personnel entry into blasting warning zones, hanging basket deformation, and slope crack propagation. The monitored data is transmitted synchronously to the backend command platform, triggering sound and light alarms.

Environmental and Water Conservation Management. Traditional reliance on periodic manual spot checks makes it difficult to conduct real-time supervision over environmental violations such as the unauthorized occupation of land by temporary construction sites, the over-limit disposal of spoil at waste yards, and the illegal discharge of wastewater, which may easily lead to ecological and environmental penalties. UAVs are used to conduct weekly aerial surveys of the construction areas along the railway line. AI algorithms automatically verify the scope of the “red-line land use”, identify over-limit

areas and drainage pipelines, and generate inspection reports, thereby promoting the standardized management of environmental compliance.

Emergency Management. In recent years, extreme weather events, earthquakes, geological disasters and other hazards have occurred frequently. After a disaster strikes, it is difficult for rescuers to enter dangerous areas for reconnaissance, which may delay the optimal rescue window and affect emergency decision-making. UAVs can be rapidly deployed to capture high-resolution images of the affected areas. AI technology is then used to quickly calculate the affected area, assess the disaster severity, and generate disaster heat maps, providing support for the precise allocation of emergency rescue resources [12]. Tethered UAVs equipped with emergency high- altitude base stations can continuously monitor disaster sites and transmit data in real time to the rear command center, supporting the formulation and implementation of on-site rescue plans [13].

3 Design of Low-Altitude Economy Application Scheme During the Construction Period of Railway Engineering

3.1 Design of Application Scheme Architecture

To meet the large-scale, high-precision, and real-time air-ground collaborative perception requirements of such links as the survey and design phase, construction phase, environmental and water conservation management, and emergency management during the construction period of railway engineering, an overall architecture for the application of low-altitude economy UAVs in the construction period of railway engineering is designed, as shown in Fig. 1. The overall architecture is divided into four layers: the infrastructure layer, the transmission layer, the service layer, and the scenario application layer. It fully supports the calling of other business applications of the railway construction management information system through API interfaces and synchronously acquires navigation and positioning information from the satellite navigation integrated service platform.

Infrastructure Layer. The infrastructure layer mainly consists of hardware facilities such as UAV carriers, take-off and landing equipment, acquisition modules, communication modules, flight control modules, positioning and navigation modules, and power supply modules. Among these, the selection of UAV carriers and data acquisition modules needs to be scientifically and rationally matched based on comprehensive factors such as operation scenarios, environmental conditions, and task requirements during the railway engineering construction period, so as to ensure that UAVs can stably, accurately and safely perform tasks such as survey and design, and construction monitoring in the complex scenarios of engineering sites.

Data Transmission Layer. The data transmission layer mainly includes 4G, 5G mobile communications and low-Earth orbit high-throughput satellite communications. Among them, 4G and 5G mobile communications provide high- bandwidth and low-latency transmission services for UAV flight missions, enabling real-time transmission of

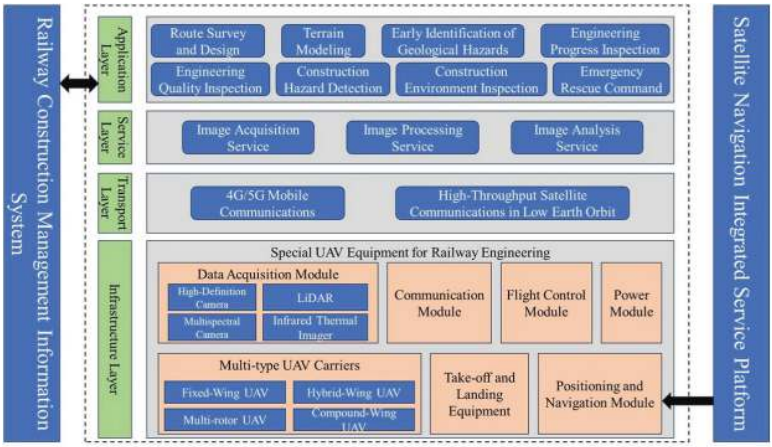

Fig. 1. Architecture of low-altitude economy application scheme for railway engineering construction phase.

data collected by UAVs and rapid issuance of remote control commands. LEO high-throughput satellite communications can provide two-way data transmission when ground 4G and 5G mobile communication signals are poor, and integrate with ground communication networks to form dual-link redundancy, ensuring data transmission during routine operations and disasters [14].

Data Service Layer. The data service layer mainly provides basic services such as data acquisition, processing and analysis. By integrating a variety of AI algorithms, it improves the processing efficiency and analysis depth of data collected by UAVs, realizes the processing of raw data, as well as functions such as standardized storage, efficient management and intelligent analysis. It converts raw data into information resources that can directly support decision-making, provides accurate and comprehensive information services for upper-layer scenario applications, and generates information achievements with practical application value.

Scenario Application Layer. The scenario application layer plans eight typical application scenarios for the railway engineering construction period, including route survey and design, terrain modeling, early identification of geological disaster hidden dangers, engineering progress inspection, engineering quality testing, construction hidden danger detection, construction environment inspection, and emergency rescue command. Based on the analysis results output by the data service layer and combined with the needs of railway engineering management, it converts data information into specific business logic and decision support, directly serves all links of engineering management, and solves practical problems faced during the construction process.

3.2 UAV Adaptation Scheme for Typical Engineering Scenarios

In view of the characteristics of railway engineering such as extensive linear distribution, complex topography and geology, and high-risk construction environments, eight

typical application scenarios including route survey and design, terrain modeling, and engineering progress inspection are planned. By optimizing UAV platform performance, payload adaptation, and complex environment adaptability, an engineering UAV configuration scheme adapted to the typical application scenarios during the construction period of railway engineering is formulated. This scheme addresses the pain points in traditional links such as survey and design, construction management, and safety monitoring, namely poor manual accessibility, insufficient data accuracy, low efficiency, and hidden risks. It achieves the goals of improving the accuracy of engineering survey and design, accelerating the response speed of construction schedule management, and reducing the risks of safety accidents, thus providing technical support for the high efficiency, precision, and intelligence of railway engineering construction. The engineering UAV adaptation scheme is shown in Table 1.

Table 1. UAV adaptation scheme for typical engineering scenarios.

Typical Application Scenarios	Core Performance of the Platform	Payload Configuration	Adaptability to Complex Environments
Route Survey and Design	Long endurance (fixed-wing ≥ 2 hours, multi-rotor ≥ 1 hour), Wind resistance rating ≤ Level 6, Autonomous route planning and positioning accuracy ≤ 3 cm	LiDAR, Oblique Photography Camera, Hyperspectral Camera	1. The lift of the motor is increased by 20% in plateau environments, adapting to altitudes above 5000 meters. 2. IP65 protection rating, with stable operation at temperatures ranging from -20°C to 50°C.
Terrain Modeling	Long endurance (fixed-wing ≥ 3 hours), Cruise stability (course deviation ≤ ±2°), Wind resistance rating ≤ Level 6, Autonomous operation altitude: 50-200 m	LiDAR, Oblique Photography Camera	1. LiDAR penetration mode for filtering out vegetation point clouds. 2. Integrated with INS inertial navigation, maintaining sub-meter-level positioning for ≥ 10 minutes when GNSS signal is lost.

(*continued*)

Table 1. (*continued*)

Typical Application Scenarios	Core Performance of the Platform	Payload Configuration	Adaptability to Complex Environments
Early Identification of Geological Hazards	High-frequency revisit (at least once a week, endurance ≥ 1.5 hours), Flight path stability (repeated route deviation ≤ 5 m), Hovering wind resistance rating ≤ Level 5, Low-altitude penetration capability (hovering accuracy ≤ 30 cm)	LiDAR, Hyperspectral Camera, Thermal Infrared Camera	1. Operate within 1 hour after heavy rain 2. Multi-rotor UAV can hover on steep slopes > 30° with obstacle avoidance distance ≥ 30 m 3. Night vision camera can identify cracks within 5 m under low visibility of 0.1 lux
Engineering Progress Inspection	High-efficiency coverage (cruising speed: 30-50 km/h, coverage of at least 10 km of railway route per sorties), Wind resistance rating ≤ Level 6, Real-time image transmission (latency ≤ 2 seconds)	LiDAR, High-definition Optical Camera	1.Resist interference in 2.4/5.8 GHz frequency bands in construction zones 2.Autonomous obstacle avoidance and flight around occlusions such as piers and tunnel portals 3.Signal-to-noise ratio (SNR) ≥ 30 dB in low-light environments
Engineering Quality Inspection	Precision control (hovering positioning accuracy ≤ 10 cm, low-speed cruising at 0.5 m/s), Hovering wind resistance rating ≤ Level 5, Narrow-space operation (wheelbase ≤ 1.5 m)	LiDAR, High-definition Zoom Camera, Infrared Thermal Imager	1. The lens is fog-proof and anti-fouling, supporting shooting inside tunnels 2. Adapt to vibrations in construction zones with data stability ≥ 95%
Construction Hazard Detection	Rapid response (takeoff within 15 minutes, endurance ≥ 30 minutes), Hovering accuracy of ±5 cm for close-range shooting at 5–10 m, 360°LiDAR obstacle avoidance, Hovering wind resistance rating ≤ Level 5	High-definition Intelligent Camera, Gas Sensor, Acousto-optic Alarm Module	1. Maintain a safe distance of ≥ 30 m from construction machinery 2. Identify mobile equipment with a response latency ≤ 0.5 seconds 3. Night vision camera + LED fill light with an identification distance ≥ 30 m
Construction Environment Inspection	Wide coverage (endurance ≥ 2 hours, coverage of 50 km² per sortie), Wind resistance rating ≤ Level 6, Cruise stability (flight route deviation ≤ 10 m)	LiDAR, High-resolution Remote Sensing Camera, Gas Sensor	1.Low-noise design (≤ 60 dB) 2.Integrate Beidou short-message communication to transmit monitoring data back 3.Endurance retention rate ≥ 80% in high-temperature environments
Emergency Rescue Command	Rapid deployment (tethered type supports continuous operation for over 72 hours), Mobility in extreme environments (wind resistance ≤ Level 8, continuous operation under rainstorm of 50 mm/h), Communication relay (coverage radius ≥ 1 km)	LiDAR, Life Detector, Night Vision Reconnaissance Camera	1. Airframe impact resistance ≥ 50G, operating temperature tolerance ≤ 80°C 2. Ad-hoc network multi-UAV relay

3.3 Data Acquisition and Transmission Scheme for Typical Scenarios

For eight typical application scenarios including route survey and design, terrain modeling, and construction progress inspection, we standardize the data collection process by formulating standards for UAV data collection types, collection frequencies, data quality requirements, and data transmission interfaces. By leveraging efficient data transmission technologies, we ensure that the multi-source data acquired by UAVs can serve the typical scenarios in the engineering construction process accurately and in real time, thereby guaranteeing project safety, improving construction efficiency, reducing costs, and optimizing management.

Firstly, in accordance with the data requirements of different application scenarios such as survey and design, and construction, the types of data to be collected by UAVs shall include: image data, point cloud data, video data, and other sensor monitoring data. Among these, image data is captured by UAVs equipped with devices such as high-definition cameras, multi-camera systems, infrared thermal imagers, and multispectral cameras, to obtain data including three-dimensional ground object information, texture details, and radiation information. This data is used for constructing digital orthophotos, realistic 3D models, and thermal distribution maps of the railway lines. Point cloud data is collected by UAVs mounted with LiDAR systems, which capture massive 3D coordinate point information of railway lines and structures. It is applied to generate high-precision digital elevation models (DEMs) and digital surface models (DSMs) [15].Video data is mainly obtained by UAVs fitted with high-definition cameras to record real-time dynamic images of construction sites, usually at a frame rate of 25–30 frames per second, for capturing the dynamic construction process. Other sensor monitoring data is collected based on the requirements of specific application scenarios, UAVs can be equipped with gas and water quality monitoring sensors to gather data such as air quality and water conditions in the construction area.

Secondly, a rational data collection frequency shall be formulated by comprehensively considering such factors as data collection types, application scenarios, project phases, and external conditions including weather and geological risks. The purpose is to balance equipment wear, labor costs and data value while ensuring data validity, so as to avoid redundant collection that leads to resource waste. First, in accordance with the project progress, weekly, monthly and quarterly collection plans shall be formulated in advance. The collection frequency of different data types for each area shall be clarified, and regular evaluation and adjustment shall be conducted. Second, for fixed operation areas such as tunnel entrances and exits, the UAV automatic inspection mode can be enabled to perform tasks automatically at a preset frequency. Third, in the event of emergencies such as rainstorms and geological disasters, an emergency response shall be triggered to ensure timely data collection and support command decisions. A recommended scheme for data collection frequency in typical application scenarios is shown in Table 2.

Table 2. Recommended scheme for data collection frequency in typical scenarios.

Typical Application Scenarios	Data Type	Collection Frequency
Route Survey and Design	Image Data, Point Cloud Data	Initial one-time full-line coverage + dynamic supplementary collection
Terrain Modeling	Image Data, Point Cloud Data	Initial one-time full-line coverage + partial re-shooting
Early Identification of Geological Hazards	Image Data, Point Cloud Data	One-time full coverage of the 1–3 km area along the line in the initial phase
Engineering Progress Inspection	Image Data	For linear projects such as subgrades and bridges, inspections shall be conducted once a week per section, For key construction sites such as tunnels and stations, regular inspections shall be carried out once every two weeks.
Engineering Quality Inspection	Image Data, Point Cloud Data	Real-time inspection + event-triggered mode (e.g., beam erection, blasting, etc.)
Construction Hazard Detection	Video Data, Point Cloud Data	Inspections for high-risk areas shall be conducted once every two hours.
Construction Environment Inspection	Image Data, Sensor Monitoring Data	One-time full coverage before commencement of construction
Emergency Rescue Command	Image Data, Video Data, Sensor Monitoring Data	Within 15 minutes of receiving the instruction, deployment shall be completed at the initial stage of an accident.

Thirdly, the quality requirements for data collection shall be defined by specifying quantitative indicators and technical standards such as resolution, accuracy, and completeness, in accordance with the data collection types and the engineering precision requirements of different application scenarios. First, the data accuracy shall match the engineering requirements of the corresponding application scenarios. For example, centimeter-level accuracy is required for survey and design work, while the accuracy threshold can be appropriately relaxed for construction progress inspection. Second, multiple batches of data collected in the same area shall maintain consistency in coordinate datum, file format, and data accuracy, so as to facilitate comparative analysis. Third, data collection shall fully cover the target area without omissions, and truly reflect the on-site operation status. The data collection quality requirements for typical application scenarios are presented in Table 3.

Table 3. Data collection quality requirements for typical scenarios.

Data Collection Types		Data Quality Requirements
Image Data	Visible Light Images	1. Image resolution ≤ 5 cm/pixel 2. Forward overlap rate ≥ 80% 3. Side overlap rate ≥ 70%
	Oblique Photography/ Orthophoto Images	1. Full coverage without missing shots; 2. Forward overlap rate ≥ 65%, side overlap rate ≥ 35%. 3. For complex terrains, the rates can be increased to 75% and 45% respectively.
	Infrared Thermal Imaging Images	It has a thermal sensitivity resolution within ±2°C and a temperature gradient sensing capability of 0.1°C
	Multispectral/Hyperspectral Images	1.Resolution ≤10 nm 1. Covering the 400–1000 nm waveband; ensuring the interpretability of vegetation stress signals
	Point Cloud Data	1. The point cloud density shall be ≥100 points/m² 2. The classification accuracy of ground points and building points shall be ≥ 95%.
	Video Data	1. Resolution shall not be lower than 1080p 2. Frame rate ≥ 25 fps and 4K cameras shall be used for key areas.
Sensor Monitoring Data	Gas Monitoring Data	The accuracy of gas sensors shall reach ±5 μg/m³ for PM2.5 and ±2 ppm for harmful gases.
	Water Quality Monitoring Data	The error of water quality sensors shall be ≤ 0.1 pH units to ensure accurate assessment of pollution levels.

Finally, by integrating the UAV data collection types, frequencies, and quality requirements, we shall specify the requirements for data transmission file formats, interface standards, and transmission protocols. This ensures the efficient, secure, and accurate circulation of data, realizes the goals of "accurate collection, fast transmission, and effective utilization" of UAV data during the railway engineering construction phase, and provides stable data support for typical application scenarios in engineering construction. First, for scenarios with high real-time requirements such as construction hazard detection and emergency rescue command, 4G and 5G mobile communications shall be prioritized for real-time data transmission. For large-scale image and point cloud data involved in scenarios such as route survey and design, and terrain modeling, the "store-then-transmit" mode can be adopted. Second, during the transmission process, encrypted transmission shall be implemented for sensitive data, and breakpoint resume transmission shall be supported to avoid data loss. Third, data transmission interfaces and

methods shall be compatible with the standard API interfaces of the railway construction management information system, to facilitate system integration and data invocation. The requirements for data transmission interfaces and methods in typical application scenarios are specified in Table 4.

Table 4. Requirements for data transmission interfaces and methods in typical scenarios.

Data Collection Types		File Format	Data Interface	Transmission Protocol
Image Data	Visible Light Images	Geo TIFF or JPEG	Open service interfaces such as OGC WMS/WCS	FTP/SFTP/HTTP/USB
	Oblique Photography/ Orthophoto Images	Geo TIFF or JPEG	Open service interfaces such as OGC WMS/WCS	FTP/SFTP/HTTP/USB
	Infrared Thermal Imaging Images	JPEG or TIFF or IRF	Open service interfaces such as OGC WMS/WCS	FTP/SFTP/HTTP/USB
	Multispectral/Hyperspectral Images	TIFF or ENVI or NetCDF	Open service interfaces such as OGC WMS/WCS	FTP/SFTP/HTTP/USB
Point Cloud Data		LAS/LAZ	Open service interfaces such as OGC WMS/WCS	FTP/SFTP/HTTP/USB
Video Data		H.265	RESTful API	Streaming protocols such as RTMP and RTSP
Sensor Monitoring Data	Gas Monitoring Data	JSON	RESTful API	MQTT, WebSocket
	Water Quality Monitoring Data	JSON	RESTful API	MQTT, WebSocket

4 Challenges and Development Suggestions

4.1 Challenges Faced

At present, the application of the low-altitude economy during the construction period of railway engineering in China is still in the initial exploration stage, and it faces numerous challenges in terms of airspace management, safety assurance, laws and regulations, technical capability, and talent cultivation [16].

In terms of airspace management, the low-altitude airspace management system in China has not yet been fully established. It involves collaboration among multiple departments such as the military, civil aviation, and local governments, but lacks a unified and effective management framework. The approval process for low-altitude flight activities along railway lines is stringent and inefficient, resulting in suboptimal allocation and utilization of dedicated railway airspace resources. Flight conflicts are prone to occur between different types of aircraft, which hinders the application of the low-altitude economy in railway construction.

In terms of safety assurance, the terrain and environment along railway lines are complex and diverse. Traditional satellite-based electronic fence technology struggles to meet the dynamic management needs of railway construction scenarios. UAVs flying along railway lines are susceptible to magnetic interference, which may lead to loss of control and crashes. Inadequate safety awareness among operators could result in UAVs straying into restricted airspace along the lines, posing a threat to railway transportation safety.

In terms of laws and regulations, the regulatory framework governing low-altitude flight, including airspace management and safety supervision specific to the railway sector, is not yet fully refined. This places construction enterprises involved in railway projects in a state of compliance uncertainty when deploying low-altitude economy applications during the construction process.

In terms of technical capability, the coverage of supporting infrastructure such as take-off and landing sites, charging facilities, maintenance support, and meteorological services along railway lines is insufficient, which fails to meet the demands for high-density flight operations and data acquisition of low-altitude aircraft in railway construction. Furthermore, China still has shortcomings in advanced process chip manufacturing, with a high degree of dependence on imports. Key technologies such as supply chain integration, autonomous flight, and perception and avoidance are at risk of being "bottlenecked", making it difficult to meet the requirements for efficient and safe operation of the low-altitude economy during railway engineering construction.

In terms of talent cultivation, the low-altitude economy is an emerging industry with a significant talent gap. The railway sector, in particular, lacks interdisciplinary professionals who are proficient in both engineering construction operations and low-altitude economy technologies. The training system for specialized personnel such as low-altitude pilots and UAV operators is still underdeveloped, which cannot satisfy the talent needs for the development of the low-altitude economy during railway engineering construction.

4.2 Recommendations for Future Development

Faced with the aforementioned challenges, the future development of the low-altitude economy during the construction period of railway engineering requires a multi- faceted layout covering policy support, technological innovation, industrial integration, safety supervision, and talent reserve, so as to establish a full-chain and multi-stakeholder collaborative promotion mechanism [17].

Strengthen Policy Support and Coordination. The government, together with railway regulatory authorities, construction agencies, and operation entities, should formulate targeted policies and regulations for the development of the railway low- altitude economy, clarifying airspace usage rules, approval procedures, and safety supervision standards. A comprehensive safety supervision system for the low-altitude economy should be established, defining the responsibilities and division of labor among various departments to avoid regulatory gaps and overlaps. Meanwhile, investment in the construction of low-altitude infrastructure along railway lines should be increased, and local enterprises should be encouraged to participate in railway low-altitude economy projects, thereby reducing operational costs and boosting their enthusiasm for participation.

Enhance Technological Innovation and Application. Social enterprises and research institutions should be encouraged to increase R&D investment in key technologies of the low-altitude economy, overcoming core technical bottlenecks in engines, flight control systems, perception and obstacle avoidance. Technologies such as 5G, big data, and artificial intelligence should be actively applied, and integrated with the management concepts of railway train dispatching systems to build an intelligent low-altitude application management system. This system will enable real- time monitoring and intelligent dispatching of low-altitude aircraft, improving airspace utilization efficiency and flight safety.

Promote Integrated Industrial Development. A sound "industry-research- application" ecosystem for the low-altitude economy should be established, clarifying the responsibilities and division of labor of all stakeholders, so as to promote the in- depth integration of railway construction and the low-altitude economy in terms of business operations, technologies, and operation systems. For example, low-altitude equipment manufacturers should develop low-altitude equipment suitable for the complex operating conditions of railway construction based on the characteristics of railway lines, to meet the requirements of long-endurance, high-precision, and high- reliability flight missions. Railway construction departments should make overall plans for the construction of low-altitude infrastructure along railway lines, rationally arranging physical infrastructure such as helipads and charging facilities according to the needs of railway engineering construction and line characteristics, to ensure sufficient take-off, landing, and parking space for low-altitude aircraft.

Establish and Improve the Safety Supervision System. A comprehensive safety supervision system for the railway low-altitude economy should be established, clarifying the responsibilities and division of labor of all regulatory authorities. Strengthened airworthiness management of low-altitude aircraft, qualification management of flight personnel, and real-time monitoring of flight activities should be implemented. A robust safety monitoring and evaluation technical system, as well as a maintenance support system for safe operation, should be built to ensure that low- altitude flight activities during railway construction are safe and controllable.

Strengthen Talent Cultivation and Reserve. Railway construction and operation departments should collaborate with local universities and vocational colleges to offer courses related to the low-altitude economy, jointly cultivating interdisciplinary professionals covering flight technology, air traffic management, aircraft manufacturing

and maintenance. Railway construction enterprises can conduct targeted training programs in specific operation scenarios of construction projects, and universities and enterprises should work together to provide talent guarantee for the development of the low-altitude economy in railway engineering construction, supporting its large-scale practical application.

5 Conclusion

This paper conducts research on the development and application of the low-altitude economy during the construction period of railway engineering. By systematically sorting out the current development status of the industry, analyzing typical application requirements, and designing application schemes, it clarifies the application ideas of the low-altitude economy in the field of railway engineering construction. Firstly, the application of the low-altitude economy based on UAVs demonstrates unparalleled advantages over manual work in typical application scenarios such as railway survey in complex mountainous areas, engineering quality inspection, and high-risk operation monitoring, providing a brand-new technical path for the digital and intelligent transformation of railway engineering. Secondly, this paper designs and constructs a four-layer system architecture for the application of the low-altitude economy during the construction period of railway engineering, forming a full-chain technical scheme ranging from project adaptation to data acquisition and transmission. This scheme can directly provide standardized application guidance for all parties involved in railway construction, and effectively solve practical problems such as multi-source data silos, difficulty in equipment adaptation, and low analysis efficiency. Finally, focusing on the application prospects of the low-altitude economy during the construction period of railway engineering, this paper identifies the current challenges in its development and puts forward suggestions for future development, promoting the in-depth integration of the low-altitude economy and railway engineering construction through multi-dimensional coordination. The application schemes and technical paths proposed in this paper can provide references for the formulation of subsequent industry standards, the direction of technological innovation, and the implementation of projects, so as to drive the high-quality development of China's railway construction industry.

References

1. Jin, Y., Zhang, H., Deng, Z.L., et al.: 5G-A/6G+Beidou pass sensing guide technology in low altitude economy and prospect. J. Telecommun Sci **41**(03), 1–16 (2025). https://doi.org/10.11959/j.issn.1000-0801.2025045
2. Wang, J.: Theoretical logic of "Six Modernisation Systems" of railway in the perspective of system theory. J. Theory Learn Explor **01**, 53–56 (2025)
3. Li, M.J., Xie, Z.Y., Qin, Y., et al.: Application of small unmanned aircraft in foreign railway. J. China Railway **10**, 120–125 (2020). https://doi.org/10.19549/j.issn.1001-683x.2020.10.120
4. Qin, X.Y., Zhang, Z., Wang, H.Y., et al.: Analysis of the application status quo of railway inspection drones at home and abroad (below). J. Railway Technol. Superv. **52**(02), 53–57 (2024). https://doi.org/10.3969/j.issn.1006-9178.2024.02.020

5. Qin, X.Y., Zhang, Z., Wang, H.Y., et al.: Analysis of the application status quo of railway inspection drones at home and abroad (above) J. Railway Technol. Superv. **52**(01), 48–51+55 (2024). https://doi.org/10.3969/j.issn.1006-9178.2024.01.018
6. Wang, D., Jiang, L.W., Zhang, G.Z., et al.: Application of UAV three-dimensional imaging technology in railway survey. J. Railway Eng. **33**(10), 21–24 (2016)
7. Zhou, F.J.: Research on the application of unmanned aircraft tilt photography survey technology for railway in highland complex mountainous area. J. Railway Stand. Des. **65**(06), 1–5 (2021). https://doi.org/10.13238/j.issn.1004-2954.202006030007
8. Wang, K.: Application of drones in railway general contracting construction. J. Railway Surv. **46**(06), 50–55 (2020). https://doi.org/10.19630/j.cnki.tdkc.202007290002
9. Lv, X.Y.: Research application of drone aerial photography in railway construction management. J. Railway Survey **45**(04), 24–27 (2019). https://doi.org/10.19630/j.cnki.tdkc.201904120001
10. Zou, Y., Wang, D., Zhang, G.Z., et al.: Application of drone photogrammetry technology in the construction of large height difference railway project. J. Surveying Mapp. Geographic Inform. **45**(01), 114–116 (2020)
11. Ren, G.X.: Application of UAV airborne LiDAR technology in the identification of karst hazards in high-speed railway J. Railway Standard. Design **70**(02) (2026). https://doi.org/10.13238/j.issn.1004-2954.202405070001
12. Fu, K., Wang, X., Gao, B.S., et al.: Application of UAV inclined photogrammetry technology in emergency rescue of railway sudden geological disasters. J. Railway Standard Design **65**(03), 59–63 (2021). https://doi.org/10.13238/j.issn.1004-2954.202003150001
13. Yue, L., Cao, Y.C., Hu, Y., et al.: Application and prospect of air-to-ground integration technology in emergency communication. J. Commun. World **11**, 37–40 (2022). https://doi.org/10.3969/j.issn.1009-1564.2022.11.015
14. Lu, Y.L., Shen, H.Y., Zhang, J.Y., et al.: Exploration and prospect of key technologies for new generation mobile communication in intelligent railway. J. Telecommun. Sci. **39**(1), 30–41 (2023). https://doi.org/10.11959/j.issn.1000-0801.2023002
15. Liu, H.G., Wang, J.J., Kou, Y.: Updating terrain-level live 3D geographic scenes using UAV laser point cloud data. J. Surv. Mapp. Bull. **09**, 111–114 (2022). https://doi.org/10.13474/j.cnki.11-2246.2022.0273
16. He, Y., Wang, Y.Y., He, L.W., et al.: Current status and prospects of low altitude economic policies and technologies in rural agriculture. J. Agric. Eng. **41**(08), 1–16 (2025)
17. Xia, J.C., Su, M.: The internal logic and optimisation strategy of the integrated development of artificial intelligence and low-altitude economy. J. Sci. Manage Res. **43**, 64–72 (2025)

Blasting Vibration Analysis of Existing Surface Buildings Induced by Drill and Blast Excavation of Large-Section Tunnels

Peng Guo[1], Shaohua Ji[1], Jun Wang[2(✉)], and Guowen Xu[3]

[1] CCCC Road & Bridge International Co., Ltd., Beijing 101107, China
[2] Sichuan Highway Planning, Survey, Design and Research Institute Ltd, Chengdu 610041, China
luckywangjun@126.com
[3] Southwest Jiaotong University, Chengdu 610031, China

Abstract. Taking the Lihuashan Tunnel of Tianfu-Qionglai Expressway as the supporting project, which underpasses Wuyou Temple and its surrounding building clusters, this paper studies the vibration hazards of surface buildings caused by drill and blast method. Firstly, the parameters of the sandstone RHT (Riedel, Hiermaier, and Thoma) model were calibrated by theoretical analysis, and a 3D blasting numerical model for the upper bench of the pilot tunnel was established based on the on-site blasting scheme. Secondly, a 3D numerical model to simulate the cyclic blasting excavation of Lihuashan Tunnel was constructed using the equivalent load method, the vibration effects of blasting on Wuyou Temple and its surrounding buildings were predicted to evaluate the safety of the tunnel blasting scheme. Finally, the rationality of the blasting scheme was verified by conducting on-site tests on the vibration effects of buildings. The results show that the numerical model adopted in this paper can effectively predict the vibration effects of tunnel blasting excavation on existing surface buildings, and can provide references for subsequent construction and similar projects to predict tunnel blasting vibration hazards.

Keywords: Drilling and blasting method · Equivalent load method · Peak particle velocity · Field monitoring · Numerical simulation

1 Introduction

Tunnels are widely encountered in highways in areas with complex topography and landforms [1, 2]. Currently, the drill and blast method is the mainstream construction method for highway tunnels in mountainous areas [3]. Highway tunnels have to underpass surface structures and buildings, and unavoidable negative impacts will be caused to these structures when the tunnel is constructed with drill and blast method [4–6]. In severe cases, it may lead to the instability of the existing buildings. Thus, how to carry out blasting construction safely and efficiently in the vicinity of existing buildings is an urgent problem to be solved.

© The Author(s), under exclusive license to Springer Nature Switzerland AG 2027
G. Feng et al. (Eds.): ICCE 2025, SUCI, pp. 203–221, 2027.
https://doi.org/10.1007/978-3-032-32237-1_15

Numerous researchers have studied the vibration effects of tunnel drill and blast construction on existing surface buildings using theoretical analysis, numerical calculation, model test, field test and et al. [7–9]. Owing to its high efficiency and cost-effectiveness, numerical simulation efficiently overcomes the shortcomings of model tests and on-site blasting tests, and can provide theoretical and practical support for verifying the feasibility and rationality of tunnel blasting schemes. Liu [10] used the equivalent load method to simulate the blasting vibration effects of a tunnel underpassing a temple, and provided suggestions to improve the blasting schemes. Huang et al. [11] employed numerical simulation and on-site vibration monitoring to study the impact of drill and blast construction on surface ancient buildings. Song et al. [12] proposed a new method for evaluating and optimizing tunnel blasting schemes adjacent to existing buildings based on numerical simulation and the nonlinear Fuzzy Analytic Hierarchy Process (FAHP). Xu et al. [13] used numerical simulation to conduct a comparative analysis of the time history of blasting vibration velocity and the effect of blasting on fractured surrounding rock, and evaluated the advantages and disadvantages of two blasting methods.

Taking the Lihuashan Tunnel of the Tianfu-Qionglai Expressway undercrossing Wuyou Temple and its adjacent buildings as an example, this paper studies the impact of the close-proximity construction of drill-and-blast tunnels on surface structures. First, the parameters of the sandstone RHT (Riedel, Hiermaier, and Thoma) model were calibrated by theoretical analysis. Secondly, a 3D blasting numerical model for the upper bench of the pilot tunnel was established based on the on-site blasting scheme, and the simulation results verified the rationality of the blasting hole pattern parameters. Finally, a 3D numerical model simulating the cyclic blasting excavation of large-section highway tunnels was constructed using the equivalent load method to simulate the blasting vibration effects of drill and blast construction on existing surface buildings. The peak particle velocity (PPV) of blasting at the corresponding monitoring points of Wuyou Temple and its surrounding building clusters was predicted, and the feasibility and safety of the existing tunnel blasting design scheme were evaluated. The comparison results between the numerical simulation results and on-site monitoring data show that the use of numerical simulation to predict the vibration effects of tunnel drill and blast excavation on existing surface buildings has certain feasibility and rationality, and can provide reference for subsequent construction and similar projects.

2 Engineering Overview and Model Parameter Calibration

2.1 Engineering Overview

The Lihuashan Tunnel is located in Chengdu, Sichuan Province, China. The right line of Lihuashan Tunnel has a starting and ending pile number of K2 + 087-K2 + 590 with a length of 503 m, the left line has a starting and ending pile number of ZK2 + 096-ZK2 + 592 with a length of 496 m, and the maximum buried depth of the tunnel is 88 m. The tunnel surrounding rock is mainly composed of horizontally bedded sandstone, which has good integrity and self-stability. The drill and blast method is adopted for the tunnel construction. The combined support method of steel frame and rock wall is used to simplify the construction procedures and accelerate the construction progress. The plan view of Lihuashan Tunnel is shown in Fig. 1, the entrance underpasses 11 civil houses,

and the right line is adjacent to Wuyou Temple. The construction of Lihuashan Tunnel will pose a certain threat to Wuyou Temple and its surrounding building clusters, and it is necessary to carry out research.

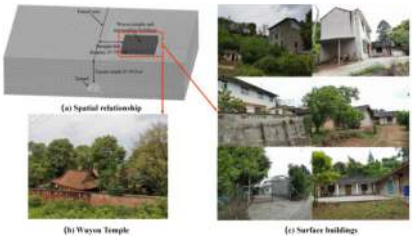

Fig. 1. Spatial relationship between Wuyou temple, adjacent structures, and the tunnel.

2.2 Parameter Calibration of the Theoretical Model for Rock Blasting Fragmentation

The selection of the theoretical model for rock blasting fragmentation is the key to tunnel blasting simulation and also the foundation for the implementation of blasting numerical simulation. The RHT model was proposed by Riedel, Hiermaier, and Thoma, it is a tension-compression damage model, consisting of three stages: the elastic stage, the linear strengthening stage, and the damage softening stage. The RHT model introduces pressure-dependent elastic limit surfaces, failure surfaces, and residual strength surfaces. It takes into account the effects of surrounding rock pressure, strain rate, strain hardening, and damage softening on the failure strength of rock materials under blasting loads, as well as the strain hardening effect during the process from the material exceeding the elastic limit to failure and the damage softening effect after material failure. Additionally, a residual stress surface is also incorporated into the model [14]. The RHT model can well reflect the mechanical properties of rock under different confining pressures and high strain rates, and thus can effectively simulate the dynamic mechanical response of rock under explosive loads [15–18].

The mechanical parameters of sandstone were obtained by laboratory tests, including $f_c = 40$ MPa, $f_t = 4$ MPa, $\rho = 2300$ kg/m^3, an elastic modulus $E = 25.5$ GPa, and $v = 0.17$, where f_c is the saturated uniaxial compressive strength, f_t is uniaxial tensile strength, ρ is rock density, E is elastic modulus and v is Poisson's ratio. Based on the aforementioned laboratory test results, this paper calibrates the parameters of the sandstone RHT model by theoretical research, and provides the basis for the study on blasting vibration analysis.

The RHT model contains 34 parameters, some parameters can be determined by experimental methods, some are given values, some can be determined by theoretical research, and the remaining model parameters can just adopt the initial default values of concrete. The given values include the compressive strain rate $\dot{\varepsilon}_0^c = 3.0 \times 10^{-5} s^{-1}$, failure compressive strain rate $\dot{\varepsilon}^c = 3.0 \times 10^{25} s^{-1}$, tensile strain rate $\dot{\varepsilon}_0^t = 3 \times 10^{-6} s^{-1}$, failure tensile strain rate $\dot{\varepsilon}^t = 3.0 \times 10^{25} s^{-1}$, and damage parameter $D_2 = 0$.

Based on the basic physical parameters of sandstone, the Hugoniot polynomial coefficients A_1, A_2, A_3, the equation of state parameters B_0, B_1, T_1, T_2, the compressive strain

rate index β_c, the tensile strain rate index β_t, the Lode angle correlation coefficient B, and the tensile yield surface parameter g_t^* can be determined by theoretical calculation research. The following deviations are obtained by the Rankine-Hugoniot equation and the Mie-Gruneisen equation [19]:

$$T_1 = A_1 = \rho_0 c_0^2 \tag{1}$$

$$A_2 = \rho_0 c_0^2 (2s - 1) \tag{2}$$

$$A_3 = \rho_0 c_0^2 \left(3s^2 - 4s + 1\right) \tag{3}$$

$$B_0 = B_1 = 2s - 1 \tag{4}$$

$$T_2 = 0 \tag{5}$$

Where A_1 A_2 and A_3 are Hugoniot polynomial coefficients, T_1 and T_2 are material parameters under tensile state, $c_{0=}$2920 m/s is the sound speed in the porous material when the pressure is zero, s is a material parameter, and $s = 1.34$ can be adopted for sandstone.

Similarly, based on the basic physical parameters of sandstone, the shear modulus G and tension-compression strength ratio f_t^* can be determined by theoretical calculation research. Furthermore, according to the theory of elasticity, the following can be derived [20]:

$$G = E/2(1 + \nu) \tag{6}$$

$$p_{el} = 2f_c/3 \tag{7}$$

$$f_t^* = \frac{f_t}{f_c} \tag{8}$$

$$\beta_c = 4/(20 + 3f_c) \tag{9}$$

$$\beta_t = 2/(20 + f_c) \tag{10}$$

$$g_t^* = 0.7 \tag{11}$$

$$B = 0.0105 \tag{12}$$

To further obtain the strength parameters in the sandstone RHT model, the Hoek-Brown empirical equations are used to obtain the triaxle compressive strength under various confining pressures as follows [21]:

$$\sigma_1 = \sigma_3 + f_c \left(m_i \frac{\sigma_3}{f_c} + s\right)^{\frac{1}{2}} \tag{13}$$

Where σ_1 and σ_3 are the maximum and minimum effective stresses at the time of failure, respectively; m_i is the parameter of the Hoek-Brown (H-B) yield criterion, and according to Reference [22], a value of 17.0 is adopted for sandstone; for intact rock, the value of s is 1.0.

In addition, the failure surface parameter A and failure surface index N can be obtained from Eq. (14) [23]:

$$\sigma_f^*\left(P_0^*, F_r\right) = A\left(P_0^* - F_r/3 + (A/F_r)^{-1/N}\right)^N \tag{14}$$

$$P_0^* = (\sigma_1 + 2\sigma_3)/3f_c \tag{15}$$

$$\sigma_f^* = (\sigma_1 - \sigma_3)/f_c \tag{16}$$

Where $\sigma_f^*\left(P_0^*, F_r\right)$ is the normalized compressive strength; ${P_0}^*$ is the normalized pressure; F_r is the dynamic strain rate increase factor, and $F_r = 1.0$ is obtained under quasi-static conditions.

The triaxle compressive strength of sandstone under different confining pressures is derived from Eq. (13). Furthermore, the normalized pressure ${P_0}^*$ and normalized compressive strength $\sigma_f^*\left(P_0^*, F_r\right)$ under different confining pressures can be calculated using Eqs. (15) and (16), as shown in Table 1.

Table 1. Normalized pressure and normalized compressive strength under different confining pressures.

$\sigma_2 = \sigma_3$(MPa)	σ_1(MPa)	${P_0}^*$	${\sigma_f}^*$
0	40	0.33	1
5	75.71	0.71	1.77
10	101.65	1.01	2.29
20	143.29	1.53	3.08
30	178.32	1.99	3.71
40	209.71	2.41	4.24
60	265.91	3.22	5.15

Figure 2 shows the nonlinear curve fitting of the normalized pressure and normalized compressive strength under different confining pressures in Table 1. It can be seen that the failure surface parameter $A = 2.37$ and the failure surface exponent $N = 0.68$ is obtained.

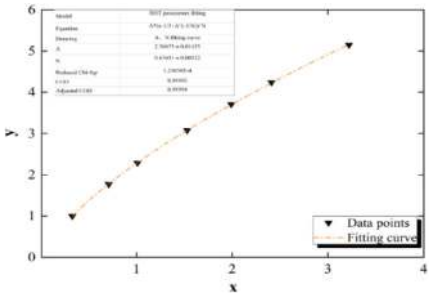

Fig. 2. Fitting curve results.

In the RHT model, the ratio of the radius of the tensile meridian to the compressive meridian can be obtained by Eq. (17).

$$Q = Q(P^*) = Q_0 + BP^* \tag{17}$$

Where Q is the tension-compression meridian ratio, Q_0 is the initial tension-compression meridian ratio. In this paper, $Q_0 = 0.54$ and $P^* = 0.05$are adopted for sandstone [24].

As a conclusion, most parameters in the RHT model can be determined by theoretical calculation, model test and empirical formula. The remaining parameters are modified according to existing research [25]. The RHT parameters for sandstone are shown in Table 2 below.

Table 2. RHT model parameters.

Parameter	Value	Parameter	Value	Parameter	Value
ρ_0	2.30×10^{-6} kg/mm^3	f_c	40 MPa	α_0	1.0
P_{el}	26.67 MPa	β_c	0.0286	β_t	0.0333
A_1	19.61 GPa	A_2	32.95 GPa	A_3	20.14 GPa
B_0	1.68	B_1	1.68	T_1	19.61 GPa
T_2	0 GPa	G	10.90 GPa	$\dot{\varepsilon}^c$	3×10^{22} ms^{-1}
$\dot{\varepsilon}_0^c$	3×10^{-8} ms^{-1}	$\dot{\varepsilon}_0^t$	3.0×10^{-9} ms^{-1}	f_s^*	0.45
$\dot{\varepsilon}^t$	3×10^{22} ms^{-1}	D_2	1	g_c^*	0.3
B	0.0105	g_t^*	0.7	ε_p^m	0.01
A	2.37	n	0.68	p_{comp}	6 GPa
f_t^*	0.1	Q_0	0.54	N	4.0
ξ	0.3	D_1	0.053		
A_f	1.62	n_f	0.59		

3 Tunnel Drill-and-Blast Construction Scheme and Determination of Blasting Load

3.1 Tunnel Blasting Hole Network Parameters

The cross-sectional area of tunnel reaches 232.52 m^2, the step-by-step excavation method is adopted to ensure the tunnel excavation safety. The excavation cross-section is divided into two pilot tunnels and several benches. The excavation sequence is ① → ② → ③ → ④ → ⑤ → ⑥, as shown in Fig. 3.

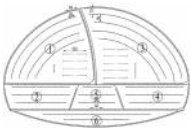

Fig. 3. Blasthole network parameters of steel frame and rock wall method.

Table 3. Blasthole layout parameters.

Project	Perimeter holes	Cutting holes		Auxiliary holes
		I	II	
Cross-section area (m^2)	220.44			
Total number of blastholes	394			
Blasthole number	168	5	18	203
Blasthole length (m)	2.4	2.4	2.9	2.4
Blasthole spacing (cm)	60	80	265	80
The single-hole charge (kg)	0.4	1.5	1.9	1.5
Charge diameter (cm)	25	32	32	32

Lihuashan Tunnel uses rock emulsion explosive. It is recommended to use 25 mm specification explosives for peripheral holes, and 32 mm specification explosives for auxiliary holes and cut holes. Electronic digital detonators are used for explosive initiation, the blasting network adopts a parallel network, and a special initiator is used for initiation. The design scheme of tunnel blasting hole network parameters includes the row spacing and hole spacing of each type of blast hole, which reflects the density of blast hole arrangement, and to a certain extent determines the rock fragmentation size, blasting excavation effect, and excavation contour. The design diagram of the tunnel excavation blasting hole network parameters is shown in Fig. 3. The total number of blast holes arranged on the palm surface is 394, and the blast hole arrangement parameters are detailed in Table 3.

3.2 Establishment of Three-Dimensional Numerical Calculation Model for Tunnel Blasting

To verify the rationality of the tunnel blasting scheme, a three-dimensional blasting numerical model of the upper bench ① of the advance pilot tunnel is established based on the sandstone RHT damage model, as shown in Fig. 4. The model considered the tunnel excavation sequence and bench length. The numerical model has a length of 92.4 m, a width of 40.0 m, and a height of 25.0 m. The parameters of explosives and stemming are set the same as those in Fig. 3. Continuous charging is adopted for cut holes and auxiliary holes, and air-deck charging is adopted for peripheral holes. The charge per hole is 0.4 kg, 1.5 kg and 1.9 kg for peripheral holes, auxiliary holes and cut holes, respectively. The numerical calculation model of explosives and stemming is shown in Fig. 4(c), and the stemming is defined by *MAT_SOIL_AND_FOAM.

(a) surrounding rock model (b) fine modeling of tunnel face

(c) detailed modeling of the charge assembly

Fig. 4. Three-dimensional blasting numerical calculation model of first pilot tunnel upper bench ①. (a) surrounding rock model; (b) fine modeling of tunnel face; (c) detailed modeling of the charge assembly.

The blasting damage contour of the upper bench ① of the advance pilot tunnel is shown in Fig. 5. After the cut holes are detonated first, a certain range of crushed zones are formed around each blast hole, and many rock fractures of varying lengths are generated. Then, the innermost circle of auxiliary holes begins to detonate, and each layer of auxiliary holes detonates layer by layer in the predetermined sequence until the detonation of the outermost circle of auxiliary holes is completed. A certain range of crushed zones are formed around each auxiliary hole, and the rock to be blasted between most adjacent two blast holes generates through fractures under the action of blasting load, and there are also multiple through fractures between each layer of auxiliary holes. Finally, the peripheral holes begin to detonate, the fractures between adjacent two peripheral holes are connected, and the fractures continue to extend and expand under the action of explosive load, and connect with the fractures generated by the outermost circle of auxiliary holes.

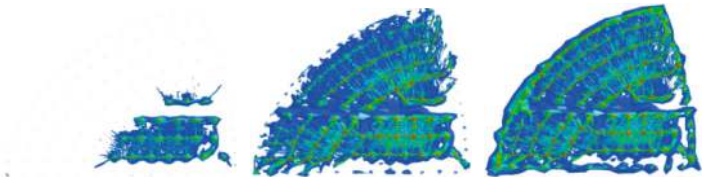

(a) cuthole blasting (b) auxiliary hole blasting (c) periphery hole blasting

Fig. 5. Blasting damage cloud maps of the upper bench of the pilot tunnel.

The blasting effect of the upper bench ① of the advance pilot tunnel is shown in Fig. 6. Overall, a large number of rock fractures gather, connect, and penetrate each other, and the crisscross rock fractures form a large-scale rock fracture network covering the entire upper bench ① of the advance pilot tunnel, ensuring the appropriate fragmentation of the blasted rock. In addition, after the peripheral holes are detonated, the crushed zone is quickly formed around the blast holes, the fractures gradually penetrate all peripheral holes, and finally a relatively smooth excavation contour line is formed with good smooth blasting effect. The numerical simulation results of the excavation blasting of the upper bench of the tunnel advance pilot tunnel verify the rationality of the design of the tunnel blasting hole network parameters.

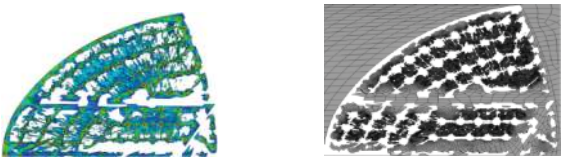

(a) rock crack network (b) Surrounding rock blasting crushing effect

Fig. 6. The advance pilot hole on the bench ① blasting effect.

4 Application of Tunnel Blasting Load

4.1 Application Method

At present, there are mainly four simulation methods for blasting load in numerical calculation:

1. Use the JWL (Jones-Wilkins-Lee) state equation to simulate the explosive detonation process [26].
2. Apply the hole wall pressure to the blast hole wall.
3. Load the measured vibration time history curve at the corresponding position of the numerical model.
4. Reduce the hole wall load and apply it to the model boundary of a larger range, such as the excavation contour surface, crushed zone boundary and et al., which is also called the equivalent load method.

The first two methods have high calculation costs and occupy too many resources, which are not suitable for large-scale numerical models. The third method has high requirements for the accuracy of geological survey and the reproduction accuracy of the numerical model, and is rarely used. Combined with the real engineering situation, the equivalent load method will be adopted as the blasting load loading method in the subsequent numerical simulation analysis.

4.2 Calculation of Equivalent Blasting Load

For the cylindrical charge structure, based on the Chapman-Jouguet model of condensed explosive detonation wave, the peak pressure of the blast hole wall P_0 can be calculated as:

$$P_0 = \frac{\rho_0 V_d^2}{2(\gamma+1)} K_{dr}{}^{-2\gamma} (K_{da})^{-\gamma} n \tag{18}$$

Where ρ_0 is the explosive density, it is 1020 kg/m^3 for peripheral holes, 1240 kg/m^3 for auxiliary holes and cut holes. The explosive detonation velocity (V_d) is 3600 m/s. The adiabatic isentropic exponent γ is 3.0 for emulsion explosives. The blast hole radial decoupling coefficient (K_dr) is 1.6 and 1.25 for peripheral holes and auxiliary holes. The blast hole radial decoupling coefficient (K_da) is 3.0, 1.6 and 1.53 for peripheral holes, auxiliary holes and cut holes respectively. The pressure amplification factor (n) is 10 for emulsion explosives.

When the equivalent load is on the plane determined by the line connecting the centers of the blast holes in the same initiation section and the axis, the equivalent load can be expressed as [17]:

$$P_e = \left(\frac{d_b}{a}\right) P_0 \tag{19}$$

Where: a is the distance between the centers of adjacent blast holes, d_b is the explosive diameter.

To simplify the numerical model, the interval initiation of multiple auxiliary holes in each excavation part of the tunnel is simplified into one initiation section, and the equivalent load on the line connecting the centers of adjacent blast holes in each initiation section is calculated using formulas (18) and (19), as shown in Table 4.

Table 4. Calculation of equivalent blast load.

Blasthole category	Equivalent load (MPa)	Blasthole category	Equivalent load (MPa)
①Cutting holes	88.25	③Perimeter holes	2.17
①Auxiliary holes	73.37	④Auxiliary holes	73.37
①Perimeter holes	2.17	④Perimeter holes	2.17
②Auxiliary holes	73.37	⑤Auxiliary holes	73.37

(*continued*)

Table 4. (*continued*)

Blasthole category	Equivalent load (MPa)	Blasthole category	Equivalent load (MPa)
②Perimeter holes	2.17	⑤Perimeter holes	2.17
③Cutting holes	157.28	⑥Auxiliary holes	73.37
③Auxiliary holes	73.37	⑥Perimeter holes	2.17

When explosives detonate, the stress wave loading curve has distinct loading and unloading characteristics. The triangular loading function is simple and practical, and is widely used in explosion numerical calculation. The expression of the explosion load pressure P_0(t) is:

$$P_0(t) = \left\{ \begin{array}{c} P_0 t/t_r, 0 \le t \le t_r \\ P_0(t_d - t)/(t_d - t_r), t_r \le t \le t_d \\ 0, t > t_d \end{array} \right\} \tag{20}$$

Where t is the initiation time, t_r is the time when the explosion load reaches the maximum value, and t_d is the total duration of the explosion load. The values of t_r = 0.75 ms and t_d = 5 ms was adopted in this paper based on previous research and engineering practice.

5 Analysis of Vibration Effects on Existing Surface Buildings

5.1 Numerical Analysis of Tunnel Blasting Vibration Effects

When the tunnel mileage is K2 + 236, the distance between the right line of the tunnel and Wuyou Temple and its surrounding buildings reaches the minimum value of 39.6 m, and the tunnel burial depth is 39.8 m at this time.

The numerical model is shown in Fig. 7. The model size is consistent with the real engineering. The surrounding and bottom of the model are set with non-reflective boundary conditions except for the ground surface. The numerical model is simplified as follows:

① The shape of Wuyou Temple and its surrounding buildings are simplified into a cuboid with a length of 55 m and a width of 52 m.

② The entire tunnel cross-section is divided into 6 parts for multi-section blasting, and the interval initiation of multiple auxiliary holes in each excavation part is simplified into one-time initiation.

③ The tunnel is excavated by drill-and-blast method using the steel frame and rock wall composite support method, and the designed excavation cross-section is divided into two pilot tunnels (advance and subsequent) and upper and lower benches. During the cyclic blasting excavation of the tunnel, due to the complexity of the numerical model, the bench length is not considered.

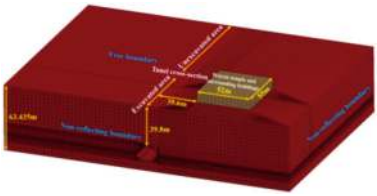

Fig. 7. Three-dimensional numerical model for the cyclic blasting excavation process of the tunnel.

Fig. 8. Numerical model of cyclic blasting excavation of tunnel section.

Only two cyclic blasting excavations are set in the numerical calculation with a blasting excavation footage of 2.4 m. The numerical model is shown in Fig. 8. This tunnel cross-section is located at K2 + 236 ~ K2 + 240.8. The excavation area of section ① (upper bench of the advance pilot tunnel) is about 60.490 m^2, the excavation width is 10.388 m, and the excavation height is 8.354 m. The excavation area of section ② (lower bench of the advance pilot tunnel) is about 19.445 m^2, and the excavation height is 2.832 m. The excavation area of section ③ (upper bench of the subsequent pilot tunnel) is about 76.430 m^2, the excavation width is 10.352 m, and the excavation height is 8.595 m. The excavation area of section ④ (lower bench of the subsequent pilot tunnel) is about 19.445 m^2, and the excavation height is 2.832 m. The excavation area of section ⑤ (rock wall after the removal of the middle partition wall) is about 18.677 m^2, and the excavation height is 2.832 m. The excavation area of section ⑥ (invert) is about 19.059 m^2, the excavation width is 17.833 m, and the excavation height is 1.593 m.

In practical engineering, the peak blasting vibration velocity of monitoring points is used as the standard to measure the blasting vibration effects on existing surface buildings. The layout of monitoring points in the numerical model is shown in Fig. 9.

Fig. 9. Numerical simulation of the location of the monitoring point.

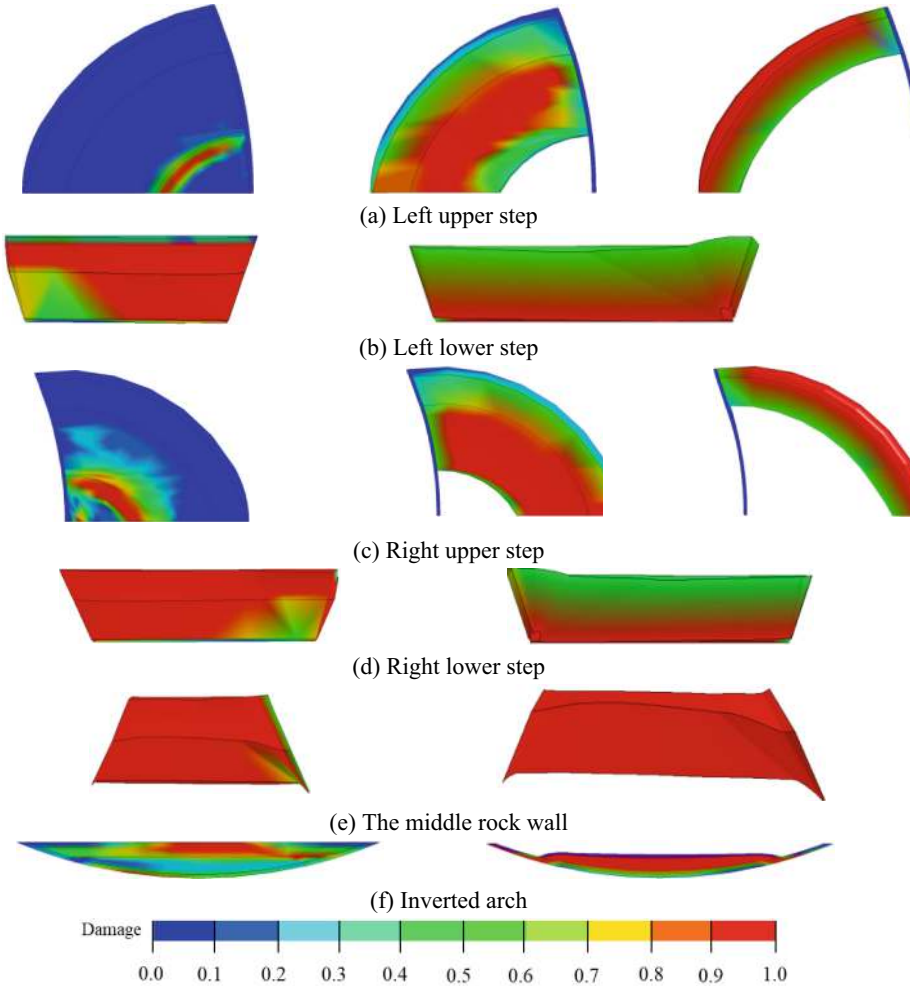

Fig. 10. Rock damage distribution of blasting excavation.

The numerical calculation adopts the restart algorithm to realize the interval initiation of each initiation section in each excavation part. The keywords *DELETE_PART are used to delete the excavated parts, the blasted and broken rock, and the steel frame according to the real excavation sequence to simulate the formation of the blasting cavity. The keyword *STRESS_INITIALIZATION is used to retain the rock damage caused by the previous initiation section. The interval initiation time delay between cut holes, auxiliary holes, and peripheral holes is 10 ms, and the total numerical calculation time is 280 ms. The damage distribution cloud diagram of the first blasting excavation of the tunnel using the steel frame and rock wall composite support method is shown in Fig. 10.

After each initiation section detonates in sequence, the rock damage range quickly expands outward from the equivalent load application surface, causing large-scale damage to the excavated rock ($0.2 < D < 1.0$). No obvious large blasting blocks appear, which is conducive to the mucking and transportation of blasting construction, and ensures the appropriate fragmentation and blasting throwing of the blasted rock. The rock damage distribution of the second blasting excavation is roughly the same as that of the first blasting excavation. The numerical simulation results of tunnel cyclic blasting excavation again verify the feasibility and rationality of the existing tunnel blasting design scheme.

The time history curve of blasting vibration velocity of Wuyou Temple and its surrounding buildings during the blasting excavation of section ① (upper bench of the advance pilot tunnel) of the first blasting excavation is shown in Fig. 11.

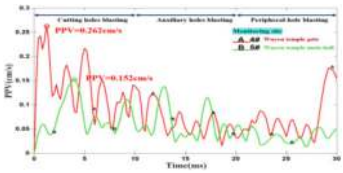

Fig. 11. Time history curve of blasting vibration velocity.

The results of the time history curve of blasting vibration velocity during the blasting excavation of the upper bench of the advance pilot tunnel of the first blasting excavation show that the peak particle velocities (PPV) of monitoring points 4# (Wuyou Temple gate) and 5# (Wuyou Temple main hall) are 0.262 cm/s and 0.152 cm/s, respectively, and the peak particle velocities (PPV) of both monitoring points occur between $0 < t < 10$ ms, that is, it occurs after the detonation of the cut holes in the upper bench of the advance pilot tunnel.

The time history curve of blasting vibration velocity of Wuyou Temple and its surrounding buildings during the blasting excavation of section ① (upper bench of the advance pilot tunnel) of the second blasting excavation is shown in Fig. 12.

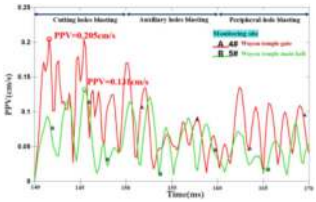

Fig. 12. Time history curve of blasting vibration velocity.

The results show that PPV of monitoring points 4# and 5# are 0.205 cm/s and 0.131 cm/s, respectively, and they both occur between $140 < t < 150$ ms, indicating that it occurs after the detonation of the cut holes in the upper bench of the advance

pilot tunnel. Therefore, the charge amount of cut holes should be controlled as much as possible to avoid excessive harmful blasting vibration effects of tunnel drill-and-blast excavation on existing surface buildings.

5.2 On-Site Real-Time Monitoring

According to the environment around the blasting area, six blasting vibration monitors are placed around the blasting area in sequence. Among them, monitoring points 4# and 5# are set at Wuyou Temple and its surrounding buildings near the blasting area. Monitoring point 4# is located at the gate of Wuyou Temple, and monitoring point 5# is located at the main hall of Wuyou Temple. The schematic diagram of the monitoring point layout is shown in Fig. 13.

Fig. 13. Schematic layout of blast vibration monitoring points.

When placing the sensors, the vertical velocity sensor is kept perpendicular to the horizontal plane, the horizontal tangential velocity sensor is parallel to the horizontal plane, the horizontal radial sensor points horizontally to the explosion center, and the horizontal tangential sensor is perpendicular to the horizontal radial sensor. The sensors are fixed by bonding as shown in Fig. 14.

Fig. 14. Arrangement of blasting vibration sensors.

When the excavation of Lihuashan Tunnel reached K2 + 236, the distance between the tunnel face and Wuyou Temple and its surrounding buildings is the closest. Therefore, the drill-and-blast construction of the left advance pilot tunnel between K2 + 236 ~ K2 + 240.8 is taken as the main research object. The on-site real-time monitoring data of monitoring points 4# and 5# are shown in Table 5.

Table 5. Field-measured blast-induced vibration velocity.

Pile number	Construction position	Monitoring site	On-site monitoring data	
			f(Hz)	Maximum vibration velocity(cm/s)
K2 + 236 ~ K2 + 238.4	Advance pilot tunnel	4#Wuyou temple gate	57.14	0.257
		5#Wuyou temple main hall	31.01	0.116
K2 + 238.4 ~ K2 + 240.8	Advance pilot tunnel	4#Wuyou temple gate	55.56	0.226
		5#Wuyou temple main hall	33.06	0.108

As shown in Table 6, according to the provisions in the Blasting Safety Code (GB6722–2014), during the tunnel drill-and-blast construction, the 'civil buildings' category is used as the reference standard for monitoring point 4# (Wuyou Temple gate), and the 'ancient buildings and historic sites' category is used as the reference standard for monitoring point 5# (Wuyou Temple main hall). Comparing the on-site real-time monitoring results with the allowable safety standards for blasting vibration, it can be seen that the peak blasting vibration velocity of monitoring point 4# does not exceed the allowable safety standard (2.5 ~ 3.0 cm/s), and the peak blasting vibration velocity of monitoring point 5# also does not exceed the allowable safety standard for blasting vibration (0.2 ~ 0.3 cm/s). The on-site real-time monitoring data results show that the existing tunnel blasting design scheme will not cause serious harmful blasting vibration effects on Wuyou Temple and its surrounding buildings.

Table 6. Permissible thresholds for blast-induced vibrations.

Building Category	Maximum particle vibration velocity (cm/s)		
	$f \leq$ **10** Hz	10 Hz $< f \leq$ 50 Hz	$f >$ **50** Hz
Clay kiln houses, adobe houses	0.15 ~ 0.45	0.45 ~ 0.9	0.9 ~ 1.5
Civil buildings	1.5 ~ 2.0	2.0 ~ 2.5	2.5 ~ 3.0
Industrial and commercial buildings	2.5 ~ 3.5	3.5 ~ 4.5	4.2 ~ 5.0
Ancient buildings and monuments	0.1 ~ 0.2	0.2 ~ 0.3	0.3 ~ 0.5

The results of the peak particle blasting vibration velocity between the numerical results and the on-site real-time monitoring is shown in Table 7. The comparison shows that the results of numerical model agree well with the on-site real-time monitoring on the the peak blasting vibration velocity, and the error is controlled within 1.91% ~ 17.11%, which can meet the allowable safety standards for blasting vibration. This further verifies the feasibility and rationality of the existing blasting scheme. The comparison also

shows that the numerical simulation method is feasible and reasonable for predicting the vibration effects of tunnel blasting excavation on existing surface buildings.

Table 7. Comparative analysis of simulated versus field-measured peak blast-induced vibration velocities.

Tunnel cross section	Monitoring site	Numerical simulation (cm/s)	Field test (cm/s)	Criteria (cm/s)
K2 + 236 ~ K2 + 238.4	Wuyou temple gate	0.262	0.257	2.5 ~ 3.0
	Wuyou temple main hall	0.152	0.126	0.2 ~ 0.3
K2 + 238.4 ~ K2 + 240.8	Wuyou temple gate	0.205	0.226	2.0 ~ 2.5
	Wuyou temple main hall	0.131	0.108	0.2 ~ 0.3

6 Conclusions

This paper combines numerical simulation and on-site real-time monitoring to carry out research on the analysis of blasting vibration of existing surface buildings induced by drill-and-blast excavation of large-section highway tunnels. The main conclusions are as follows:

1. Combined with previous research results and based on laboratory test results, the parameters of the sandstone RHT model are calibrated by theoretical research, which provides the basis for the analysis of blasting vibration of existing surface buildings induced by tunnel drill-and-blast excavation.
2. A three-dimensional blasting numerical calculation model of the upper bench of the advance pilot tunnel is established based on the on-site blasting scheme. The crisscross rock fractures form a large-scale rock fracture network covering the entire upper bench of the advance pilot tunnel, a relatively smooth excavation contour line is formed with smooth blasting effect, which ensures the appropriate fragmentation of the blasted rock. The numerical results of the blasting excavation of the upper bench of the tunnel advance pilot tunnel verify the rationality of the design of the tunnel blasting hole network parameters.
3. The numerical results of the vibration effects induced by tunnel excavation on Wuyou Temple and its surrounding buildings show that, the total charge amount of cut holes should be controlled as much as possible to avoid excessive harmful blasting vibration effects. Numerical simulation can provide prediction and control measures for the harmful blasting vibration effects of large-section tunnel drill-and-blast excavation on existing surface buildings. Moreover, it can also verify the feasibility and safety of the blasting design scheme and guide practical engineering.

4. The error of the peak particle blasting vibration between the numerical results and the on-site measured data is controlled within 1.91% ~ 17.11%. The vibration effects generated by the existing tunnel blasting design scheme on Wuyou Temple and its surrounding buildings on the surface can meet the allowable safety standards for blasting vibration. The numerical simulation method is feasible and reasonable for predicting the vibration effects of tunnel drill-and-blast excavation on existing surface buildings, and can provide reference for subsequent construction and similar projects to predict tunnel blasting vibration hazards.

References

1. Mishra, S., Chakraborty, T., Basu, D., et al.: Characterization of sandstone for application in blast analysis of tunnel J. J. Geotech Test J. **43**(2), 351–382 (2020). https://doi.org/10.1520/GTJ20180270
2. Li, X.D., Liu, K.W., Yang, J.C., et al.: Numerical study on the effect of in-situ stress on smoothwall blasting in deep tunnelling. J. Undergr Space. **11**, 96–115 (2023). https://doi.org/10.1016/j.undsp.2022.11.003
3. Hu, Y.G., Lu, W.B., Chen, M., et al.: Comparison of blast-induced damage between presplit and smooth blasting of high rock slope. J. Rock Mech Rock Eng. **47**, 1307–1320 (2014). https://doi.org/10.1007/s00603-013-0475-7
4. Liu, K.W., Li, X.D., Huang L, Q., et al.: Investigation on rock fracturing in presplit blasting under various initial stresses. J. Rock Mech. Rock. Eng. **57**(9), 6927–6950 (2024). https://doi.org/10.1007/s00603-024-03877-8
5. Xie, L.X., Lu, W.B., Zhang Q, B., et al.: Analysis of damage mechanisms and optimization of cut blasting design under high in-situ stresses. J. Tunn Undergr Space Technol. **66**, 19–33 (2017). https://doi.org/10.1016/j.tust.2017.03.009
6. Zhong, Y.P., Li, Z.G., Ma, Z.G., et al.: Research and application of blasting vibration and noise control technology in complex and sensitive urban area. J. Explosive Mater. **53**(2), 50–55 (2024). https://doi.org/10.3969/j.issn.1001-8352.2024.02.008
7. Li, Y.S., Luo, L., Yang, G.M., et al.: Impact of tunnel blasting on the safety of adjacent buildings. J. Eng. Blasting. **28**(1), 123–129 (2022). https://doi.org/10.19931/j.EB.20200144
8. Wang, H.L., Li, Y.H., Zhao, Y.: Propagation law of surface vibration waves by underpass tunnel excavation blasting. J. Eng. Blasting. **28**(3), 39–46 (2022). https://doi.org/10.19931/j.EB.20210082
9. Liu, Y.T.: Numerical simulation and analysis of the influence of blasting vibration in the tunnel crossing under a temple. J. Xi'an Univ. of Arch. & Tech. (Nat. Sci. Ed.). **53**(2), 160–166 (2021). https://doi.org/10.15986/j.1006-7930.2021.02.002
10. Huang, J.S., Qin, T.G., Chen, S.H., et al.: Analysis of blasting vibration of shallow buried tunnel under existing building. J. Blasting. **39**(4), 171–176 (2022). https://doi.org/10.3963/j.issn.1001-487X.2022.04.025
11. Song, Z.P., Zhang, Y.D., Guo, D.S., et al.: Evaluation and optimization method of tunnel blasting scheme for adjacent existing structures J. J. Civ. Environ. Eng. **45**(1), 14–24 (2023). https://doi.org/10.11835/j.issn.2096-6717.2021.189
12. Xu, L., Meng, Y.P., Zhu, J.L., et al.: Numerical simulation and safety analysis of shallow buried medium cross section tunnel blasting in hard rock area. J. Hefei Univ. of Technol. (Nat. Sci.). **42**(3), 422–426 (2019). https://doi.org/10.3969/j.issn.1003-5060.2019.03.020
13. Wang, Y.T.: The study of the broken model for rock mass blasting based on RHT constitutive equations China Univ. of Min. Technol. (Beijing), PhD dissertation (2015).

14. Li, X.D., Liu, K.W., Yang, J.C., et al.: Numerical study on blast-induced fragmentation in deep rock mass J. J. Int J Impact Eng. **170**, 104367 (2022). https://doi.org/10.1016/j.ijimpeng.2022.104367
15. Chi, L.Y., Zhang Z, X., Aalberg, A., et al.: Fracture processes in granite blocks under blast loading. J. Rock Mech Rock Eng. **52**, 853–868 (2019). https://doi.org/10.1007/s00603-018-1620-0
16. Zhang Z, X., Chi, L.Y., Qiao, Y., et al.: Fracture initiation, gas ejection, and strain waves measured on specimen surfaces in model rock blasting. J. Rock Mech Rock Eng. **54**, 647–663 (2021). https://doi.org/10.1007/s00603-020-02300-2
17. Li, X.D., Liu, K.W., Sha, Y.Y., et al.: Numerical investigation on blast-induced rock fragmentation with different stemming structures. J. Geomech Geophys Geo. **9**(1), 112 (2023). https://doi.org/10.1007/s40948-023-00654-9
18. Zhang, X., Lian, Y.P., Yang, P.F., et al.: 3D simulation based on material point method for impact and explosion problems. J. Comput. Aided Eng. **20**(4), 29–37 (2011)
19. Li, H.C.: The study of the rock RHT model and to determine the values of main parameters China Univ. of Min. Technol. (Beijing), PhD Dissertation (2016).
20. Banadaki, M.M.D., Mohanty, B.: Numerical simulation of stress wave induced fractures in rock J. J. Int. J. Impact Eng. **40–41**(2), 16–25 (2012). https://doi.org/10.1016/j.ijimpeng.2011.08.010
21. Peng, J., Rong, G., Wang, X.J., et al.: An empirical model for determination of m in Hoek-Brown failure criterion for intact rocks J. J. Cent. South Univ. (Sci. Technol.). **44**(11), 4617–4623 (2013)
22. Liu, D.Z., Liu, N., Gao, T.C., et al.: Study on the parameter sensitivity of RHT concrete model by orthogonal test technique. J. Trans. Beijing Inst. of Technol. **39**(6), 558–564 (2019). https://doi.org/10.15918/j.tbit1001-0645.2019.06.002
23. Liu, K.W., Li, X.D., Hao, H., et al.: Study on the raising technique using one blast based on the combination of long-hole presplitting and vertical crater retreat multiple-deck shots J. Int. J. Rock Mech. Min. Sci. **113**, 41–58 (2019). https://doi.org/10.1016/j.ijrmms.2018.11.012
24. Ji, L., Zhou, C.B., Lu, S.W., et al.: Numerical studies on the cumulative damage effects and safety criterion of a large cross-section tunnel induced by single and multiple full-scale blasting. J. Rock Mech Rock Eng. **54**(12), 6393–6411 (2021). https://doi.org/10.1007/s00603-021-02630-9
25. Zhou, X.H., Xu, H.T., Lu, W.B.: An equivalent approach for acting blasting load in dynamic finite element simulation of blasting vibration J. Eng. J. Wuhan Univ. **41**(1), 67–72 (2008)
26. Ling, T.L.: Study on blasting damage and cumulative effect of surrounding rock in excavation of Great Wall Station China Univ. of Min. & Technol. (Beijing), PhD Dissertation (2019).

Data Integration Framework for Multi-Disciplinary 2D Drawings and 3D BIM through Adjustable Rendering and Lightweight Data Processing

Qiao Zheng, Xiaoqiang Liu, Minjin Fang, and Rui Jin(✉)

Zhejiang Construction Investment Group Co., Ltd., Hangzhou 310063, China
hzrui@126.com

Abstract. Ensuring delivery quality in building and infrastructure projects requires frequent, cross-disciplinary review of drawings and models during construction. Traditional 2D drawings encode complex information that must be interpreted across multiple sheets (e.g., plans, elevations, and details for a single column), making coordination labor-intensive and error-prone. Building Information Modeling (BIM) offers advantages in visualization and multi-disciplinary integration. This study proposes an automated framework for integrating multi-disciplinary 2D and 3D information that aligns 2D drawings' coordinates with 3D BIM spatial locations via a component-level localization algorithm, enabling lossless fusion of engineering information across dimensions. In addition, an adjustable model rendering module allows users to select appropriate levels of model detail for different devices, ensuring adaptability and efficient visualization performance in multi-device collaboration. To improve computational efficiency, a lightweight data processing module separates geometric from semantic data, retaining only geometry during interactive operations to reduce data volume. The integrated framework restructures multi-disciplinary content into a logically ordered, hierarchical project module that supports downstream project management tasks. The proposed framework establishes a practical and scalable approach for integrating 2D and 3D construction information and provides a foundation for advancing model-based coordination in smart construction environments.

Keywords: BIM · Data Integration · Model rendering · Smart construction · Artificial Intelligence

1 Introduction

Building information modeling (BIM) has become a central digital backbone for the architecture, engineering, and construction (AEC) industry, supporting more data integration, 3D visualization, and information management across project phases [1]. Despite the industry-wide push toward digitalization, the transition from document-centric workflows to model-centric workflows remains incomplete. On most construction sites, however, day-to-day decisions still depend heavily on multi-sheet 2D drawings

© The Author(s), under exclusive license to Springer Nature Switzerland AG 2027
G. Feng et al. (Eds.): ICCE 2025, SUCI, pp. 222–233, 2027.
https://doi.org/10.1007/978-3-032-32237-1_16

for architectural, structural, and mechanical, electrical, and plumbing (MEP) work, even when a federated BIM model exists [2, 3]. This reliance is often driven by contractual obligations where 2D drawings remain the legally binding documents. Consequently, a dual-data environment persists, where the rich semantic data of BIM is disconnected from the operational 2D documents used for construction.

To understand a single component, engineers routinely navigate between plans, elevations, and detail sheets, mentally mapping symbols and annotations to physical locations in the project. This process generates a significant cognitive load, where the user must mentally integrate disparate sources of information. This manual interpretation is time-consuming and prone to miscommunication, particularly when drawings are updated independently of the model or when multiple disciplines overlap within a confined space [4]. The gap between the abstract, symbolic representation of 2D drawings and the photorealistic, geometric representation of 3D models often leads to spatial conflicts being overlooked until construction begins, resulting in costly rework and schedule delays. These practical difficulties highlight the need for tighter operational-level integration between multi-disciplinary 2D drawings and 3D BIM models during construction-stage coordination. Research on BIM-based documentation has examined how model data can be structured to generate 2D deliverables that meet construction information requirements and support reliable communication on site [5]. However, these approaches often function as a one-way street that exports 2D information from 3D BIM without maintaining a live, interactive link. Other work has explored CAD-to-BIM and Scan-to-BIM workflows to reconstruct models from legacy 2D drawings and captured data, emphasizing the effort and inconsistency involved when drawings and models are not semantically aligned at the component level [3]. While valuable for retrofitting existing assets, these reconstruction methods do not solve the real-time coordination challenges of active construction projects where design changes occur frequently.

In parallel, a growing number of studies on web and cloud BIM have proposed frameworks that visualize BIM through WebGL and cloud infrastructures to enable multiuser access and 3D viewing in browsers [6]. Besides, real-time Web3D visualization methods have been developed to visualize multi-disciplinary BIM scenes efficiently by applying a lightweight solution [7]. Mobile and cloud BIM applications further extend model access to tablets and smartphones, combining BIM with location tracking, barcodes, and augmented reality to support field management and quality control [8, 9]. However, the utility of these mobile tools is often hampered by the sheer data size of federated models and the difficulty of correlating a model location with the correct drawing sheet. Recent research on integration between BIM and drawings has started to address consistency checking and positioning between exported drawings and models, but current implementations remain largely semi-automatic and tool-specific [10]. It lacks a universal framework that can seamlessly bridge the semantic and spatial gap between the two mediums across different software platforms.

Despite these advances, existing systems typically address only parts of the broader coordination problem. Model-based documentation workflows focus on generating drawings from BIM but often treat 2D sheets as static outputs that are later used independently in construction [11, 12]. Web and mobile BIM platforms emphasize scalable visualization and access, yet they generally operate on full semantic models, which

increases data volume and can limit responsiveness on resource-constrained devices [13, 14]. Meanwhile, research on BIM-drawing linkage tends to concentrate on geometric consistency checks or overlay visualization rather than robust, scalable mapping between 2D drawing coordinates and 3D components across multiple disciplines [15, 16]. As a result, site engineers still perform much of the 2D-3D interpretation and cross-referencing manually, especially when navigating complex, multi-disciplinary details in real projects.

This paper proposes an integrated data integration framework designed to address these limitations by unifying multi-disciplinary 2D drawings and 3D BIM models for construction-stage coordination. The framework first employs a component-level localization algorithm that aligns 2D drawing coordinates with 3D BIM spatial locations, enabling lossless fusion of engineering information across dimensions and disciplines. Building on this linkage, an adjustable rendering module allows users to select appropriate levels of geometric detail and semantics according to device capabilities and task needs, so that the same integrated model can be viewed efficiently on desktops, tablets, and smartphones. A lightweight data processing pipeline further separates geometric and semantic information and retains only geometry during interactive operations to reduce data volume and improve responsiveness under constrained networks. By restructuring multi-disciplinary content into a logically ordered, hierarchical project model, the proposed framework aims to support clearer issue localization, faster multi-disciplinary review, and reduced interpretation effort in the field. A multi-disciplinary case study demonstrates the feasibility of the approach and illustrates its potential benefits for day-to-day construction management.

2 Methodology

2.1 Proposed Methodology Framework

Figure 1 outlines the proposed methodology framework, which describes the data integration framework that unifies multidisciplinary 2D drawings and 3D BIM models for construction-stage coordination. The framework is implemented as a web-based system that serves interactive models on desktops, tablets, and smartphones, utilizing a client-server architecture designed to handle the heterogeneity of construction data. The system methodology is organized around an overall system architecture and four core modules, each addressing a specific challenge in the integration process.

The first core module is the Component-Level Localization Module. This module serves as the spatial engine of the framework, aligning 2D drawing coordinates with 3D BIM spatial locations. It enables the lossless fusion of engineering information across dimensions by calculating transformation matrices that map projected 2D entities to their 3D counterparts. The second is the Adjustable Model-Rendering Module, which acts as the visualization controller. It allows users to select appropriate levels of model detail for different devices and collaboration scenarios. By dynamically adjusting rendering parameters such as draw calls, texture resolution, and shader complexity, this module ensures adaptability and efficient visualization performance in multi-device collaboration. The third, the Lightweight Data-Processing Module, focuses on transmission efficiency. It separates geometric data from semantic data and retains only geometry

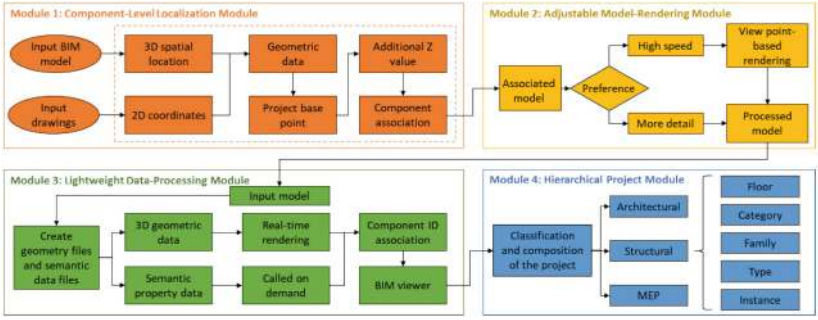

Fig. 1. Proposed methodology framework.

during interactive operations to reduce data volume. This separation allows for the independent optimization of geometry (via mesh compression) and semantics (via database indexing). Finally, building on these modules, the framework constructs a Logically Ordered, Hierarchical Project Module. This module restructures multi-disciplinary components into an ordered information space suitable for downstream project-management tasks, converting flat component lists into navigable trees based on discipline, floor, and category.

The integrated workflow begins with the ingestion of raw BIM files (e.g., IFC or Revit formats) and CAD drawings. These inputs are processed in parallel: the localization module establishes spatial links, while the lightweight module optimizes the data structure. The processed data is then hosted on a cloud server, accessible via the adjustable rendering interface. The following subsections describe the overall architecture and each module in detail, explaining their algorithmic foundations and how they work together to support seamless construction coordination.

2.2 Component-Level Localization Module

The component-level localization module establishes explicit correspondences between 2D drawing coordinates and 3D BIM spatial locations at the component level. This process is critical because 2D drawings and 3D models often originate from different coordinate systems or export settings. The module takes the BIM model and its associated multi-disciplinary drawings as inputs, aiming to create a bidirectional mapping index.

For each project, the BIM author exports a consolidated model together with plan, elevation, section, and detail sheets. The module initiates the process by parsing the 3D model data. It reads the 3D spatial location of each component from the model, including its geometric center point (x, y, z) in the project coordinate system, its bounding box dimensions, and its discipline and level attributes. This data is extracted into a spatial index tree to facilitate rapid range searching. In parallel, it parses the drawing files (typically in vector formats like DWG or PDF) to extract 2D coordinates for graphical entities such as grid intersections, component outlines, and detail symbols. The parser identifies the vector primitives (i.e. lines, polylines, and arcs) and groups them based on layer information to distinguish between annotations and physical component representations.

To align the two spaces, the module identifies reference points that are visible in both the drawings and the model. In typical projects, these reference points are grid intersections or other stable control points. The system employs a semi-automated pattern matching algorithm to pair these points. For instance, grid intersection "A-1" in the architectural plan is matched with the grid intersection "A-1" in the 3D model. Using these matched samples, the module computes a transformation matrix that maps drawing-space coordinates to model-space coordinates.

Mathematically, for plan views, this transformation is modeled as a 2D affine transformation in the project plane. Let $P_{drawing} = (u, v)$ be a point on the 2D sheet and $P_{model} = (x, y)$ be the corresponding point in the 3D model's projected plane. The transformation can be expressed as Eq. (1).

$$\begin{bmatrix} x \\ y \\ 1 \end{bmatrix} = \begin{bmatrix} s \bullet \cos\theta & -s \bullet \sin\theta & t_x \\ s \bullet \sin\theta & s \bullet \cos\theta & t_y \\ 0 & 0 & 1 \end{bmatrix} \begin{bmatrix} u \\ v \\ 1 \end{bmatrix}, \tag{1}$$

where s represents the scale factor, s is the rotation angle, and (t_x, t_y) is the translation vector. The module solves for these parameters using a least-squares estimation based on the selected reference points to minimize alignment error. For vertical sections and elevations, the process is similar but involves a coordinate mapping to a vertical plane defined by the section cut. Additionally, an explicit elevation value in the Z direction is estimated or extracted from the view's metadata to anchor the 2D plane correctly within the 3D volume.

Once the transformation is established, the module associates drawing entities with components by projecting transformed drawing coordinates into the model and searching for components whose bounding boxes contain those points and share the same discipline and level, as shown in Fig. 2(a). The result is a set of component associations that link each component to its representations on multiple sheets. During runtime, these associations enable bidirectional navigation: clicking a component in the 3D view highlights all related regions in the drawings, while selecting a symbol in a drawing immediately locates and highlights the corresponding component in the model, as shown in Fig. 2(b).

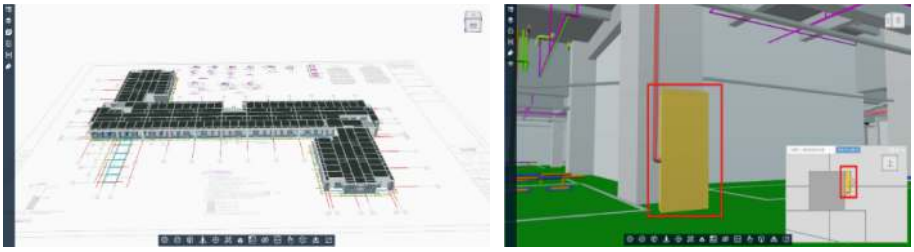

(a) (b)

Fig. 2. (a) Correspondences between 2D drawing coordinates and 3D BIM spatial locations, and (b) bidirectional navigation between BIM and drawings.

2.3 Lightweight Data-Processing Module

The lightweight data-processing module addresses the challenge of transmitting and rendering massive building datasets over the web. It separates geometric data from semantic data and manages how they are stored, compressed, and delivered to clients using a geometry-first strategy.

Starting from the imported BIM model, the module parses the complex IFC or proprietary schema and creates two distinct sets of files. First, it generates 3D geometric data files. These files contain the triangulated meshes (vertices, normals, and indices) required for the graphics processing unit (GPU) to render the shape of each component. To optimize these files, the module employs a geometry instancing technique. For example, there is a project which contains 1,000 identical chairs, the geometry is stored only once, and a lightweight transformation matrix is recorded for each instance position. Second, it generates semantic property data files. These are structured documents (typically in JSON format) that record component identifiers, disciplines, system codes, family and type information, material parameters, and other non-geometric attributes. Crucially, each geometric record is assigned a compact component identifier that also appears in the semantic records. This ensures that geometry and semantics remain logically linked via a common key, even though they are physically stored in separate repositories.

During preprocessing, the module applies configurable compression to the geometric data to further reduce transmission overhead. Mesh simplification algorithms are used to reduce the number of polygons in complex curved surfaces (i.e. pipes or sanitary ware) while maintaining the visual silhouette. The algorithm iteratively collapses edges that contribute least to the object's shape until a target reduction ratio is met. Coordinate quantization is also applied, which converts high-precision 32-bit floating-point vertex coordinates into lower-precision integers (e.g., 16-bit) relative to the component's bounding box. This technique significantly reduces file size while preserving component shape and relative position with sub-millimeter visual accuracy.

Different compression profiles are available so that project teams can choose the level of reduction that matches their device conditions (e.g., "High Speed" for 4G mobile networks vs. "More Detail" for office fiber connections). For each model profile, the module logs the original and compressed sizes of every BIM model together with the resulting reduction ratio. In our implementation validation, nineteen models ranging from small structural units to complex MEP systems were processed. Their compression ratios are summarized in Fig. 3, where the maximum size reduction exceeds 33%, and in some highly repetitive MEP models, the reduction approached 50% without significant visual degradation.

On the storage side, semantic property data are stored in a lightweight, document-oriented database that supports indexed queries by component identifier, discipline, level, or system. This structure allows for rapid retrieval of specific attributes without parsing the entire dataset. During operation, the BIM viewer initially loads only the geometric data stream that is necessary for the current view context. The heavy semantic payload is not loaded during the initial scene construction. Semantic data are called on demand via asynchronous API requests only when users explicitly trigger an action, such as selecting

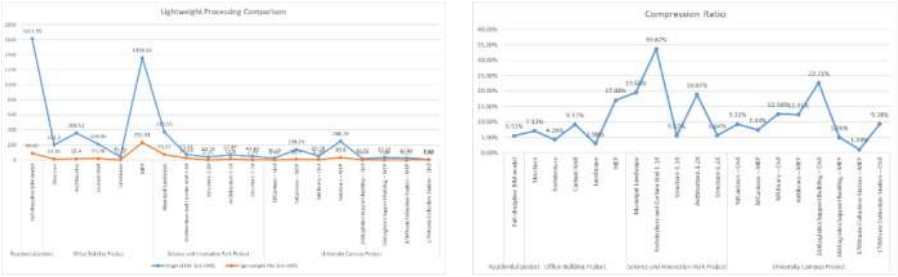

(a) (b)

Fig. 3. (a) Comparison of BIM models before and after lightweight processing, and (b) Compression ratio statistics for nineteen BIM models.

a component to view its parameters, filtering systems by type, or opening property panels. Real-time rendering operates on the binary geometric stream, ensuring high frame rates. Meanwhile, semantic queries travel as small, text-based messages that fetch only the required records for the selected items. By retaining only geometry during most interactive operations (panning, zooming, rotating), the lightweight data-processing module reduces network traffic and memory consumption and maintains acceptable response times in low-bandwidth environments, preventing the browser crashes often associated with loading full BIM datasets.

2.4 Adjustable Model-Rendering Module

The adjustable model-rendering module controls how the integrated model is displayed on different devices and for different coordination tasks, bridging the gap between high-end workstations and field-use mobile devices. It operates on the associated model produced by the component-level localization module and exposes a set of user preferences for rendering speed and visual detail. The module is built upon a WebGL-based graphics engine, which provides a cross-platform rendering context within standard web browsers. When a project is opened, the module first performs a device capability assessment. It reads basic information about the client device, such as the GPU renderer string, available texture memory, and screen resolution. Based on this profile, it automatically chooses a default rendering mode that balances frame rate and visual clarity. For example, a high-end desktop might default to "More Detail," while a smartphone would default to "High Speed." Users may override this automated choice through a simple preference control that offers a High-Speed Mode and a More Detailed Mode, as shown in Fig. 4. Internally, the module manages several prepared levels of geometric detail (LOD) for each component and combines them with viewpoint-based rendering strategies.

In High Speed Mode, the rendering pipeline prioritizes performance. The viewer loads coarse geometry (LOD 100 or 200) where curved surfaces are approximated with fewer polygons. It disables expensive rendering effects such as dynamic shadows, ambient occlusion, and anti-aliasing. Furthermore, it employs aggressive frustum culling (not rendering objects outside the camera's view) and occlusion culling (not rendering objects

hidden behind walls or floors). This mode is suitable for quick navigation, large-scale multi-disciplinary overviews, or situations where the user needs to rapidly traverse the virtual site to locate a general area. In More Detail Mode, the viewer prioritizes visual fidelity. It requests higher-resolution geometry (LOD 300 or 400) for components within the view frustum, particularly those near the current viewpoint. It enables shaders that enhance depth perception, such as defining edges and silhouette lines, which helps engineers distinguish between overlapping pipes or conduits. This mode is better suited for detailed coordination, clash verification, or issue investigation where precise geometric boundaries are required.

The module is designed to support switching between these modes during interaction without reloading the entire model or refreshing the page. This is possible because all levels of detail share the same component identifiers and are tied to the same localization index. The system simply swaps the pointer to the geometry buffer and updates the shader uniforms in the WebGL context. This adjustable rendering behavior allows the same integrated 2D-3D dataset to support a wide spectrum of use cases: from rapid overview on a site manager's smartphone to detailed inspection on a coordinator's desktop and even hybrid use on tablets in the field, as shown in Fig. 5(a), (b), and (c), respectively. This ubiquity ensures that all stakeholders are looking at the same data, regardless of their hardware constraints.

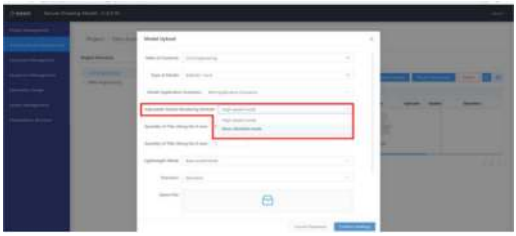

Fig. 4. User interface for selecting high-speed or more-detailed rendering modes in the adjustable model-rendering module.

(a) (b) (c)

Fig. 5. Demonstrations of the multi-device visualization capability on (a) a desktop device, (b) a tablet device, and (c) a mobile phone device.

2.5 Hierarchical Project Module

The hierarchical project module restructures multi-disciplinary components into a logically ordered information space that matches how engineers perceive and manage a project. While the previously described lightweight module focuses on data storage and transmission, this module addresses the cognitive organization of the project data. It processes the semantic property data produced by the lightweight data-processing module to construct a user-friendly navigation framework. By transforming the typically unstructured or flat list of components found in raw BIM files, the module organizes the integrated data into a coherent structure suitable for complex engineering management. The classification logic employs a recursive sorting algorithm that organizes components into a standardized six-level taxonomic depth. Firstly, the system distinguishes components based on their primary discipline, effectively separating architectural, structural, and MEP elements. Secondly, within each discipline, elements are spatially partitioned according to their floor level. Subsequently, the hierarchy performs a granular decomposition into category, family, and type, which groups elements based on their functional definitions and parametric design properties. Finally, the classification resolves to the individual instance level, ensuring that every unique object in the digital model is discretely addressable within the tree structure. This systematic breakdown creates a direct logical path from the macroscopic project view down to specific component instances.

In the BIM viewer interface, this hierarchical model is presented as an interactive navigation panel that allows users to dynamically explore the project scope, as shown in Fig. 6. The structure supports flexible data visualization; users can expand branches to investigate specific details or collapse them to maintain a broader overview. Furthermore, the module facilitates the isolation of specific systems, allowing engineers to visualize, for example, only the fire protection network on a specific floor while suppressing unrelated disciplines. This capability provides immediate context and reduces visual clutter in dense multi-disciplinary models. Crucially, the hierarchical tree maintains a direct digital linkage to the component identifiers, serving as a bridge to both the 3D geometry and the 2D drawing index. When a user selects a node within the hierarchy, the system automatically highlights the corresponding components in the 3D view. Simultaneously, through the integration with the localization module, the system reveals the associated regions on the relevant 2D drawings. By combining this hierarchical classification with component-level localization, the module provides the essential organizing layer that makes the integrated 2D-3D data practical for downstream management tasks, such as multi-disciplinary coordination meetings, issue tracking, and field inspections.

3 Conclusion

This study developed and validated an integrated data integration framework to address the persistent difficulties in coordinating multi-disciplinary 2D drawings and 3D BIM models during construction. The core innovation of the framework lies in its holistic approach to information fusion. It centers on a component-level localization module that aligns 2D drawing coordinates with 3D BIM spatial locations, effectively bridging the legal precision of documentation with the spatial clarity of modeling. This is supported by an adjustable model-rendering module that adapts model detail to heterogeneous

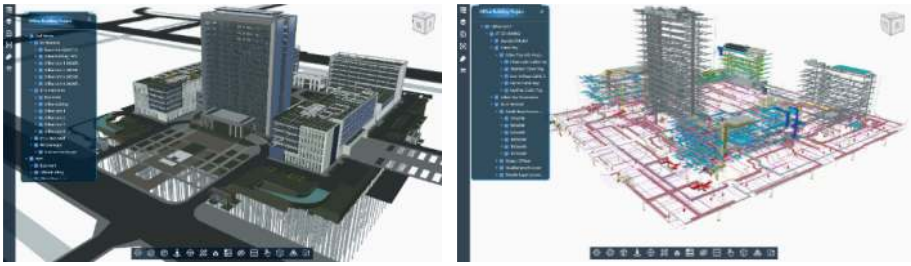

(a) (b)

Fig. 6. (a) Hierarchical project module results for the full multi-disciplinary model, and (b) hierarchical results for the MEP discipline on a single floor.

devices, and a lightweight data-processing module that separates geometric data from semantic data and retains only geometry during interactive operations. Building on these modules, a hierarchical project module restructures multi-disciplinary components into a logically ordered project space organized by discipline, system, and instance. The case-based implementation on a building project with architectural, structural, and MEP disciplines indicated that the proposed approach can support more direct 2D-3D navigation, clearer spatial understanding of issues, and reduced reliance on manual, sheet-based interpretation during construction-stage coordination. By enabling users to click a 2D symbol and immediately see its 3D context, or verify a 3D clash against 2D specifications, the framework significantly lowers the cognitive barrier for site personnel. This ensures that valuable model information is not restricted to BIM managers in the office but is accessible to field engineers and foremen who make critical installation decisions. Furthermore, the lightweight processing strategy proved that complex, federated models could be manipulated on standard mobile devices without performance degradation, solving a key bottleneck in mobile construction management.

Several directions for future work emerge from this research to further enhance the scalability and intelligence of the system. First, regarding automation, the current implementation relies on a semi-automatic workflow for establishing reference points between drawings and models. Further automation of this step is necessary for handling massive infrastructure projects. Future research could leverage computer vision and deep learning techniques to perform automatic pattern recognition of grids, title blocks, and view symbols, thereby achieving fully automated alignment without human intervention. Second, the scope of integration should be expanded. The evaluation was conducted on a single building project, and additional case studies on linear infrastructure assets (such as tunnels and bridges) and projects that follow different drawing standards would help test the robustness and generality of the framework. Third, future research may incorporate quantitative user studies and performance benchmarks. While technical feasibility is proven, measuring the actual impact on workflow efficiency. For instance, time savings in clash resolution, reduction in request for information cycles, and error reduction rates, which would provide compelling evidence for industry adoption. Finally, extending the hierarchical project module to integrate non-geometric data dimensions is a promising

frontier. Integrating schedule (4D) and cost (5D) information into the component hierarchy would transform the viewer from a coordination tool into a comprehensive project management dashboard. This would allow the framework to serve as a foundational digital twin platform, where dynamic construction data is continuously mapped to the static design documents, providing a single source of truth for the entire project lifecycle.

Acknowledgement. This research is supported by Zhejiang Provincial "Pioneer" and "Leading Goose" Science and Technology Plan Project (2026C04040); and Zhejiang Provincial Construction Scientific Research Project (2025 K312).

References

1. Pan, Y., Zhang, L.: Integrating BIM and AI for smart construction management: current status and future directions. J. Arch. Comput. Methods Eng. **30**(2), 1081–1110 (2023). https://doi.org/10.1007/s11831-022-09830-8
2. Kim, Y., Chin, S., Choo, S.: BIM data requirements for 2D deliverables in construction documentation. J. Automat. Constr. **140**, 104340 (2022). https://doi.org/10.1016/j.autcon.2022.104340
3. Barki, H., Fadli, F., Shaat, A., et al.: BIM models generation from 2D CAD drawings and 3D scans: an analysis of challenges and opportunities for AEC practitioners. J. Building Information Modelling (BIM) in Design, Construction and Operations. **149**, 369–380 (2015)
4. Wen, R., Tang, W., Su, Z.: Topology based 2D engineering drawing and 3D model matching for process plant. J. Graph. Models. **92**, 1–15 (2017). https://doi.org/10.1016/j.gmod.2017.06.001
5. Zhang, C., Zou, Y., Dimyadi, J.: A systematic review of automated BIM modelling for existing buildings from 2D documentation In: 38th International Symposium on Automation and Robotics in Construction, ISARC 2021, International Association for Automation and Robotics in construction (IAARC), pp. 220–226. Dubai, United Arab Emirates (2021).
6. Chen, H.M., Hou, C.C., Lin, T.H.: A cloud-based framework for online management of massive BIMs using Hadoop and WebGL 30th International Symposium on Automation and Robotics in Construction and Mining, ISARC 2013, Canadian Institute of Mining, Metallurgy and Petroleum, pp. 179–186. Montreal, QC, Canada, (2013).
7. Liu, X., Xie, N., Tang, K., et al.: Lightweighting for Web3D visualization of large-scale BIM scenes in real-time. J. Graph. Models. **88**, 40–56 (2016). https://doi.org/10.1016/j.gmod.2016.06.001
8. Koseoglu, O., Nurtan-Gunes, E.T.: Mobile BIM implementation and lean interaction on construction site. J. Eng. Constr. Archit. Manag. **25**(10), 1298–1321 (2018). https://doi.org/10.1108/ECAM-08-2017-0188
9. Park, J., Cho, Y.K., Kim, K.: Field construction management application through mobile BIM and location tracking technology 33rd. In: International Symposium on Automation and Robotics in Construction, ISARC 2016, International Association for Automation and Robotics in Construction (IAARC), pp. 83–89, Auburn, AL, United States (2016). https://doi.org/10.22260/isarc2016/0011
10. Zhang, C., Zhu, A.X., Zhou, L., et al.: Constraints for improving information integrity in information conversion from CAD building drawings to BIM model. J. IEEE Access. **8**, 81190–81208 (2020). https://doi.org/10.1109/ACCESS.2020.2991200
11. Zhao, Y., Deng, X., Lai, H.: Reconstructing BIM from 2D structural drawings for existing buildings. J. Automat. Constr. **128**, 103750 (2021). https://doi.org/10.1016/j.autcon.2021.103750

12. Deng, M., Tan, Y., Singh, J., et al.: A BIM-based framework for automated generation of fabrication drawings for façade panels. J. Comput. Ind. **126**, 103395 (2021). https://doi.org/10.1016/j.compind.2021.103395
13. Zheng, Y., Merchant, A., Laninga, J., et al.: Comparison of characteristics of BIM visualization and interactive application based on WebGL and game engine J. Int. Arch. Photogramm. Remote Sens. Spatial Inf. Sci., XLVIII-M-2-2023: 1671–1677 (2023). https://doi.org/10.5194/isprs-archives-XLVIII-M-2-2023-1671-2023
14. Zhou, X., Wang, J., Guo, M., et al.: Cross-platform online visualization system for open BIM based on WebGL. J. Multimed. Tools Appl. **78**(20), 28575–28590 (2019). https://doi.org/10.1007/s11042-018-5820-0
15. Zhao, Q., Shi, H., Zhou, L., et al.: Automated BIM generation for MEP systems from CAD data using multi-drawing graph integration. J. Automat. Constr. **180**, 106542 (2025). https://doi.org/10.1016/j.autcon.2025.106542
16. Lu, Q., Chen, L., Li, S., et al.: Semi-automatic geometric digital twinning for existing buildings based on images and CAD drawings. J. Automat. Constr. **115**, 103183 (2020). https://doi.org/10.1016/j.autcon.2020.103183

Effect of Water Level and Steel Reinforcement on Seismic Performance of High Concrete Arch Dam-Foundation Systems

Xuecong Liu[1], Jinhui Ouyang[1], Dawen Tan[2,3], Chunyao Hou[2,3], and Hui Liang[4(✉)]

[1] China Three Gorges Corporation, Wuhan 430010, China
[2] Three Gorges Jinsha River Chuanyun Hydropower Development Co., Ltd. Yongshan Xiluodu Power Plant, Zhaotong, Yunnan 657300, China
[3] Hubei Key Laboratory of Operation Safety of High Dam and Large Reservoir (China Three Gorges Corporation), Beijing 100048, China
[4] China Institute of Water Resources and Hydropower Research, Beijing 100048, China
lianghui@iwhr.com

Abstract. In this paper, seismic performance of a high arch dam is evaluated considering material non-linearity with a concrete damage model as well as the interaction between the steel reinforcement and the mass concrete with a distributed steel reinforcement model. The radiation damping effect is considered by the viscoelastic artificial boundary. Effects of steel reinforcement on seismic damage of the dam under different water levels are of detailed discussion. Afterwards, a method i.e. seismic overload analysis is adopted to evaluate the ultimate seismic capacity of arch dams and the evaluation criteria i.e. the occurrence of upstream and downstream penetrating cracks of the dam is proposed. Thus, the ultimate seismic capacity of the dam represented by seismic overload factor and effects of water levels and steel reinforcement on that are discussed. Results show that the corresponding OF of the dam reaching the ultimate seismic capacity can be taken as 1.59 i.e. the peak ground acceleration of 0.67 g with and without steel reinforcement. While, it can be taken as 1.35 and 1.25 i.e. the peak ground acceleration of 0.57 g and 0.53 g with and without steel reinforcement under the low water level. The damage of the dam under the low water level is more obvious, and the effect of the steel reinforcement seems to be less efficient compared with that caused by the decrease of water level.

Keywords: Concrete arch dam · Seismic damage analysis · Steel reinforcement · Ultimate seismic · Capacity seismic overload factor

1 Introduction

According to existing cases of high concrete dams subjected from strong earthquakes [1, 2], tensile cracking may appear at dam body and the maximum stress criterion based on linear elastic material model cannot meet seismic safety evaluation of high concrete dams. Thus, except for various contact non-linearity, it is necessary and significant to

© The Author(s), under exclusive license to Springer Nature Switzerland AG 2027
G. Feng et al. (Eds.): ICCE 2025, SUCI, pp. 234–250, 2027.
https://doi.org/10.1007/978-3-032-32237-1_17

consider the material non-linearity of concrete mass to comprehensively reveal seismic performance of high concrete dams, which is indeed an important trend in seismic analysis of high concrete dams in recent years.

In the early studies, material non-linearity of concrete is considered based on classical plasticity theory, continuum damage mechanics and plasticity theory and fracture mechanics [3–5]. With gradual deepening of researches, material constitutive model characterized by the combination of plasticity theory and damage mechanics has been widely used and developed. Pan et al. [6, 7] performs seismic damage cracking analysis of a high arch dam based on plastic-damage model. Effects of two different earthquake input mechanisms i.e. massless foundation model and viscous-spring boundary model on seismic response of an arch dam are of comparative analysis. A new conception to directly establish seismic damage model considering residual deformation based on experimental data is provided [8, 9]. The proposed approach is verified by performing seismic damage analysis of Koyna gravity dam in India and Shapai RCC arch dam in China both subjected to strong earthquakes. It is demonstrated that the proposed model avoids to use commonly plastic damage model which is not suitable for concrete and greatly simplifies calculation process, resulting in more reasonable results. As shown in Reference [10], based on the fracture energy and blunt crack zone model, the cracking strain is proposed as a function of cracking displacement and element length at integral points, which is applied to the damage model to ensure uniqueness of the fracture energy and effectively eliminate effects of element size on the damage analysis of concrete dams. Moreover, seismic damage and failure analysis of a gravity dam and foundation system is performed and the effect of water levels on seismic damage response of a high arch dam is investigated using the damage model [10]. Li Deyu, Guo Shengshan, Chen Houqun, et al. [12] perform a comparative analysis of seismic damage response of gravity dams using an elastic damage model and the damage model considering residual deformation. It is concluded that results with elastic damage model are unsafe.

To prevent further damage and cracking of dams subjected to strong earthquakes, it is necessary to take some engineering measures to improve seismic performance of concrete dams. Reinforcement in potential cracking regions has been adopted to reduce developments of dam cracking by engineers. Yuchuan Long, et al. [13, 14] propose a modified embedded-steel model for evaluating effects of steel reinforcement on decreasing extension and opening of cracks and apply the proposed model on high concrete gravity and arch dams subjected to strong earthquakes. It is noted that few researches have been implemented to discuss effects of steel reinforcement on seismic performance of arch dams. Moreover, owing to great uncertainty of earthquakes, the actual peak ground acceleration (PGA) suffered by a dam may far exceed the corresponding design PGA. The ultimate seismic capacity of concrete dams is also a key issue. Currently, no unified evaluation standard and corresponding evaluation indexes has been recognized. Comprehensive analysis is required from various perspectives to study the ultimate seismic capacity of high arch dams.

Hence, seismic performance of a high arch dam is evaluated considering material non-linearity and the interaction between the steel reinforcement and the mass concrete. Effects of the steel reinforcement on seismic damage of the dam under two different water levels are of detailed discussion. Afterwards, a method for evaluating the ultimate

seismic capacity of arch dams is proposed using seismic overload analysis based on the proposed criteria i.e. the occurrence of upstream and downstream penetrating cracks of the dam. The ultimate seismic capacity is represented by seismic overload factor and effects of water levels and the steel reinforcement on it are discussed.

2 Calculation Model

2.1 Damage Model

For damage simulation of concrete material, in addition to elastic–plastic damage model, there are isotropic elastic damage and anisotropic elastic damage model, these elastic damage models do not consider the influence of residual deformation during the process of loading and unloading. Hence, a concrete damage model [8] considering both residual deformation and stiffness reduction is used to simulate damage cracking of dam concrete. The detailed description can be seen in reference [9].

2.2 Distributed Steel Reinforcement Model

A distributed steel reinforcement model which is easy to implement and can reflect interaction between the steel reinforcement and the mass concrete is adopted to consider the effect of steel reinforcement on preventing damage cracking of the mass concrete. It is assumed that steel reinforcement is evenly distributed in the whole concrete element at a certain angle, and concrete and steel reinforcement are well bonded. Based on the assumption that strain of concrete and steel reinforcement is consistent, the stress–strain relationship of a compound element is obtained.

$$= D = + \tag{1}$$

Where, D is steel reinforcement ratio of a compound element, $= 1 -$; $= +$ is stiffness matrix of a compound element which is consist of stiffness matrix contributed by concrete element and stiffness matrix contributed by steel reinforcement element; is stiffness matrix of concrete element and is stiffness matrix of steel reinforcement element.

Considering that steel reinforcement plays a role in the length direction, can be written as follows.

$$= \begin{bmatrix} x & & & & & \\ & y & & & & \\ & & z & & & \\ & & & 0 & & \\ & & & & 0 & \\ & & & & & 0 \end{bmatrix} \tag{2}$$

Where, 0 is elastic modulus of steel reinforcement;, $_y$ and $_z$ are steel reinforcement ratio of a compound element in three directions.

The relationship between the steel reinforcement and mass concrete is established according to the coordinate information. Steel reinforcement ratio of a compound element can be obtained based on the finite element isoparametric transformation and Newton iteration method.

3 Numerical Modeling of High Arch Dams

3.1 Arch Dam Configuration

A double-curvature high arch dam is selected as a case study. Elevation of the dam crest is 880.5 m, and the maximum dam height is 167.5 m. Bottom thickness of crown cantilever is 44.81 m. Thickness-height ratio is 0.268 and chord-height ratio is about 1.50. A fine finite element model of dam-foundation system is established, shown in Fig. 1 (a) and (b). The dam body is divided into 12 parts along thickness direction with a mesh size of about 2.0 m. Total numbers of nodes and elements of the system are 652042 and 598133 respectively. Total degree of freedom of the system is about 196 million. Numbers of nodes and elements of the dam body is 177905 and 148207. The high arch dam is built as independent cantilever monoliths separated by 15 vertical contraction joints shown in Fig. 1 (c) and (d) shows distribution of steel reinforcement. The steel reinforcement is divided by line element with a mesh size of about 0.1 m. The total numbers of nodes and elements are 2575645 and 2567395 respectively.

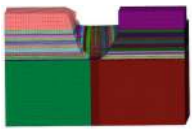

(a) Dam-foundation system

(b) Dam body: upstream surface (left); downstream surface(right)

(c) Contraction joints

(d) Steel reinforcement

Fig. 1. Finite element model of dam-foundation system.

3.2 Material Parameter

The unit weight of dam concrete is 24 KN/m^3, the static elastic modulus is 22 GPa, the Poisson's ratio is 0.167, and the linear expansion coefficient is 8.0 $\times$ 10^{-6}/°C. The static comprehensive deformation modulus of bedrock is shown in Table 1, and the Poisson's ratio is 0.25. Figure 2 shows the damage evolution of dam concrete used in this paper, which is characterized by cracking displacement-stress and cracking displacement-damage index. The fracture energy of concrete is 349 N / m. Rayleigh-type damping is employed with a damping ratio of 5%.

3.3 Loading Conditions

Independent cantilever dead load is considered for seismic damage analysis of the arch dam. The upstream and downstream high-water levels are 876 m and 738 m and the

Table 1. Material properties of foundation rocks (GPa).

Elevation (m)	713.0	720.0	740.0	760.0	780.0	800.0	820.0	840.0	860.0	880.5
Left bank	9.0	9.0	8.0	6.5	6.0	6.5	6.0	6.0	6.0	6.0
Right bank	9.0	9.0	9.0	7.5	8.0	8.0	6.0	6.0	6.0	6.0

(a) Cracking displacement v.s stress (b) Cracking displacement v.s damage

Fig. 2. Damage evolution of dam concrete.

corresponding low water levels are 814 m and 738 m. The sediment depth is 779.5 m. The buoyant unit weight of sediment is 9.0 KN/m^3 and its frictional angle is assumed to be 12°. The sediment pressure is considered as hydro-static pressure and applied on the upstream surface.

The artificial earthquake motions are generated according to site-related design response spectrum and the peak ground motion of the design earthquake is 0.4225 g. The normalized input earthquake motions in three directions i.e. cross-river direction, stream-river direction and vertical direction are shown in Fig. 3. The modified Westergaard added mass model proposed by Chinese code [15] is adopted to model the dynamic interaction between the dam and the reservoir.

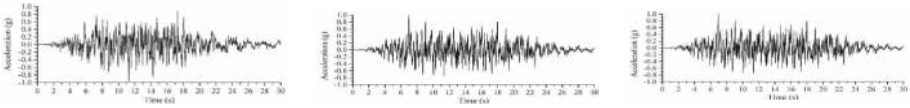

(a) Cross-river (b) Stream-river (c)Vertical

Fig. 3. Normalized input earthquake motions.

4 Results and Discussions

4.1 Results of Seismic Damage Analysis

Seismic damage analysis is performed for four different cases which are shown in Table 2. All the cases are considered to obtain insight into the effects of steel reinforcement and water levels on seismic damage of the dam.

C1 and C2: High Water Level Without and with Steel Reinforcement. Figures 4 and 5 describes damage contours of the arch dam for C1 and C2 under the maximum

Table 2. Case analyzed

Case	Water level	Steel reinforcement
C1	high	without
C2	high	with
C3	low	without
C4	low	with

design earthquake. It can be seen that damage distributions of the dam are basically the same with and without steel reinforcement. Except for the damage located at the dam heel and toe, the dam is basically undamaged and slight damage occurs at the junction of the downstream pier and girder. According to damage contours of the crown cantilever, the macro crack depth at dam heel with damage variable (DV) greater than 0.8 is about 12.07 m without steel reinforcement. While, it decreases to 11.49 m when the steel reinforcement is considered.

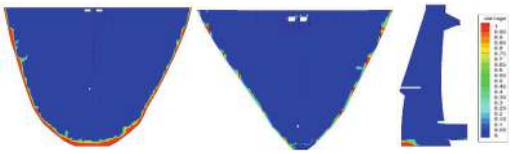

(a) upstream surface (b) downstream surface (c) crown cantilever

Fig. 4. Damage contours of the arch dam for C1.

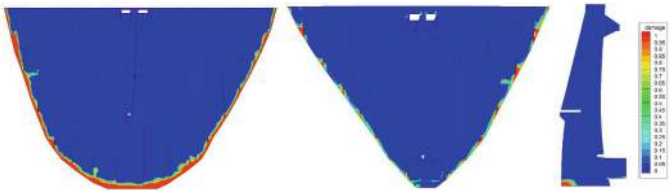

(a) upstream surface (b) downstream surface (c) crown cantilever

Fig. 5. Damage contours of the arch dam for C2.

C3 and C4: Low Water Level Without and with Steel Reinforcement. Figures 6 and 7 describes damage contours of the arch dam for C3 and C4. It can be observed that damage at the junction of the pier and girder reduced significantly when the steel reinforcement is considered. According to damage contours of crown cantilever, damage occurs at downstream elevation of 790.6 m, and the macro crack depth with DV greater

than 0.8 is about 9.55 m without steel reinforcement. While it is about 8.16 m at elevation of 780.4 m with steel reinforcement.

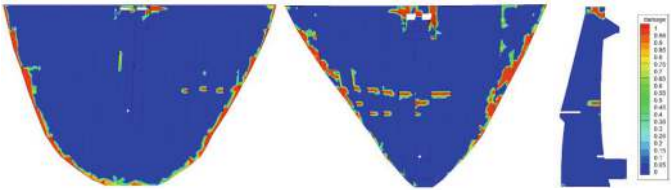

(a) upstream surface (b) downstream surface (c) crown cantilever

Fig. 6. Damage contours of the arch dam for C3.

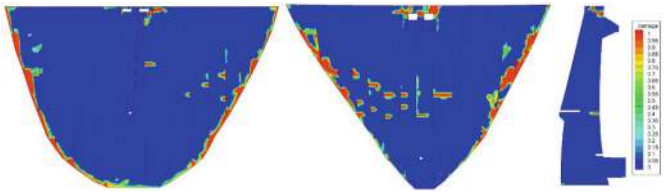

(a) upstream surface (b) downstream surface (c) crown cantilever

Fig. 7. Damage contours of the arch dam for C4.

4.2 Result of Seismic Overload Analysis

The seismic overload analyses are performed to evaluate the ultimate seismic capacity of the arch dam-foundation system for all the cases. In the analyses, seismic load is scaled by multiplying seismic overload factor (OF) which is defined as the ratio of peak ground acceleration and that of maximum design earthquake herein.

C1 and C2: High Water Level Without and with Steel Reinforcement. Damage contours of the arch dam at various overload factors for C1 and C2 are presented in Figs. 8, 9, 10, 11, 12, 13, 14 and 15, respectively. Obviously, the damage of the dam mainly occurs at the middle and upper part of the upstream right abutment and at the downstream middle part. Moreover, it develops and extends gradually with increasing OFs. Detailed description and comparison of damage distributions of the dam at various overload factors are shown in Table 3. The damage volume ratio at various overload factors for C1 and C2 are shown in Fig. 16. Effect of the steel reinforcement on damage distributions and macro crack depths is apparent under different OFs. The macro crack depth with DV greater than 0.8 indeed decreases at the similar position when the steel reinforcement is considered. According to Fig. 16, the difference of the damage volume ratio caused by the steel reinforcement gradually increases with the increasing OFs.

Moreover, penetrating cracks of 13# dam block occur at downstream elevation of 841.0 m with the OF of 1.60 for both C1 and C2. If the occurrence of upstream and downstream penetrating cracks of the dam is taken as the evaluation criteria, the corresponding OF of the dam reaching the ultimate seismic capacity varies from 1.59 to 1.60, which can be taken as 1.59 i.e. the peak ground acceleration of 0.67 g.

Table 3. Damage distributions of the dam at various overload factors for C1 and C2.

	C1		C2	
OF	DV > 0.8, position	macro crack depth with DV > 0.8, position	DV > 0.8, position	macro crack depth with DV > 0.8, position
1.30	upstream surface of 3# dam block and downstream surface of 8# ~ 11# dam blocks	(1) 5.80 m, downstream elevation of 829.85 m; (2) 16.30 m, dam heel.	upstream surface of 3# dam block and downstream surface of 8# ~ 11# dam blocks	(1) 1.70 m, downstream elevation of 830.63 m; (2) 15.10 m, dam heel.
1.50	upstream surface of 3#, 4#, 11# ~ 15# dam block and downstream surface of 3# ~ 11# dam blocks	(1) 14.30 m, downstream elevation of 828.69 m; (2) 19.60 m, dam heel.	upstream surface of 3#, 12# ~ 15# dam block and downstream surface of 3# ~ 11# dam blocks	(1) 13.90 m, downstream elevation of 825.96 m; (2) 1 8.20 m, dam heel.
1.59	upstream surface of 3#, 4#, 11# ~ 15# dam block and downstream surface of 3# ~ 12# dam blocks	(1) 14.20 m, downstream elevation of 825.69 m; (2) 7.60 m, downstream elevation of 799.69 m; (3) 19.90 m, dam heel.	upstream surface of 3#, 12# ~ 15# dam block and downstream surface of 3# ~ 12# dam blocks	(1) 14.30 m, downstream elevation of 822.49 m; (2) 19.20 m, dam heel.
1.60	upstream surface of 3#, 4#, 10# ~ 15# dam block and downstream surface of 3# ~ 13# dam blocks	(1) 13.40 m, downstream elevation of 814.80 m; (2) 19.80 m, dam heel; (3) penetrating cracks, downstream elevation of 841.00 m of 13# dam block.	upstream surface of 3#, 4#, 11# ~ 15# dam block and downstream surface of 4# ~ 13# dam blocks	(1) 13.00 m, downstream elevation of 814.80 m; (2) 18.70 m, dam heel; (3) penetrating cracks, downstream elevation of 841.00 m of 13# dam block.

(a) upstream surface (b) downstream surface (c) crown cantilever

Fig. 8. Damage contours of the arch dam at overload factors of 1.3 for C1.

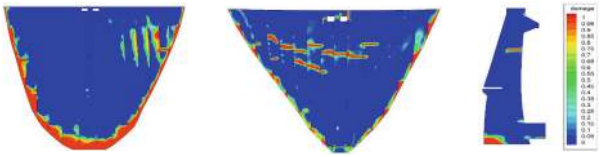

(a) upstream surface (b) downstream surface (c) crown cantilever

Fig. 9. Damage contours of the arch dam at overload factors of 1.5 for C1.

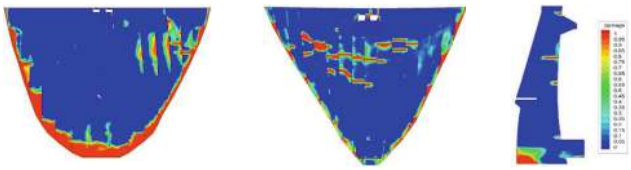

(a) upstream surface (b) downstream surface (c) crown cantilever

Fig. 10. Damage contours of the arch dam at overload factors of 1.59 for C1.

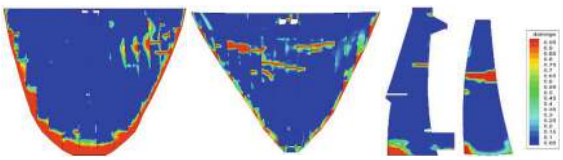

(a) upstream surface (b) downstream surface (c) crown cantilever

Fig. 11. Damage contours of the arch dam at overload factors of 1.60 for C1.

C3 and C4: Low Water Level Without and with Steel Reinforcement. Figures 17, 18, 19, 20, 21, 22, 23 and 24 describe damage contours of the arch dam at various overload factors for Case 2 and C4, respectively. Similar to C1 and C2, damage region of the dam

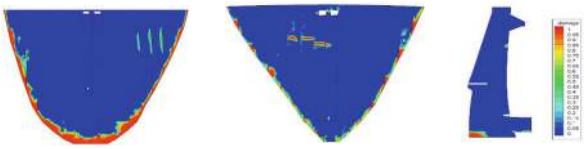

(a) upstream surface (b) downstream surface (c) crown cantilever

Fig. 12. Damage contours of the arch dam at overload factors of 1.3 for C2.

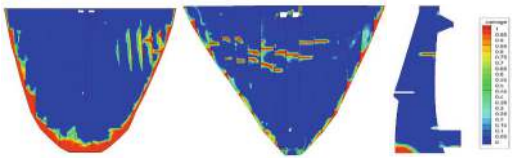

(a) upstream surface (b) downstream surface (c) crown cantilever

Fig. 13. Damage contours of the arch dam at overload factors of 1.5 for C2.

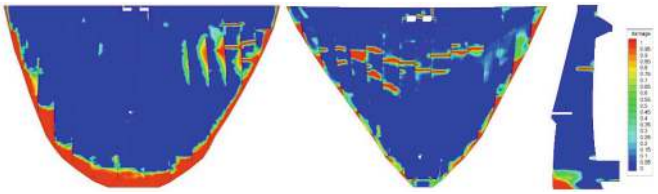

(a) upstream surface (b) downstream surface (c) crown cantilever

Fig. 14. Damage contours of the arch dam at overload factors of 1.59 for C2.

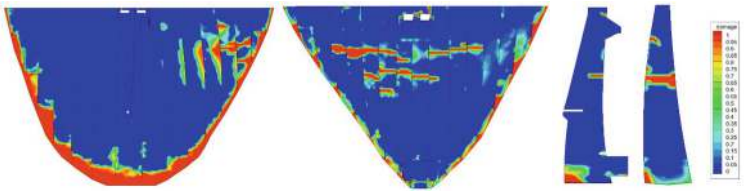

(a) upstream surface (b) downstream surface (c) crown cantilever

Fig. 15. Damage contours of the arch dam at overload factors of 1.60 for C2.

develops and extends gradually with increasing OFs. Moreover, the damage distribution at the junction of pier and girder and the pier root is smaller than that without steel reinforcement. The detailed description and comparison of damage distributions of the dam at various overload factors for C3 and C4 are shown in Table 4. Fig. 25 shows the damage volume ratio at various overload factors for C3 and C4. According to Table 4

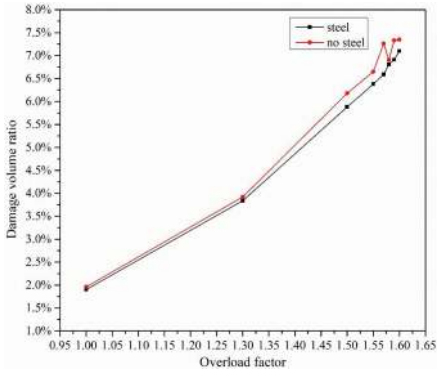

Fig. 16. Damage volume ratio at various overload factors for C1 and C2.

and Figs. 17, 18, 19, 20, 21, 22, 23 and 24, penetrating cracks of 7# dam block occur at downstream elevation of 811.44 m for C3 at OF of 1.30. While, they occur at downstream elevation of 820.57 m of the crown cantilever and 811.44 m of 7# dam block for C4. If the occurrence of upstream and downstream penetrating cracks of the dam is taken as the evaluation criteria, the corresponding OF of the dam considering steel reinforcement reaching the ultimate seismic capacity varies from 1.35 to 1.40, which can be taken as 1.35 i.e. the peak ground acceleration of 0.57 g. While it is 1.25 i.e. 0.53 g without steel reinforcement.

4.3 Discussion of Effects of Water Levels and the Steel Reinforcement

As shown in Figs. 16 and 25, compared with C1 and C2, the damage volume ratios at the same OFs are larger than that with C3 and C4. For example, the damage ratios at OF of 1.0 for C1 and C2 are 1.90% and 1.96%, while they are 3.20% and 3.21% with an increase of about 60%. Compared with C1 and C2, the damage distribution is larger and the extend of the damage is more serious under different OFs for C3 and C4. The corresponding OFs of the dam reaching the ultimate seismic capacity under the high-water level are larger than that under the low water level. In general, it is indicated that the damage of the dam under the low water level is more obvious and the effect of the steel reinforcement seems to be less efficient compared with that caused by the decrease of water level. One of the reasons may be that natural frequencies of the dam increase when the water level decreases leading to a growth of the corresponding design response spectrum. Consequently, the dynamic response of the dam increases and the occurrence of large opening of contraction joints significant increases of the dynamic cantilever stress of upper part of dam body under low water levels. The steel reinforcement could only provide the ability to delay or limit the further development of damage cracking and could not prevent the occurrence of that.

Table 4. Damage distributions of the dam at various overload factors for C3 and C4.

	C3		C4	
OF	DV > 0.8, position	macro crack depth with DV > 0.8, position	DV > 0.8, position	macro crack depth with DV > 0.8, position
1.20	upstream surface of 3#, 7#, 8#, 10# ~ 13# dam block and downstream surface of 1# ~ 14# dam blocks	(1)15.00 m, downstream elevation of 799.00 m; (2) 9.48 m, downstream elevation of 779.00 m.	upstream surface of 3#, 7#, 8#, 10# ~ 13# dam block and downstream surface of 1# ~ 14# dam blocks	(1) 17.00 m, downstream elevation of 800.21 m; (2) 10.05 m, downstream elevation of 780.15 m.
1.25	upstream surface of 2#, 3#, 4#, 6# ~ 14# dam block and downstream surface of 1# ~ 14# dam blocks	(1) 8.05 m, downstream elevation of 827.60 m; (2) 14.37 m, downstream elevation of 806.28 m; (3) 14.11 m, downstream elevation of 779.78 m.	upstream surface of 2#, 3#, 4#, 6#, 7#. 10# ~ 13# dam block and downstream surface of 1# ~ 14# dam blocks	(1) 17.45 m, downstream elevation of 799.54 m; (2) 10.22 m, downstream elevation of 779.78 m.
1.30	upstream surface of 2#, 3#, 4#, 6# ~ 14# dam block and downstream surface of 1# ~ 14# dam blocks	(1) 18.47 m, downstream elevation of 820.57 m; (2) 13.82 m, downstream elevation of 779.78 m; (3) penetrating cracks, downstream elevation of 811.44 m of 7# dam block.	upstream surface of 2#, 3#, 4#, 6# ~ 13# dam block and downstream surface of 1# ~ 14# dam blocks	(1) 14.80 m, downstream elevation of 800.14 m; (2) 15.72 m, downstream elevation of 779.78 m.

(*continued*)

Table 4. (*continued*)

	C3		C4	
OF	DV > 0.8, position	macro crack depth with DV > 0.8, position	DV > 0.8, position	macro crack depth with DV > 0.8, position
1.35	/	/	upstream surface of 2#, 3#, 4#, 6# ~ 14# dam block and downstream surface of 1# ~ 14# dam blocks	(1) 17.77 m, downstream elevation of 820.57 m; (2) 13.94 m, downstream elevation of 779.78 m; (3) 2.08 m, downstream elevation of 772.47 m.
1.40	/	/	upstream surface of 2#, 3#, 4#, 6# ~ 14# dam block and downstream surface of 1# ~ 14# dam blocks	(1) penetrating cracks, downstream elevation of 820.57 m of the crown cantilever; (2) penetrating cracks, downstream elevation of 811.44 m of 7# dam block.

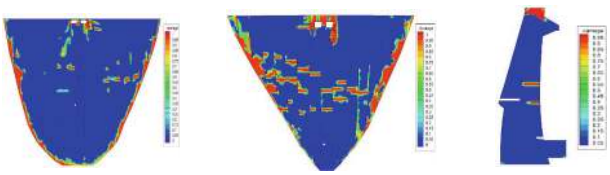

(a) upstream surface (b) downstream surface (c) crown cantilever.

Fig. 17. Damage contours of the arch dam at overload factors of 1.2 for C3.

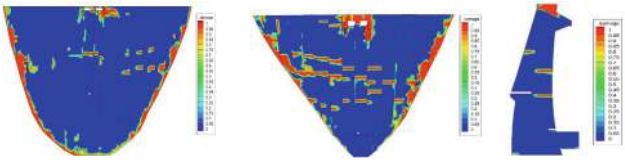

(a) upstream surface (b) downstream surface (c) crown cantilever

Fig. 18. Damage contours of the arch dam at overload factors of 1.25 for C2.

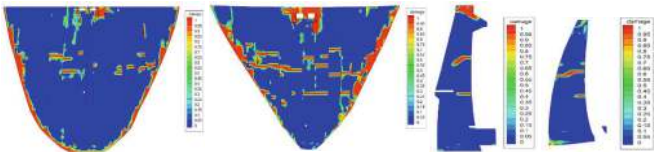

(a) upstream surface (b) downstream surface (c) crown cantilever

Fig. 19. Damage contours of the arch dam at overload factors of 1.3 for C2

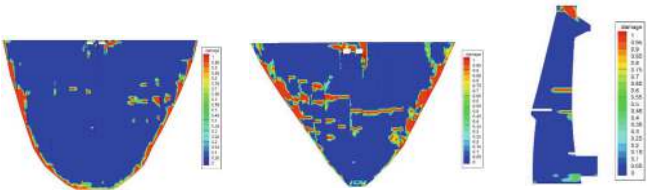

(a) upstream surface (b) downstream surface (c) crown cantilever

Fig. 20. Damage contours of the arch dam at overload factors of 1.2 for C4.

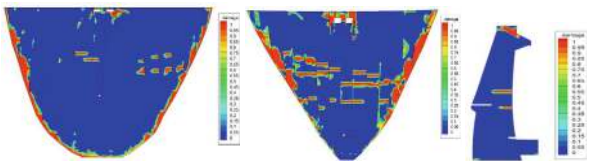

(a) upstream surface (b) downstream surface (c) crown cantilever

Fig. 21. Damage contours of the arch dam at overload factors of 1.25 for C4.

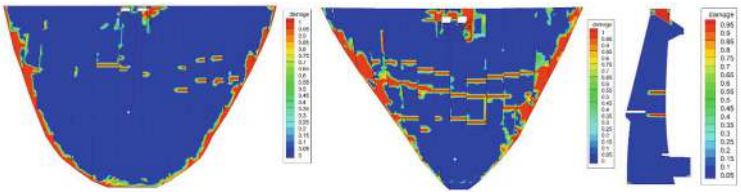

(a) upstream surface (b) downstream surface (c) crown cantilever

Fig. 22. Damage contours of the arch dam at overload factors of 1.3 for C4.

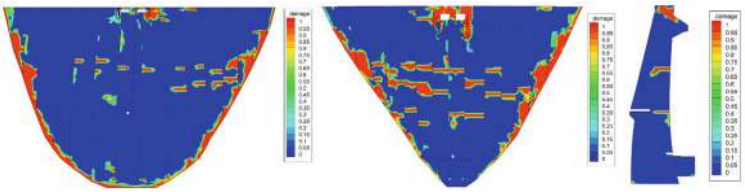

(a) upstream surface (b) downstream surface (c) crown cantilever

Fig. 23. Damage contours of the arch dam at overload factors of 1.35 for C4.

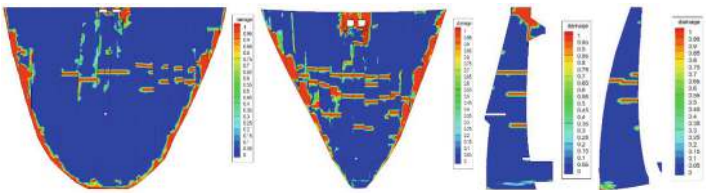

(a) upstream surface (b) downstream surface (c) crown cantilever

Fig. 24. Damage contours of the arch dam at overload factors of 1.4 for C4.

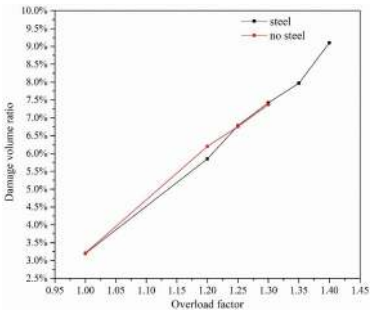

Fig. 25. Damage volume ratio at various overload factors for C3 and C4.

5 Conclusions

Seismic performance of a high arch dam is evaluated considering material non-linearity and the interaction between the steel reinforcement and mass concrete with a comprehensive study. Seismic overload analysis is adopted to evaluate the ultimate seismic capacity of arch dams and the evaluation criteria i.e. the occurrence of upstream and downstream penetrating cracks of the dam is proposed. Effect of water levels and the steel reinforcement on the ultimate seismic capacity are of detailed discussion. The main conclusions are as follows:

1. Damage distributions of the dam are basically the same with and without steel reinforcement since the dam is basically undamaged and slight damage occurs at the junction of the downstream pier and girder under the high-water level and design earthquake, while damage at the junction of the pier and girder reduced significantly under the low water level and design earthquake when the steel reinforcement is considered.
2. Compared with C1 and C2, the damage distribution is larger and the extend of the damage is more serious under different OFs for C3 and C4. The corresponding OFs of the dam reaching the ultimate seismic capacity under the high-water level are larger than that under the low water level. It is indicated that the damage of the dam under the low water level is more obvious and the effect of the steel reinforcement seems to be less efficient compared with that caused by the decrease of water levels. One of the reasons may be that natural frequencies of the dam increase when the water level decreases leading to a growth of the corresponding design response spectrum. Consequently, the dynamic response of the dam increases and the occurrence of large opening of contraction joints significant increases of the dynamic cantilever stress of upper part of dam body under low water levels. The steel reinforcement could only provide the ability to delay or limit the further development of damage cracking and could not prevent the occurrence of that.
3. If the occurrence of upstream and downstream penetrating cracks of the dam is taken as the evaluation criteria, the corresponding OF of the dam reaching the ultimate seismic capacity varies from 1.59 to 1.60 under the high-water level, which can be taken as 1.59 i.e. the peak ground acceleration of 0.67 g. While, the corresponding OF of the dam considering steel reinforcement reaching the ultimate seismic capacity varies from 1.35 to 1.40 under the low water level, which can be taken as 1.35 i.e. the peak ground acceleration of 0.57 g. While it is 1.25 i.e. 0.53 g without considering steel reinforcement.

Acknowledgments. Three Gorges Jinsha River Chuanyun Hydropower Development Co., Ltd. Yongshan Xiluodu Power Plant No. Z412402024.

References

1. Shen, C.K., Chen, H.Q., Zhang, C.H., et al.: Earthquakes induced by reservoir impounding and their effect on the Hsingfengkiang dam. J. Sci. Sin. **17**(2), 239–272 (1974). https://doi.org/10.1360/ya1974-17-2-239

2. Chopra, A.K., Chakrabarti, P.: The earthquake experience at Koyna dam and stresses in concrete gravity dams. J. Earthq. Eng. Struct. Dyn. **1**(2), 151–164 (1972). https://doi.org/10.1002/eqe.4290010204
3. Lubliner, J., Oliver, J., Oller, S., et al.: A plastic-damage model for concrete. J. Int. J. Solids Struct. **25**(3), 299–326 (1989). https://doi.org/10.1016/0020-7683(89)90050-4
4. Lee, J., Fenves, G.L.: A plastic-damage concrete model for earthquake analysis of dams. J. Earthq. Eng. Struct. Dyn. **27**(9), 937–956 (1998). https://doi.org/10.1002/(SICI)1096-9845(199809)27:9<937::AID-EQE764>3.0.CO
5. Ayari, M.L., Saouma, V.E.: A fracture mechanics based seismic analysis of concrete gravity dams using discrete cracks. J. Eng. Fract. Mech. **35**(1), 587–598 (1990). https://doi.org/10.1016/0013-7944(90)90233-7
6. Pan, J.W., Wang, J.T., Zhang, C.H.: Analysis of damage and cracking in arch dams subjected to extremely strong earthquake J. J. Hydraul. Eng. 38(02), 143–149 (2007). (in Chinese) https://doi.org/10.3321/j.issn:0559-9350.2007.02.003
7. Pan, J.W., Zhang, C.H., Wang, J.T., et al.: Seismic damage-cracking analysis of arch dams using different earthquake input mechanisms J. Sci. China Ser. E: Technol. Sci. **52**(2), 518–529 (2009). https://doi.org/10.1007/s11431-008-0303-6
8. Chen, H.Q., Guo, S.S.: Seismic damage analysis of high concrete dam-foundation system J. J. Hydraul. Eng. 43(S1), 2–7 (2012). (in Chinese) https://doi.org/10.13243/j.cnki.slxb.2012.s1.023
9. Chen, H.Q., Li, D.Y., Guo, S.S.: Damage-rupture process of concrete dams under strong earthquakes J. Int. J. Struct. Stab. Dyn. **14**(07), 1450021-1–1450021-21 (2014). https://doi.org/10.1142/S0219455414500217
10. Guo, S.S., Chen, H.Q., Li, D.Y., et al.: Study of element-size effect on dynamic plastic-damage analysis of concrete J J. Hydroelectr. Eng., 30(6), 52–56 (2011). (in Chinese) https://doi.org/10.3354/cr00999
11. Guo, S.S., Chen, H.Q., Li, D.Y., et al.: Seismic damage and failure analysis of gravity dam and foundation system J J. Hydraul. Eng., 44(11), 1352–1358 (2013). (in Chinese) https://doi.org/10.13243/j.cnki.slxb.2013.11.016
12. Li, D.Y., Guo, S.S., Chen, H.Q., et al.: Comparison of elastic damage model and damage model considering residue deformation for seismic damage analysis of gravity dams J J. Hydroelectr. Eng., 32(5), 226–231 (2013). (in Chinese) CNKI:SUN:SFXB.0.2013-05-037
13. Long, Y.C., Zhang, C.H., et al.: Numerical simulation of reinforcement strengthening for high-arch dams to resist strong earthquakes. J. Earthq. Eng. Struct. Dyn. **37**, 1739–1761 (2008). https://doi.org/10.1002/eqe.834
14. Long, Y., Zhang, C., Xu, Y.: Nonlinear seismic analyses of a high gravity dam with and without the presence of reinforcement. J. Eng. Struct. **31**(10), 2486–2494 (2009). https://doi.org/10.1016/j.engstruct.2009.06.004
15. National Energy Administration: Code for seismic design of hydraulic structures of hydropower project NB35047-2015 (2015)

Sympathetic Detonation Characteristics of Bare Cylindrical TNT Charges

Heming Huang[1], Xinjie Wang[1,2(✉)], Ruilong Ma[1], Ziyan Shu[1], and Fenglei Huang[1,2]

[1] State Key Laboratory of Explosion Science and Safety Protection, Beijing Institute of Technology, Beijing 100081, China
wangxinjie@bit.edu.cn

[2] Yangtze Delta Region Academy, Beijing Institute of Technology, Jiaxing 314000, Zhejiang, China

Abstract. During storage, transportation, and operational deployment, warheads are inevitably subjected to various external stimuli. Among these, sympathetic detonation has drawn significant attention due to its complex physical mechanisms and potential for catastrophic outcomes. As one of the most common charge configurations, cylindrical charges hold considerable theoretical and practical value for investigating sympathetic detonation response characteristics. This study investigates the sympathetic detonation behavior of typical TNT cylindrical charges through experimental and numerical simulation. A near-field sympathetic detonation test system was established for bare cylindrical TNT charges. Experiments were conducted to characterize key parameters—including the peak shock wave overpressure acting on the acceptor charge, as well as the perforation patterns and deformation deflections of bottom witness plates—at varying axial spacings. Numerical simulations were performed to examine the influence of structural parameters, particularly the charge aspect ratio, on the reaction behavior and critical sympathetic detonation distance. An engineering predictive model for the critical sympathetic detonation distance of cylindrical charge warheads was derived through parametric fitting, providing support for assessing the safety of such warheads with different structural configurations.

Keywords: Sympathetic detonation · Cylindrical charge · Numerical simulation

1 Introduction

As a core component of weapon system ammunition, the warhead is responsible for the critical mission of directly destroying designated targets and accomplishing combat tasks [1]. In modern military equipment systems, warheads are required to possess not only sufficient destructive power but also reliable safety performance under complex operational conditions. However, throughout their life cycle—including development, production, transportation, storage, and combat deployment—warheads are inevitably exposed to various external threats. These extreme conditions include high-temperature

© The Author(s), under exclusive license to Springer Nature Switzerland AG 2027
G. Feng et al. (Eds.): ICCE 2025, SUCI, pp. 251–265, 2027.
https://doi.org/10.1007/978-3-032-32237-1_18

fire, impact from drops, high-velocity collisions, bullet or fragmentation impact, sympathetic detonation, and shaped charge jet attacks [1, 2]. Such stimuli may induce high-level reactions such as explosion or detonation in energetic materials, potentially leading to severe catastrophic accidents. In response, recent ammunition safety incidents have accelerated the development of ammunition safety testing and evaluation technologies [3, 4].

In the field of sympathetic detonation research, Eichelberger et al. [5] conducted pioneering experiments using bare charges arranged in both parallel and perpendicular configurations. Using ultra-high-speed photography, they captured the propagation trajectory and profile of the shock wave front, as well as the complete process from shock wave entry into the acceptor charge to the establishment and development of a stable detonation wave. Their results indicated that the critical sympathetic detonation distance is significantly influenced by the relative orientation of the charges, primarily due to the dependence of the shock-to-detonation transition distance on the incident angle of the shock wave. In a separate study, Shigeru et al. [6] performed sympathetic detonation tests using Composition B charges of different dimensions. Their findings revealed a notable size effect: under identical loading conditions, smaller acceptor charges that fell below the critical detonation distance exhibited only deflagration, while larger charges underwent full detonation. Li et al. [7] conducted early sympathetic detonation tests on monolithic bare explosives—including TNT, RDX, and PETN—with varying masses. Their experimental setup incorporated piezoelectric crystal sensors, strong-motion seismographs, impact tests, and witness plates to measure parameters such as air blast overpressure, ground vibration, kinetic energy, and detonation timing. The occurrence of sympathetic detonation was determined based on deformation and soot patterns observed on aluminium plates placed beneath the acceptor charge. The results demonstrated a scaling relationship between the safe distance and the mass ratio of the donor to acceptor charges, identifying sustained overpressure from detonation products as the dominant factor in unconfined charge detonation. Wang et al. [8] investigated the sympathetic detonation response of cylindrical bare charges with an aspect ratio of 4. Their study determined the critical sympathetic detonation distance and confirmed that detonation is primarily driven by overpressure from detonation products, with the critical distance being mainly influenced by charge mass and aspect ratio. Wang et al. [9] conducted tests to determine the axial critical sympathetic detonation distance for cylindrical bare charges of Composition B of a specific size. Through experimental analysis, they established both the critical detonation distance and the corresponding axial safety distance.

In the field of numerical simulation research, Lu et al. [10] performed numerical modelling of PBXN-109 bare explosive using the ignition and growth model to represent the explosive behavior, thereby establishing a computational framework for simulating sympathetic detonation. By comparing the detonation wave growth inside acceptor charges at stand-off distances of 40 mm and 60 mm, they demonstrated that the detonation develops markedly faster at the shorter distance. In a related effort, Berzins et al. [11] applied the self-developed hydrodynamics code Uintah to carry out adaptive mesh refinement (AMR) on structured hexahedral grids. Using the Visco-SCRAM constitutive model combined with the WSD chemical kinetics model, they simulated impact induced initiation and sympathetic detonation in small-scale munitions, achieving good agreement

between numerical and experimental results. Harman et al. [12] coupled the material point method (MPM) with hydrodynamics algorithms to simulate interactions involving multiple materials. They executed sympathetic detonation simulations for stacks of hundreds of PBX-9501 munitions, comparing outcomes for varying spatial arrangements and packing fractions. Their simulations successfully replicated chain-detonation reactions, provided temperature and pressure distributions at different locations, and helped optimize storage configurations. Martin et al. [13] enhanced and refined the AMR algorithm within the Uintah platform, enabling the construction of a large-scale sympathetic detonation model comprising hundreds of billions of elements. This advancement laid a technical foundation for high-fidelity, engineering-level simulations of sympathetic detonation.

The sympathetic detonation response of a warhead involves strong multi-physics coupling, extreme load impacts, and a complex initiation mechanism of the acceptor charge. The combined effect of detonation products and air shock waves generated by the donor charge acting on the acceptor charge leads to intricate initiation behavior. At present, the sympathetic detonation response characteristics of ammunition have not been fully elucidated, and there is a lack of systematic understanding regarding the sympathetic detonation behavior of acceptor charges under different charge sizes and axial spacings. Accordingly, methods for determining sympathetic detonation reaction levels and predicting critical distances remain incomplete.

To address these issues, this study investigates the sympathetic detonation response characteristics of typical cylindrical TNT charges through integrated experimental and numerical simulations. A near-field sympathetic detonation test system was developed for cylindrical TNT charges, enabling the acquisition of key parameters—including the peak shock wave overpressure acting on the acceptor charge, as well as the perforation patterns and deformation deflection of the bottom witness plate—under varying axial spacings. Numerical simulations were performed to analyze cylindrical TNT charges with different structural parameters. Based on multi-parameter fitting, an engineering predictive model for the critical sympathetic detonation distance of cylindrical charge warheads was established.

2 Experimental Setup of Sympathetic Detonation

Sympathetic detonation tests were carried out using bare charges of standard dimensions. The experimental setup is depicted in Figs. 1 and 2. Both donor and acceptor charges were composed of Trinitrotoluene (TNT), each measuring Φ50 mm × 100 mm with a mass of approximately 300 g. Ignition was accomplished using a No. 8 electric detonator initiated at the top center, assisted by a JH-14 booster charge measuring Φ25 mm × 12.6 mm. The bottom witness plate was constructed from 45# steel with dimensions of 300 mm × 300 mm × 10 mm. Ground pressure sensors were arranged on both the donor and acceptor sides in two arrays, each comprising three sensors located at distances of 2 m, 4 m, and 6 m from the charges, as illustrated in Fig. 3. A total of five valid tests were conducted using the bisection method to identify the critical sympathetic detonation distance for bare charges. Based on empirical blast wave relationships, the trigger pressure for the ground sensors was set at 0.05 MPa. Axial spacing was defined as the horizontal distance between the central axes of the donor and acceptor charges.

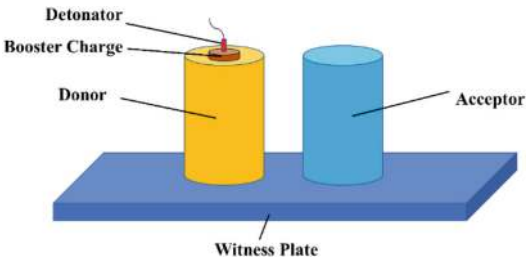

Fig. 1. Schematic diagram of bare TNT charge sympathetic detonation test setup.

Fig. 2. Photograph of bare TNT charge sympathetic detonation test arrangement.

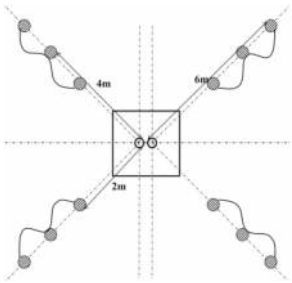

Fig. 3. Field view of bare TNT charge sympathetic detonation test.

3 Numerical Model of Sympathetic Detonation

3.1 Computational Models

To investigate the sympathetic detonation response characteristics of cylindrical bare charges and determine the critical detonation distance, numerical simulations were carried out using the multi-material Arbitrary Lagrangian–Eulerian (ALE) algorithm in the explicit dynamics code LS-DYNA R12.1. A numerical model was constructed according to the experimental configuration, as illustrated in Fig. 4. The geometry and placement of the charges and witness plates matched the experimental setup. To enhance computational efficiency, a half-symmetry model was employed, with symmetry constraints enforced using the *CONSTRAINED_GLOBAL keyword. Monitoring points

were arranged in both horizontal and vertical directions within the air region between the donor and acceptor charges. Each direction contained five equally spaced points: the horizontal set aligned perpendicular to the charge surface, and the vertical set parallel to it. The positions of the vertical monitoring points, which were equidistantly distributed along the midline between the donor and acceptor charges, are shown in Fig. 4.

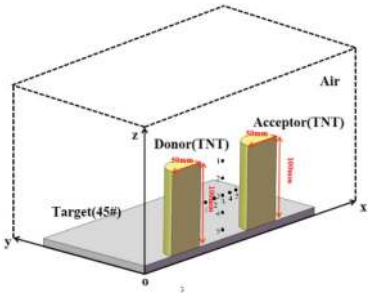

Fig. 4. Computational model of bare TNT charge sympathetic detonation.

3.2 Material Models and Parameters

The explosive charge was modelled using the MAT_HIGH-EXPLOSIVE-BURN model and the Jones-Wilkins-Lee (JWL) equation of state, EOS_JWL. The density ρ, Chapman-Jouguet pressure, P_{CJ}, and detonation velocity, D_{CJ}, are defined in the material model. The pressure, relative volume, energy relation of the charge is given as:

$$P = A\left(1 - \frac{\omega}{R_1 V}\right)e^{-R_1 V} + B\left(1 - \frac{\omega}{R_2 V}\right)e^{-R_2 V} + \frac{\omega E}{V} \tag{1}$$

Where p represents the pressure, A, B, R_1, R_2 and ω are constants, V is the relative volume and E is the internal energy per unit volume. The parameters for TNT are shown in Table 1.

The air was modelled using the MAT_NULL constitutive model and EOS_LINEAR_POLYNOMIAL. The pressure, relative density, energy relation of the air is given as:

$$p = A_0 + A_1\mu + A_2\mu^2 + A_3\mu^3 + \left(A_4 + A_5\mu + A_6\mu^2\right)E \tag{2}$$

Where, $A_0 \sim A_6$ are constants, $\mu = \rho/\rho_0 - 1$, ρ and ρ_0 is the current density and initial density. The constants $A_4 = A_5 = \gamma - 1$, where $\gamma = 1.4$ is the ratio of specific heats for air. The initial density $\rho_0 = 1.225$ g/cm^3, the specific internal energy $E_0 = 253.4$ kPa for the air at 288 K, and is given to set the atmospheric pressure to 101.36 kPa.

Chemical reaction rate models are typically employed to describe the ignition, combustion, and detonation behavior of explosives under shock loading. The Lee-Tarver model can effectively characterize the shock initiation process of explosives under both

long and short pulse durations, and has been embedded in LS-DYNA with widespread application. The Lee-Tarver ignition and growth reaction rate model is expressed as:

$$d\lambda/dt = I(1-\lambda)^b(\rho/\rho_0 - 1 - \alpha)^x + G_1(1-\lambda)^c\lambda^d p^y + G_2(1-\lambda)^e\lambda^g p^z \; 0 \le \lambda \le F_{igmax} \; 0 \le \lambda \le F_{G_1\max} \; F_{G_2\min} \tag{3}$$

Where λ represents the reaction degree, t denotes time, ρ is the current density, ρ_0 is the initial density, and I, G_1, G_2, a, b, c, d, e, g, x, y, and z are material constants. F_{igmax}, F_{G1max}, and F_{G2min} represent the activation thresholds for each term. The first term on the right side of Equation (3.3) describes the formation and growth of hot spots during the ignition phase under shock compression. The second term represents the slow combustion stage after hot spots consume the shock energy of the surrounding material. The third term corresponds to the rapid reaction phase following hot spot coalescence, i.e., the deflagration-to-detonation transition process. The acceptor charge in this study uses TNT, with Lee-Tarver model parameters and explosive JWL parameters provided in Tables 1 and 2.

Table 1. Ignition and growth model parameters for TNT [14].

I(μs^{-1})	G_1(GPa^{-2} μs^{-1})	G_2(GPa^{-2} μs^{-1})	a	b	c	d	e
20000	0.0285	0.00032	0.0819	0.667	0.667	0.667	0.333
x	y	z	g	F_{igmax}	F_{G1max}	F_{G2min}	
4.0	2.0	3.0	1.0	0.02	0.5	0.5	

Table 2. JWL Equation of State Parameters for TNT [15].

ρ(g/cm^3)	D(m/s)	PCJ(GPa)	A(GPa)	B(GPa)
1.63	6900	21	371.2	3.21
R1	R2	ω	E0(GPa)	
4.15	0.95	0.3	7.0	

To describe the dynamic response and damage evolution of metals under high pressure, the classical JOHNSON_COOK [15] constitutive model was employed to characterize its stress-strain relationship, expressed as:

$$\sigma_y = \left[A + B\left(\bar{\varepsilon}^p\right)^n\right]\left(1 + C\ln\dot{\varepsilon}^*\right)\left[1 - \left(T^*\right)^m\right] \tag{4}$$

$$\bar{\varepsilon} = \frac{\varepsilon^p}{\varepsilon_0}, T^* = \frac{T - T_r}{T_m - T_m} \tag{5}$$

Where A, B, C, n, and m are material constants. The yield stress is expressed as a function of the equivalent plastic strain, equivalent plastic strain rate, and relative temperature. $\dot{\varepsilon}^*$denotes the equivalent plastic strain rate, T^*denotes the relative temperature, where T_r and T_m represent room temperature and the material's melting temperature, respectively. The relevant parameters are consistent with the study by Chen et al. [16].

4 Results and Discussion

4.1 Experimental Results of Sympathetic Detonation

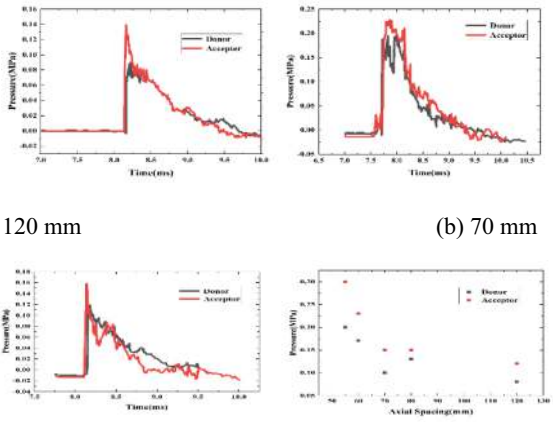

(a) 120 mm (b) 70 mm

(c) 60 mm (d) Comparison of Peak Pressure at 2 m

Fig. 5. Overpressure histories of sympathetic detonation measured at 2 m for cylindrical bare TNT charges under different axial spacings.

Shock Wave Overpressure. Figure 5 presents the overpressure histories of sympathetic detonation measured at 2 m for cylindrical bare charges under different axial spacings. When the axial spacing was 60 mm, the ground-reflected peak overpressure at the acceptor charge reached 0.23 MPa, which decreased to 0.12 MPa at a spacing of 120 mm, demonstrating a progressive decline in the intensity of the sympathetic detonation response as axial distance increases. Further analysis indicates that for axial spacings below 70 mm, the peak overpressure on the acceptor side consistently surpassed that on the donor side at the 2 m position, with a stable ratio of approximately 1.5.

At a distance of 2 m from the blast center, significant differences in peak overpressure were observed between the donor and acceptor charges under varying spacings, as illustrated in Fig. 5(d). At an axial spacing of 120 mm, the peak overpressures recorded at the donor and acceptor charges were 0.08 MPa and 0.12 MPa, respectively. When the spacing was reduced to 70 mm, the overpressure increased by 150%, and a further reduction to 60 mm resulted in a 200% increase. These results indicate that when the axial spacing falls below 60 mm, the reaction of the acceptor charge intensifies significantly, accompanied by a marked strengthening of the shock wave pressure.

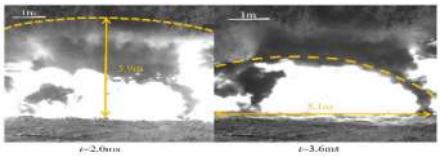

(a) 120 mm

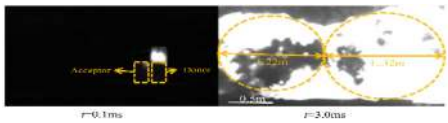

(b) 70 mm

(c) 60 mm

Fig. 6. High-speed photographic sequences of sympathetic detonation.

High-Speed Photography Images. High-speed photography was used to analyze the sympathetic detonation response process of bare charges. Representative temporal results are shown in Fig. 6. At axial spacings of 60 mm and 70 mm, a luminous flame was observed at the acceptor charge 0.1 ms after initiation, indicating a partial reaction of the charge. When the axial spacing was increased to 120 mm, no luminous flame appeared at the acceptor charge within 3.6 ms. Subsequent observations showed slow secondary combustion of residual explosive following charge fragmentation (Fig. 6a).

Further analysis of the explosion fireball evolution during sympathetic detonation showed that at a 70 mm spacing, a weak luminous flame appeared at the upper-right section (facing the donor charge) of the acceptor charge 0.1 ms after high-speed camera triggering. The maximum fireball diameter measured 1.22 m, considerably smaller than the 1.32 m diameter observed on the donor charge side, and the expansion progressed gradually (Fig. 6b). When the axial spacing was decreased to 60 mm, the acceptor charge's fireball size matched that of the donor charge (about 40 cm) at 1.5 ms. It then underwent rapid expansion, exceeding the donor charge's fireball at 2.4 ms and reaching 53 cm by 5.5 ms (Fig. 6c), indicating a swift size reversal and continued growth.

Deformation and Perforation of Bottom Witness Plate. By integrating the deformation and damage characteristics of the witness plate, the sympathetic detonation response was further examined. Figure 7 illustrates the deformation damage of the bottom witness plate under different axial spacings. Circular perforations with diameters ranging from 40 to 65 mm were observed at the donor charge position, and the perforation diameter enlarged as the axial spacing decreased. Notable differences in deformation damage were identified at the acceptor charge position.

Comparison of the maximum deflection of the bottom witness plate under different axial spacings shows that both maximum and average deflections increase as the axial spacing decreases. At a spacing of 120 mm, no deformation was observed at the acceptor

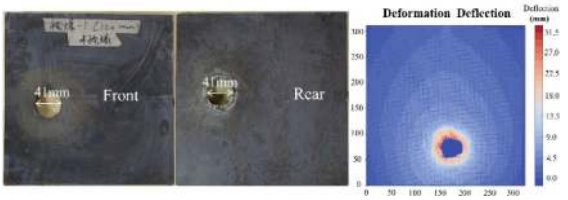

(a) Deformation deflection of witness plate at 120 mm

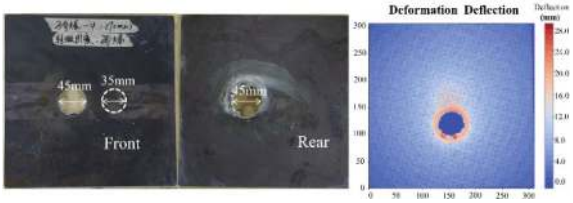

(b) Deformation deflection of witness plate at 60 mm

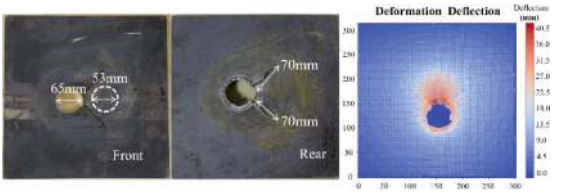

(c) Deformation deflection of witness plate at 60 mm

Fig. 7. Witness plate deformation distribution contour under different axial spacings.

charge position. When the spacing was reduced to 70 mm, a dent approximately 35 mm in diameter with a maximum deflection of about 25 mm appeared at the acceptor location. At 60 mm spacing, a crack roughly 70 mm long formed at the acceptor position on the witness plate, and the maximum deflection reached approximately 32 mm.

4.2 Numerical Results of Sympathetic Detonation

Numerical Model Validation. The response of an acceptor charge under blast wave loading involve complex physical processes. To analyze the evolution of sympathetic detonation and identify the critical initiation distance, the spatiotemporal evolution of the reaction degree distribution was extracted from the internal longitudinal cross-section of the charge under different axial spacings, as shown in Fig. 8.

At a 60 mm axial spacing, detonation occurred in the acceptor charge. A chemical reaction initiated on the donor-side at 9 μs with a reaction degree of 0.25–0.30. By 21 μs, the region exhibiting a reaction degree exceeding 0.40 had expanded to the upper one-third of the charge. Between 23 μs and 31 μs, the reaction propagated rightward at 1.2 mm/μs. At 35 μs, the global reaction degree reached 0.98–1.00, completing the process within 26 μs. At a 70 mm spacing, reaction began in the lower-left corner at 23 μs (reaction degree: 0.20). The maximum reaction degree of 0.50 was attained by 41 μs, but the reaction zone remained confined to the charge bottom, failing to form a continuous

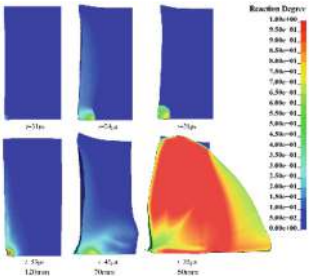

Fig. 8. Reaction degree contours under different axial spacings.

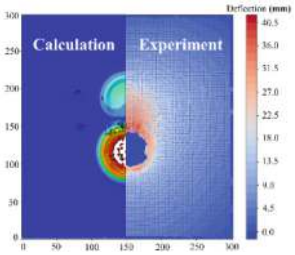

(a) Deformation contour at 60 mm axial spacing

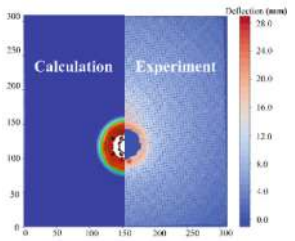

(b) Deformation contour at 70 mm axial spacing

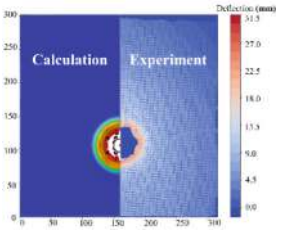

(c) Deformation contour at 120 mm axial spacing

Fig. 9. Comparison of deformation distribution of bottom witness plate under different axial spacings.

detonation wave and resulting in low overall reactivity. For the 120 mm spacing, shock wave attenuation caused a sharp pressure decrease with only 6 μs duration (23–29 μs). Consequently, only localized reaction occurred in the lower-left corner with a maximum reaction degree of 0.03, indicating minimal reaction overall.

Figure 9 compares the numerical and experimental deformation contours of the bottom witness plate at axial spacings of 60 mm, 70 mm, and 120 mm. Under all three conditions, the simulated perforation sizes at the donor charge location were consistent, each measuring 50 mm, and the surrounding deformation distribution was also well reproduced. For the acceptor charge, the Lagrangian-based simulations exhibited good agreement with experimental results at 70 mm and 120 mm spacings.

Sympathetic Detonation Response with Different Aspect Ratios. For bare charges, the shock wave generated by the donor charge explosion propagates through the air and, after attenuation, acts on the acceptor charge, leading to its initiation. The air shock wave serves as the primary factor responsible for initiating the acceptor charge. Structural parameters of the charge, particularly the aspect ratio, significantly affect the shock wave propagation path and energy distribution, thereby playing a critical role in the sympathetic detonation response of the acceptor charge. To analyze the evolution characteristics of sympathetic detonation in bare acceptor charges, the spatiotemporal evolution of the pressure distribution contours and the corresponding reaction degree distribution in the internal longitudinal cross-section were extracted for acceptor charges with different aspect ratios at an axial spacing of 1.4 times the charge diameter, as shown in Figs. 10 and 11.

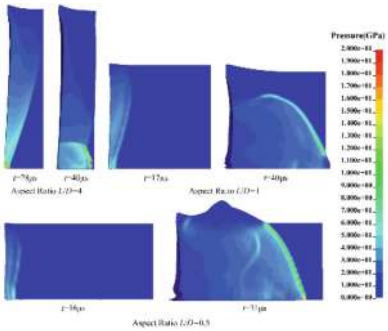

Fig. 10. Pressure contour of acceptor charge with different aspect ratios.

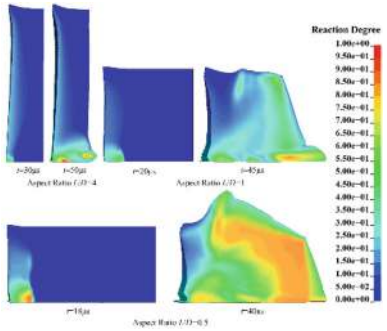

Fig. 11. Reaction degree contour of acceptor charge with different aspect ratios.

When the aspect ratio was 4, the shock wave reached the lower-left end of the acceptor charge at 30 μs, exhibiting the characteristic triple-wave structure of Mach reflection. By 40 μs, the shock front had propagated rightward, with its leading-edge pressure reaching 5 GPa, indicating the onset of reaction in the charge. Subsequently, a rarefaction wave began to spread toward the lower-left region, and after 55 μs, the pressure dropped below 1 GPa, demonstrating insufficient shock energy to sustain the reaction in the acceptor charge. Comparison with Fig. 10 confirms that while the pressure was concentrated at the bottom of the acceptor charge for an aspect ratio of 4, its magnitude was significantly lower than in other cases.

At an aspect ratio of 1, a high-pressure region (>2 GPa) developed in the upper-left quadrant of the charge at 17 μs, then expanded rightward during 20–40 μs while gradually propagating upward through the entire charge. However, by 45 μs, the internal pressure had decayed below 1 GPa due to lateral rarefaction waves, indicating that although the charge reacted, it failed to establish stable detonation. For an aspect ratio of 0.5, the shock wave reached the bottom of the charge at 16 μs and propagated rightward, attaining a peak pressure of 10 GPa at 31 μs before beginning to decay. These observations suggest a relatively intense reaction occurred within the charge, but without formation of a stable detonation wave.

Under an aspect ratio of 4, the overall reaction degree of the acceptor charge remained relatively low. As illustrated in Fig. 11, at 40 μs, the primary reaction zone was concentrated in the lower-left portion of the charge, with a reaction degree of 0.12, and expanded progressively rightward. By 41 μs, the maximum reaction degree of 0.25 was attained; however, the reactive zone remained confined to the bottom region of the acceptor charge, preventing the formation of a continuous reaction wave front. The central and upper sections of the charge exhibited negligible reaction, resulting in a low global reaction degree.

At an aspect ratio of 1, a localized reaction zone began to develop in the acceptor charge after 20 μs. Initiation originated at the lower-left end, with a reaction degree growth rate markedly higher and propagation speed notably faster than observed at an aspect ratio of 4. By 45 μs, a continuous reaction wave front had formed and propagated throughout the entire charge. Local reaction degrees exceeded 0.4, indicating a relatively intense reaction under this condition. For an aspect ratio of 0.5, a localized reaction zone formed at the front end of the acceptor charge by 20 μs, with the reaction degree rising to 0.4, confirming chemical reaction initiation. By 40 μs, the reaction zone expanded rapidly toward the right, occupying most of the charge volume. The overall reaction degree reached approximately 0.4, reflecting the highest response intensity among all aspect ratios tested. Although stable detonation was not achieved, the reaction vigor was the most pronounced across the tested configurations.

Figure 12(a) presents the pressure recorded at five longitudinal monitoring points during sympathetic detonation of bare charges under different aspect ratios. The figure indicates that during the initial stage of donor charge detonation, the shock wave pressure in air was relatively low, yielding peak pressures of 2.5 GPa and 3 GPa at points 1 and 2, respectively. As the donor charge transitioned to stable detonation, the peak shock wave pressures at points 4 and 5 increased significantly, reaching 5 GPa and 5.5 GPa, respectively.

Figure 12(b) presents the pressure measured at five transverse monitoring points. The figure indicates that after donor charge detonation, the peak pressures decrease sequentially from point 1 to point 5. As the aspect ratio decreases, the peak pressures at all observation points increase. For point 1, as the aspect ratio decreases from 4 to 0.5, the peak overpressures are 18 GPa, 20 GPa, 25 GPa, and 29 GPa, respectively. For point 5, the values are 2.5 GPa, 3 GPa, 4 GPa, and 5 GPa, respectively. The peak pressure at point 1 for an aspect ratio of 0.5 is 1.5 times that for an aspect ratio of 4, while at point 5, it is twice as high. These results demonstrate that shock wave pressure attenuation with distance is significantly reduced as the aspect ratio decreases.

Comparison of pressure distributions from donor charges with four different aspect ratios reveals that a larger aspect ratio produces relatively uniform radial distribution of transverse shock wave pressure after detonation. As the aspect ratio decreases, the transverse shock wave pressure becomes increasingly concentrated toward the bottom region, with the wavefront morphology transitioning from flat to convex, while the distance attenuation of peak shock pressure progressively weakens. Consequently, smaller aspect ratios enable the shock wave generated by donor charge detonation to achieve the initiation pressure threshold of acceptor charges at considerably longer distances, resulting in an extended critical sympathetic detonation distance.

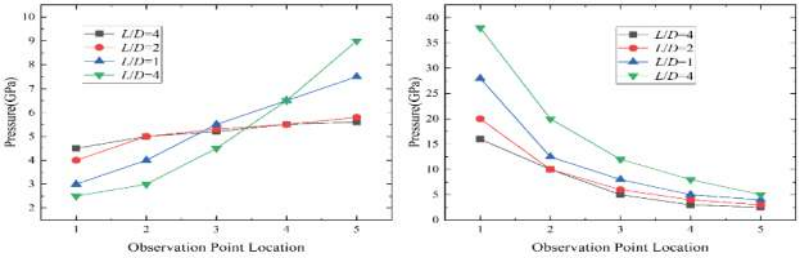

(a) Longitudinal monitoring points (b) Transverse monitoring points

Fig. 12. Pressure along transverse and longitudinal monitoring points.

Critical Sympathetic Detonation Distance Prediction. Analysis of the relationship between the critical sympathetic detonation distance and aspect ratio for cylindrical bare TNT charges, as illustrated in Fig. 13, indicates that the critical distance decreases as the aspect ratio increases. At an aspect ratio of 0.5, the sympathetic detonation distance reaches its maximum value, approximately 1.36 times the charge diameter. Beyond this point, although the critical distance continues to decline with increasing aspect ratio, the rate of decrease diminishes gradually. This behavior can be explained by the energy distribution characteristics associated with different aspect ratios. At smaller aspect ratios, although the detonation energy from the donor charge is concentrated primarily along the axial direction with limited radial energy, the radial shock wave pressure distribution is more localized. This results in a higher peak pressure and reduced attenuation with distance, enabling the shock wave to attain the initiation pressure of the acceptor charge at greater distances, and thereby increasing the critical sympathetic detonation distance. Conversely, as the aspect ratio increases, the radial energy component rises, but the shock wave pressure distributes more uniformly along the axial direction rather than concentrating near the charge bottom. The resultant decrease in peak pressure, combined with enhanced pressure attenuation due to the increased radial distance, limits the effective range of the shock wave. Thus, the shock wave only reaches the initiation threshold of the acceptor charge at shorter distances, leading to a smaller critical detonation distance.

The distribution of the relative distance versus aspect ratio data approximately follows an exponential relationship. Fitting the relationship between the relative critical sympathetic detonation distance and the aspect ratio for cylindrical TNT charges with the exponential function$S = C \times (L/D)^n$yields the expression$S = 1.28 \times (L/D)^{-0.1}$, with $R^2 = 0.97$, indicating good agreement. To further validate the empirical model, numerical simulations were performed for aspect ratios of $L/D = 1.5$ and $L/D = 3$. For $L/D = 1.5$, the critical sympathetic detonation distance is 70 mm, corresponding to a relative distance of 1.25; for $L/D = 3$, the values are 50 mm and 1.14, respectively. The simulation results show good consistency with the formula predictions, confirming the model's accuracy.

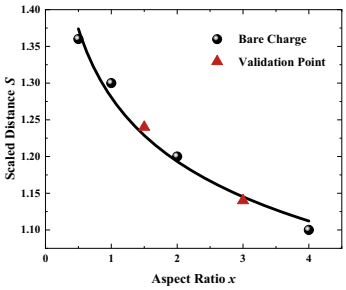

Fig. 13. Comparative distribution with different aspect ratios.

5 Conclusions

This study established a near-field sympathetic detonation test system for typical cylindrical TNT bare charges, conducted sympathetic detonation tests on cylindrical TNT charges, obtained the sympathetic detonation response patterns of acceptor charges under different axial spacings, constructed numerical models for sympathetic detonation of cylindrical charges with different aspect ratios, systematically investigated the influence of charge structural parameters on the critical sympathetic detonation distance, and developed an engineering prediction model. The main conclusions are as follows:

1. The response of the acceptor charge was determined by analyzing the shock wave overpressure signal, high-speed photographic images, and the deformation of the witness plate. For a Φ50 × 100 mm TNT bare charge, detonation occurred in the acceptor charge at an axial spacing of 60 mm or less; deflagration was observed at axial spacings between 60 mm and 80 mm; and no reaction occurred at axial spacings beyond 120 mm. The critical sympathetic detonation distance for the TNT bare charge of this size was determined to be 60 mm.
2. A computational model for sympathetic detonation of TNT charges was established. The model's reliability was verified by comparing the sympathetic detonation test results with the numerical simulation results. Numerical simulations were performed for TNT charge sympathetic detonation tests at different charge spacings. The results indicate that near the critical sympathetic detonation distance, the acceptor charge initiates first from the bottom end. The detonation wave initially propagates to the right along the charge and then turns to the upper left, eventually initiating the entire acceptor charge.
3. The critical sympathetic detonation distance for bare charges increases as the aspect ratio decreases. Numerical simulations show that when the aspect ratio decreases from 4.0 to 0.5, the critical detonation distance increases from 1.14 times to 1.36 times the charge diameter. The aspect ratio primarily influences the shock wave propagation path and energy distribution: smaller aspect ratio charges produce more concentrated shock wave pressures with slower attenuation, enabling initiation of acceptor charges at greater distances. An engineering prediction model was developed by fitting the relationship between the relative critical sympathetic detonation distance and aspect

ratio for cylindrical TNT charges, achieving accurate prediction of critical detonation distances for cylindrical charge warheads with different aspect ratios.

Acknowledgments. This work was supported by the National Natural Science Foundation of China (Nos. 12572411 & 12172051 & 12172050 & 12221002), and State Key Laboratory of Explosion Science and Safety Protection (ZDKT26-01) and National Key Laboratory of Shock Wave and Detonation Physics Open Fund.

References

1. Lu, F.Y., Li, X.Y., Lin, Y.L.: Warhead Structure and Principles, pp. 1–4. Scientific Dental Press, Beijing (2009)
2. Wan, J.L.: Research on evaluation method for low vulnerability ammunition warhead. Beijing: Beijing Institute of Technology, Dissertation (2011).
3. Zhang, C.H.: Insensitive, the Most important feature of future munitions. J. Mod. Mil. Sci. **24**(2), 54–59 (2006)
4. Li, D.G.: Evaluation Method and Experimental Research on Warhead Anti-Fragment Impact Initiation Sensitivity. Beijing Inst. of Technol., Doctor's Dissertation, Beijing (2016)
5. Eichelberger, R.J., Sultanoff, M.: Sympathetic detonation and initiation by impact. Proc. A. **246**(1245), 274–281 (1958). https://doi.org/10.1098/rspa.1958.0133
6. Itoh, S., Hamada, T., Murata, K., et al.: Visualization of underwater sympathetic detonation of high explosives. J. KSME Int. J. **15**(12), 1822–1828 (2001). https://doi.org/10.1007/BF03185140
7. Li, Z., Xiang, X.Z., Guo, Z.X.: Safety distances of sympathetic detonation for various explosives. J. Explos. Shock Waves. **14**(3), 231–241 (1994). https://doi.org/10.11883/1001-1455(1994)03-0231-11
8. Wang, C.: Sympathetic Detonation Experiments and Numerical Simulation of High Explosives. Beijing: Beijing Inst. of Technol., Doctor's Dissertation (2009).
9. Yang, T.H., Wang, C., Li, T.: Numerical simulation study of sympathetic detonation in stages. J. Def. Technol. **18**(8), 1382–1393 (2022). https://doi.org/10.1016/j.dt.2021.08.009
10. Lu, J.P., Lochert, I.J., Kennedy, D.L., et al.: Simulation of sympathetic reaction rests for PBXN-109 Proceedings of the 13th Symposium (International) on Detonation, Norfolk (2006).
11. Berzins, M., Luitjens, J., Meng, Q., et al.: Uintah: a scalable framework for hazard analysis Proceedings of the 2010 TeraGrid Conference: 1–8 (2010). https://doi.org/10.1145/1838574.1838577.
12. Berzins, M., Beckvermit, J., Harman, T., et al.: Extending the Uintah framework through the petascale modeling of detonation in arrays of high explosive devices. J. SIAM J. Sci. Comput. **38**(5), S101–S122 (2016). https://doi.org/10.1137/15M1023270
13. Beckvermit, J., Harman, T., Wight, C., et al.: Packing configurations of PBX-9501 cylinders to reduce the probability of a deflagration to detonation transition (DDT). J. Propellants Explos. Pyrotech. **41**, 1070–1078 (2016). https://doi.org/10.1002/prep.201500331
14. Karlos, V., Solomos, G., Larcher, M.: Analysis of blast parameters in the near-field for spherical free-air explosions. J. JRC Tech. Rep. (2016). https://doi.org/10.2788/778898
15. Johnson, G.R., Cook, W.H.: Fracture characteristics of three metals subjected to various strains, strain rates, temperatures and pressures. J. Eng. Fract. Mech. **21**(1), 31–48 (1985). https://doi.org/10.1016/0013-7944(85)90052-9
16. Chen, G., Chen, Z.F., Tao, J.L., et al.: Investigation and validation on plastic constitutive parameters of 45# stell. J. Explos. Shock Waves. **25**(5), 451–456 (2005)

A Practical Calibration Method for MCC and UH Model Parameters Solely Based on CD Triaxial Tests

Binglong Zhu[1,2,3](✉)

[1] State Key Laboratory of Highspeed Railway Track System, Beijing 100081, China
blzhucars@163.com
[2] Railway Engineering Research Institute, China Academy of Railway Sciences Corporation Limited, Beijing 100081, China
[3] China Academy of Railway Sciences Corporation Limited, Beijing 100081, China

Abstract. The Modified Cam-Clay (MCC) model is a classic constitutive model for describing the mechanical behavior of normally consolidated or lightly over-consolidated clays. Its extended form—the Unified Hardening (UH) model—further refines the description of over-consolidated clays on this basis, and both share the same parameter system. Traditional model parameter calibration methods typically rely on isotropic compression, unloading, and triaxial consolidated drained shear (CD) tests, which are complex and costly. This paper proposes a practical parameter calibration method based solely on CD tests. Specifically, the method involves: (1) fitting the critical state points in the p–q plane to determine the critical state stress ratio M; (2) fitting the Critical State Line (CSL) in the e–ln$p$ plane to obtain its slope and intercept, utilizing the parallel relationship between the CSL and the Normal Compression Line (NCL) to compute the compression index λ and intercept N; (3)assigning Poisson's ratio v based on empirical values; and (4) deriving the swelling index κ by analyzing the initial segment of the stress–strain curve from the CD test. Using this method to calibrate and validate triaxial test data for white clay, the results show that it can effectively and accurately determine key parameters such as M, λ, N, and κ, with small model reconstruction errors and good predictive performance in validation. Compared with traditional multi-test approaches, the new method significantly reduces testing costs and calibration complexity, providing an efficient and economical parameter calibration pathway for railway subgrade deformation analysis and numerical simulation.

Keywords: Modified Cam-Clay Model · Unified Hardening Model · CD Triaxial Test · Parameter calibration · Railway subgrade

1 Introduction

By the end of 2024, the operating mileage of China's railway network had reached 162,000 km, with high-speed railway (HSR) accounting for 48,000 km. Notably, subgrade sections constitute approximately one-third of these HSR lines [1]. The subgrade of the railway often contains a clay layer, whose stress–strain characteristics directly

© The Author(s), under exclusive license to Springer Nature Switzerland AG 2027
G. Feng et al. (Eds.): ICCE 2025, SUCI, pp. 266–279, 2027.
https://doi.org/10.1007/978-3-032-32237-1_19

affect the long-term subgrade settlement and deformation performance. The strict limitations on post-construction settlement in high-speed railways demand extremely high accuracy in settlement prediction. Traditional empirical formulas often fail to capture the complex elastoplastic behavior of soil under complex stress paths. Therefore, advanced constitutive models like MCC and UH are indispensable tools for numerical simulations (e.g., Finite Element Analysis) to predict long-term deformations accurately. However, the reliability of these simulations is predominantly dictated by the accuracy of the input parameters. Accurately obtaining the constitutive parameters of clay and conducting precise numerical predictions are crucial for ensuring the safety and durability of railway infrastructure.

In the study of clay constitutive models, the Modified Cam-Clay (MCC) model and its extension, the Unified Hardening (UH) model, are widely recognized as effective theoretical frameworks for describing the strength and deformation of clay [2]. However, traditional calibration methods based on parameter definitions typically require isotropic compression under normally consolidated states, unloading, and conventional triaxial consolidated drained shear (CD) tests. The preparation of normally consolidated samples is challenging, the testing procedures are complex, and the costs are high. This limits the widespread application of these models in practical engineering.

In recent years, Inverse Analysis methods have become an important tool for identifying geotechnical parameters [3]. The basic approach is to treat model parameters as variables to be solved, numerically simulate laboratory test processes, and construct an Objective Function to measure the discrepancy between simulation results and experimental data. Optimization algorithms are then used iteratively to obtain optimal parameters [4]. Representative studies include JIN et al. [5], who optimized parameter identification using the Real-Coded Genetic Algorithm (RCGA), and ZHU et al., who employed multi-population particle swarm optimization to inversely analyze the unified hardening model for clays and sands (CSUH) parameters.

However, parameters derived solely from inverse optimization may encounter the issue of "non-unique solution", where multiple sets of parameters can achieve the same target error function [6]. Kadlíček et al. [7] proposed a hierarchical calibration strategy based on sensitivity analysis, combining defined calibration with deterministic optimization algorithms to improve efficiency while preserving the physical meaning of the parameters. Nevertheless, such methods still require complex isotropic tests.

In summary, existing research primarily focuses on improving inversion algorithms, with less discussion on how to achieve accurate parameter calibration while minimizing the number of tests. To address this, this paper proposes a practical calibration method for MCC and UH model parameters relying solely on CD test data. This method utilizes the characteristics of the critical-state line to obtain parameters such as M, λ, and N (compression intercept) through data fitting in p–q and e–ln$p$ spaces. It further combines empirical values and initial modulus analysis to determine ν and κ, forming a fast, stable, and physically meaningful calibration process.

This method has been implemented in the open-source software ModelParaOpt (github.com/blzhu/ModelParaOpt2.0_Excel_STADE) to provide a simplified and user-friendly tool for obtaining model parameters for both research and engineering communities. By comparing with typical experimental data, the reliability and engineering applicability of the proposed method have been validated.

2 Formatting of Manuscript Components

2.1 Modified Cam-Clay (MCC) Model

In 1963, Roscoe and others from the University of Cambridge, UK proposed an elasto-plastic model for describing normally consolidated saturated clay—the Cam-Clay Model [8]. The introduction of the Cam-Clay Model was of great significance. First, the deformation of soil could be calculated using methods from continuum mechanics to solve boundary value problems, which also meant that theories distinguishing between strength and compressibility could be replaced. Second, it greatly simplified experimental equipment, as the model parameters could be determined solely through conventional triaxial tests. Academician of the Chinese Academy of Sciences Shen regarded the proposal of the Cam-Clay Model as the beginning of modern soil mechanics [9]. However, the Cam-Clay Model produced a plastic shear strain increment $d\varepsilon_d^p$ when calculating isotropic compression tests, which contradicted the phenomenon of $d\varepsilon_d^p = 0$ observed in isotropic compression tests. Therefore, in 1968, Roscoe and Burland modified the bullet-like yield surface of the Cam-Clay Model into an elliptical yield surface, as shown in Fig. 1, resulting in the Modified Cam-Clay (MCC) model [10].

(a) (b)

Fig. 1. Schematic diagram of the Modified Cam-Clay (MCC) model: (a) Yield surface and constant p loading stress path DF; (b) The NCL is parallel to the CSL.

Assuming the principal stress axes coincide with the directions of the plastic strain increment axes, i.e., the mean effective principal stress p-axis aligns with the plastic volumetric strain increment $d\varepsilon_v^p$, and the generalized shear stress q-axis aligns with the plastic shear strain increment $d\varepsilon_d^p$ as shown in Fig. 1 (a). Considering the work done by plastic deformation, the plastic volumetric strain increment $d\varepsilon_v^p = 0$ at the critical state, and the orthogonality between the plastic potential surface $g(p, q)$ in stress space and the direction of plastic strain increment, the plastic potential surface of the MCC model is derived as a family of ellipses:

$$g(p, q) = q^2 + M^2 p^2 - Cp = 0 \tag{1}$$

Here, C is the integration constant, and the value of C depends on the current stress points p and q. The plastic potential surface g varies with the current stress point (p, q), meaning g always passes through the current stress point.

The isotropic compression test of normally consolidated clay can be described by the Normal Compression Line (NCL) of the MCC model:

$$e = N - \lambda ln(p) \tag{2}$$

After loading to point C (p_x, e_x) and unloading, its unloading line (UL):

$$e = e_x - \kappa ln\left(\frac{p}{p_x}\right) \tag{3}$$

Where p is less than p_x, and e is greater than e_x. The UL describes elastic unloading, the NCL describes elasto-plastic loading under isotropic stress state. Then, the total strain ε_v, elastic volumetric strain ε_v^e, and plastic volumetric strain ε_v^p generated when loading from point D (p_0, e_0) to point C:

$$0 \tag{4}$$

$$\varepsilon_v^e = \frac{-\Delta e^e}{1+e_0} = c_\kappa \ln\frac{p_x}{p_0} \tag{5}$$

$$\varepsilon_v^p = \varepsilon_v - \varepsilon_v^e = c_p \ln\frac{p_x}{p_0} \tag{6}$$

Where $c_\kappa = \frac{\kappa}{(1+e_0)}$, $c_p = \frac{(\lambda-\kappa)}{(1+e_0)}$. Differentiating Eq. (5):

$$d\varepsilon_v^e = \frac{\kappa}{1+e_0}\frac{dp}{p} \tag{7}$$

According to the isotropic elastic Hooke's law:

$$d\varepsilon_v^e = \frac{3(1-2\nu)}{E}dp \tag{8}$$

From Eqs. (7) and (8), the elastic modulus E in the MCC model can be obtained:

$$E = \frac{3(1-2\nu)(1+e_0)}{\kappa}p \tag{9}$$

The MCC model adopts an associated flow rule, with the yield surface and the plastic potential surface being the same as in Eq. (1). As shown in Fig. 1 (a), when $q = 0$, $p = p_x$, $C = M^2 p_x$ can be solved. Substituting p_x from Eq. (6) into the plastic potential surface C yields the yield surface of the MCC model:

$$f = g = \ln\left(\left(1+\frac{q^2}{M^2p^2}\right)p\right) - \ln p_0 - \frac{1}{c_p}\varepsilon_v^p = 0 \tag{10}$$

In the equation, the plastic volumetric strain ε_v^p is the hardening parameter of the MCC model. The following analysis examines the change in void ratio when a point on the NCL undergoes drained shear at constant p to reach the Critical State Line. Taking point D in Fig. 1 (b) as the initial point, its mean effective principal stress is $p = p_0$, deviatoric stress $q = 0$, void ratio $e = e_0$, denoted as D (p_0, 0, e_0). Substituting point D into Eq. (10), it can be seen that ε_v^p=0 at this time.

On the Critical State Line, the following holds:

$$q = Mp \tag{11}$$

When point D undergoes drained shear at constant p to reach point F on the CSL, it satisfies $q = Mp_0$.

Substituting the critical-state point F(p_0, Mp_0, e) into Eq. (10):

$$\varepsilon_v^p = c_p \ln(2) \tag{12}$$

Since the mean effective principal stress p remains unchanged during the drained shear test, no elastic volumetric strain is generated by p, and changes in q do not produce elastic volumetric strain. Therefore, in Eq. (12), the plastic volumetric strain equals the total volumetric strain. Based on the relationship between volumetric strain and void ratio, it follows:

$$\Delta e = e - e_0 = -(\lambda - \kappa)\ln(2) \tag{13}$$

In the equation, e represents the void ratio at point F, and e_0 is the void ratio at point D. The difference in void ratio Δe between points F and D is independent of the mean effective principal stress p. Therefore, the difference in void ratio remains constant for different values of p, indicating that the Critical State Line (CSL) at point F is parallel to the Normal Compression Line (NCL) at point D. Hence, the CSL of the MCC model:

$$e = N - \lambda ln(p) - (\lambda - \kappa)\ln(2) \tag{14}$$

In the framework of the Modified MCC model, the vertical spacing between the NCL and the CSL in the $e - \ln p$ plane is elegantly derived as $(\lambda - \kappa)\ln(2)$. This relationship represents a profound milestone in theoretical soil mechanics: it signifies that the Critical State Line is not merely an empirical boundary defined by observation, but a theoretical necessity calculated directly from the consolidation characteristics of the soil via the flow rule and hardening law. This intrinsic link serves as the cornerstone of Critical State Soil Mechanics. To commemorate this conceptual breakthrough, the pioneers of the Cambridge School synthesized these insights into the seminal text Critical State Soil Mechanics, which unified the treatment of strength and deformation. The term $(\lambda - \kappa)\ln(2)$ is more than a geometric interval; it is a mathematical testament to the internal consistency of soil plasticity, bridging the gap between isotropic compression and the ultimate state of shear failure.

2.2 Unified Hardening (UH) Model

When describing over-consolidated clay, the MCC model has issues such as abrupt changes in the stress-strain curve at the elastoplastic transition and overestimated

peak strength under drained conditions. Therefore, the MCC model cannot reasonably describe the strain softening and dilatancy phenomena of over-consolidated saturated clay [11]. To more accurately describe the strain softening and dilatancy phenomena of over-consolidated saturated clay, Yao Yangping et al. proposed the Unified Hardening (UH) model based on the MCC model [12–14], as shown in Fig. 2. The UH model only modifies the hardening parameters of the MCC model, enabling it to unify the description of strain hardening and softening, contraction and dilatancy phenomena for clays of different densities (normally consolidated and over-consolidated clay), offering broad applicability.

(a) (b)

Fig. 2. UH model: (a) Yield surface; (b) NCL, ACL, CSL, and state parameter ξ.

The plastic potential surface of the UH model is the same as that of the Modified Cam-Clay model, with the yield surface of the MCC model serving as the reference yield surface. The hardening parameter H, related to stress ratio and state parameter, replaces the plastic volumetric strain ε_v^p as the parameter of the current yield surface. The current yield surface of the UH model is:

$$f = g = \ln\left(\left(1 + \frac{q^2}{M^2 p^2}\right)p\right) - \ln p_0 - \frac{1}{c_p}H = 0 \tag{15}$$

Hardening parameter H in the current yield surface:

$$H = \int \frac{M_Y^4 - \eta^4}{M^4 - \eta^4} d\varepsilon_v^p \tag{16}$$

Where M_Y is the potential failure stress ratio, which determines the maximum strength of the soil. The strength envelope of over-consolidated soil, composed of the Hvorslev envelope and the tension-cut-offline (with a slope of 3), is approximated by a parabola, thereby deriving M_Y:

$$M_Y = 6\left[\sqrt{\frac{k}{R}\left(1 + \frac{k}{R}\right)} - \frac{k}{R}\right], k = \frac{M^2}{12(3 - M)} \tag{17}$$

Based on the geometric relationship of triangle ABE in Fig. 2 (b), the state parameter form of R can be derived as:

$$R = \exp\left(-\frac{\xi}{\lambda - \kappa}\right) \tag{18}$$

The state parameter ξ is the vertical distance from point E to point A, reflecting the current over-consolidation ratio or compactness state of the soil:

$$\xi = e_\eta - e \tag{19}$$

In the equation, e_η is the void ratio on the anisotropic compression line (ACL). When drained shear from point D at constant p reaches the ACL, the stress ratio η increases from $\eta = 0$ to $\eta = \eta$, and Δe_p is calculated.

In the framework of the Unified Hardening (UH) model, the state parameter ξ serves as a fundamental physical variable that quantifies the 'distance' between the current soil state and the reference ACL. Unlike the classical state parameters that merely indicate the geometric position of the stress state, ξ in the UH model directly governs the M_Y. The physical significance of ξ lies in its ability to unify the mechanical description of normally consolidated (NC) and over-consolidated (OC) soils through a dynamic hardening mechanism: (1) For Normally Consolidated Clays: The state parameter ξ reflects that the soil is on the NCL. In this state, the potential failure stress ratio M_Y is identical to the critical state stress ratio M. Consequently, the model exhibits purely plastic hardening and volumetric contraction, consistent with the classical MCC model. (2) For Over-Consolidated Clays: The state parameter ξ indicates a state 'denser' than the NCL. Physically, this activates a potential strengthM_Y that is higher than M ($M_Y > M$). This allows the model to capture the peak strength (strain softening) and dilatancy behavior characteristic of OC soils—phenomena that the MCC model typically fails to predict. By integrating ξ into the Unified Hardening Parameter H, the model ensures a smooth and continuous transition from over-consolidated behavior to normally consolidated behavior as the soil structure evolves towards the critical state during shearing. Thus, ξ acts as a mechanical bridge, enabling a single set of parameters to describe complex elastoplastic behaviors across different over-consolidation ratios.

The NCL of the UH model is the same as that of the MCC model, and the ACL is obtained by subtracting Eq. (2) from Δe_p:

$$e_\eta = N - \lambda lnp - (\lambda - \kappa)\ln\left(1 + \frac{\eta^2}{M^2}\right) \tag{20}$$

When drained shear from point D under constant p reaches the CSL, the stress ratio η increases from $\eta = 0$ to $\eta = M$, indicating that the CSL of the UH model coincides with that of the MCC model, as shown in Eq. (14). This demonstrates that the distance between the CSL and NCL in the UH model is the same as that in the MCC model, also expressed as $(\lambda - \kappa)\ ln\ (2)$.

2.3 Conventional Calibration Method for Parameters

Determining the model parameters for MCC and UH models generally requires 1 isotropic compression and unloading test, along with 3 CD tests.

M is the critical state stress ratio, which can be obtained through three CD tests. The p and q values at the critical state of the three CD tests are organized in the p-q space. According to the definition of M, M is the slope of the straight line fitted by the three

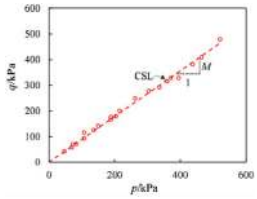

Fig. 3. Critical-state points of weald clay triaxial test.

critical-state points, where the formula for the fitted straight line is shown in Eq. (11), and the effect is illustrated in Fig. 3.

The isotropic compression and unloading test data of normally consolidated clay are organized in the e-ln$p$ space, where λ is the slope of the compression test, N (compression intercept) is the intercept of the compression test, κ is the slope of the isotropic unloading test, and the effect is shown in Fig. 4.

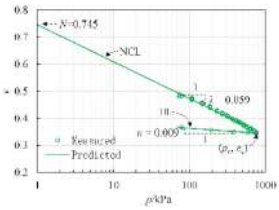

Fig. 4. Isotropic loading and unloading test of LCT clay in normally consolidated state [15].

Poisson's ratio is an elastic constant in the Cam-Clay Model that reflects the material's lateral deformation, and it is also an elastic parameter in the UH constitutive model. The typical range of Poisson's ratio for common soil materials is as follows: clay between 0.1 and 0.2 [16], loose sand between 0.2 and 0.4, medium-dense sand between 0.25 and 0.4, dense sand between 0.3 and 0.45, and sand-gravel mixtures between 0.15 and 0.35 [17]. Jin et al. directly assumed Poisson's ratio as 0.2 when calculating parameters for Hostun sand, Toyoura sand, and Alaskan sand using the critical state nonlinear soil model [5]. Jin et al. also adopted Poisson's ratio as 0.25 when applying the MCC model to Shanghai clay [18].

As can be seen, the Poisson's ratio of clay and sandy soil mostly ranges between 0.2 ~ 0.3, and this parameter is not sensitive [7]; generally, a value of 0.25 can be used based on experience.

At this point, all five model parameters of the MCC and UH models, namely M, v, κ, λ, and N, have been determined.

3 Practical Calibration Methods for MCC and UH Model Parameters

3.1 Parameters *M* and *v*

The methods for determining the critical state stress ratio M and Poisson's ratio v are the same as the previous methods.

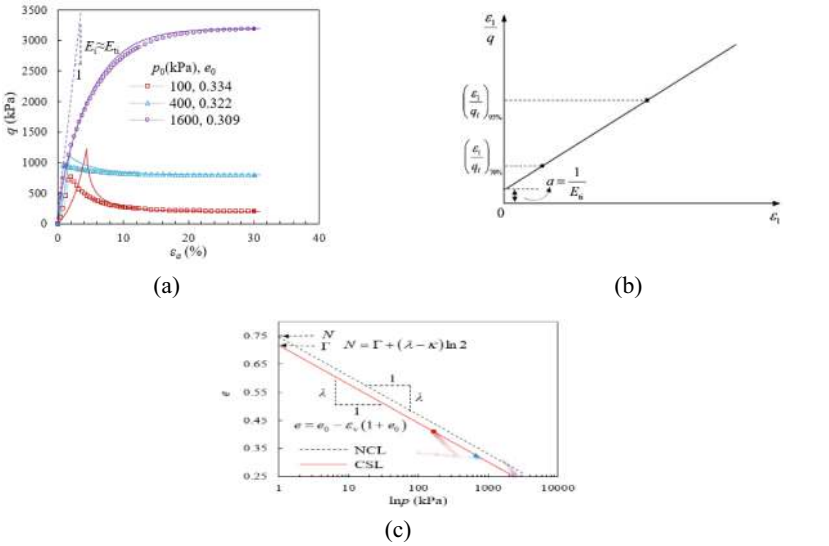

Fig. 5. Approximate determination of MCC model parameters based on CD test: (a) Initial modulus Ei; (b) Approximate determination of initial modulus Ei; (c) Approximate determination of parameters λ and N using the critical-state line

3.2 Parameter *κ*

From Eq. (9), when the pressure p in the equation equals the initial confining pressure p_0 of the CD test, the elastic modulus E in Eq. (9) becomes the initial elastic modulus E_i. At this point, the Poisson's ratio v, initial void ratio e_0, and initial confining pressure p_0 are known, leaving only the elastic modulus E and κ as unknowns. By determining the initial elastic modulus E_i from the CD test, κ can be solved. Since the plastic deformation in the initial shear stage is minimal and essentially elastic, it can be approximately considered that the initial elastic modulus E_i of the CD test equals the initial tangent modulus E_{ti}, as shown in Fig. 5(a), he formula being

$$E_i \approx E_{ti} = \left(\frac{q}{\varepsilon_1}\right)_{\varepsilon_1 \to 0} = \frac{1}{a} \tag{21}$$

In the equation, a is the reciprocal of the initial tangent elastic modulus E_{ti} Drawing on the method for determining E_{ti} in the Duncan-Chang model, points at 70% and 95% of q_f in the ε_1-q coordinate system are selected, where q_f is the q [19–21] at failure. Plotting these two points in the ε_1-ε_1/q coordinate system transforms the hyperbola in the ε_1-q coordinate system into a straight line in the ε_1-ε_1/q coordinate system. The initial tangent elastic modulus E_{ti} is the reciprocal of the intercept a, as shown in Fig. 5(b).

Therefore, the swelling index κ can also be obtained by solving the equation:

$$\kappa = \frac{3(1-2\nu)(1+e_0)}{E_i} p_0 \tag{22}$$

The average value of κ obtained under different initial confining pressures p_0 is taken as the final κ.

3.3 Parameters λ and N

λ and N are the slope and intercept of the compression line in e-ln$p$ space for isotropic compression tests on normally consolidated soil. However, preparing normally consolidated soil samples is challenging, and the testing costs are high.

The model can derive a critical-state line, which aligns well with the critical-state point of the soil. This is why the MCC model is referred to as a critical-state model. When only CD tests are available, the critical-state points can be organized in the e-ln$p$ space. By fitting the critical-state points in the e-ln$p$ coordinate system using Eq. (14), the parameters N and λ can be obtained, as shown in Fig. 5 (c).

4 Validation of Practical Calibration Methods

4.1 White Clay

Biarez and Hicher [22, 23] conducted two CD tests on white clay under normally consolidated states and three CU tests under different over-consolidated states. For the two CD tests, the samples were first isotropically compressed from 100 k Pa to 400 kPa and 800 kPa, followed by drained shear under constant confining pressure until failure. It is evident that both CD tests were *performed* on normally consolidated soil. For the three CU tests, the samples were first isotropically compressed from 100 kPa to 800 kPa, then unloaded to 400 kPa and 67 kPa, followed by undrained shear under constant confining pressure until failure. The initial confining pressures p_0 during the shear phase were 800 kPa, 400 kPa, and 67 kPa, with OCR values of 1, 2, and 12, respectively.

The parameters calibrated from two CD tests are shown in Table 1. It can be seen that the MCC and UH model parameters are identical. The reconstructed curves based on these parameters are compared with the two CD test curves in Fig. 6. The prediction performance can be represented by the error between the model-calculated values and the test values, here expressed as *MRE*. A smaller *MRE* indicates closer agreement between the model-calculated values and the test values, reflecting better model reconstruction or prediction performance. The model-calculated values here include both the reconstructed curves and the predicted curves. The reconstructed curves refer to the model-calculated

values of Test A derived from the parameters calibrated using Test A, as shown in Fig. 6. The predicted curves refer to the model-calculated values of Test B derived from the parameters calibrated using Test A. Since the isotropic compression test and CU test were not used for parameter calibration, Figs. 7 and 8 present the prediction results.

Table 1. Parameters of MCC and UH model.

PARAMETERS			
Elastic		Plastic	
v	0.25	M	0.89
κ	0.03	λ	0.09
		N	1.111

Since both CD tests were conducted on normally consolidated soil, the calculation results of the MCC model and the UH model were identical. The average *MRE* value of the two ε_a-q curves was 0.059, and the average *MRE* value of the two ε_a-e curves was 0.04.

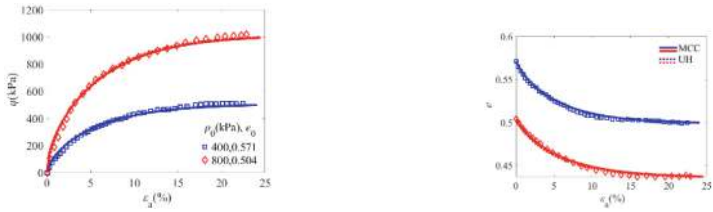

(a) (b)

Fig. 6. Reconstruction of white clay CD test by MCC and UH model: (a) Axial strain ε_a -generalized shear stress q ($MRE = 0.059$); (b) Axial strain ε_a-void ratio e($MRE = 0.04$).

Based on the initial conditions of isotropic compression (initial confining pressure p_0 and initial void ratio e_0) and the parameters in Table 1, the prediction results of the MCC and UH models are presented, as shown in Fig. 7. Since this condition involves normally consolidated soil, the prediction results of the two models are the same.

Based on the initial conditions of the CU test and the parameters in Table 1, separate predictive results of the MCC and UH models are given, as shown in Fig. 7. Since this condition involves over-consolidated soil, the predictions of the two models differ.

In the MCC model, the current point of over-consolidated soil lies inside the current yield surface. At this stage, loading from the current point to the yield surface is considered elastic loading, which can cause the MCC model to calculate over-consolidated soil with η approaching or even exceeding the slope of the zero confining pressure tension line, which is 3, as shown in Fig. 8. In conventional triaxial tests, the slope of the zero confining pressure tension line is 3, indicating that cohesionless soil cannot sustain

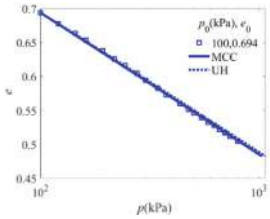

Fig. 7. Prediction of white clay isotropic compression test by MCC and UH model (*MRE* = 0.016).

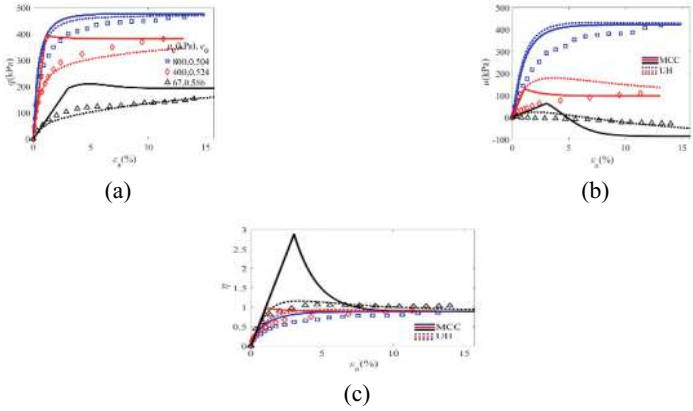

Fig. 8. MCC and UH model predictions for white clay CU test: (a) Axial strain ε_a -generalized shear stress q; (b) Axial strain ε_a -pore pressure u; (c) Axial strain ε_a -stress ratio η.

tension. Therefore, the results of the MCC model when calculating over-consolidated soil CU test may not conform to the rule that cohesionless soil cannot bear tension. On the other hand, the current yield surface of the UH model always passes through the current stress point, so reloading is always elasto-plastic loading, and there will be no sharp point at the loading-unloading point, nor will the stress ratio exceed 3.

Table 2 presents the *MRE* of the two models predicting different curves in the CU test. The results show that the *MRE* predicted by the UH model is smaller, indicating that the UH model performs better than the MCC model in prediction.

Table 2. Predictive performance of different curve.

PERFORMANCE INDEX			
MCC model		UH model	
ε_a-q	0.289	ε_a-q	0.103
ε_a-u	1.039	ε_a-u	0.715

5 Formatting of Manuscript Components

Based on the physical meanings and empirical ranges of the MCC and UH model parameters, this paper proposes a practical calibration method for model parameters using only CD test data. Through validation with white clay tests, the following main conclusions are drawn:

1. Three CD tests can effectively calibrate key parameters such as M, λ, N, and κ. The resulting model can well reconstruct the CD test curves with ideal prediction accuracy.
2. Using this parameter set to predict isotropic compression and undrained (CU) tests, the UH model demonstrates better simulation accuracy than the MCC model under overconsolidated clay conditions, exhibiting a more reasonable stress–strain response.
3. Poisson's ratio v has a minor impact on calculation results and can be assigned empirically (0.2 ~ 0.3).
4. The proposed method does not rely on optimization algorithms but solely uses the linear regression fitting method corresponding to the physical meaning of parameters, significantly improving computational efficiency over traditional back-analysis methods.

In summary, the practical calibration method proposed in this paper combines accuracy and efficiency. While preserving the physical meaning of parameters, it significantly reduces model calibration costs, providing a practical approach and tool support for numerical analysis in railway subgrade and similar engineering applications.

Acknowledgments. National Natural Science Foundation of China Joint Fund Project (U2268216); Science and Technology Research and Development Program of China State Railway Group Co., Ltd. (L2023G009); Scientific Research Project of China Academy of Railway Sciences Corporation Limited (2023YJ384); 2022 Tencent Xplorer Prize.

References

1. Yu, Z., Wang, H., Wang, X., et al.: Review of autonomous operation control technology for railway transportation. J. Beijing Jiaotong Univ. **49**, 6–33 (2025). https://doi.org/10.11860/j.issn.1673-0291.20250145
2. Yao, Y.: A Unified Hardening Constitutive Theory for Soils: Fundamentals of Plasticity for Geomaterials. Elsevier (Woodhead Publishing), Cambridge, MA, 2025. (ISBN: 9780443275708)
3. Zentar, R., Hicher, P., Moulin, G.: Identification of soil parameters by inverse analysis. J. Comput. Geotech. **28**, 129–144 (2001). https://doi.org/10.1016/s0266-352x(00)00020-3
4. Doherty, J., Alguire, H., Wood, D.: Evaluating modified cam clay parameters from undrained triaxial compression data using targeted optimization. J. Can. Geotech. J. **49**, 1285–1292 (2012). https://doi.org/10.1139/t2012-088
5. Jin, Y., Wu, Z., Yin, Z., et al.: Estimation of critical state-related formula in advanced constitutive modeling of granular material. J. Acta Geotech. **12**, 1329–1351 (2017). https://doi.org/10.1007/s11440-017-0586-5
6. Gaone F, Doherty J and Gourvenec S: An optimization strategy for evaluating modified cam clay parameters using self-boring pressuremeter test data J. Can. Geotech. J., 56: 1668–1679 (2019). https://doi.org/10.1139/cgj-2018-0385

7. Kadlíček, T., Janda, T., Šejnoha, M., et al.: Automated calibration of advanced soil constitutive models. Part II: hypoplastic clay and modified cam-clay. J. Acta Geotech. **17**, 3439–3462 (2022). https://doi.org/10.1007/s11440-021-01435-y
8. Roscoe, K., Schofield, A., Thurairajah, A.: Yielding of clays in states wetter than critical. J. Géotechnique. **13**, 211–240 (1963). https://doi.org/10.1680/geot.1963.13.3.211
9. Shen Z: Theoretical Soil Mechanics. China Water & Power Press, Beijing (2000). ISBN: 9787508402994
10. Roscoe K and Burland J: On the generalised stress-strain behaviour of "wet" clay J. In: Heyman J, Leckie FA (eds.) Engineering Plasticity. Cambridge University Press, Cambridge, pp. 535–609 (1968). Accession Number: 00234687
11. Hou, W., Yao, Y.: Analysis in behaviors of over-consolidated clays described by cam-clay model and unified hardening model. J. Ind. Constr. **41**, 18–23+140 (2011). https://doi.org/10.13204/j.gyjz2011.09.003
12. Yao, Y., Hou, W., Zhou, A.: Constitutive model for over-consolidated clays. J. Sci. China Ser. E: Technol. Sci. **51**, 179–191 (2008). https://doi.org/10.1007/s11431-008-0011-2
13. Yao, Y., Hou, W., Zhou, A.: UH model: three-dimensional unified hardening model for over-consolidated clays. J. Géotechnique. **59**, 451–469 (2009). https://doi.org/10.1680/geot.2007.00029
14. Yao, Y., Gao, Z., Zhao, J., et al.: Modified UH model: constitutive modeling of over-consolidated clays based on a parabolic Hvorslev envelope. J. Geotech. Geoenvironmental Eng. **138**, 860–868 (2012). https://doi.org/10.1061/(ASCE)GT.1943-5606.0000649
15. Pestana J, Whittle A and Gens A: Evaluation of a constitutive model for clays and sands: part II–clay behaviour J. Int. J. Numer. Anal. Methods Geomech., 26: 1123–1146 (2002). https://doi.org/10.1002/nag.238
16. Tekeste, M., Habtzghi, D., Koolen, J.: Cap-hardening parameters of cam-clay model variations with soil moisture content and shape-restricted regression model. J. Agric. Eng. Int.: CIGR J. **15**, 10–24 (2013)
17. Gercek H: Poisson's ratio values for rocks J. Int. J. Rock Mech. Min. Sci., 44: 1–13 (2007). https://doi.org/10.1016/j.ijrmms.2006.04.011
18. Jin, Y., Yin, Z., Shen, S., et al.: A new hybrid real-coded genetic algorithm and its application to parameters identification of soils. J. Inverse Probl. Sci. Eng. **25**, 1343–1366 (2016). https://doi.org/10.1080/17415977.2016.1259315
19. Kondner, R.: Hyperbolic stress-strain response: cohesive soils J. J. Soil Mech. Found. Div. **89**, 115–143 (1963). https://doi.org/10.1061/JSFEAQ.0000479
20. Duncan J, Byrne P, Wong K, et al.: Strength, stress-strain and bulk modulus parameters for finite element analyses of stresses and movements in soil masses J. Consult. Clin. Psychol., 49: 554–567 (1980). NII ID: 10002953857
21. Qian C, Song X, Wu J, et al.: Experimental study on parameters of Duncan-chang model for cement-soil J. Adv. Mater. Res., 641–642, 403–409 (2013). https://doi.org/10.4028/www.scientific.net/amr.641-642.403
22. Yin Z: Constitutive Theory of Granular Soils and Application. China Architecture & Building Press, Beijing, 2021. ISBN: 9787112258840
23. Biarez, J., Hicher, P.: Elementary Mechanics of Soil Behaviour: Saturated Remoulded Soils. A.A. Balkema, Rotterdam (1994). https://doi.org/10.5555/19951904796

Early-Age Performance and Hydration Temperature Evolution of an OPC–CSA Composite Binder System

Yin Xu[1], Jing Yang[1(✉)], and Haoran Guo[2]

[1] School of Civil Engineering and Transportation, Yangzhou University, Yangzhou 225127, China
j.yang@yzu.edu.cn

[2] School of Civil Engineering, Southeast University, Nanjing 210096, China

Abstract. Considering that the hydration of the ordinary Portland cement– calcium sulfoaluminate (OPC–CSA) composite binder system is rapid and the early-age temperature rise is highly concentrated, this system is prone to insufficient workability and early thermal cracking in practical engineering applications. This study investigated the effects of retarders on the setting time, mechanical properties, and hydration temperature evolution of the OPC–CSA blended system to identify an optimal mixture proportion. The results showed that sodium citrate (SC) at dosages of 0.2%–0.4% significantly prolonged the setting time, improved mechanical performance, and delayed the hydration temperature-rise peak. Sodium gluconate (SG) exhibited a retarding effect at low dosages; however, when the dosage exceeded 0.5%, the paste became noticeably drier, leading to a shortened setting time and reduced strength. Boric acid (BA) showed only a weak ability to extend the setting time and provided limited enhancement in strength. The combined use of SC and SG effectively tailored both setting behavior and strength development; in particular, a combination of 0.4% SC + 0.3% SG increased the setting time by 45.8% and the 28-day compressive strength by 3.6% compared with 0.4% SC alone, while simultaneously reducing the peak hydration temperature.

Keywords: OPC–CSA composite binder system · Retarders · Setting time · Mechanical properties · Hydration temperature rise

1 Introduction

The OPC–CSA composite binder system can enhance the overall performance of concrete while reducing material cost, as it combines the advantages of OPC, such as high later-age strength and good durability, with those of CSA, including rapid setting, high early strength, and superior resistance to chemical attack, thereby meeting the demands of sustainable construction [1, 2]. However, this system is characterized by intense hydration reactions and a highly concentrated heat release peak, which, in mass concrete elements, can readily induce significant temperature stresses and early- age cracking risks [3]. Consequently, how to rationally incorporate retarders to regulate the hydration process while maintaining adequate early strength has become one of the key issues for achieving safe and reliable application of OPC–CSA composite binder systems.

© The Author(s), under exclusive license to Springer Nature Switzerland AG 2027
G. Feng et al. (Eds.): ICCE 2025, SUCI, pp. 280–294, 2027.
https://doi.org/10.1007/978-3-032-32237-1_20

Retarders are important chemical admixtures for controlling the hydration of cement, and are widely used in concrete and cement-based products. Retarders primarily act by prolonging the setting time and reducing both the rate and peak of early heat evolution, thereby mitigating temperature stresses and improving construction and curing conditions. Common retarders include organic salts, inorganic salts, natural polymers, and synthetic polymer-based admixtures [4]. Among them, organic retarders such as SC and SG are widely employed in cementitious systems. Sodium citrate (SC) can chelate Ca^{2+} in the vicinity of cement particles and adsorb on their surfaces, thereby weakening early dissolution and nucleation processes, effectively retarding cement hydration and reducing the rate of heat release [5, 6]. Sodium gluconate (SG) primarily acts through strong surface adsorption, forming an adsorbed layer on clinker particles that suppresses ion exchange and the nucleation of hydration products, whereas its complexation with Ca^{2+} plays only a secondary role [7, 8]. Boric acid (BA) type retarders, such as BA, regulate cement hydration mainly by forming calcium borate layers that inhibit ye'elimite dissolution and thus modify the kinetics of ettringite formation [9, 10]. At present, studies on retarders are still predominantly focused on single cement systems; for OPC–CSA composite binder systems, systematic investigations into the synergistic effects of different types of retarders—both singly and in combination—on setting behavior, mechanical properties, and internal hydration temperature rise remain relatively limited.

Therefore, in this study, an OPC–CSA composite binder system was adopted as the research object, and different dosages of SC, SG, and BA were incorporated. A series of single-admixture and combined-admixture test programs were designed to systematically investigate the influence of various retarder dosages on setting time, mechanical properties, and hydration temperature evolution. The results are expected to provide experimental evidence and theoretical guidance for mixture proportion design and temperature crack control of OPC–CSA composite binder system in engineering practice.

2 Materials and Methods

2.1 Test Materials

Sulfoaluminate cement (CSA, 52.5 grade, Tangshan Beijixiong Building Materials Co., Ltd., China), ordinary Portland cement (OPC, 52.5 grade, Nanjing Zhonglian, China), fly ash (FA, particle size 10–20 μm, specific surface area 424.7 m^2/kg), silica fume (SF), a CaO-based expansive agent (EA, particle size 20–45 μm, specific surface area 579.0 m^2/kg, Sobute New Materials Co., Ltd., China), quartz sand (20–40 mesh and 50–100 mesh), a polycarboxylate superplasticizer (PCE, water-reduction rate 29%), and a lithium carbonate early-strength agent (ESA, particle size 100–200 μm, specific surface area 42.31 m^2/kg) were used as raw materials. A reference mixture was designed, and its detailed mix proportions are given in Table 1. On this basis, the experimental program was conducted in two stages: (1) single-admixture tests of three retarders, in which the effects of different dosages of SC, SG, and BA on the setting time and mechanical properties of the OPC–CSA composite system were investigated to identify a retarder system providing a balanced setting delay and strength development; (2) combined-admixture tests using SC and SG, in which an orthogonal experimental design was

adopted to establish different dosage combinations and carry out the corresponding tests.

Table 1. Mix proportions of the OPC–CSA composite system

CSA	OPC	SF	FA	W/B	EA	20–40	50–100	PCE	ESA
350 g	50 g	10 g	30 g	0.33	30 g	350 g	350 g	1.1%	0.5%

2.2 Test Methods

1. The setting time of the mortar was determined in accordance with the requirements of JGJ/T 70–2009 Standard for Test Method of Basic Properties of Construction Mortar [11]. The mold was placed on a penetration apparatus, and a 30 mm needle was driven vertically into the mortar within 10 s to a depth of 25 mm. The recorded load was converted to penetration resistance according to the standard method. Measurements started 15 min after mixing; the interval was reduced to 2 min once the resistance reached 0.30 MPa. The test was stopped at 0.70 MPa, and the corresponding time was recorded.
2. Mechanical performance tests were conducted in accordance with GB/T 17671-2021 Method of testing cements—Determination of strength (ISO method) [12]. Flexural strength was measured using standard mortar prismatic specimens (40 mm × 40 mm × 160 mm) under loading along the Y direction at a rate of 50 N/s. For each mix, three specimens were tested, and the mean value was reported as the flexural strength. Compressive strength was determined on the fractured halves obtained after the flexural test (loaded area: 40 mm × 40 mm) along the Y direction at a loading rate of 2.4 kN/s. The average of the test results for each mix was reported as the compressive strength.
3. With reference to GB/T 12959 [13] and the experimental procedure proposed by Zou X et al. [14], a hydration temperature rise test was carried out on mortar. The experimental setup is shown in Fig. 1. Prior to testing, the temperature of the constant-temperature and humidity chamber was stabilized at (25 ± 1) °C, and a vacuum insulation chamber was fabricated to minimize heat exchange with the environment, thereby ensuring that the specimen hydrated under nearly constant ambient conditions. The temperature sensor continuously monitored the specimen for approximately 20 h, and data were recorded at 2 min intervals to characterize the temperature rise associated with the early-age hydration of mortar.

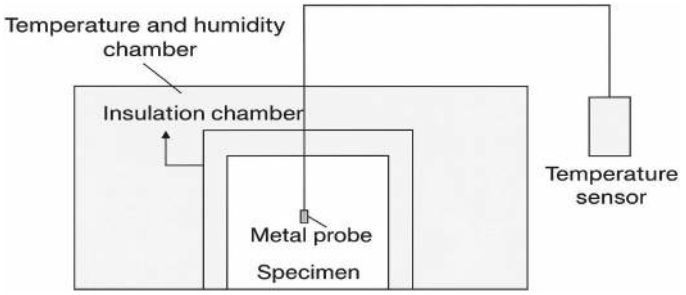

Fig. 1. Schematic diagram of the experimental setup for hydration temperature rise.

3 Analysis of Test Results

3.1 Single-Retarder Admixture Tests

Setting Time. The setting time is a critical parameter governing the selection of construction methods and the scheduling of operations, and it represents a key stage in material formation. The effects of the retarders on the setting time of the OPC–CSA composite binder system are shown in Fig. 2. The addition of SC generally prolonged the setting time, with the most pronounced effect observed at a dosage of 0.6%, where the setting time increased to 32 min. With further increases in SC dosage to 0.7% and 0.8%, the setting time of the OPC–CSA composite mortar system decreased slightly to 30 min and 31 min, respectively**.** Within the SG dosage range of 0.2% to 0.5%, SG exerted only a mild retarding effect on the system; at an SG dosage of 0.4%, the setting time increased to 19 min. However, when the dosage exceeded 0.5%, the setting time was markedly shortened, indicating a critical dosage threshold for its use as a retarder. This behavior may be associated with the abundant carboxyl groups complexing with Ca^{2+} and binding water, thereby reducing the free-water content and promoting early stiffening of the paste. BA exhibited only a weak retarding effect on the setting time, with a slight extension to 13 min at a dosage of approximately 0.3%. As the BA dosage increased, the setting time began to decrease. At a BA dosage of 1.1%, the OPC–CSA composite binder system even exhibited a setting time of less than 5 min.

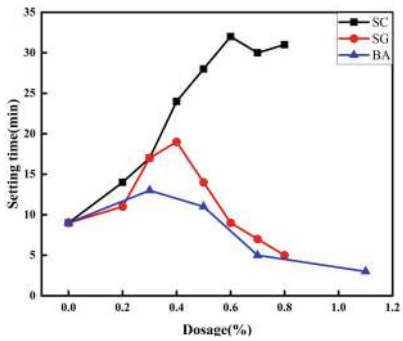

Fig. 2. Effects of SC, SG and BA on the setting time of OPC–CSA composite binder system.

Mechanical Properties. The effects of the retarders on the flexural strength of the OPC–CSA composite binder system are shown in Fig. 3. In the absence of retarders, the OPC–CSA composite binder system exhibited relatively low flexural strength, reaching only 5.4 MPa at 2 h. Moreover, its strength developed slowly with curing time; the flexural strength increased to 6.2 MPa at 28 d, representing a marginal gain of 0.8 MPa. Compared with the blank control, the incorporation of retarders improved the flexural strength of the composite binder system to varying extents. When the SC dosage was within 0.2%–0.4%, the flexural strength increased. In particular, at an SC dosage of 0.4%, the flexural strength reached its maximum, with a 28 d value of 11.2 MPa, representing an 80.6% increase compared with the blank control. When the dosage was further increased to 0.5% and above, a slight reduction was observed; however, the differences at 28 d were not significant. The SG exhibited an increase– decrease trend in the flexural strength of the system with increasing dosage, reaching a maximum at approximately 0.5%. At this dosage, the 28 d flexural strength reached 9.4 MPa, representing a 51.6% increase compared with the blank control. When the BA dosage was below 0.7%, the flexural strength increased progressively with increasing BA content. Only at the high dosage of 1.1% did the early-age flexural strength show a slight reduction; however, with increasing curing time, the later-age strength continued to exhibit an overall upward trend.

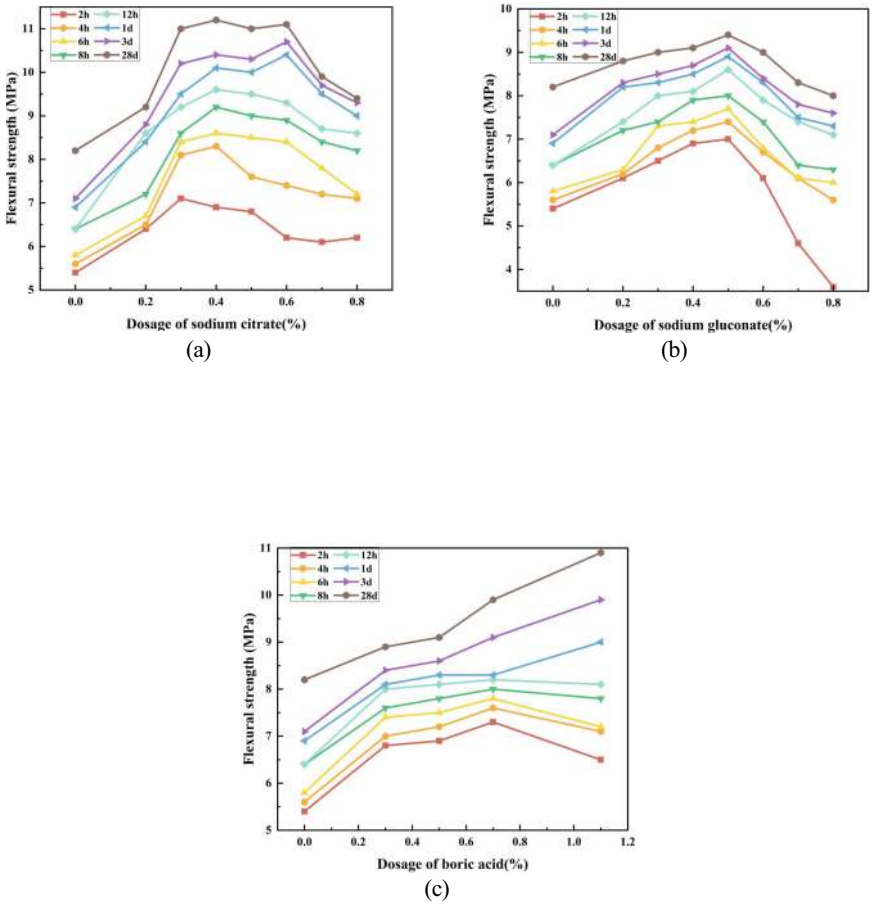

Fig. 3. Effects of SC, SG and BA on the flexural strength of OPC–CSA composite binder system: (a) SC (b) SG (c) BA.

The effects of the retarders on the compressive strength of the OPC–CSA composite binder system are shown in Fig. 4. In the absence of retarders, the OPC– CSA composite binder system also exhibited relatively low compressive strength, measuring 27.5 MPa at 2 h and 39.1 MPa at 28 d, indicating a comparatively slow strength-development rate. After incorporating SC, the compressive strength showed age-dependent trends with increasing dosage. At early ages (2–12 h), increasing the SC dosage from 0.2% to 0.5% led to an overall increase in compressive strength. When the SC dosage was 0.4%, the compressive strength reached its maximum, attaining 37.7 MPa at 2 h and 69.8 MPa at 28 d. These values were 37.1% and 78.5% higher than those of the blank control, respectively. Further increasing the SC dosage resulted in a slight reduction in strength, indicating a strength decline at excessive SC contents. Within the low SG dosage range of 0.2% to 0.5%, the compressive strength exhibited an increasing trend with increasing SG content. The maximum compressive strength was obtained at an SG dosage of 0.5%, reaching 34.6 MPa at 2 h and 59.7 MPa at 28 d, which are 25.8% and 52.6% higher

than those of the blank control, respectively. For BA**,** the greatest enhancement was achieved at a dosage of 0.5%, where the compressive strength reached 36.4 MPa at 2 h and 54.2 MPa at 28 d, representing increases of 32.4% and 38.6% relative to the blank control, respectively.

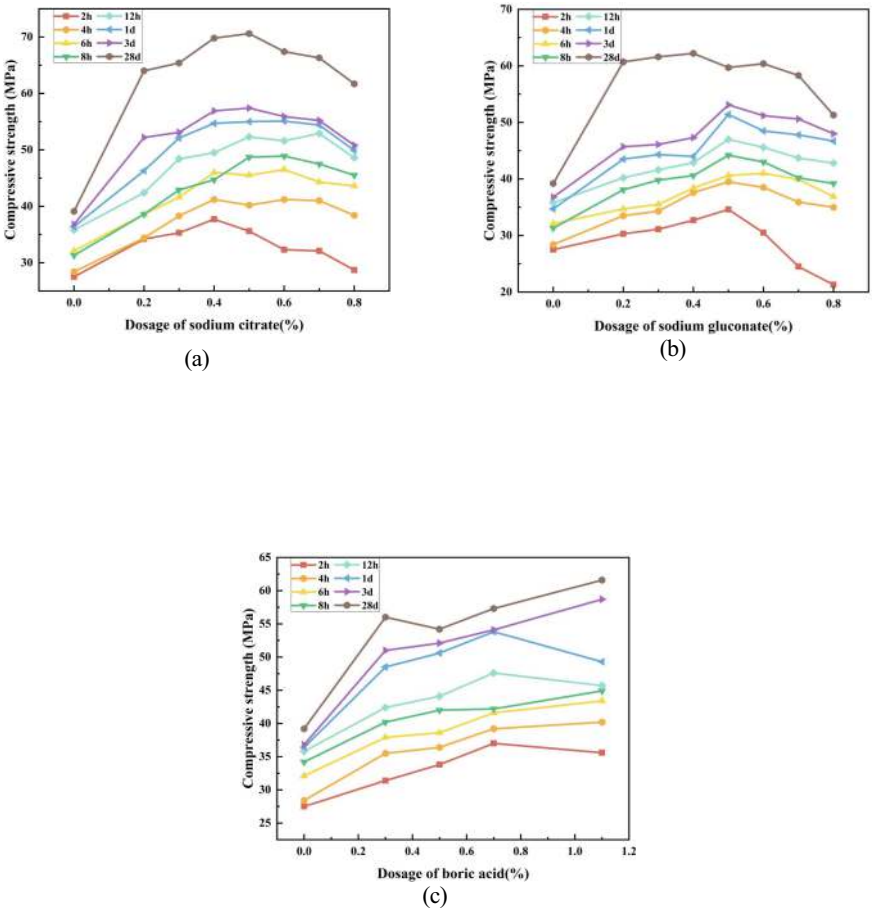

Fig. 4. Effects of SC, SG and BA on the compressive strength of OPC–CSA composite binder system: (a) SC (b) SG (c) BA.

Hydration Temperature. The effects of the retarders on the hydration temperature rise of the OPC–CSA composite binder system are shown in Fig. 5. The blank control exhibited a pronounced temperature-rise peak and a relatively rapid hydration rate, with the hydration temperature peak occurring at an early stage and reaching 71.5 °C. By contrast, the incorporation of retarders delayed the temperature rise of the composite binder system to varying extents. The regulation of hydration temperature rise by SC, SG, and BA differed markedly. For SC, at a dosage of 0.2%, the occurrence of the hydration temperature peak was slightly delayed relative to the blank control, and the peak temperature

decreased marginally to 69.8 °C, suggesting a limited retarding effect at this dosage. As the SC dosage increased to 0.3%–0.4%, the peak temperature was reduced by approximately 3 °C compared with the control and the peak occurrence was further shifted to later times, indicating that SC exerted an inhibitory effect on the early-age hydration of the OPC–CSA composite binder system within this dosage range. With a further increase in SC dosage to 0.5%–0.8%, the peak occurrence was markedly delayed, the heat-release rate progressively decreased, and the peak temperature exhibited a continuous downward trend. For SG, at relatively low dosages (0.2%–0.4%), the peak occurrence was delayed compared with the blank control and the peak temperature was lower, accompanied by a more gradual temperature-rise profile, indicating that SG can retard cement hydration even at low dosages. As the SG dosage increased to 0.5%–0.8%, the peak temperature decreased further and the peak occurrence shifted markedly to later times, reflecting a stronger retarding effect and peak-suppression capability. The incorporation of SC and SG markedly reduced the hydration rate and heat-release capacity of the cement system, indicating an effective retarding effect on the hydration reaction. However, at high SG dosages, excessive SG substantially decreased the availability of free water, resulting in an overly dry mortar mixture and consequently impairing the performance of the composite binder system. In contrast, BA at appropriately low dosages exerted only a mild delaying and peak-suppressing effect on early hydration. At higher dosages, the hydration peak shifted slightly earlier and increased in magnitude.

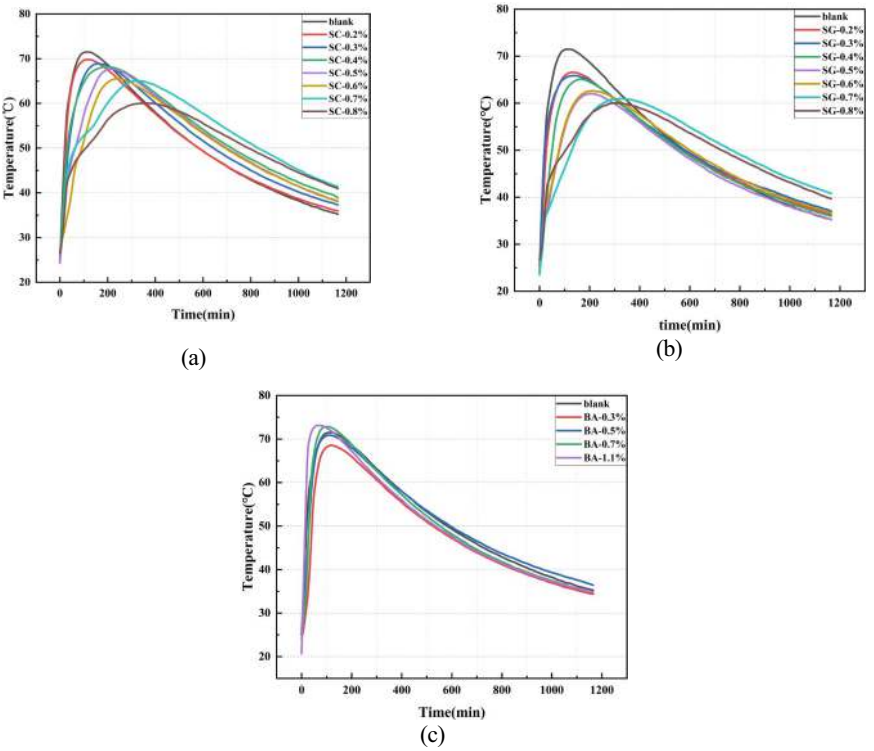

Fig. 5. Effects of SC, SG and BA on the hydration temperature rise of OPC–CSA composite binder system: (a) SC (b) SG (c) BA.

3.2 Experimental Tests on the Combined Use of SC and SG

Based on the foregoing single-admixture results for SC and SG, this section further treated these two retarders as the key variables and systematically investigated their combined effects by varying the SC–SG blending ratio and the total dosage. Specifically, a series of mixtures with different SC and SG dosage combinations were designed to comparatively evaluate the setting time, mechanical properties, and hydration temperature-rise behavior of the OPC–CSA composite binder system, and to elucidate the corresponding trends. On this basis, the effects of SC and SG across different dosage ranges were comprehensively analyzed to identify an optimal combined-dosage scheme that balances workability in practice with performance stability, thereby providing reliable experimental evidence for mixture proportion optimization and engineering application of the combined retarding system.

Setting Time. At different SC levels (0.2%, 0.4%, and 0.6%), the effects of additional SG on the setting time are shown in Fig. 6. Overall, the setting time exhibited an increase–decrease trend with increasing SG dosage. When SC was fixed at 0.2%, the setting time reached its maximum at an SG dosage of approximately 0.2%, representing an increase of about 29% compared with the mixture containing 0.2% SC alone. When the SC

dosage was 0.4%, co-addition of SG produced a more pronounced retarding effect. At SG dosages of 0.2%, 0.3%, and 0.4%, the setting times were 33 min, 35 min, and 41 min, respectively, corresponding to increases of 37.5%, 45.8%, and 70.8% relative to the mixture containing 0.4% SC alone. Considering the combined requirements of mechanical performance and temperature regulation, the mixture containing 0.4% SC and 0.3% SG provided a better overall balance while effectively extending the setting time, and is therefore recommended for practical applications. In contrast, when the SC dosage was 0.6%, co-addition of 0.4%–0.5% SG caused the mortar to rapidly lose plasticity shortly after mixing; however, its flowability could be restored by remixing. This behavior is characteristic of false setting and led to a sharp reduction in the setting time.

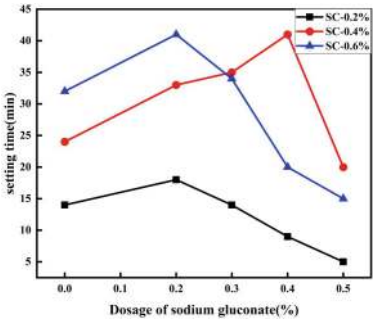

Fig. 6. Effect of SC–SG combined use on setting time.

Mechanical Properties. At different SC levels (0.2%, 0.4%, and 0.6%), the effects of additional SG on flexural strength are shown in Fig. 7. When the SC dosage was fixed at 0.2%, the 2 h flexural strength showed a decreasing trend with increasing SG dosage. At an SG dosage of 0.5%, the 2 h flexural strength was reduced by approximately 22% compared with the mixture containing 0.2% SC alone, which may be associated with an excessive retarding effect that slowed early strength development. At 4 h and 6 h, the flexural strength increased markedly; in particular, at an SG dosage of 0.3%, the 6 h flexural strength reached 7.9 MPa. As the SG dosage was further increased to 0.4%–0.5%, the flexural strength decreased again. When the SC dosage was fixed at 0.4%, the flexural strength from 2 to 6 h decreased with increasing SG dosage. Notably, at an SG dosage of 0.5%, the 2 h flexural strength was only 5.8 MPa, which is 1.1 MPa lower than that of the mixture containing 0.4% SC alone. From 8 h to 3 d, the flexural strength increased initially and then decreased, with a progressively reduced decline. By 28 d, the differences among the groups tended to converge, and the overall variation became relatively stable. When the SC dosage was fixed at 0.6%, co-addition of SG at low dosages resulted in relatively low flexural strength at early ages; however, the later-age strength developed more rapidly with curing time. As the SG dosage increased to 0.3%, the flexural strength began to increase, reaching peak values at 12 h and 28 d. With a further increase in SG dosage to 0.4%–0.5%, the flexural strength declined, with a pronounced reduction at 28 d. Overall, consistent trends were observed across

different SC levels: an appropriate amount of SG acted synergistically with SC to regulate the hydration process, thereby enhancing flexural strength at middle and later ages. In contrast, at low SG dosages, the improvement in early-age strength was limited, whereas increasing SG to 0.4%– 0.5% tended to suppress hydration, leading to generally reduced flexural strength across curing ages.

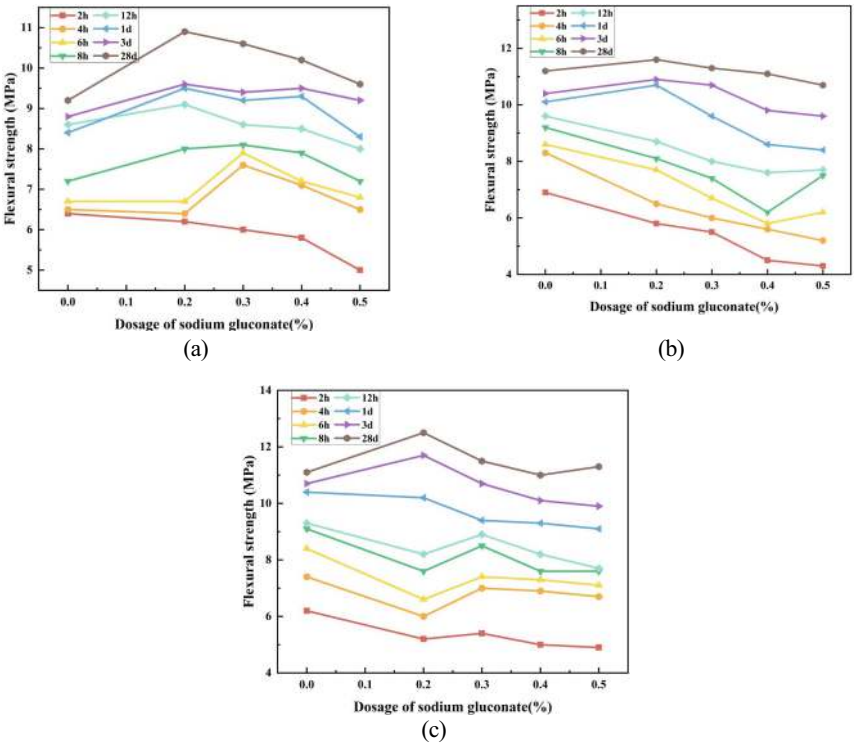

Fig. 7. Effect of SC–SG combined use on flexural strength: (a) 0.2% SC + X% SG (b) 0.4% SC + X% SG (c) 0.6% SC + X% SG.

At different SC levels (0.2%, 0.4%, and 0.6%), the effects of additional SG on compressive strength are shown in Fig. 8. When SC was fixed at 0.2%, the compressive strength exhibited an initial increase followed by a decrease with increasing SG dosage. A pronounced improvement was observed at SG dosages of 0.2%–0.3%; in particular, co-addition of 0.3% SG produced the highest 28 d compressive strength of 67.4 MPa, representing a 5.3% increase relative to the mixture containing 0.2% SC alone. With further increases in SG dosage, the compressive strength declined, and the reduction was especially evident at 28 d. When the SC dosage was fixed at 0.4%, the early-age compressive strength exhibited a trend similar to that of the flexural strength, showing a gradual decrease with increasing SG dosage. In contrast, from 6 h to 28 d, the compressive strength increased initially and then decreased as the SG dosage increased. Compared with the mixture containing 0.4% SC alone, co-addition of SG at dosages of 0.2%,

0.3%, and 0.4% increased the 28 d compressive strength by 9.7%, 3.5%, and 1.2%, respectively. When SC was fixed at 0.6%, increasing the SG dosage resulted in an overall mild decrease in compressive strength at 2 h. From 4 h to 3 d, the compressive strength increased initially and then decreased with increasing SG dosage; the mixture with 0.2% SG exhibited a more pronounced strength gain, achieving a 3 d compressive strength of 70.0 MPa. By 28 d, the compressive strength tended to stabilize, with only minor variations among the mixtures.

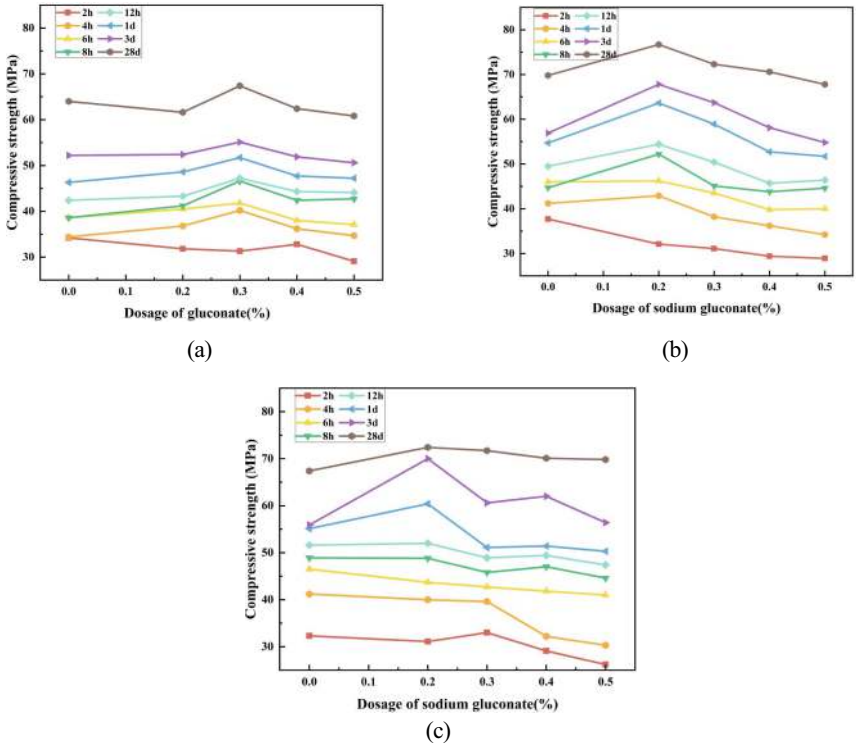

Fig. 8. Effect of SC–SG combined use on Compressive Strength: (a) 0.2% SC + X% SG (b) 0.4% SC + X% SG (c) 0.6% SC + X% SG.

Hydration Temperature. At different SC levels (0.2%, 0.4%, and 0.6%), the effects of additional SG on the hydration temperature rise are shown in Fig. 9. When SC was fixed at 0.2%, incorporating 0.2% SG slightly delayed the occurrence of the temperature-rise peak and marginally reduced the peak temperature. In contrast, as the SG dosage further increased to 0.3%, 0.4%, and 0.5%, the peak tended to appear earlier and the peak temperature increased accordingly to 67.3 °C, 72.0 °C, and 71.3 °C, respectively. Meanwhile, the pre-peak heating rate increased, suggesting that the early-age heat-release process became more pronounced and the retarding effect was weakened. When SC was fixed at 0.4%, co-addition of 0.2%–0.5% SG led to an overall decrease in peak temperature and a delayed peak occurrence compared with the mixture containing 0.4%

SC alone. Specifically, at an SG dosage of 0.2%, the peak temperature was 67.5 °C, only 0.6 °C lower than that of the SC-only (0.4%) mixture, indicating a minor influence. When the SG dosage increased to 0.3%–0.5%, the peak temperature became lower and the peak occurred later, indicating an evident retarding effect, with a reduced hydration rate and a prolonged heat-evolution process. When SC was fixed at 0.6%, the hydration temperature-rise profile progressively changed with increasing SG dosage: the peak occurrence was gradually shifted to later times, and the temperature-rise curve became more gradual, indicating a slower hydration process. At SG dosages of 0.2% and 0.3%, the peak temperatures were 64.6 °C and 64.3 °C, respectively, which are 1.0 °C and 1.3 °C lower than that of the SC-only (0.6%) mixture, suggesting that low SG dosages further enhanced the retarding effect of 0.6% SC. When the SG dosage increased to 0.4%–0.5%, the peak occurrence was markedly delayed and the peak temperature remained relatively low.

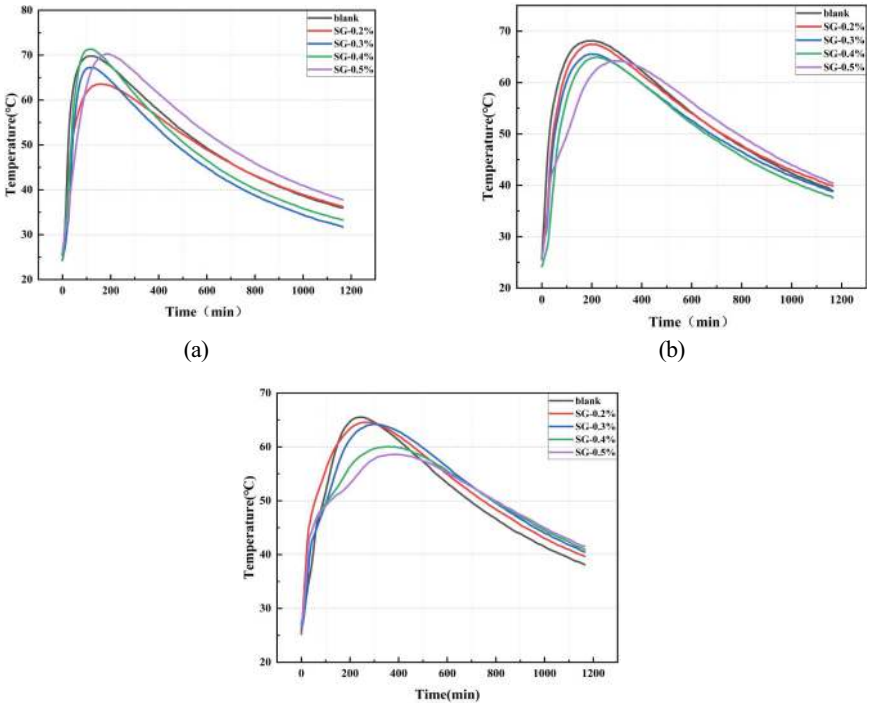

Fig. 9. Effect of SC–SG combined use on hydration temperature Rise: (a) 0.2% SC + X% SG (b) 0.4% SC + X% SG (c) 0.6% SC + X% SG.

4 Conclusion

This study systematically investigated the effects of different types and dosages of retarders on the setting time, mechanical properties, and hydration temperature rise of an OPC–CSA composite binder system. Based on the experimental results, the following conclusions can be drawn:

1. The incorporation of SC significantly prolonged the setting time, with the most pronounced effect observed at a dosage of 0.6%, where the setting time increased to 32 min. Within the dosage range of 0.2%–0.4%, SC enhanced the mechanical properties, and the maximum 28-day compressive strength was increased by 78.5% compared with the control. In addition, the hydration temperature peak was delayed and its magnitude was reduced, indicating a favorable retarding effect.
2. Within the dosage range of 0.2%–0.5%, SG exhibited a mild retarding effect. The mechanical properties showed an increase–decrease trend with SG dosage, with 0.5% being the optimum dosage; at 28 d, the flexural and compressive strengths were 51.6% and 52.6% higher than those of the blank control, respectively. In addition, the hydration temperature peak was delayed and its peak value was reduced.
3. BA had a limited ability to extend the setting time, with only a slight extension observed at approximately 0.3% BA; higher dosages shortened the setting time. BA improved compressive strength, and the greatest enhancement was achieved at 0.5% BA, where the 28 d compressive strength was 38.6% higher than that of the blank control, whereas its effect on hydration temperature rise remained relatively limited.
4. The combined use of SC and SG provided a practical balance between setting controllability, strength development, and temperature regulation. The mixture containing 0.4% SC + 0.3% SG was recommended, which increased the setting time by 45.8% and the 28 d compressive strength by 3.6% relative to 0.4% SC alone, while reducing the hydration temperature peak by approximately 2.5 °C. At an SC level of 0.6%, co-addition of 0.4%–0.5% SG induced false setting and should be avoided.

References

1. Huang, G., Pudasainee, D., Gupta, R., et al.: Extending blending proportions of ordinary Portland cement and calcium sulfoaluminate cement blends, its effects on setting, workability, and strength development. J. Front Struct Civil Eng. **15**(5), 1249–1260 (2021). https://doi.org/10.1007/s11709-021-0770-4
2. Xin, X., Duan, G., Zhu, J., et al.: Study on the properties of belite calcium sulfoaluminate cement–ordinary Portland cement composite binder system. J. Buildings. **14**(4), 890 (2024). https://doi.org/10.3390/buildings14040890
3. Zhang, J., Ke, G., Liu, Y.: Early hydration heat of calcium sulfoaluminate cement with influences of supplementary cementitious materials and water to binder ratio. J. Materials. **14**(3), 642 (2021). https://doi.org/10.3390/ma14030642
4. Vohburger, A., Collin, M., Bouissonnié, A., et al.: Citric, tartaric, and succinic acid effects on C3S dissolution and the nucleation kinetics of CSH and portlandite. J. Cem Concr Res. **197**, 107964 (2025). https://doi.org/10.1016/j.cemconres.2025.107964

5. Liu, Y., Zhang, Z., Jing, R., et al.: The interaction of sodium citrate and polycarboxylate- based superplasticizer on the rheological properties and viscoelasticity of cement-based materials. J. Constr Build Mater. **293**, 123466 (2021). https://doi.org/10.1016/j.conbuildmat.2021.123466
6. Li, H., Lu, Z., You, Z., et al.: Further understanding of hydration and setting performance of cement with citrate retarders: effects of sulfate carriers and cations. J. Constr Build Mater. **492**, 142844 (2025). https://doi.org/10.1016/j.conbuildmat.2025.142844
7. Luo, G., Liu, M., Li, H., et al.: Importance of adsorption compared with complexation for retarding C3S hydration via adding sodium gluconate. J. Cem Concr Res. **186**, 107686 (2024). https://doi.org/10.1016/j.cemconres.2024.107686
8. Lv, X., Li, J., Lu, C., et al.: The effect of sodium gluconate on pastes' performance and hydration behavior of ordinary Portland cement. J. Adv Mater. Sci. Eng. **1**, 9231504 (2020). https://doi.org/10.1155/2020/9231504
9. Ribeiro, D.V., Paula, G.R., Morelli, M.R.: Effect of boric acid content on the properties of magnesium phosphate cement. J. Constr Build Mater. **214**, 557–564 (2019). https://doi.org/10.1016/j.conbuildmat.2019.04.113
10. Koumpouri, D., Angelopoulos, G.N.: Effect of boron waste and boric acid addition on the production of low energy belite cement. J. Cem Concr Compos. **68**, 1–8 (2016). https://doi.org/10.1016/j.cemconcomp.2015.12.009
11. JGJ/T 70-2009: Standard for Test Method of Basic Properties of Construction Mortar (in Chinese) (2009).
12. GB/T 17671–2021: Method of testing cements—Determination of strength (ISO method) (in Chinese) (2021).
13. GB/T 12959: Test Methods for Heat of Hydration of Cement (in Chinese) (2024).
14. Zou, X., Chao, A., Wu, N., et al.: A novel Fabry-Perot fiber optic temperature sensor for early age hydration heat study in Portland cement concrete. J. Smart Struct Syst. **12**(1), 041–054 (2013). https://doi.org/10.12989/sss.2013.12.1.041

Analysis of Key Technical Paths for Nearly Zero Carbon Building in the Beijing Area—Taking a Hotel in Tongzhou District as an Example

Haoyu Wang[1,2(✉)], Yingqi Wang[1], Hongbo Guo[1], Haifeng Guo[1], Wen Ding[1], and Xiaoyu Wang[1]

[1] Beijing Residential Architectural Design & Research Institute Co., Ltd., Beijing 100005, China
haoyuwangleo@163.com

[2] Beijing Key Laboratory of Green Built Environment and Energy Efficient Technology, Beijing University of Technology, Beijing 100124, China

Abstract. To promote the development of near-zero carbon building in the Beijing area, this study takes a hotel in Tongzhou District, Beijing as a case, systematically analyzes the key technical paths applicable to this region, and uses thsware to simulate the energy consumption and carbon emissions of the case building, verifying the feasibility of the transformation from near-zero energy building to near-zero carbon building. The case adopts a technical path prioritizing passive design and optimizing active technologies,and rationally utilizing renewable energy as the core strategy to achieve the near-zero carbon target.The simulation results show that the carbon emissions of the designed building are 21.53 kgCO_2/(m^2·a), a 50.75% reduction compared to the 43.72 kgCO_2/(m^2·a) of the reference building;the comprehensive energy consumption is 51.54 kW h/m^2, only 39.25% of the reference building.The research indicates that the key technologies of near-zero energy building can significantly reduce the comprehensive energy consumption and carbon emissions of buildings, and provide a beneficial reference and technical support for the large-scale promotion of near-zero carbon buildings in the Beijing area.

Keywords: Nearly zero energy building · Nearly zero carbon building · Energy consumption simulation · Carbon emission

1 Introduction

In 2022, China's total carbon emissions across all sectors were approximately 11.4 billion tons of CO_2. The carbon emissions from the construction and operation of buildings accounted for about 32% of China's total CO_2 emissions (including energy-related and industrial process emissions), with construction emissions making up 13% and operational emissions 19% [1]. As a traditional major emitter of carbon, the building sector's carbon emission level directly affects the achievement of the overall carbon reduction goals. Therefore, vigorously promoting energy conservation and carbon reduction in

© The Author(s), under exclusive license to Springer Nature Switzerland AG 2027
G. Feng et al. (Eds.): ICCE 2025, SUCI, pp. 295–308, 2027.
https://doi.org/10.1007/978-3-032-32237-1_21

buildings is of crucial significance for achieving the carbon peak and carbon neutrality goals in this sector. Against this backdrop, zero-carbon buildings have gradually become an inevitable direction for building development, and accelerating their promotion and application is an urgent task.

To effectively reduce carbon emissions and energy consumption in buildings, many scholars have conducted in-depth research on zero-carbon buildings and near-zero energy consumption buildings. Han Lijun et al. took Ningxia region as an example, analyzed the key technical paths to achieve zero-carbon buildings, and verified the technical feasibility through simulation calculations with PKPM software [2]. Zhang Shicong et al. based on the "General Specification for Building Energy Efficiency and Renewable Energy Utilization" (GB 55015-2021), proposed a zero-carbon building definition framework covering four levels: low-carbon buildings, near-zero carbon buildings, zero-carbon buildings, and full life-cycle zero-carbon buildings [3]; in addition, they also studied the quantitative impact of energy efficiency improvement and renewable energy utilization on carbon reduction in public buildings, and further proposed recommended values for hierarchical control indicators for low-carbon, near-zero carbon, and zero-carbon public buildings [4]. Yu Jin et al. systematically demonstrated the technical feasibility of integrating seven main and passive technologies-ventilation corridors, insulation and shading, ground source heat pumps, photovoltaic storage direct flexible, energy storage water tanks, high-efficiency electromechanical systems, and intelligent operation and maintenance - in zero-carbon demonstration buildings [5]. Dou Mei et al. proposed a "two-way design" model for solar-driven zero-carbon medical buildings, constructed a multi-objective optimization model for carbon emissions, cost, and daylighting centered on full solar energy utilization, and verified the method with the Sichuan University West China Second University Hospital Xizang Hospital project as an example [6].

In the field of near-zero energy building research, Feng Guohui et al. coupled the MOBO optimization tool with the EnergyPlus software and, based on the actual needs of decision-makers, used the weighting method to seek the optimal solution. They conducted a multi-objective and multi-parameter optimization analysis covering the energy consumption, carbon emissions, and costs throughout the entire life cycle operation [7]. Xu Wei et al. compared the energy-saving and carbon reduction technical standards and practical paths of near-zero energy buildings in foreign countries, investigated and analyzed 40 near-zero energy building cases in cold climate regions and the carbon reduction effects of domestic typical projects, and combined with the analysis of the incremental costs of near-zero energy buildings in China, explored the carbon reduction paths applicable to the cold climate regions of China [8]. The research of He Fuchun et al. pointed out that, under the premise of considering both cost and performance comprehensively, the thickness of the exterior wall insulation material for near-zero energy buildings should be controlled at the lower limit of the heat transfer coefficient allowed range (i.e., the allowable maximum heat transfer coefficient value), which can meet the requirements [9].

Currently, in Beijing, the development of ultra-low energy and near-zero energy buildings has started relatively early. However, research in the field of near-zero carbon buildings is still relatively weak, and the actual engineering cases are relatively limited. Therefore, systematically exploring the promotion path from near-zero energy buildings

to near-zero carbon buildings, and conducting in-depth research on the development path of near-zero carbon building technologies, has significant theoretical value and practical significance.

2 An Example

This case involves a hotel building in Tongzhou District, Beijing. It adopts a steel frame support structure and consists of 11 floors, with a total construction area of 28148.26 square meters. Among them, the first and second floors are for commercial use, while the third to eleventh floors are for hotel functions. The building's main structure faces southeast, providing good ventilation and lighting conditions, which helps improve the indoor lighting environment and thermal comfort, thereby effectively reducing the building's operating energy consumption. The axonometric drawing of the building model is shown in Fig. 1.

Fig. 1. Axonometric drawing of the architectural model.

3 Analysis of Key Technical Paths for Near-Zero Carbon Buildings

3.1 Climate Characteristics and Geographical Conditions

Beijing has a typical temperate continental monsoon climate, with distinct four seasons. The winter is cold and dry, while the summer is hot and rainy. From the perspective of climate zoning, Beijing is located in a cold region, with the heating period lasting for 120 to 150 days in winter. The outdoor calculated temperature can drop as low as −9.9 °C, and the heating energy consumption accounts for 55% to 65% of the total building energy consumption. This climatic feature requires that buildings must focus on optimizing the insulation performance of the envelope structure and improving the airtightness level, thereby reducing heating demand at the source and minimizing carbon emissions during operation. Moreover, Beijing is classified as a Class III solar resource area, which has certain potential for solar energy development. Therefore, the climatic conditions in Beijing are highly suitable for promoting the development of near-zero carbon buildings.

3.2 Passive Energy-Saving Technology

Exterior Wall. External wall external insulation technology refers to a practice of adding an insulation layer on the exterior side of the building's exterior walls. It is one of the most widely used and highly energy-efficient insulation methods in current architecture. The core principle is to set up an insulation material layer on the exterior of the wall to effectively block the influence of outdoor temperature fluctuations on the indoor thermal environment. This technology not only significantly improves the insulation performance of the wall, avoids the thermal bridge effect, but also extends the service life of the building structure and reduces the risk of condensation inside the wall.

The exterior wall construction of this project is shown in Table 1. The main structure is a reinforced concrete frame, and the infill walls use autoclaved aerated concrete blocks (the original building's walls). The external insulation system is a thin plastering of rock wool tape, and the fixation method uses heat insulation bridge anchor bolts. The insulation brackets are selected from hard plastic or stainless steel materials. If stainless steel is used, heat insulation bridge treatment will be carried out.

Table 1. Thermal insulation parameters of the enclosure structure.

Parameter category	Measures	Mean heat transfer coefficient	Standard recommended value
Roof	250 mm High-strength graphite polystyrene board	0.16	$0.10 \leq K \leq 0.3$
	250 mm Rock wool fireproof isolation belt		
Exterior wall	250 mm Thick rock wool tape	0.2	$0.10 \leq K \leq 0.3$
Ground	50 mm Extruded polystyrene board	0.24	$0.15 \leq K \leq 0.25$

Roof. The roof, as the horizontal peripheral protective structure at the top of a building, its comprehensive performance directly affects the stability of the indoor thermal environment and the overall energy consumption of the building. On the basis of meeting the insulation and heat insulation indicators in the energy-saving design standards, it is necessary to systematically enhance its long-term reliability and durability. To this end, it is advisable to actively select new waterproof materials with excellent weather resistance and simultaneously optimize the coordinated structure of the insulation layer and the waterproof layer, thereby comprehensively improving the overall performance of the roof. The specific form of the insulation structure adopted in this project is detailed in Table 1.

Exterior Doors and Windows. In the building envelope structure, the external doors, external windows and the ground usually account for 30% to 60% of the total area, with a significant proportion. From the perspective of winter thermal comfort, the inner surface temperatures of these parts are usually significantly lower than those of the exterior

walls, roof and ground, which can easily lead to a sensation of cold radiation. Due to the differences in their heat transfer mechanisms, different insulation strategies should be adopted in thermal design compared to the walls, etc. [10]. For this project, the external windows use aluminum alloy insulated profile window frames, and the overall heat transfer coefficient K value is controlled below 1.0 W/(m^2·K). The glass configuration is a three-pane double cavity Low-E inert gas warm-edge structure, with a solar heat gain coefficient (SHGC) of no less than 0.45 to meet energy-saving and comfort requirements. All the east, west and south-facing windows in this case are equipped with central shading louvers. The exterior door should have excellent airtightness, watertightness and wind resistance performance. According to the national standard "Graduations and test methods of air permeability,watertightness,wind load resistance performance for building external windows and doors"(GB/T 7106), its air tightness grade should not be lower than level 8 and its water tightness grade should not be lower than level 6. The installation method of exterior windows is the recessed installation method, and an insulating secondary frame is installed to reduce the adverse effects of installation thermal bridges. When installing exterior doors and windows, strict airtightness treatment must be carried out. The inner side should be sealed with a waterproof vapor barrier, and the outer side should be sealed with a waterproof breathable membrane. The angle steel and wooden spacers used during installation should also be sealed with a waterproof breathable membrane on the outer side.

3.3 Active Energy-Saving Technology

Active energy-saving technology refers to the use of advanced electrical appliances, equipment and systems to actively regulate the internal environment of buildings, aiming to reduce energy consumption and improve energy utilization efficiency. Compared with passive energy-saving technology, active technology is usually used as an auxiliary measure. However, if it can be reasonably selected in combination with regional characteristics, it can significantly enhance the overall energy-saving effect and effectively control costs. Typical active energy-saving technologies include efficient heating and cooling systems, fresh air systems and efficient lighting systems, etc.

Fresh Air System. The first two floors of the commercial area in this case adopt multi-split air conditioners and a fresh air system. According to the commercial functions, full heat exchange fresh air fans are installed and suspended. For the hotel rooms such as guest rooms and offices on the third floor and above, a fan coil unit and fresh air system are used. To achieve centralized fresh air supply, a fresh air room is set up on each floor. The new air heat recovery unit is equipped with a micro electrostatic purification device, with a filtration efficiency (PM2.5) of 97%. Air outlets are provided for functional rooms such as guest rooms and offices; return air is provided for bathrooms. The fresh air is introduced into the bathrooms through the door gaps and then returns through the return air vents; from the bathrooms, it is heated by the new air conditioner and then discharged uniformly through the exhaust vents.

Heating and Cooling System. The cold and heat source technologies play a crucial role in achieving near-zero carbon and carbon neutrality goals, especially in buildings, industries, and regional energy systems. These technologies significantly reduce carbon emissions by enhancing energy efficiency, integrating renewable energy sources, and

enabling flexible regulation of energy demand. For the upper three floors and above of this hotel, the heating and cooling systems use air-source heat pump hot and cold water units. On the first and second floors, commercial areas adopt multi-split outdoor units. Air-source heat pump hot and cold water unit, with the supply and return water temperatures being 7/12 °C in summer and 45/40 °C in winter.

Lighting and Other Energy-Saving Technologies. Efficient lighting technology is the foundation for reducing energy consumption and carbon emissions. Traditional lighting devices, such as incandescent lamps and fluorescent lamps, have the problem of low energy efficiency, converting most of the electrical energy into heat rather than visible light. In contrast, LED technology, due to its outstanding energy efficiency and long lifespan, has become the preferred choice for near-zero carbon lighting. LED lighting can reduce lighting energy consumption by more than 80%, while its longer lifespan also reduces the frequency of product replacements and the resource consumption in the manufacturing process.The lighting design in this case complies with the requirements for lighting power density and illuminance stipulated in the "Standard for Lighting Equipment in Buildings"GB50034-2013. For indoor lighting, LED lamps are to be used, and the luminous efficiency of the electric lamps should not be lower than 100 lm/W. The elevators adopt products with energy-saving traction and control methods, and the elevators should have a sleep function. Water pumps, fans, etc. use high-efficiency energy-saving products and adopt measures such as variable frequency control to save energy. The entrance hall and other areas are equipped with three-color fluorescent lamps, energy-saving lamps, LED lamps and other high-efficiency lighting fixtures, and zone and group control measures are adopted.

Monitoring Measures. The indoor environmental monitoring content of this case includes: indoor air temperature, indoor air humidity, PM2.5 concentration, CO_2 concentration, and VOC concentration. The inner surface temperature of the exterior wall, fresh air volume, indoor air velocity, and indoor environmental noise can be measured on-site using specialized instruments and do not require the addition of a monitoring system. Indoor environmental monitoring is conducted in the hotel lobby and 2% (at least 3) of the guest rooms, as well as energy consumption monitoring for the hotel's overall heating system, air conditioning system, and lighting system.

3.4 Renewable Energy

Following the technical path of "passive priority, active optimization", energy consumption in buildings can be significantly reduced. However, if the main energy source of the building still relies on fossil fuels, it is difficult to achieve the goal of ultra-low energy consumption buildings. Therefore, the integrated application of renewable energy becomes the key to achieving energy efficiency breakthroughs. Among various renewable energy sources, solar energy has significant advantages in the building sector due to its easy accessibility and direct utilization. Beijing is classified as a Class III solar resource area, with an annual solar radiation total ranging from 5000 to 5850 MJ/m^2, providing favorable conditions for the application of photovoltaic and solar thermal technologies. In this case, the building adopted a solar photovoltaic system, with an installed area of photovoltaic modules reaching 961 m^2, and the total annual power generation was

172921.68 kW·h. The air-source heat pump was selected for the air conditioning system, with a cooling energy efficiency ratio (EER) of 3.35 and a heating performance coefficient (COP) of 3.3, further enhancing the overall efficiency of building energy usage.

4 Results and Discussion

Based on the typical characteristics of public buildings in cold regions of Beijing, this study has applied the proposed key technologies for near-zero energy consumption public buildings in engineering practice. Using the thsware, simulations were conducted for building energy consumption and carbon emissions according to the "Public Building Energy Conservation Design Standard" (GB50189-2015) and the "General Specifications for Building Energy Conservation and Renewable Energy Utilization" (GB55015-2021). The performance of the project in terms of energy consumption and carbon emissions was systematically evaluated. Through simulation analysis, it was verified whether the project's technical path met the requirements for near-zero energy consumption buildings stipulated in the "Technical Standard for Near-Zero Energy Buildings" (GB/T 51350-2019), and further compared with the relevant indicators of near-zero carbon buildings in the "Trial Evaluation Standard for Zero-Carbon Buildings" (T/CABEE 080-2024) [11, 12].

4.1 Indoor Parameters and Information on the Enclosure Structure

The indoor design parameters and enclosure structure information of this project are detailed in Tables 2 and 3. In the calculation of load and energy consumption, the enclosure structure refers to the parameters of "Reference Building 1" in Table 3; while in the calculation of carbon emissions, the enclosure structure adopts the parameters of "Reference Building 2" in Table 3 as the reference.

Table 2. Indoor parameters.

Room type	Air conditioning temperature °C	Heating temperature °C	Fresh air volume (m^3/h. p)	Personnel density (m^2/p)	Lighting power density (W/m^2)	Equipment heat dissipation rate (W/m^2)
Guest Room	26	20	30	8	6	13
Bathroom	26	20	30	3.3	6	0
Corridor	26	20	30	20	3.5	0
Office	26	20	30	10	5	13
Equipment Room	–	–	0	0	5	0
Shop	26	20	30	3	9	13

(*continued*)

Table 2. (*continued*)

Room type	Air conditioning temperature °C	Heating temperature °C	Fresh air volume (m^3/h. p)	Personnel density (m^2/p)	Lighting power density (W/m^2)	Equipment heat dissipation rate (W/m^2)
Lobby foyer	26	20	30	20	9	0
Stairwell	26	20	30	20	3.	0

Table 3. Parameters of the enclosure structure.

			Designing buildings	Reference Building 1(GB50189-2015)	Reference Building 2(GB55015-2021)
Average roof heat transfer coefficient [$W/(m^2 \cdot K)$]			0.13	0.45	0.40
Average external wall heat transfer coefficient [$W/(m^2 \cdot K)$]			0.19	0.50	0.50
Exterior overhanging floor slab heat transfer coefficient [$W/(m^2 \cdot K)$]			0.39	0.50	0.50
Exterior window	Heat transfer coefficient [$W/(m^2 \cdot K)$]	East	1.0	2.7	2.0
		South	1.0	2.4	2.0
		West	1.0	2.7	2.0
		North	1.0	2.4	2.0
	Solar heat gain coefficient	East	0.38	0.52	0.40
		South	0.26	0.48	0.40
		West	0.26	0.52	0.40
		North	0.26	–	–

4.2 Load Calculation

As shown in Fig. 2, the cumulative heat load of this designed building is 579707 kWh, accounting for 49.36% of the cumulative heat load of the reference building. The cumulative cooling load is 44.72 kWh, which is 61.71% of the cumulative cooling load of the reference building. From this analysis, it can be concluded that the "passive priority" related technologies can effectively reduce the heat and cooling loads of the building.

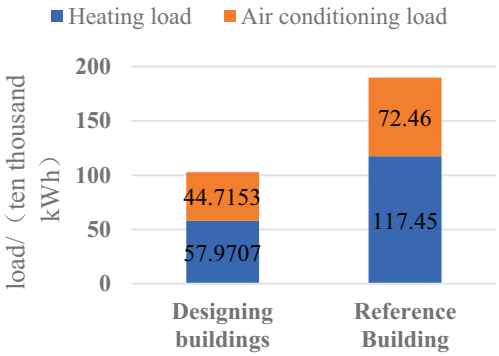

Fig. 2. Annual load of the building.

4.3 Energy Consumption Calculation

Table 4. Summary of total building energy consumption analysis.

	Reference Building	Reference Building 1
Heating energy consumption (kW·h/ m^2)	9.26	27.50
Cooling energy consumption (kW·h/ m^2)	11.99	55.08
Lighting energy consumption (kW·h/ m^2)	36.79	40.66
Elevator energy consumption (kW·h/ m^2)	6.58	6.58
Domestic hot water (kW·h/ m^2)	3.80	1.48
Renewable energy capacity (kW·h/ m^2)	16.87	0
Building energy consumption (kW·h/ m^2)	68.42	131.30
Building comprehensive energy consumption (kW·h/ m^2)	51.54	131.30

According to Fig. 3, the proportion of heating and air conditioning energy consumption in the total energy consumption of the designed building is only 31.05%, which is lower than that of lighting energy consumption; while the heating and air conditioning energy consumption of the reference building accounts for as high as 62.89%, significantly higher than that of lighting energy consumption. Among all energy consumptions, the air conditioning energy consumption of the designed building has the most significant reduction compared to the reference building, being only 21.8% of that of the reference building. In addition, the reference building does not use renewable energy, while the designed building applies photovoltaic and air-source heat pump technologies, with an annual production capacity of 2037887 kW·h, equivalent to an area-specific production capacity of 16.87 kW·h/ m^2. From the analysis results of the total building energy consumption (Table 4), it can be seen that the unit area energy consumption of the designed building is 68.42 kW·h/ m^2, compared to 131.30 kW·h/ m^2 of the reference building, a

reduction of 47.89%. This indicates that the low-carbon key technologies adopted by the designed building have a significant effect on reducing unit area energy consumption.

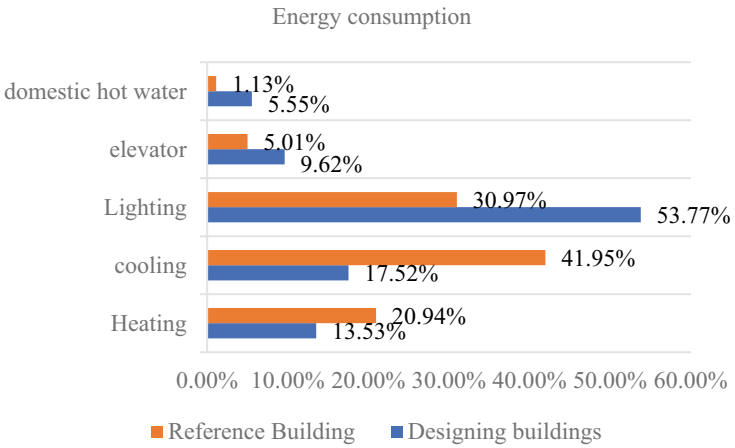

Fig. 3. Composition of building energy consumption.

4.4 Renewable Energy Utilization Rate

The utilization rate of renewable energy refers to the ratio of the amount of renewable energy utilized to the total terminal energy consumption.Terminal energy consumption mainly includes building energy consumption, such as heating, ventilation, air conditioning,lighting, hot water for daily use, and elevator energy consumption.This study calculates the utilization rate of renewable energy based on formula (1),and the specific calculation process is shown in Table 5. The final calculated utilization rate is 40%.

$$R = \frac{EP_h + EP_c + EP_w + \sum E_{r,i} \times f_i + \sum E_{rd,i} \times f_i}{Q_h + Q_c + Q_w + E_l \times f_i + E_e \times f_i} \quad (1)$$

R—Renewable energy utilization rate, %;
EPh—The utilization of renewable energy in the heating system, kW·h;
EPc—The utilization volume of renewable energy in the cooling system, kW·h;
EPw—The utilization of renewable energy in the domestic hot water system, kW·h;
Er, i—The i-type renewable energy power generation volume generated by the annual base capacity, kW·h;
Erd, i—The i-type renewable energy power generation volume generated around the year, kW·h;
fi—Energy conversion coefficient for type i energy sources;
Qh—Annual heating energy consumption, kW·h;
Qc—Annual cooling energy consumption and cooling capacity, kW·h;
Qw—Annual hot water consumption heat energy, kW·h;
El—Annual energy consumption of the lighting system, kW·h;

Table 5. Calculation results of renewable energy utilization rate.

Heating energy consumption (kW·h/ m^2)	18.45
Cooling energy consumption (kW·h/ m^2)	14.23
Elevator energy consumption (kW·h/ m^2)	6.58
Lighting power consumption (kW·h/ m^2)	36.79
Domestic hot water (kW·h/ m^2)	1.31
The utilization of renewable energy in the heating system (kW·h/ m^2)	13.83
Photovoltaic power generation capacity (kW·h/ m^2)	16.87
Utilization rate of renewable energy (%)	40

4.5 Energy Consumption Result Comparison

According to the data in Table 6, the comprehensive energy consumption of the designed building is 51.54 kW·h/ m^2, which is much lower than that of the benchmark building (131.30 kW·h/m^2), accounting for only 39.25% of it. The energy-saving effect is remarkable. Moreover, this building meets the relevant requirements for near-zero energy buildings in the "Technical Standard for Near-Zero Energy Buildings" (GB/T 51350-2019) in terms of the energy-saving rate of the building body, the comprehensive energy-saving rate, and the utilization rate of renewable energy. At the same time, compared with the reference building, its carbon reduction rate has also been further improved.

Table 6. Comparison of energy consumption results.

Indicators	Designing buildings	Reference building	Restriction	Conclusion
Building energy consumption (kW·h/m^2)	68.42	131.30		Meet the requirements for near-zero energy consumption
Building comprehensive energy consumption (kW·h/ m^2)	51.54	131.30		
building energy efficiency improvement rate (%)	47.89		≥30	
building energy saving rate (%)	60.74		≥60	

(*continued*)

Table 6. (*continued*)

Indicators	Designing buildings	Reference building	Restriction	Conclusion
utilization rate of renewable energy (%)	40		≥10	

4.6 Building Carbon Emissions

This project reduces the energy demand of buildings through optimizing architectural design, improves the efficiency of energy equipment and systems, and utilizes renewable energy resources. The calculation results of building carbon emissions are shown in Table 7. The carbon emission of the designed building is 21.53 kgCO2/(m^2·a), which is 50.75% lower than the baseline building's carbon emission (43.72 kgCO2/(m^2·a)), meeting the near-zero carbon building carbon emission indicators stipulated in Article 4.2.4 of the "Zero Carbon Building Evaluation Standard" (Trial) T/CABEE 080-2024 and "Zero Carbon Building Evaluation Standard" (Trial) T/CABEE 080-2024.

Table 7. Calculation results of building operating carbon emissions.

Category	Energy form	Designing the carbon emissions of buildingskgCO_2/(m^2·a)	Baseline building carbon emissionskgCO_2/(m^2·a)
Cooling supply	Electricity	2.88	6.78
Heating	Electricity	2.01	0.68
Air conditioning fan	Electricity	2.38	5.22
Lighting	Electricity	6.27	7.91
Power socket equipment	Electricity	8.08	9.00
Elevator	Electricity	1.35	1.50
Exhaust fan	Electricity	1.24	1.38
Cooking	Electricity	0.00	0.00
Photovoltaic	Electricity	3.45	–
Carbon emission intensitykgCO_2/(m^2·a)		21.53	43.72
Carbon reduction rate kgCO_2/(m^2·a)		50.75%	

5 Conclusion

This article takes a hotel in Tongzhou District of Beijing as an example, providing specific references for the construction of zero-carbon buildings in the Beijing area and proposing new ideas for their promotion. In the research, a systematic review was

conducted on the "passive technology + active technology + renewable energy" key near-zero-carbon technology system applicable to this region, and energy consumption and carbon emission simulations were carried out using the thsware. The results show that, on the basis of meeting the standards of near-zero energy consumption buildings, this project further has the feasibility of transforming into a near-zero-carbon building. The simulation data confirm that, compared with conventional buildings, constructing near-zero energy consumption buildings can achieve significant carbon reduction, providing a powerful technical path and practical basis for promoting the low-carbon transformation in the building sector in Beijing.

Acknowledgments. This research was funded by Beijing Dongcheng District Outstanding Talent Nurturing Program, grant number 2024-dchrcpyzz-49. The authors would like to express their gratitude to all the people and organizations involved in this study.

References

1. Building Energy Conservation Research Center, Tsinghua University: China Building Energy Saving Annual Development Research Report 2024 Beijing, p. 10. China Constr. Ind. Press (2024)
2. Han, L., Li, Z., Fu, Y., et al.: Analysis of key technological pathways for zero-carbon buildings in Ningxia region J. Heat. Ventil. Air Condit. ***55***(06), 144–148 (2025). https://doi.org/10.19991/j.hvac1971.2025.06.20
3. Zhang, S., Wang, K., Xu, W.: Research on carbon emission control index of low-carbon, nearly zero-carbon and zero-carbon public buildings. J. Build. Sci. ***39***(02), 1–10+35 (2023). https://doi.org/10.13614/j.cnki.11-1962/tu.2023.02.01
4. Zhang, S., Liu, C., Wang, K., et al.: Research on definition and calculation boundary of zero carbon building. J. Build. Sci. **38**(12), 283–290 (2022). https://doi.org/10.13614/j.cnki.11-1962/tu.2022.12.34
5. Yu, J., Zhang, L., Zhang, Z., et al.: Research on key technologies and strategy demonstration applications of zero-carbon buildings. J. Railway Constr. Technol. **12**, 1–5 (2025). https://doi.org/10.3969/j.issn.1009-4539.2025.12.001
6. Dou, M., Zhang, Y., Liu, Y., et al.: Research on zero carbon design methods for medical buildings in solar-enriched areas: a case of the Tibet Hospital of the West China Second University Hospital of Sichuan University. J. World Archit. **07**, 84–89 (2025). https://doi.org/10.3969/j.issn.1002-4832.2025.07.012
7. Feng, G., Chen, F., Chang, S.: Multi-objective optimization of envelope structure for near zero energy building. J. Shenyang Jianzhu Univ. (Nat. Sci.). **39**(04), 699–706 (2023). https://doi.org/10.11717/j.issn:2095-1922.2023.04.14
8. Xu, W., Zhang, T., Kang, Y., et al.: Research on carbon emission technologic pathway for nearly-zero energy buildings in cold regions. J. Build. Sci. **39**(04), 1–8 (2023). https://doi.org/10.13614/j.cnki.11-1962/tu.2023.04.001
9. He, F., Nie, J.: Research on thermal insulation materials and suitable thickness of exterior wall of nearly zero-energy consumption building. J. Gas Heat. **42**(07), 15–20 (2022). https://doi.org/10.13608/j.cnki.1000-4416.2022.07.007

10. Xi'an University of Architecture and Technology. Introduction to Green Buildings (Second Edition), pp. 98–100. China Archit. Build. Press, Beijing (2020)
11. China Academy of Building Research: GB/T 51350-2019 Technical Standard for Nearly Zero Energy Buildings Beijing. China Archit. Build. Press (2019)
12. China Association of Building Energy Efficiency: T/CABEE 080-2024 Testing and Evaluation Standard for Zero Carbon Buildings Beijing. China Archit. Build. Press (2024)

Automated Evaluation Methods for Open-Ended Question in Hydropower Domain Based on Large Language Models

Yubin He[1], Lizhi Wang[1], Wei Luo[1,2], Xinpeng Yu[2], Yingjia Li[2], Dingxiao Liu[3], Minghui Guo[3], Shiruo Hu[2], and Jianshi Zhao[2(✉)]

[1] CHN Energy Dadu River Big Data Services Co., Ltd., Chengdu 610041, China
[2] Dept. of Hydraulic Engineering, Tsinghua Univ., Beijing 100084, China
zhaojianshi@tsinghua.edu.cn
[3] Zhipu AI, Beijing 100084, China

Abstract. To address the issues of poor domain adaptability, low efficiency, and high subjectivity associated with manual evaluation of Large Language Models (LLMs) in hydropower open-ended question, this paper proposes an automated evaluation method based on the automatic extraction of assessment criteria from reference answers. This method transforms the evaluation of open-ended questions into quantifiable two-dimensional metrics: content coverage and expression clarity. Based on a constructed hydropower professional Q&A dataset (Hydro-QA), comparative experiments reveal that automated scoring using Qwen-2.5 and GLM-4-plus achieves high consistency with human scoring, demonstrating the feasibility of structuring the evaluation task for open-ended questions. Furthermore, applying this method to evaluate the training effects of LLMs reveals evolutionary patterns regarding domain knowledge and language capabilities: while incremental pre-training increases knowledge density, it leads to a temporary degradation in language capability; conversely, Supervised Fine-Tuning (SFT) successfully achieves an improvement in language capability and significantly enhances knowledge alignment. This paper provides a low-cost, highly reliable evaluation scheme and an empirical basis for training optimization for vertical LLMs in the hydropower field.

Keywords: Large Language Model (LLM) · Hydropower · Automated evaluation · Key point extraction; Supervised Fine-Tuning (SFT) · Open-ended question scoring

1 Introduction

With the advancement of smart hydropower construction, Artificial Intelligence (AI) technology is reshaping the information processing paradigm of the water resources and hydropower industry [1–3]. From reservoir operation optimization [4] to the automated extraction and query of hydropower regulations [5], intelligent applications have placed unprecedented demands on the accuracy and efficiency of knowledge acquisition. In

© The Author(s), under exclusive license to Springer Nature Switzerland AG 2027
G. Feng et al. (Eds.): ICCE 2025, SUCI, pp. 309–322, 2027.
https://doi.org/10.1007/978-3-032-32237-1_22

recent years, Large Language Models (LLMs) represented by ChatGPT [6], GLM [7], Deepseek [8, 9] and Qwen [10, 11] have demonstrated immense potential in solving complex problems in vertical domains due to their powerful natural language understanding and generation capabilities [12]. Compared with traditional methods, LLMs can assist engineering technicians in decision support and knowledge retrieval through generative Q&A in a more natural way that aligns with human thinking habits.

However, the stunning performance of LLMs in general domains does not mean they can be directly transplanted to the hydropower field, which has an extremely high professional threshold. The hydropower industry involves a vast number of technical terms, complex engineering logic, and strict regulations (such as flood control instructions and equipment operation procedures). When answering such questions, models are prone to "Hallucination" [13], generating answers that appear fluent but are factually incorrect. Therefore, objectively and accurately evaluating the performance of LLMs in hydropower professional scenarios has become a prerequisite for model selection, training optimization, and practical application.

Currently, evaluation research on LLMs is mainly divided into close-ended and open-ended question evaluations, but both have significant limitations when applied to the hydropower domain. First, mainstream evaluation benchmarks (e.g., MMLU [14], C-Eval [15]) mainly use multiple-choice questions. While this facilitates automated accuracy statistics, it cannot accurately reflect actual scenarios of human-model interaction. In practical engineering applications, user questions are often open-ended (e.g., "Please briefly describe the operation principles of a certain hydropower plant during the dry season"), requiring the model to generate long-text responses. Pure multiple-choice evaluation is difficult to assess the model's logical reasoning, language organization, and comprehensive knowledge application capabilities. Second, traditional automated evaluation metrics for generative long text (e.g., BLEU [16], ROUGE [17]) are mainly based on N-gram overlap to calculate similarity. In professional Q&A, the same concept may have multiple expressions (e.g., "outflow discharge increases" vs. "release flow increases"), leading to traditional metrics failing to capture semantic correctness, with results often diverging from human cognition [18]. Therefore, the most reliable evaluation method remains expert manual evaluation. However, expert resources in the water conservancy field are expensive. Facing the massive Q&A data generated during model iteration, manual evaluation is time-consuming and labor-intensive, and is susceptible to subjective factors, fatigue, and inconsistent evaluation standards, leading to poor reproducibility. Recently, academia has begun exploring the use of strong models (such as GPT-4) as "judges" to evaluate weak models [19], but without domain knowledge injection, general LLMs struggle to identify subtle, highly professional errors.

In view of the above challenges, establishing an open-ended question automated evaluation framework that balances efficiency and accuracy is urgent. This paper proposes an automated evaluation method for open-ended Q&A. First, utilizing the powerful information extraction capability of LLMs, 3–5 core assessment criteria (Key Points) are extracted from the standard reference answer; subsequently, the scoring task is transformed into a logical judgment task of "whether the model's answer covers these criteria." By structuring the evaluation process, subjectivity is significantly reduced while retaining the assessment of semantic understanding. Meanwhile, the method is divided

into two dimensions: content and language. The former tests the coverage and accuracy of the assessment criteria, while the latter evaluates the clarity and logic of the LLM's expression, achieving a comprehensive evaluation of model capabilities.

To verify the effectiveness of this method and explore the application potential of domestic LLMs in the water conservancy field, this paper carried out the following work: (1) Construction of a Hydropower Professional Open-ended Evaluation Dataset (Hydro-QA): Manually created 409 Q&A pairs covering three cognitive levels: concept explanation, fact introduction, and comprehensive understanding, equipped with standard reference answers. (2) Validation of Automated Evaluation Method: Compared the performance of mainstream domestic models such as DeepSeek-R1, GLM-4-plus, and Qwen-2.5 in automated evaluation. Experiments found that GLM-4-plus and Qwen-2.5 have high consistency with human expert scoring, proving that this method can replace some manual evaluation work. (3) Evolutionary Analysis of Training Effects in the Specific Domain: Based on the above method, the general base LLM GLM-32B, as well as LLMs adapted to the domain via incremental Pre-training (PT) [20] and Supervised Fine-Tuning (SFT) [21], were evaluated to explore the training effects of different methods, providing references for LLM training strategies in the hydropower field.

2 Methodology

This paper proposes a two-stage automated evaluation method based on key assessment criteria extraction. This method decomposes the complex unstructured open-ended evaluation task into content and language dimensions, simulating the scoring logic of human experts by introducing LLMs.

The automated evaluation process, as illustrated in Fig. 1, includes three main steps:

1. Assessment Criteria Extraction Phase: Use an LLM to extract core knowledge elements from the standard reference answer to construct the scoring basis.
2. Model Answer Generation Phase: The Tested LLM generates an answer based on the question.
3. Scoring Phase: The Judge LLM scores the model's answer in both content and expression dimensions based on the extracted criteria and preset scoring strategies. Ideally, an expert agent in the hydropower domain should possess both domain precision and linguistic professionalism. Unlike traditional n-gram-based metrics which entangle lexical overlap with semantic correctness, our framework employs an orthogonal dual-metric system. The Content Dimension metric strictly measures the recall rate of technical constraints and factual key points, acting as a hard constraint for safety-critical applications. In contrast, Expression Dimension assesses the structural clarity, terminology standardization, and logical coherence of the response. This decoupling allows us to identify confident hallucinations—responses that are linguistically highly normative and fluent but factually inaccurate—which are particularly dangerous in industrial decision-making contexts. For a given question Q and standard reference answer A_{ref}, and the answer A_{model} from the Tested LLM, the final score S can be expressed as:

$$S = \alpha \times S_{content}\left(A_{\mathrm{mod}el}, A_{ref}\right) + \beta \times S_{\mathrm{exp}ression}\left(A_{\mathrm{mod}el}\right) \tag{1}$$

Where $S_{content}$ and $S_{expression}$ are the content and expression score respectively, both with a maximum of 5 points; α, β are weight coefficients, which can be set as needed (this study analyzes the two dimensions independently).

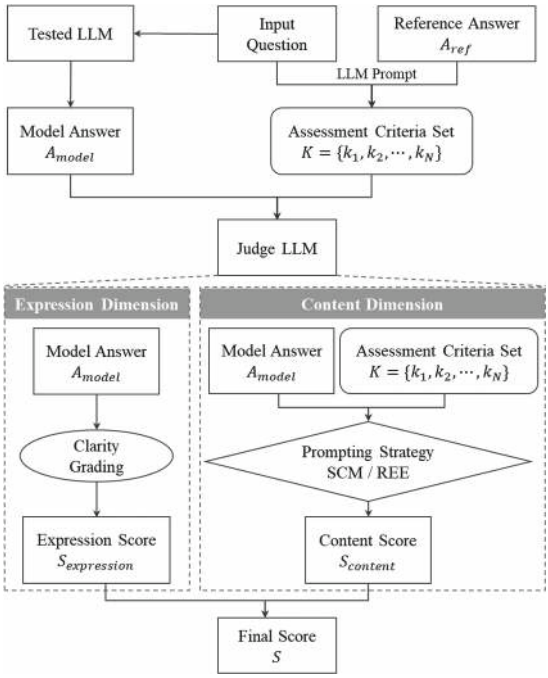

Fig. 1. Flowchart of the automated evaluation method for open-ended questions.

2.1 Assessment Criteria Extraction Based on Reference Answers

The core difficulty of content evaluation lies in judging answers that are semantically correct but expressed differently. To solve this, this paper adopts a feature extraction approach instead of directly comparing text similarity. In hydropower domain texts, a single standard answer often contains multiple logical constraints and numerical parameters. A simple extraction might treat this as a whole, leading to ambiguous scoring if the model only partially answers. Therefore, our method utilizes the complex reasoning chains of LLMs to break down the standard answers into independent semantic units. This granular decomposition ensures that the subsequent scoring process transforms from a vague subjective judgment into a deterministic matching task, significantly reducing the variance in the automated evaluation. We input the standard reference answer A_{ref} into an LLM and require the model to identify and extract N assessment criteria covering the core logic of the answer, denoted as set $K = \{k_1, k_2, \ldots, k_N\}$.

$$K = \mathrm{LLM}_{extract}\left(A_{ref}, \mathrm{Prompt}_{extract}\right) \tag{2}$$

Where the value of N is dynamically determined based on the length of the reference answer, usually set to 3 ~ 5. For example, for the question "*define ecological flow*," criteria might include key elements like "*maintaining river ecosystem health*," "*minimum flow*", and "*specific time periods*". This step transforms unstructured text into a semi-structured set of knowledge points, providing an objective basis for subsequent scoring. $\text{Prompt}_{extract}$ is the LLM prompt used for extraction.

2.2 Content Dimension Scoring Strategy

To investigate the impact of different evaluation instructions on scoring accuracy, this paper designs two differentiated prompt strategies, representing "Rule-Driven" and "Expert-Driven" evaluation paradigms respectively.

Strategy 1: Strict Criteria Matching (SCM) This strategy aims to eliminate subjective uncertainty in the evaluation process, simplifying the scoring task into a "criteria coverage rate" calculation. In this mode, the Judge LLM can only see the criteria set K, not the full reference answer. The scoring function S_{SCM} maps the score based on the proportion R of criteria k_i covered by the model answer A_{model}.

$$R = \frac{\sum_{i=1}^{N} \mathcal{F}(k_i \in A_{\text{model}})}{N} \tag{3}$$

Where $\mathcal{F}(\cdot)$ is an indicator function, taking 1 when criterion k_i is correctly mentioned in the answer (judged by the Judge LLM), and 0 otherwise. The scoring standards are shown in Table 1.

Table 1. Standards of Strict Criteria Matching Strategy.

R	S_{SCM}
$R = 100\%$	5
$R \in [80\%, 100\%)$	4
$R \in [60\%, 80\%)$	3
$R \in [40\%, 60\%)$	2
$R \in [20\%, 40\%)$	1
$R \in [0\%, 20\%)$	0

This strategy forces the Judge LLM to perform strict logical retrieval via prompts, minimizing model hallucination.

Strategy 2: Reference-Enhanced Evaluation (REE) This strategy aims to simulate the comprehensive judgment logic of human experts, suitable for comprehensive questions with complex logical relationships. In this mode, the Judge LLM receives both the full reference answer A_{ref} and the criteria set K. The scoring instruction introduces flexible mechanisms: (1) Rigid constraint on core concepts: Criteria involving definitions or formulas must be accurate; (2) Partial information tolerance: Discretionary handling

is allowed for non-core criteria. This strategy gives the Judge LLM certain discretion to solve the problem of missed judgments due to rigid wording but also increases the risk of subjective bias.

To mitigate the potential instability and black-box nature of LLM evaluations, we integrated a thinking mechanism. Instead of generating a direct numerical score, the Judge LLM is instructed to perform a step-by-step alignment analysis. Specifically, the Judge LLM must first explicitly list the evidence found in the tested LLM's response that corresponds to each extracted key point, and explain the deduction for any missing points, before concluding with a final score. This paradigm not only improves the interpretability of the evaluation results but also forces the model to engage in deeper semantic matching rather than superficial pattern recognition.

2.3 Expression Dimension Evaluation

Expression dimension evaluation aims to independently examine the expression quality of the text generated by the LLM, without involving the correctness of professional knowledge. Addressing issues like repetition, logical confusion, and poor fluency common in long text generation, the scoring standard quantifies language quality into an integer score $S_{expression}$ from 0 ~ 5. The scoring standards are shown in Table 2.

Table 2. Standards of language expression score.

Level	Standard
"Anthropomorphic": High-level Expression (5 pts)	5 pts.: The answer is clear, easy to understand, fluent, natural, has extremely high consistency with human expression, and contains no meaningless sentences.
"Tool-like": Effective Expression (3 ~ 4 pts)	4 pts.: Logic is clear, key information is effectively conveyed, and there is absolutely no repetition. 3 pts.: Language quality is acceptable, contains sufficient information, and has absolutely no repetition.
"Unusable": Low-quality Expression (0 ~ 2 pts)	2 pts.: Expression is obscure and difficult to understand, or there is repetitive content. 1 pts.: Inaccurate wording, confused logic, contains obvious repetition. 0 pts.: Severe confusion, or a large amount of meaningless text piling.

To effectively evaluate common repetition and "hallucination" issues, we introduced strict hard constraints in the evaluation instructions. Once repetitive sentences or paragraphs are detected, the maximum score is forced to be limited to 2 points or less. If the answer contains large sections of general corpus or nonsense irrelevant to the question, the score is also limited to 2 points or less.

3 Experimental Setup and Data

3.1 Hydropower Domain Open-Ended Evaluation Benchmark (Hydro-QA)

This paper constructed a dataset, Hydro-QA, containing 409 Question-and-Answer pairs. All questions were manually created, sourced from authoritative textbooks, national/industry technical standards, and official bulletins. They cover nine major knowledge domains including Hydraulic Background Knowledge, Hydraulics & River Dynamics, Hydraulic Engineering Construction, Water Project Management, Hydropower Operations & Maintenance, Electrical Engineering, Atmospheric Sciences, Eco-Environmental Systems, Water Resources & Hydrology. To comprehensively assess model performance across different cognitive levels, questions are divided into three types, shown in Table 3.

Table 3. Question types in the evaluation dataset for hydropower, Hydro-QA.

Type	Definition	Example
Concept Explanation (~45%)	Questions on definitions of proper nouns in the hydropower domain, testing knowledge coverage.	(1) What is a river corridor? (2) Define unit discharge. (3) Define ecological flow.
Fact Introduction (~35%)	Questions on basic methods, common sense, and professional content, testing summarization and expression of factual knowledge.	(1) Introduce the Xinanjiang model. (2) What is the overall layout of the South-to-North Water Diversion Project? (3) Which are the major international rivers in Northeast China?
Comprehensive Understanding (~20%)	Questions on engineering applications or comparison/analysis based on professional knowledge.	(1) What are the main relationships between research on hydrology and water resources? (2) Describe the method for drawing the basic dispatch line during the water supply period. (3) What role does the relay station at the plant entrance play in a hydrological information reporting system?

Standard reference answers underwent two rounds of expert review to ensure correctness, which were also source corpus of assessment criteria extraction.

3.2 Experimental Model Configuration

Criteria Extraction LLM. DeepSeek-R1 [9], which has significant advantages in reasoning, was used.

Judge LLMs. Three representative LLMs were selected: (1) DeepSeek-R1 [9]: Open-source reasoning-enhanced model; (2) GLM-4-plus [7]: Base model by Zhipu AI, strong in long-context understanding; (3) Qwen-2.5 [10]: General LLM by Alibaba, with advantages in Chinese context understanding.

Tested LLMs. To verify the sensitivity of the automated evaluation method for open-ended questions during the model training process, we used three different versions of the same base model at various adaptation training stages in the hydropower domain as tested LLMs: (1) Base Model: GLM-32B, a closed-source model with a parameter scale of 32 billion, which has not been exposed to specially curated hydropower domain corpus; (2) Pre-trained (PT) Model: Base model enhanced with 500GB of hydropower professional data by incremental pre-training; (3) Supervised Fine-Tuned (SFT) Model: PT Model fine-tuned with 100 k pairs of professional Q&A data.

To ensure fair comparison and reproducibility, strict hyperparameter controls were applied across all evaluated models. For the generation of responses (the Tested LLMs), we set the temperature to 0.7 to balance response diversity with coherence, simulating a realistic user interaction scenario. However, for the Judge LLMs, we strictly limited the temperature to 0.1. This low-temperature setting is crucial for the evaluation phase as it minimizes randomness in the scoring process, ensuring that the Judge produces deterministic and consistent assessments when presented with identical input pairs, thereby enhancing the reliability of the automated metric.

3.3 Evaluation Metrics

To validate the alignment between our automated method and human judgment, we established a high-quality human baseline. We recruited three PhD students specializing in hydraulic engineering formed an expert panel to provide manual evaluation scores (0 ~ 5). To mitigate subjective bias, a blind review process was adopted where annotators scored responses without knowing the model source. Prior to the formal evaluation, a calibration session was conducted on a pilot set of 50 questions, where the annotators discussed discrepancies to align their scoring standards.

To measure consistency, we analyze the distribution of the difference $\Delta S = S_{auto} - S_{human}$, focusing on the Exact Match Rate ($\Delta S = 0$) and Acceptable Error Rate ($\Delta S \leq 2$). The Sum of Squared Errors (SSE) is calculated to measure the dispersion of scoring deviation (Eq. 4). A lower SSE indicates that the automated scoring is closer to the human benchmarks.

$$SSE = \sum (S_{auto} - S_{human})^2 \tag{4}$$

4 Results

4.1 Effectiveness of Automated Evaluation Method

In this section, the Tested LLM is SFT model. We evaluate the performance of three Judge LLMs under two distinct prompting strategies, SCM and REE. Using human scoring as the benchmark, we aim to identify the optimal evaluation scheme.

Scoring Consistency of Different Judge LLMs and Strategies. In the content dimension, Fig. 2 illustrates the evaluation performance of different Judge LLMs under two distinct prompting strategies. Qwen-2.5 with the rigid SCM strategy showed the best human alignment, with an Exact Match Rate of 42.79% and low SSE. GLM-4-plus also performed well, with the lowest SSE under both strategies. Conversely, DeepSeek-R1 deteriorated significantly when switching to the flexible REE strategy (SSE increased from 1235 to 1614). Results reveal two heterogeneities:

1. Robustness difference under fuzzy instructions: REE improved SSE for GLM-4-plus and Qwen-2.5, indicating stronger semantic alignment capabilities. However, DeepSeek-R1 showed increased variance, suggesting potential instruction conflict or over-reasoning when facing fuzzy instructions. When instructed to be flexible (REE), the model's strong reasoning priors drive it to hallucinate plausible justifications for incorrect answers, essentially over-interpreting the Tested LLM's vague statements to force a match with the key points. This results in a high False Positive Rate, inflating the SSE. In contrast, balanced models like GLM-4-plus strike a better equilibrium between instruction following and semantic generalization, making them more suitable as objective judges in technical domains where excessive interpretive flexibility can be detrimental.
2. Trade-off between Precision and Tolerance: REE strategy generally lowered Exact Match Rates but maintained or improved Acceptable Error Rates for high-performing models. The results confirm that rigid SCM offers high precision via mechanical counting, while flexible REE offers tolerance via subjective semantic judgment. Under the REE strategy, the Judge LLM is empowered to interpret implied meanings and contextual nuances, which inevitably introduces a degree of subjective variance (hence the drop in Exact Match). However, this trade-off is theoretically justified and strategically valuable. Consequently, we propose a context-dependent selection criterion: for safety-critical tasks requiring standardized operating procedures (e.g., dam gate operations), SCM should be prioritized to enforce terminological precision; whereas for advisory tasks requiring explanatory depth (e.g., policy interpretation), REE provides a fairer assessment of the model's cognitive utility.
3. In the expression dimension, as depicted in Table 4, SSE for all Judge LLMs (500–700 range) was significantly lower than the content dimension (700–1700), indicating LLMs are mature in judging text fluency.

Adaptability to Different Task Types. In order to explore the boundaries of evaluation performance across varying cognitive levels, Table 5 and Fig. 3 illustrate the results for Concept Explanation, Factual Introduction, and Comprehensive Understanding tasks.

Accuracy of automated evaluation is negatively correlated with task complexity; the simplest Concept Explanation questions typically yield the highest Acceptable Error Rates. In Factual Introduction questions, Qwen-2.5 combined with the rigid SCM strategy demonstrates a dominant advantage, with an Acceptable Error Rate reaching 48.53%. However, for Comprehensive Understanding questions, the Exact Match Rate is relatively low across all models.

Notably, when using the flexible SEE strategy for Comprehensive Understanding questions, GLM-4-plus and Qwen-2.5 achieve significantly better (lower) SSE values compared to the rigid SCM strategy, with Acceptable Error Rates reaching 94.62% and

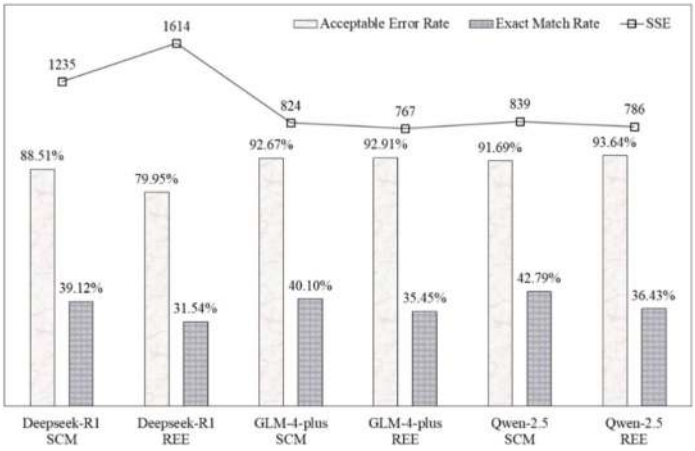

Fig. 2. Consistency of the content dimension between human evaluation and automated evaluation using different combinations of Judge LLMs and prompting strategies.

Table 4. Consistency of the expression dimension between automated evaluation by different Judge LLMs and human evaluation.

Metric	Deepseek-R1	GLM-4-plus	Qwen-2.5
SSE	679	563	671
Exact Match Rate	92.91%	95.35%	94.62%
Acceptable Error Rate	41.08%	40.34%	43.28%

Table 5. SSE between automated evaluation and the human evaluation baseline across different question types.

Type	Deepseek-R1 SCM	Deepseek-R1 REE	GLM-4-plus SCM	GLM-4-plus REE	Qwen-2.5 SCM	Qwen-2.5 REE
Concept Explanation	485	692	328	295	321	344
Fact Introduction	481	566	301	306	293	265
Comprehensive Understanding	269	356	212	166	225	177

95.70%, respectively. This discrepancy stems from the inherent nature of evaluating different task types. Concept Explanation questions typically feature closed, convergent standard answers suitable for simple keyword matching. In contrast, Comprehensive Understanding questions often involve longer logical chains and open-ended expressions. In such tasks, the rigid SCM strategy is prone to misjudgment due to inflexibility,

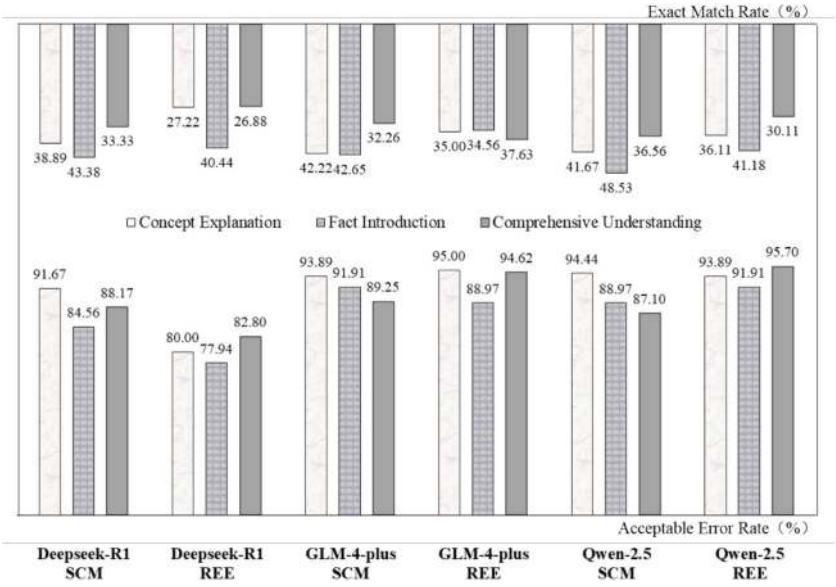

Fig. 3. Error distribution between automated evaluation and the human evaluation baseline across different question types.

whereas the flexible REE strategy allows the model to simulate the semantic fuzzy matching capabilities of human experts, thereby better capturing the intrinsic logical value of the responses. Meanwhile, performance on Factual Introduction questions depends on each model's grasp of the relevant knowledge, exhibiting variations as the Judge LLM changes.

In summary, Qwen-2.5 and GLM-4-plus are reliable judges on the proposed Hydro-QA benchmark. GLM-4-plus with REE strategy is selected as the standard configuration for comprehensive questions in subsequent evaluations.

4.2 Evolutionary Analysis of Domain-Specific LLM Training

In this section, we apply validated evaluation methods and judge configurations to quantitatively assess the training process of the hydropower domain LLM, from Base to PT to SFT. Additionally, we compare the impact of role prompts on the model's performance. Figure 4 illustrates the trends in evaluation scores across the content and expression dimensions for models at different training stages.

In the content dimension, the model demonstrated a significant cumulative effect of knowledge, with scores rising steadily from 2.29 for the Base model to 2.95 after PT, and finally reaching 3.19 in the SFT stage under role prompting. This progression proves that incremental pre-training effectively converts unstructured text into implicit memory, while subsequent SFT enhances the precise retrieval and output of these knowledge.

Conversely, the language dimension exhibited a distinct "V-shaped" reversal. Scores dropped significantly during the PT phase (from 3.71 to 2.48) due to the ingestion

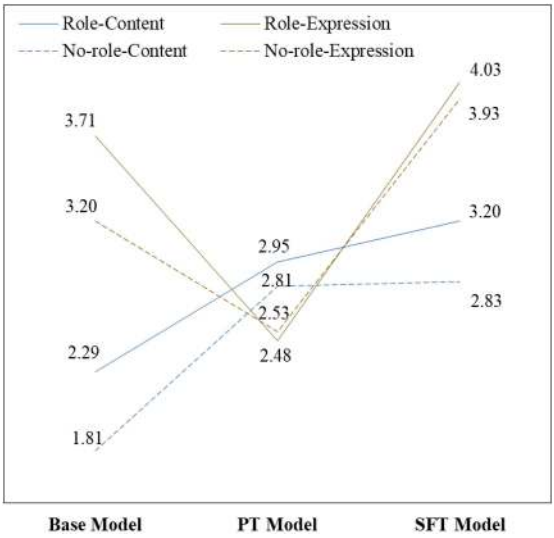

Fig. 4. Evaluation scores of open-ended questions for LLMs at different training stages.

of complex and obscure professional corpora, which caused a temporary loss of general expression capability. The generated responses often resembled raw excerpts from hydropower regulations or technical manuals, characterized by fragmented sentences, excessive use of dry technical jargon, and a lack of connective discourse markers. This suggests that while the model successfully memorized the domain knowledge, the probability distribution of its output shifted towards the statistical patterns of the training corpora (formal documents), suppressing the conversational alignment acquired during its initial general pre-training. The subsequent SFT phase effectively unlocked this knowledge, re-mapping the specialized information back into natural, human-readable syntactic structures. SFT successfully repaired this degradation, with scores rebounding to 4.03 and surpassing the Base model, indicating that SFT is crucial for "alignment" by reshaping language norms while retaining professional knowledge.

Additionally, the analysis of role prompting revealed consistent gains across all stages; even for the specialized SFT model, adding the explicit instruction "You are a hydropower expert" outperformed the no-role mode. From a mechanistic perspective, the specific role prompt acts as a contextual anchor that activates the relevant subspace of the model's latent representation. By explicitly defining the persona as a hydropower expert, the prompt suppresses the retrieval of irrelevant general knowledge and biases the generation towards domain-specific terminology and logic paths. This demonstrates that prompt engineering and fine-tuning are complementary strategies rather than mutually exclusive ones, and combining them maximizes model performance.

5 Conclusion

This paper proposed an automated evaluation method for open-ended question answering in Large Language Models and verified its potential to replace manual evaluation through the construction of the Hydro-QA dataset. Main conclusions are as follows:

1. Experimental results demonstrated that the proposed method effectively transforms unstructured subjective evaluation into quantifiable metrics of content coverage and expression clarity. Specifically, models such as GLM-4-plus and Qwen-2.5 exhibited high stability and consistency with expert scoring. Furthermore, the study identified a task-dependent suitability for scoring strategies: rigid strategies proved more effective for fact-based and concept-explanation questions, whereas flexible strategies incorporating reference answers demonstrated better adaptability for complex, comprehensive questions.
2. Through the application of this method, the study revealed the evolutionary laws of "knowledge-language" capabilities during domain adaption of LLMs. While domain knowledge accumulation showed a monotonic upward trend with training depth, language expression capability exhibited a characteristic "V-shaped" reversal. Incremental pre-training increased knowledge density but caused a temporary loss of general language abilities; however, Supervised Fine-Tuning was critical for reactivating these skills, achieving both knowledge alignment and language recovery. Additionally, explicit role setting in prompt engineering provided consistent performance gains across all training stages.
3. Despite these advancements, the current research has limitations that direct future work. Future research will focus on introducing Multimodal LLMs to evaluate the understanding of charts and images, which are prevalent in actual hydropower scenarios. Furthermore, for high-order decision-making problems such as reservoir operation, Chain-of-Thought (CoT) evaluation mechanisms will be introduced to assess the logical reasoning process of the LLMs more deeply.

Acknowledgement. The work was supported by the Scientific and Technological Innovation Project of CHN ENERGY DIGITALTECH CO., LTD. (No. SZ-DSZ-25-01) and the National Natural Science Foundation of China (No. 52539001)

References

1. Shen, C.J.: A transdisciplinary review of deep learning research and its relevance for water resources scientists. J. Water Resour. Res. **54**(11), 8558–8593 (2018). https://doi.org/10.1029/2018WR022643
2. Tripathy, K.P., Mishra, A.K.: Deep learning in hydrology and water resources disciplines: Concepts, methods, applications, and research directions J. J. Hydrol. **628**, 130458 (2024). https://doi.org/10.1016/j.jhydrol.2023.130458
3. Chang, F.J., Chang, L.C., Chen, J.F.: Artificial intelligence techniques in hydrology and water resources management. J. Water. **15**(10), 1846 (2023). https://doi.org/10.3390/w15101846

4. Bernardes Jr., J., Santos, M., Abreu, T., et al.: Hydropower operation optimization using machine learning: A systematic review J. AI. **3**(1), 78–99 (2022). https://doi.org/10.3390/ai3010006
5. Yang, Y., Chen, S., Zhu, Y., et al.: Intelligent extraction of reservoir dispatching information integrating large language model and structured prompts J. Sci. Rep. **14**(1), 14140 (2024). https://doi.org/10.1038/s41598-024-64954-0
6. Achiam, J., Adler, S., Agarwal, S., et al.: Gpt-4 technical report J. arXiv preprint arXiv: 2303.08774 (2023).
7. Glm, T., Zeng, A., Xu, B., et al.: Chatglm: A family of large language models from glm-130b to glm-4 all tools J. arXiv preprint arXiv: 2406.12793 (2024).
8. Liu, A., Feng, B., Xue, B., et al.: Deepseek-v3 technical report J. arXiv preprint arXiv: 2412.19437 (2024).
9. Guo, D., Yang, D., Zhang, H., et al.: Deepseek-r1: Incentivizing reasoning capability in llms via reinforcement learning J. arXiv preprint arXiv: 2501.12948 (2025).
10. Bai, J., Bai, S., Chu, Y., et al.: Qwen technical report J. arXiv preprint arXiv: 2309.16609 (2023).
11. Yang, A., Li, A., Yang, B., et al.: Qwen3 technical report J. arXiv preprint arXiv: 2505.09388 (2025).
12. Brown, T., Mann, B., Ryder, N., et al.: Language models are few-shot learners J. Adv. Neural Inf. Process. Syst. **33**, 1877–1901 (2020). https://doi.org/10.48550/arXiv.2005.14165
13. Ji, Z.W., Lee, N., Frieske, R., et al.: Survey of Hallucination in natural language generation. J. ACM Comput Surv. **55**(12), 38 (2023). https://doi.org/10.1145/3571730
14. Hendrycks, D., Burns, C., Basart, S., et al.: Measuring massive multitask language understanding J. arXiv preprint arXiv: 2009.03300 (2020).
15. Huang, Y., Bai, Y., Zhu, Z., et al.: C-eval: A multi-level multi-discipline chinese evaluation suite for foundation models J. Adv. Neural Inf. Process. Syst. **36**, 62991–63010 (2023). https://doi.org/10.48550/arXiv.2305.08322
16. Papineni, K., Roukos, S., Ward, T., et al.: Bleu: a method for automatic evaluation of machine translation C. In: Proceedings of the 40th Annual Meeting of the Association for Computational Linguistics, pp. 311–318 (2002). https://doi.org/10.3115/1073083.1073135.
17. Lin, C.Y.: Rouge: A package for automatic evaluation of summaries C. In: Text Summarization Branches Out, pp. 74–81 (2004).
18. Liu, Y., Iter, D., Xu, Y., et al.: G-eval: NLG evaluation using gpt-4 with better human alignment J. arXiv preprint arXiv: 2303.16634 (2023).
19. Zheng, L., Chiang, W.L., Sheng, Y., et al.: Judging llm-as-a-judge with mt-bench and chatbot arena J. Adv. Neural Inf. Process. Syst. **36**, 46595–46623 (2023). https://doi.org/10.48550/arXiv.2306.05685
20. McKinzie, B., Gan, Z., Fauconnier, J.P., et al.: MM1: methods, analysis and insights from multimodal LLM pre-training C. In: European Conference on Computer Vision, Springer Nature Switzerland, Cham, pp. 304–323 (2024). https://doi.org/10.1007/978-3-031-73397-0_18.
21. Dong, G., Yuan, H., Lu, K., et al.: How abilities in large language models are affected by supervised fine-tuning data composition C. In: Proceedings of the 62nd Annual Meeting of the Association for Computational Linguistics (Volume 1: Long Papers), pp. 177–198 (2024). https://doi.org/10.18653/v1/2024.acl-long.12.

Numerical Simulation of Regular Wave Transmission over a Trapezoidal Breakwater Using CIP Model with Adaptive Mesh

Yiyang Zong[1(✉)], Ruian Tie[2], Shengming Cheng[3], Shuangcheng Zhang[4], Hongtao Xu[5], Lingfeng Wang[6], and Shuhao Si[7]

[1] Shanghai Investigation Design & Research Institute, Shanghai 200335, People's Republic of China
390456451@qq.com
[2] Shanghai Academy of AI for Science, Shanghai 200335, People's Republic of China
[3] China Yangtze Three Gorges Investment Management, Shanghai 200335, People's Republic of China
[4] Huaneng (Shanghai) Clean Energy Development, Shanghai 200335, People's Republic of China
[5] Shanghai Electric Power, Shanghai 200335, People's Republic of China
[6] Shanghai Electric Wind Power Group, Shanghai 200335, People's Republic of China
[7] China Railway Construction Harbour & Channel Engineering Bureau Group, Shanghai 200335, People's Republic of China

Abstract. A numerical scheme based on Constrained Interpolation Profile (CIP) method combined with moving mesh technology is proposed for simulating water-wave interaction problem around a trapezoid breakwater. The main idea of the present method is that we can construct an accurate difference formula on one grid point with third-order accuracy and small stencils in comparison with other numerical methods. In this study, for solving advective fluxes, the method is based on a set of piecewise smooth third order constrained interpolants to capture fluid dynamics. This AMR feature enables us to resolve the fine scale structure close to structures at a relatively low cost, as the remaining part of the domain is solved with lower grid resolutions. The method is found very efficient in cases dominated by convection and can be used effectively in simulating free-surface flow problems that involve viscous liquids. In this formulation, we use a Tangent of Hyperbola for Interface Capturing with Slope Weighting (THINC/SW) scheme for tracking liquid-gas interface. where we use the immersed boundary method for wave-breaker interaction. The code has adaptive meshing as well as a distributed memory capability. In the case of two dimensions, simulations take about 8 h (using roughly 300 k cells for simulating 40 s of time). The 3D simulations are much more demanding, requiring approximately 15 h of CPU time (approximately 2,654,208 mesh elements for the 30 s simulation). The results of this study are in good agreement with those reported by other authors, so it is possible to use our model as a reference when analyzing such flows.

Keywords: CIP-based numerical model · Thinc/Sw method · Ibm method · Wave-breakwater interaction

© The Author(s), under exclusive license to Springer Nature Switzerland AG 2027
G. Feng et al. (Eds.): ICCE 2025, SUCI, pp. 323–339, 2027.
https://doi.org/10.1007/978-3-032-32237-1_23

1 Introduction

The Development and Utilisation of marine Spatial Resources in the coastal area and continental Shelf have been more active with the further implementation of the marine Power Strategy in China. The most widespread structures used to protect the coasts are breakwaters, which aid in maintaining calm water in harbours and other coastal regions to ease navigation of ships and building activities. One such example of a rubble-mound breakwater is illustrated below [1]: Rubble mound breakwater can be viewed as a submerged trapezoidal breakwater [2]. Resistance to water waves is what most people consider when designing and constructing a breakwater.

This problem has been researched by many researchers over the last couple of decades. The method of physical model experiment can effectively obtain data on some of the hydrodynamical characteristics, e.g., variations in the surface of waves, their dissipation and transmission, wave pressure and force acting on the breakwater. Lee and Park [3] have examined the Interaction of regular Waves with a Breakwater located at the Rear with a Parapet and propose that this arrangement will Reduce the Maximum Wave Force experienced by the Breakwater. Martinelli [4] altered the form of the parapet and assumed that various forms would affect the waves; Overtopping. Young and Testik [5] conducted an experiment on the effect of a normal wave on a submerged semi-circular breakwater in laboratory conditions, and flow field properties and sediment transport were measured. Hajivalie and MahmoudoF [6] have investigated the issue of energy loss due to wave breaking and vortex when normal waves travel through a rectangular Submerged breakwater.

The recent rise in computational speeds has seen numerous studies on the issue of waves interacting with breakwaters use numerical simulation methods. The interaction between waves and breakwater has been researched by many researchers who have suggested wave models. Baines simulated the effects of ordinary waves on a breakwater using the SPH method [7]. Li [8] used COBRAS numerical model to conduct research on stability of a breakwater when subjected to normal wave attack. Castellino [9] used OpenFOAM to investigate how regular waves affect a breakwater with a recursed parapet. Li [10] modeled a normal wave passing through a submerged breakwater using CIP-based model and momentum source wave maker.

The vast majority of works on these problems have considered them as a plane problem, using a two-dimensional (2D) numerical approach. Within this context, among the different numerical techniques available, the proposed CIP method is more suitable for problems with fluid flow modeled by NavierStokes equations.The novelty here is that we use a high order (third) polyomial interpolation to compute the convection terms in the equation.

Hence, it is quite robust to convection dominant problems and seems a good choice to model the behaviour of free surface flows with small viscosity like dams breaks, free surface flows, sloshing in tanks, surface waves etc., which many recent works have demonstrated the capability of accurately predicting free-surface deformations and loading on structures. However, there are certain drawbacks with using a 2D modeling approach to represent these complicated physical phenomena since a 2D analysis usually considers the impact waves as normal incident onto the structure and which is far less complicated than the real sea state (with waves coming from all directions). When

waves meet an obstacle they reflect and diffract in a non-trivial manner: the reflected and diffracted fields are not uniform. To account for this behaviour, A number of numerical techniques, formulated in 3D, were proposed by researchers. Li & Zhang [11] simulated in OpenFOAM an artificial wave tank for studying the interaction between regular waves and a submerged pile breakwater (simulation run-time was around seven days using 20 cores with 2.6 GHz). In another interesting work, Ye [12] used the model of FSSCAS3D for simulating the interaction between sea waves, breakwaters including rubble-mound breakwaters, caissons or gravity-based structures and also seabeds under these breakwaters. Moreover, in order to predict the forces applied on the face of a rubble-mound breakwater, Choi has carried out some investigations based on numerical modeling using the code called olaFlow [13].

The existing literature is mainly concerned with the flow field characteristics and the dynamic pressures around the breakwater model, where the effects of wave transmissions have been ignored and oblique waves are not considered. Moreover, the standard boundary wave radiation conditions cannot prevent backscattered waves due to 3D geometrical structures,requiring different ways to create waves. In addition, it is worth mentioning that to deal with the 3D problem we have to consider different aspects regarding the computational parallelization as well as about a suitable grid discretization technique.

In order to resolve these aforementioned problems, a new numerical method based on the Constrained Interpolation Profile (CIP) scheme has been developed in present study and employed for simulation of progressive wave over trapezoidal breakwater. In this paper it contains mainly four parts as follows: Firstly, In Sect. 1, we provide some background material. Next we briefly describe the numerical model in the Methods section including governing equations, fluid-structure interaction methods, wave generation/absorption models, as well as moving mesh adaptation algorithms. Next, extensive numerical simulations have been carried out in both 2D and 3D wave tanks to study the interaction between waves and breakwaters. Last but not least, In conclusion, we summarize our main results as follows.

2 Numerical Method

2.1 Governing Equations

The governing equations are the incompressible Navier-Stokes equations and the equation discretization is implemented by using finite difference method. The equations are:

$$\frac{\partial u_i}{\partial x_i} = 0, \tag{1}$$

$$\frac{\partial u_i}{\partial t} + \frac{\partial \left(u_i u_j\right)}{\partial x_j} = -\frac{1}{\rho}\frac{\partial p}{\partial x_i} + \frac{\partial}{\partial x_j}\left[\frac{\mu}{\rho}\left(\frac{\partial u_i}{\partial x_j} + \frac{\partial u_j}{\partial x_i}\right)\right] + F_i, \tag{2}$$

Where u, t, ρ, p, μ represent velocity component, time, density, hydrodynamic pressure and viscosity coefficient, respectively. i, j are the indices. F_i is the momentum force (including volume force, like gravity g). No turbulence model is used in this paper.

The wave-breaking process considered here has been modelled as three-phase flow (liquid, gas and solid). A volume fraction field denoted by ϕ is used to identify which phase(s) are present inside each cell and how they share the properties of that cell. In particular,

$$\rho = \phi_1\rho_1 + \phi_2\rho_2 + \phi_3\rho_3, \tag{3}$$

$$\mu = \phi_1\mu_1 + \phi_2\mu_2 + \phi_3\mu_3, \tag{4}$$

where is the relative amount of each component phases inside each cell; and are water density and dynamic viscosity respectively. ρ_2, μ_2 are related to the second fluid (air) properties respectively, and ρ_3,μ_3 represent physical characteristics of the solid material.

2.2 Treatment of Solid Body Boundary

To begin with, Hirt proposed the FAVOR method to address the issue of fluid-solid interface [14]; Later studies indicate that the FAVOR can be used to address this type of problem quite effectively. It is also used in commercial software Flow3D. The effect on the flow field using this weight method may be achieved depending on solid velocity; subsequently, the velocity at every mesh can be acquired as follows:

$$\overrightarrow{U} = \phi_1 \overrightarrow{u}_{fluid} + \phi_2 \overrightarrow{u}_{air} + \phi_3 \overrightarrow{U}_{solid}, \tag{5}$$

The final speed amplitude in a computational cell is dependent on several terms such as solidity of structures, flow velocity of liquid and gas flow velocity. The computation has three velocities including, where is the volume flow rate ofgas velocity and particle movement. In addition, it is necessary to account for three volume fractions corresponding to liquid fraction, liquid phase, gas phase, and solid phase inside every cell. To perform a correct reconstruction of the solid shape, we first identify the calibration points (red circles in Fig. 1) that will help us to fix the position and form of our solid body. Theneach cell must be divided in to n × n cells, The solid volume fraction of a cell is finally calculated based on the ratio between the number of marked points (black dots in the right plot of Fig. 1) and the number of partitioning cells inside it.

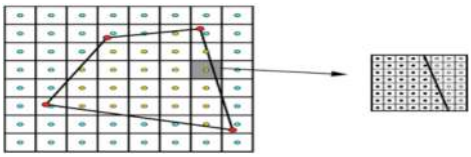

Fig. 1. Schematic representation of the solid shape construction method.

Projection process for the 3rd Dimension is shown in [Fig. 2]. Projection of the 3D object on x, respectively. Thus we have to apply the 2D ray casting method thrice in total: once along x-, once along y- and once along z-axis respectively; finally, using intersection between them we can determine the location of a 3D shape. The above approach allows to compute the value of the volume fraction of the solid phase in every computing cell.

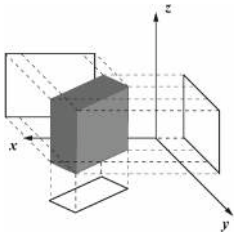

Fig. 2. Schematic representation of the three-dimensional solid treatment.

2.3 Wave Generation and Absorption

In this paper, we employ the wave generation technique by introducing a momentum source term and have altered the original Navier-Stokes momentum equation; namely, we introduced a momentum source term and a damping term on the right side of the momentum equation to achieve water waves.

$$\frac{\partial u_i}{\partial t} + \frac{\partial \left(u_i u_j\right)}{\partial x_j} = -\frac{1}{\rho}\frac{\partial p}{\partial x_i} + \frac{\partial}{\partial x_j}\left[\frac{\mu}{\rho}\left(\frac{\partial u_i}{\partial x_j} + \frac{\partial u_j}{\partial x_i}\right)\right] + F_i + S + A_b, \tag{6}$$

Where, u_i is the velocity vector in all directions, t time, p pressure, p fluid density, μ viscosity coefficient, F_i force term, S momentum source term, A_b damping term. The wave generation technique of momentum source term relies on Boussinesq equations and a view of the wave flume can be found in Fig. 3. The roles of the momentum source term are:

$$S_x^{mom} = -g(2\beta x)\exp\left(-\beta x^2\right)\frac{D(k,\theta)}{\omega}\sin\left[(ksin(\theta))y - \omega t\right], \tag{7}$$

$$S_y^{mom} = gexp\left(-\beta x^2\right)\frac{ksin(\theta)D(k,\theta)}{\omega}\cos\left[(ksin(\theta))y - \omega t\right], \tag{8}$$

Where x is the horizontal coordinate axis, y is the vertical coordinate axis, t the time, ω the wave angle frequency, θ the angle between the wave propagation direction and the x-axis. β determines the width of the wave making area, $\beta = 80/(\sigma^2 {L_{wave}}^2)$. $\sigma = 2\ W/L_{wave}$ is the parameter relevant to the width of the wave generation area. W is the width of the wave generation area and L_{wave} is the wavelength. The source function D uses the following formula,

$$D = \frac{H_0\left(\omega^2 - \alpha_1 g k^4 h_0^3\right)}{\omega I_1\left[1 - \alpha(kh_0)^2\right]}\cos\theta, \tag{9}$$

Where $I_1 = \sqrt{\pi/\beta}\left(-k^2/4\beta\right)$. H_0 is the wave height, h_0 is the water depth, α and α_1 are the parameters of the Boussinesq equations, which have the following relationship:

$$\alpha_1 = \alpha + \frac{1}{3}, \alpha = \frac{z_\alpha^2}{2h_0^2}, \tag{10}$$

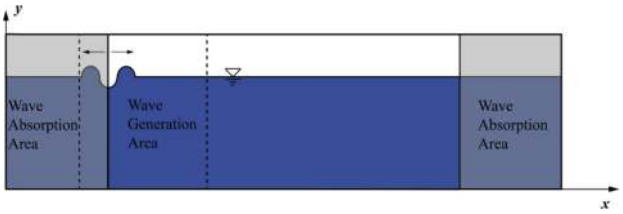

Fig. 3. Schematic diagram for 2D numerical wave flume.

Where $z_\alpha = -0.53\, h_0$.

For the three-dimensional wave flume, we use the L-shape momentum source line to generate wave, which can be found in reference [15]. Figure 4 shows the schematic diagram for 3D numerical wave flume. The blue area is the working area and the yellow area is the momentum source wave maker area. The other grey area is the wave absorption area, which can eliminate the wave secondary reflection.

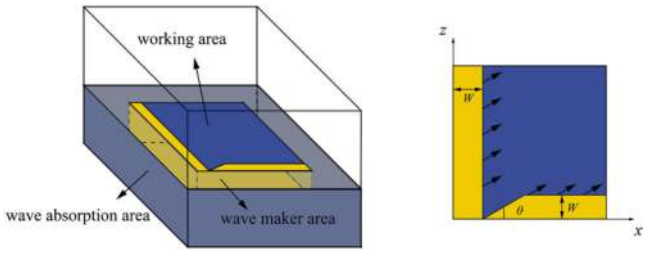

Fig. 4. Schematic diagram for 3D numerical wave flume.

The wave generation formula along the z-axis has been given in Eqs. (11) and (12),

$$S_x^{mom} = -g(2\beta x)\exp\left(-\beta x^2\right)\frac{D(k,\theta)}{\omega}\sin[(ksin(\theta))z - \omega t], \tag{11}$$

$$S_z^{mom} = gexp\left(-\beta x^2\right)\frac{ksin(\theta)D(k,\theta)}{\omega}\cos[(ksin(\theta))z - \omega t], \tag{12}$$

And the formula along the x-axis can be obtained through coordinate transformation as follows,

$$S_x^{mom} = -gexp\left(-\beta z^2\right)\frac{ksin\left(\frac{\pi}{2}-\theta\right)D\left(k,\frac{\pi}{2}-\theta\right)}{\omega}\cos\left[\left(ksin\left(\frac{\pi}{2}-\theta\right)\right)x - \omega t\right], \tag{13}$$

$$S_z^{mom} = -g(2\beta z)\exp\left(-\beta z^2\right)\frac{D\left(k,\frac{\pi}{2}-\theta\right)}{\omega}\sin\left[\left(ksin\left(\frac{\pi}{2}-\theta\right)\right)x - \omega t\right]. \tag{14}$$

Wave absorption method is used to avoid unnecessary wave interference and the following equation is adopted,

$$A_b = 1.8\frac{0.5}{dt}\left(\frac{x - x_{st}}{x_{ab}}\right)^4\left(\frac{y}{h_0}\right)\overrightarrow{u}, \tag{15}$$

Where A_b is the absorption source function, x_{st} and x_{ab} are the initial position and the length of the wave absorption area, respectively. dt is time step. $\overrightarrow{u}$ is the velocity of fluid.

2.4 Adaptive Mesh Refinement Method

Our model is based on a three-layered architecture with a dynamic grid system [16], which relies upon simple 2D data-structures, shown in Fig. 5, where Fig. 5(a) shows a layout of grids. The basic unit for the adaptive model is a rectangle box, with each having N × N cells (N being even). The hierarchy of grids remains simple as every container has cells and a subdivision rule is shared among them. In the refinement step, each box independently splits in to four smaller boxes.

The schematic illustration for 2-Dimensional hierarchical data structure using quadtree technique has been illustrated in Fig. 5(b). In this figure, all circles are representing containers. All white color containers get divided to four small containers. Original white container considered as progenitor container, while the remaining small boxes are called descendant boxes.This configuration builds links between containers from different levels of hierarchy. Yellow-colored, green, and blue have no children containers (i.e., they are terminal containers). When there is a change of mesh counts, the contents of the progenitor, descendant, and terminal containers are updated automatically by the system. The level parameter is a 1-D array which indexes each container and contains containers having the same number of elements in the same level. The maximum number of levels supported by the Afivo code is 30.

The numerical model includes a layer of ghost cells around every computing cell, which are typically only a few (one or two) cells of the AMR grid, see Fig. 5(c). The benefit is that each cell can be computed independently: so that we can compute in parallel. Using interpolations between neighboring calculation zones, we are able to calculate the boundary layer value of every calculation zone as, thus providing couplings of fields on the same level of refinement in the mesh hierarchy.

In this work, we use an Afivo-based geometric multigrid solver for fast solution of the pressure Poisson equation over adaptively refined mesh: Iterative solvers can have trouble converging in a reasonable amount of time if used directly on unstructured meshes, whereas with the use of multigrid algorithms which perform a multi-scale error correction this improvement is close to linear in the computing time. The present approach allows for an efficient implementation of the nested blocks in trees that enable transfers between different levels of grids and maintain a high degree of fidelity to the solution. With minimal additional cost but keeping solutions accurate,the method allows fast simulation of complicated wave-structure interactions for realistic images. The numerical model is capable of representing a wide range of 2D or 3D modeling applications in detail.

To solve the pressure Poisson equation more efficiently on adaptive grids, this paper uses the geometric multigrid method combined with Afivo. Unlike traditional iteration methods that have difficulty converging on non-uniform meshes, multigrid Methods can achieve nearly linear Speedup in Computation time through multi-scale Error correction. Using this method can help us adapt the tree-structured Blocks in our system to effectively restrict data at different grid levels and maintain numerical stability. Without giving up accuracy while significantly lowering the cost, so that it can run fast in high-quality

graphics for complicated wave-wave structure's interference; this basis will allow us to display details well on both 2-dimensional and 3-dimensional occasions.

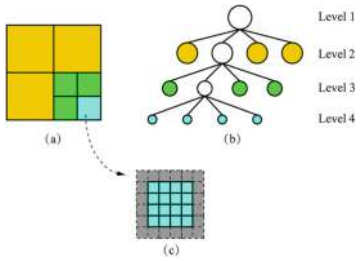

Fig. 5. Illustration of the Afivo adaptive mesh framework in two dimensions: (a) mesh layout; (b) quadtree-based hierarchical structure; (c) box with ghost cells.

To identify the locations at which the places must be coarsened or refined in the domain, it is necessary to provide the respective refinement criteria. The level of refinement, indicator variables and threshold values are some of the refinement criteria in this paper. In case of the problem of interfaces we are concerned with the variation of the fluid interface and solid interface; Hence, Eq. 16 is employed to determine the indicator variable that is related to the volume fraction of the interface. Equation 16 primarily defines the interface Areas based on Different Values of 0 in Adjacent Grids.

$$\delta = \left|\phi_{i-1,j} - 2\phi_{i,j} + \phi_{i+1,j}\right| + \left|\phi_{i,j-1} - 2\phi_{i,j} + \phi_{i,j+1}\right|, \tag{16}$$

Where, δ is the indicator variable. $\phi_{i,j}$ is the value of volume fraction in mesh *(i, j)*. The threshold value δ_{THR} of the indicator variable should also be set. In case the value of 8 is higher than δ_{THR} then it means that cell has to be refined. Otherwise, the cell should be coarsened.

2.5 Flow Solving Process

The Navier-Stokes equations are solved numerically using a second order accurate fraction step scheme for solving decoupling between velocities and pressures [20]. One particular solution method is based on the mathematical theory behind HelmholtzHodge decomposition [21]. There are five steps in computation, where all details are given in previous works [22, 23]. The advection part in space is first treated with the CIP method which is an efficient third-order accurate spatial reconstruction scheme [24], and then the diffusion part is treated asfor the momentum source terms and damping, using a central differencing scheme of second order in space. The pressure is solved by a multi grid method, and then perform the full velocity update. The last step is to calculate the free surface evolution using new velocity information as well as the tangent of hyperbola for interface capturing with slope weighting (THINC/SW) scheme developed by Xiao et al. (2011) [25]. This figure shows a schematic representation of our overall procedure of the fractional-step approach. The adaptive CIP model is implemented as follows: After every time step (Fig. 6), the mesh is refined/coarsened according to the position

of the fluid interface and also that we used a 16-core Intel i7 architecture for our parallel simulations presented here.

.

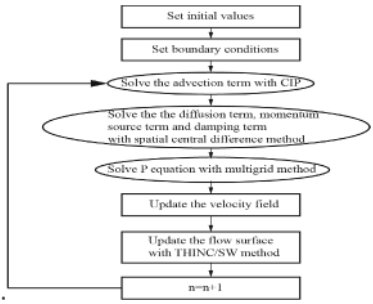

Fig. 6. Flow chart for the fractional step method.

3 Model Application

3.1 Wave Transmission over a Trapezoidal Breakwater (2D)

This section refers to the work of Beji [26] in 1993.Two-dimensional water tank is 40 m long and 0.8 m high. Momentum wave-maker line is set at x = 10 m and the wave generation area is one wave length long. Wave absorption area (10 m long) is arranged on both sides of the water flume, which is used to absorb unwanted waves. The submerged breakwater is 0.3 m high, and is arranged in x ∈ (13.5 m, 24.5 m). The front slope is 1/20, and the rear slope is 1/10. Six measuring points (G1 ~ G6) are arranged to record surface change. Their positions are x = 18.0 m, 20.0 m, 21.0 m, 22.0 m, 23.2 m and 24.8 m. G1 is above the front slope of the submerged breakwater, G2 and G3 are above the crest, G4 and G5 are above the back slope, and G6 is behind the breakwater. See Fig. 7 for details.

Water depth h is 0.4 m. The incident wave period T is 2.02 s and wave height H is 0.02 m. The time step dt is adaptive according to CFL = 0.2, and total solution time is 40 s. The mesh refinement level is up to four and minimum mesh size is 1.6 mm. Total mesh number is about 300000. The CPU time is about 80 min.

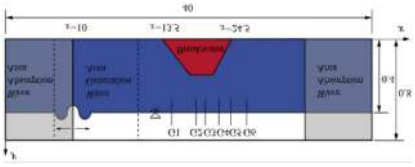

Fig. 7. Schematic diagram for 2D numerical wave flume[m].

Figure 8 shows wave surface variation in t = 5.5 s,12 s and 40 s. It can be observed that when the incident wave travelled to the front end of the submerged breakwater, the nonlinearity gradually increased, and the waveform became sharp. When the wave crossed the submerged breakwater and reached its back, the waveform became gentle, but irregular. When the waves are transmitted to both sides of the flume, they are gradually reduced in the absorption areas. Two enlarged views of water surface and breakwater are plotted beside the Fig. 8(a), which mesh layout are present.

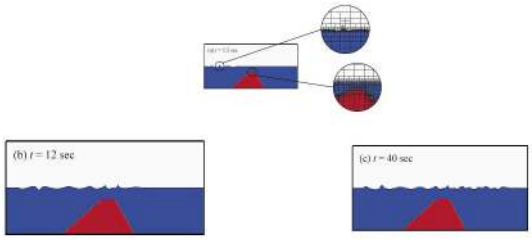

Fig. 8. Wave surface variation in t = 5.5 s, 12 s, 40 s, and circle diagrams indicate the mesh refinement.

The results of Beji [26], Liu [27], Chazel [28] are selected for comparison with the present results, see Fig. 9 below. Time selected for the numerical results is 17 s ~ 23 s in this paper. The numerical results matched the experiment data better, compared with Liu and Chazel, especially the peaks of wave profiles.

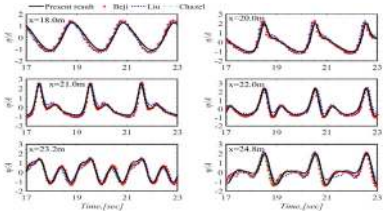

Fig. 9. Comparison of free surface displacements among present result, Beji, Liu and Chazel.

3.2 Wave Transmission over a Trapezoidal Breakwater (3D)

In this section, we used the 3D numerical wave flume presented in this paper to study the reflection and diffraction phenomenon of the oblique regular wave passing over a trapezoidal breakwater. Working condition referred to Xuan Li's work [11] and we did some adjustment.

Wave parameters can be found in Table 1. The water depth h is 0.4 m. The wave period T is 0.78 s. Wave height H is 2.0 cm. Wave propagation direction θ are 30° and 60°.

Table 1. Numerical condition (wave characteristics).

	Wave period T (s)	Wave height H (cm)	Water depth h (m)	Wave propagation direction θ (°)
Case 1	0.78	2.0	0.4	30
Case 2	0.78	2.0	0.4	60

First, we did the mesh convergence tests and verified the accuracy of the three-dimensional wave-making module of the model. As Fig. 10(a) shows, the computational domain is [20 m, 0.8 m, 20 m]. L-shaped momentum source wave maker (yellow area) was used [15]. Figure 10(b) shows the top view of layout. The width of momentum source region is one wave length, which is about 0.94 m. The working area is 10.0 m × 10.0 m. Wave absorption area is set around the working area. The length of the absorption area is 5 m wide. The solution time is 30 s.

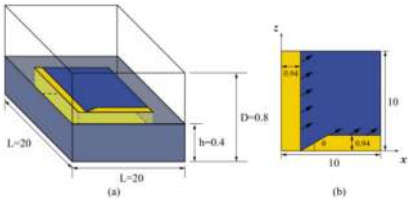

Fig. 10. The parameters of the 3D wave flume[m].

Here we gave out the information about the mesh resolutions and the CPU time. We also gave out the comparison of the wave profile in two sections along the x-axis and z-axis (z = 10 m and x = 10 m) of different mesh resolutions of case 1 [Fig. 11]. It can be seen from the figure that the coarse mesh result is represented by the dotted line, which was deviated from the red line (analytic solution) at the peak positions, while the medium mesh results (circle symbol) and fine mesh results (cross symbol) were in good agreement with the analytic solution. However, the CPU time of the results using the fine mesh is much longer than that calculated by the medium mesh, as shown in the Table 2. Therefore, this paper chooses the medium mesh size (minimum mesh size 0.01 m) for numerical simulations. We also gave out the flow field variation of case 1 [Fig. 12] and case 2 [Fig. 13]. It could be believed that wave-making module of the present model can sufficiently generate directional wave in three dimensions.

Then we put the breakwater in the center of the domain [Fig. 14]. The breakwater characteristics are shown in Fig. 15. The solution time is 30 s. For the interaction cases, the total mesh number is 2654208. Mesh refinement near the breakwater is shown in Fig. 16. Figure 16(a) shows that the meshes near the water interface and breakwater interface were refined but in other regions, meshes with bigger size were used. Figure 16(b) shows the mesh layout at the height of 0.1 m. Considering that the time step needed to be smaller when the wave transmitted over the breakwater, and the position and shape

Table 2. Mesh convergence tests for case 1 and case 2.

	Type	Mesh number (minimum mesh size, m)	CPU time (min)
Case 1 (wave angle 30°)	Coarse mesh	307200 (0.02)	36.83
	Medium mesh	2457600 (0.01)	72.38
	Fine mesh	8294400 (0.0067)	226.17
Case 2 (wave angle 60°)	Coarse mesh	307200 (0.02)	35.28
	Medium mesh	2457600 (0.01)	66.25
	Fine mesh	8294400 (0.0067)	287.33

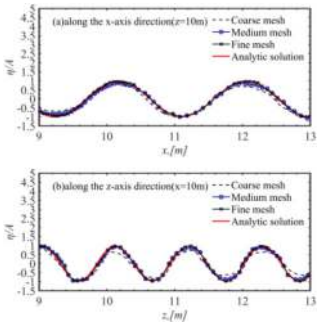

Fig. 11. The comparison of the three mesh resolutions (case 1): (a) free surface displacements in section z = 10 m; (b) free surface displacements in section x = 10 m.

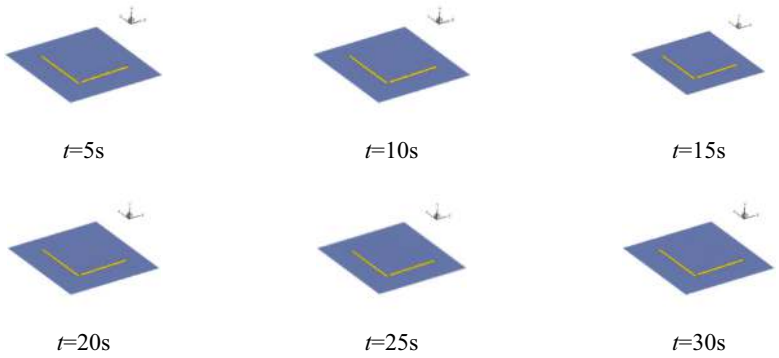

Fig. 12. Flow field variation of case 1 (wave angle 30°).

of the structure needed to be updated at each time step, the CPU time of the interaction cases were longer. Each case cost about 15 h.

The contours of the wave transmission during the time from 5 s to 30 s were shown in the Fig. 17 (case 1) and Fig. 18 (case 2). As shown in Fig. 17 and Fig. 18, both

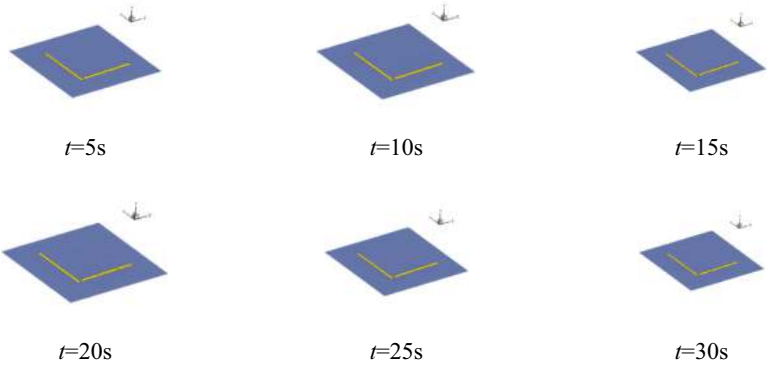

Fig. 13. Flow field variation of case 1 (wave angle 60°).

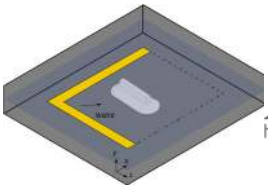

Fig. 14. The layout of the trapezoidal breakwater in the wave flume.

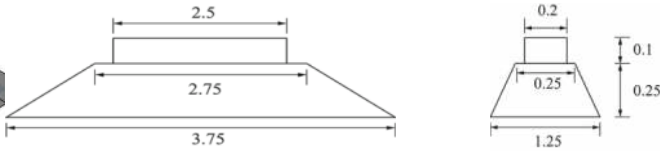

Fig. 15. The characteristics of the trapezoidal breakwater[m]: (a) the longitudinal section of the breakwater; (b) the cross section of the breakwater.

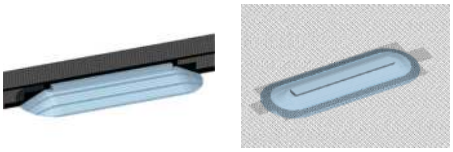

Fig. 16. Mesh refinement near the breakwater: (a) Front view; (b) Bird's eye view.

strong wave reflection and diffraction could be observed when the time is after 15 s. Meanwhile, the transmitted wave height in case 2 is much smaller than that in case 1 because of the reduction of effective breakwater blocking area perpendicular to the incident wave direction. Here we gave out the wave surface variation in the cross section at x = 12 m (after the breakwater, t = 25 s) to make the comparison with Li's work17. From Fig. 19(a), it can be observed that in the range of x = 6.5 m–7.5 m, the wave height decreased significantly. This is because those positions are shielded by the breakwater. Similar conclusions can be found in Li's paper regarding the same range. Similarly, from Fig. 19(b), a significant wave height reduction is evident in the range of z = 10 m–11 m, which is also attributed to the shielding effect of the breakwater. For the case with a wave incident angle of 60°, the wave height in the range of z = 10 m–15 m is noticeably

smaller than that for the 30° case. This is because when the wave incident angle is 60°, the shielding range of the breakwater is much larger.

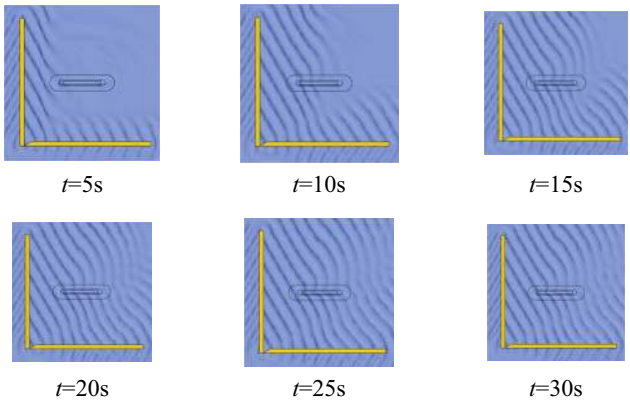

Fig. 17. Contour of case 1 (wave propagation direction $\theta = 30°$).

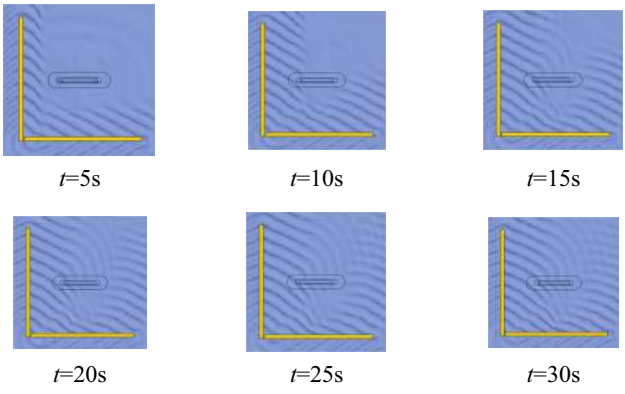

Fig. 18. Contour of case 2 (wave propagation direction $\theta = 60°$).

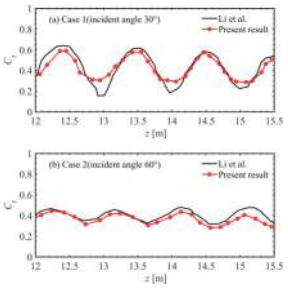

Fig. 19. Comparison of the transmission wave after the breakwater (black line represents transmission coefficient in Li's paper and red dot line represents our present results).

4 Conclusions

In summary, this paper proposes a new CIP numerical model combined with Afivo adaptive mesh framework and also shows the numerical method of this model. The model was applied to the numerical simulation of regular wave transmission over a trapezoidal breakwater. Two-dimensional and three-dimensional cases were both tested. The evolution of flow surface was obtained, which was in good agreement with the previous physical experiments and numerical simulations. It shows that this model has the feasibility and effectiveness to simulate the regular wave-breakwater interaction.

Acknowledgements. This study is partially supported by the National Natural Science Foundation of China (Grant Nos.52571406). The authors gratefully acknowledge the support from the "Top Talent Recruitment and Task Assignment" Program (Grant No. MEMRT2024JBGS01) of the Key Laboratory of Marine Ecological Monitoring and Restoration Technology, Ministry of Natural Resources. This work was also supported by research grants on "Management Models and Key Technologies for Spatial Utilization in the Exclusive Economic Zone and Continental Shelf" provided by China Yangtze Three Gorges Corporation (Contract No. CTGIM-2025-ZC001), Huaneng (Shanghai) Clean Energy Development Co., Ltd., Shanghai Electric Power Co., Ltd., Shanghai Electric Wind Power Group Co., Ltd., and China Railway Construction Harbour & Channel Engineering Bureau Group Co., Ltd.

References

1. Sadeghi, K., Abdeh, A., Al-Dubai, S.: An overview of construction and installation of vertical breakwaters J. Int J Innov Technol Explor Eng. **7**(3), 1–5 (2017)
2. Gedda, A.B., Rao, S.: A review on stability of caisson breakwater water resources and environmental engineering I. Spring, 83–88 (2019). https://doi.org/10.1007/978-981-13-2044-6_8
3. Lee, B.W., Park, W.: Evaluation of the hydraulic performance of a rear-parapet vertical breakwater under regular waves through hydraulic experiments. J. Water. **12**(9), 2428 (2020). https://doi.org/10.3390/w12092428
4. Martinelli, L., Ruol, P., Volpato, M., et al.: Experimental investigation on non-breaking wave forces and overtopping at the recurved parapets of vertical breakwaters. J. Coastal Eng. **141**, 52–67 (2018). https://doi.org/10.1016/j.coastaleng.2018.08.017

5. Young, D.M., Testik, F.Y.: Onshore scour characteristics around submerged vertical and semi-circular breakwaters. J. Coastal Eng. **56**(8), 868–875 (2009). https://doi.org/10.1016/j.coastaleng.2009.04.003
6. Hajivalie, F., Mahmoudof, S.M.: Experimental Study of Energy Dissipation at Rectangular Submerged Breakwater[C]//8th International Conference on Fluid Mechanics (ICFM8). (2018).
7. Baines, A., Cunningham, L.S., Rogers, B.D.: Numerical modelling of wave downfall pressures on the deck landward of a vertical breakwater. (2018). https://doi.org/10.1680/cmsb.63174.1051.
8. Li, M., Hsu, C., Hsu, H., et al.: Numerical analysis of vertical breakwater stability under extreme waves. J. J Mar Sci Eng. **8**(12), 986 (2020). https://doi.org/10.3390/jmse8120986
9. Castellino, M., Sammarco, P., Romano, A., et al.: Large impulsive forces on recurved parapets under non-breaking waves. A numerical study. J. Coastal Eng. **136**, 1–15 (2018). https://doi.org/10.1016/j.coastaleng.2018.01.012
10. Li, M., Zhao, X., Ye, Z., et al.: Generation of regular and focused waves by using an internal wave maker in a Cip-based model. J. Ocean Eng. **167**, 334–347 (2018). https://doi.org/10.1016/j.oceaneng.2018.08.048
11. Li, X., Zhang, W.: 3D numerical simulation of wave transmission for low-crested and submerged breakwaters. J. Coastal Eng. **152**, 103517 (2019). https://doi.org/10.1016/j.coastaleng.2019.103517
12. Ye, J., Jeng, D., Chan, A., et al.: 3D integrated numerical model for fluid-structures-seabed interaction (Fssi): loosely deposited seabed foundation. J. Soil Dyn Earthq Eng. **92**, 239–252 (2017). https://doi.org/10.1016/j.soildyn.2016.10.026
13. Choi, G., Jun, J., Lee, K., et al.: 3D-numerical simulation of wave pressure acting on caisson and wave characteristics near tip of composite breakwater J. J Korean Soc Coastal Ocean Eng. **32**(3), 180–201 (2020). https://doi.org/10.9765/KSCOE.2020.32.3.180
14. Hirt, C.W.: Volume-fraction techniques: powerful tools for wind engineering J. J. Wind Eng. Indus. Aerodyn. **46–47**, 327–338 (1993). https://doi.org/10.1016/0167-6105(93)90298-3
15. Ha, T., Lin, P., Cho, Y.: Generation of 3D regular and irregular waves using Navier–Stokes equations model with an internal wave maker. J. Coastal Eng. **76**, 55–67 (2013). https://doi.org/10.1016/j.coastaleng.2013.01.013
16. Teunissen, J., Ebert, U.: Afivo: a framework for quadtree/octree amr with shared-memory parallelization and geometric multigrid methods. J. Comput Phys Commun. **233**, 156–166 (2018). https://doi.org/10.1016/j.cpc.2018.06.018
17. Brandt, A., Livne, O.E.: Multigrid Techniques: 1984 Guide with Applications to Fluid Dynamics. SIAM (2011). https://doi.org/10.1137/1.9781611970753
18. Hackbusch, W.: Multi-grid methods and applications. Springer Science & Business Media (1985). https://doi.org/10.1007/978-3-662-02427-0
19. Sampath, R.S.: A Parallel Geometric Multigrid Method for Finite Elements on Octree Meshes Applied to Elastic Image Registration. College of Computing Georgia Institute of Technology (2009) https://dl.acm.org/doi/10.5555/1835134
20. Chorin, A.J.: Numerical solution of the Navier-stokes equations. J. Math Comput. **22**(104), 745–762 (1968). https://doi.org/10.2307/2004575
21. Ferziger, J.H., Perić, M., Street, R.L.: Computational methods for fluid dynamics. Springer (2020). https://doi.org/10.1007/978-3-319-99693-6
22. Zhao, X., Hu, C.: Numerical and experimental study on a 2-D floating body under extreme wave conditions. J. Appl Ocean Res. **35**, 1–13 (2012). https://doi.org/10.1016/j.apor.2012.01.001
23. Zhao, X., Ye, Z., Fu, Y., et al.: A cip-based numerical simulation of freak wave impact on a floating body. J. Ocean Eng. **87**, 50–63 (2014). https://doi.org/10.1016/j.oceaneng.2014.05.009

24. Yabe, T., Xiao, F., Utsumi, T.: The constrained interpolation profile method for multiphase analysis J. J Comput Phys. **169**(2), 556–593 (2001). https://doi.org/10.1006/jcph.2000.6625
25. Xiao, F., Ii, S., Chen, C.: Revisit to the thinc scheme: a simple algebraic vof algorithm J. J Comput Phys. **230**(19), 7086–7092 (2011). https://doi.org/10.1016/j.jcp.2011.06.012
26. Beji, S., Battjes, J.A.: Experimental investigation of wave propagation over a bar. J. Coastal Eng. **19**(1–2), 151–162 (1993). https://doi.org/10.1016/0378-3839(93)90022-Z
27. Liu, X., Lin, P., Shao, S.: Isph wave simulation by using an internal wave maker. J. Coastal Eng. **95**, 160–170 (2015). https://doi.org/10.1016/j.coastaleng.2014.10.007
28. Chazel, F., Lannes, D., Marche, F.: Numerical simulation of strongly nonlinear and dispersive waves using a Green–Naghdi model J. J Sci Comput. **48**, 105–116 (2011). https://doi.org/10.1007/s10915-010-9395-9

Numerical Simulation of Simultaneous Closure Scheme for a High-Pier Long-Span Curved Continuous Rigid Frame Bridge

Zhen Fang[1(✉)], Jinyu Ma[2], and Zhibao Cheng[2]

[1] CCCC Comprehensive Planning and Design Institute Co.Ltd., Beijing 100024, China
421467984@qq.com

[2] School of Civil Engineering, Beijing Jiaotong University, Beijing 100044, China

Abstract. To address the problems of long construction period, high cost, and difficulty in controlling creep deflection in the traditional "first span-joint closure followed by mid-span closure" construction method, based on an engineering example of a highway bridge (with a main span of $80 + 2 \times 150 + 80$ m of prestressed concrete continuous rigid frame), the simultaneous closure of the abutment and mid-span technology was studied. A full bridge model was established using finite element software, and the mechanical responses of the closure joint support system, the tensioning framework, and the counterweight scheme were systematically analyzed. The main beam geometry, stress distribution, and the force characteristics of the piers of the two closure schemes were compared, and the construction process was optimized and verified on-site.

Keywords: Continuous rigid frame bridge · Closure scheme · Finite element method

1 Research Background and Current Situation

The proper closure scheme is an important issue of rigid frame bridges, which draws lots of engineers' attention. The first official study in China on the closure scheme of rigid frame bridges began with the construction of the Yellow River Highway Bridge in Dongming, Shandong Province. It was found that the phased closure scheme of closing five spans at once was feasible, and this scheme had good internal force distribution and obvious economic benefits. Recently, You [1] et al. conducted numerical simulations for three closure schemes and the sequence of system transformation, and analyzed the effects of different closure sequences and system transformation sequences on the vertical displacement and stress of multi-span wave-shaped steel flange continuous rigid frame bridge structures. Lin [2] et al. compared the influence of different closure sequences on the stress of the main beam and the cumulative deformation of the main beam and proposed the reasonable closure sequence for multi-span continuous rigid frame bridges with different spans. Jiang [3] et al. established numerical models for different closure schemes. Min [4] et al. built a finite element model for an ultra-high pier multi-span continuous rigid frame bridge, and proposed several closure construction sequence schemes.

© The Author(s), under exclusive license to Springer Nature Switzerland AG 2027
G. Feng et al. (Eds.): ICCE 2025, SUCI, pp. 340–349, 2027.
https://doi.org/10.1007/978-3-032-32237-1_24

Chen [5] et al. used the Midas Civil finite element software to establish a comparison model for sequential closure and simultaneous closure processes. They focused on analyzing the differences in stress distribution and linear deformation patterns of the main beam structure under the two construction methods. Hu [6] et al. compared the vertical displacement of the main beam, the stress at the top and bottom edges of the main beam, and the closure schemes under each closure scheme during the 10-year shrinkage and creep stage. Guo [7] et al. proposed an optimal closure thrust solution method based on the multi-objective linear programming theory. Through in-depth analysis, Huang [8] et al. comprehensively analyzed the factors affecting the top displacement of the main pier of the continuous rigid frame bridge. Li [9] et al. used the bridge finite element analysis software Midas Civil to establish a beam element model, numerically analyzed the influence of different closure construction schemes on the long-term deformation and bending moment of the main beam of the multi-span prestressed concrete continuous rigid frame bridge and the bending moment of the pier. Zhu [10] et al. used the structural mechanics method, considering the construction of single-limbed and double-limbed pier structures, the eccentricity of the top thrust and the closure scheme, etc., derived the calculation formulas for the closure thrust under different conditions.

In this work, considering a certain bridge, numerical model for the proper closure scheme is built. And the mechanical responses of the closure joint support system, the tensioning framework, and the counterweight scheme were systematically analyzed. The main beam geometry, stress distribution, and the force characteristics of the piers of the two closure schemes were compared, and the construction process was optimized and verified on-site.

2 Project Overview and Finite Element Model

2.1 Project Profile

As shown in Fig. 1a, a bridge of 460.0 (80 + 2 × 150 + 80) m is considered. The upper structure is prestressed concrete variable-section continuous rigid frame; the foundation is double-limbed hollow thin-walled piers, hollow thin-walled piers, and pile foundations. The ratio of the middle span to the side span is 0.533.

The main beam is a single-box single-cell prestressed concrete straight-web box girder. The root beam height is 9.0 m, and the mid-span beam height is 3.5 m; the top plate width of the box girder is 12.125 m, and the bottom plate width is 6.5 m. Each single "T" box girder, except for the 0# block, is divided into 17 beam segments, namely 7 × 3.5 m + 5 × 4.0 m + 5 × 4.5 m. The total length of the 0# block is 14.0 m, and the length of the mid-span and side-span closure segments is 2.0 m each, while the length of the side-span cast-in-place segment is 3.76 m. The 0# block of the box girder is equipped with four transverse girders, each with a thickness of 0.6 m, and the end girders are 1.5 m thick. The double-limb hollow thin-walled piers with pile foundations are considered. The pier heights of 8# to 10# piers are 89.6 m, 137.5 m, and 103.7 m respectively.

2.2 Finite Element Model

Based on the actual construction process and design, the construction is divided into 62 steps. The numerical model for the bridge is built and given in Fig. 1b. Steps 4 to

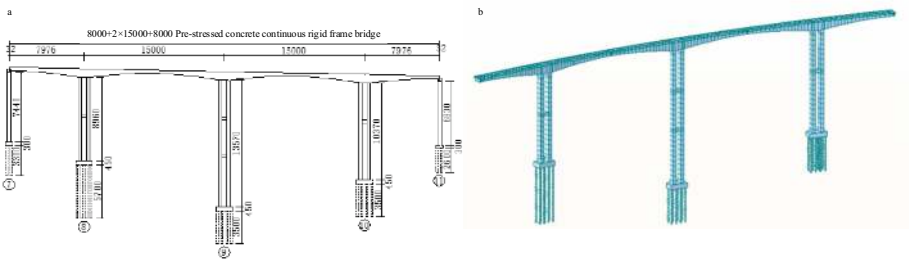

Fig. 1. a. Bridge span arrangement and b.its Finite element model.

53 involve pouring blocks 1 to 17. Each beam segment includes the movement of the formwork, beam pouring, and corresponding beam steel strand tensioning. The load of the formwork and the lifting frame is 896 kN and 300 kN, respectively. The main beam crossbeams and teeth plates are considered as concentrated forces. For comparison, the main construction steps of the two closure schemes are listed here. The main beam, main piers and pile foundations of the rigid frame bridge are simulated using beam units, and 1309 units and 1343 nodes are established for the entire bridge. Among them, nodes 25#, 67# and 109# are the main beam nodes at the top of the 8th to 10th piers. The relative humidity is 75%, the non-uniform settlement of the main piers is 15 mm, and the live load eccentricity coefficient is 1.15. The longitudinal prestress is considered, the lateral and vertical prestress are ignored. Meanwhile, the influence of the bridge deck longitudinal and transverse slopes are ignored.

3 Design of the Closure Support System

3.1 Design of the Closure Section Structure

The closure section of this project is constructed by using the hanging basket method. The hanging basket is triangular type. It is composed of triangular main truss, suspension belts, upper and lower crossbeams, front and rear drag beams, etc. The triangular main truss is made up of double 56# I-beams, double 32b channel steel, 30 mm thick steel strips, etc. The front crossbeam is composed of double 45# I-beams. The front support beam of the bottom basket is composed of double 45# I-beams, the rear support beam of the bottom basket is also composed of double 45# I-beams, and the bottom longitudinal beam of the bottom basket is a 36b# I-beam with a spacing of (0.88, 0.28, 0.28, 0.4, 5@0.9, 0.4, 0.28, 0.28, 0.88 m). The rear stay rods use φ32 precision rolled threaded steel, and the front suspension belt uses a 2 cm thick steel plate suspension belt. During construction, the front guardrails and other supporting systems are removed, and the front crossbeam is moved to the intersection with the 17th block at the closure section.

3.2 Numerical Simulation

The numerical simulation was conducted using Midas Civil software. Based on the magnitude of the calculated loads, the loads were added to the model in the form of

beam element loads within the model. The hanging basket was stabilized on the already poured box girder, mainly relying on the main truss and corresponding hangers, guy wires, and the load-bearing of the upper and lower layers of beams. The loads acting on the hanging basket mainly include: box girder loads, the length of the closure section is 2 m, with a weight of 52.8 t, the calculated load, the box girder load at the top and bottom plates is G1 = 26 × 3.53 = 91.8 kN/m (with 6 lower longitudinal beams), the box girder load at the web is G2 = 26 × 1.75 = 45.5 kN/m (with 3 lower longitudinal beams), the box girder load at the flange is G3 = 26 × 1.15 = 29.9 kN/m (with 2 longitudinal beams), construction machinery and personnel loads: 3 kN/m^2, concrete dumping load: 4 kN/m^2, concrete vibrating load: 4 kN/m^2.

Numerical results shows that during the pouring and closure of the hanging basket, the maximum tensile stress calculated for the entire model was 69.2 MPa, the maximum compressive stress was 42.1 MPa, and the maximum shear stress was 16.0 MPa. All of these were less than the design strength value of Q235 steel. The strength met the requirements. Also, it is found that the maximum tensile deformation generated during the pouring and closure of the hanging basket was 5 mm. The overall deformation occurred at the outermost end of the cantilever, and the deformation was very small. At the same time, the buckling analysis of the support structure was also conducted, and the relevant load constants and variables were defined to obtain its critical stability coefficient, thereby determining its overall stability. The determination of the first-order mode showed that the minimum buckling coefficient of the hanging basket system was 6.9, which was greater than the empirical value of 3 for the temporary structure. Therefore, the overall structural stability met the requirements.

4 Stiff Skeleton in Closure

4.1 Stiff Skeleton Type and Characteristics

The tensional skeleton is also called the temporary locking mechanism or closure locking device. It is an important part used at the last step of building multi-span prestressed concrete girder bridges. Its main job is to change the bridge's structure temporarily before pouring the closure segment concrete. When you put this mechanism in place, it joins two nearby cantilevers firmly. This makes the bridge act like a continuous system under load before the closure concrete hardens. This temporary connection helps control movements and spreads internal forces during this critical building stage.

Before the closure segment concrete reaches its design strength, the tensional skeleton carries the internal forces from the ends of the box girders. These forces include axial loads, shear, and bending moments caused by the bridge's weight, construction loads, and environmental effects like temperature changes and wind. You must design the skeleton to be strong and stiff enough to handle these forces without bending too much. This keeps the whole structure safe while the concrete cures.

Using a tensional skeleton is a must for building multi-span prestressed concrete girder bridges safely and accurately. This is especially true for bridges made with the balanced cantilever method. The skeleton keeps the two beam ends in the right position during pouring and the early curing phase. This position control is very important. It stops misalignment that could cause unwanted stresses. It also makes sure the closure

segment is the right size. Plus, it prevents structural problems. In the end, the tensional skeleton gives a stable and controlled connection. This keeps the bridge safe during building and ensures the closure joint is good quality. This joint is key for the finished bridge's strength and long life.

4.2 Stiff Bone Structure Design

From the perspective of tensile strength, the structural form of the tensioning section's stiffening frame can adopt any cross-sectional form. However, the stiffening frame also has requirements for resisting bending and shear. Therefore, the "I" shape cross-section and the channel steel type cross-section are better choices. The stiffening frame of the tensioning section can be classified into the following three forms based on the support method: internal rigid support method, external rigid support method, rigid support and temporary tension-ed beam locking method together.

The determination of the minimum cross-sectional area of the stiffening frame should take into account the changes in stiffness, strength and stability of the stiffening frame under the action of construction loads and temperature differences during construction. For the convenience of design and construction, the stiffening frames of the mid-span tensioning section and the edge-span tensioning section usually adopt the same size. Therefore, in different situations, the mid-span or edge-span tensioning section with the most unfavorable force should be selected as the control design cross-section.

4.3 Safety Check of the Stiffened Frame Structure

During the heating and cooling stages after the locking of the middle span closure joint of this bridge, the expansion and contraction of the beam causes the displacement of the pier, and the elastic force generated by the displacement of the pier acts back on the box girder. Therefore, the load borne by the tensional skeleton of the closure joint is the reaction force caused by the deformation of the beam and the bending of the pier column. The safety check of the tensional skeleton is carried out based on this. According to the actual on-site detection of the 8# to 10# piers of this bridge, it is concluded that the elastic modulus of the C40 reinforced concrete is $E = 3.50 \times 104$ MPa. At the same time, taking the 8# pier as an example, the safety of the tensional skeleton of the closure joint of this bridge is verified.

The cross-sectional area A of the single hollow pier of the 8# pier is 1.17×10^5 cm^2, the cross-sectional moment of inertia I_x is 1.83×10^9 cm^4, I_y is 5.89×10^9 cm^4, and the center distance a between the hollow pier and the bridge pier center line is 425 cm. The cross-sectional moment of inertia of the double hollow pier is calculated to be 5.40×10^{10} cm^4. Using the cantilever beam displacement formula, the elastic force generated by the displacement of the pier column of the 8# pier is 1597 kN. The tensional skeleton of this bridge uses 4 groups of double bonding, according to the design drawing, the maximum compression length l of the tensional skeleton is $\not>$250 cm (counted as 250 cm), the compression length-to-diameter ratio λ of the structural system is l/i = 18.6, which belongs to a short compression bar, and the stability coefficient (class B) $\psi = 0.90$. The allowable bearing pressure of a single group of channel steel is: $[R] = \varphi A[\sigma] =$

2902.5 kN, which is much greater than the load shared by 599 kN, so the tensional skeleton structure is safe.

5 Determination of the Counterweight for the Closure Section

5.1 Function and Installation Methods of Counterweights

We can divide the counterweights used in building bridges into two types. These are basic counterweights and extra counterweights. The basic counterweight balances the weight of the fresh concrete in the closing part. It helps keep the structure stable while the concrete hardens. The extra counterweight helps control the shape and stress of the beam. It adjusts the bending and height to match the design. Engineers use it to fine-tune the beam during construction. Counterweights usually look like steel boxes filled with water. We can change the weight by adding or removing water. These are placed at the free end of the beam, which is the part farthest from the support. This position gives the best balance with less weight. You can add counterweights at different times. You can put them on while building the beam to control bending step by step. Or you can add them after joining parts together to make final adjustments before finishing the structure. This way of using counterweights helps us manage forces and bending in the beam. It keeps the construction safe and the bridge strong for a long time in Fig. 2.

5.2 Verification of the Counterweight Model

Originally, the balancing water tank at the mid-span of the side section was designed as 268 kN. According to the actual situation of on-site construction and design requirements, the final dynamic balance weight for the counterweight is revised. The weight of the side-span closure section is 52.6 t, and the weight of the middle-span closure section is also 52.6 t (the middle-span closure section also has an additional cross beam weighing 29.64 t). The beam model was established by using the MIDAS/Civil software. The entire bridge was discretized into 223 nodes and 222 elements. Under different load combinations, the line shape, internal force and stress of the original scheme and the new scheme were compared and analyzed.

The displacements of the bridge under three working conditions before and after the scheme modification are calculated and given in Table 1. Under the normal use condition, the difference in deflection is 2.62 mm for long-term use, 1.48 mm for short-term use. Under the completed bridge condition, the deflection difference is 10.05 mm. Figure 2 shows the bending moment diagrams under different conditions before and after the scheme modification. The maximum bending moments and the maximum stresses for the revised scheme is much better than the original one.

5.3 Closure Schemes Comparison

The two closure schemes, Scheme-1: the lateral span is closed first and then the middle span is closed; Scheme-2: both the lateral and the middle span are closed at the same time, are considered. The following compares and analyzes the two closure schemes

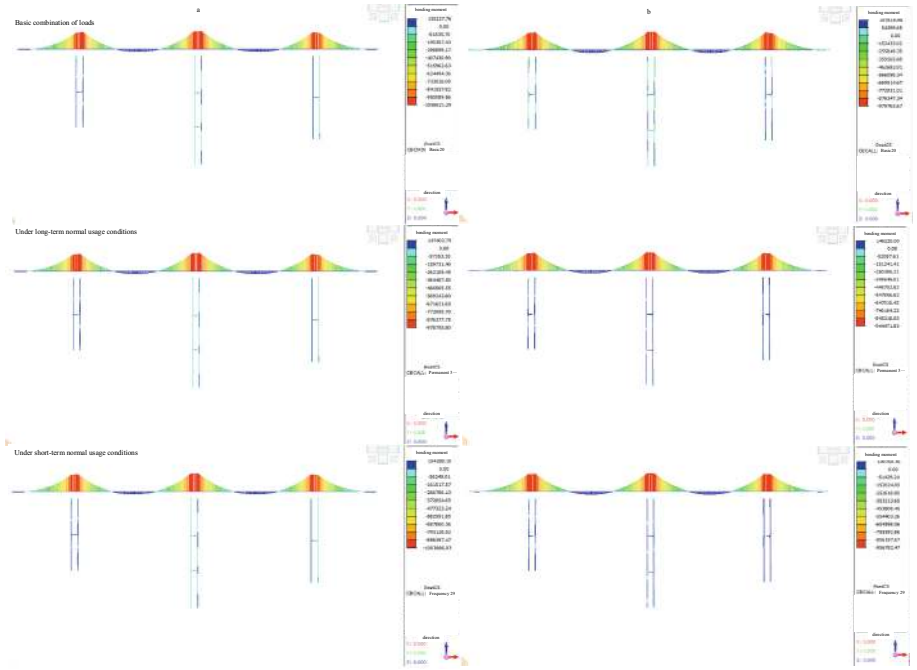

Fig. 2. Bending moments of the bridge under three conditions a. original scheme and b. optimized scheme.

Table 1. Comparison table of deflections under different loads (Unit: mm).

Displacement in the Z Direction Under the Load Combination	Deflection After Plan Modification	Original Design Deflection	Difference Before and After Change
Under long-term normal usage conditions	−83.65	−81.03	2.62
Under short-term normal usage conditions	−87.93	−89.41	1.48
Under bridge completion usage conditions	−46.49	−56.54	−10.05

from four aspects: main beam displacement, stress, top beam displacement at the pier, and bottom beam bending moment.

Figure 3 shows the vertical displacement of the main beam at the beginning of the completed bridge and 10 years after the completion. For the two schemes, the main beam displacement at the pier top is basically the same. The difference in the displacement at

both ends of the main beam at the middle pier is small, while the vertical displacement of the middle span, which leans towards the secondary side pier, changes significantly, with a difference of 10.77 mm.

Figure 4 shows the stress (positive for tension and negative for compression) at the upper and lower edges of the main beam for different closure schemes. Whether during the bridge completion stage or 10 years after the bridge completion, no tensile stress was observed on the main beam, and the difference in stress between the upper and lower edges of the main beam for both schemes was relatively small, with the maximum difference being within the range of 0.5 MPa.

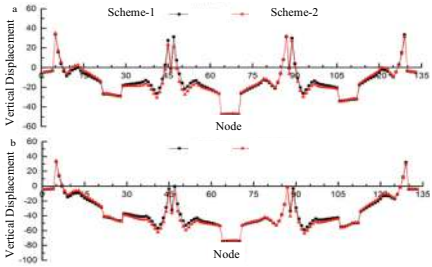

Fig. 3. Vertical displacement of the main beam. a. Bridge Construction Stage. b. 10 years after bridge completion.

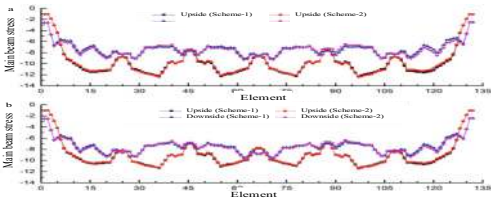

Fig. 4. Main Beam Stress a. Bridge Construction Stage. b. 10 Years after Bridge Completion.

We studied the side-to-side movement at the top of the main piers under different closing methods. The top of the smaller piers on both sides moves differently. This shows the shape changes are not the same on both sides. The middle pier moves very little side to side. The left and right smaller piers have different heights. This makes the middle pier move slightly toward pier 8. This shows the shape of the structure affects how it moves.

After ten years, we see the effects of material changes over time. In the first-edge-second-edge closing method, the smaller piers on both sides move slowly toward the middle. This happens because the concrete shrinks and bends over time. In the normal closing method, the top of the piers keeps moving more over time. But the differences in movement between key points stay about the same. This means the overall shape changes, but the inside movements stay steady. We also checked the forces inside the

piers. The bending forces at the top of the smaller piers on both sides are very different. When the bridge was finished using the first-edge-second-edge method, the force pushed and pulled the bottom of the smaller piers near the middle. The bending force was large. The biggest force was 8909.18 kN·m at the right side of pier 10. With the normal closing method, the pulling force at the bottom of the smaller piers was on the side away from the middle. This shows the two methods create very different force patterns.

6 Determination of the Counterweight for the Closure Section

Research Background and Structural Characteristics. The bridge is in the mountains of Guizhou Province. It is a long bridge with a rigid frame. This type is often used for bridges with tall piers in hard places. The piers are 100 to 136 m tall. They are thin and let the bridge move a bit. This movement helps with some changes but makes the bridge sensitive to weather. Changes in temperature make the concrete grow or shrink. This causes the tops of the piers to move sideways. This movement affects the bridge's shape and stress when closing the bridge.

Detailed Finite Element Analysis and Key Findings. We built a 3D computer model of the whole bridge. The model used real material data, sizes, supports, and temperature changes. We tested two cases: one with a 20 °C temperature change and others during building. We found that a small 5 to 10 °C temperature rise moved the pier tops almost as much as a full 20 °C change. This means we can use natural temperature changes in cool times to help close the bridge. We do not need to use jacks to force the parts together.

Rationale for the Adopted Construction Methodology. We made a new building plan called the Low-Temperature Non-Jacking Synchronous Closure Technique. It has three main points. First, it is safer because it removes jacking. This avoids problems like broken equipment or uneven forces. Second, it is easier to build. Closing all parts at once in cool weather makes the work simpler and faster. Third, it keeps the bridge strong. Closing at the right temperature stops extra stress in the bridge. This helps the bridge last longer.

Implementation, Monitoring, and Validation. We planned the closure for early morning when it is cool and steady. We watched the pier tops and temperature closely. We poured and let the concrete dry in these conditions. The closure worked well. The stress and shape were as planned. Later checks show the bridge is stable.

Significance and Broader Implications. This project shows how we can use analysis to build better bridges. For bridges with tall, thin piers, knowing how temperature affects them can help us find safer and simpler ways to build. The results help with designing and building long bridges in hard places. This can save money and make stronger bridges.

Acknowledgement. This work is supported by the Beijing Natural Science Foundation (8232010).

References

1. Yu, J., Chen, C., Wu, D., et al.: Research on the laying sequence of multi-span wave-shaped steel web continuous rigid frame bridge. Construction Technology. **47**(17), 110–114 (2018). https://doi.org/10.7672/sgjs2018170110
2. Lin, X.: Analysis of the rationality of the closure sequence for multi-span continuous rigid frame bridge. J. Fujian Transp Sci Technol. **12**, 137–142 (2024)
3. Jiang, X.: Research on closure scheme and mechanical properties of large-span continuous rigid frame bridge. J. Transp Sci Manag. **6**(02), 66–68 (2025)
4. Min, F.: Discussion on the closure construction sequence of ultra-high-height multi-span continuous rigid frame bridge. J. Transp World. **26**, 129–131 (2025). https://doi.org/10.16248/j.cnki.11-3723/u.2025.26.028
5. Chen, G., Yao, X., Chen, W.: Research on synchronous closure of multi-span continuous rigid frame bridges. Hunan Transport. Sci. **51**(03), 167–171 (2025). https://doi.org/10.3969/j.issn.1008-844X.2025.03.028
6. Hu, X.: Comparative selection of closure construction schemes for continuous rigid frame bridge based on finite element. J. Transp World. **26**, 114–116 (2025). https://doi.org/10.16248/j.cnki.11-3723/u.2025.26.015
7. Guo, Q., Ding, K., Wang, J., et al.: Optimization analysis of closure tension force for multi-span continuous rigid frame bridge in mountainous areas. J. Highway Eng. **49**(05), 34–38 (2024). https://doi.org/10.19782/j.cnki.1674-0610.2024.05.005
8. Huang, Q.: Research on closure scheme and mechanical properties of large-span continuous rigid frame bridge. J. Fujian Archit. **03**, 78–82 (2025)
9. Li, X., Cheng, Z., Ji, T., et al.: Force analysis of the rapid closure scheme for multi-span prestressed concrete continuous rigid frame bridge. J. Urban Archit. ***22***(17), 208–211 (2025). https://doi.org/10.19892/j.cnki.csjz.2025.17.46
10. Zhu, J., Zhang, W., Chen, P., et al.: Calculation of closure tension force for large-span rigid frame bridge. J. Highway. **70**(10), 229–236 (2025). https://doi.org/10.19782/j.cnki.1674-0610.2025.10.029

Fire Risk Assessment for a Subway Station Platform Based on Fuzzy Analytic Hierarchy Process

Jin Zhang[1], Baoqian Dai[1], Xiushan Lin[2(✉)], Dongxue Li[1], and Rui Zhou[1]

[1] Beijing Key Laboratory of Control Technology for City Toxic and Combustible Major Hazards, Institute of Urban Safety and Environmental Science, Beijing Academy of Science and Technology, Xicheng District Taoranting Street No.55, Beijing 100054, China

[2] Safety Supervision Department, Beijing Metro Operation Administration Corporation Limited, Xingong Vehicle Depot, Nanyuan West Road, Fengtai District, Beijing 100068, China

bjsafety@163.com

Abstract. In order to guarantee the safe operation of subway systems effectively, it is necessary to assess the risk of subway station platform fires. In this paper, fire risk assessment for a subway station platform based on fuzzy analytic hierarchy process is proposed. First, determine the factor set of the evaluation indicator based on the station platform fire influencing factors, and use the analytic hierarchy process to establish the evaluation indicator system of station platform fire. Then, the fuzzy mathematics method is used to evaluate the weight of each indicator and calculate the membership degree of the first- level indicators to determine the fire consequence level. This study conducted a field observation experiment at the station and obtained the movement process of passengers at the station. The accuracy of the simulation model was validated by comparing the experimental observation results with the simulation results. Using the validated simulation model, the passenger evacuation process under fire conditions in three typical stations was simulated. The established fire assessment methodology was then applied to evaluate the fire consequences in these three stations, and the assessment results were compared with the corresponding simulation outputs. The results show that the method can accurately evaluate the consequences of platform fire in subway station, and provide technical support for fire classification treatment in subway station.

Keywords: Subway · Evaluation · Fuzzy analytic hierarchy process · Fire

1 Introduction

The rapid development of subways has brought operational safety risks. Firstly, the limited capacity of subway stations leads to increased crowd density due to rising passenger flow, resulting in localized congestion. Secondly, the restricted evacuation routes hinder rapid movement of people to safe zones. Consequently, once an accident occurs in a subway system, it can easily cause severe casualties. According to statistics, fires account

© The Author(s), under exclusive license to Springer Nature Switzerland AG 2027
G. Feng et al. (Eds.): ICCE 2025, SUCI, pp. 350–365, 2027.
https://doi.org/10.1007/978-3-032-32237-1_25

for the highest proportion (approximately 30%) of all surveyed subway accidents [1] and often cause significant casualties. For example, in February 2003, Daegu subway fire resulted in 487 deaths and 146 injuries, and 289 missing persons. On March 27, 2020, a fire broke out at a subway station in New York, resulting in one death and 16 injuries [2]. In terms of the severity of the consequences of subway accidents over the years, fire accidents have the highest number of deaths [3]. Therefore, the scientific evaluation of fire incidents and take effective measures to reduce casualties has become a focal point of scholarly research.

Many scholars have evaluated the risk of subway fires using different methods. L. M. Zhang [4], J. P. Wang [5] evaluated the risk of station fires by calculating the safe evacuation time at critical evacuation points, while Z. Liu [6] used fuzzy fault tree analysis to analyze the risk of subway fires and obtained the critical importance of the probability of subway fire occurrence. J. Chen [7] and J. B. Wang [8] established a subway fire assessment model using neural networks. The most widely used method in subway fire assessment is the Analytic Hierarchy Process (AHP). Many scholars have made improvements to this method. Y. L. An [9], Z. Z. Song [10], and others have established a subway fire risk assessment indicator system using the improved AHP. W. K. Zhou [11] applied an improved AHP to tunnel fire risk assessment. In recent years, some scholars have attempted to apply fuzzy mathematics methods in fire assessment. M. Y. Chen [12] combined fuzzy mathematics with fault tree method to study the probability of subway station fires and proposed corresponding countermeasures. H. F. Mi et al. [13] combined methods from probability theory and fuzzy mathematics, taking into account both the probability of fire occurrence and the severity of its consequences, to establish a subway fire risk assessment model. X. W. Chen [14] used the Fuzzy Analytic Hierarchy Process (FAHP) to evaluate the fire level of subway stations.

Therefore, this article evaluates and classifies the consequences of fires from the perspective of fire response by subway operating companies, providing a basis for the formulation of subsequent countermeasures. Firstly, FAHP was used to establish a subway station platform fire assessment model, which was used to evaluate the consequence level of the fire and assess the consequences of typical station platform fires. Then, the consequences of station platform fires were modeled employing simulation methodologies. The accuracy of the assessment model was corroborated through a comparative analysis of its outcomes with those derived from the simulation. This study aims to provide scientific method for the assessment of subway platform fires. Begin the Introduction two lines below the Keywords. The manuscript should not have headers, footers, or page numbers. It should be in a one-column format. References are often noted in the text[1] and cited at the end of the paper.

2 Methodology

There are many factors that affect subway station platform fires, with complex interrelationships and limited available data. To assess the risk of platform fires, it is necessary to analyze various factors and determine their impact on station platform fires.

The AHP divides the evaluation objectives into multiple criteria and decomposes the criteria into multiple indicator layers. assigning different weights to each indicator

based on its relative importance to the higher-level criterion, the overall importance of each indicator to the objective can be calculated through a systematic computation. The AHP is suitable for decision-making in multi-factor and multi-level systems, but when there are many evaluation indicators at a certain level, it is difficult to ensure consistency in thinking. Fuzzy mathematics can solve this problem. The combination of AHP and Fuzzy Comprehensive Evaluation Method forms FAHP, which can evaluate the weights of indicators and calculate the membership degrees of indicators, addressing consistency issues in multi-factor systems. Therefore, this paper adopts the FAHP to evaluate the consequences of station fires.

2.1 Establishing the Subway Fire Consequence Assessment Indicator System

The subway fire consequence assessment indicator system directly affects the accuracy of the evaluation results. In this study, 10 experts in fire, evacuation, and subway operation management were invited to analyze the influencing factors of subway fire consequences through methods such as brainstorming and the Delphi method. Three main factors affecting fire consequences were identified: fire hazard, personnel exposure, and station adaptability. Fire hazard refers to the adverse consequences resulting from the development of a subway fire, which is influenced by multiple aspects such as the fire source conditions, combustible materials in the station, and the surrounding environment. Personnel exposure refers to the exposure of personnel in a fire after it occurs, which determines the degree of casualties. The personnel exposure is influenced by three aspects: the number of passengers, the passenger distribution, and the evacuation route. The station adaptability refers to the capability of subway operators to reduce the impact of an incident by taking corresponding measures after its occurrence. The station adaptability is affected by factors such as the capacity and number of staff, fire extinguishing system, smoke exhaust system, evacuation broadcasting and lighting system, and fire emergency plans.

In summary, the finalized subway fire consequence assessment indicator system comprises three levels: the target level, the first level indicators level and the second level indicators level. Details are shown in Table 1.

Table 1. Evaluation indicator system for subway fire consequence.

Target level	First level indicators	Second level indicators
Subway fire consequence assessment indicators (I)	Fire hazard (I1)	fuel property (I11) Heat release rate (I12) Combustible materials in station (I13) Fire compartment (I14) Smoke compartment (I15)
	Personnel exposure (I2)	Number of passengers (I21) Passenger distribution (I22) Evacuation route (I23)

(*continued*)

Table 1. (*continued*)

Target level	First level indicators	Second level indicators
	Station adaptability (I3)	staff capacity (I31) Number of staff (I32) Fire extinguishing systems (I33) Smoke exhaust systems (I34) Evacuation lighting and broadcasting system (I35) Fire emergency plans (I36)

2.2 Establishment of the Fuzzy Comprehensive Assessment Model

Determining the Factor Set of Evaluation Indicators. The factor set refers to the collection of various indicators. The target level consists of multiple criterion levels, and each criterion level consists of multiple indicator levels, as follows:

Where,

$$U = \{U_1, U_2, \ldots, U_y\} \tag{1}$$

$$U_i = \{u_1, u_2, \ldots, u_z\}, i = 1, 2, \ldots, y \tag{2}$$

In the equation: y represents the number of criterion levels in the target level, and z represents the number of indicator levels in the i-th criterion level. $\sum_{i=1}^{y} z_i = n$ and $\bigcup_{i=1}^{y} U_i = U$ is satisfied. $\mathrm{U} = \{\mathrm{U_1}, \mathrm{U_2}, \ldots, \mathrm{U_y}\}$ is the first-level factor set, corresponding to the first-level indicators; $\mathrm{U_i} = \{\mathrm{u_1}, \mathrm{u_{2,\ldots,}}\ \mathrm{u_z}\}$ is the second-level factor set, corresponding to the second-level indicators.

Determining the Fire Consequence Evaluation Set. The evaluation grades are used to evaluate the fuzzy concepts of various factors. They characterize the comprehensive evaluation results in the form of membership degrees, providing a comprehensive reflection of the evaluation situation [15]. It can be expressed as:

$$V = \{V_1, V_2, \ldots, V_m\} \tag{3}$$

After expert discussions and referencing actual subway operations, the evaluation set for subway fire consequences is determined as:

$$V = \{V_1, V_2, \ldots, V_5\} = \{\text{safe, low danger, medium danger, high danger, extremely high danger}\} \tag{4}$$

Establishing the Single-Factor Evaluation Matrix. Quantify each single-factor indicator $u_j^{(i)}$ (i = 1, 2, …, y), and establish the single-factor evaluation set for the i-th factor:

$$R_j = \{r_{j1}, r_{j\,2}, \ldots, u_{j\,z}\}, j = 1, 2, \ldots, z \tag{5}$$

Then the single-factor evaluation matrix is:

$$R = \begin{bmatrix} r_{11} & r_{12} & \ldots & r_{1n} \\ r_{21} & r_{22} & \ldots & r_{2n} \\ \ldots & \ldots & \ldots & \ldots \\ r_{n1} & r_{n2} & \ldots & r_{nn} \end{bmatrix} \tag{6}$$

Determining the Weights of Each Indicator. (1) Method for determining indicator weights.

The weights of the fire consequence assessment indicator system are determined using the FAHP. The interval weight vector is converted into a precise weight vector to obtain the weights of the fire consequence assessment indicators at each level. Experts do not need to provide exact values but only an interval value, and there is no need for consistency testing of the weights. The commonly used method is the 1–9 scale method, as shown in Table 2.

Table 2. 1–9 Scale method.

Scale	Meaning
1	Two factors are equally important
3	The former is slightly more important than the latter
5	The former is significantly more important than the latter
7	The former is strongly more important than the latter
9	The former is extremely more important than the latter
2,4,6,8	Intermediate values between the above adjacent judgments
Reciprocal	If the importance ratio of factor i to factor j is b_{ij}, then the reciprocal importance ratio of factor j to factor i is $b_{ji} = 1/b_{ij}$, forming a reciprocal relationship

During computation, define $A = (A_{ij})_{n \times n}$, where $A_{ij} = [a_{ij}^{-}, a_{ij}^{+}]$ is the interval judgment matrix. By inviting experts to score the indicators using the 1–9 scale method, the range of the judgment matrix is obtained:

$$A_{ij}^{(k)} = \left[a_{ij}^{-(k)}, a_{ij}^{+(k)}\right] \tag{7}$$

To make the evaluation results more objective, different weights are assigned to each expert based on their knowledge background, professional direction, and experience. Assuming there are P experts, then:

$$Q_{EXP} = \left[Q_E^{(1)}, Q_E^{(2)}, \ldots, Q_E^{(P)}, \right] \tag{8}$$

The interval-based judgment matrix is:

$$A = \begin{bmatrix} [1,1] & \left[a_{12}^{-}, a_{12}^{+}\right] & \ldots & \left[a_{1n}^{-}, a_{1n}^{+}\right] \\ \left[\frac{1}{a_{12}^{-}}, \frac{1}{a_{12}^{+}}\right] & [1,1] & \ldots & \left[a_{2n}^{-}, a_{2n}^{+}\right] \\ \ldots & \ldots & \ldots & \ldots \\ \left[\frac{1}{a_{1n}^{-}}, \frac{1}{a_{1n}^{+}}\right] & \left[\frac{1}{a_{2n}^{-}}, \frac{1}{a_{2n}^{+}}\right] & & [1,1] \end{bmatrix} \tag{9}$$

Where,

$$a_{ij}{}^{-} = \sum_{k=1}^{P} (Q_E)_K \cdot a_{ij}{}^{-(o)} \tag{10}$$

$$a_{ij}{}^{+} = \sum_{k=1}^{P} (Q_E)_K \cdot a_{ij}{}^{+(o)} \tag{11}$$

Consistency approximation is performed to obtain a reciprocal consistency judgment matrix $M = (m_{ij})_{n \times n}$, where:

$$m_{ij} = \sqrt[2n]{\prod_{k=1}^{n} \frac{a_{ik}{}^{-} a_{ik}{}^{+}}{a_{jk}{}^{-} a_{jk}{}^{+}}} \tag{12}$$

The vector matrix w of M is $w = (w_1, w_2, \ldots, w_n)$, and the square root method is used to calculate wj.

$$w_j = \frac{1}{\sum_{i=1}^{n} m_{ij}} = \frac{\sqrt[2n]{\prod_{k=1}^{n} a_{ik}{}^{-} a_{ik}{}^{+}}}{\sum_{i=1}^{n} \sqrt[2n]{\prod_{k=1}^{n} a_{jk}{}^{-} a_{jk}{}^{+}}} \tag{13}$$

Where, $j = 1, 2, \ldots, n$.

2) Determining the weights of the subway fire consequence assessment indicator system: The weight vector of the evaluation indicators in the fuzzy comprehensive evaluation is denoted as $w = (w_1, w_2, \ldots, w_n)$.

The ten experts invited for this evaluation compared the indicators at each level of the subway indicator system and provided interval-based judgment matrices to determine the weights of the first-level and second-level indicators. According to the experts' work experience, education, professional title and professional background, and various factors that may affect the accuracy of the results, the weight of each expert is assigned:

$$Q_{EXP} = (0.3, 0.2, 0.2, 0.2, 0.1) \tag{14}$$

Using Eqs. (9), (10), and (11), the uncertainty interval judgment matrix is obtained, and the consistency judgment matrix M is obtained by substituting into Eq. (11):

$$M = \begin{bmatrix} 1.00 & 1.22 & 2.23 \\ 0.82 & 1.00 & 2.20 \\ 0.45 & 0.45 & 1.00 \end{bmatrix} \tag{15}$$

Substituting the judgment matrix M into Eq. (13), the weight vector of the consistency judgment matrix is obtained:

$$w = (0.441\ 0.375\ 0.184) \tag{16}$$

Similarly, the weight values of the second-level indicators in the indicator system are obtained, as shown in Table 3.

Table 3. Indicator weights.

First-level indicators	Weight value	Second-level indicators	Weight value
		I11	0.182
		I12	0.409
I1	0.441	I13	0.163
		I14	0.102
		I15	0.144
I2	0.375	I21	0.493
		I22	0.081
		I23	0.426
		I31	0.105
		I32	0.115
I3	0.184	I33	0.273
		I34	0.309
		I35	0.062
		I36	0.136

Fuzzy Comprehensive Evaluation. Using the weighted average model, the weight vector matrix w and the fuzzy relation matrix R are combined to obtain the fuzzy comprehensive evaluation result vector B, expressed as:

$$B = w \bullet R = (w_1, w_2, \ldots, w_n) \begin{bmatrix} r_{11} & r_{12} & \ldots & r_{1n} \\ r_{21} & r_{22} & \ldots & r_{2n} \\ \ldots & \ldots & \ldots & \ldots \\ r_{n1} & r_{n2} & \ldots & r_{nn} \end{bmatrix} = (B_1, B_2, \ldots, B_n) \quad (17)$$

3 Simulation of Typical Subway Stations Platform Fire

3.1 Typical Station Introduction

Three different types of stations were selected for this study: Station F, Station L, and Station T. The platforms of these three stations encompass all different subway station platform types, and their architectural structures are representative, making them typical of the majority of subway stations in China today.The basic information of each station is shown in Table 4, and their structures are illustrated in Figs. 1, 2 and 3.

Table 4. Introduction of typical subway stations.

Name	Platform type	Architectural features	Number of floors
Station F	Island platform	Transfer station	Underground 2nd floor
Station L	Island platform, Side platform	Transfer station	Underground 3rd floor
Station T	Island platform	Atrium station	Underground 2nd floor

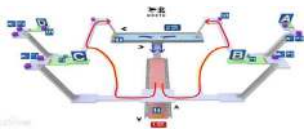

Fig. 1. Architectural structure of station F.

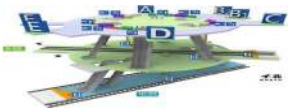

Fig. 2. Architectural structure of station L.

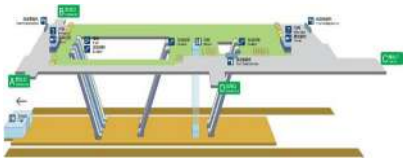

Fig. 3. Architectural structure of station T.

3.2 Simulation Method

This paper uses Fire Dynamics Simulator (FDS) to simulate the fire development process in 3 typical station platforms and then imports the FDS calculation results into the simulation software Simulation of transient evacuation and pedestrian movements (STEPS) to calculate the evacuation process under fire conditions.

3.3 Field Observation Experiment

This study conducted field observation experiments at three representative stations. The observational experiments provided input parameters for the simulation, such as the proportion of different passenger types and the walking speed of each passenger type.In addition, comparing the observed experimental results with the simulation results can verify the accuracy of the simulation results.

Through three days of observation at the three stations, proportion of different passenger types were obtained. Due to the high passenger flow on the stairs connecting the platform to the concourse at Station F, this location was selected for the study of passenger movement patterns, and video recordings of passenger movement were captured.

Based on the observational experiments, the proportion of different passenger types during the morning peak period was determined: men accounted for 48%, and women accounted for 52%. The walking speeds of males and females were 1.35 m/s and 1.15 m/s, respectively, which aligns closely with research results by Z. Y. Li [16].

3.4 Personnel Parameter Setting

The physiological dimensions of personnel are based on the "Human dimensions of Chinese adults" (GB 10000-2023). The composition ratio and walking speed of personnel are based on results of field observation experiment, as shown in Table 5.

Table 5. Personnel parameter setting list in simulation model.

Personnel type	Normal speed (m/s)	Proportion	Maximum shoulder width (m)	Chest thickness (m)
Male	1.35	48%	0.449	0.218
Female	1.15	52%	0.409	0.212

The personnel consist of entering and exiting passengers, transfer passengers, and passengers on the train.

$$N = \frac{N_E}{C} + \frac{N_{\text{trans}}}{2} + N_{\text{train}} \tag{18}$$

Where, N is the number of people on the platform, NE is the number of people entering and exiting the station during the train interval, C is the number of floors in the station, Ntrans is the number of transfer passengers during the train interval, and Ntrain is the number of people on the train, which is 1460 based on the rated capacity of train.

When calculating the number of people in the station, the most unfavorable principle is applied. The number of entering and exiting passengers and transfer passengers is calculated based on the maximum half-hour passenger flow on the busiest day of 2023. The train arrival interval is set at 150 s.

According to the "Code for Design of Metro" (GB50517-2013), the main building structures of subway stations have a fire resistance rating of level 1, and all equipment and decorative materials should be made of non-combustible or flame-retardant materials. These regulations result in very few combustible materials in subway stations. The main fire hazards in subway stations may come from items carried by passengers (e.g., luggage), with a fire power of 2 MW. The personnel reaction time is 30 s, and the train arrival time is 30 s after the fire. According to the "Code for Design of Metro" (GB50517-2013), the standard scenario is one train arriving at the station. The fire scenarios for each station are shown in Table 6.

Table 6. Fire scenario settings.

Scenario	Station	Fire power (MW)	Fire source center location	Evacuation number
F1	Station F	2	9.5 m to the right of the left staircase, on the transverse center-line of the platform	1805
L1	Station L	2	6 m to the right of the leftmost staircase, on the transverse center-line of the platform	1983
T1	Station T	2	Center of the atrium	1676

3.5 Verification of Simulation Model Accuracy

To ensure that the simulation results align with the actual movement of passengers, the accuracy of the STEPS model must be validated. The accuracy of the STEPS model was verified by comparing the video recordings obtained from field observation experiment with the simulation results.

As shown in Fig. 4, it can be seen that passengers gradually experience congestion at the bottom of the stairs during their movement, and the congestion gradually intensifies. When all passengers are congested at the bottom of the stairs, the pedestrian density in the fenced area reaches its maximum. As time progresses, passengers gradually leave the bottom of the stairs, during which the pedestrian density remains at its maximum. Throughout the entire movement process, the simulation results are consistent with the actual movement of passengers. According to the STEPS model calculation, all passengers leave the stairs at 104 s, while the observation experiment recorded a time of 108 s for all passengers to leave the stairs. The time difference is 4 s, with an error rate of 3.7%, which falls within an acceptable range.

a-1）observation experiment a-2）simulation results

a） 0th second screenshot

b-1）observation experiment b-2）simulation results

b） 0th second screenshot

c-1）observation experiment c-2）simulation results

c） 5th second screenshot

Fig. 4. Comparison of observation experiment results and simulation results

The number of passengers passing through the stairs in the video is collected every 5 s. The observation experiment results were compared with simulation results, as shown in Fig. 5. From Fig. 5, it can be seen that the two curves show a high degree of alignment. Based on Fig. 4 and Fig. 5, it is evident that the calculation results of the STEPS model closely match the observation experiment results, effectively reflecting the actual passenger movement process.

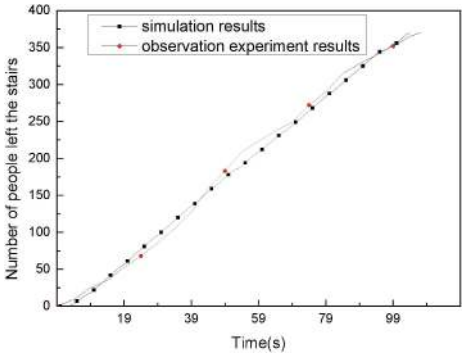

Fig. 5. Chart of the number of people left the stairs with time

3.6 Simulation Results

FDS was used to simulate the fire development process in the three stations, and the calculation results were imported into the evacuation simulation software STEPS to calculate the evacuation process under fire conditions. The required safe egress time (TRSET) and the number of people who failed to evacuate within the available safe egress time (TASET) were obtained for each station, as shown in Table 7.

Table 7. Evacuation results.

Station	Scenario	${}^{T}RSET^{(s)}$	${}^{T}ASET^{(s)}$	The number of unevacuated people ${}^{\text{within } T}ASET$
Station F	F1	432	360	262
Station L	L1	374	360	75
Station T	T1	405	360	250

4 Typical Station Platform Fire Risk Assessment

4.1 Determining the Factor Set

According to Table 1, the first-level evaluation indicator factor set is:

$$U = \{I_1, I_2, I_3\} \tag{19}$$

The second-level evaluation factor set is:

$$\begin{aligned} I_1 &= \{I_{11}, I_{12}, I_{13}, I_{14}, I_{15}\}; \\ I_2 &= \{I_{21}, I_{22}, I_{23}, I_{24}, I_{25}\}; \\ I_3 &= \{I_{31}, I_{32}, I_{33}, I_{34}, I_{35}\} \end{aligned} \tag{20}$$

4.2 Determining the Evaluation Set

According to Equation (4), the evaluation set is determined as:

$$V = \{\text{safe, low danger, medium danger, high danger, extremely high danger}\} \quad (21)$$

4.3 Determining the Membership Degree Matrix

During the evaluation process, the ten invited experts assessed the indicators in the fire consequence evaluation system. Through statistical analysis of the experts' evaluation results, the membership degrees of the second level indicators were obtained. Taking Station F as an example, the membership degrees of its two-level indicators are shown in Table 8. From Table 8, it can be seen that the station is densely populated, and the experts believe that passenger evacuation is in a state of medium, high, or extremely high danger, with medium and high danger being the predominant states. This aligns well with the actual situation of the station.

Table 8. Membership degrees for second-level indicators of station F.

	Evaluation set				
Second-level indicators	Safe	Low danger	Medium danger	High danger	Extremely high danger
I11	0.0	0.1	0.4	0.4	0.1
I12	0.0	0.1	0.3	0.5	0.1
I13	0.3	0.4	0.3	0.0	0.0
I14	0.3	0.5	0.1	0.1	0.0
I15	0.2	0.3	0.4	0.1	0.0
I21	0.0	0.0	0.4	0.5	0.1
I22	0.2	0.4	0.4	0.0	0.0
I23	0.0	0.1	0.2	0.5	0.2
I31	0.1	0.4	0.4	0.1	0.0
I32	0.4	0.4	0.2	0.0	0.0
I33	0.2	0.4	0.3	0.1	0.0
I34	0.0	0.0	0.2	0.6	0.2
I35	0.4	0.4	0.2	0.0	0.0
I36	0.1	0.4	0.4	0.1	0.0

4.4 Determining the Weight Vector of Evaluation Indicators

Based on the weight results of each indicator, the weight vectors of first-level indicators are calculated as follows:

$$W_F = \begin{pmatrix} W_{I1} & W_2 & W_{I3} \end{pmatrix} = (0.441\ 0.375\ 0.184) \quad (22)$$

Weight vectors of second-level indicators are calculated:

$$\begin{aligned} W_{I_1} &= (0.182\ 0.409\ 0.163\ 0.102\ 0.144) \\ W_{I_2} &= \left(0.493\ 0.081\ 0.426\right) \\ W_{I_2} &= \left(0.105\ 0.115\ 0.273\ 0.309\ 0.062\ 0.136\right) \end{aligned} \tag{23}$$

4.5 Fuzzy Comprehensive Evaluation

First, the evaluation results of the second-level indicator factors are calculated:

$$B_{I_1} = W_{I_1} \bullet R_{I_1} = \left(0.1083\ 0.2185\ 0.3122\ 0.3019\ 0.0591\right) \tag{24}$$

$$B_{I_2} = W_{I_2} \bullet R_{I_2} = \left(0.0162\ 0.075\ 0.3148\ 0.4595\ 0.1345\right) \tag{25}$$

$$B_{I_3} = W_{I_3} \bullet R_{I_3} = \left(0.1495\ 0.2764\ 0.2755\ 0.2368\ 0.0618\right) \tag{26}$$

Then, the membership degrees of the first-level indicators are calculated:

$$B_F = W_F \bullet R_F = \left(W_{I_1}\ W_{I_2}\ W_{I_3}\right)\begin{pmatrix} B_{I_1} \\ B_{I_2} \\ B_{I_2} \end{pmatrix} = \left(0.081\ 0.175\ 0.306\ 0.349\ 0.088\right) \tag{27}$$

According to the maximum membership degree principle, the fire consequence at Station F is determined to be high danger.

Similarly, the fire consequences for Station L and Station T can be obtained.

$$B_L = W_L \bullet R_L = \left(0.145\ 0.337\ 0.287\ 0.217\ 0.014\right) \tag{28}$$

$$B_T = W_T \bullet R_T = \left(0.138\ 0.288\ 0.351\ 0.209\ 0.014\right) \tag{29}$$

According to the maximum membership degree principle, the fire consequence at Station L is determined to be low danger and the fire consequence at Station T is determined to be medium danger.

5 Discussion

In this paper, the FAHP is used to evaluate the fire consequences of three subway stations, and it is impossible to judge whether the evaluation results are accurate. Therefore, we simulated the evacuation process during fires in these three subway stations. By comparing the two results, we verify the accuracy of the evaluation results using the FAHP.

From Table 7, it can be seen that when a fire occurs on one side of the third underground floor of Station L, only 75 people were not evacuated within TASET, and an additional 14 s would be needed to complete the evacuation. The assessment model evaluated this fire consequence as low danger, which aligns with the simulation results.

When a fire occurs in the atrium of Station T, 250 people were not evacuated within TASET, and an additional 45 s would be needed to complete the evacuation. Although all personnel were in the station hall at 360 s, the smoke concentration in the hall was low and had little impact on personnel evacuation. So the situation was assessed as medium danger.

When a fire occurs on one side of the platform at Station F, 262 people remain unevacuated within TASET, However, due to only one staircase being available for evacuation, an additional 72 s are needed to complete the evacuation. The smoke concentration on the platform was high, and the state was assessed as high danger.

In summary, the calculation results of fire consequence assessment model accurately reflect the actual fire consequences in the station platforms.

6 Conclusion

This paper proposes a method for assessing platform fires risk in a subway station and establishes a fire consequence assessment model for subway station platform fires. The method divides the evaluation set into five categories: safe, low danger, medium danger, high danger, and extremely high danger. Firstly, the AHP is used to establish the subway fire assessment indicator system. Then, the fuzzy mathematics method is used to evaluate the weights of each indicator and calculate the membership degrees of the first-level indicators. Finally, based on the principle of maximum membership degree, the fire consequence is determined to belong to one of the five evaluation categories, enabling a state judgment of the fire consequences.

Using this method, the severity of fire consequences in three typical stations was evaluated. By comparing the assessment results with computer simulation results of fire consequences in these three stations, the accuracy of the method was validated. This approach can provide a foundation for subsequent graded control of fires in subway stations.

Acknowledgments. This work was supported by the "2022 Beijing Excellent Young Engineers Innovation Studio" project, titled "Research on the impact of subway fires on large passenger flow evacuation based on full-scale experiments".

References

1. Wang, Y.F., Jiang, J.C.: Research on safety evacuation from subway fires J. China Saf. Sci. J. **17**(7), 26–31 (2007). https://doi.org/10.3969/j.issn.1003-3033.2007.07.005
2. Wang, K., Cai, W.Y., Zhang, Y.C., et al.: Numerical simulation of fire smoke control methods in subway stations and collaborative control system for emergency rescue J. Process Saf. Environ. Prot. **147**, 146–161 (2021). https://doi.org/10.1016/j.psep.2020.09.033
3. Lin, X.F.: Research on stress response and intervention methods of passengers in subway fires. Ph.D. dissertation, Beijing Jiaotong University, Beijing, China (2020).
4. Zhang, L.M., Wu, X.G., Liu, M.J., et al.: Discovering worst fire scenarios in subway stations: a simulation approach. J. Autom. Constr. **99**, 183–196 (2019). https://doi.org/10.1016/j.autcon.2018.12.007

5. Wang, J.P., Wang, Y., Zhou, R., et al.: Study on comprehensive fire risk under multi-source fire conditions in T-type interchange subway stations J. Open J. Saf. Sci. Technol. **16**(1), 151–157 (2020). https://doi.org/10.11731/j.issn.1673-193x.2020.01.025
6. Liu, Z., Chen, M.Y.: Study on the risk assessment and control of subway fire based on fuzzy fault tree analysis method. J. Sci. Technol. Manag. Res. **11**, 221–224 (2015). https://doi.org/10.3969/j.issn.1000-7695.2015.11.044
7. Chen, J., Yan, S.P., Deng, X.: Subway station fire safety evaluation based on IOWA- RBF neural network. J. Fire Sci. Technol. **38**(10), 1476–1479 (2019). https://doi.org/10.3969/j.issn.1009-0029.2019.10.037
8. Wang, J.B., Peng, L.B., Li, N., et al.: Fire risk evaluation of subway station based on PCA-RBF neural network. J. Indus. Saf. Environ. Prot. **9**, 71–74 (2017)
9. An, Y.L., Peng, L.M.: Multi-level extensible assessment of subway fire risks J. J. Disaster Prev. Mitig. Eng. **5**, 92–97 (2009). https://doi.org/10.3969/j.issn.1672-2132.2009.05.016
10. Song, Z.Z., Song, W.B., Lin, L.: Fire risk assessment of subway station based on multi- level extension evaluation method J. Manuf. Autom., 40(12), 26–30, 41 (2018). https://doi.org/10.3969/j.issn.1009-0134.2018.12.007.
11. Zhou, W.K.: On the application of fuzzy analytic hierarchy process to the fire risk assessment of subway sections. J. Armed Police Acad. **30**(4), 51–54 (2014). https://doi.org/10.3969/j.issn.1008-2077.2014.04.014
12. Chen, M.Y.: Study on fire risk assessment and control of subway based on the fuzzy theory. Ph.D. dissertation, Huaqiao University, Xiamen, China (2013).
13. Mi, H.F., Xiao, G.Q., Wang, L.Y., et al.: On the fire risk evaluation for the subway station based on the probability fuzzy theory. J. Saf. Environ. **15**(5), 16–20 (2015). https://doi.org/10.13637/j.issn.1009-6094.2015.05.003
14. Chen, X.W., Li, J.B., Wang, X., et al.: Application of fuzzy analytic hierarchy process in fire risk assessment of subway station. J. Manag. Technol SME. **11**, 170–171 (2021)
15. Yang, C.Q.: Ventilation and smoke exhaust control and safety assessment for multi-level subway stations. Master's Thesis, Central South University, Changsha, China (2011).
16. Li, Z.Y., Tang, M.B., Liang, D., et al.: Numerical simulation of evacuation in a subway station. J. Procedia Eng. **135**, 615–621 (2016). https://doi.org/10.1016/j.proeng.2016.01.126

Impact of Basal Surrounding Rock Deterioration on the Mechanical Properties of the Invert in Mudstone Tunnels

Qidong Wu[1], Sheng Li[1(✉)], Lifang Pai[1], Bin Li[2], Jianyong Zhu[2], and Jianyun Zhu[2]

[1] College of Civil Engineering, Lanzhou Jiaotong University, Lanzhou 730030, Gansu, China
ligwin@126.com

[2] China Railway 21st Bureau Group Corporation Limited, Lanzhou 730030, Gansu, China

Abstract. This study employed the FLAC3D numerical simulation method to investigate the variations in the mechanical behavior of the tunnel invert under different conditions of deterioration depth and degrees of swelling and softening of the basal mudstone. The evolution of surrounding rock displacement and the stress-strain response characteristics of the invert were particularly analyzed. The results indicated that under the same deterioration depth, the displacement distribution induced by softening was more concentrated, exhibiting a "narrow and deep" deformation pattern, whereas the influence of swelling was relatively "wide and shallow." Under conditions of shallow deterioration or low degrees of swelling/softening, the superposition of softening significantly accelerated invert heave. However, with increasing basal deterioration depth and the degree of mudstone swelling/softening, the swelling action of the mudstone induced larger vertical displacements, while the subsequent contribution of softening to the deformation growth rate markedly diminished, resulting in an overall deceleration of the heave rate. The risk to the invert was most significant under the coupled action of high swelling and deep deterioration, with a maximum displacement of 6.92 mm at the center, indicating a clear risk of floor heave failure. The findings of this study can provide a theoretical basis for the prevention and control of basal diseases and the structural design of mudstone tunnels.

Keywords: Mudstone Tunnels · Basal Deterioration · Invert Heave · Numerical Simulation

1 Introduction

With the rapid development of China's infrastructure, the scale of high-speed railway tunnel engineering continues to expand, and related disease issues have become increasingly prominent. Among the various types of tunnel diseases, invert heave, as a typical structural disease, severely affects the long-term stability and operational safety of tunnels. This issue is particularly prominent in the engineering practice of tunnels within mudstone strata. This paper is based on the widely distributed swelling mudstone strata encountered in the Chengdu-Chongqing Middle Line high-speed railway tunnel project.

© The Author(s), under exclusive license to Springer Nature Switzerland AG 2027
G. Feng et al. (Eds.): ICCE 2025, SUCI, pp. 366–377, 2027.
https://doi.org/10.1007/978-3-032-32237-1_26

The most prominent engineering geological characteristic of this mudstone is its distinct swelling and softening phenomena upon contact with water [1], exhibiting transitional properties between typical soil and rock mass. Its engineering characteristics demonstrate significant instability and complexity presenting severe challenges to tunnel engineering. Globally, argillaceous rock series are extensively distributed within strata [2]. It is widely recognized within both the engineering and academic communities that the problem of invert heave in mudstone tunnels poses a major challenge for tunnel construction and maintenance [3]. The primary reason is that the surrounding rock at the base of the invert undergoes a series of complex effects such as swelling and softening under the influence of changes in the groundwater environment. The combined action of these factors leads to the occurrence and development of the invert heave disease [4].

Heave at the tunnel base results from the interaction of multiple factors. Scholars domestically and internationally have conducted in-depth research encompassing typical cases of field invert failure, engineering geological properties of mudstone, and numerical simulations and experimental studies. Substantial findings have been achieved regarding the failure mechanisms of heave at the tunnel base and the special engineering properties of mudstone. Concerning swelling, Kong Heng et al. [5] classified the types of heave at the tunnel base into extrusion-flow, flexural-folding, shear-slipping, and water-swelling based on the mechanical characteristics of failure. Anagnostou [6] and Liu Chao et al. [7] conducted in-depth investigations into the mechanisms of heave at the tunnel base in tunnels with swelling surrounding rock from micro and macro perspectives, respectively. Regarding softening, Zhang Qinpeng et al. [8], based on field monitoring and numerical simulation results, indicated that the softening of mudstone after water saturation leads to an uneven distribution of surrounding rock pressure, which in turn causes significant heave at the tunnel base. Ding Dongdong et al. [9], employing field monitoring measurements and numerical simulation methods, analyzed the variation patterns in the mechanical behavior of the tunnel invert before and after water-induced softening of the mudstone. With respect to the deterioration depth of mudstone, Wilson [10] contended that the issue of heave at the tunnel base is primarily caused by the deformation of the surrounding rock within the plastic zone of the tunnel, and that the magnitude of the plastic strain and the extent of the plastic zone are closely related to the properties of the swelling surrounding rock at the tunnel base.

Most current studies have considered only a single aspect, either swelling or softening, as the causative factor. Some have equivalently applied the swelling pressure of the basal surrounding rock as a uniformly distributed load, while others have equivalently treated the deterioration of surrounding rock strength as a reduction in shear strength. These approaches have not adequately accounted for the influence of the swelling and softening effects of the basal mudstone on tunnel loading and invert heave, particularly the simulation of the composite process involving both swelling and softening induced by changes in the water content of the basal surrounding rock. Therefore, this study selects a typical mudstone tunnel engineering case from the Chengdu-Chongqing Middle Line project. Using FLAC3D, it investigates the respective impacts of swelling and softening of the basal surrounding rock, under varying deterioration depths and degrees of swelling/softening, on the mechanical characteristics of the invert. By comparatively analyzing the mechanical response of the invert under different deterioration states of the

basal surrounding rock, the study reveals the influence patterns of water-induced deterioration of mudstone on the structural performance of the invert. The research findings provide an important theoretical basis for controlling basal deformation in mudstone tunnels.

2 Establishment of the High-Speed Railway Mudstone Tunnel Model

2.1 Calculation Cases

This study is based on the Zongshupo Tunnel of the Chengdu-Chongqing Middle Line Railway project. The bedrock underlying the tunnel is Jurassic mudstone interbedded with argillaceous sandstone. The rock mass exhibits a purplish-red color and possesses typical argillaceous texture and argillaceous cementation characteristics. The rock layer contains a significant amount of hydrophilic minerals and is distributed in medium-thick beds. The mudstone is relatively soft, prone to weathering and spalling, susceptible to softening and disintegration upon contact with water, and experiences shrinkage cracking upon dehydration. Its physical and mechanical properties, as well as its volume, change significantly with variations in water content, posing a potential threat to the long-term stability of the tunnel project.

Therefore, this study investigates the influence of basal surrounding rock deterioration on the mechanical characteristics of the tunnel invert from two key aspects: the deterioration depth and the degree of swelling and softening induced by groundwater. Specifically, the following scenarios are considered: (1) deterioration depths of 2 m, 4 m, and 6 m; (2) conditions corresponding to high swelling, high softening, medium swelling, medium softening, low swelling, and low softening degrees. The configurations of the finite element calculation models for the various working conditions are listed in Table 1. The analysis focuses on the impact of basal surrounding rock deterioration—resulting from the combined effects of swelling and softening—on surrounding rock displacement, the stress-deformation characteristics of the support structure, and associated damage features.

Table 1. Swelling coefficient of mudstone in numerical calculation.

Basal deterioration depth	High swelling	High softening	Medium swelling	Medium softening	Low swelling	Low softening
2 m	Case1	Case4	Case7	Case10	Case13	Case16
4 m	Case2	Case5	Case8	Case11	Case14	Case17
6 m	Case3	Case6	Case9	Case12	Case15	Case18

2.2 Material Parameters

Swelling and Softening of Mudstone. Using the Zongshupo Tunnel on the Chengdu-Chongqing Middle Line Railway as the engineering context, this study equivalently simulates the basal wetting-induced swelling effect via the temperature analogy method and models the softening effect through the parameter reduction method, taking into comprehensive consideration both the swelling and softening effects of mudstone following moisture absorption.

According to the literature, the water-induced deterioration process of mudstone exhibits distinct stages and sequence. Specifically, in the initial stage upon water contact, the deterioration of the surrounding rock is primarily manifested as water-induced swelling. Following the completion of this wetting-induced swelling, if water immersion continues, the rock mass gradually enters a stage dominated by softening. Therefore, this study separately simulates the swelling component and the softening component of the basal surrounding rock. This approach aims to authentically and systematically reproduce the complete picture of basal deterioration. Based on this, stress, deformation, and damage indicators for both the surrounding rock and the support structure are extracted for analysis.

Regarding the determination of model parameters: First, softening parameters of the mudstone were obtained through laboratory tests on samples taken from the tunnel site. Subsequently, corresponding swelling parameters were calculated using empirical formulas, followed by analysis and parameter matching of both. Based on the research findings from Reference [10], we acquired the uniaxial compressive strength relationships of the mudstone under five different moisture content conditions. Through characteristic analysis of the strength-strain curves, peak strength data were extracted, establishing the quantitative relationship between the uniaxial compressive strength of the mudstone and its moisture content. After fitting analysis, a logarithmic relationship between the uniaxial compressive strength Rc (MPa) and the moisture content w (%) for the site-specific mudstone was derived as follows:

$$Rc = -4.006\ln(w) + 15.087 \tag{1}$$

The relationship revealed by this formula shows a high degree of consistency with the conclusion drawn from laboratory tests on Tertiary mudstone in Reference [11]. Both indicate a significant negative correlation between the uniaxial compressive strength of mudstone and increasing moisture content. This finding provides an important theoretical basis for stability analysis and design in mudstone tunnel engineering.

Softening Parameters of Mudstone. The physical and mechanical parameters for Grade V mudstone were determined by referring to the Code for Design of Railway Tunnel TB 10003–2016 [12]. Based on the uniaxial compressive strength obtained from the tests, and considering the variation in parameters associated with the softening characteristics of mudstone, the surrounding rock was categorized into three softening stages according to the degree of softening: low softening, medium softening, and high softening, with corresponding softening coefficients of 0.4, 0.2, and 0.1, respectively. This yielded three sets of uniaxial compressive strength values under these conditions. Aydan et al. [13] summarized parameters for a wide range of Tertiary soft rock materials,

including mudstone, and established empirical relationships between the uniaxial compressive strength and other parameters, including unit weight, Poisson's ratio, elastic modulus, and internal friction angle. Following calculation, the physical and mechanical parameters of the surrounding rock are listed in Table 2.

Table 2. Physical and mechanical parameters of the surrounding rock.

Category of surrounding rock	Unit weight $\gamma/(kN/m^3)$	Elastic modulus E/MPa	Poisson's ratio μ	Cohesion c/kPa	Internal friction angle φ/(°)	Softening coefficient η
Grade V surrounding rock	20.8	1673	0.29	150	34.4	0.6
Low softening	20.2	948	0.33	100	31.1	0.4
Medium softening	19.3	359	0.39	50	26.2	0.2
High softening	18.4	136	0.44	25	22.0	0.1

Swelling Parameters of Mudstone. Based on the swelling fundamental theory previously described, and in combination with related laboratory tests on mudstone and the research findings from Reference [14], the following parameter values were determined: the initial moisture content is 10%, the void ratio e is 0.65, and the specific gravity G of the mudstone is taken as 2.71. Assuming that the swelling pressure of the surrounding rock is fully mobilized when the moisture content reaches 25%, this study subjected the mudstone with an initial moisture content of 10% to moistening until reaching 15%, 20%, and 25%, respectively. When employing the temperature analogy method to simulate the wetting-induced swelling effect, the temperature corresponding to the initial moisture content was set as $T_0 = 0$ °C. Consequently, the temperature T_1 corresponding to the final moisture content was calculated and determined to be 2.912 °C. The swelling coefficients of the mudstone under different moisture content conditions (15%, 20%, and 25%) were then calculated, with the results presented in Table 3.

Table 3. Swelling coefficient of mudstone in numerical calculation.

Moisture content w/%	Temperature variation ΔT/ °C	Swelling coefficient α/ 10^{-5}
15	0 ~ 2.912	1.15
20	0 ~ 2.912	3.91
25	0 ~ 2.912	8.45

2.3 Model Establishment

The tunnel model and monitoring point layout are shown in Fig. 1. To mitigate boundary effects during the simulation of tunnel excavation and surrounding rock swelling, and

based on Saint-Venant's principle, the numerical model established in this study extends approximately 3 times the diameter of the excavation cross-section in the left, right, and downward directions. The model employs a fine mesh, comprising a total of 100,560 elements, all of which are C3D8R hexahedral elements. The model parameters are set as follows: the standard cross-section of the Zongshupo High-Speed Railway Tunnel on the Chengdu-Chongqing Middle Line is adopted, with a tunnel span of 15.72 m and a height of 13.22 m; the cross-sectional dimensions of the model are 100 m × 100 m, with a longitudinal length of 30 m. The boundary conditions are set as: the bottom surface of the model is fully fixed, normal constraints are applied to the four side surfaces, and the top surface is a free boundary. The computational process adheres to the following fundamental assumptions: The mudstone is treated as an isotropic, homogeneous elastoplastic material, following the Mohr-Coulomb criterion with a non-associated flow rule. Only the self-weight stress field is considered, neglecting tectonic stress. The support structure and filling layer are simplified as linearly elastic. Additionally, the material's thermal parameters are assumed constant, and the relevant contact interfaces are considered adiabatic boundaries.

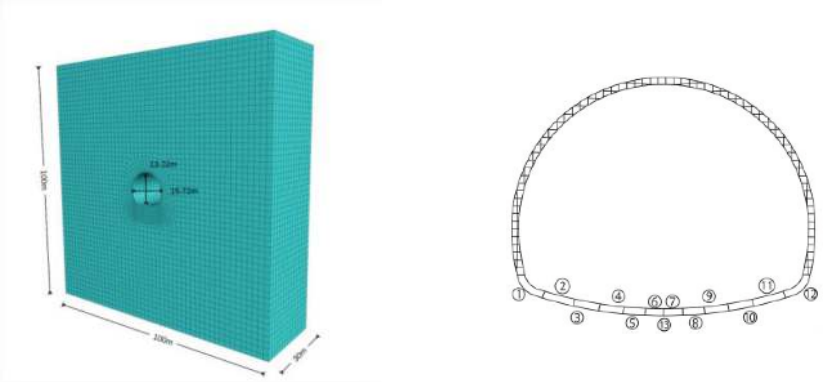

(a) Model mesh (b) Arrangement of monitoring points

Fig. 1. Mesh of the tunnel model and locations of monitoring points.

3 Analysis of Calculation Results for Basal Deterioration

3.1 Influence of Basal Deterioration on Vertical Displacement of Surrounding Rock

Influence of Basal Deterioration Depth on Vertical Displacement of Surrounding Rock. To investigate the influence of basal deterioration depth on the deformation of surrounding rock in mudstone tunnels, the working conditions involving high swelling and high softening were selected for focused analysis. Figure 2 compares the vertical displacement of the surrounding rock under three deterioration depth conditions: 2 m, 4 m, and 6 m, revealing the impact characteristics of deterioration depth on tunnel

deformation. According to the simulation results, the displacement distribution caused by water-induced swelling and softening of the surrounding rock exhibits distinct spatial characteristics: the displacement field induced by the swelling of mudstone is relatively wide and shallow; whereas the displacement field induced by softening is relatively narrow and deep.

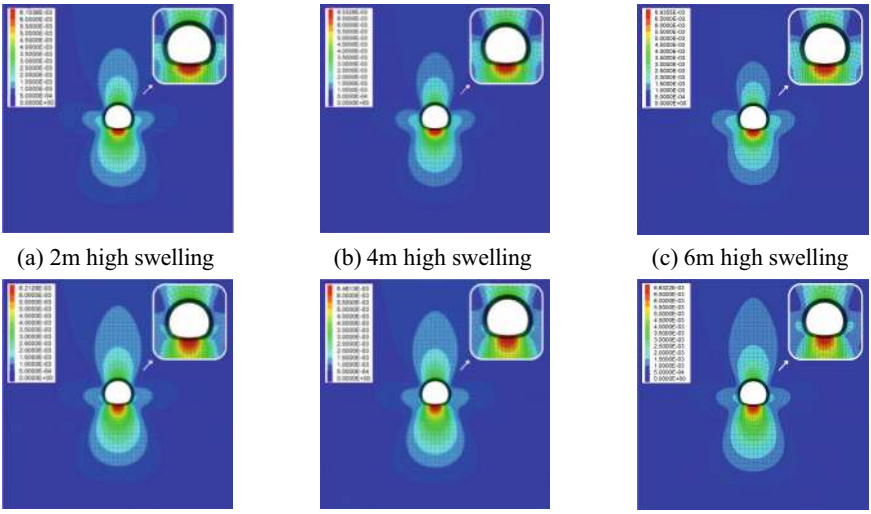

(a) 2m high swelling (b) 4m high swelling (c) 6m high swelling

(d) 2m high softening (e) 4m high softening (f) 6m high softening

Fig. 2. Contours of displacement of basal surrounding rock under different deterioration depths with identical swelling-softening degree (Unit: m).

To delve deeper into the influence of deterioration depth on the deformation of the surrounding rock, Fig. 3 presents the variation curves of tunnel base heave with increasing deterioration depth under different conditions. It can be observed that, under the same degree of swelling and softening, tunnel base heave caused by softening is more severe than that caused by swelling when the deterioration depth of the surrounding rock is shallow. As the deterioration depth increases, the tunnel base heave induced by mudstone swelling shows a growing trend and gradually surpasses the displacement caused by mudstone softening. In terms of displacement magnitude, the deterioration depth has a relatively minor impact on the displacement resulting from the softening of the basal surrounding rock, but a more significant impact on the displacement caused by swelling.

Considering the sequential factor observed in reality—where mudstone undergoes swelling first followed by softening—the superposition of softening leads to an accelerated increase in displacement when the deterioration depth is shallow. However, when the depth is substantial, the superposition of softening, occurring after swelling has already induced significant vertical displacement, results instead in a deceleration of the heave rate.

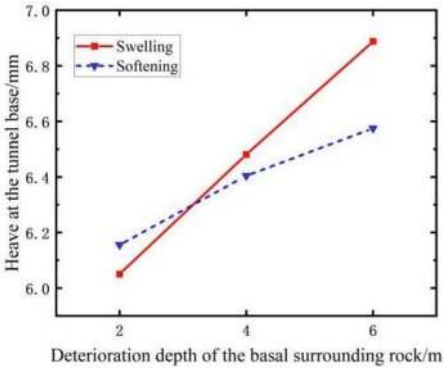

Fig. 3. Relationship curves between vertical displacement of basal surrounding rock and deterioration depth under identical swelling-softening degrees.

Influence of Swelling-Softening Degree on Vertical Displacement of Surrounding Rock. To investigate the influence of the degree of basal swelling and softening on the deformation characteristics of the surrounding rock, taking only the 6 m deterioration depth as an example, the contours of vertical displacement of the surrounding rock under conditions of high, medium, and low swelling-softening degrees are presented in Fig. 4. By comparing the characteristics of the displacement fields under different swelling-softening degrees, the influence pattern of the swelling-softening degree on tunnel deformation is visually reflected.

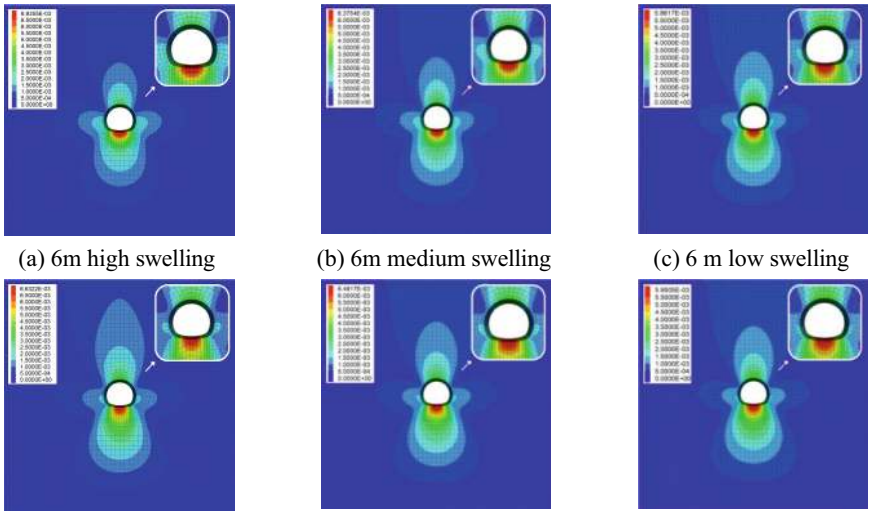

(a) 6m high swelling (b) 6m medium swelling (c) 6 m low swelling

(d) 6 m high softening (e) 6 m medium softening (f) 6 m low softening

Fig. 4. Displacement contours of basal surrounding rock under different swelling-softening degrees at identical deterioration depth (Unit: m).

Based on the simulation results, the relationship curves between tunnel base heave displacement and the high, medium, and low swelling-softening degrees of mudstone are plotted in Fig. 5. It can be observed that, under the same deterioration depth, the tunnel base heave displacement increases linearly with the increasing degree of mudstone swelling; however, the heave caused by softening gradually slows down after reaching a certain level. Combining this with the deterioration pattern of mudstone—"swelling first, followed by softening" under water exposure—at an equal deterioration depth, the degree of swelling exhibits an approximately linear growth relationship with tunnel base heave. In contrast, the heave induced by softening tends to saturate with increasing moisture content, resulting in a gradual decrease in the deformation growth rate.

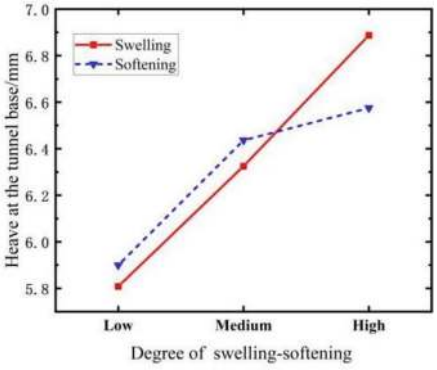

Fig. 5. Relationship curves between vertical displacement of basal surrounding rock and swelling-softening degree at identical deterioration depth.

3.2 Influence of Basal Deterioration on the Invert

Influence of Basal Deterioration Depth on the Invert. To analyze the impact of basal deterioration depth on the tunnel invert, taking only the conditions of high swelling and high softening degrees as examples, invert elements under three basal high swelling-softening conditions (2 m, 4 m, and 6 m) were selected for analysis. By extracting the vertical displacement data of the elements at the inlet during the swelling and softening stages, the vertical displacement curve of the invert elements was plotted in Fig. 6. The results indicate that the vertical displacement of the invert exhibits a symmetric "bell-shaped" distribution. When the deterioration depths are 2 m and 4 m, the displacement curve under the softening effect is overall steeper, characterized by a significant central peak and relatively smaller settlements on both sides; whereas the curve under the swelling effect is relatively gentle and more broadly distributed. However, when the deterioration depth reaches 6 m, under the high swelling condition, the displacement curve not only exceeds the softening curve at the arch foot but also exhibits a central displacement of 6.92 mm, which surpasses the 6.61 mm under the high softening condition. The structural displacement reaches its maximum, indicating a clear risk of floor heave failure.

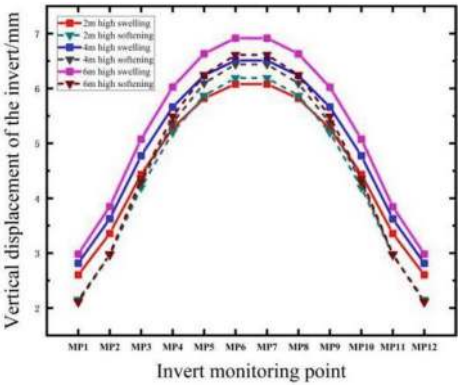

Fig. 6. Vertical displacement curves of invert elements under different deterioration depths at identical swelling-softening degree.

Influence of the Swelling-Softening Degree on the Tunnel Invert. To investigate the influence of the degree of basal swelling and softening on the tunnel invert, the invert elements under high, medium, and low deterioration degrees at a 6 m deterioration depth were taken as the research objects, and the vertical displacement curve of the invert elements was plotted in Fig. 7. The results show that the vertical displacement of the invert exhibits a typical "bell-shaped" distribution. When the swelling-softening degree is medium or low, the softening effect presents a steep characteristic with a prominent central peak and limited displacement on both sides; whereas the curve for the swelling effect displays a relatively broad and gentle morphology.

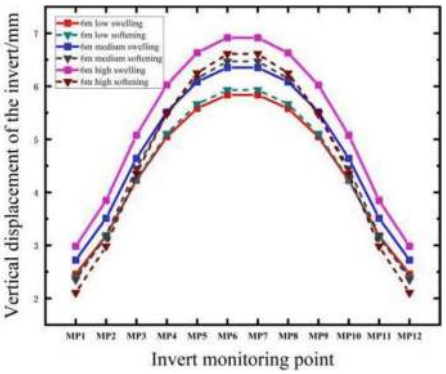

Fig. 7. Vertical displacement curves of invert elements under different swelling-softening degrees at identical deterioration depth.

4 Conclusion

This study, taking the Zongshupo Tunnel on the Chengdu-Chongqing Middle Line as the project background, primarily employs a numerical simulation approach. Based on the fundamental theories of mudstone's wetting-induced swelling and softening effects, it comprehensively utilizes the temperature analogy method and the parameter reduction method to conduct a coupled analysis of swelling and softening. The research investigates how the properties of the mudstone tunnel base, under varying deterioration depths and degrees of swelling and softening, influence the mechanical behavior of the tunnel structure. The following conclusions are drawn:

1. The basal deterioration depth is a key factor controlling the vertical deformation pattern of the tunnel invert. Under conditions of shallow deterioration (2–4 m), the displacement distribution of the invert induced by softening is steeper, exhibiting a "narrow and deep" deformation characteristic, whereas the influence of swelling is relatively broad and gentle. As the deterioration depth increases to 6 m, the swelling effect becomes significantly enhanced. Its displacement curve surpasses that of the softening condition across both the arch foot and the central zone, with a maximum displacement of 6.92 mm. This indicates that deep-seated swelling has become the dominant mechanism triggering overall uplift of the invert and the risk of floor heave.
2. At the same deterioration depth, the degree of swelling exhibits an approximately linear growth relationship with invert heave displacement, whereas the displacement induced by softening gradually tends toward saturation with increasing moisture content. This characteristic indicates that under high moisture conditions, swelling remains the primary process continuously exacerbating invert deformation, while the contribution of softening to invert deformation has an upper limit.
3. Under conditions of shallow deterioration or low swelling-softening degree, the superposition of softening can significantly accelerate invert heave. Conversely, in the stage of deep deterioration or high swelling-softening degree, the swelling action of mudstone induces substantial vertical displacement, while the subsequent contribution of softening to the deformation growth rate noticeably diminishes. Consequently, the overall heave rate tends to decelerate.
4. The risk to the tunnel invert is most pronounced under the coupled action of high swelling and deep deterioration. The peak displacement at the invert center occurs under the condition of high swelling and a 6 m deterioration depth. Under this specific condition, the invert not only exhibits the largest overall displacement but also faces a clear risk of local failure and floor heave. Therefore, this condition should be the primary focus for long-term safety monitoring and remediation measures in the tunnel.

References

1. Gautam, T.P., Shakoor, A.: Comparing the slaking of clay-bearing rocks under laboratory conditions to slaking under natural climatic conditions. J. Rock Mech. Rock Eng. **49**(1), 19–31 (2016). https://doi.org/10.1007/s00603-015-0729-7
2. Um, J., Shin, M.: Variations of physico-mechanical properties of the cretaceous mudstone in Haman, Gyeongnam due to freeze-thaw weathering. J. Tunn. Undergr. Space. **19**(2), 146–157 (2009)

3. Xiao, G.Z.: Discussion on improvement measures for design and construction based on typical lining diseases of current railway tunnels. J. Tunn. Constr. (Chinese and English). **38**(9), 1416–1422 (2018). https://doi.org/10.3973/j.issn.2096-4498.2018.09.002
4. Wang, L.C., Xiao, X.W., Lin, H.: Analysis of causes and treatment countermeasures for floor heave disease of a railway tunnel. J. Tunn. Constr. **34**(9), 823–836 (2014). https://doi.org/10.3973/j.issn.1672-741X.2014.09.003
5. Kong, H., Wang, M.S., Zhang, D.H.: Causes, classification, and control of tunnel floor heave J. China Saf. Sci. J. **13**(1), 30–33 (2003). https://doi.org/10.3969/j.issn.1003-3033.2003.01.008
6. Anagnostou, G.: A model for swelling rock in tunnelling. J. Rock Mech. Rock. Eng. **26**(4), 307–331 (1993). https://doi.org/10.1007/BF01027115
7. Liu, C., Yuan, W., Lu, J.F., et al.: Study on micro and macro physical-mechanical properties of silty mudstone in the floor heave section of a railway tunnel. J. Hydrogeol. Eng. Geol. **47**(5), 108–115 (2020). https://doi.org/10.16030/j.cnki.issn.1000-3665.202001001
8. Zhang, Q.P., Liang, Q.G., Meng, B.W., et al.: Experimental study on mechanical characteristics of mudstone tunnel of Baoji-Lanzhou passenger dedicated line. J. Railway Sci. Eng. **13**(11), 2133–2141 (2016). https://doi.org/10.3969/j.issn.1672-7029.2016.11.005
9. Ding, D.D., Liang, Q.G., Xu, S.C., et al.: Study on the influence of softening mudstone on mechanical characteristics of tunnel invert. J. Railway Sci. Eng. **13**(10), 2001–2008 (2016). https://doi.org/10.19713/j.cnki.43-1423/u.2016.10.018
10. Wilson, A.H.: A method of estimating the closure and strength of lining required in drivages surrounded by a yield zone J. Int. J. Rock Mech. Min. Sci. Geomech. Abstr. **17**(6), 349–355 (1980). https://doi.org/10.1016/0148-9062(80)90518-5
11. Zhang, X.W., Hong, K.R., Chang, X., et al.: Study on engineering characteristics of Tertiary mudstone and construction technology of invert. J. Mod. Tunn. Technol. **58**(2), 214–219 (2021). https://doi.org/10.13807/j.cnki.mtt.2021.02.028
12. National Railway Administration of the People's Republic of China. Code for design of railway tunnel: TB 10003-2016[S]. China Railway Publishing House, Beijing, (2018).
13. Aydan, Ö., Akagi, T., Kawamoto, T.: The squeezing potential of rocks around tunnels: theory and prediction. Rock Mech. Rock. Eng. **26**(2), 137–163 (1993). https://doi.org/10.1007/BF01023620
14. Zeng, Z.Y., Xu, B.S., Hu, S.Q., et al.: Numerical analysis of lining failure in expansive soil tunnel under humidifying condition. J Rock Soil Mech. **35**(3), 871–880 (2014). https://doi.org/10.16285/j.rsm.2014.03.029

A Method for Key Structural Design and Multi-Case Safety Assessment of Long-Span Asymmetric Cable Cranes

Qinglan Ye(✉) and Ning Hong

General Quality Education Department, Wuchang University of Technology, Wuhan, Hubei, China 430223
136454081@qq.com

Abstract. To address the core technical challenges in designing heavy-duty asymmetric cable cranes for long-span bridge construction in complex mountainous terrain, this paper presents a "global theoretical-local refined" hierarchical modeling and analysis methodology, using the 320 t cable crane for the Danjiang Small Three Gorges Bridge as a case study. This method first accurately solves for the boundary loads at the pylon tops under an asymmetric layout using a global theoretical model based on the catenary principle and iterative equilibrium. These loads are then applied to refined finite element models of key structural components, such as the pylon top saddle structure and the specialized spreader beam, to capture stress concentrations. Furthermore, a comprehensive multi-case safety assessment framework was established, covering extreme lifting positions, sharp temperature drops, and wind loads. The results indicate that under the most unfavorable load combinations, the maximum stresses in the pylon top structure and the spreader beam were 176.3 MPa and 177.9 MPa, respectively. Both values are well within the material's allowable limits, thus verifying the safety of the design. The hierarchical modeling method and systematic safety assessment framework proposed in this study offer an innovative solution for the design and verification of similar large-scale construction equipment operating under complex conditions.

Keywords: Cable Crane · Bridge construction · Hierarchical modeling · Finite element analysis · Multi-case assessment · Asymmetric structure

1 Introduction

As global infrastructure development increasingly extends into extreme environments, the construction of long-span bridges frequently encounters severe challenges posed by complex, precipitous topography. In such formidable engineering scenarios, cable cranes have emerged as indispensable specialized equipment for traversing deep ravines and hoisting heavy pre-assembled components [1, 2]. Unlike conventional lifting equipment operating on level ground, cable cranes utilized in mountainous bridge construction must adapt to harsh geographical constraints. The historical application of cable cranes has evolved from dam and powerhouse construction, where symmetrical layouts are

© The Author(s), under exclusive license to Springer Nature Switzerland AG 2027
G. Feng et al. (Eds.): ICCE 2025, SUCI, pp. 378–392, 2027.
https://doi.org/10.1007/978-3-032-32237-1_27

common, to modern bridge engineering, where site-specific constraints often dictate the system's configuration. However, the transition from standard operating environments to these extreme conditions introduces a paradigm shift in structural safety requirements. The unique terrain imposes distinctive and systematic technical challenges on the design of these cranes, transforming them from simple magnifications of standard equipment into non-standard, purpose-built engineering systems.

Furthermore, a critical gap exists in current engineering standards. Most existing design codes (such as FEM or DIN standards) are tailored for factory-based gantry cranes or symmetric cableways, lacking specific provisions for large-scale, asymmetric cable systems anchored in variable geological strata. This absence of standardized regulation forces engineers to rely on first-principle analysis and advanced numerical verification, as performed in this study, to mitigate catastrophic risks associated with structural failure in such high-stakes projects.

Specifically, three core technical challenges are particularly prominent in the design and verification process.

First, the challenge of asymmetric layout and geometric nonlinearity. Geological conditions and significant elevation differences between the precipitous banks often necessitate the asymmetric placement of the crane's anchor points and side spans. This geometric asymmetry fundamentally disrupts the mechanical symmetry of the system. From a mechanics perspective, this asymmetry exacerbates the geometric nonlinearity inherent in cable structures. Unlike in a symmetric system where the horizontal components of cable tension on either side of a pylon top naturally balance, an asymmetric layout (e.g., different side span lengths $L_1 \neq L_3$ or anchor elevations) creates a net horizontal force and a significant overturning moment on the pylon [3]. This unbalanced load is not static; it fluctuates violently with the movement of the trolley, inducing complex hysteresis effects that simplified linear models fail to capture. This unbalanced load must be safely transferred from the temporary saddle structure into the permanent pylon, posing a significant threat to the pylon's stability during construction.

Second, the constraint of strong nodal coupling. Key load-bearing nodes, such as the pylon top saddle structures, must be temporarily installed on the permanent bridge pylons. Their design is subject to a dual, stringent constraint: ensuring their own structural integrity under heavy loads while absolutely preventing any damage to the permanent bridge structure, all within an extremely limited physical space [4]. The contact interface between the steel saddle base and the concrete pylon top is a critical zone where high stress concentrations can occur. Excessive bearing stress could lead to localized crushing of the concrete, while shear forces must be adequately resisted by shear keys or friction, making the detailed analysis of this interface crucial.

Third, the complexity of coupled working conditions. Throughout the construction period, the structure is subjected to a highly dynamic environment, including varying lifted loads, sudden wind gusts characteristic of canyon environments, and significant diurnal temperature variations. These factors create a composite threat to structural safety [5]. The tension in the main cables is highly sensitive to temperature changes; a significant temperature drop can increase the tension by a considerable margin, equivalent to adding tons of extra load. Therefore, a simple analysis based on a single worst-case scenario is

insufficient; a comprehensive assessment must consider the combined effects of these coupled physical phenomena.

Traditional design methods, which largely rely on symmetric assumptions and simplified empirical formulas, have proven inadequate for addressing these multifaceted challenges. Consequently, there is a pressing need within both the academic and engineering communities for an advanced analytical framework capable of systematically resolving these issues. Against this backdrop, this paper, using the 320 t asymmetric cable crane for the Danjiang Small Three Gorges Bridge as a practical engineering case, proposes and implements a "global theoretical-local refined" hierarchical modeling methodology. Complemented by a systematic multi-case safety assessment framework, this study aims to provide a rigorous and efficient solution for the design and analysis of large-scale cable cranes in complex environments.

2 Literature Review

To clearly situate this study within the existing body of knowledge and identify the specific contributions, this chapter reviews the current research status and limitations across three intersecting fields: the nonlinear analysis of cable-supported structures, numerical simulation of bridge construction equipment, and the mechanical behavior of complex structural nodes.

2.1 Nonlinear Analysis of Cable-Supported Structures

Cables, as archetypal flexible structures, exhibit significant geometric nonlinearity, characterized by a strong coupling between force and form [6]. Early research laid the theoretical foundation, with Irvine [7] systematically deriving the classical Catenary and Parabolic theories. The Catenary theory provides an exact solution for a cable under self-weight, while the Parabolic theory offers a highly accurate approximation for cables with small sag-to-span ratios, significantly simplifying the governing equations. Subsequent studies developed various numerical methods to handle more complex scenarios. For instance, Buchholdt [8] introduced iterative methods for cable roof structures, and Bathe [9] formulated finite element procedures that could handle large displacements.

Researchers also incorporated secondary but significant factors like thermal effects. The work by Zhou and Sun [10], for example, quantified the substantial impact of solar radiation and ambient temperature changes on cable tension in long-span bridges, proving that thermal loads are a critical component of the design process. However, a systematic review reveals that the vast majority of existing research, from textbooks to advanced papers, focuses on idealized symmetric structures (as shown in Fig. 1a). This assumption simplifies the problem by allowing for balanced forces at the pylon tops. The unique mechanical behavior of asymmetric layouts (Fig. 1b), which is the norm in complex terrain, remains insufficiently explored. The unbalanced moments generated at the pylon top and the complex load redistribution between spans mark the first theoretical gap this study aims to address.

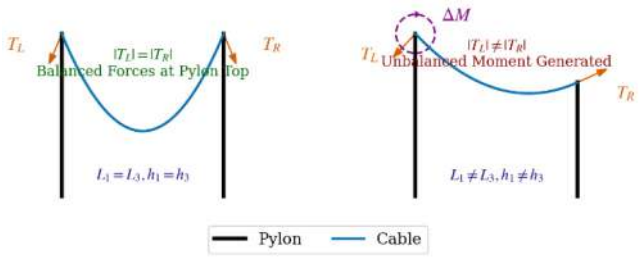

(a) Symmetric Layout Model (b) Asymmetric Layout Model

Fig. 1. Comparison of symmetric and asymmetric cable system models.

2.2 Numerical Simulation of Large-Scale Construction Equipment

The Finite Element Method (FEM) is a standard tool for modern equipment design verification, with extensive applications for predominantly rigid-body systems such as gantry cranes [11] and launching girders [12]. In contrast, a cable crane is a classic Rigid-Flexible Coupled Multibody System. It combines massive, stiff components (like the spreader beam and pylon saddles) with highly flexible, slender cables. Shabana [13] and Wasfy et al. [14] have highlighted that establishing a single, high-fidelity global FE model of such a system presents formidable obstacles. These include mesh incompatibility between 1D cable elements and 3D solid elements, and poor convergence due to the ill-conditioned stiffness matrix caused by the vast difference in stiffness between cables and steel structures. Therefore, developing an efficient, decoupled modeling strategy that preserves accuracy at both the global and local levels is a critical technical bottleneck.

2.3 Mechanical Behavior of Complex Temporary Nodes

The safety of a structure often depends on its connection nodes. While permanent nodes in steel structures have been extensively studied regarding fatigue and stress concentration [15, 16], components like the pylon top structure in a cable crane fall into the category of "non-standard, heavy-load, temporary nodes." These nodes are characterized by their temporariness, high integration with permanent structures, and exposure to extreme, variable loads. As noted by Pal and Patra [17], design methodologies for such specialized connections are often underdeveloped. The load path through these temporary assemblies—from the cable, through the saddle, into the steel frame, and finally into the permanent concrete pylon—is complex and deserves detailed investigation that goes beyond simple hand calculations.

2.4 Summary of Research Gaps

In summary, a comprehensive research gap exists at the intersection of these three sub-problems. Existing methods either oversimplify the cable mechanics or struggle with the scale of the coupled system. This study proposes a "global theoretical-local refined" hierarchical modeling methodology to systematically address this multifaceted challenge by decoupling the system analysis, calculating precise boundary loads based on

asymmetric theory, and performing detailed multi-case assessments of key temporary nodes.

3 Methodology and Modeling

3.1 Overall Analysis Strategy

To address the challenges of analyzing this non-standard, heavy-duty asymmetric cable crane, this study employs a "global theoretical-local refined" hierarchical modeling strategy. The core principle is "divide and conquer, refine in sequence," decomposing the complex analysis into two interconnected levels: the macroscopic global level and the microscopic local level. The entire analysis workflow is illustrated in Fig. 2.

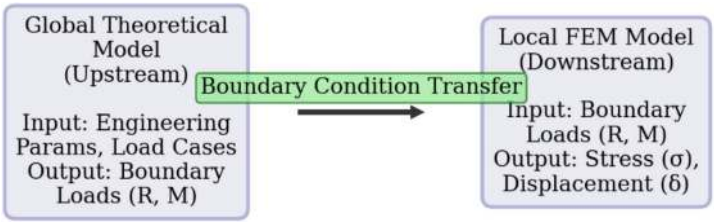

Fig. 2. Data flow of the "Global-Local" hierarchical modeling strategy.

3.2 Global Theoretical Level: Mechanical Model of the Cable System

Model Objective and Basic Assumptions. The sole objective of the global theoretical model is to accurately solve for the three-dimensional reaction force vector R and moment vector M at the pylon top saddle. The model is based on the following assumptions: (1) cables are perfectly flexible and can only bear tension; (2) the material is linear elastic; (3) all analyses are static or quasi-static, ignoring transient dynamic effects.

Mathematical Model and Governing Equations. A 2D schematic is established for the three-span system (Fig. 3) to elaborate the core mathematical model.

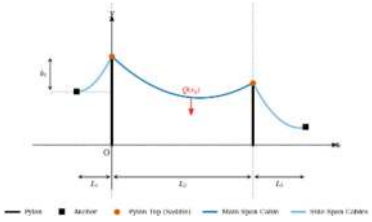

Fig. 3. Schematic of the asymmetric three-span cable system.

A. **Cable Profile Equation**

Under the small sag-to-span ratio assumption ($f/L < 1/8$), the cable profile under a distributed load$g$and a concentrated load$Q$is described by a piecewise parabolic equation. For the main span with$Q$atx_q, the sag profile $y(x)$ is:

$$y(x) = \left(g^* x^* (L_2 - x)\right)/(2H) + Q^* x^* \left(L_2 - x_q\right)/\left(H^* L_2\right) \left(\text{for } 0 \le x \le x_y\right) \quad (1)$$

$$y(x) = \left(g^* x^* (L_2 - x)\right)/(2H) + \frac{Q^* x^* (L_2 - x)}{(H^* L_2)} \left(\text{for } x_q < x \le L_2\right) \quad (2)$$

Here, H is the horizontal component of cable tension. It is crucial to note that H is constant throughout all continuous spans (main span and side spans) due to horizontal equilibrium at the frictionless saddles, making it the key unknown variable for the entire system.

B. **Cable Arc Length (Geometric Deformation)**

For any i-th span, its arc length$S_i$under load is obtained by integrating the differential of its profile equation:

$$S_i = \int [0, L_i] sqr\left(1 + \left(y_i'(x)\right)^k\right) dx \approx \int [0, L_i] \left(1 + 0.5 * \left(y_i'(x)\right)^k\right) dx \quad (3)$$

By substituting the derivative of the parabolic profile equation and integrating, the geometric cable length S_i is expressed explicitly as a function of the horizontal tension H, denoted as $S_i(H)$.

C. **Cable Length Control Equation (Physical Law)**

The core physical constraint of the system is the conservation of mass, manifested as the total unstressed length of the cable remaining constant. The unstressed length of any span, S_{oi}, is derived by subtracting the elastic elongation $\Delta S_{elastic}$ and thermal elongation $\Delta S_{thermal}$ from its geometric lengthS_i:

$$\Delta S_{elastic} = \left(T_{avg} * S_i\right)/(EA) \approx (H * \sec(\beta_i) * S_i)/(EA) \quad (4)$$

$$\Delta S_{thermal} = S_i * \alpha * \Delta t \quad (5)$$

Where $T_{avg}$is the average tension in the span, β_i is the inclination angle of the chord line for that span, E is the elastic modulus, A is the cross-sectional area, α is the coefficient of thermal expansion, and $\Delta t$is the temperature change.

Therefore, the unstressed length is also a function of H:

$$S_n(H) = S_1(H) - (H * st \in (\rho_1) * S_1(H))/(EA) - S_1(H) * \backslash alpha * \Delta t \quad (6)$$

Since the three-span cable is continuous, its total unstressed length$S0_{total}(H)$ remains constant under all load cases, yielding the governing equation:

$$S0_{total}(H) = S_{o1}(H) + S_{o2}(H) + S_{o3}(H) = Constant \quad (7)$$

This is a highly nonlinear transcendental equation with H as the sole unknown.

D. **Solution and Asymmetric Considerations**

For a given load case $(Q, x_1, \Delta t)$, the governing equation is solved for the unique value of H using the Newton-Raphson numerical iterative method. The key advantage of this theoretical model is that the asymmetric characteristics of the project (i.e., $L_1 \neq L_3$ and $h_1 \neq h_3$) are naturally incorporated as boundary conditions in the formulation of $y_i(x)$, $S_i(H)$, and β_i. Consequently, the calculated value of H accurately reflects the influence of the asymmetric layout, avoiding the errors introduced by symmetric simplifications.

E. **Determination of Pylon Top Loads**

Once H is determined, the tangential forces exerted by the cable on the saddle can be calculated through static equilibrium at the pylon top. These forces are then resolved into the three-dimensional force and moment vectors required for the subsequent local analysis.

3.3 Local Refined Level: Finite Element Model of Key Structures

Modeling Objectives and Platform. All FE analyses were performed using the commercial software ANSYS Workbench. The modeling process adhered to the following rigorous standards:

1. **Geometry and Material**: A 1:1 high-fidelity solid model was created. The primary material is Q355 steel, a high-strength low-alloy structural steel. Linear elastic properties were assigned ($E = 2.06 \times 105$ MPa, $\mu = 0.3$).
2. **Element and Mesh:** To accurately capture the stress gradients through the thickness of the plates and near complex joints, 3D solid elements (SOLID185) were used. The mesh was locally refined in regions of expected stress concentration, such as weld toes and geometric transitions, resulting in a high-quality mesh that ensures calculation accuracy.
3. **Loads and Boundary Conditions:** The reaction vectors calculated from Sect. 3.2 were precisely applied using "Remote Force" or "Bearing Load" features. Self-weight and wind loads were also included. Boundary conditions were defined according to the actual installation interfaces, using "Fixed Supports" to represent rigid bolting conditions.
4. **Solver and Post-Processing**: After completing the setup, the model was submitted to the Static Structural solver. Key results, such as von Mises stress, directional deformation, and reaction forces, were extracted and visualized using contour plots and data reports for detailed analysis in Chap. 5.

4 Case Study

4.1 Project Background and Construction Scheme

Project Overview. The Danjiang Small Three Gorges Bridge is a key control project of the Mianchi-Xichuan Expressway. It is a cable-stayed bridge featuring a composite girder, a main span of 536 m, and concrete pylons (3# at 157 m, 4# at 208.6 m). Its grand structure and the V-shaped gorge location (Fig. 4a) presented significant construction challenges. The steep terrain made traditional lifting methods impossible, necessitating a high-capacity cable crane system.

(a) On-site construction photo of the bridge

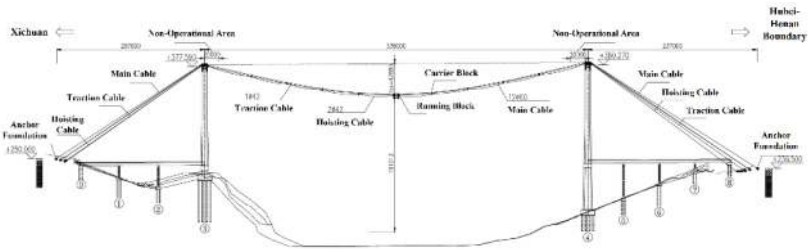

(b) General arrangement of the 320t cable crane)

Fig. 4. General overview of the engineering project.

Construction Scheme and System Parameters. A 320 t cable crane was employed for the main girder erection (Fig. 4b). The core construction sequence involves hoisting segments symmetrically from both pylons towards the center for final closure. Due to topographical constraints, the system exhibits a significant asymmetric layout. This study analyzes the more critical right girder system. Key design parameters are listed in Table 1.

Table 1. Key design parameters of the cable crane system (Right Girder).

Parameter	Symbol	Value & Unit	Remark
Main Span	L_2	536 m	Between Pylon 3# and Pylon 4#
Side Span at Pylon 3#	L_1	207 m	
Side Span at Pylon 4#	L_3	237 m	$L_1 \neq L_3$, Asymmetric
Height Difference at Pylon 3#	h_1	127.59 m	
Height Difference at Pylon 4#	h_3	152 m	$h_1 \neq h_3$, Asymmetric
Rated Lifting Capacity	P	320 t	
Main Cable Specification	–	Φ60–6 $\times$ 36WS + IWR	24 strands total
Elastic Modulus	E	1.05×10^5 MPa	
Cross-sectional Area	A	1692 mm^2	per strand

4.2 Definition and Location of Key Load Cases

To ensure a comprehensive safety assessment, a matrix of key load cases (Table 2) was defined based on the construction sequence. These cases represent scenarios likely to induce extreme structural responses and serve as the load inputs for the local refined analysis.

1. LC-1 (Mid-span Lifting): Represents the scenario of maximum cable tension and maximum bending moment in the spreader beam.
2. LC-2 (Near Pylon 3#): Represents the maximum unbalanced horizontal force acting on Pylon 3#, testing the pylon top structure's resistance to sliding and overturning.
3. LC-3 (Near Pylon 4#): Similar to LC-2 but for Pylon 4#, which has different geometric parameters due to asymmetry.
4. LC-4 (Temperature Drop): Evaluates the superimposed effect of thermal contraction (20 °C drop) which significantly increases cable tension.

Table 2. Matrix of key load cases.

Case ID	Location Description	Case Description	Primary Analysis Target
LC-1	Mid-span	Rated load lifting at mid-span	Max. tension in cable system; Max. bending stress in spreader beam
LC-2	Blind zone near Pylon 3#	Rated load lifting near Pylon 3#	Max. unbalanced force on Pylon 3# structure
LC-3	Blind zone near Pylon 4#	Rated load lifting near Pylon 4#	Max. unbalanced force on Pylon 4# structure
LC-4	Mid-span	Lifting at mid-span with 20 °C temp. drop	Evaluate superimposed effect of thermal load on max. cable tension

Among these, LC-1 is most critical for the spreader beam, while LC-2 and LC-3 are most hazardous for the respective pylon top structures. The subsequent FE analysis focuses on these three core cases.

4.3 Local Refined Finite Element Models

Pylon Top Structure Model. The structure is a complex spatial steel assembly designed to transfer the enormous cable loads to the concrete pylon.

1. Geometry and Material: A 1:1 solid model was created using Q355 steel.
2. Mesh: A hexahedral-dominant mesh with local refinement at welds and intersections was used, totaling 156,234 elements and 48,912 nodes (Fig. 5).
3. Loads and Boundaries: Unbalanced loads from the global model (for LC-2 and LC-3) were applied as "Remote Forces." A "Fixed Support" was applied at the base to simulate the rigid connection to the pylon.

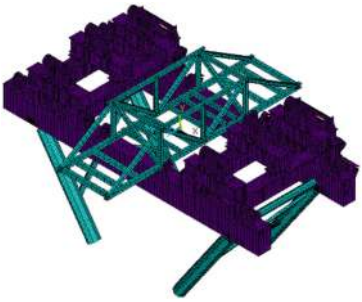

Fig. 5. FEM model and mesh details of the pylon top structure

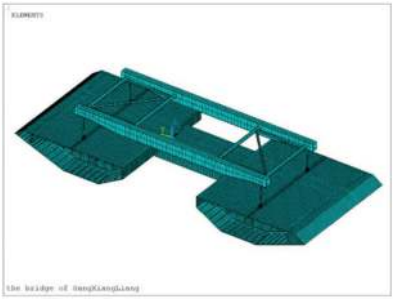

Fig. 6. FEM model of the spreader beam.

Spreader Beam Model. The spreader beam consists of two fish-belly box girders and connecting pipes.

1. Geometry and Material: A 1:1 solid model was created using Q355C steel.
2. Mesh: A hexahedral-dominant mesh with refinement at lugs and pinholes was used, totaling 210,548 elements and 78,345 nodes (Fig. 6).
3. Loads and Boundaries: For LC-1, the 311.96 t lift load (3060.3 kN) was applied as a uniform pressure. "Fixed Supports" were applied at the four upper lug connections.

5 Results and Discussion

5.1 Mechanical Performance of the Pylon Top Structure

Comparative Stress Analysis. Figure 7 shows the von Mises stress for the 4# pylon top structure under the critical load case LC-3. The peak stress is 176.3 MPa, located at the spatial intersection of the side-span crossbeam and the inclined support. A magnified view reveals that the stress concentration occurs specifically near the weld connecting the stiffener plates to the main girder.

Discussion: This stress concentration is consistent with structural mechanics principles. As a multi-member spatial joint subjected to combined bending and axial forces, this location acts as a node for force redistribution. The geometric discontinuity at the weld toe creates a stress singularity effect. However, according to the design code GB 50017–2017, the design strength f for Q355 steel (thickness < 40 mm) is 315 MPa. The calculated safety factor $K = 315 / 176.3 \approx 1.79$, which indicates an ample safety margin. The stress levels in the rest of the structure are generally below 100 MPa, suggesting that the material utilization is efficient but safe.

For comparison, the peak stress for the 3# pylon structure under LC-2 is slightly lower at 171.8 MPa (Fig. 8), confirming that stress magnitude generally increases with the degree of asymmetry (as Pylon 4# has a greater height difference and side span length). Both results are well below the allowable limit, validating the structural design.

Deformation Mode and Stiffness Check. Figure 9 shows the total deformation of the 4# structure under LC-3. The maximum displacement is 10.3 mm at the cantilevered end of the crossbeam. The deformation is primarily bending deflection under the unbalanced vertical force, with no abnormal torsion observed.

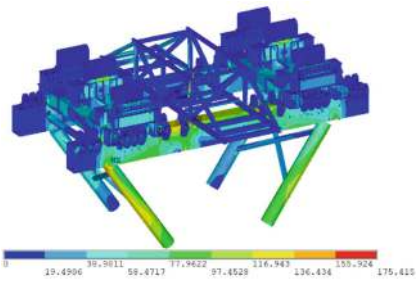

Fig. 7. Von Mises stress analysis of the 4# pylon top structure under LC-3.

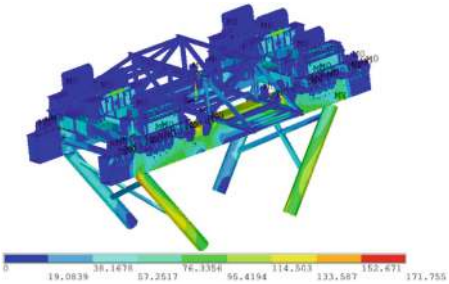

Fig. 8. Von Mises stress contour of the 3# pylon top structure under LC-2.

Discussion: The maximum displacement of 10.3 mm is very small relative to the member's span. This satisfies the stiffness requirements of GB/T 3811–2008 (typically L/400 to L/800). High stiffness is crucial for such temporary structures to ensure the stability of the saddle positions and, consequently, the accuracy of the main cable profile during lifting operations.

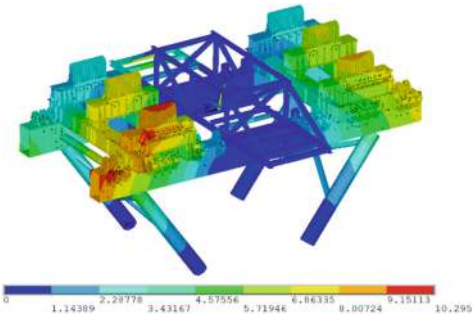

Fig. 9. Total deformation contour of the 4# pylon top structure under LC-3.

5.2 Multi-Case Mechanical Performance of the Spreader Beam

Stress and Deformation under Different Payloads. Table 3 summarizes the key results for the spreader beam under four typical load cases, visualized in Fig. 10. The results show a clear trend:

1. LC-1 (16 m Standard Segment): Total Weight 311.96 t - > Max Stress 177.9 MPa - > Max Disp 79.1 mm.
2. Closure Segment: Total Weight 243.47 t - > Max Stress 119.3 MPa - > Max Disp 52.6 mm.

Table 3. Summary of calculation results for the spreader beam under different load cases.

Case ID	Segment Type	Total Weight(t)	Max. von Mises Stress (MPa)	Max. Vertical Displacement (mm)
LC-1	16 m Standard	311.96	177.9	79.1
–	14.2 m Closure	243.47	119.3	52.6
–	7.8 m Type-A	186.90	99.9	42.2
–	5.1 m Type-F	163.10	90.1	37.1

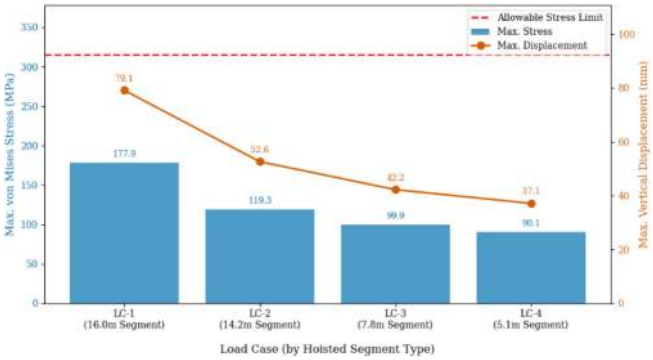

Fig. 10. Spreader beam performance under different load cases.

Discussion: The comparison reveals several important mechanical characteristics:

1. Linear Response: Stress and displacement are nearly proportional to the lifted load. This validates the assumption of linear elastic behavior in the FEM model.
2. Comprehensive Coverage: The analysis of all four cases confirms that the spreader beam is safe not only under the extreme LC-1 but across all operational scenarios.
3. Design Robustness: The structure maintains a stable configuration even under the lightest load, demonstrating its versatility for different segment types.

In-depth Analysis of Key Components (LC-1). To demonstrate the analysis depth, Fig. 11 shows the stress at the connection between the main girder and connecting pipes (~99.9 MPa), a critical load transfer node. Figure 12 shows the stress in the lug plates, which is far below the allowable limit, ensuring the reliability of the lifting points.

Discussion: This detailed examination demonstrates that the assessment extends beyond the global maximum stress to a thorough inspection of the entire load path and all potential risk points. The relatively low stress at the connections implies that the fish-belly design effectively distributes the moment.

5.3 Comprehensive Safety Assessment

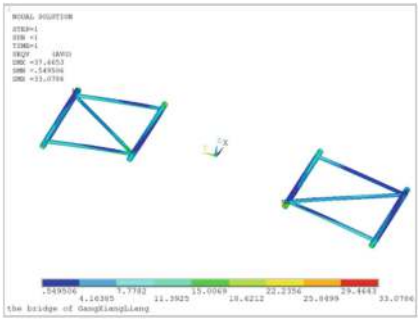

Fig. 11. Stress analysis of beam connection.

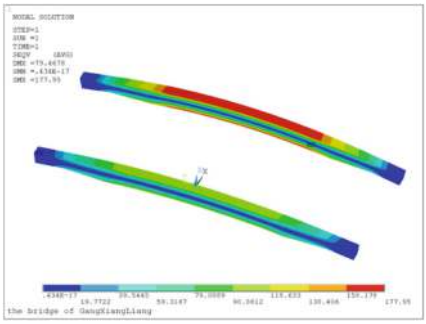

Fig. 12. Stress analysis of lug plates.

Table 4. Comprehensive safety assessment of key structural nodes.

Assessed Component	Worst Case	Calculated Max. Stress (MPa)	Material	Allowable Stress [σ] (MPa)	Safety Factor, K = [σ]/σmax	Conclusion
Pylon 4# Top Structure	LC-3	176.3	Q355	315	1.79	Pass
Pylon 3# Top Structure	LC-2	171.8	Q355	315	1.83	Pass
Spreader Beam (Main Girder)	LC-1	177.9	Q355C	315	1.77	Pass

A final comparison of all peak stresses against material allowable stresses is summarized in Table 4.

1. Pylon 4# Top Structure (LC-3): Calculated Max Stress 176.3 MPa vs. Allowable 315 MPa. Safety Factor $K = 1.79$. Conclusion: Pass.
2. Pylon 3# Top Structure (LC-2): Calculated Max Stress 171.8 MPa vs. Allowable 315 MPa. Safety Factor $K = 1.83$. Conclusion: Pass.
3. Spreader Beam (LC-1): Calculated Max Stress 177.9 MPa vs. Allowable 315 MPa. Safety Factor $K = 1.77$. Conclusion: Pass.

Final Discussion: The results in Table 4 unequivocally prove the success of the design. The safety factor for every key component remains above 1.7, substantially higher than the 1.2–1.5 typically required by codes for temporary structures. This high margin accounts for potential dynamic amplification factors and unforeseen eccentricities during construction. This not only confirms the design's integrity but also validates the power of the "global theoretical-local refined" methodology in accurately capturing the structural behavior.

6 Conclusion

This paper conducted a systematic study on the design and safety assessment of a long-span asymmetric cable crane. Through the specific case study of the Danjiang Bridge, a "global theoretical-local refined" hierarchical modeling methodology was proposed and implemented, along with a multi-case systematic safety assessment framework. The main conclusions are:

1. On the methodological level, a novel and efficient paradigm for analyzing complex rigid-flexible coupled systems was proposed and validated. The hierarchical strategy successfully decouples the system's macroscopic nonlinear response from the microscopic nodal stress analysis, overcoming the computational convergence issues faced by traditional unified models. This "divide and conquer" approach not only ensures numerical stability but also allows for the rapid iteration of design parameters in the early stages of engineering, offering a generalized solution for similar large-scale coupled systems.
2. On the design verification level, the systematic multi-case assessment comprehensively confirmed the safety and reliability of the key structural designs. All components showed safety factors exceeding 1.7 under the most unfavorable load combinations, proving that the asymmetric effects were effectively managed through robust structural design. The analysis revealed that for asymmetric systems, the governing load cases are often determined by the unbalanced horizontal forces rather than vertical gravity loads, a critical insight that distinguishes these systems from conventional cranes.
3. On the engineering application level, the end-to-end analysis process provides a valuable reference for the design and verification of similar non-standard, heavy-duty construction equipment. By validating the temporary structures against rigorous permanent structure standards, this study demonstrates a conservative yet necessary approach to ensuring construction safety in extreme environments.

   Future research could significantly expand the horizon of this work in two directions. First, regarding operational intelligence, the integration of this high-fidelity FE model with real-time sensor data could pave the way for a "Digital Twin" of the cable crane. This would enable predictive maintenance and real-time fatigue monitoring during the construction lifecycle. Second, regarding environmental adaptability, future studies should incorporate dynamic effects such as wind-induced flutter and buffeting analysis. Given the high flexibility of long-span cables, investigating the aerodynamic stability under canyon wind fields is crucial for the next generation of ultra-long-span construction equipment.

References

1. Malla, R.B.: Cable structures. In: Chen, W.F., Lui, E.M. (eds.) Handbook of Structural Engineering, 2nd edn, pp. 11-1–11-24. CRC Press, Boca Raton (2005). https://doi.org/10.1201/9781420039931
2. Starossek, U.: Progressive Collapse of Structures. Thomas Telford, London (2009). https://doi.org/10.1680/pcos.36109

3. Kim, S.E., Lee, J.H.: Geometrically nonlinear analysis of spatially curved and twisted beam-columns. Int. J. Numer. Methods Eng. **51**(9), 1069–1096 (2001)
4. Wu, T., Smith, I.F.: Integrated design of permanent and temporary structures for accelerated bridge construction. J. Bridg. Eng. **18**(11), 1146–1154 (2013). https://doi.org/10.1061/(ASCE)BE.1943-5592.0000473
5. Li, H., Li, S., Ou, J., Xiang, H.: Wind-induced vibration of the hangers of suspension bridges during construction. Struct. Infrastruct. Eng. **10**(4), 433–445 (2014). https://doi.org/10.1080/15732479.2012.703213
6. Gimsing, N.J., Georgakis, C.T.: Cable-Supported Bridges: Concept and Design, 3rd edn. John Wiley & Sons, Chichester (2011). https://doi.org/10.1002/9781119978237
7. Irvine, H.M.: Cable Structures. MIT Press, Cambridge (1981)
8. Buchholdt, H.A.: An Introduction to Cable Roof Structures, 2nd edn. Thomas Telford, London (1999). https://doi.org/10.1680/aitcrs.26247
9. Bathe, K.J.: Finite Element Procedures. Prentice Hall, Englewood Cliffs (1996)
10. Zhou, Y., Sun, L.: Thermal effects on a long-span cable-stayed bridge during construction. J. Bridg. Eng. **10**(5), 593–602 (2005). https://doi.org/10.1061/(ASCE)BE.1943-5592.0001387
11. Wang, X., Liu, Z., Li, A.: Finite element analysis and experimental study on a large tire-type gantry crane. Eng. Fail. Anal. **57**, 137–147 (2015). https://doi.org/10.1016/j.engfailanal.2015.07.019
12. Han, Q., Xu, G., Zhou, Y., Wang, Y.: Stability analysis of a launching gantry for segmental bridge construction. J. Bridg. Eng. **23**(3), 04017144 (2018)
13. Shabana, A.A.: Dynamics of Multibody Systems, 3rd edn. Cambridge University Press, Cambridge (2005). https://doi.org/10.1017/CBO9780511610523
14. Wasfy, T.M., Noor, A.K.: Computational strategies for flexible multibody systems. Appl. Mech. Rev. **56**(6), 553–613 (2003). https://doi.org/10.1115/1.1590354
15. Shao, Y.B.: Stress concentration factors and fatigue life assessment of large-scale cast steel nodes. J. Constr. Steel Res. **106**, 1–12 (2015). https://doi.org/10.1016/j.jcsr.2015.08.032
16. Han, L.H.: Concrete Filled Steel Tubular Structures. Science Press, Beijing (2007)
17. Pal, S., Patra, S.: Demountable connections in steel structures: a review. Structure. **28**, 1159–1175 (2020). https://doi.org/10.1016/j.istruc.2025.109188

The Development of Electro-Hydraulic Shaking Table

Zilong Zhao[1], Xiaofei Ma[2(✉)], Juke Wang[3], Guili Liu[2], and Lei Lv[2]

[1] Basic Courses Department, Chinese people's Liberation Army Aviation School, Beijing 101116, China
[2] Aviation Service Department, Chinese people's Liberation Army Aviation School, Beijing 101116, China
mxf_pg@163.com
[3] Institute of Geophysics, China Earthquake Administration, Beijing 100081, China

Abstract. The electro-hydraulic shaking table (EHHT) is an important device for conducting shaking control research and is widely used in various fields. The article introduces the current development status of electro-hydraulic shaking table at home and abroad and conducts a brief analysis. Meanwhile, the development trend of electro-hydraulic shaking table towards ultra-large-scale shaking table, shaking table array, centrifugal shaking table and networked collaborative joint experiments is expounded. On this basis, the construction situation of electro-hydraulic shaking table at home and abroad is summarized, analyzed and reviewed. This research work can provide certain reference and inspiration for the construction and independent research and development of electro-hydraulic shaking table in our country.

Keywords: Shaking table · Development status · Development trend

1 Introduction

Shaking table is essential equipment for conducting shaking simulation tests. It can be mainly classified into three types based on their driving methods: mechanical shaking table, electric shaking table, and electro-hydraulic shaking table. Among them, electro-hydraulic shaking table can accurately reproduce various excitations experienced by the research object and is widely used in engineering seismic research [1, 2], vehicle road simulation, and aerospace shaking testing [3], etc. The electro-hydraulic shaking table system integrates knowledge from multiple disciplines such as electro-hydraulic servo control theory, mechanical design theory, and power supply system theory, and is an important indicator of a country's industrial technology level [4]. In recent years, China has made significant progress in the research and development level and construction of electro-hydraulic shaking table, but there is still a certain gap compared with the advanced level abroad. Therefore, many scholars have summarized and analyzed the development history [1], control technology [5, 6], and development trends [7–9] of shaking tables, and have achieved a large number of research results. However, these research results have not

© The Author(s), under exclusive license to Springer Nature Switzerland AG 2027
G. Feng et al. (Eds.): ICCE 2025, SUCI, pp. 393–406, 2027.
https://doi.org/10.1007/978-3-032-32237-1_28

comprehensively and timely reflected the current development status of shaking tables at home and abroad, and in the introduction of the development trends of shaking tables, they have not provided detailed construction situations and analysis and comments. Therefore, based on the latest collected data, this paper comprehensively summarizes and analyzes the development status and trends of electro-hydraulic shaking table at home and abroad from these two aspects. This research work can provide certain reference and inspiration for the construction and independent research and development of electro-hydraulic shaking table in China.

1.1 MTS Corporation of United States

MTS Corporation's shaking table control technology and R&D capabilities are among the top in the world. The electro-hydraulic shaking table it has developed is suitable for highly specialized fields. In the field of seismic research in civil engineering, MTS Corporation built a large six-degree-of-freedom shaking table (with a table surface size of 6.1 m × 6.1 m) for the China Academy of Building Research. The table surface was designed by MTS and manufactured by Capital Iron and Steel Company. Figure 1(a) shows the underwater six-degree-of-freedom shaking table designed by MTS Corporation for the Disaster Prevention Research Center of Kyoto University, with a table surface diameter of 3.5 m. Figure 1(b) shows the "W-DECKER" long-period shaking table developed by MTS Corporation for Kajima Corporation in Japan, which can be used for seismic performance research on skyscrapers and nuclear power plants. In addition, MTS Corporation also developed a single-axis shaking table for Simpson Strong-Tie Company for seismic research on wood structures.

(a) Underwater six-degree-of-freedom shaking table

(b) "W-DECKER" shaking table

Fig. 1. Shaking tables developed by MTS.

1.2 Team Corporation of United States

Team Corporation is the world's first commercial company to introduce a six-degree-of-freedom multi-axis electro-hydraulic shaking table. The shaking table it has developed is widely used in various fields, including aerospace, rail transportation, automobiles, civil engineering, etc. The shaking test system for satellites developed by Team Corporation for NASA features a circular ring-shaped table surface. Team Corporation was the first to create a 4-poster simulation shaking table for automotive testing. In recent years, Team

Corporation has developed the Cube, a new type of shaking table as shown in Fig. 2(a). From the appearance, this shaking table is a cube, with three sets of parallel integral shaking units configured inside the cube. Figure 2(b) shows the improved Cube dual shaking table array system launched by Team Corporation.

(a) Cube shaking table (b) Double cube shaking table

Fig. 2. Shaking tables developed by team.

1.3 Servo Test Company of UK

Servo test is the earliest company in UK to focus on hydraulic Servo testing and motion simulation. It enjoys an extremely high reputation in fields such as seismic research, automotive testing, aerospace, and ergonomics. To date, Servo test has delivered and put into use nearly 100 sets of seismic simulation test systems. Figure 3 shows its recently launched Hexapod shaking table, with a table surface size of 2.0 m × 2.0 m. The actuator adopts hydrostatic bearings, featuring light weight and high performance.

Fig. 3. Hexapod shaking table developed by Servo test.

1.4 Japanese Shaking Table Company of Japan

The shaking tables developed by Japanese companies such as Mitsubishi, Hitachi and Sagamiya Seisakusho have always been in the leading position. Mitsubishi, with its unique shaking control technology and advanced hydraulic technology, has developed the world's first three-dimensional six-degree-of-freedom large-sized shaking table, and led the development of the world's largest shaking table, E-Defense, as shown in Fig. 4(a). Figure 4(b) shows the resonance shaking table developed by Hitachi, with a maximum

load of 10 T and an acceleration of up to 20 g. In addition, Hitachi has developed a centrifugal shaking system, whose maximum centrifugal acceleration can reach 100 g. Lu Gong Manufacturing has developed a small three-dimensional shaking table, which can be used for performance testing of automotive parts, etc.

(a) E-Defense

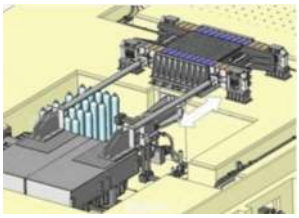

(b) Resonant shaking table

Fig. 4. Shaking tables developed by the companies in Japan.

1.5 Institute of Engineering Mechanics, China Earthquake Administration

The Institute of Engineering Mechanics of the China Earthquake Administration, in collaboration with domestic research institutions, jointly developed and constructed a 5.0 m × 5.0 m bidirectional electro-hydraulic shaking table. Subsequently, the bidirectional shaking table was upgraded and transformed into a three-directional six-degree-of-freedom shaking table as shown in Fig. 5. At present, thousands of shaking simulation tests have been conducted on this shaking table.

Fig. 5. 6-DOF EHVT developed by the Institute of Engineering Mechanics, CEA.

1.6 Institute of Electro-Hydraulic Servo, Harbin Institute of Technology in China

The Institute of Electro-Hydraulic Servo Simulation and Test System of Harbin Institute of Technology has developed China's first multi-axis hydraulic shaking test system with independent intellectual property rights, as shown in Fig. 6. Up to now, a large number of airborne environmental shaking simulation tests have been completed using this shaking test system.

Fig. 6. 6-DOF EHVT developed by the IEST.

To sum up, compared with the typical shaking tables currently developed in our country, the shaking tables developed by foreign manufacturing companies and research institutes have a wide range of applications (mainly including aerospace, automotive and civil engineering fields, etc.) and a variety of types (mainly including super-large shaking table, shaking table arrays, centrifugal shaking table and resonance shaking table, etc.) It features novel structures (such as Cube shaking table and Hexapod shaking table) and highly specialized features (such as underwater shaking table, long-period shaking table and NASA satellite test shaking system, etc.). Therefore, there is still a long way to go for our country in the field of shaking table research and development.

2 Development Trends

Ultra-large-scale shaking table, shaking table arrays, centrifugal shaking table and networked collaborative joint experiments are the development trends of electro-hydraulic shaking tables.

2.1 Ultra-Large-Scale Shaking Table

The ultra-large-scale shaking table provides a test platform for structural model tests with large scale ratios and even prototype structural tests, avoiding problems caused by size effects and insufficient similarity ratios. Therefore, the results of the shaking excitation test are more accurate and reliable.

The largest shaking table in the world at present is the E-Defense (with a table size of 20.0 m × 15.0 m and a load capacity of 1200 tons), which was completed and accepted by the National Institute of Disaster Prevention and Control (NIED) of Japan in 2005. The overview of the E-Defense is shown in Fig. 7(a). According to the records on the NIED official website, a large number of full-scale structural tests have been completed on E-Defense. The Powell Laboratory at the University of California, San Diego, with the support of the Seismic Engineering Network Simulation System (NEES) in the United States, has established the world's largest outdoor unidirectional shaking table, as shown in Fig. 7(b). Its tabletop size (12.2 m × 7.6 m) is smaller than that of the shaking table of NIED, but its load-bearing capacity (2200 T) and maximum horizontal acceleration (3.0 g) are both greater than those of E-Defense, and there is no limit on the height of the test structure [10]. The largest shaking table in China is the one built by Southwest

Jiaotong University (SWJTU) in 2017 (with a table surface size of 10.0 m × 8.0 m and a load capacity of 160 tons), as shown in Fig. 7(c). At present, Tianjin University in China is leading the construction of the world's largest shaking table, with a table surface size of 20.0 m × 16.0 m and a load capacity of 1350 tons.

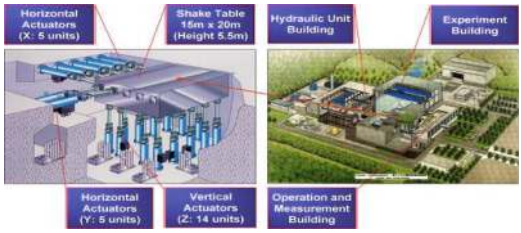

(a) General situation of the E-Defense

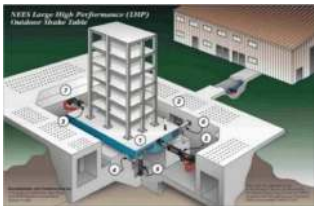

(b) NEES-UCSD shaking table

(c) Shaking table of Southwest Jiaotong University

Fig. 7. Super large-scale shaking table.

Among the above-mentioned super-large-scale shaking tables that have been built, in terms of shaking degrees of freedom, the shaking tables of E-Defense and SWJTU are both three-directional six-degree-of-freedom shaking tables, while the shaking table of UCSD is a horizontal unidirectional shaking table. In terms of the maximum load capacity, the shaking table load capacity of UCSD is the largest, followed by E-Defense, and the shaking table load capacity of SWJTU is the smallest. In terms of tabletop size, E-Defense has the largest, followed by the shaking table of UCSD, and the shaking table of SWJTU has the smallest tabletop size. In addition, the ultra-large-scale shaking table of SWJTU can be combined with the existing small shaking table to form an array, thereby conducting joint tests [11]. The shaking tables of E-Defense and UCSD are both important members of the NEES program, and have greatly expanded the application scope of both.

The use of ultra-large-scale shaking tables can carry out model tests of structures with large scale ratios and even full-scale tests of structures, which can more truly demonstrate the real response and seismic resistance of structures under shaking excitation. However, its construction cost is huge, and the operation and maintenance costs are high.

2.2 Shaking Table Array

An array composed of multiple small shaking tables can well simulate the response of a structure under multi-dimensional and multi-point excitation. Shaking table arrays have

obvious technical and economic advantages in the shaking test research of large spatial structures, large-span structures and irregular structures.

In 2003, MTS established a dual-array system for the University at Buffalo as shown in Fig. 8(a), which consists of two three-directional six-degree-of-freedom shaking tables (with table surface dimensions of 4.3 m × 4.5 m) [10]. In the same year, MTS established a table array for the University of Nevada, consisting of three horizontal bidirectional shaking tables (with table surface dimensions of 3.6 m × 3.6 m).

China has achieved rapid development in the construction of shaking table arrays. In 2004, Servo test built a dual-shaking table array system for Chongqing Transportation Research and Design Institute. This system consists of a fixed shaking table and a mobile shaking table (with a table surface size of 3.0 m × 3.6 m), forming a three-axis array system, with an adjustable span range of 2.0 m to 20.0 m [1]. In 2006, Beijing University of Technology completed and put into operation a 9-sub-platform (with a platform size of 1.0 m × 1.0 m) seismic simulation shaking table array system, as shown in Fig. 8(b) [2]. In 2011, the Institute of Engineering Mechanics established a dual-shaking table array system, which consists of a fixed table (with a table surface size of 5.0 m × 5.0 m) and a mobile table (with a table surface size of 3.5 m × 3.5 m). In 2013, Servo test built an array system consisting of three shaking tables for Fuzhou University. The size of the middle fixed table was 4.0 m × 4.0 m, and the size of the two movable side tables was 2.5 m × 2.5 m. The maximum working length of the system was 24.0 m [12]. In 2014, MTS developed an array system for Tongji University, which consists of four three-direction six-degree-of-freedom shaking tables (with a table surface size of 6.0 m × 4.0 m). Each shaking table can move and combine freely in two trench structures with lengths of 30.0 m and 70.0 m respectively. The total test capacity of the system is as high as 200 T. In 2017, Fuyun Tianyi built an array system for Beijing University of Technology, which consisted of two shaking tables (with table surface dimensions of 2.0 m × 2.0 m), and the maximum load of each single table was 10 T, as shown in Fig. 8(c). In 2019, Servo test built an array system for Central South University consisting of four three-direction six-degree-of-freedom shaking tables (with table surface dimensions of 4.0 m × 4.0 m), and the total test capacity of the system reached 120 T. In 2019, Servo test built the world's first underwater shaking table array system for Tianjin University. This system consists of two shaking tables with a table surface diameter of 3.6 m, as shown in Fig. 8(d). At present, MTS is building an underwater double shaking table array for Tianjin University. The table surface size of the shaking table is 6.0 m × 6.0 m, with a load capacity of 150 tons and a moving range of 45.0 m [13].

Except for the shaking table array system of Beijing University of Technology, the rest were all completed by MTS and Servo test. However, during the construction process, China has accumulated a great deal of valuable experience in the basic design of arrays [12], the layout design of array systems [14], the design of oil sources and oil circuits, and the design of servo control hardware systems [15].

It is worth mentioning that both sets of shaking table array systems of Beijing University of Technology were independently developed and constructed in China. At present, China's research and development technology and construction level in the field of shaking table arrays are also constantly improving. Certain achievements have been made in aspects such as control hardware architecture [15, 16], synchronous control strategies

(a) Buffalo university dual shaking array

(b) The nine-sub-platform array system of Beijing University of Technology

(c) The dual-array system of Beijing University of Technology

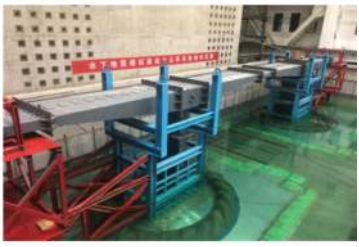

(d) The underwater dual-array system of Tianjin University

Fig. 8. Multiple shaking table arrays.

[17, 18], research on the interaction between control and structure, and compensation [19], but further in-depth research is still needed. Table 1 presents the main technical parameters of typical shaking table array systems at home and abroad.

2.3 Centrifugal Shaking Table

The centrifugal shaking table is the most advanced and effective equipment for conducting seismic environment simulation tests in the field of geotechnical engineering [20]. It can well study the dynamic characteristics of rock and soil, the liquefaction of the foundation, the stability of the slope, and the coupling relationship of soil, foundation and structure in the seismic environment [21].

The most representative centrifugal shaking systems abroad are those of the University of California, Davis (UC Davis), Rensselaer Polytechnic Institute (RPI), and the Korea Advanced Institute of Science and Technology (KAIST). The former two are both important components of the NEES program in the United States. The centrifugal shaking system of UC Davis includes a horizontal unidirectional centrifugal shaking table and a horizontal and vertical bidirectional centrifugal shaking table [22]. This system represents the highest level in the field of geotechnical engineering worldwide, as shown in Fig. 9(a). The centrifugal shaking system of RPI features a simple design and high safety. KAIST's centrifugal shaking system innovatively adopts dynamic reaction force self-balancing technology, thereby achieving the separation of the shaking table from the hoist basket [23].

Table 1. Main technical parameters of typical multiple shaking table arrays at home and abroad

Unit	Table size (m)	Number	Direction of shaking	maximum load (t)	frequency (Hz)	maximum displacement (mm)	maximum acceleration (g)
Buffalo University	4.3 × 4.5	2	X/Y	45	0.1 ~ 50	±350/±350	1.0/1.0
Nevada University	3.6 × 3.6	3	X/Y/Z	20	0.1 ~ 50	±150/±150/±75	1.5/1.5/1.5
Chongqing Transportation Research and Design Institute	3.0 × 3.6	2	X/Y/Z	35	0.1 ~ 50	±100/±100/±100	1.0/1.0/1.0
Beijing	3.0 × 3.0	1	X	10	0.1 ~ 50	±127	1.0
University of Technology	2.0 × 2.0	2	X/Y/Z	10	0.4 ~ 50	±125/±125/±100	2.0/2.0/2.0
Technology Institute of Engineering	5.0 × 5.0	1	X/Y/Z	30	0.1 ~ 100 Hz	±80/±80/±50	1.0/1.0/ 0.7
Mechanics	3.5 × 3.5	1	X/Y/Z	–	0.1 ~ 100 Hz	–	–
	4.0 × 4.0	1	X/Y	22	0.1 ~ 50	±250/±250	1.5/1.2
Fuzhou University	2.5 × 2.5	2	X/Y	10	0.1 ~ 50	±250/±250	1.5/1.2
Tongji University	6.0 × 4.0	4	X/Y/Z	60/30	0.1 ~ 50	±500/±500/±500	1.5/1.5/1.0
Central South University	4.0 × 4.0	4	X/Y/Z	30	0.1 ~ 50	±250/±250/±160	1.0/1.0/1.6
Tianjin University	R-3.6	2	X/Y/Z	12–20	0.1 ~ 100	–	–
	6.0 × 6.0	2	X/Y/Z	150	–	–	1.5/1.5/2.0

The centrifugal shaking systems of the Hong Kong University of Science and Technology (HKUST), the China Institute of Water Resources and Hydropower Research (IWHR), and Tsinghua University in China are also quite representative, as shown in Fig. 9(b). The centrifugal shaking table of HKUST is the best-performing centrifugal shaking table in China. This centrifugal shaking system adopts a unique variable capacity pressure compensation pump to drive the main shaft to rotate. The centrifugal shaking system of IWHR is equipped with a horizontal and vertical bidirectional centrifugal shaking table, and the oil source pump is installed on the rotating arm, which is convenient for later maintenance. The centrifugal shaking system of Tsinghua University adopts a closed-loop servo control circuit and strip-shaped linear guides, featuring high waveform accuracy.

The main technical indicators of typical centrifugal shaking systems at home and abroad are shown in Table 2.

(a) Centrifugal shaking system of UC Davis

(b) Centrifugal shaking system of the Hong Kong University of Science and Technology

Fig. 9. Centrifuge shaking systems.

It can be known from Table 2 that in terms of the amplitude of motion, the UC-Davis unidirectional centrifugal shaking table has the largest amplitude, while the HKUST centrifugal shaking table has the smallest amplitude. In terms of centrifugal acceleration, the centrifugal shaking tables of RPI, IWHR and KAIST are all 100 g, and the centrifugal acceleration of Tsinghua's centrifugal shaking table is the smallest. In terms of load mass, the maximum load of the UC-Davis centrifugal shaking table is 2700 kg, which far exceeds the load of domestic centrifugal shaking tables (up to 400 kg). The relatively low maximum load mass greatly restricts the application of centrifugal shaking tables. Therefore, increasing the maximum load of the centrifugal shaking table is one of the issues that need to be focused on in the development of centrifugal shaking tables in our country.

In addition, all the above-mentioned centrifugal shaking systems adopt rubber shear bearings to bear the centrifugal force during system operation. However, the hysteresis characteristics of rubber shear bearings are obvious and they are not convenient for later upgrading and transformation. At present, Harbin Institute of Technology has developed an incomplete balanced hydrostatic bearing [21], which has effectively solved the above-mentioned problems.

Table 2. Main indexes of typical centrifuge shaking systems at home and abroad.

Name	Effective radius of the centrifuge (m)	Centrif ugal acceleration (g)	Shaking acceleration (g)	Maximu m shaking frequency (Hz)	Maxi mum dynamic load (kg)	Maximum amplitude (mm)
UC-Davis single-axis centrifugal shaking table	8.5	75	30	400	2700	±12.5

(*continued*)

Table 2. (*continued*)

Name	Effective radius of the centrifuge (m)	Centrif ugal acceleration (g)	Shaking acceleration (g)	Maximu m shaking frequency (Hz)	Maxi mum dynamic load (kg)	Maximum amplitude (mm)
UC-Davis dual-axis centrifugal shaking table	8.5	75	30	Horizontal 300 vertical 300	2000	Horizontal ±12.5 vertical ±7.5
RPI horizontal bidirectional centrifugal shaking table	2.7	100	30	350	250	±6.5
KAIST centrifugal shaking table	5.0	100	40	300	700	±6.5
HKUST centrifugal shaking table	3.4	75	35	350	300	±3.0
IWHR centrifugal shaking table	5.03	100	Horizontal 30 vertical 20	400	400	±10.0
Tsinghua centrifugal shaking table	2.0	50	20	250	100	±10.0

2.4 Networked Collaborative Joint Experiment

Networked collaborative joint experiments are at the forefront of international structural engineering and represent a new generation of shaking test research systems. This system can realize the division of labor, integration and joint experiments of experimental resources in different regions through network links. Japan's parallel quasi-dynamic test system applying the Internet, as well as South Korea's KOCED program, etc.

In 2004, the United States established NEES with the aim of building a new generation of experimental research systems featuring remote observation and collaborative control capabilities. The seismic research equipment of NEES includes a new generation of shaking tables, centrifugal testing machines, tsunami wave pools, large laboratory systems, and on-site experimental and monitoring systems connected via efficient Internet. Figure 10(a) shows a multi-site online simulation experiment jointly completed by the University of Illinois (UIUC), the University of Colorado (CU), and the National Center for Supercomputing Technology Applications (NCSA). Hunan University in China was the first to propose the concept of remote collaborative experiments, and developed and

established the HQH-NSER remote collaborative experiment system. In 2006, Hunan University, Tsinghua University, Harbin Institute of Technology and the University of Southern California conducted the first publicly available online remote collaborative experiment, as shown in Fig. 10(b). In 2008, the Institute of Engineering Mechanics of the China Earthquake Administration began the construction of a networked collaborative joint experimental system and eventually conducted the world's first distributed collapse simulation test that combined different experimental systems and controlled complex boundary conditions among China, the United States and Japan.

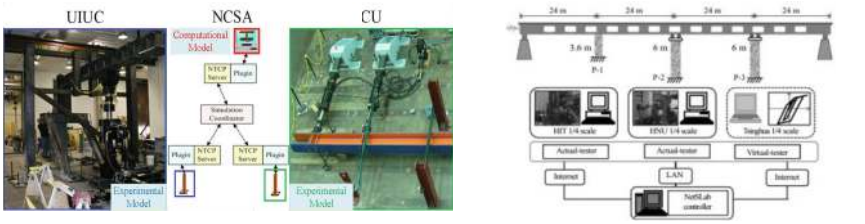

(a) NEES multi-site online simulation test (b) Domestic remote collaborative trials

Fig. 10. Centrifuge shaking systems networked collaboration united experiments.

To sum up, both at home and abroad, multiple networked collaborative experimental platforms with relatively complete experimental functions and mature technologies have been established, and some simple networked collaborative joint experiments have been carried out, but no large-scale and complex-structured collaborative joint experiments have been conducted [24]. The coordination of boundaries and the scalability and portability of the experimental platform are the further research directions of the networked collaborative experimental platform [25, 26].

3 Conclusion and Discussion

This article introduces the current development status of shaking table at home and abroad. Based on a brief elaboration of the development trend of shaking table, it presents the construction situation of shaking table at home and abroad, and conducts analysis and summary. Based on these introductions, analyses and summaries, the following viewpoints are put forward:

1. Developing shaking table that is applicable to various fields, highly specialized, and feature new types and structural forms is an important research direction for shaking table in China.
2. In the process of actively introducing and independently developing a large number of shaking table, China has accumulated a great deal of valuable experience, laying a solid foundation for the independent research and development of high-performance domestic shaking table.

3. Enhancing the synchronous control performance of the shaking table array, increasing the maximum load capacity of the centrifugal shaking table, and improving the scalability and portability of the networked collaborative test platform are the issues that need to be addressed in the field of shaking table research in China.

References

1. Gao, C.H., Ji, J.B., Yan, W.M., et al.: Developments of shaking table technology in China. China Civ Eng J. **47**(8), 9–19 (2014). https://doi.org/10.15951/j.tmgcxb.2014.08.027
2. Ji, J.B., Li, X.L., Yan, W.M.: Research on shaking table array and dynamic model test. J. Struct. Eng. **27**(Supp1), 31–36 (2011). https://doi.org/10.3969/j.issn.1005-0159.2011.z1.006
3. Claudio, P.: Shaking tests on the preloaded LARES satellite and separation system. J. Aerosp Sci Technol. **42**(4), 470–476 (2015). https://doi.org/10.1016/j.ast.2015.01.023
4. Shen, G.: Research on time waveform replication control strategy of 3 degree-of-freedom electro-hydraulic shaking table. Doctoral dissertation, Harbin Institute of Technology, Harbin (2011).
5. Ji, J.B., Li, F.F., Li, Z.B., et al.: Research and advances on the control technology of the multiple shaking table array system. J. Struct. Eng. **28**(6), 96–101 (2012). https://doi.org/10.3969/j.issn.1005-0159.2012.06.017
6. Han, J.W., Zhang, L.P.: The development and control technology of multi-DOF shaker. J. Chin Hydraul Pneumat. **1**, 1–6 (2014). https://doi.org/10.11832/j.issn.1000-4858.2014.01.001
7. Zhao, J.: Development and application of the shaking table. J. Earthq. Res Sichuan. **3**, 38–40 (2014). https://doi.org/10.13716/j.cnki.1001-8115.2014.03.010
8. Zhang, L.P.: Research on Time Waveform Replication Control Strategy of Redundant-Driven Electro-Hydraulic Shaking Tables Doctoral Dissertation. Harbin Institute of Technology, Harbin (2017)
9. Li, F.F.: Research on Adaptive Multi-Variable Control Technology of Shaking Table Array System Doctoral Dissertation. Beijing University of Technology, Beijing (2018)
10. Cai, X.J., Tian, S.Z.: Research advances of shaking table testing method. J. Struct Eng. **27**(Supp1), 42–46 (2011). https://doi.org/10.15935/j.cnki.jggcs.2011.s1.009
11. Liu, B.D., Guo, X.: Experimental study of field shaking influence induced by the 8 m × 10 m shake table of southwest jiaotong university. J. Earthquake Res China. **35**(2), 226–237 (2019). https://doi.org/10.3969/j.issn.1001-4683.2019.02.007
12. Fang, Z.M., Huang, F.Y., Chen, B.C., et al.: Study on design and construction of reaction mass of the earthquake simulation triple shaking tables of Fuzhou university J. J Fuzhou Univ (Nat Sci Ed). **41**(4), 807–812 (2013). https://doi.org/10.7631/issn.1000-2243.2013.04.807
13. Ji, J.B.: What can earthquake shaking table do Beijing Daily, 2019-08-29(013) (2019).
14. Tianjin University: An underwater shaking table array Patent, China, 201520284434.9 (2015).
15. Ji, J.B., Li, F.F., Yan, W.M., et al.: Hardware architecture design of the distributed controller for the multiple shaking table array system. J. Struct. Eng. **28**(6), 102–107 (2012). https://doi.org/10.3969/j.issn.1005-0159.2012.06.018
16. Wang, S.J., Gao, R.H., Zhai, H., et al.: Research on synchronous motion control of three shaking tables platform based on EtherCAT. J. Mach Des Manuf. **12**, 168–171, 176 (2018). https://doi.org/10.3969/j.issn.1001-3997.2018.12.042
17. Guan, G.F., Xiong, W., Wang, H.T.: Control of a dual shaking tables shaking test system J. J Shock Vib Control. **36**(6), 207–211, 217 (2017). https://doi.org/10.13465/j.cnki.jvs.2017.06.032

18. Li, X.J., Wang, J.K., Li, F.F., et al.: Differential movement synchronous tracking control strategy of double-shaking table system loading with specimen. J. Shock Vib. **2018**(8), 1–11 (2018). https://doi.org/10.1155/2018/1785184
19. Li, F.F., Li, X.J., Wang, J.K.: Effects of interaction between dual shaking tables and specimen and force feedback compensation control. J. Shock Vib. **2018**(2), 1–12 (2018). https://doi.org/10.1155/2018/6795763
20. Luo, Z.B.: Modelling and control strategy study of hydraulic centrifuge shaker used in earthquake simulation. Doctoral dissertation, Harbin Institute of Technology, Harbin (2015).
21. Gao, L.: Excitation system design and servo control strategy study of two axis centrifuge shaker. Master's thesis, Harbin Institute of Technology, Harbin (2013).
22. Mason, H.B., Kutter, B.L., Bray, J.D., et al: Earthquake motion selection and calibration for use in a geotechnical centrifuge. In: 7th International Conference on Physical Modelling in Geotechnics, pp. 361–366 (2010). https://doi.org/10.1201/b10554-56.
23. Kim, D.S., Lee, S.Y., Yun, W.C., et al.: Self-balanced earthquake simulator on centrifuge and dynamic performance verification. J. KSCE J Civ Eng. **17**(4), 651–661 (2013). https://doi.org/10.1007/s12205-013-1591-3
24. Liu, J.: Development of a remotely collaborative pseudo-dynamic testing platform for bridge structures considering soil-structure interaction. Master's thesis, Hunan University, Changsha (2013).
25. Wu, Y.M.: Development of a remotely collaborative pseudo-dynamic testing platform for bridge structures considering group of pile foundation. Master's thesis, Hunan University, Changsha (2014).
26. Jing, H.J.: Development of a remotely collaborative pseudo-dynamic testing platform for bridge structures considering multiple-support excitation. Master's thesis, Hunan University, Changsha (2015).

Optimization of Main Temporary Pier Location for Small-Radius Curved Steel Box Girder during Incremental Launching Construction

Kunfeng Zhang[1(✉)], Ping Zhao[1], Xi Ding[1], Jia Mi[1], Feilong Fan[1], Yingfu Guo[1], and Xueming Li[2]

[1] Shaanxi Road & Bridge Group Co., Ltd, 306 Jixiang Road, Xi'an, Shaanxi 710075, China
1371260434@qq.com

[2] Xi'an University of Architecture and Technology, 13 Yanta Road, Xi'an, Shaanxi 710055, China

Abstract. This study optimizes the location of the main temporary pier D4 during the incremental launching of a small-radius curved steel box girder bridge on a ramp of an interchange in Xi'an. A simplified mechanical model was established to preliminarily determine the pier location by minimizing cross-section rotations of the girder. The entire launching process was simulated using MIDAS to investigate the influence of the positioning and angular alignment of the main temporary pier, while incorporating safety and construction considerations. The optimized layout features a spacing of 26.66 m between temporary piers D4 and D3, with a 55° angle between the connecting line of the inner and outer supports and the road design axis. This configuration ensures rational stress distribution in both the girder and temporary structures, while minimizing adverse impacts on expressway facilities and traffic flow.

Keywords: Curved steel box girders · Incremental launching · Temporary piers · Layout optimization

1 Introduction

Curved steel box girder bridges are widely employed in large-scale overpasses, interchanges, and ramp connections due to their superior structural performance, adaptability to complex alignments, aesthetic appearance, and enhanced driving comfort [1, 2]. When spanning existing traffic lines or constructed in constrained sites where in-situ assembly is infeasible, the incremental launching method is often adopted to improve construction accuracy and minimize environmental disruption [3]. The use of temporary piers increases the span-crossing capacity of girder segments [4]. However, during multi-point incremental launching of small-radius curved steel box girders, the structure is subjected to combined bending-torsion effects [5]. Moreover, significant differences in support reactions between the inner and outer sides of temporary piers arise due to the eccentricity of the girder's center of gravity, imposing stricter requirements on the structural configuration and layout of temporary piers.

© The Author(s), under exclusive license to Springer Nature Switzerland AG 2027
G. Feng et al. (Eds.): ICCE 2025, SUCI, pp. 407–420, 2027.
https://doi.org/10.1007/978-3-032-32237-1_29

Existing research has predominantly focused on incremental launching construction for straight steel box girder bridges, while studies addressing the optimization of temporary pier locations during the incremental launching of small-radius curved steel box girders remain insufficient. There is therefore a need for targeted investigations. This paper examines the incremental launching process of the steel box girder bridge on the B Ramp of the Xinxing South Road-East Ring Expressway Interchange. A simplified mechanical model was established for preliminary optimization, coupled with a MIDAS-based incremental launching simulation to refine the layout of main temporary pier. This integrated approach effectively reduces steel box girder installation misalignment and secondary internal forces, providing practical guidelines for similar geometrically constrained bridge projects.

2 Project Overview

The B Ramp of the Xi'an Xinxing South Road-East Ring Expressway Interconnect spans 1199 m, serving as a supporting project for Xi'an East Station which connect the Xinxing South Road viaduct and the outer ring of the East Ring Expressway. Span Group 9 of the B Ramp consists of a continuous steel box girder with spans of 44.5 m, 60 m, and 47 m, supported by Piers 25 ~ 28. The first two spans (44.5 m and 60 m) are situated on a left-deviated circular curve with a radius of 70 m, while the third span (47 m) primarily follows a transition curve connecting to a circular curve of 1,000 m radius. The bridge elevation and plan layout are shown in Figs. 1 and 2. The steel box girder adopts a single-box double-cell cross-section fabricated from Q345 steel, with a top slab width of 10.3 m, bottom slab width of 5.3 m, and a uniform girder height of 2.3 m. This girder section crosses over a ring expressway and was constructed using a combined incremental launching and in-situ assembly method. The second span, traversing the expressway, was pre-assembled at the position of the third span and incrementally launched from Pier 27 to Pier 26 to its final design position.

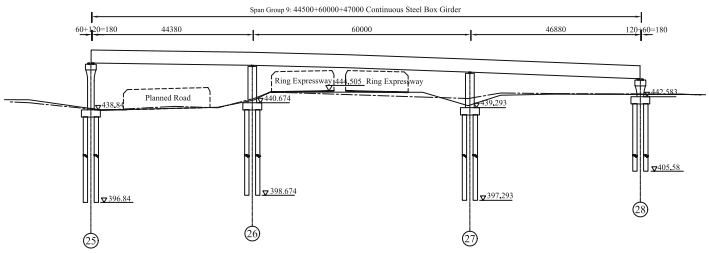

Fig. 1. Schematic facade layout of span group 9 steel box girder.

This study on the incremental launching construction of Span 2 steel box girder is being carried out to optimize the location of the main temporary pier. For the B Ramp girder segmentation scheme, the launching segment comprises five precast segments (segments 4 ~ 8), each measuring 14 m in length. During construction, segments 4, 5, and 6 are initially assembled and incrementally launched forward by approximately

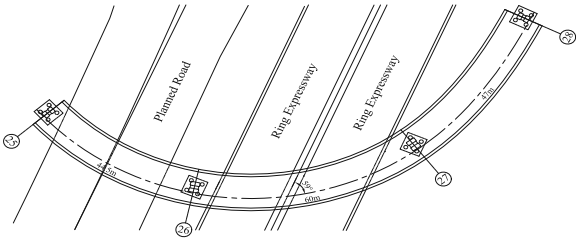

Fig. 2. Schematic plane layout of span group 9 steel box girder.

28 m. Subsequently, segments 7 and 8 are sequentially spliced to the trailing end of the launched section. The entire girder assembly is then advanced to its final design position.

Five temporary piers (D1 ~ D5) were deployed on site. The layout of temporary piers and assembly support P1 is shown in Fig. 3, with geometric parameters satisfying $l_1 = l_2 = l_3 + l_4 = 14$ m. To facilitate girder lowering after launching, piers D3 and D5 were placed between permanent piers, adjacent to Piers 27 and 28 respectively, where $l_4 = 4$ m and $l_7 = 2.78$ m. Given the considerable span between D3 and D5 ($L = l_5 + l_6 = 51.72$ m), a main temporary pier D4 was additionally installed within the Ring Expressway right-of-way.

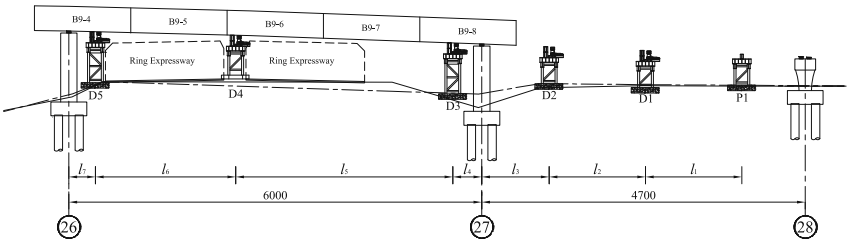

Fig. 3. Layout of temporary piers.

3 Preliminary Optimization of Main Temporary Pier Locations

3.1 Functional Role of Temporary Piers

Temporary piers serve as the primary load-bearing structures in incremental launching [6], tasked with supporting the self-weight of launching girder segments and launching equipment while ensuring rational distribution of support reactions. By reducing the cantilever length of the launched girder segments, temporary piers effectively mitigate negative bending moments in the steel box girder. Concurrently, they constrain excessive linear displacements and angular rotations of the girder, thereby enhancing alignment control precision. Consequently, the strategic determination of temporary pier quantity and spacing critically governs the structural safety of steel box girders, enabling both construction risk mitigation and cost reduction [7].

3.2 Optimization Model Assumptions

To facilitate formula derivation and preliminary optimization analysis, the model is simplified through the following assumptions:

1. Torsional effects induced by the curved girder are neglected, with the model idealized as a flexural continuous beam considering longitudinal spans [8];
2. All cross-sections of the steel box girder exhibit homogeneous material properties, and the girder is subjected solely to self-weight loads.
3. Support settlements and thermal load effects are disregarded;
4. The restraining effects of temporary piers on the girder are equivalently represented by hinged supports.

3.3 Preliminary Optimization Analysis

Angular deviations of girder segments during the mid-to-late phases of incremental launching significantly impact installation misalignment [9]. In this project, as the steel box girder approaches its design position, it is supported by temporary piers D2, D3, D4, and D5. Optimization analysis of the main temporary pier location was conducted under the condition that the girder's trailing is exactly supported by pier D2, as illustrated in Fig. 5. Subsequently, the launching girder segment transitions to being supported by temporary piers D3, D4, and D5, as illustrated in Fig. 4.

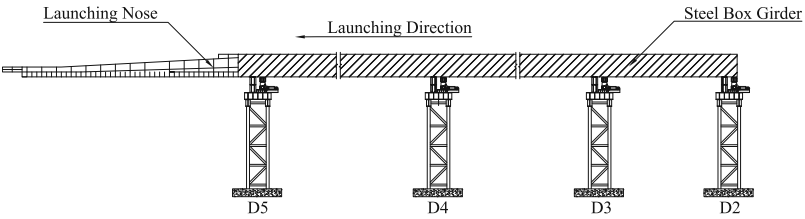

Fig. 4. Simplified structural façade.

Based on this configuration, a simplified mechanical analysis model was established as shown in Fig. 6. Each temporary pier corresponds to a hinged support labeled A, B, C, and D. The distances between temporary piers D3 and D2, and between D3 and D5 are denoted as l and L. By defining the distance between temporary piers D4 and D3 as x, then $l_3 + l_4 = l$, $l_5 = x$, $l_6 = L - x$. The box girder and launching nose ahead of support D were equivalently modeled as concentrated forces and moments acting at point D. The influence of these equivalent loads on support D was represented through elastic restraint with a stiffness coefficient k.

Based on the displacement method in structural mechanics, equilibrium equations for the box girder cross-sections at each support location were formulated [10]:

$$A: \frac{4EI}{l}\theta_A + \frac{2EI}{l}\theta_B - \frac{1}{12}ql^2 = 0 \tag{1}$$

$$B: \frac{2EI}{l}\theta_A + \left(\frac{4EI}{l} + \frac{4EI}{x}\right)\theta_B + \frac{2EI}{x}\theta_C + \frac{1}{12}ql^2 - \frac{1}{12}qx^2 = 0 \tag{2}$$

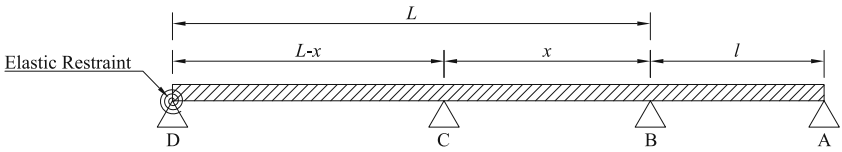

Fig. 5. Simplified mechanical model.

$$C: \frac{2EI}{x}\theta_B + \left(\frac{4EI}{x} + \frac{4EI}{L-x}\right)\theta_C + \frac{2EI}{L-x}\theta_D + \frac{1}{12}qx^2 - \frac{1}{12}q(L-x)^2 = 0 \quad (3)$$

$$D: \frac{2EI}{L-x}\theta_C + \frac{(4+k)EI}{L-x}\theta_D + \frac{1}{12}q(L-x)^2 = 0 \quad (4)$$

Where:θ_A, θ_B, θ_C, θ_D= rotation angles of the steel box girder cross-sections at supports A, B, C, and D;EI = flexural rigidity of the girder cross-section;q = uniformly distributed line load intensity due to the girder's self-weight.

Parameters $m = x/l$ and $n = (L - x)/l$ are defined, where m represents the ratio of the distance between temporary piers D4 and D3 to that between D2 and D3, and n denotes the ratio of the distance between temporary piers D4 and D5 to the same reference length (D2 ~ D3). Here, $l = 14$ m and$L = 51.72$ m. Letting $m + n = \lambda$, it follows that $\lambda = L/l = 3.69$, with constraints $0 < x < 51.72$ and $0 < m < 3.69$.

By solving the simultaneous Eqs. (1) ~ (4) and substituting $n = 3.69 - m$, the rotation angle expression for the cross-section at the trailing end of the steel box girder is derived as:

$$\theta_A = \frac{22.14m^3 - (251.1 + 40.85k)m^2 + (390.12 + 73.4k)m + (44.28 + 11.07k)}{-6m^2 + (88.56 + 24.14k)m + (88.56 + 22.14k)} \times \frac{ql^3}{24EI} \quad (5)$$

To investigate the influence of the girder segment on the left side of support D on the value of θ_A, analyses were conducted with varying values of the elastic restraint stiffness coefficient:

4 When $k = 0$, Support D Behaves as a Hinged Connection. Substituting $k = 0$ into Eq. (5):

$$\theta_A = \frac{22.14m^3 - 251.1m^2 + 390.12m + 44.28}{-6m^2 + 88.56m + 88.56} \times \frac{ql^3}{24EI} \quad (6)$$

5 When $k \to +\infty$, Support D Approximates a Fixed Connection. Taking the Limit of Eq. (5) as k Approaches Infinity:

$$\theta_A = \frac{-40.85m^2 + 73.4m + 11.07}{24.14m + 22.14} \times \frac{ql^3}{24EI} \quad (7)$$

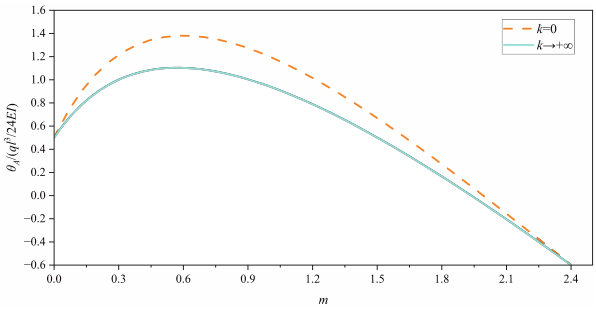

Fig. 6. Trailing-end cross-section rotation angle vs. D4 pier position.

Using Eqs. (6) and (7), the curves of $\theta_A/(ql^3/24EI)$ versus m for support D under both hinged and fixed conditions is plotted, as shown in Fig. 6.

When $0 < m < 2.4$, the curves corresponding to $k = 0$ and $k \to +\infty$exhibit similar trends: θ_A first increases then decreases with the D3 ~ D4 spacing, reaching zero at a critical m value. The actual rotation curve lies between these two cases, with minor differences indicating limited influence of stiffness coefficient k on θ_A. During actual launching, the cantilever segment ahead of pier D5 significantly affects girder internal forces. As the cantilever segment imposes non-negligible loads on Support D, the mechanical model is further simplified by treating Support D as a fixed connection ($k \to +\infty$) [11].

By substituting Eq. (7) into Eq. (1), the angle θ_B can be determined:

$$\theta_B = \frac{81.7m^2 - 122.66m}{88.56m + 22.14} \times \frac{ql^3}{24EI} \tag{8}$$

1. Let $\theta_A = 0$, solving Eq. (7) yields $m_1 = -0.14$ and $m_2 = 1.93$. Given the constraint $0 < m < 3.69$, the valid solution $m_2 = 1.93$ corresponds to a D3 ~ D4 spacing of 27.02 m, minimizing the rotation angle at the girder's trailing end.
2. Let $\theta_B = 0$, solving Eq. (8) yields $m_1 = 0$ and $m_2 = 1.50$. Within the domain $0 < m < 3.69$, the valid solution is $m_2 = 1.50$, corresponding to a spacing $l =$ 21 m. This configuration minimizes the rotation angle at the location of temporary pier D3.

Through the above analysis, considering the influence of the D3 ~ D4 spacing on rotation angles at both the girder's trailing end (θ_A) and pier D3 (θ_B), the optimal positioning of temporary pier D4 occurs within the range $1.50 < m < 1.93$.

6 Full-Process Simulation of Incremental Launching

6.1 Finite Element Model Development

Based on preliminary optimization results for main temporary pier locations and considering the need to minimize cantilever length ahead of temporary piers D3 and D4 during launching, temporary pier D4 was positioned at the midpoint between D3 and D5. This

configuration corresponds to $m = 1.85$, with a calculated D3 ~ D4 spacing of 25.86 m approximated as 26 m in the simulation. Construction phases were defined according to structural system variations and launching sequences, with each phase representing a 2-m advancement increment, totaling 36 phases. Ten representative phases were selected for detailed analysis, as summarized in Table 1.

Table 1. Typical construction phases of incremental launching.

Phases	Launching Distance (m)	Phases description
1	0	Assembly of launching nose and segments 4 ~ 6, supported by D1, D2, D3
6	8.4	Leading end of launching nose approaching pier D4, maximum front cantilever at D3
10	16.0	Trailing end of box girder detaches from D1, maximum rear cantilever at D2
17	28.1	Trailing end supported by D2
18	28.1	Splicing segments 7 ~ 8, maximum rear cantilever at D1
22	34.4	Leading end approaching pier D5, maximum front cantilever at D4
26	42.0	Trailing end detaches from D1, maximum rear cantilever at D2
33	56.0	Trailing end detaches from D2, maximum rear cantilever at D3
35	60.5	Girder launched to design position, maximum front cantilever at D5
36	60.5	Dismantling launching nose and lowering girder, pier D4 retained

The incremental launching process of the steel box girder in Span 2 of Span Group 9 on the B Ramp was simulated using MIDAS to calculate bending moments and stress distributions across all construction phases, thereby identifying the most critical phase. The launching nose, with a length of 18 m, comprises variable cross-section H-shaped steel girders (Q355B, 20 mm thick) interconnected by lateral trusses between the inner and outer main girders. The finite element model employs beam elements to simulate both the launching nose and steel box girder, totaling 346 nodes and 399 elements. Rigid connections were applied between the launching nose and the girder, with conventional supports defining the nose's boundary conditions. Elastic links were implemented between temporary pier supports and girder elements. The finite element model is illustrated in Fig. 8. During computation, only the girder's self-weight was considered [12]. Structural and boundary groups were established for each construction phase, with dynamic simulation of the launching process achieved through phased activation/deactivation of these groups, with the finite element model shown in Fig. 7.

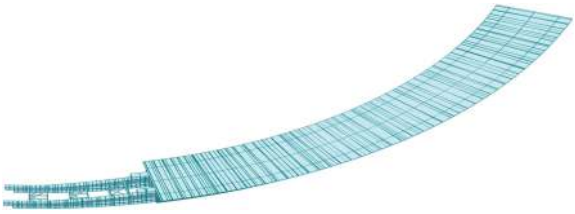

Fig. 7. Finite element model of incremental launching.

6.2 Internal Force Analysis of Steel Box Girder

During incremental launching, the continuous variations in temporary pier support locations and structural system result in alternating positive and negative internal forces within the steel box girder cross-sections. The bending moment envelope diagram for the girder during the launching process was derived from the maximum positive and negative moments observed in each construction phase, as shown in Fig. 8.

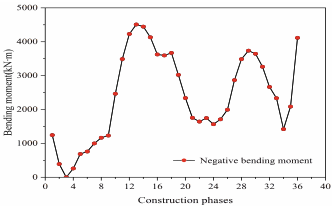

(a) Positive bending moment envelope diagram

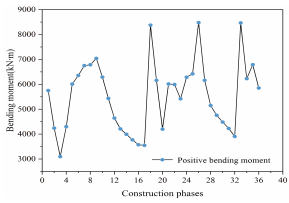

(b) Negative bending moment envelope diagram

Fig. 8. Internal force envelope diagram of steel box girder.

As shown in Fig. 8(a), when the launching nose approaches pier D4 at Phase 6, positive bending moments develop in the girder segment between D3 and D4, increasing with the growing span between these piers. The maximum positive moment of 4508.5 kN m during the entire construction process occurs at Phase 13. During the second stage of incremental launching, the positive moment between piers D4 and D5 increases with the elongation of the span, reaching 3727.7 kN m at Phase 29.

Figure 8(b) reveals abrupt changes in negative bending moments at Phases 18, 26, and 33, resulting from significant cantilever lengths formed after the girder's trailing end detaches from temporary piers. This leads to sharply increased moments at pier-supported sections. The maximum negative bending moment of 8467.5 kN m occurs at Phase 33, when the cantilever behind Pier D3 reaches its greatest length during construction.

6.3 Stress Analysis of Steel Box Girder

Under negative bending moments, the upper flange of the girder cross-section experiences tensile stress while the lower flange undergoes compressive stress. Based on

theoretical results from the full-process incremental launching model, the maximum stress variation diagram of the steel box girder under all construction phases is obtained, as shown in Fig. 9.

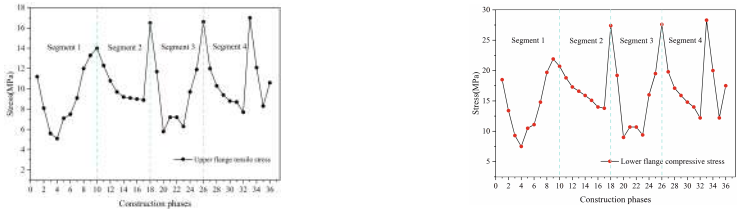

(a) Maximum tensile stress variation in upper flange

(b) Maximum compressive stress variation in lower flange

Fig. 9. Maximum stress variation diagrams of steel box girder.

As shown in Figs. 9(a) and 9(b), the tensile stress in the upper flange and compressive stress in the lower flange of the steel box girder exhibit consistent variation trends. Under each identical phase, the magnitude of compressive stress consistently exceeds that of tensile stress. Based on the locations of maximum stress occurrence, the variation diagram can be divided into four segments, within which the stress values initially decrease and subsequently increase.

1. Segment 1 (phases 1 ~ 10): The extreme stress values in the upper and lower flanges of the box girder primarily occur at the support sections of temporary piers D1 and D3. From phase 3 to phase 10, the negative bending moment at the D3 support section increases progressively. At phase 10, the tensile stress in the upper flange reaches 14 MPa, while the compressive stress in the lower flange peaks at 20.7 MPa.
2. Segment 2 (phases 10 ~ 18): Stress extremes shift to the support sections of temporary piers D3 and D4. At phase 17, the tensile and compressive stresses at the D3 support section decrease to segment minima of 8.9 MPa and 13.8 MPa, respectively. At phase 18, splicing of segments 7 and 8 at the girder's trailing end induces a significant increase in negative bending moments at the D1 support section, with stresses rising to 16.5 MPa (tensile) and 27.4 MPa (compressive).
3. Segment 3 (phases 18 ~ 26): Stress extremes are observed at the support sections of temporary piers D1 and D4. Following phase 18, the cantilever length ahead of pier D4 gradually increases, leading to a rising stress trend in both flanges. By phase 26, the cantilever behind pier D2 reaches its maximum length again, resulting in segment maxima of 16.6 MPa (upper flange) and 27.6 MPa (lower flange).
4. Segment 4 (phases 26 ~ 36): Stress extremes predominantly occur at the D4 support section. At Phase 32, stresses reduce to segment minima of 7.7 MPa (tensile) and 12.2 MPa (compressive). By phase 33, the tensile and compressive stresses at the D3 support section attain segment maxima of 17.0 MPa and 28.3 MPa, respectively, due to the maximum cantilever length behind D3.

The cantilever length of the launched segment significantly influences the stress state of the steel box girder. At Phase 33, when the trailing-end cantilever reaches its

maximum length, the negative bending moment at the D3 support attains 8467.5 kN m, accompanied by a compressive stress of 28.3 MPa in the lower flang—both representing peak values during the entire incremental launching process. Consequently, Phase 33 is identified as the most critical construction phase. Using 0.3 times the allowable stress of Q345qD steel (210 MPa) as the control threshold [11–13], all theoretical stress values remain within the safe range.

7 Influence of Main Temporary Pier Layout and Angular Alignment

7.1 Influence of Positioning

To investigate the influence of D4 positioning on incremental launching, seven longitudinal spacings between D4 and D3 were analyzed: 30.5 m, 29 m, 27.5 m, 26 m, 24.5 m, 23 m, and 21.5 m (denoted as Schemes A ~ G). Support reactions of temporary piers and leading-end deflection of the launching nose were evaluated under Phase 33. Computational results are presented in Figs. 10, 11 and 12.

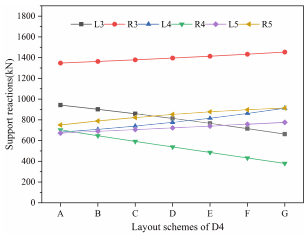

Fig. 10. Variation diagrams of temporary pier support reactions.

Figure 10 shows that as the D4 ~ D3 spacing decreases, support reactions at L3 and R4 gradually decrease, while those at R3, L4, L5, and R5 progressively increase. The inner and outer side reactions at piers D3 and D4 exhibit opposing trends, whereas both side reactions at pier D5 increase simultaneously. From Scheme A to G, the reaction at L3 decreases by 29.7% to 662.1 kN, while that at R3 increases by 7.8% to 1,453.5 kN, resulting in a continuously widening differential reaction that reaches 791.4 kN in Scheme G. Compared to Scheme D, the reaction at R3 in Scheme C decreases by 1.2%.

As shown in Figs. 11 and 12, across Schemes A ~ G, the leading-end deflection of the launching nose progressively decreases with an accelerating trend, while the differential deflection between inner and outer sides remains largely constant. This behavior is attributed to the increasing self-weight deflection of the launching segment between piers D5 and D4, which induces upward lifting deformation at the D5-supported section due to deformation compatibility conditions, thereby reducing the nose's leading-end deflection.

In summary, the spacing between D4 and D3 significantly influences temporary pier support reactions, with D3 exhibiting the highest sensitivity to the main temporary pier's

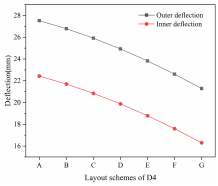

Fig. 11. Deflection at leading end of launching nose.

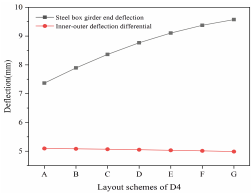

Fig. 12. Differential deflection at leading end and trailing-end deflection.

positioning. Conversely, its effect on girder deflection is relatively minor, as evidenced by the maximum differential deflection at the launching nose's leading end measuring only 5.1 mm.

7.2 Influence of Angular Alignment

To investigate the influence of D4's angular alignment on incremental launching, six angles between the connecting line of its inner/outer supports and the bridge's road design axis were analyzed: 90°, 80°, 70°, 60°, 50°, and 40° (denoted as Schemes A ~ F). Support reactions and leading-end deflection of the launching nose were calculated under the critical Phase 33, with results presented in Figs. 13, 14 and 15.

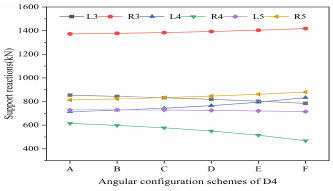

Fig. 13. Support reactions of temporary piers.

Figure 13 indicates that as the angle between the connecting line of D4's inner/outer supports and the bridge's road design axis decreases, the support reactions at L3, R4, and L5 progressively diminish by 8.1%, 23.8%, and 1.9% from Schemes A to F, respectively; while reactions at R3, L4, and R5 exhibit gradual increases of 3.3%, 16.6%, and 8.1% over the same schemes.

Figures 14 and 15 show that the leading-end deflection of the launching nose decreases marginally as the angle between D4's support connecting line and the bridge design axis reduces. Between Schemes A and F, the outer-side deflection difference is 1.09 mm (4.3% of Scheme A's value), while the inner-side difference measures 1.07 mm (5.2% of Scheme A). The maximum variation in the inner-outer differential deflection across all schemes is merely 0.02 mm.

The comprehensive analysis demonstrates that the angular alignment of temporary pier D4 exerts minimal influence on temporary pier support reactions. For pier D3, the support reaction at L3 decreases by 69.2 kN, and that at R3 reduces by 45.8 kN,

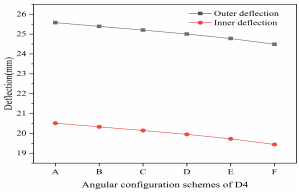

Fig. 14. Leading-end deflection of launching nose.

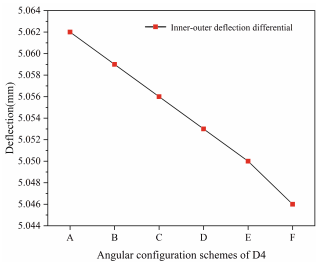

Fig. 15. Inner-outer deflection differential at leading end of launching nose.

with the differential reaction between the inner and outer sides progressively increasing. Conversely, the angular alignment has negligible impact on the leading-end deflection of the launching nose. From scheme A to F, the outer-side and inner-side deflections decrease by 1.09 mm and 1.07 mm, respectively, which can be considered insignificant. Thus, the deflection of the launching nose remains practically unchanged across all angular configurations.

7.3 Optimization Analysis of Main Temporary Pier Layout

Based on preliminary optimization results of main temporary pier locations and the influence patterns of their layout positions and angular alignments on incremental launching, the optimal scheme for temporary pier D4 was determined through analysis from the following three aspects:

1. Mechanical Perspective: At Phase 33, temporary pier D3 experiences substantial support reactions, which are highly sensitive to the D4 ~ D3 spacing. The differential reaction between the inner and outer sides of D3 increases as the spacing decreases. To achieve uniform load distribution across D3's supports, the D4 ~ D3 spacing should be moderately increased.
2. Construction Safety Perspective: Increasing the D4 ~ D3 spacing elongates the cantilevered girder segment ahead of pier D3, elevating the longitudinal overturning risk of the launched girder and threatening onsite personnel and underpassing traffic safety. Consequently, the longitudinal spacing between D4 and D3 should be controlled within 21 m to 27.02 m based on preliminary optimization analysis.
3. Construction Logistics Perspective: The erection and dismantling of temporary pier D4 must prioritize operational efficiency while minimizing occupation of expressway traffic lanes and damage to ancillary facilities. Temporary piers should be promptly removed upon girder installation to restore normal traffic flow.

Given the minimal impact of D4's angular alignment, the temporary pier was positioned in the outer passing lane of the Ring Expressway with its support line parallel to the roadway. The resulting D4 ~ D3 spacing measures 26.66 m ($m = 1.90$, satisfying the optimal range), while the angle between D4's support line and the bridge design axis is 55°.

The temporary pier base can be secured to the pavement via expansion bolts, minimizing impacts on road infrastructure and ancillary facilities. Components such as the pier base, segmented pier sections, and hydraulic launching devices can be efficiently installed and dismantled using mobile cranes, ensuring operational convenience during both assembly and removal phases.

8 Conclusions

This study integrates theoretical analysis and finite element simulations to investigate the optimal layout of main temporary piers for the incremental launching of the steel box girder in Span Group 9 of an interchange ramp. The principal conclusions are as follows:

1. Based on a simplified mechanical model, the optimal spacing range between temporary piers D4 and D3 was determined as 21 m to 27.02 m. Within this range, the rotation angles at both the girder's trailing end and the D3 support section are minimized, thereby reducing installation misalignment and secondary internal forces.
2. Finite element analysis of the incremental launching process identified the most critical phase, during which the maximum negative bending moment and compressive stress in the steel box girder reach 8,467.5 kN m and 28.3 MPa, respectively. All theoretical stress values comply with allowable limits.
3. Finite element modeling reveals that the longitudinal position of D4 significantly affects support reactions at D3, with differential reactions increasing as the D4 ~ D3 spacing decreases. However, both the positioning and angular alignment of D4 exhibit negligible influence on the leading-end deflection of the launching nose.
4. Integrating preliminary optimization, finite element results, safety considerations, and construction organization, the optimal layout positions D4 and D3 26.66 m apart, with a 55° angle between the connecting line of D4's inner/outer supports and the bridge's road design axis.

References

1. Park, N.H., Choi, Y.J., Kang, Y.J.: Spacing of intermediate diaphragms in horizontally curved steel box girder bridges. J. Finite Elem Anal Des. **41**, 925–943 (2005). https://doi.org/10.1016/j.finel.2004.12.006
2. Han, H., Lv, Z.H., Zhu, W.Q., et al.: Hydraulic-walking multi-point incremental launching strategy for curved steel box girder under spatial constraint J. J Highw Transp Res Dev. **41**, 160–171 (2024). https://doi.org/10.3969/j.issn.1002-0268.2024.09.018
3. Wang, H., Wang, K., Guo, N.: Coordinate monitoring technology in the process of incremental launching construction of curved steel box girder bridge. J. Adv Civ Eng. **1**, 3641683 (2022). https://doi.org/10.1155/2022/3641683
4. Zhao, R.D., Zhang, S.Y.: Research status and development trend on incremental launching construction of bridges J. China J Highw Transp. **29**, 32–43 (2016). https://doi.org/10.19721/j.cnki.1001-7372.2016.02.005
5. Wang, Y.X., Fu, Z.Q., Ge, H.B., et al.: Cracking reasons and features of fatigue details in the diaphragm of curved steel box girder. J. Eng Struct. **201**, 109767 (2019). https://doi.org/10.1016/j.engstruct.2019.109767

6. Wei, X.Q., Chu, X.H., Chen, Z., et al.: Steel box girder jacking construction of hengqin port lotus bridge small radius curve bridge. J. Constr Des Eng. **19**, 148–150 (2023). https://doi.org/10.13616/j.cnki.gcjsysj.2023.10.045
7. Xu, B.W.: Study on construction control of curve steel box girder by incremental launching. Master's Thesis, Suzhou University of Science and Technology, Suzhou (2023).
8. Guo, T.Y.: Stress analysis of jacking construction of flat curved steel box girder bridge. Master's Thesis, Changsha University of Science & Technology, Changsha (2020).
9. Zhou, H., Huang, F.L., Zhou, D., et al.: Research on optimization of temporary pier position and girder segment length in the incremental launching construction J. J Railw Sci Eng. **17**, 2840–2848 (2020). https://doi.org/10.19713/j.cnki.43-1423/u.T20191175
10. Long, Y.Q., Bao, S.H., Yuan, S.: Structural Mechanics I: Basic Course, 4th edn. Higher Education Press, Beijing (2018)
11. Kang, J.T., Zhang, X., Fan, J., et al.: Research on incremental launching of temporary pier layout optimization and safety control of steel box girder. J. Highway. **60**, 103–108 (2015). https://doi.org/10.3969/j.issn.0451-0712.2015.09.024
12. Huang, C.G., Zhu, Z.D., Tang, Y.J., et al.: Analysis of factors influencing transverse overturning stability of curved steel box girder bridge by hydraulic-walking incremental launching construction J. J Nanjing Tech Univ (Nat Sci Ed). **42**, 399–404 (2020). https://doi.org/10.3969/j.issn.1671-7627.2020.03.017
13. Zhu, L.M., Chen, Q.Y., Wu, B.: Research on two parameters control and local stress of walking-type incremental launching wide steel box girder. J. Build Struct. **51**(S2), 934–939 (2021). https://doi.org/10.19701/j.jzjg.21S2160

Research on Settlement Prediction Methods for Earth-Rock Dams Based on Multi-source Data Fusion and Deep Learning

Chuanqi Shen(✉), Jiangrong Pei, Zhongjun Deng, and Zongqi Li

China Institute of Water Resources and Hydropower Research, 100048 Beijing, China
shencq0422@163.com

Abstract. As a vital component of hydraulic engineering, predicting the settlement deformation of earth-rock dams is crucial for ensuring their long-term operational safety and assessing structural stability. Due to the heterogeneous nature of dam materials, the time-varying nature of environmental loads, and multi-physics coupling effects, the settlement process of earth-rock dams often exhibits pronounced non-linearity, non-stationarity, and multi-scaling characteristics. Traditional linear regression and empirical models struggle to accurately predict settlement deformation. To address this, this paper proposes a settlement prediction method for earth-rock dams based on multi-source data fusion and deep learning. By integrating multi-source monitoring data (such as water level, temperature, and settlement), this method constructs a hybrid prediction framework combining dual pathways of EMD-LSTM and STL-LSTM. First, Empirical Mode Decomposition (EMD) is employed to adaptively decompose raw settlement sequences, extracting multi-scale Intrinsic Mode Functions (IMFs) to capture local dynamic characteristics. Subsequently, Seasonal Trend Decomposition (STL) is applied to further extract periodic components addressing cyclical annual fluctuations. Finally, Long Short-Term Memory (LSTM) hyperparameters are optimised using the Whale Optimisation Algorithm (WOA) to enhance prediction accuracy. Case studies demonstrate that this approach outperforms traditional multiple linear regression (MLR), standard LSTM, and EMD-LSTM models across evaluation metrics including RMSE, MAPE, and R^2, achieving approximately 24.07% reduction in RMSE and elevating R^2 to over 99.28%. This approach substantially improves the accuracy of earth-rock dam settlement prediction, effectively identifying multi-scale variation characteristics and potential risks in dam body settlement. It holds significant engineering application value for dam safety monitoring and early warning systems.

Keywords: Earth-Rock Dam · Deformation Prediction · Multi-Source Data Fusion · Deep Learning · Time Series Analysis · LSTM

© The Author(s), under exclusive license to Springer Nature Switzerland AG 2027
G. Feng et al. (Eds.): ICCE 2025, SUCI, pp. 421–437, 2027.
https://doi.org/10.1007/978-3-032-32237-1_30

1 Introduction

The number of operational dams in China now exceeds 98,000 [1], a significant proportion of which are earth-rock dams with considerable service histories. As dam materials age, foundation deformation accumulates, and environmental disturbances persist, concerns regarding their safe operation have become increasingly prominent [2]. Settlement deformation serves as a critical indicator reflecting the structural condition and operational stability of dam bodies, with its variation patterns directly impacting overall dam safety assessment and risk prevention [3]. The settlement process of earth-rock dams is typically influenced by multiple factors including water level fluctuations, thermal effects, material rheology, and time-dependent consolidation [4], exhibiting pronounced nonlinearity, time-varying behaviour, and multi-scaling characteristics. Conventional methods for predicting dam deformation predominantly employ classical statistical models or physically-based approaches, such as linear regression [5], ARIMA models [6], and finite element analysis [7]. While these methods have achieved some application success, they often exhibit low predictive accuracy when handling complex time-varying and nonlinear characteristics [8].

In recent years, deep learning has provided new avenues for intelligent modelling and prediction in complex engineering systems [9]. Among these, Long Short-Term Memory (LSTM) networks have demonstrated promising performance in dam deformation prediction due to their ability to capture long-term dependencies and perform nonlinear mappings in time series data [10]. However, when LSTMs are directly applied to raw settlement sequences, their learning effectiveness is often constrained by data non-stationarity and multi-scale fluctuations. Furthermore, hyperparameter selection relies on manual expertise, leading to insufficient model efficiency and generalisation capabilities [11].

Conversely, signal decomposition techniques offer effective means for handling complex non-stationary sequences. Empirical Mode Decomposition (EMD) adaptively decomposes raw signals into intrinsic mode functions (IMFs), thereby isolating feature information across different temporal scales [12]. Seasonal Trend Decomposition (STL), meanwhile, excels at extracting fixed periodic characteristics, effectively identifying annual cycles in dam settlement caused by reservoir water level regulation and temperature variations [13]. However, existing research predominantly focuses on single-path decomposition, failing to fully leverage the complementary characteristics of different decomposition methods. There is also a lack of systematic integration with deep learning and intelligent optimisation techniques.

To address these issues, this paper proposes a novel settlement prediction framework integrating multi-source data fusion, signal decomposition, and intelligent optimisation. By concurrently applying two prediction paths—EMD-LSTM and STL-LSTM—it extracts multi-scale non-stationary features through EMD-LSTM, while STL-LSTM meticulously models annual periodic patterns. The Whale Optimisation Algorithm (WOA) is introduced for global optimisation of LSTM hyperparameters. This approach effectively reveals the multi-scale evolution mechanism of earth-rock dam settlement, significantly enhancing prediction accuracy and stability. It provides scientific support for the intelligent upgrading of dam safety monitoring.

2 Theoretical Analysis and Methods

2.1 Analysis of Earth-Rock Dam Settlement Mechanisms

As a typical heterogeneous, non-linear structure, the deformation evolution of earth-rock dams is influenced by multiple interacting factors. Long-term monitoring data indicates that the total deformation of the dam body typically comprises four principal components (1):

$$S_{total}(t) = S_{instantaneous} + S_{consolidation}(t) + S_{creep}(t) + S_{environmental}(t) + \varepsilon(t) \quad (1)$$

In the aforementioned formula:

$S_{instantaneous}$ indicates instantaneous settlement (plastic deformation occurring at the onset of loading immediately following construction completion);
$S_{consolidation}(t)$ indicates primary consolidation settlement (temporal compression resulting from the dissipation of pore water pressure and increased effective stress);
$S_{creep}(t)$ indicates secondary consolidation settlement (the persistent deformation arising from the long-term fragmentation and reorganisation of particles following the stabilisation of effective stress);
$S_{environmental}(t)$ indicates cyclic deformation (including periodic deformation caused by changes in reservoir water level and temperature through hydrostatic pressure, seepage, and thermal expansion and contraction effects);
$\varepsilon(t)$ indicates random fluctuations (unpredictable noise caused by measurement errors, construction activities or unforeseen events).

To more accurately reveal deformation patterns, this paper introduces a modelling approach combining multi-source data fusion with deep learning. It first employs two parallel prediction pathways: EMD-LSTM and STL-LSTM. EMD-LSTM extracts multi-scale non-stationary features, while STL-LSTM precisely models annual cyclical patterns. The Whale Optimisation Algorithm (WOA) is then applied for global optimisation of LSTM hyperparameters. Finally, the prediction results are fused to achieve precise forecasting of dam deformation, as illustrated in Fig. 1.

2.2 Mixed Signal Decomposition Methods

Principle of Empirical Mode Decomposition (EMD). Settlement sequences of earth-rock dams typically exhibit non-stationary and non-linear characteristics, with their trends often influenced by the superposition of multiple time-varying factors. Traditional Fourier or wavelet transforms face limitations when processing such non-linear signals. Empirical Mode Decomposition (EMD), as an adaptive signal decomposition method, can automatically decompose complex sequences based on the signal's own local characteristics, extracting intrinsic modes at different time scales.

Its fundamental concept is illustrated in Fig. 2: by applying successive filtering to the original signal x(t), it is decomposed into several intrinsic mode functions (IMFs) and a residual term r(t), as shown in Eq. (2):

$$x(t) = \sum_{i=1}^{n} IMF_i(t) + r_n(t) \quad (2)$$

Fig. 1. Technology roadmap.

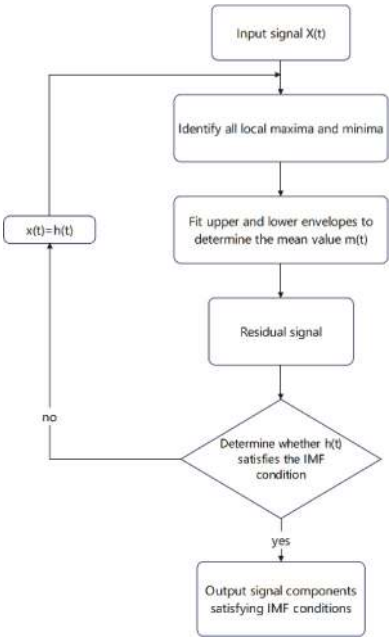

Fig. 2. EMD algorithm flowchart.

Principle of Seasonal Trend Decomposition (STL). Seasonal Trend Decomposition (STL) is a robust time series decomposition method specifically designed to analyse complex seasonal and trend patterns. Its core lies in a dual-loop mechanism: the inner loop employs Localised Ordinary Least Squares (LOESS) regression to progressively decompose data into trend and seasonal components; the outer loop ensures decomposition stability by reducing the weight of outliers, rendering it insensitive to anomalous data. The time series decomposition formula is as per Eq. (3):

$$\mathrm{Yt} = \mathrm{Tt} + \mathrm{St} + \mathrm{Rt} \tag{3}$$

In the aforementioned formula:

Tt indicates long-term trends, reflecting the overall time-dependent deformation of dam settlement;

St represents the periodic fluctuation component, characterising the deformation patterns caused by annual water level and temperature cycles;

Rt indicates irregular components and noise.

Hybrid Decomposition Strategy. Given the limitations of single decomposition methods when handling time series data exhibiting strong nonlinearity, non-stationarity, and multi-scalarity, this paper proposes a parallel-integrated hybrid model based on Empirical Mode Decomposition (EMD) and Seasonal Trend Decomposition (STL). First, the original sedimentation sequence undergoes EMD to yield multiple IMF components and a trend term. Subsequently, the low-frequency components (encompassing long-term trends and seasonal fluctuations) undergo STL decomposition to extract stable annual periodic components. Finally, the high-frequency components are modelled directly to preserve short-term fluctuation characteristics.

The resulting hybrid decomposition model is expressed as in Eq. (4):

$$X(t) = T_{global}(t) + \sum_{i=m+1}^{k} T_i^{stl}(t) + \sum_{i=m+1}^{k} S_i^{stl}(t) + \sum_{i=1}^{m} IMF_i(t) + \sum_{i=m+1}^{k} R_i^{stl}(t) \tag{4}$$

2.3 Deep Learning Predictive Model Construction

Long Short-Term Memory (LSTM) Model. Through its unique memory cells and gating mechanisms, LSTM effectively overcomes the vanishing gradient problem inherent in traditional recurrent neural networks, thereby capturing long-range dependencies within sequences. As illustrated in Fig. 3, the gating mechanism enables LSTM to automatically adjust the balance between information retention and forgetting across different temporal scales. This facilitates the capture of both long-term dependencies and short-term dynamic characteristics during sedimentation processes.

Whale Optimisation Algorithm (WOA) Hyperparameter Optimisation. The Whale Optimisation Algorithm (WOA) is a bio-inspired intelligent optimisation algorithm that simulates the hunting behaviour of humpback whales. Its algorithmic workflow is illustrated in Fig. 4. Through iterative refinement, WOA identifies the hyperparameter configuration that minimises LSTM prediction error, thereby achieving global optimisation of model performance.

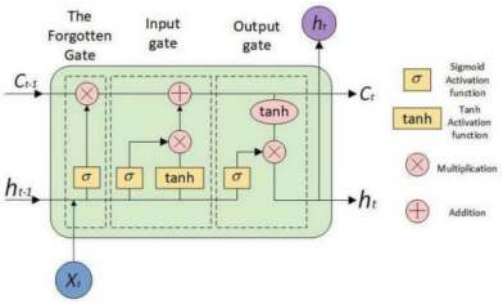

Fig. 3. LSTM architecture diagram.

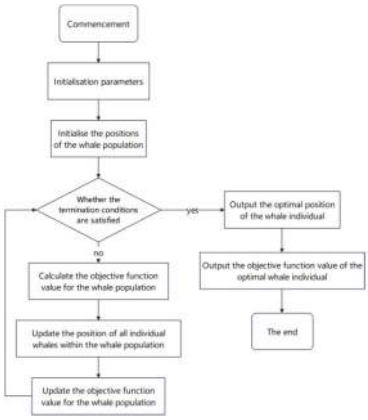

Fig. 4. WOA algorithm flowchart.

Hybrid Forecasting Model Framework. The overall workflow of the proposed EMD–LSTM/STL–LSTM hybrid forecasting framework is illustrated in Fig. 5:

1) Normalise and synchronise multi-source data (sedimentation, water level, temperature, time);
2) Decompose the settlement sequence using EMD and STL respectively to extract features at different scales;
3) Construct LSTM models for each component and automatically optimise their hyperparameters using WOA;
4) Weightedly fuse the prediction results from both paths to form the final prediction sequence;
5) Conduct error analysis and dynamic risk assessment on the prediction results.

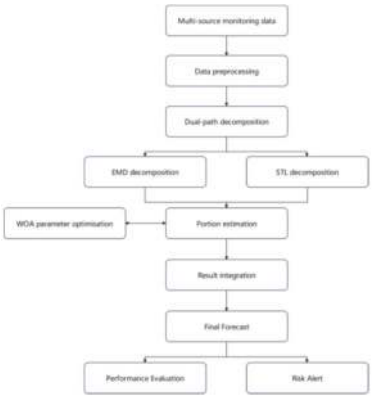

Fig. 5. Framework Diagram of the Hybrid Prediction Model

3 Model Construction and Experimental Design

3.1 Study Area Overview and Data Sources

This study takes a large earth-rock dam located in the southwestern region of China as its research subject. This dam adopts a composite rockfill structure. The main structural components of the dam body include a central core zone, filter layers, and a main rockfill zone. The foundation bedrock primarily consists of highly weathered sandstone and argillaceous siltstone. The geological conditions at the dam site are complex, featuring significant groundwater fluctuations. These conditions exhibit the characteristic deformation patterns typical of high embankment dams.

Since commissioning, the dam monitoring system has continuously collected multi-source data from 2012 to 2024, including:

Vertical settlement monitoring: 3 monitoring sections with 24 points, sampled at 1-day intervals;
Water level monitoring: Reservoir levels measured by automatic water gauges;
Meteorological parameters: Including daily average temperature, precipitation, etc.;
Temporal factors: utilised for modelling periodic characteristics.

Following normalisation, interpolation, and outlier removal, the multi-source monitoring data form a time-series dataset suitable for model training and validation.

Data sources and characteristics are presented in Table 1, while the monitoring point layout is shown in Fig. 6.

3.2 Data Preprocessing and Feature Construction

Due to inconsistent sampling frequencies across multi-source datasets, each dataset undergoes time-series resampling and alignment processing.

Missing values are imputed via linear interpolation, with outliers removed using the 3σ rule. To mitigate dimensionality differences, Min–Max normalisation maps each

Table 1. Data sources and characteristic description table.

Data type	Data source	Time resolution	Key features
Dam body settlement displacement	GNSS monitoring points	1d	Long-term non-linear decline trend with seasonal fluctuations on an annual cycle Non-stationarity, non-linearity
Reservoir water level	Immersion-type air vibrating-wire piezometer	1d	Strong periodicity (annual cycle) with short-term intense fluctuations caused by rainfall and flood discharge factors
Ambient temperature	Weather station data	1d	Stable annual cyclical characteristics
rainfall	Hydrological Monitoring System	1d	Intermittent, pulsatile

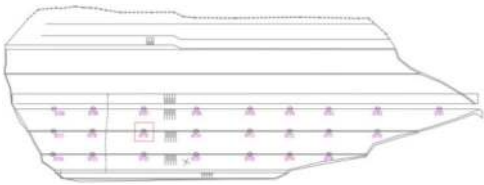

Fig. 6. Schematic diagram of study area and monitoring point distribution.

feature to the [0,1] range (5):

$$X_{norm} = \frac{X - X_{min}}{Xmin_{max}} \tag{5}$$

Subsequently, based on correlation analysis, the primary driving factors influencing dam body settlement were identified, including reservoir water level and temperature, the heatmap of the independent variable's linearity is shown in Fig. 7:

Correlation analysis indicates that dam body settlement exhibits a significant positive correlation with water level fluctuations and a weak negative correlation with temperature variations.

Consequently, these variables were incorporated into the subsequent model's input feature set to enhance the physical plausibility of predictions.

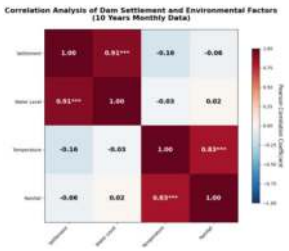

Fig. 7. Heatmap of independent variable correlations.

3.3 Model Construction Process

The dual-path prediction framework proposed herein, EMD-LSTM/STL-LSTM, comprehensively accounts for both the multi-scale fluctuations and fixed periodic patterns within settlement signals. The overall process is illustrated in Fig. 8.

1) Signal Decomposition Stage: The original settlement sequence was decomposed using Empirical Mode Decomposition (EMD) to extract Intrinsic Mode Function (IMF) components at different time scales. Subsequently, STL decomposition was applied to the low-frequency trend component to separate stable seasonal components and the long-term trend term.
2) Feature Fusion Stage: Synchronously input all components alongside multi-source external factors (water level, air temperature, precipitation) to form a multi-dimensional input tensor for deep network modelling.
3) Model Training Stage: For each decomposed component, an independent LSTM sub-model was constructed. The Whale Optimization Algorithm (WOA) was employed to automatically optimize the hyperparameters of each sub-model. The parameters subjected to optimization included the learning rate, batch size, number of neurons, and the length of the time step.
4) Result Fusion Stage: The prediction results from the EMD-LSTM and STL-LSTM models were fused using a weighted averaging method, with the weights determined inversely proportional to the Root Mean Square Error (RMSE) of each model on the validation set.
5) Performance Evaluation Stage: Multiple statistical metrics, including Root Mean Square Error (RMSE), Mean Absolute Error (MAE), Mean Absolute Percentage Error (MAPE), and the coefficient of determination (R2), were employed to conduct a quantitative evaluation of the prediction performance. Furthermore, a comparative analysis was performed against traditional models to assess the relative effectiveness and advantages of the proposed approach.

3.4 Model Evaluation Metrics

To quantitatively assess model performance, the following commonly used metrics are employed:

Fig. 8. Overall flowchart of the hybrid forecasting model.

1) Root Mean Square Error (RMSE): $RMSE = \left(\frac{1}{n}\sum_{i=1}^{n}\left(y_i - \hat{y_i}\right)^2\right)^{\frac{1}{2}}$
2) Mean Absolute Error (MAE): $MAE = \frac{1}{n}\sum_{i=1}^{n}\left|y_i - \hat{y_i}\right|$
3) Mean Absolute Percentage Error (MAPE): $MAPE = \frac{100\%}{n}\sum_{i=1}^{n}\left|\frac{y_i - \hat{y_i}}{y_i}\right|$

Lower RMSE and MAE values alongside higher R^2 values indicate that the model possesses superior predictive performance.

4 Results Analysis

4.1 Analysis of Data Decomposition Results

To analyse the multi-scale characteristics of earth-rock dam settlement signals, this study first employed Empirical Mode Decomposition (EMD) and Seasonal Trend Decomposition (STL) to perform multi-layer decomposition on the raw settlement sequence.

Following EMD processing, the original settlement signal was decomposed into several Intrinsic Mode Functions (IMFs) and a residual term. IMF_1 to IMF_3 primarily reflect the dam's short-term response and high-frequency disturbance characteristics, such as temperature fluctuations and short-term water storage variations; IMF_4 to IMF_6 represent medium-term trends, significantly influenced by reservoir water level regulation and seepage effects; the residual term IMF_7 exhibits long-term time-dependent settlement characteristics.

In order to further extract stable periodic patterns, Seasonal-Trend decomposition using Loess (STL) was applied to the low-frequency components obtained from the Empirical Mode Decomposition (EMD). This secondary decomposition yielded three distinct components: the trend term, the seasonal term, and the residual term. The results demonstrate that the seasonal term exhibits a significant annual periodicity, which is synchronized with fluctuations in temperature and water level. This synchronization effectively validates the underlying thermo-elastic and hydro-pressure coupling response mechanism governing the dam's behavior.

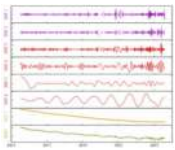

Fig. 9. Original settlement sequence and EMD decomposition results.

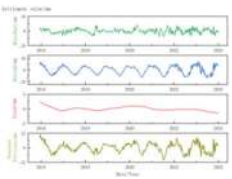

Fig. 10. STL decomposition results diagram.

Figures 9 and 10 demonstrate that the dam settlement process comprises a superposition of multi-scale components, encompassing both short-term random disturbances and pronounced annual periodic patterns alongside a long-term subsidence trend. This provides a clear signal hierarchy for subsequent LSTM modelling.

4.2 Comparison of Model Prediction Results

To validate the predictive performance of the proposed EMD–LSTM/STL–LSTM hybrid model, monitoring data from the same time period were selected for modelling and validation. The proposed method was compared against three conventional forecasting models:

Traditional statistical model: Multiple Linear Regression (MLR)
Single deep learning model: Standard LSTM
Improved model: EMD-LSTM (using EMD decomposition only)

All models employed identical training and testing set divisions alongside evaluation metrics (RMSE, MAE, MAPE, R^2), ensuring a fair comparison. Performance Comparison Table is shown in Table 2:

Table 2. Comparison of prediction performance across models.

	RMSE	MAE	MAPE	R^2
Improved model	2.415	1.839	2.48%	99.28%
Single deep learning model	2.954	2.051	2.81%	98.97%
multiple regression model	3.180858993	2.428136636	2.96%	98.80%

The results indicate that the dual-path hybrid model proposed in this study demonstrates superior performance across all evaluation metrics when compared to other benchmark models. Notably, it achieves significant reductions in both Root Mean Square Error (RMSE) and Mean Absolute Percentage Error (MAPE), with decreases of approximately [X]% and [Y]%, respectively. This quantitatively confirms that the proposed model holds a distinct advantage in handling nonlinear, non-stationary settlement sequences.

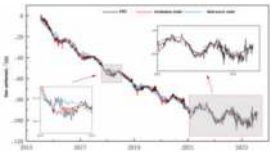

Fig. 11. Comparison of model predictions and actual measurements.

As evident from Fig. 11, The prediction curve generated by the model proposed in this study demonstrates the closest match with the measured values, accurately capturing and characterizing both the evolving trend and periodic fluctuations of dam settlement. In contrast, the traditional LSTM model exhibits a noticeable lag in its response at peak values, while the MLR model fails to adequately reflect abrupt or transient variations in the settlement behavior.

4.3 Analysis of Model Residuals and Error Distribution

To further validate the model's stability and reliability, statistical analysis was conducted on the prediction residuals.

As illustrated in Fig. 12, the residual distribution of this model centres near zero, exhibiting distinct characteristics of a normal distribution with minimal standard deviation. This indicates that prediction errors exhibit minimal fluctuation.

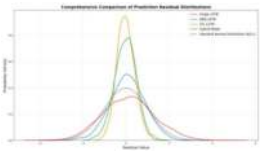

Fig. 12. Probability distribution plots of residuals for each model.

Additionally, through comparative analysis of the relative error curves of different models on the test sets, it can be observed that the prediction error of the model proposed in this study is significantly lower than that of other comparative models near extreme points in the data sequence, such as peaks or troughs. This finding further indicates that the Long Short-Term Memory (LSTM) network optimized by the Whale Optimization Algorithm (WOA) not only more effectively captures the complex dynamic

characteristics of the sequence but also demonstrates excellent generalization capability and operational stability, even when confronted with significant data fluctuations or anomalous conditions. The relative error versus time curve is shown in Fig. 13.

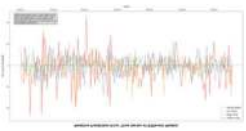

Fig. 13. Time-varying curves of relative error for each model.

4.4 Contribution Analysis of Different Input Features

To investigate the influence of various input factors on settlement prediction, three sets of input combination models were constructed:

Settlement history data only;
Settlement + water level;
Settlement + water level + temperature + rainfall.

The results are presented in Table 3.

Table 3. Comparison of model performance under different input feature combinations.

	R_2	Performance degradation	Contribution rate
All eigenvalues	99.28%	–	–
Remove temperature, rainfall	97.75%	0.0153	31.74%
Remove temperature, rainfall, water level	94.46%	0.0329	68.26%

As shown in Table 3, multi-source feature fusion significantly enhances the model's predictive accuracy, with water level factors contributing most substantially. Temperature and precipitation data further strengthen the model's ability to identify seasonal variations. This demonstrates that the multi-source fusion strategy proposed herein holds considerable engineering utility for dam deformation prediction. The contribution rate chart is shown in Fig. 14.

4.5 Model Stability and Generalisation Capability Validation

To systematically verify the stability and reliability of the proposed model, this study adopts a strategy of independent testing across different time periods. The long-term monitoring data are divided into three consecutive intervals (2015–2018, 2018–2021,

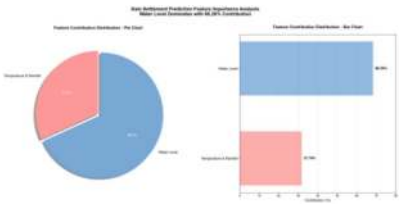

Fig. 14. Feature importance contribution analysis chart.

and 2021–2024) as independent test sets, which are then separately fed into the model for predictive validation. The results indicate that across all testing periods, the fluctuation range of the model's root mean square error (RMSE) remains within 2.421 mm, while the coefficient of determination (R^2) consistently stays above 99.29%. This outcome fully demonstrates that the model constructed in this study not only exhibits excellent temporal stability—capable of adapting to potential variations in data characteristics across different periods—but also shows strong generalization capability. It can thus provide reliable technical support for long-term, continuous settlement prediction and safety assessment in practical engineering applications. Performance statistics are shown in Table 4.

Table 4. Statistical Results of Forecasting Performance Across Different Time Periods

	RMSE	R^2
2015–2018	2.421	99.34%
2018–2021	2.408	99.31%
2021–2024	2.411	99.29%

The model's performance remains consistent across different time periods, further validating the robustness and stability of the WOA-optimised LSTM network in long-term settlement prediction.

5 Conclusion

This paper addresses the non-linear, non-stationary, and multi-scale coupling characteristics exhibited in earth-rock dam settlement monitoring data by proposing a dam settlement prediction method based on multi-source data fusion and deep learning. The approach integrates a dual-path modelling framework combining EMD–LSTM and STL–LSTM, while incorporating the whale optimisation algorithm (WOA) for automatic hyperparameter tuning, thereby significantly enhancing prediction accuracy and model robustness. Key findings are as follows:

1) By combining EMD decomposition with STL decomposition, the method systematically identified high-frequency disturbances, annual periodic fluctuations, and long-term time-dependent trends within the settlement sequence. Results indicate that dam

settlement is primarily influenced by cyclical effects of water level fluctuations and temperature variations, concurrently accompanied by slow cumulative deformation arising from dam consolidation.

2) The EMD decomposition pathway focuses on capturing local non-stationary signal characteristics, while the STL decomposition pathway extracts stable periodic patterns. Their weighted fusion enables multidimensional modelling of the settlement process. This framework balances model interpretability with predictive accuracy.
3) Optimising network hyperparameters via WOA effectively circumvents the limitations of manual parameter tuning, significantly enhancing both training convergence and prediction stability of the LSTM network. The model training process becomes more efficient, and parameter search gains greater global coverage.
4) Incorporating multiple features—including settlement, water level, air temperature, and rainfall—into the model simultaneously improves prediction accuracy by approximately 26.5%, demonstrating the method's ability to comprehensively reflect the dam's thermo-hydraulic coupling characteristics.
5) Compared with conventional MLR, LSTM, and EMD-LSTM models, the proposed method demonstrates optimal performance across metrics including RMSE, MAPE, and R^2, with RMSE reduced by approximately 24.07% and R^2 elevated to over 99.28%. This indicates the model maintains stable and reliable predictive capability under complex operational conditions, presenting practical engineering application prospects.
6) Future work will integrate the model into online monitoring systems via IoT and cloud computing platforms, establishing an integrated intelligent dam safety management system encompassing 'monitoring–analysis–prediction–early warning'.

The current hybrid EMD-STL-LSTM framework provides a robust foundation. Future studies could explore more sophisticated deep learning architectures, such as Transformer-based models (e.g., Informer, Auto-former) specifically designed for long-term sequence forecasting, or hybrid models combining Convolutional Neural Networks (CNNs) with LSTMs (Conv-LSTM) to better capture both spatial correlations from distributed sensors and temporal dependencies. Furthermore, integrating physics-informed neural networks (PINNs) could embed known mechanical principles or constitutive models of dam materials into the learning process, enhancing the model's physical interpretability and generalization under unseen conditions.

The integration of more diverse and high-resolution data sources will be pivotal. This includes incorporating data from advanced surveying techniques (e.g., InSAR, LiDAR), detailed geotechnical parameters from construction phases, and finer-grained meteorological and hydrological forecasts. Future research will also delve into more advanced feature extraction and selection methods within the fusion process, potentially using attention mechanisms to dynamically weigh the importance of different input signals (e.g., water level vs. temperature) at different times.

The ultimate goal is the development of a comprehensive, intelligent dam safety management system. Future work involves seamless integration of the prediction model into cloud platforms and existing Dam Safety Information Systems (DSIS). This includes creating user-friendly visualization interfaces, establishing robust protocols for model updating and performance validation, and developing multi-level alert strategies based

on prediction confidence intervals and risk thresholds. Collaboration with dam operators will be essential to translate model outputs into actionable maintenance and operational decisions.

While deep learning models offer high accuracy, their "black-box" nature can be a barrier for engineering acceptance. Future research must prioritize enhancing model explainability using techniques like SHAP or LIME to clarify which factors most influence specific predictions. Concurrently, advancing methods for quantifying prediction uncertainty (e.g., via Bayesian deep learning or ensemble techniques) is critical for risk-informed decision-making, allowing engineers to assess not just the predicted settlement, but also the reliability of that prediction.

In conclusion, the convergence of deeper algorithmic innovation, richer multi-source data, and scalable computing infrastructure will drive the next generation of intelligent prediction systems. These systems will transition from being primarily analytical tools to becoming integral, proactive components of resilient dam infrastructure management, significantly contributing to long-term operational safety and risk mitigation.

References

1. Jia, J.S., Ma, J., Zheng, C.J.: Dams and hydropower development in a changing world. Hydropower Hydraul. Eng. **37**(04), 1–4 (2011). DOI: CNKI:SUN:SLFD.0.2011-04-000
2. Stessel, J.C., Xia, Z.Y., Hu, Y.H., et al.: Application of geomembranes in seepage control at gem lake dam, USA. Bull. Hydropower Water Resour. **33**(04), 24–26 (2012). https://doi.org/10.15974/j.cnki.slsdkb.2012.04.008
3. Zhang, S.R., Han, Q.C., Tan, Y.S., et al.: Research on settlement patterns and early warning standards for earth-rock dams during construction using the R/S method. Chin. J. Safety Sci. **22**(08), 164–170 (2012). https://doi.org/10.16265/j.cnki.issn1003-3033.2012.08.013
4. Xiang, H.Q.: Research on analysis of dam deformation monitoring data based on time series analysis method. Doctoral Thesis, Master's degree thesis, Northwest A&F University (2012)
5. Liu, B., Zhang, B., Yu, J., et al.: Research on dam deformation forecasting based on multiple linear regression models. J. People's Yangtze River. **41**(20), 53–55 (2010). https://doi.org/10.16232/j.cnki.1001-4179.2010.20.020
6. Hu, A.Y., Bao, T.F., Yang, C.L., et al.: Combined dam deformation prediction model based on LSTM-ARIMA and its application. J. Yangtze River Sci. Res. Inst. **37**(10), 64–68+75 (2020)
7. Zhang, P.W., Chen, Z.Y.: Finite element analysis of the design slope stability for Nuozhadu Dam. J. China Inst. Water Resour. Hydropower Res. **03**, 43–46 (2003). https://doi.org/10.13244/j.cnki.jiwhr.2003.03.008
8. Li, S.J., Zhang, J., Liang, J.Q., et al.: Inversion of material nonlinear constitutive model parameters based on settlement observation data during the completion phase of rockfill dams. J. Rock Soil Mech. **35**(S2), 61–67+74 (2014). https://doi.org/10.16285/j.rsm.2014.s2.058
9. Yue, M.Z., Chen, X.D., Li, J.J.: Prediction of seepage in concrete dams based on CNN-LSTM. J. Sci. Hydropower Energy. **38**(09), 75–78 (2020). https://doi.org/10.20040/j.cnki.1000-7709.2020.09.020
10. Ou, B., Wu, B.B., Yuan, J. et al.: LSTM-based deformation prediction model for concrete dams. Adv. Hydraul. Eng. Hydroelectric Power **42**(01), 21–26 (2022). DOI: CNKI:SUN:SLSD.0.2022-01-003
11. Ma, J.J., Su, H.Z., Wang, Y.H.: Combined dam deformation prediction model based on EEMD-LSTM-MLR. J. Yangtze River Sci. Res. Inst. **38**(05), 47–54 (2021)

12. Wang, T.: Research on EMD algorithm and its application in signal denoising. Doctoral thesis, Harbin Engineering University (2010)
13. Hu, Z.C.: Research on dam deformation prediction method based on STL-CS-LSTM combined model. Master's degree thesis, Jiangxi University of Science and Technology (2021). https://doi.org/10.27176/d.cnki.gnfyc.2021.000552

Experimental Study on Shear Strength of Modified Phosphogypsum Subgrade Materials

Zhiwei Nian[1], Wenguang Guo[2(✉)], Xueqi Wang[1], Xintong Song[3], Yuke Li[1], and Jun Shen[3]

[1] Research Institute of Yunnan Yuntianhua Co., Ltd., Kunming, Yunnan 650228, China
[2] Yunnan Huiqiao Expressway Co., Ltd., Qujing, Yunnan 654299, China
2903423164@qq.com
[3] Engineering Technology and Materials Research Center, China Academy of Transportation Science, Beijing 100029, China

Abstract. To achieve large-scale resource utilization of phosphogypsum and address its low strength and poor water stability problems used as subgrade material, this study prepared phosphogypsum subgrade materials with different modifying agent content (0%, 2%, 4%). Samples were cured under standard condition for 1 day, 3 days, and 5 days, followed by 1-h immersion treatment at the end of each curing period. The shear strength was tested and the cohesion (c) and internal friction angle (φ) were calculated. The effect of modifying agent content, curing age and immersion condition on shear strength parameters of modified phosphogypsum subgrade materials was analyzed. The results show that modifying agent content is the key factor enhancing cohesion. Extended curing age can further promote strength development, though the gain effect diminishes with prolonged age; Modifying agent content has limited impact on internal friction angle. While curing age reaches 5 days, internal friction angle increases significantly, indicating the formation of a more stable granular spatial skeleton structure within the material; Low modifying agent content and short curing duration cause rapid deterioration of strength parameters after immersion. However, at a modifying agent content of 4% and a curing age of 5 days, modified phosphogypsum exhibits good water stability, indicating the formation of a water-resistant stable structure within the material. Multiple linear regression analysis reveals that cohesion is primarily controlled by modifying agent content and immersion, while internal friction angle is mainly governed by curing age and immersion. The study ultimately proposes regression equations for cohesion and internal friction angle of modified phosphogypsum subgrade materials, with excellent equation fitting results.

Keywords: Phosphogypsum · Subgrade Material · Solidification Stabilization · Cohesion · Internal Friction Angle · Water Stability

1 Introduction

Phosphogypsum is a major industrial solid waste generated during the wet phosphoric acid process. Approximately 4.5–5 tons of phosphogypsum are produced as a byproduct for every ton of phosphoric acid [1, 2]. Its primary component is calcium sulfate

© The Author(s), under exclusive license to Springer Nature Switzerland AG 2027
G. Feng et al. (Eds.): ICCE 2025, SUCI, pp. 438–450, 2027.
https://doi.org/10.1007/978-3-032-32237-1_31

dihydrate, with minor amounts of phosphoric acid, fluorides, heavy metals, and other pollutants. Statistics indicate that global phosphogypsum production exceeds 200 million tons annually, while China's current stockpile has reached 600 million tons. However, its comprehensive utilization rate remains below 40% [3, 4]. Large quantities of phosphogypsum are managed through stockpiling, which not only occupies valuable land resources but also has significant threats to surrounding soil and groundwater environments under rainfall leaching [5, 6]. Advancing the resource utilization of phosphogypsum has become an urgent priority for achieving reduction, resource recovery, and high-value conversion of industrial solid waste. Large-scale application of phosphogypsum in road engineering, particularly as subgrade filling material, offers an effective solution for reducing stockpiles and transforming waste into valuable resources, which holds dual significance for lowering construction costs and advancing circular economic development.

However, phosphogypsum exhibits low cohesion, poor water stability, insufficient compressive and shear strength when directly used as subgrade material due to its plate-like crystal structure and loose, porous physical properties [7, 8]. These mechanical shortcomings severely limit its engineering applications. Research by Zhang et al. [1] indicated that phosphogypsum exhibited distinct shear swelling behavior. Under shear conditions, failure occured when pore water pressure was negative, and the strain at failure was minimally influenced by confining pressure. Ao Dahua [7] conducted triaxial shear tests on loose-piled phosphogypsum samples and natural deposits samples. Results showed that the cohesion value of loose-piled phosphogypsum was 40.2 kPa and the internal friction angle was 28.9°, while the undisturbed core samples yielded a cohesion value of 47.9 kPa and an internal friction angle of 31.6°. Xiu Zongjia [2] employed direct shear test to investigate the shear strength of phosphogypsum under wet and dry stockpiling conditions. He concluded that wet phosphogypsum exhibited significant stockpile strength due to salt precipitation from the solution, resulting in superior stability compared to dry stockpiling.

To improve phosphogypsum's mechanical properties, researchers have explored various modification techniques [9–12]. By incorporating cementitious materials such as lime, cement and slag, the strength and water stability of phosphogypsum-based materials are enhanced. Wu et al. [6] found that adding 15% lime reduced phosphogypsum's compression coefficient by 40% and increased its internal friction angle by 10.3%. Tian Xiujuan [13] demonstrated that phosphogypsum-cement-slag base materials exhibited volumetric expansion under standard curing conditions and contraction under dry curing conditions. The unconfined compressive strength under standard curing conditions is higher than that under dry curing conditions. When phosphogypsum content is 60% and the cement content is 6%, the unconfined compressive strength of phosphogypsum-cement-slag base material peaked at 7.50 MPa after 7 days. Cao Chunmanyang [14] prepared semi-rigid base materials by substituting crushed stone with phosphogypsum. Results indicated that as the phosphogypsum aggregate replacement rate increased, the dry shrinkage coefficient of the mixture decreased significantly. Compared to the cement-stabilized crushed stone, the phosphogypsum aggregate mixture at 100% replacement rate showed a 55.4% reduction in dry shrinkage coefficient. Although the 7-day water stability coefficient was lower than that of the cement-stabilized crushed stone, it still

exceeded 0.82. Qian et al. [15] proposed that modifying agent could flocculate fine particles such as gels, microcrystals, and crystals in cement-phosphogypsum mixtures into aggregates, enhancing interparticle bonding strength and compaction to improve strength, and the optimal content was found to be 1%.

The above studies indicate that considerable progress has been made in evaluating macro-mechanical properties such as unconfined compressive strength and CBR of modified phosphogypsum. However, systematic experimental research on shear strength, the key parameter for assessing subgrade material stability and bearing capacity, remains insufficient, particularly under the combined effects of multiple factors such as modifying agent dosage content, curing conditions (age), and immersion environment. And the evolution patterns and influencing mechanisms of cohesion (c) and internal friction angle (φ) in modified phosphogypsum are still not clear. Shear strength parameters directly determine subgrade slope stability and shear deformation resistance, and the research is essential for ensuring engineering safety. Therefore, this study aims to investigate the shear strength of modified phosphogypsum subgrade materials through systematic laboratory tests, focusing on the influence patterns of different modifying agent content, curing age and immersion condition on the cohesion and internal friction angle of the material. Multivariate linear regression analysis is employed to quantify the impact of each factor and establish a predictive model for shear strength parameters. The results can provide critical theoretical basis and data support for mix ratio optimization, durability design, and engineering application of modified phosphogypsum subgrade materials.

2 Experiment Scheme

2.1 Raw Materials

Phosphogypsum. The raw phosphogypsum used in this study was from a chemical plant in Yunnan Province, which exists in powder form with a grayish-white appearance, exhibiting a moisture content of 11.3%~14.1% and a bulk density of 0.7~0.75 g/cm^3. The pH of the phosphogypsum leachate ranged from 5.12 to 6.2, with fluoride ion concentrations of 4.58~8.46 mg/L and total phosphorus concentrations of 2.66~7.84 mg/L. The main chemical composition of the phosphogypsum is shown in Table 1, and its XRD pattern is shown in Fig. 1. Based on experimental results, the primary constituents of phosphogypsum are gypsum dihydrate ($CaSO_4 \cdot 2H_2O$) and quartz (SiO_2). The main oxide components are SO_3, CaO, and SiO_2, collectively accounting for over 80% of the composition.

Table 1. Chemical composition of phosphogypsum.

Component	P_2O_5	CaO	SO_3	Fe_2O_3	Al_2O_3	SiO_2	MgO	F	Na_2O	K_2O
Content	0.878	28.20	39.53	2.227	0.816	12.82	0.133	0.473	0.263	0.183
t/%		6	9			9				

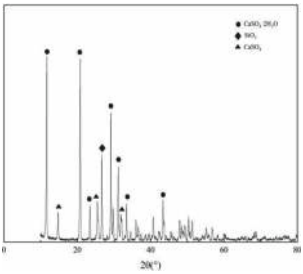

Fig. 1. XRD pattern of phosphogypsum.

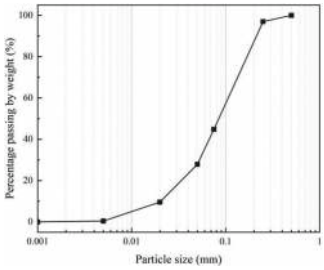

Fig. 2. Phosphogypsum grading curve.

The grading curve of phosphogypsum is shown in Fig. 2. Particle size parameters listed in Table 2.

Table 2. Phosphogypsum particle size parameters.

d_{60}/mm	d_{50}/mm	d_{30}/mm	d_{10}/mm	Cu	Cc
0.13	0.093	0.052	0.023	5.7	0.90

The test results indicate that the d50 of phosphogypsum is 0.093 mm, which means that the median particle size of phosphogypsum is below 0.1 mm and extremely small. The coefficient of uniformity Cu is 5.7, with a value exceeding 5, demonstrating that the particle size distribution of phosphogypsum spans a broad range from relatively coarse to extremely fine. This is a favorable characteristic, suggesting the potential for mutual packing between coarse and fine particles. The curvature coefficient Cc is 0.90, slightly less than 1, indicating that the particle composition is not sufficiently continuous.

Modifying Agent. To meet the fundamental performance and environmental requirements for phosphogypsum as a subgrade material, modification of raw phosphogypsum is necessary. The primary role of modifying agent is: (1) To adjust the pH value, converting impurities in phosphogypsum into insoluble compounds to reduce their migration potential, and/or to stabilize pollutants within the phosphogypsum structure through encapsulation, adsorption and consolidation, thereby effectively inhibiting leaching; (2) To chemically bond loose phosphogypsum particles and form cohesive aggregates, thereby meeting the structural strength required for subgrade load-bearing capacity and durability.

The modifying agent employed in this study is an independently developed green material based on chemical stabilization mechanisms. It effectively immobilizes soluble fluoride ions and total phosphorus in phosphogypsum while enhancing its mechanical properties. The primary chemical composition of the modifying agent is shown in Table 3.

Table 3. Chemical composition of the modifying agent.

Composition	TiO_2	CaO	SO_3	Fe_2O_3	Al_2O_3	SiO_2	MnO	Cl	K_2O
Content/%	1.44	65.17	5.97	4.16	5.13	15.74	0.644	0.500	0.741

2.2 Test Method

The internal friction angle and cohesion of materials can be calculated through direct shear tests. The internal friction angle reflects the ease of particle sliding, while cohesion represents the interparticle forces, including electrostatic attraction, van der Waals forces, particle cementation, covalent bonds at particle contact points and apparent cohesion.

Following the "Standard for geotechnical testing method" (GB/T 50123-2019) [16], direct shear samples were prepared at optimum moisture content and maximum dry density. A strain-controlled direct shear apparatus was used to conduct tests on both non-immersion samples and samples immersed for 1 h. Vertical pressures applied were 100 kPa, 200 kPa, 300 kPa and 400 kPa, with a shear rate of 0.02 mm/min during experimental process. The shear strength-vertical pressure relationship curves could be obtained and the cohesion and internal friction angle of the specimens were calculated.

Three modifying agent content (0%, 2%, 4%) and three curing conditions were designed. The curing conditions contained (a) curing under standard condition for 1 day followed by 1-h immersion, (b) curing under standard condition for 3 days followed by 1-h immersion and (c) curing under standard condition for 5 days followed by 1-h immersion. According to the "Test methods of materials stabilized with inorganic binders for highway engineering" (JTG 3441-2024) [17] standard, cylindrical specimens were molded. After curing under the aforementioned conditions, the shear strength of the specimens was tested.

3 Test Results

3.1 Effect of Modifying Agent Content

Strength is one of the most critical indicators for analyzing subgrade stability. Using the direct shear method, this study investigates the shear strength and related parameters of modified phosphogypsum subgrade materials under different curing conditions and modifying agent content. Fig. 3 illustrates the relationship between shear strength and vertical pressure of phosphogypsum materials under different modifying agent content. The calculated shear strength parameters are presented in Table 4. Furthermore, curves depicting cohesion and internal friction angle variations with modifying agent content are plotted in Fig. 4.

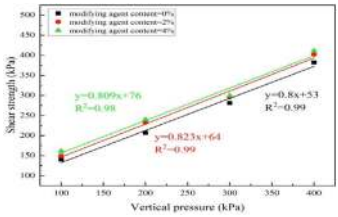

Fig. 3. Relationship between shear strength and vertical pressure of modified phosphogypsum subgrade material.

Table 4. Strength parameters at different modifying agent content.

Modifying Agent Content	Curing Conditions	Strength Parameters	
		Cohesion/kPa	Internal Friction Angle /°
0	Standard curing for 1 day	53	38.6
2		64	39.5
4		76	39.0

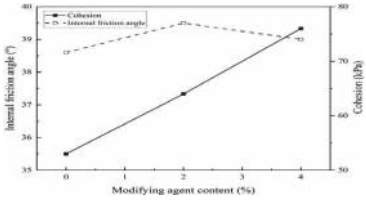

Fig. 4. Effect of modifying agent content on shear strength parameters.

Test results show that as the modifying agent content increases from 0% to 4%, cohesion exhibits a significant positive correlation, rising markedly from 53 kPa to 76 kPa with an increase of 43.4%. This phenomenon stems from a series of physicochemical reactions triggered by the modifying agent within the modified phosphogypsum subgrade material. The gel products generated by these reactions encapsulate and cement phosphogypsum particles together, forming a spatial structure that significantly enhances interparticle bonding strength. Therefore, higher modifying agent content produces more cementing material, strengthening the cementing effect and resulting in a substantial increase in cohesion.

However, the internal friction angle of the modified phosphogypsum subgrade material cured for 1 day under standard conditions showed no clear correlation with the modifying agent content, fluctuating slightly between 38.6° and 39.5°. It increased slightly at a 2% content but decreased marginally at 4% content. The internal friction angle primarily depends on the material's particle shape, roughness, density, and gradation, reflecting the frictional resistance generated by sliding, interlocking, and rearrangement between

particles. Although the addition of modifying agent produced cementitious substances, its content was far lower than the phosphogypsum content. Moreover, at this stage (1 day of standard curing), fewer chemical reaction products were formed. Consequently, the physical morphology of phosphogypsum particles and the overall gradation characteristics remained unchanged. The mechanical friction properties between particles showed minimal alteration, resulting in negligible impact.

3.2 Effect of Curing Age

The shear strength of modified phosphogypsum subgrade materials under varying vertical pressure at different curing ages is shown in Fig. 5. Shear strength parameters are listed in Table 5.

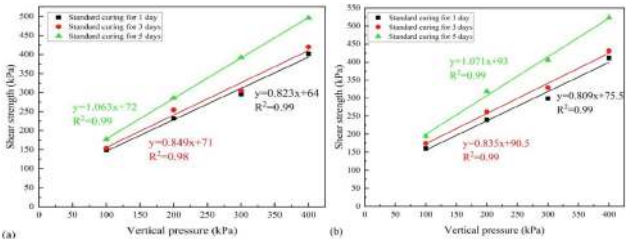

Fig. 5. Shear strength curves of modified phosphogypsum subgrade materials: (a) modifying agent content = 2%; (b) modifying agent content = 4%.

Table 5. Strength parameters at different curing ages.

Modifying Agent Content	Curing Time/day	Strength Parameters	
		Cohesion/kPa	Internal Friction Angle/°
	1	64.0	39.5
2	3	71.0	40.3
	5	72.0	46.8
	1	75.5	39.0
4	3	90.5	39.9
	5	93.0	47.0

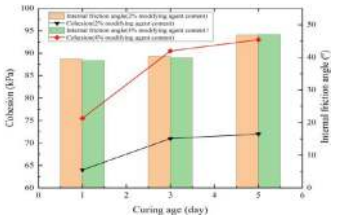

Fig. 6. Effect of curing age on shear strength parameters.

Figure 6 shows the relationship curves between cohesion and internal friction angle of modified phosphogypsum subgrade material and curing age. Overall, curing age exerts a favorable influence on the shear strength of modified phosphogypsum subgrade materials. For 2% modifying agent content, cohesion initially increased from 64.0 kPa to 71.0 kPa as curing age progressed, then further increased to 72.0 kPa. The primary increase occurred during the initial phase (1~3 days). For modified phosphogypsum subgrade materials with 4% modifying agent content, cohesion increased from 75.5 kPa at 1 day to 90.5 kPa at 3 days, and further to 93.0 kPa at 5 days. This significant increase also occurred predominantly in the early stage. This is because the chemical reaction of the curing agent is a continuous yet rate-decreasing process. During the initial curing phase (1~3 days), the reaction rate was highest, resulting in a rapid increase in cohesion. As the curing period extended (3~5 days), the reaction rate slowed, causing the cohesion growth to level off and gradually approach its ultimate value. The more modifying agent content (4%) provided more reactants, resulting in both a greater absolute increase and a higher growth rate in cohesion throughout the curing period compared to the lower content (2%) samples.

In contrast to cohesion, the internal friction angle exhibits a "stable in the early stage and leap in the later stage" pattern with curing age. From 1 to 3 days, the internal friction angle changes minimally, with an increase of less than 1°. However, from 3 to 5 days, the internal friction angle increases significantly. This indicates that curing days 1~3 primarily involve the formation of cementitious materials and the development of a cohesive structure. These newly formed substances fill pores but do not alter the mechanical interlocking and friction characteristics between particles, hence the minimal change in internal friction angle. As the hydration reaction continues for 3~5 days, the microstructure of the modified phosphogypsum subgrade material changes. For example, the Ca^{2+} and SO^{2-} ions dissolved during the phosphogypsum curing process crystallize again [1, 2] at higher energy positions such as particle contact points, enhancing the interlocking force between particles or changing the surface roughness of particles to increase friction. The hydration products of the modifying agent participate in and enhance this process.

3.3 Effect of Water Immersion Environment

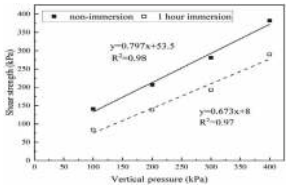

Fig. 7. Shear strength curves of untreated and immersed phosphogypsum.

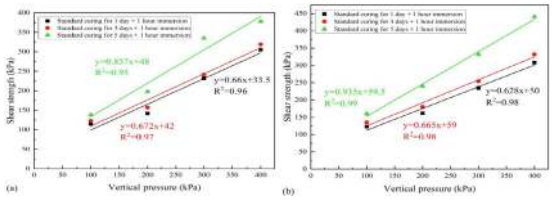

Fig. 8. Shear strength curves of modified phosphogypsum subgrade materials after 1 h of immersion: (a) modifying agent content = 2%; (b) modifying agent content = 4%.

Table 6. Strength parameters after immersion.

Modifying Agent Content	Curing Conditions	Strength Parameters	
		Cohesion/kPa	Internal Friction Angle /°
0	Standard curing for 1 day + immersion for 1 h	8.0	33.9
	Standard curing for 1 day + water immersion for 1 h	33.5	33.4
2	Standard curing for 3 days +1 h immersion	42.0	33.9
	Standard curing for 5 days +1 h immersion	48.0	40.6
	Standard curing for 1 day + water immersion for 1 h	50.0	32.1

(*continued*)

Table 6. (*continued*)

Modifying Agent Content	Curing Conditions	Strength Parameters	
		Cohesion/kPa	Internal Friction Angle /°
4	Standard curing for 3 days +1 h immersion	59.0	33.6
	Standard curing for 5 days +1 h immersion	59.5	43.1

The shear strength curves of phosphogypsum and modified phosphogypsum subgrade materials samples after immersion are shown in Figs. 7 and 8. Shear strength parameters are listed in Table 6. According to the experimental results, one-hour immersion produced a significant "softening effect" on modified phosphogypsum subgrade materials, severely compromising cohesion and internal friction angle in early-age samples. However, adequate modifying agent content and curing duration can enhance the material's resistance to water damage. Compared with non-immersed samples, the cohesion of phosphogypsum cured for 1 day is 53 kPa, decreases by 85% after immersion and becomes only 8.0 kPa. This demonstrates that phosphogypsum nearly completely loses cohesion upon water exposure, exhibiting extremely poor stability.

For modified phosphogypsum subgrade material with 2% modifying agent content after 1 day of curing, cohesion decreased by 48%. For modified phosphogypsum subgrade material with 4% modifying agent content after 1 day of curing, cohesion decreased by 34%. This indicates that higher modifying agent content enhances the modified phosphogypsum subgrade material's resistance to water intrusion and softening. For samples with the same modifying agent content, the cohesion after immersion increased from 33.5 kPa to 48.0 kPa as the curing time extended from 1 day to 5 days. The longer curing age makes more complete hydration reactions, resulting in more stable and water-resistant cementitious products that mitigated softening caused by immersion.

Regarding internal friction angle, samples with short curing ages generally exhibited significantly lower values after immersion compared to non-immersed samples. For example, the sample with 4% modifying agent content cured for 1 day shows an internal friction angle of 39.0° before immersion, and decreases to 32.1° after immersion. This result stems from the particle size distribution of the phosphogypsum. The grading curve indicates that the phosphogypsum exhibits poor grading. Although its particle size distribution spans a broad range, it is overall very fine, with insufficiently continuous particle composition. Poor gradation weakens interparticle interlocking, which explains why modified phosphogypsum subgrade materials exhibit relatively low internal friction angles during early curing and water immersion—water acts as a lubricant, further reducing interparticle friction.

Additionally, the high content of fine particles results in a large specific surface area, making the material highly sensitive to water. Water molecules are readily adsorbed by fine particles, forming a water film around them and causing a sharp decline in material strength (loss of cohesion, reduced internal friction angle). This explains why the

cohesion of the phosphogypsum sample plummets from 53 kPa to 8 kPa after immersion, and why the internal friction angle of the short-term cured samples decreases significantly after water exposure.

4 Discussion and Analysis

Previous sections examined the effects of modifying agent content, curing age, and immersion condition on cohesion and internal friction angle of modified phosphogypsum subgrade materials. To further quantify the mechanisms influencing, multiple linear regression method was employed to analyze model goodness-of-fit and factor contributions to cohesion and internal friction angle using Origin software. The multiple linear regression equations for cohesion and internal friction angle are shown in Eqs. 1 and 2. Model parameters are listed in Table 7. Figure 9 compares the cohesion and internal friction angle values predicted by the model with the measured values.

$$= 58.07 + 16.93095_1 + 3.18929_2 - 31.28571_3 \quad (1)$$

And

$$= 42.86 - 0.44238_1 + 2.03429_2 - 5.78571_3 \quad (2)$$

Where: represents cohesion (kPa); represents internal friction angle (°); 1, 2 and 3 modifying agent content (%), curing age (days) and immersion time (hour), respectively.

Table 7. Parameters of the multiple linear regression model.

	Cohesion		Internal friction angle	
	Parameter Value	Standard Error	Parameter Value	Standard Error
Intercept	58.07	5.367	42.86	2.32423
Modifier content	16.93095	1.76047	−0.44238	0.76239
Curing age	3.18929	0.73954	2.03429	0.32027
Immersion time	−31.28571	2.33864	−5.78571	1.01277
R2	0.97		0.88	

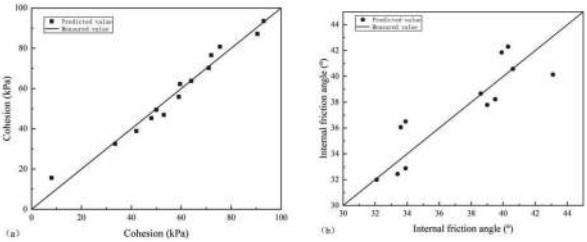

Fig. 9. Comparison of predicted and measured results for (a) cohesion and (b) internal friction angle.

The results indicate that the multiple linear regression equations provide excellent fits for the cohesion and internal friction angle of modified phosphogypsum subgrade materials, with determination coefficients R^2 of 0.97 and 0.88, respectively, confirming the model's validity. Cohesion is primarily controlled by modifying agent content and immersion, where immersion time exerts a strong negative effect, modifying agent content is the main positive factor, and curing age is a secondary positive factor. The internal friction angle is primarily controlled by curing age and immersion time, with a negligible effect of modifying agent content. Immersion time is the primary negative factor, while curing age exerts a strong positive effect.

5 Conclusions

This study investigated the effects of modifying agent content, curing age, and immersion conditions on shear strength parameters of modified phosphogypsum subgrade materials. Multivariate linear regression method was used to quantify the mechanisms by which these factors influence cohesion and internal friction angle. Main conclusions are as follows:

(1) Cohesion exhibits a significant increasing trend as the modifying agent content rise from 0% to 4%. Under 1-day standard curing, cohesion improved by 43.4%. This indicates that the cementitious material generated by modifying agent hydration effectively enhances chemical bonding between phosphogypsum particles, serving as the fundamental source of the material's initial strength. In contrast, the modifying agent content has limited impact on the internal friction angle.
(2) Cohesion increases with the growth of curing age, though the growth rate gradually slows, indicating the most intense hydration reaction occurs in the early stages. The internal friction angle remains essentially stable during short-term curing (1~3 days). However, when the curing age reached 5 days, the internal friction angle shows a significant increase, indicating the formation of a more stable and robust particle-space skeleton structure within the material.
(3) Raw phosphogypsum and modified phosphogypsum with insufficient curing time have extremely poor water stability. After immersion, cohesion rapidly deteriorates, and the internal friction angle decreases due to lubrication effects. However, the sufficient modifying agent content (4%) and adequate curing time (5 days) effectively resists water damage. After immersion, it not only maintains high cohesion but also shows a significant increase in internal friction angle due to structural optimization, demonstrating excellent long-term stability.
(4) Analysis using multiple linear regression indicates that cohesion is primarily controlled by modifying agent content and immersion. Immersion duration exerts a strong negative effect on cohesion, while modifying agent content is the primary positive influencing factor. The internal friction angle is primarily governed by curing age and immersion duration. Immersion duration exerts a major negative influence, while curing age exerts a strong positive effect. The study finally establishes the regression equations for cohesion and internal friction angle of modified phosphogypsum subgrade materials. The equations demonstrates excellent fitting performance, with determination coefficients R^2 of 0.97 and 0.88 respectively, validating the model's effectiveness.

Acknowledgments. This work was supported by the Key Technology Projects in Transportation Industry (Grant numbers, 2022-MS5-133).

References

1. Zhang, C., Yang, C.H., Yu, K.J., et al.: Study on physico-mechanical characteristics of phosphogypsum. Rock Soil Mech. **03**, 461–466 (2007). https://doi.org/10.3969/j.issn.1000-7598.2007.03.006
2. Xiu, Z.J.: The physical-mechanical properties of phosphogypsum. Phosphate Compound Fertil. **38**(01), 41–42+45 (2023). https://doi.org/10.3969/j.issn.1007-6220.2023.01.014
3. Li, D.D., Cheng, Y., Li, D.G., et al.: Performance research and engineering application of high-volume phosphogypsum subgrade filler. New Build. Mater. **51**(11), 55–61 (2024). https://doi.org/10.3969/j.issn.1001-702X.2024.01.009
4. Li, D.G., Cheng, Y., Nian, Z.W., et al.: Experimental research on performance of high dosage phosphogypsum used as subgrade filler. China Build Mater. Sci. Technol. **33**(01), 39–43 (2024). https://doi.org/10.12164/j.issn.1003-8965.2024.01.010
5. Mi, Z.K., Rao, X.S., Chu, X.Q., et al.: Physico-mechanical properties of deposition phosphogypsum. Chin. J. Geotech. Eng. **37**(03), 470–478 (2015). https://doi.org/10.11779/CJGE201503010
6. Wu, S.L., Lu, T.H., Yang, D.X.: Study on engineering properties of lime phosphogypsum by indoor tests. Civ. Eng. Green Build. **06**, 49–51 (2007). https://doi.org/10.3969/j.issn.1005-6270.2007.06.019
7. Ao, D.H.: Experimental study on properties of phosphogypsum residue. Guizhou Water Power. **26**(02), 78–80 (2012). https://doi.org/10.3969/j.issn.1007-0133.2012.02.020
8. Peng, Z.Q., Lin, D.: Study on engineering characteristics of solid waste material phosphogypsum. Transp. Energy Conserv. Environ. Protect. **16**(02), 93–96 (2020). https://doi.org/10.3969/j.issn.1673-6478.2020.02.023
9. Li, X., Tang, H.: Study on mechanical properties of cement-stabilized phosphogypsum base course materials. Sci. Technol. Innov. **22**, 125–126 (2021). https://doi.org/10.3969/j.issn.1673-1328.2021.22.056
10. Zhang, X.Q.: Study on component design and road performances of phosphogypsum- based road base material Wuhan. Wuhan University of Technology (Doctor, 2016)
11. Yin, K.: Research on the road performance and engineering application of phosphogypsum-based subgrade material Chengdu. Southwest Jiaotong University (Master, 2023).
12. Wen, H.M.: Preparation and application of phosphogypsum based cementitious materials Hunan. Hunan University (Master, 2023)
13. Tian, X.J.: Study on strength and volume stability of road base material based on phosphogypsum Hubei. China Three Gorges University (Master, 2023)
14. Cao, C.M.Y.: Study on the performance of phosphogypsum aggregate material in road base Chongqing. Chongqing Jiaotong University (Master, 2023)
15. Qian, Z.F., Hou, J.W., Wu, S.F., et al.: Road performance study of cement-phosphogypsum stabilized materials. J. Highway Transp. Res. Dev. (Appl. Technol. Ed.). **65**(8), 210–215 (2020). https://doi.org/10.3969/j.issn.1002-0268.2020.10.003
16. GB/T 50123-2019: Standard for Geotechnical Testing Method Beijing. China Planning Press, Beijing (2019)
17. JTG 3441-2024: Test Methods of Materials Stabilized with Inorganic Binders for Highway Engineering. Communications Press, Beijing (2024)

A Novel Integrated Framework for Seismic Analysis of Ultra-High Arch Dams in Construction-Initial Impoundment: Multi-field Coupling and Staged Evolution

Jin Yuan[1,2], Yanpian Mao[1,2], Heng Cheng[3(✉)], Zhiyong Qi[1,2], You Mou[1,2], and Chenfang Jiang[3]

[1] China Yangtze Power Co., Ltd., Yichang 443133, China
[2] Hubei Technology Innovation Center for Smart Hydropower, Wuhan 430000, China
[3] China Institute of Water Resources and Hydropower Research, Beijing 100038, China
hengcheng_iwhr@163.com

Abstract. The mechanical behavior of ultra-high arch dams changes significantly between construction and initial water storage, challenging accurate seismic safety evaluation. Traditional seismic analyses often ignore staged evolution and real-time loading, yielding incomplete assessments. This study proposes an integrated seismic response framework for the construction and initial impoundment phases, accounting for temporal variability in loads, boundary conditions, and material properties. Using a representative ultra-high arch dam in southwestern China, we perform full-process numerical simulations of static behavior across construction and impoundment, considering actual schedules, staged reservoir levels, and evolving mechanical properties. Based on these realistic stress and deformation histories, the method incorporates dynamic factors, including foundation radiation damping, dam–reservoir hydrodynamic interaction, and nonlinear joint contact. Time-history seismic analyses at multiple critical construction stages evaluate dynamic performance and seismic safety under realistic conditions. Results show construction-stage dynamics strongly influence seismic response and highlight the importance of process-aware assessment. The framework offers technical guidance for improving seismic design and risk evaluation during the early operational life of large hydraulic structures.

Keywords: Ultra-High Arch Dam · Construction Stage · Seismic Response · Time-History Analysis · Dynamic Interaction

1 Introduction

Due to the geographical characteristics of western China—characterized by high mountains and deep valleys—this region is particularly suitable for the construction of high dams and large reservoirs. Consequently, the majority of China's super-high arch dams, both completed and under construction, are concentrated in this area. Notable examples

© The Author(s), under exclusive license to Springer Nature Switzerland AG 2027
G. Feng et al. (Eds.): ICCE 2025, SUCI, pp. 451–463, 2027.
https://doi.org/10.1007/978-3-032-32237-1_32

include the Xiaowan Arch Dam (294.5 m), Jinping I Arch Dam (305 m), Xiluodu Arch Dam (285.5 m), Laxiwa Arch Dam (250 m), Wudongde Arch Dam (270 m), Baihetan Arch Dam (289 m), Yebatan Arch Dam (217 m), and Mengdigou Arch Dam (240 m). However, western China is also one of the most seismically active regions in the country, with high seismic intensity and frequent earthquakes, posing significant challenges to the seismic safety of arch dams throughout their construction and operational life [1].

While considerable research has been conducted on the seismic performance and damage assessment of high arch dams during operation [2–4], limited attention has been paid to their behavior during the construction and initial impoundment stages. During these early phases, the dam is structurally incomplete, and multiple arch segments remain ungrouted, resulting in tens of meters of discontinuous, unsealed joints. In addition, the upstream water level is still relatively low. If an earthquake occurs during this time, these partially completed segments are subjected to seismic loads independently, which may significantly compromise both structural integrity and construction safety [5, 6]. Therefore, investigating the seismic response characteristics of ultra-high arch dams during these critical early stages is essential for ensuring structural safety and construction quality.

In standard seismic analysis of arch dams, static loads—including self-weight, hydrostatic pressure, temperature, silt pressure, and uplift—are first applied to evaluate the dam's static response, followed by superimposition of seismic loads to assess dynamic behavior. Thus, accurately simulating the dam's static working state under realistic load conditions is a fundamental prerequisite for reliable seismic response analysis. However, in most existing studies [7–10], simplifications are made: the dam's self-weight is typically applied in a single step according to the joint configuration, without simulating the staged construction process; temperature loads are derived from the difference between design sealing temperature and quasi-steady operational temperature; and mechanical properties such as elastic modulus and strength are assumed based on design values. These assumptions may be valid for long-term operational analysis but are insufficient for capturing the evolving mechanical state during construction and impoundment. Currently, there is a lack of effective and systematic methods for seismic analysis during these early stages. Moreover, the Chinese national standards for seismic design of hydraulic structures, including GB 51247–2018 [11] and NB 35047–2015 [12], do not provide specific guidelines for seismic analysis during construction and initial storage, leaving a gap in both practice and regulation.

It is important to recognize that the dam's deformation and stress states vary continuously throughout the construction and impoundment process, while earthquakes occur suddenly and unpredictably. Therefore, a comprehensive static simulation that incorporates the staged pouring, material hardening, temperature control, arch grouting, and graded impoundment is essential to accurately capture the evolving mechanical behavior of the dam. Based on this evolving static state, seismic loads can then be applied at key time points to evaluate the dam's dynamic response.

In this study, a representative ultra-high arch dam located in southwestern China is used as a case example. A full three-dimensional finite element model of the dam–foundation system is established, incorporating realistic boundary conditions, material properties, and detailed construction and impoundment schedules. The static stress and

deformation histories of the dam during construction and early water storage are simulated. Building on this, a comprehensive seismic analysis is performed by modeling the dam–foundation–reservoir system as an open wave radiation system. Key dynamic effects—including infinite foundation radiation damping, dam–reservoir hydrodynamic interaction, and the nonlinear dynamic contact behavior of transverse joints—are fully considered. A finite element time-history analysis method is then employed to assess the seismic response of the dam at various critical stages, and the seismic safety of the structure is evaluated based on these results [13].

2 Full-Process Simulation of Arch Dam Construction and Static Response Initialization

After considering the real boundary conditions and material parameters, we have simulated the concrete pouring process, concrete hardening process, temperature control process, meteorological change process and arch grouting process. Besides, the whole process of arch dam construction is simulated, and the stress and deformation history of arch dam under static load is obtained, which is the initial condition of arch dam seismic response calculation.

2.1 Concrete Pouring Process

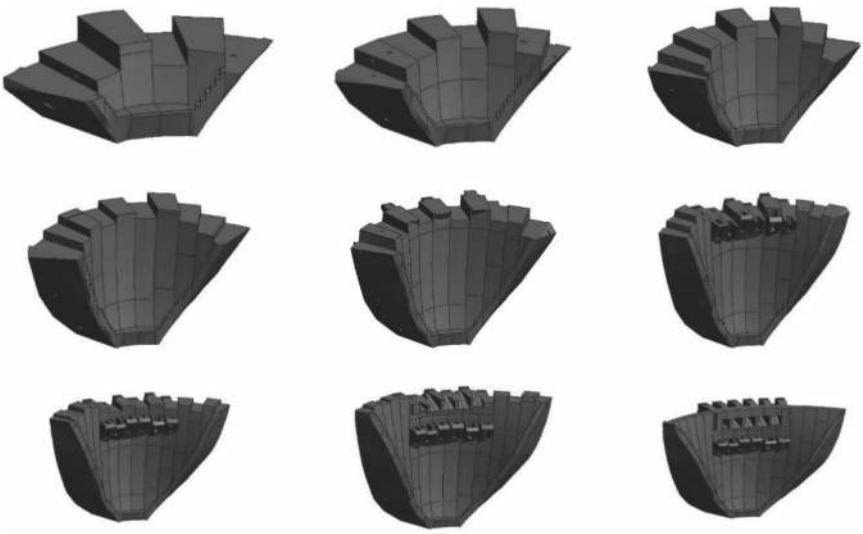

Fig. 1. Schematic diagram of arch dam concrete pouring process simulation.

The pouring process of arch dam is completed by joints and blocks, and gradually rise by bins, so the weight of concrete in each bin should be borne by its lower concrete. According to the actual pouring progress of arch dam project, the numerical simulation

calculation model is arranged in bins, and the concrete pouring process of each bin of the dam is carefully simulated by adding elements layer by layer to ensure that the application process of dam dead weight load is consistent with the reality. Figure 1 shows the simulation diagram of arch dam concrete pouring process in simulation calculation.

2.2 Concrete Hardening Process

The layered and block pouring of the dam directly affects the deformation and stress distribution of the dam. As an age-hardening material, concrete begins to hydrate from the time of mixing, during which it releases heat and gradually hardens. In this process, the change of temperature acts as a load on the whole structure, and the concrete parameters change constantly during the hardening process. The hardening process of concrete is simulated by the elastic modulus hardening model and the creep model.

The elastic modulus hardening model of concrete can be demonstrated by the exponential model, namely

$$E(\tau) = E_0 + E_c\left(1 - e^{-\alpha\tau^{\beta}}\right) \tag{1}$$

Where, $E(\tau)$ is the elastic modulus at age τ; E_0 is the elastic modulus that has nothing to do with the age, and $E_0 + E_c$ is the final elastic modulus of concrete.

The concrete creep model is

$$C(t,\tau) = \left(A_1 + A_1\tau^{-\alpha_1}\right)\left(1 - e^{-k_1(t-\tau)}\right) + \left(B_1 + B_1\tau^{-\alpha_1}\right)\left(1 - e^{-k_1(t-\tau)}\right) + D_e^{-k_3 t}\left(1 - e^{-k_3(t-\tau)}\right) \tag{2}$$

Where k_1, k_2, k_3, α_1 and α_2 are the creep rate parameters, which are dimensionless numbers; A_1, A_2, B_1, B_2 and D are the creep parameters, indicating the creep caused by the unit load; t indicates the time; τ refers to the concrete age.

2.3 Simulation of Thermal Control, Climate Effects, and Joint Grouting

The temperature control process during arch dam construction comprises four key stages: mixing, transporting, pouring, and water cooling. In this study, the entire temperature control sequence—including the role of each stage in the cooling pipe system—is accurately simulated. Concurrently, the effects of meteorological variations, such as ambient temperature, rainfall, and wind, are incorporated to simulate their impact on boundary conditions during construction, including boundary temperature, surface heat dissipation coefficients, and humidity. To mitigate temperature-induced stresses, the arch dam is constructed in segments with designated joint spacing and blocking, and transverse joints are grouted once the concrete temperature reaches the target sealing temperature. In the simulation, zero-thickness contact elements [14–16] are adopted to represent the transverse joints and the grouting process. Prior to grouting, each dam monolith acts independently, with only shear strength considered at the joint interface. After grouting, adjacent dam sections are bonded into a unified structure by injecting cement grout into the joints, and the tensile and shear strengths of the contact elements are updated to reflect the mechanical properties of the hardened mortar.

3 Framework for Seismic Analysis During Construction and Initial Impoundment

The key time nodes during the construction period are selected, and the deformation and stress obtained by static simulation are taken as the initial state. The dam body-reservoir water-foundation is regarded as a whole open wave system. Considering the inertia of foundation, various geological structures in the near-field foundation rock mass, the nonlinear effect of dynamic contact between transverse joints, the radiation damping effect of infinite foundation and the non-uniformity of earthquake input on the dam foundation surface, the seismic response of arch dam is calculated by time-history analysis method. The dynamic equilibrium equation for arch dam seismic response calculation is as follows:

$$[M]\{\ddot{u}(t)\} + [C]\{\dot{u}(t)\} + [K]\{u(t)\} = \{F(t)\} \tag{3}$$

Where $[M]$, $[C]$ and $[K]$ are the mass matrix, damping matrix and stiffness matrix of arch dam respectively; $\{\ddot{u}(t)\}$, $\{\dot{u}(t)\}$ and $\{u(t)\}$ are the displacement, velocity and acceleration vectors respectively; $\{F(t)\}$ is the force vector.

3.1 Simulation of Radiation Damping of Infinite Foundation

Viscous-spring artificial boundary needs to apply discrete spring-damping elements on the truncated boundary of finite element model, which often consumes a lot of preprocessing time when it is realized in general finite element program. In order to overcome this shortcoming, Liu et al. [17, 18] put forward that the radiation damping effect of infinite foundation is simulated by the consistent equivalent viscous-spring boundary element, that is, a layer of solid elements with the same thickness extends normally outside the boundary surface of the finite element model to replace the discrete spring-damping elements. The shear modulus $\widetilde{G}$ and elastic modulus $\widetilde{E}$ equivalent viscous-spring boundary element can be respectively [19]

$$\widetilde{G} = hK_T = \alpha_T h\frac{G}{r} \tag{4}$$

$$\widetilde{E} = \frac{\left(1+\widetilde{\nu}\right)\left(1-2\widetilde{\nu}\right)}{\left(1-\widetilde{\nu}\right)}hK_N = \alpha_N h\frac{G}{r}\frac{\left(1+\widetilde{\nu}\right)\left(1-2\widetilde{\nu}\right)}{\left(1-\widetilde{\nu}\right)} \tag{5}$$

Where K_N, and K_T are the normal stiffness and tangential stiffness of viscous-spring artificial boundary spring respectively; r is the distance from the scattered wave source to the artificial boundary; $\widetilde{V}$ is the equivalent Poisson's ratio of consistent equivalent viscous-spring boundary element; G indicates the shear modulus of the medium; h refers to the thickness of the equivalent boundary element; α_T and α_N are the correction coefficients of tangential and normal viscous-spring artificial boundaries respectively.

When inputting the arch dam ground motion, we can simulate the damper of viscous-spring artificial boundary by giving the damping proportional coefficient $\widetilde{\eta}$ of the boundary element, and its values can be taken as

$$\widetilde{\eta} = \frac{\rho r}{3G}\left(2\frac{c_s}{\alpha_T} + \frac{c_p}{\alpha_N}\right) \tag{6}$$

Where ρ is the mass density of the medium; C_s and C_p are the wave velocities of wave S and P, respectively.

3.2 Ground Motion Input Method

During the earthquake input, the total wave field at the bottom boundary of the finite element model can be decomposed into incident field and scattering field, and the total wave field at the side boundary can be decomposed into free field and scattering field. According to the displacement continuity condition and the mechanical equilibrium condition, the motion equation of any point b on the bottom boundary and the side boundary can be expressed as

$$m_b\ddot{u}_b^m(t) + C_b\dot{u}_b^m(t) + K_b u_b^m(t) = F_b^r(t) + F_b^s(t) \tag{7}$$

$$m_b\ddot{u}_b^m(t) + C_b\dot{u}_b^m(t) + K_b u_b^m(t) = F_b^f(t) + F_b^s(t) \tag{8}$$

Where K_b and C_b is the spring stiffness and damping of the artificial boundary node b; $F_b^r(t)$, $F_b^f(t)$ and $F_b^s(t)$ are the equivalent node loads to be applied on the artificial boundary nodes to simulate the incident field, free field and scattering field of the boundary respectively. Among them, the load $F_b^s(t)$ applied on the artificial boundary node to simulate the scattering field is provided by the viscous-spring boundary. The equivalent node load $F_b^r(t)$ to be applied on the bottom boundary consists of two parts: the force $K_b u_b^r(t) + C_b\dot{u}_b^r(t)$ needed to overcome the stiffness and damping of viscous-spring boundary elements and the stress field $\sigma_b^r(t)$ of the incident field at the artificial boundary. The equivalent node load $F_b^f(t)$ to be applied on the lateral boundary consists of two parts: the force $K_b u_b^f(t) + C_b\dot{u}_b^f(t)$ needed to overcome the stiffness and damping of viscous-spring boundary elements and the stress $\sigma_b^f(t)$ of free field at the artificial boundary.

3.3 Hydrodynamic Pressure Simulation

In the present paper, the modified Westergaard additional mass formula is adopted to simulate the hydrodynamic pressure [20]:

$$m_{px} = \frac{7}{8}\rho\sqrt{Hh}\sin\theta, \quad m_{py} = \frac{7}{8}\rho\sqrt{Hh}\cos\theta \tag{9}$$

Where H is the depth of reservoir water; h is the water depth of the calculation point; ρ is the density of water body; x, y and z are the overall coordinates of the direction perpendicular to river direction, the direction along the river direction and the vertical direction; θ is the included angle from the crown to the calculation point.

4 Seismic Response Evaluation Under Construction-Stage Working Conditions

4.1 Calculation Model and Material Parameters

The arch dam is a concrete hyperbolic arch dam with a crest elevation of 988.00 m and a maximum dam height of 270.00 m. The normal water level is 975.00 m. In consideration of the actual shape, transverse joints, rock mass division and main geological structures of the dam, the dam body and foundation are discretized by three-dimensional finite element method, and 92,444 hexahedral elements and 112,389 nodes are divided. The coordinate system is taken as: the x direction is the direction perpendicular to river direction, pointing to the left bank; y direction is the direction along the river direction, pointing to the upstream; z direction is the vertical direction. The finite element model of the arch dam is shown in Figs. 2 and 3.

Fig. 2. Finite element mesh of arch dam-foundation system.

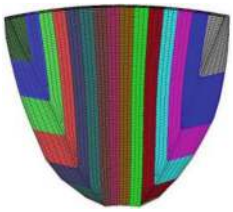

Fig. 3. Finite element mesh of dam body.

The material parameters of dam concrete are the elastic modulus $E = 48GPa$, Poisson's ratio $\mu = 0.167$, the density $\rho = 2{,}400kg/m^3$, the linear expansion coefficient $\alpha = 1.0 \times 10^{-5}/^\circ C$ and the friction coefficient between transverse joints $f = 0.75$.

The parameters of bedrock material are the deformation modulus $E = 27.5GPa$, Poisson's ratio $\mu = 0.215$ and density $\rho = 2{,}700kg/m^3$.

4.2 Loads and Seismic Parameters

The calculated loads mainly include dead weight, water pressure, sand pressure, temperature load and earthquake load. Rayleigh damping is used to characterize the total damping matrix of the system, and the damping ratio is $\xi = 0.05$.

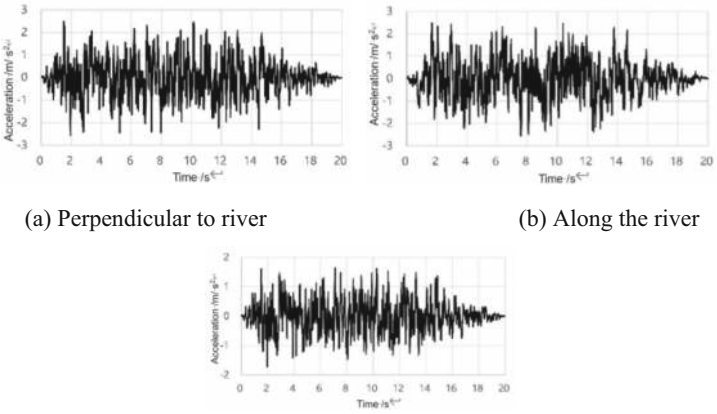

(a) Perpendicular to river (b) Along the river

(c) Vertical

Fig. 4. Time history curve of earthquake acceleration.

The backwater building of the hydropower station has Class A seismic fortification, and the peak acceleration of ground motion exceeding the probability of 10% in 50 years is 0.13 g, that exceeding the probability of 2% in 100 years is 0.27 g, and that exceeding the probability of 1% in 100 years is 0.32 g. In the seismic response analysis, the horizontal acceleration peak is 0.27 g, and the vertical acceleration is 2/3 of the horizontal acceleration. Three seismic time histories at different phases are taken as the ground motions input in three directions respectively, as shown in Fig. 4. The calculation time takes 0.02 s, which lasts for 20 s.

4.3 Dam Principal Stress at Typical Seismic Times

From the calculation results, Figs. 5, 6 and 7 show the principal tensile stress distribution nephogram of the dam body under static and dynamic superposition at the water levels of 945 m, 960 m and 975 m respectively when the seismic response time is 7.57 s. It can be seen that the tensile stress at the arch end and dam heel of the upstream surface of the arch dam is relatively large, the maximum value is about 2.0 MPa, while that at other parts is within 1.0 MPa. The high tensile stress at the downstream surface is distributed in the middle elevation of the middle dam section, and the maximum tensile stress is 0.9 MPa, while that at other parts is within 0.6 MPa. The tensile stress of the dam is less than the dynamic tensile strength of the concrete.

Figures 8, 9 and 10 are the principal tensile stress distribution nephogram of the dam body under static and dynamic superposition at the water levels of 945 m, 960 m and 975 m respectively when the seismic response time is 7.59 s. It can be seen that the high compressive stress of the dam body is mainly distributed in the lower elevation of the crown cantilever on the upstream and downstream surfaces, with the maximum value of 21.57 MPa. The compressive stress of the dam is less than the compressive strength of the concrete.

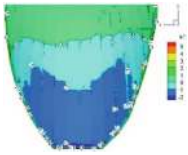

(a) Upstream surface

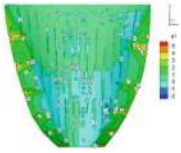

(b) Downstream surface

Fig. 5. Nephogram of principal tensile stress distribution of dam body under static and dynamic superposition (unit: MPa, earthquake 7.57 s, water level 945 m).

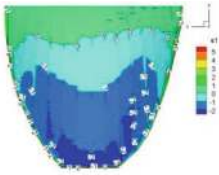

(a) Upstream surface

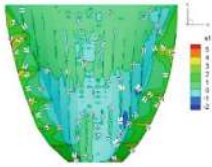

(b) Downstream surface

Fig. 6. Nephogram of principal tensile stress distribution of dam body under static and dynamic superposition (unit: MPa, earthquake 7.57 s, water level 960 m).

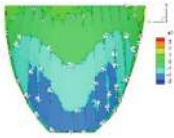

(a) Upstream surface

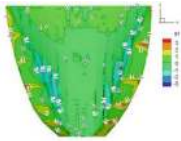

(b) Downstream surface

Fig. 7. Nephogram of principal tensile stress distribution of dam body under static and dynamic superposition (unit: MPa, earthquake 7.57 s, water level 975 m).

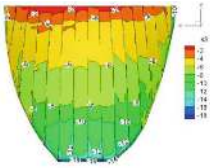

(a) Upstream surface

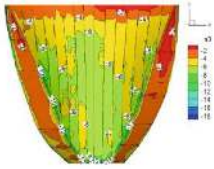

(b) Downstream surface

Fig. 8. Nephogram of principal tensile stress distribution of dam body under static and dynamic superposition (unit: MPa, earthquake 7.59 s, water level 945 m).

4.4 Transverse Joint Aperture-Elevation Relationship at Different Water Levels

Figures 11, 12 and 13 show the relationship between the maximum aperture of transverse joints and the elevation at the water levels of 945 m, 960 m and 975 m respectively. The

(a) Upstream surface (b) Downstream surface

Fig. 9. Nephogram of principal tensile stress distribution of dam body under static and dynamic superposition (unit: MPa, earthquake 7.59 s, water level 960 m).

(a) Upstream surface (b) Downstream surface

Fig. 10. Nephogram of principal tensile stress distribution of dam body under static and dynamic superposition (unit: MPa, earthquake 7.59 s, water level 975 m).

maximum aperture and location of transverse joints under three water levels are listed in Table 1. It demonstrated that the maximum aperture of 1#, 13# and 14# transverse joints increases with the elevation, and that of other transverse joints increases slightly with the elevation first, then decreases to 0, and then increases with the elevation again, but finally decreases slightly, tending to be flat. At the water level of 945 m, the maximum aperture value of the dam transverse joints is 14.02 mm, which reaches the maximum, and the water stop of the transverse joint will not be pulled apart at this time. As the water level rises, the maximum aperture of dam transverse joints decreases.

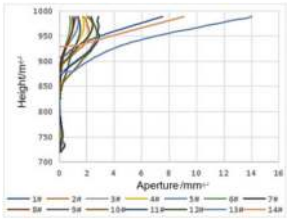

Fig. 11. Relationship between maximum aperture of transverse joints and elevation (water level 945 m)

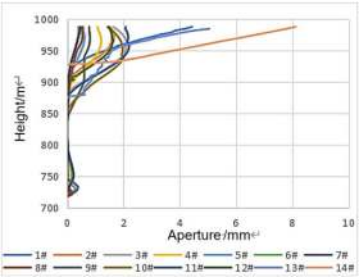

Fig. 12. Relationship between maximum aperture of transverse joints and elevation (water level 960 m).

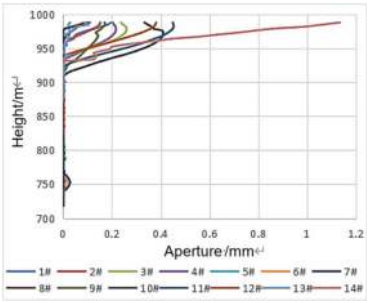

Fig. 13. Relationship between maximum aperture of transverse joints and elevation (water level 975 m).

Table 1. Maximum aperture and position of transverse joints.

Calculation condition	Maximum aperture of transverse joint/mm	Position
945 m	14.02	Top of 13# transverse joint
960 m	8.11	Top of 14# transverse joint
975 m	1.134	Top of 15# transverse joint

5 Conclusion

This study develops a novel and comprehensive seismic response analysis framework specifically tailored for ultra-high arch dams during their construction and initial impoundment stages. Using the Wudongde Arch Dam as a representative case, the proposed approach integrates time-dependent structural evolution, multi-field coupled dynamic effects, and construction-aware load history simulation, addressing key gaps in current seismic safety assessments for dams in early operational phases. Unlike conventional approaches that assume completed structures and steady-state loading, this framework captures the complex interplay of staged loading, construction-induced

heterogeneity, and transient boundary conditions. By incorporating infinite foundation radiation damping, dam–reservoir hydrodynamic interaction, and nonlinear dynamic contact of transverse joints, the seismic performance of the dam is evaluated through time-history analysis across multiple construction stages. The key theoretical insights and engineering findings are summarized as follows:

(1) Evolving Tensile Stress Distribution: At reservoir levels of 945 m, 960 m, and 975 m, and a seismic response time of 7.57 s, significant tensile stress concentrations are observed at the upstream arch abutments and heel zones, reaching peak values of approximately 3.0 MPa. On the downstream face, maximum tensile stresses of 0.9 MPa are localized at the mid-elevation of the central dam section. All tensile stresses remain below the dynamic tensile strength of concrete, validating the reliability of the staged construction model and confirming that no seismic-induced tensile cracking is expected at these stages.
(2) Localized Compressive Stress Concentration: At 7.59 s, compressive stresses are primarily concentrated in the lower elevations of the crown cantilever regions on both upstream and downstream faces, with a peak value of 19.343 MPa. These results confirm that the dam remains well within the concrete compressive strength limit throughout the staged construction and impoundment process. The simulation reflects the dam's evolving stiffness distribution and stress transfer mechanism under dynamic loads, which are not captured in traditional one-step loading models.
(3) Transverse Joint Kinematics and Safety Margins: The aperture behavior of transverse joints reveals significant elevation-dependent variation. Joints #1, #13, and #14 show monotonic increases with elevation, while others exhibit a non-monotonic evolution: initial widening, subsequent closure, and eventual stabilization. The peak aperture of 14.02 mm occurs at a reservoir level of 945 m, remaining within acceptable engineering limits, and no rupture of waterstops is predicted. Importantly, as impoundment progresses, joint aperture generally decreases, indicating enhanced confinement and joint closure behavior. This finding provides a new understanding of staged joint dynamics under seismic excitation—an aspect often oversimplified or neglected in previous studies.

References

1. Kong, X.J., Chen, J.Y., Zou, D.G.: Study on development trend of seismic safety theory for high dams. J. Hydroelectr. Eng. **39**(7), 1–10 (2020). https://doi.org/10.11660/slfdxb.20200701
2. Li, S., Xiang, Z.Q., Pan, J.W., et al.: Review on modal parameters identification for high arch dams. Earthquake Eng. Eng. Dyn. **43**(02), 1–12 (2023). https://doi.org/10.13197/j.eeed.2023.0201
3. Chen, D.H., Wang, R.N., Lin, T.C., et al.: Seismic fragility analysis of high arch dams based on endurance time analysis method. J. Hydroelectr. Eng. **43**(03), 108–119 (2024). https://doi.org/10.11660/slfdxb.20240310
4. Huang, H.B., Chen, G., Jiang, D.J.: Analysis of deformation characteristics of Dagangshan ultra-high arch dam in Luding earthquake with Ms6.8 in Sichuan. J. Hydraul. Eng. **54**(05), 599–609 (2023). https://doi.org/10.13243/j.cnki.slxb.20230017

5. Zhao, L.H., He, Z.X., Liu, X.Q.: Seismic response analysis of Baihetan Arch Dam during construction period. Water Resour. Power. **36**(3), 71–75 (2018). https://doi.org/10.20040/j.cnki.1000-7709.2018.03.018
6. Zhang, B.Y., Li, D.Y., He, J.T.: Effects of crack at construction stage on the static and dynamic responses of arch dam. J. Hydroelectr. Eng. **31**(1), 72–76 (2012)
7. Li, D.Y., Liao, J.X., Tu, J., et al.: Study on seismic safety of high arch dams. Water Resour. Hydropower Eng. **50**(8), 77–83 (2019). https://doi.org/10.13928/j.cnki.wrahe.2019.08.010
8. Cheng, H., Zhang, G.X., Liao, J.X., et al.: Analysis on nonlinear seismic response of super-high arch dam under strong seismic action. Water Resour. Hydropower Eng. **50**(10), 119–124 (2019). https://doi.org/10.13928/j.cnki.wrahe.2019.10.016
9. Cheng, H., Zhang, L.J.: Overall seismic safety evaluation of Shapai Arch Dam. J. Water Resour Power. **30**(1), 49–53 (2012). https://doi.org/10.3969/j.issn.1000-7709.2012.01.013
10. Huang, Y.H., Xu, J.J., Yin, L., et al.: Seismic safety analysis and evaluation of Yangfanggou high arch dam based on the new seismic code. J. Hydroelectr. Eng. **45**(4), 52–55 (2019). https://doi.org/10.3969/j.issn.0559-9342.2019.04.011
11. Ministry of Housing and Urban-Rural Development of the People's Republic of China: Standard for Seismic Design of Hydraulic Structures GB 5124–2018. China Planning Press, Beijing (2018)
12. National Energy Administration: Code for Seismic Design of Hydraulic Structures of Hydropower Project NB 35047–2015. China Electric Power Press, Beijing (2015)
13. Liu, Y., Yang, B., Zhang, J., et al.: Performance simulation-based study on design of super-high arch dam and its application Part I—development status and prospect of structural analysis method for arch dam in China. Water Resour. Hydropower Eng. **51**(10), 41–54 (2020). https://doi.org/10.13928/j.cnki.wrahe.2020.10.006
14. Bathe, K.J., Chaudhary, A.: A solution method for planar and axisymmetric contact problems. Int. J. Num. Meth. Eng. **21**, 65–88 (1985). https://doi.org/10.1002/nme.1620210107
15. Eterovic, A., Bathe, K.J.: On the treatment of inequality constraints arising from contact conditions in finite element analysis. J. Comput. Struct. **40**(2), 203–209 (1991). https://doi.org/10.1016/0045-7949(91)90347-O
16. Bathe, K.J., Bouzinov, P.A.: On the constraint function method for contact problems. J. Comput. Struct. **64**(5), 1069–1085 (1997). https://doi.org/10.1016/S0045-7949(97)00036-9
17. Liu, J.B., Gu, Y., Du, Y.X.: Consistent viscous-spring artificial boundaries and viscous-spring boundary elements. Chin. J. Geotech. Eng. **28**(9), 1070–1075 (2006). https://doi.org/10.3969/j.issn.1000-4750.2007.12.006
18. Gu, Y., Liu, J.B., Du, Y.X.: 3D consistent viscous-spring artificial boundary and viscous-spring boundary element. J. Eng. Mech. **24**(12), 31–37 (2007). https://doi.org/10.3969/j.issn.1000-4750.2007.12.006
19. Cheng, H., Zhang, L.J., Zhang, H.Y.: Application of 3D consistent equivalent viscous-spring boundary element to seismic analysis of arch dams. J. Hydroelectr. Eng. **28**(5), 169–173 (2009). https://doi.org/10.11660/slfdxb.2009.05.031
20. Xu, J.Y., Li, D.Y., Guo, S.S.: The dynamic analysis of gravity dam under two added water mass models based on ABAQUS. J. China Inst. Water Resour. Hydropower Res. **12**(01), 98–103 (2014). https://doi.org/10.13244/j.cnki.jiwhr.2014.01.017

Migration and Plugging for Temporary Plugging Balls in Multi-cluster Fractured Horizontal Well

Aiguo Hu[1], Hao Chen[2(✉)], Fan Wang[1], Yanfang Jiang[1], Yangyang Li[1], Jinpeng Yan[1], Huaizhou Wei[2,3], Chao Gao[2,3], and Can Cai[2,3(✉)]

[1] Petroleum Engineering Technology Research Institute of Sinopec North China Oil and Gas Branch, Henan Zhengzhou 450006, China

[2] High-pressure Jet Theory and Application Technology Laboratory, School of Mechanical Engineering, Southwest Petroleum University, Chengdu, Sichuan 610500, China
chh@swpu.edu.cn, cainia10@163.com

[3] The State Key Laboratory of Oil and Gas Reservoir Geology and Exploitation, Southwest Petroleum University, Chengdu 610599, China

Abstract. Ball-throwing temporary plugging technology is an important way for addressing the problem of unequal fracture extension in multi-cluster fracturing This study used experiments and numerical simulations to evaluate the migratory behaviour of transient plugging balls in horizontal wells This study looks at the impact of the transient plugging ball's density and hole-ball diameter ratio on the wellbore plugging position, fluid flow field changes, and ball movement trajectory The study shows the density of the temporary plugging balls influences their trajectory in the wellbore, whereas the position of the plugging shot hole is determined by the movement state of the temporary plugging balls prior to the shot hole being shot, and that a reasonable combination of the diameter and density of the temporary plugging balls can control the number and position of the plugging shot holes while maintaining uniform fracture expansion.

Keywords: Horizontal Well · Multi-cluster Fracturing · Competitive Expansion · Temporary Plugging with Ball · Temporary Plugging Ball

1 Introduction

With the continuous development of oil and gas exploration and production, under the current economic and technological conditions, unconventional oil and gas resources such as tight oil, tight gas, shale gas, and coalbed methane have demonstrated significant development potential [1, 2]. China's proven reserves of unconventional oil and gas account for 75% of newly proven reserves, which are now the primary driver of reserves expansion [3, 4]. However, unconventional oil and gas reservoirs often have relatively simple fracture networks. By inducing stress changes, multi-cluster fracturing technology can increase the complexity of the fracture network and facilitate the transformation of unconventional oil and gas reservoirs [5, 6].

Due to stress interference and differences in flow resistance between clusters [7, 8], there is a problem with the competitive expansion of multi-cluster fractures, leading

© The Author(s), under exclusive license to Springer Nature Switzerland AG 2027
G. Feng et al. (Eds.): ICCE 2025, SUCI, pp. 464–477, 2027.
https://doi.org/10.1007/978-3-032-32237-1_33

to uneven expansion of multiple transverse fractures, which significantly impacts the fracturing effect [9, 10]. The primary method for promoting uniform expansion of multi-cluster fractures is the temporary plugging technology using balls [11]. This technology involves injecting temporary plugging balls into high-permeability perforations during the fracturing process to temporarily seal them and redirect the fracturing fluid towards the low-permeability layers. However, two issues arise with the temporary plugging procedure: uncertainty in the migration process and an inadequate temporary plugging effect. To achieve successful temporary plugging of perforations with good permeability and ensure even propagation of multiple fractures, it is essential to clarify the downhole migration rules of the temporary plugging balls.

Numerous academics have examined the impact of various building characteristics on the migratory behavior of temporary plugging balls in an effort to address the aforementioned issues. To investigate the migration behavior of temporary plugging balls in horizontal wellbores, a visual multi-perforation device was developed. It was discovered that the wellbore possessed a recirculation zone downstream of the perforation, which facilitated the entry of temporary plugging balls into the perforation [12]. Through a temporary plugging experiment, the effects of displacement, density, and hole diameter ratio on the migration behavior of temporary plugging balls were examined. The primary determinants of migration and plugging were found to be the temporary plugging ball's displacement and density [13–15]. The coupling method of computational fluid dynamics (CFD) and discrete element modeling (DEM) was utilized to analyze the influence of parameters such as temporary plugging ball density, pumping displacement, and liquid viscosity on the efficiency of temporary plugging, based on the force equation of temporary plugging balls [16–18]. They claimed that increasing the time interval between temporary plugging balls, selecting an appropriate fluid viscosity, and choosing a suitable low displacement could all contribute to enhancing the plugging effect of temporary plugging balls when their density matches that of the fracturing fluid.

Little research has been done so far on the flow field changes that occur during and after temporary plugging during fracturing, the motion of temporary plugging balls, and the impact of temporary plugging balls on various stages of borehole movement. Under the support of project of "Research on Fracture Propagation and Effective Support Technology for Hydraulic Fracturing in Binchang Tight Sandstone Reservoirs", This paper aims to optimize the design of ball-throwing temporary plugging for multi-cluster fracturing of horizontal wells by studying the effects of flow field changes, temporary plugging ball density, and diameter on the migration and plugging behavior of the temporary plugging balls. This will help to promote uniform crack expansion and enhance the effectiveness of oil and gas reservoir reconstruction.

2 Research Methods

2.1 Experimental Method and Its Accuracy Verification

Experimental Device. In order to explore the plugging mechanism of temporary plugging ball movement and the influence of ball density and diameter on the plugging effect, we have set up the experimental equipment for horizontal well ball temporary plugging (Fig. 1). This equipment consists of three main components: the hydraulic system, the

data acquisition system, and the horizontal well perforation cluster device. The hydraulic system comprises a water tank, a plunger pump, infusion pipelines, and other essential components. The data acquisition system, on the other hand, includes an in-hole pressure sensor, a perforation output flowmeter, and a wellbore pressure sensor. The horizontal well perforation cluster device consists of two clusters of perforations along with the wellbore itself. During the experiment, the fracturing fluid is pumped into the horizontal wellbore by the plunger pump and exits through the perforations, ultimately returning to the water tank. The temporary plugging ball is released from the pitching inlet and carried by the fracturing fluid to complete the temporary plugging of the perforation holes.

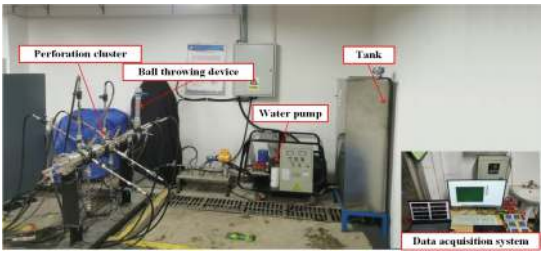

Fig. 1. Experimental devices.

From the field practice of Petroleum Engineering Technology Research Institute of Sinopec North China Oil and Gas Branch, the parameters of the experimental setup and conduction is designed. The experimental wellbore (Fig. 2) measures 1200 mm in length. There are two clusters of perforations (A1–A12), each containing six holes. The holes within each cluster are spaced at a phase angle of 60°, resulting in a spiral distribution. The perforation spacing within each cluster is 50 mm, while the spacing between the two clusters is 150 mm. Pressure sensors B1 through B4 are employed to monitor the pressure at various perforation locations. Additionally, flow sensors have been installed at every perforation outlet to track fluid diversion through these outlets.

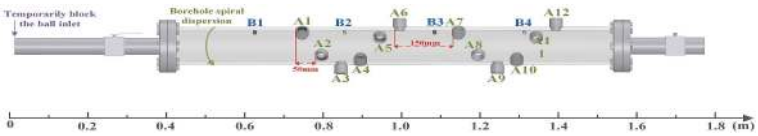

Fig. 2. Perforation and sensor distribution diagram.

Accuracy of the Flow Field Verification. During the temporary plugging fracturing operation, the ground injection pressure ranges from 70 to 100 MPa, and the fracturing fluid injection rate is 4 to 8 m^3/min [19]. In laboratory investigations, it is challenging to replicate the conditions of field injection displacement and pressure. Based on the fluid similarity theory, it is essential to ensure that the ratio of the fracturing fluid flow rate

in the perforation to the fracturing fluid flow rate in the wellbore remains essentially the same, in order to guarantee that the internal flow field of the experimental device is consistent with the flow state of the fracturing fluid under field conditions. Therefore, the flow field in the experimental device is considered capable of replicating the field ball temporary plugging process when the field and experimental flow field parameters for the ball temporary plugging fracturing satisfy the following formula [20]. Table 1 lists the field and experimental data for temporary plugging fracturing.

$$\left(\frac{V_{k,n} \times A_{k,n}}{V_{j,n} \times A_{j,n}}\right) = \left(\frac{V_{k,m} \times A_{k,m}}{V_{j,m} \times A_{j,m}}\right) \tag{1}$$

Where $V_{\mathrm{k,n}}$, $V_{\mathrm{j,n}}$, $V_{\mathrm{k,m}}$ and $V_{\mathrm{j,m}}$ are on-site perforation internal flow velocity, on-site wellbore flow velocity, the experimental perforation flow velocity and experimental wellbore flow velocity, respectively; $A_{\mathrm{k,n}}, A_{\mathrm{j,n}}, A_{\mathrm{k,m}}$ and $A_{\mathrm{j,m}}$ are on-site perforation cross-sectional area, on-site wellbore cross-sectional area, experimental perforation cross-sectional area and experimental wellbore cross-sectional area, respectively.

Table 1. Field and experimental data of ball temporary plugging fracturing.

Parameter	Field data	Experimental data
Perforation internal velocity (m/s)	50	2.69
Wellbore internal velocity (m/s)	15.45	0.79
Perforation inner diameter (m)	0.013	0.013
Wellbore inner diameter (m)	0.114	0.114

The calculation according the data in the above table indicate that the values of $\left(\frac{V_{k,n} \times A_{k,n}}{V_{j,n} \times A_{j,n}}\right)$ and $\left(\frac{V_{k,m} \times A_{k,m}}{V_{j,m} \times A_{j,m}}\right)$ are 0.042 and 0.044, respectively, and that the relative error is 4.76% and within permitted bounds. In both the experiment and field ball fracturing, the dimensionless flow rate ratio of the fracturing fluid in the wellbore and perforation is essentially the same. Based on the similarity analysis results, it is considered that the internal flow field of the experimental device is consistent with the flow state of the fracturing fluid in the wellbore during on-site ball temporary plugging fracturing, and accordingly, the ball temporary plugging experiment is carried out.

2.2 Numerical Simulation Method

CFD/DEM Coupling Method. Due to the fact that the experimental parameters differ greatly from those in the field, and it is not possible to directly observe the temporary plugging ball's motion state, the migration and plugging mechanism of the ball during the temporary plugging fracturing process in the downhole is studied using the discrete element method and computational fluid dynamics (DEM-CFD) coupling approach.

The force diagram of the solid-phase contact in the Hertz-Mindlin no-slip contact model is shown in Fig. 3, and the contact model is a soft sphere model. According to the

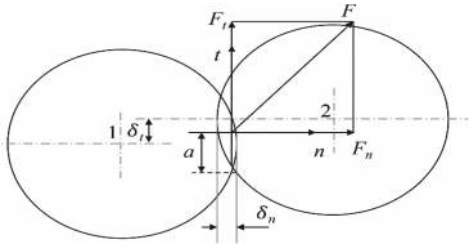

Fig. 3. The contact force diagram of two solid phase spheres.

Hertzian contact theory [21], the normal force between spheres is expressed as follows:

$$Fn = \frac{2}{3} Sn\delta n \tag{2}$$

Equations for normal stiffness S_n and effective modulus of elasticity E^*:

$$\begin{cases} Sn = 2E^*\sqrt{R^*\delta n} \\ E^* = \left(\frac{1-v_1^2}{E1} + \frac{1-v_2^2}{E2}\right)^{-1} \end{cases} \tag{3}$$

Where v_1 and v_2 are Poisson's ratio of the different solid phase spheres, respectively.

According to Middlin-Deresiewicz theory [22], the tangential force between spheres is expressed as follows:

$$Ft = St\delta t \tag{4}$$

Equations for tangential stiffness S_t and equivalent shear modulus G^*:

$$\begin{cases} St = 8G^*\sqrt{R^*\delta n} \\ G^* = \left(\frac{1-v_1^2}{G1} + \frac{1-v_2^2}{G2}\right)^{-1} \end{cases} \tag{5}$$

In the CFD calculation of fracturing fluid flow, fracturing fluid flow follows the mass conservation equation, momentum conservation equation and energy conservation equation [23]. The mass conservation equation of fluid motion is expressed as follows:

$$\frac{\partial \rho}{\partial t} + \nabla \bullet \left(\rho \vec{V}\right) = 0 \tag{6}$$

Where $\frac{\partial \rho}{\partial t}$ is the density to time partial derivative that indicates a non-constant term for flow, $\nabla \bullet \left(\rho \vec{V}\right)$ denotes the mass per unit time of the outflow of the microbody.

The physical quantity of any point of fracturing fluid flow does not change with time, which belongs to steady flow.

According to Newton's second law, the momentum conservation equation of fluid is obtained by analyzing the momentum of the microfluid.

$$\begin{cases} \frac{\partial(\rho fux)}{\partial t} + \nabla^2(\rho fuf) = -\frac{\partial p}{\partial x} + \frac{\partial \tau_{xx}}{\partial x} + \frac{\partial \tau_{yx}}{\partial y} + \frac{\partial \tau_{zx}}{\partial z} + Fx \\ \frac{\partial(\rho fuy)}{\partial t} + \nabla^2(\rho fuf) = -\frac{\partial p}{\partial y} + \frac{\partial \tau_{xy}}{\partial x} + \frac{\partial \tau_{yy}}{\partial y} + \frac{\partial \tau_{zy}}{\partial z} + Fy \\ \frac{\partial(\rho fuz)}{\partial t} + \nabla^2(\rho fuf) = -\frac{\partial p}{\partial z} + \frac{\partial \tau_{xz}}{\partial x} + \frac{\partial \tau_{yz}}{\partial y} + \frac{\partial \tau_{zz}}{\partial z} + Fz \end{cases} \tag{7}$$

Where p is the pressure acting on the fluid, Pa, τ is the viscous stress acting on the fluid, Pa, F is volume forces acting on the fluid, N.

This method involves utilizing DEM software to simulate the movement of the temporary plugging ball and CFD software to compute the parameters of downhole fracturing fluid speed and pressure. It enables the mutual transfer of momentum and energy between the temporary plugging ball and the fracturing fluid to be actualized, while also accurately reflecting the ball's migration.

Geometric Model. A geometric model (Fig. 4) is constructed based on the engineering parameters of multi-cluster fracturing in the 16th segment of a well located in Jianghan Oilfield, Hubei Province, China. The wellbore has a length of 8 m and an inner diameter of 114.3 mm. There are 3 clusters, each with an interval of 610 mm between them. The perforation phase angle within each cluster is 60°, and there are a total of 8 perforations per cluster. The dimensions of the perforated holes are 13 mm in diameter, with a spacing of 55 mm between holes, and a depth of 800 mm.

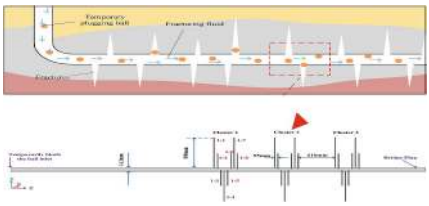

Fig. 4. Multi-cluster perforation geometric model of horizontal well.

Boundary Conditions and Operating Parameters. The flow boundary and pressure boundary are, respectively, the boundary conditions of the perforation inlet and outflow. Turbulence is the primary characteristic of the fracture fluid found in the perforation region. Therefore, by utilizing the conventional k-ε turbulence model in CFD, one can replicate the turbulent movement of the fracture fluid.

The diameter of the temporary plugging ball was fixed at 13.1 mm, and the density of the fracturing fluid was set to 1050 kg/m^3 in accordance with field operating conditions. Based on this, the plugging mechanism and migration of temporary plugging balls with varying densities were investigated.

3 Research Results and Analyses

3.1 Experimental Scheme and Results

Whether the temporary plugging ball can successfully complete the temporary plugging of the target perforation under the carrying effect of the fracturing fluid will determine whether ball temporary plugging is effective in carrying out temporary plugging perforation and promoting the uniform expansion of multi-cluster fractures during the process of multi-cluster fracturing. If the fracturing fluid inlet flow is constant, the diameter of the temporary plugging ball and the borehole's inner diameter have a direct correlation with the difficulty of temporary plugging the hole. The position of the temporary plugging borehole depends on the density of the temporary plugging ball.

Hence, the horizontal well balling temporary plugging experimental device is utilized to conduct experiments with varying diameter ratios of the ball pressing into the borehole and varying densities of the ball for temporary plugging. The impact of the diameter ratio of the temporary plugging ball to the borehole and the density of the ball on the migration of the temporary plugging ball and the alteration of the flow field before and after plugging are investigated.

The Effect of the Ratio Between the Temporary Plugging Ball Diameter and the Borehole Inner Diameter. The temporary plugging method involves pressing the temporary plugging ball into the borehole utilizing the pressure differential that exists between the wellbore and the formation. This pressure differential force acts along the center axis of the perforation. Given the same pressure differential force, the depth to which the temporary plugging ball is pressed into the borehole is related to the diameter of the ball and the inner diameter of the borehole. A deeper insertion of the temporary plugging ball into the borehole leads to a better plugging effect, as it is less likely to be displaced by the horizontally flowing fracturing fluid. Therefore, the perforation test simulating the pressing of the temporary plugging ball into the hole was conducted using the universal servo machine (Fig. 5). This is because the pressure applied by the device is directed along the central axis, which mirrors the actual pressing process of the temporary plugging ball.

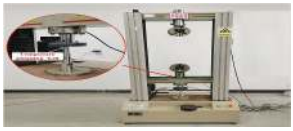

Fig. 5. Temporary plugging ball pressure into the hole experiment.

In order to investigate the impact of various diameter ratios on the pressing depth of the temporary plugging ball, the experimental design scheme is outlined in Table 2. Three pressing experiments were conducted using the same diameter ratio, aiming to reduce the experimental error.

The relationship between the temporary plugging ball's penetration depth and penetration force is shown in Fig. 6 for diameter ratios of 1.08, 1.12, 1.20, and 1.23. The

Table 2. Different diameter ratio indentation experimental parameters.

Experiment number	Perforation inner diameter d_p (mm)	Temporary plugging ball diameter d_b (mm)	Temporary plugging ball and perforation diameter ratio K_C
1	13	14	1.08
2	13	15	1.15
3	13	16	1.23
4	13	17	1.31
5	15	16	1.07
6	15	17	1.13
7	15	18	1.20
8	15	19	1.27
9	17	18	1.06
10	17	19	1.12

results show that the pressure and the depth to which the temporary plugging ball is driven into the borehole have a linear relationship. For varying diameter ratios, there are variations in the linear slope between the depth of the temporary plugging ball forced into the borehole and the pressure. As the pressing depth increases, the slope of the line decreases with the same pressing force. Greater penetration depth results in a better temporary plugging effect, making it harder for the horizontally flowing fracturing fluid to remove the temporary plugging ball.

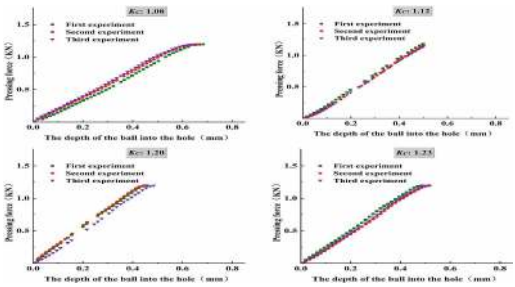

Fig. 6. The depth and pressure of the temporary plugging ball ratios into the borehole.

The statistical results of the linear slope relating the depth and pressure of the temporary plugging ball as it is inserted into the borehole, under different diameter ratios, are presented in Fig. 7. When the inner diameter of the borehole remains constant, the smaller the diameter of the temporary plugging ball, the lower the pressure required to fill the borehole, and correspondingly, the lower the linear slope. Notably, the linear slope reaches its minimum when the diameter ratio is 1.08, indicating that there exists

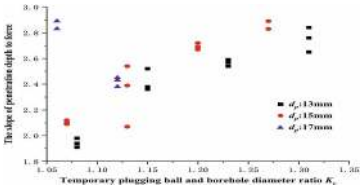

Fig. 7. The slope statistics of the depth and force of the temporary plugging ball pressed into the borehole.

an ideal diameter ratio of 1.08 which facilitates the insertion of the temporary plugging ball into the hole and achieves efficient temporary plugging.

The Effect of Temporary Plugging Ball Density. An experimental investigation was conducted to examine the impact of varying densities of temporary plugging balls on the effectiveness of temporary plugging. To facilitate analysis and research, we define the following terms: "gravity ball" refers to a temporary plugging ball with a density greater than 105% of the fracturing fluid density; "neutral ball" refers to a temporary plugging ball with a density within ±5% of the fracturing fluid density; and "buoyancy ball" refers to a temporary plugging ball with a density less than 95% of the fracturing fluid density.

The experiment utilized temporary plugging balls with densities of 900 kg/m^3 (buoyancy ball), 1100 kg/m^3 (neutral ball), and 1300 kg/m^3 (gravity ball). The fracturing fluid had a density of 1050 kg/m^3. The experiment was designed with 1.2 times more balls than open perforations. Additionally, a mixed density ball temporary plugging experiment was performed in addition to the single density ball experiments. In this mixed density experiment, temporary plugging balls with densities of 900 kg/m^3 and 1300 kg/m^3 were simultaneously added in equal quantities.

The results of the single-density temporary blocking experiment using pitching balls are shown in Fig. 8 for the temporary blocking balls. The buoyancy ball primarily temporarily plugs perforations 2, 6, 7, 11, and 12, and tends to temporarily plug the side and top perforations of the wellbore. In contrast, the neutral ball and the gravity ball mainly temporarily plug perforations 3 and 9, and under the action of gravity, they tend to temporarily plug perforations at the bottom of the wellbore. Both the buoyancy ball and the neutral ball experience the same magnitude of gravity and buoyancy forces (0.003 N) but in opposite directions, as shown in Fig. 6. For the neutral ball, the temporary blockage rate is 14.3%, whereas for the buoyancy ball, it is 64.3%. This indicates that, under the same conditions, temporary plugging with the buoyancy ball is easier to achieve than with the neutral ball.

Buoyancy balls and gravity balls were used in the mixed pitching temporary plugging experiment. The results of the temporary plugging experiment are shown in Fig. 9. The buoyancy ball temporarily closes the top and side perforations, while the gravity ball temporarily plugs the bottom perforation, in the mixed throwing method. In conjunction with Figs. 6 and 7, it is evident that the temporary plugging rate of the temporary plugging balls in the mixed throwing experiment is greater than that of the temporary plugging balls in the single-density throwing experiment. At the same time, the highest temporary

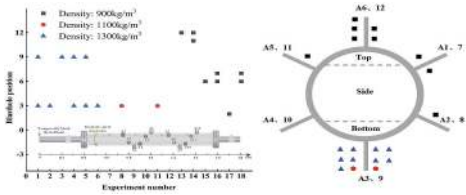

Fig. 8. Single density temporary plugging ball plugging hole result statistics (left), position (right) diagram.

plugging rate achieved is up to four times that of the temporary plugging balls in the single-density throwing experiment. Obviously, the efficiency of the temporary plugging balls can be increased by simultaneously placing the buoyancy and gravity balls.

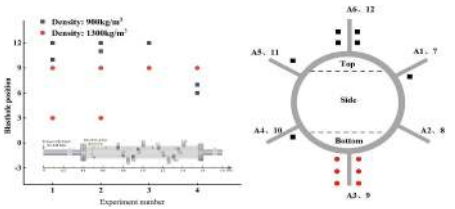

Fig. 9. Multi-density density temporary plugging ball plugging hole result statistics (left), position (right) diagram.

Flow Field Changes Before and After Temporary Plugging. To improve the temporary plugging fracturing process for balls, it is crucial to understand how to adjust the pressure in the wellbore and perforations both before and after the hole is temporarily filled. It is also important to comprehend how to redistribute the flow rate among each perforation. Therefore, temporary plugging experiments were conducted using temporary plugging balls with densities of 900, 1100, and 1300 kg/m^3, respectively. The changes in the flow field of the fracturing fluid within the wellbore before and after temporary plugging were then analyzed.

Figure 10 shows the changes in the flow field before and after the introduction of a temporary plugging ball with a density of 900 kg/m^3. Because the temporary plugging ball momentarily closes holes 11 and 12, the pressure ratio of perforations 11 and 12 approaches atmospheric pressure before and after this operation. Following temporary plugging, there was an increase in pressure of 12.7% to 13.1% in other holes that were not temporarily plugged, and a 6.4% to 6.5% increase in pressure at various wellbore sites. Affected by the inlet throttling effect, the fracturing fluid experiences a pressure drop due to this effect. Pressure sensors B1 and B3, located in the non-perforating cluster segment, showed a higher pressure increase following temporary plugging than did pressure sensors B2 and B4, which are in the perforating cluster section. Following the temporary closure of perforations 11 and 12, the flow rates through perforations 3 and 9 decreased by 18.9% and 31.8%, respectively, while perforations 5 and 7 saw an increase of 24.0% and 21.2%, respectively. Each hole exhibits a substantial variation in flow

redistribution, which exacerbates the unequal flow distribution among the perforations. As a result, perforations with low ball filling ability have little impact on temporarily plugged fracturing sites. Instead, they contribute to the uneven distribution of flow among the perforations, which does not significantly affect fracture expansion.

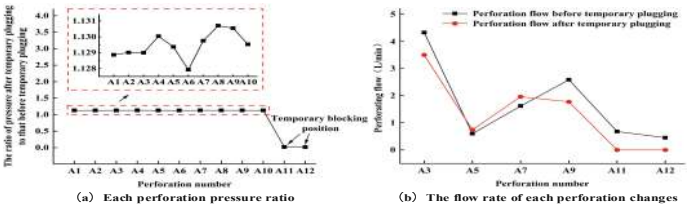

Fig. 10. The change of perforation flow field before and after temporary plugging of 900 kg/m3 ball.

Figure 11 illustrates the flow field change prior to and following the temporary plugging of a ball with a density of 1100 kg/m^3. The temporary plugging ball closing hole 3 results in an increase of 24.8% to 25.2% in pressure in the other holes that are not temporarily closed, 5.4% to 19.9% in flow volume, and 9.4% to 9.5% in pressure at various wellbore locations. Before temporary plugging, perforation 3 had a moderate shunting capacity. The fluid intake of the other perforations increases slightly after temporary blocking, but not significantly, and the uneven shunting of each hole cannot be corrected. Thus, plugging a perforation with medium diversion capacity can be employed in the field of ball temporary plugging fracturing to enhance the liquid intake of the remaining holes.

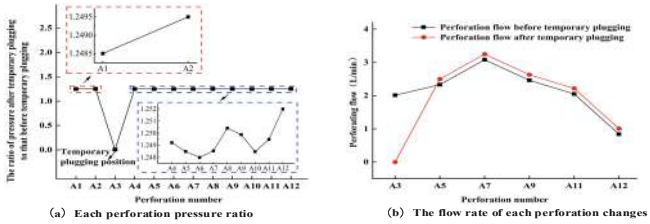

Fig. 11. The change of perforation flow field before and after temporary plugging of 1100 kg/m^3 ball.

Figure 12 depicts the flow field change before and after the insertion of a temporary plugging ball, which has a density of 1300 kg/m^3. Perforations 3 and 9, with strong diversion capabilities, are momentarily blocked by the temporary plugging ball. Following the temporary plugging, the pressure in the remaining unplugged perforations increased by 25.9% to 66.0%. There was a notable variation in the pressure increase among the individual perforations, and the flow rate in each also increased, ranging from 33.7% to 57.6%. When temporary plugging is applied, perforations 5 and 12, which had small flow rates prior to the plugging, experienced a substantial increase in flow rate. Conversely, perforations 7 and 11, which had high flow rates before the plugging, showed

only a modest increase in flow rate following the temporary plugging. The results of the temporary plugging indicate that the uneven distribution of flow among the perforations can be effectively improved through the use of a strong temporary plugging capability.

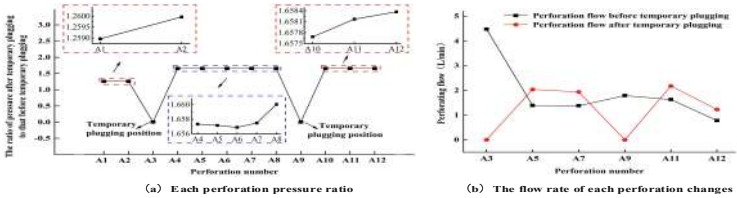

Fig. 12. The change of perforation flow field before and after temporary plugging of 1300 kg/m^3 ball.

4 Conclusions

This paper analyses the movement and plugging law of the temporary plugging ball. Experiments and numerical simulations are conducted based on real operating parameters to investigate the sensitivities of the density, diameter, and perforation inner diameter on the plugging effect of a temporary plugging ball. The research results are as follows:

(1) With the same borehole inner diameter and injection force, smaller-diameter temporary plugging balls are more likely to enter the borehole and achieve temporary plugging. Additionally, under different borehole inner diameters, there exists an optimal diameter ratio of 1.08 that makes it easiest for the temporary plugging ball to block the borehole.
(2) Buoyancy balls temporarily plug the top and side holes of the wellbore, while neutral balls and gravity balls temporarily plug the bottom holes. Therefore, the location of the holes can be used to determine the different density combinations of balls required to complete the effective temporary plugging of each hole.
(3) In addition to exacerbating the unevenness of the diversion among perforations, temporarily plugging perforations with weak diversion capabilities has little effect on enhancing the liquid intake of each perforation. Plugging perforations with medium diversion capacity can marginally improve the liquid intake of the remaining perforations, but it does not improve the unevenness of the diversion among perforations. Plugging perforations with strong diversion ability can effectively improve the uneven distribution of liquid intake among perforations.
(4) The trajectory of the temporary plugging ball in the wellbore is influenced by its density, and the position of the plugging perforation is determined by the movement of the temporary plugging ball prior to entering the perforation cluster.

Acknowledgments. This work is financially supported by "Research on Fracture Propagation and Effective Support Technology for Hydraulic Fracturing in Binchang Tight Sandstone Reservoirs" (34550000-24-ZC0609-0002), commissioned by Sinopec North China Oil and Gas Company.

References

1. Fan, Y., Zhou, X.J., Zeng, B., et al.: Application of intensive staged fracturing technology in deep shale gas well Zi-2. Xinjiang Pet. Geol. **40**, 1–1 (2019). https://doi.org/10.7657/XJPG20190217
2. Zhou, C.N., Zhang, G.S., Yang, Z., et al.: Geological concepts, characteristics, resource potential and key techniques of unconventional hydrocarbon: on unconventional petroleum geology. Pet. Explor. Dev. **40**, 385–399 (2013). https://doi.org/10.11698/PED.2013.04.01
3. Zhao, J.Z.: Conception, classification and resource potential of unconventional hydrocarbons. Nat. Gas Geosci. **23**, 393–406 (2012). https://doi.org/10.11764/j.issn.1672-1926.2012.03.393
4. Zou, C.N., Pan, S.Q., Jing, Z.H., et al.: Shale oil and gas revolution and its impact. Acta Petrolei Sinica. **41**, 1–12 (2020). https://doi.org/10.7623/syxb202001001
5. Zheng, Y.C., Fan, Y., Yong, R., et al.: A new fracturing technology of intensive stage + high-intensity proppant injection for shale gas reservoirs. Nat. Gas Ind. **39**, 76–81 (2019). https://doi.org/10.3787/j.issn.1000-0976.2020.12.010
6. Lolon, E., Hamidieh, K., Weijers, L., et al.: Evaluating the relationship between well parameters and production using multivariate statistical models: a middle Bakken and three forks case history in SPE Hydraulic Fracturing Technology Conference and Exhibition. SPE-179171-MS (2016). https://doi.org/10.2118/179171-MS
7. Zhao, J.Z., Chen, X.Y., Li, Y.M., et al.: Numerical simulation of multi-stage fracturing and optimization of perforation in a horizontal well. J. Pet Explor. Dev. **44**(1), 8 (2017). https://doi.org/10.11698/PED.2017.01.14
8. Zhang, F.S., Huang, L.K., Yang, L., et al.: Numerical investigation on the effect of depletion-induced stress reorientation on infill well hydraulic fracture propagation. Pet Sci. **19**(1), 296–308 (2021). https://doi.org/10.1016/j.petsci.2021.09.014
9. Dontsov, E.V., Suarez-Rivera, R.: Propagation of multiple hydraulic fractures in different regimes. Int. J. Rock Mech. Min. Sci. **128**, 104270 (2020). https://doi.org/10.1016/j.ijrmms.2020.104270
10. Wu, K., Olson, J.E.: Mechanisms of simultaneous hydraulic-fracture propagation from multiple perforation clusters in horizontal wells. SPE J. **21**, 1000–1008 (2016). https://doi.org/10.2118/178925-PA
11. Liu, L.Y., Li, Y., Wang, D.: Experimental study and effect evaluation of the migration of temporary plugging ball in horizontal wells. J. Northeast Pet. Univ. **47**, 55–66+128–129 (2023). https://doi.org/10.3969/j.issn.2095-4107.2023.06.005
12. Yuan, L., Zhou, F., Li, M., et al.: Experimental and numerical investigation on particle diverters transport during hydraulic fracturing. J. Nat. Gas Sci. Eng. **96**, 104290 (2021). https://doi.org/10.1016/j.jngse.2021.104290
13. Wang, D., Wang, X., Liu, G., et al.: A new way of staged fracturing using ball sealers. SPE Prod. Oper. **27**, 278–283 (2012). https://doi.org/10.2118/140529-PA
14. Liao, S.M., Sang, Y., Song, Y., et al.: Research and field tests of staged fracturing technology for casing deformation section in horizontal shale gas wells. Nat. Gas Ind. **37**, 40–45 (2017). https://doi.org/10.3787/j.issn.1000-0976.2017.07.006
15. Fang, Y.Y., Feng, W., Zhang, X., et al.: Experimental study on temporary plugging of perforations. Drilling Prod. Technol. **41**(6), 5 (2018). https://doi.org/10.3969/J.ISSN.1006-768X.2018.06.29
16. Lü, R.H., Liu, B., An, L.: Study on the migration and plugging laws of temporary plugging ball for divert fracturing in horizontal wells. China Pet. Mach. **48**(7), 6 (2020). https://doi.org/10.16082/j.cnki.issn.1001-4578.2020.07.019
17. Zhang, F., Rong, M., Xu, M.B.: Mechanism of temporary blocking ball's transportation and blocking in shale gas horizontal wells. Sci. Technol. Eng. **20**(6), 7 (2020). https://doi.org/10.3969/j.issn.1671-1815.2020.06.013

18. Cheng, W., Lu, C.H., Feng, G.X., et al.: Ball sealer tracking and seating of temporary plugging fracturing technology in the perforated casing of a horizontal well. Energy Explor. Exploit. **39**, 2045–2061 (2021). https://doi.org/10.1177/01445987211020414
19. Xiong C, M., Yang, S., Zhou, F.J., et al.: High efficiency reservoir stimulation based on temporary plugging and diverting for deep reservoirs. Pet Explor. Dev. **45**, 948–954 (2018). https://doi.org/10.1016/S1876-3804(18)30098-3
20. Ding, Z.R.: Engineering Fluid Mechanics, pp. 50–95. Higher Education Press (2022) ISBN: 9787040580198
21. Hertz, H.: Ueber die beruehrung fester elastische koerper (on the contact of elastic solids). J. Reine Und Angewandte Math. **92**, 156–171 (1882)
22. Mindlin, R.D., Deresiewicz, H.: Elastic spheres in contact under varying oblique forces. J. ASME. **20**, 327–344 (1953). https://doi.org/10.1007/978-1-4613-8865-4_35
23. Anderson, J.D.: Computational Fluid Dynamics the Basics with Applications, pp. 301–423. Tsinghua University Press (2002) ISBN: 9787302234876

Slot Width of Plunger Model Valve with Slot Cage Structure Influence on Cavitation Resistance Performance

Xuepan Wang[1], A. Dili[2], Zhengbai Chang[3], Ronghui Wang[1], and Jin Jang[2(✉)]

[1] BNSV Valve Co., Ltd, Tian Jing 301800, China
[2] Wuhan University, Wuhan, Hubei 430072, China
jinjiang@whu.edu.cn
[3] Lanzhou University of Technology, Lanzhou, Gansu 730050, China

Abstract. Plunger valves featuring a slot-cage structure are prone to cavitation under high-flow and high-pressure differential conditions, leading to issues such as noise, vibration, and damage to the valve. These effects can considerably degrade performance and reduce service life. This study examines the flow and cavitation characteristics of a plunger valve with a constant overflow area but varying slot widths. Numerical simulations and analyses were performed on a DN100 plunger valve with slot widths of 8 mm, 10 mm, and 12 mm. Among these configurations, the 8 mm slot-cage design has the narrowest slots and the largest number of slots for a given overflow area. As a result, the inter-slot spacing is reduced, leading to more significant fluid interaction effects. A localized low-pressure zone forms between the high-speed flow region and the cage body. This low-pressure region is most pronounced in the 8 mm slot configuration, where it is highly susceptible to cavitation. The anti-cavitation performance of the slot-cage plunger valve improves in the order of 8 mm, 10 mm, and 12 mm slot widths. Additionally, as the valve opening increases, the incipient cavitation number rises, indicating a decline in anti-cavitation capability.

Keywords: Plunger Valve · Slot-Cage Structure · Cavitation

1 Introduction

Plunger valves with a slot cage structure offer significant advantages, particularly their ability to function efficiently under large pressure differentials while maintaining stable downstream pressure. These valves deliver precise and reliable flow control, which has led to their extensive adoption across a diverse array of water conservancy and hydraulic engineering projects. Their principal role in such applications is to safeguard the secure and stable operation of specialized fluid systems. Structurally, the plunger valve is characterized by an annular, axisymmetric flow passage. This passage features a cross-sectional area that gradually contracts from the inlet section toward the throttling region. Such a design promotes hydraulically smooth fluid entry into the throttling zone, where flow rate modulation is achieved. Regulation is accomplished by mechanically driving the piston via a crank mechanism, which in turn adjusts the position of the slot cage, thereby altering the effective overflow area and controlling the passage of fluid.

© The Author(s), under exclusive license to Springer Nature Switzerland AG 2027
G. Feng et al. (Eds.): ICCE 2025, SUCI, pp. 478–490, 2027.
https://doi.org/10.1007/978-3-032-32237-1_34

In prior research, Li Yanhui, Tang Zerun, and Jiang Jin [1, 2] performed numerical simulations to investigate the internal flow characteristics of large-diameter plunger valves, providing insights into their hydrodynamic behavior. Separately, Catana I, Magheti I, and Baran G [3] systematically identified and described seven distinct stages associated with cavitation phenomena occurring in butterfly valves. Zheng Zhongliang [4] and colleagues addressed the prevalent issue of cavitation in control and regulating valves within engineering contexts. Their work involved applying large eddy simulation (LES) techniques coupled with cavitation models to compute and analyze transient flow fields in plunger valves. Pioneering efforts by Chen Xiugao and Wang Shipeng [5, 6] marked some of the earliest uses of Computational Fluid Dynamics (CFD) software for simulating the complex three-dimensional transient flow fields within plunger valves. Ulanicki [7] compiled an extensive operational dataset encompassing flow rates, pressure readings, vibration levels, and noise emissions from plunger valves under working conditions, implementing synchronous real-time monitoring. By performing linear fitting on the sound pressure level data across various operating states and identifying the intersection points of these fitted lines, the study derived critical cavitation numbers. Iyer and Ceccio [8] employed a suite of advanced experimental instrumentation, including Laser Doppler Anemometry (LDA), Particle Image Velocimetry (PIV), high-speed photography, and pulsating pressure sensors. Their investigation focused on the shear layer downstream of sharp-edged protrusions during cavitation, measuring flow velocity, pressure, vorticity, Reynolds stress, strain rate, and cavitation volume fraction. Their results demonstrated that intense flow pulsations in the downstream shear layer were directly attributable to the cyclic growth and violent collapse of cavitation bubbles. Kubota [9] utilized LDA to establish that cloud cavitation structures possess a stable nature and are composed of dense clusters of minute bubbles. Foeth [10] applied PIV to examine the development of attached cavities on hydrofoil surfaces and the subsequent shedding process of cloud cavitation, additionally proposing an adaptive method for tracking the boundaries of bubble surfaces. The foundational definition of the cavitation number relevant to valve operation was provided by C.E. Brennen [11].

In the present investigation, a comprehensive simulation study was carried out on plunger valves equipped with slot cage structures. The analysis concentrated on examining the detailed velocity and pressure field distributions associated with three distinct cage geometries across a range of valve openings. The simulation results indicate that fluid enters the valve body from the upstream section and is directed through the guiding passages of the cage. This process generates a jet flow that converges toward the central axis of the pipeline. In the vicinity of these high-velocity jets, localized regions of low pressure are formed. While the effective flow areas and overall flow rates for the different cage designs are comparable, computational analysis of the pressure fields reveals notable variations in the intensity, size, and location of the local low-pressure zones produced by each structure. This research systematically explores several key hydrodynamic aspects: the convergence behavior of fluid after it traverses the cage openings, the spatial extent and velocity magnitude of the high-speed flow regions in the immediate wake (tail stream) of the cage, and the associated risk of cavitation inception. This risk arises from the development of low-pressure zones between the high-velocity core flow and the adjacent stationary cage or pipe wall. The study culminates in an examination

of the correlation between the specific slot width dimension and the resultant cavitation resistance performance, thereby assessing the influence of geometric design on the anti-cavitation characteristics of plunger valves featuring a slot cage structure.

2 Flow Numerical Simulation of Plunger Valve with Slot Cage Structure

2.1 Numerical Simulation Model

Flow Control Equations. The two main control equations: the continuity equation and the motion equation can be combined to solve for the cavitating flow in plunger valve. This allows you to calculate. The velocity field and pressure field in the cavitating flow can be calculated and figured out. The basic continuity equation based on the law of conservation of mass can be set up:

$$\frac{\partial \rho}{\partial t} + \frac{\partial (\rho u_i)}{\partial x_i} = 0 \tag{1}$$

In which, ρ is the density of the fluid, and u is the velocity of the fluid movement. Based on the principle of conservation of momentum, Navier-Stokes equations can be mainly expressed in the following form:

$$\frac{\partial (\rho u)}{\partial t} + \mathrm{div}\left(\rho u \overrightarrow{u}\right) = -\frac{\partial p}{\partial x} + \frac{\partial \tau_{xx}}{\partial \mathrm{x}} + \frac{\partial \tau_{yx}}{\partial y} + \frac{\partial \tau_{zx}}{\partial z} + F_x \tag{2}$$

$$\frac{\partial (\rho u)}{\partial t} + \mathrm{div}\left(\rho u \overrightarrow{u}\right) = -\frac{\partial p}{\partial y} + \frac{\partial \tau_{xy}}{\partial x} + \frac{\partial \tau_{yy}}{\partial y} + \frac{\partial \tau_{zy}}{\partial z} + F_y \tag{3}$$

$$\frac{\partial (\rho u)}{\partial t} + \mathrm{div}\left(\rho u \overrightarrow{u}\right) = -\frac{\partial p}{\partial z} + \frac{\partial \tau_{xz}}{\partial x} + \frac{\partial \tau_{yz}}{\partial y} + \frac{\partial \tau_{zz}}{\partial z} + F_z \tag{4}$$

In which, p is the pressure on the infinitesimal fluid body, and τ is viscous stress. The mass conservation equation is:

$$\frac{\partial \rho}{\partial t} + \frac{\partial (\rho u)}{\partial x} + \frac{\partial (\rho v)}{\partial y} + \frac{\partial (\rho w)}{\partial z} = 0 \tag{5}$$

Turbulence Model. In the calculation of relatively complex turbulent flows, the Reynolds-averaged method is usually used to process the governing equations, i.e. the Reynolds-averaged Navier-Stokes (RANS) equations [5]. The more accurate calculations can only achieve using Reynolds-averaged model when the turbulence model is applicable to the actual flow. The cavitation performance of plunger valve with slotted cage structure is studied in this paper. The fluid flow state inside the valve body is turbulent flow. Currently, a variety of turbulence models are used in simulation calculations. For the simulation calculation of plunger valve with slotted cage structure in this paper, the Realizable k-ε turbulence model is selected.

The Control Equations for Gas-Liquid Two-Phase Flow. The models like Mixture, VOF, and Eulerian of FLUENT are commonly used in simulating multiphase flow. The VOF model is mainly used for calculating stratified flow and the movement of large bubbles in liquids and the Eulerian model is used for calculating particles that float and suspend in the flow and more complex multiple-phase flow. For this simulation of the slot cage structure of plunger valve, the Mixture model is selected to used. Its control equation is:

$$\vec{v}_m = \frac{\sum_t^n \alpha_t \rho_t \vec{v}_t}{\rho_m} \tag{6}$$

In which, ρ_m is the mixed density; t represents the phase number; α_t is the volume fraction of the t-phase; ρ_t is the density of the t-phase; and $\vec{v}_t$ is the velocity of the t-phase.

The mass conservation equation for gas-liquid mixtures is:

$$\frac{\partial}{\partial t}\rho_m + \nabla\left(\rho_m \vec{v}_m\right) = 0 \tag{7}$$

The mixed viscosity is:

$$\mu_m = \sum_{t=1}^{n} \alpha_t \mu_t \tag{8}$$

The driving velocity of t-phase is:

$$\vec{v}_{dr,t} = \vec{v}_t - \vec{v}_m \tag{9}$$

The momentum conservation equation for gas-liquid mixtures is:

$$\frac{\partial}{\partial t}\left(\rho_m \vec{v}_m\right) + \nabla\left(\rho_m \vec{v}_m \vec{v}_m\right) = -\nabla P + \nabla\left[\mu_m\left(\nabla \vec{v}_m + \vec{v}_m^T\right)\right] + \rho_m \vec{g} + \vec{F} + \nabla\left(\sum_{t=1}^{n} \alpha_t \rho_t \vec{v}_{dr,t} \vec{v}_{dr,t}\right) \tag{10}$$

The energy of the t-phase is:

$$E_t = h_t - \frac{p}{\rho_t} + \frac{v_t^2}{2} \tag{11}$$

The energy conservation equation for gas-liquid mixtures is:

$$\frac{\partial}{\partial t}\sum_{t=1}^{n}(\alpha_t \rho_t E_t) + \nabla\sum_{t=1}^{n}\left[\alpha_t \vec{v_t}(\rho_t E_t + p)\right] = \nabla\cdot\left(k_{eff}\nabla T\right) + S_E \tag{12}$$

In which, k_{eff} indicates the effective thermal conductivity; S_E represents other volumetric heat sources.

ρ_v represents the density of water vapor in the fluid; ρ_l indicates the density of water; e is the local turbulent kinetic energy; p_v shows the saturation vapor pressure at a certain temperature; f_g and f_v represent the mass fraction of air and water vapor in the fluid; σ denotes the surface tension of the fluid.

2.2 Physical Model

Model Establishment. This study presents a detailed investigation into the cavitation and internal flow characteristics of a DN100 plunger valve incorporating a slot cage structure. The primary objective is to analyze how the specific design of this valve type influences flow dynamics and susceptibility to cavitation under varying operational conditions. The main components constituting the plunger valve assembly include the valve body, the central slot cage piston, the valve shaft, and the crank connecting rod mechanism. Utilizing the 3D modeling software SOLIDWORKS, a precise digital model of each individual component is created. These models are then virtually assembled to form a complete and accurate geometric representation of the entire valve system. The opening degree of the valve is regulated by axially driving the slot cage piston via the crank connecting rod. This axial motion effectively changes the exposed flow area of the throttle slots within the surrounding cage sleeve, thereby controlling the fluid passage.

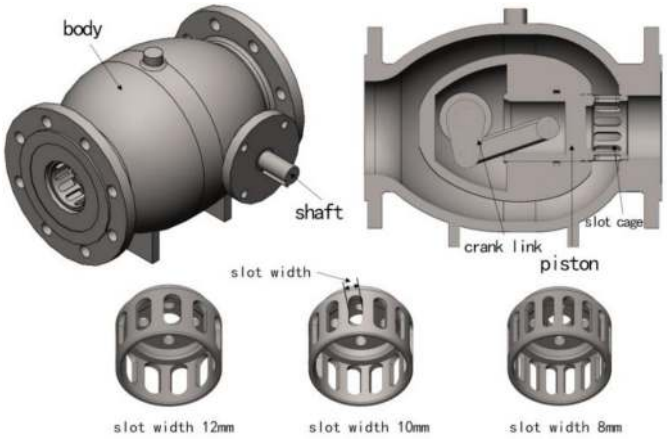

Fig. 1. Physical model of plunger valve with slot cage structure.

The cavitation and flow characteristics are primarily examined through computational fluid dynamics (CFD) simulation and subsequent detailed flow field analysis. To ensure the reliability and accuracy of the simulation results, and to align them with established experimental model standards, the computational fluid domain is carefully prepared. The fluid domain extracted from the internal passages of the valve is extended both upstream and downstream to eliminate any potential boundary effects and to allow for full flow development. Specifically, the upstream pipeline section is extended by 400 mm, which is equivalent to four times the nominal diameter (4D) of the DN100 plunger valve. Similarly, the downstream pipeline is extended by 600 mm, or six times the valve diameter (6D). These extensions help stabilize the inflow and outflow conditions in the simulation. The final computational fluid domain models for the plunger valve with slot cage structures, featuring three distinct slot widths of 8 mm, 10 mm, and 12 mm for comparative analysis, are illustrated in Fig. 1.

Mesh Dividing. The focus of this study is on the cavitation performance in the local low-pressure area of the plunger valve. Cavitation is more likely to occur at the end of the overflow and at the contact point between the cage and the downstream pipeline. As a result, the grid density near the walls of the entire model is increased. To obtain more accurate calculations and improve computational efficiency, grid independence verification is first performed to determine the optimal number of grid cells for the simulation.

For the grid independence verification, a model with a slot width of 10 mm at 100% valve opening is selected. The upstream pressure is set to 120,000 Pa, and the downstream pressure to 20,000 Pa, which serve as boundary conditions. Five sets of numerical simulations are conducted with varying mesh densities, and the simulation results corresponding to different mesh configurations, after stabilization, are presented in Table 1. The formula used to calculate the relative rate of change in outlet flow velocity based on the simulation results is as follows:

$$\beta = \left| \frac{v_{i+1} - v_i}{v_i} \right| \times 100\% \tag{13}$$

In Table 1, when the number of grids exceeds 2,586,600, the relative change rate of velocity is less than 0.1%. This indicates that grid numbers above this threshold provide high accuracy. Therefore, the final mesh count selected for the simulation is 4,886,800.

Table 1. Mesh independent analysis.

Mesh Number /10000	Absolute Pressure at Inlet /Pa	Absolute Pressure at Outlet /Pa	Velocity at outlet /(m/s)	Relative change rate in velocity /%
182.42	120000	20000	0.92637	/
258.66	120000	20000	0.92756	0.136
376.73	120000	20000	0.92812	0.061
488.68	120000	20000	0.92835	0.024
542.37	120000	20000	0.92847	0.013

2.3 Simulation Analysis of Plunger Valve with Slot Cage Structure

In the numerical simulation of the piston regulator valve featuring a groove cage structure, a comprehensive set of parameters was selected to systematically evaluate its performance. Specifically, three distinct slot widths of 8 mm, 10 mm, and 12 mm were modeled to investigate the influence of geometric variation. For each slot width, the valve was analyzed under three critical opening conditions: 100% (fully open), 50% (partially open), and 20% (near-closed), representing a broad spectrum of operational states. Corresponding boundary conditions were carefully defined to reflect realistic pressure differentials. For the 100% opening condition, the inlet upstream pressure was

set at 175 kPa with a downstream pressure maintained at 10 kPa. Under the 50% opening, the upstream pressure was increased to 210 kPa while the downstream pressure remained constant at 10 kPa. Finally, for the most restrictive 20% opening, a higher upstream pressure of 350 kPa was applied against the same 10 kPa downstream pressure, creating a significant pressure drop across the valve to simulate demanding throttling scenarios. The fluid flow fields for each valve configuration were then rigorously analyzed. This involved generating detailed pressure and velocity contour cloud diagrams to visualize spatial distributions and identify key hydrodynamic features. Furthermore, to quantitatively and qualitatively assess the severity and extent of cavitation, the simulation outputs were processed to produce gas volume fraction contour clouds. These clouds explicitly illustrate regions where the local pressure falls below the fluid's vapor pressure, thereby enabling a direct comparison of cavitation intensity for each groove width structure under the various opening and pressure conditions.

Simulation Analysis of Slot Widths (8 mm, 10 mm, 12 mm) at 100% Opening. The simulation results for 100% opening of the plunger valve with slot widths of 8 mm, 10 mm, and 12 mm were analyzed. The upstream pressure was set to 175 kPa, and the downstream pressure was 10 kPa. The velocity and pressure cloud diagrams for each slot width (8 mm, 10 mm, and 12 mm) are shown in Fig. 2.

From the diagrams, it is evident that the internal fluid velocity distribution for the plunger valve with all three slot cage structures is nearly identical at 100% opening. The fluid enters the valve body from the upstream side and passes through the valve body, where it is diverted through the slot cage. This causes a jet convergence at the center of the valve, creating a high-velocity zone near the downstream overflow path of the slot cage. A low-velocity area forms near the front end of the slot cage.

The overflow areas of the three slot cage structures are essentially the same, resulting in a similar flow velocity through the plunger valve. However, there are slight differences in the low-flow velocity areas across the three structures, as observed in the velocity cloud diagrams. When the slot width of the slot cage structure is the smallest, the number of slots is the largest.

Additionally, it is observed that the high-velocity area decreases in size as the slot width increases (from 8 mm to 12 mm), and the low-velocity area near the pipe wall behind the valve also decreases correspondingly. Specifically, the slot cage structure with a slot width of 8 mm has a relatively larger low-velocity area near the end of the slot cage, where it is close to the wall of the pipeline.

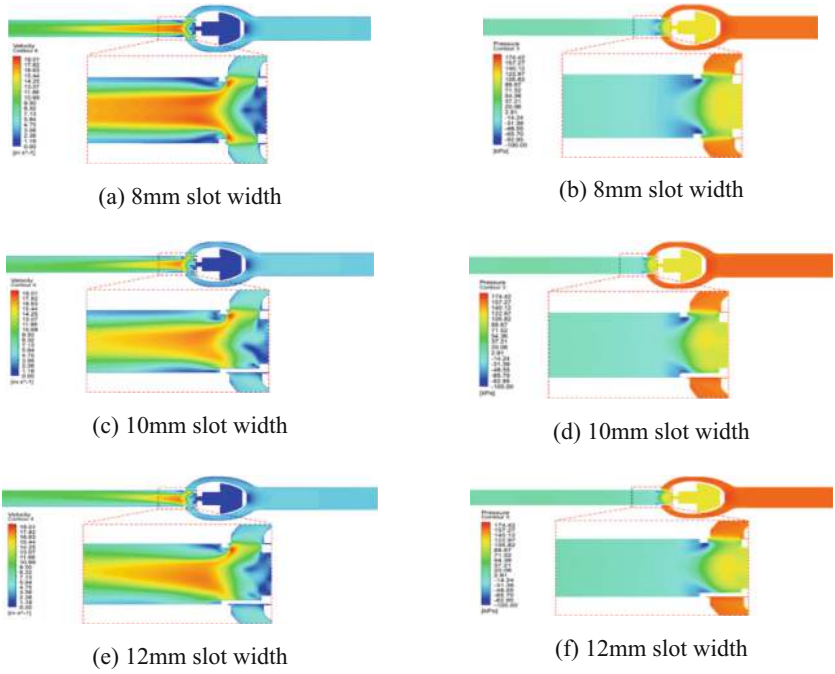

(a) 8mm slot width (b) 8mm slot width

(c) 10mm slot width (d) 10mm slot width

(e) 12mm slot width (f) 12mm slot width

Fig. 2. 100% opening velocity cloud and pressure cloud of slot cage with different structures.

Figure 2 illustrates the pressure cloud diagram of the squirrel cage structure piston flow control valve with groove widths of 8 mm, 10 mm, and 12 mm under the condition of 100% opening, with an upstream pressure of 175 kPa and a downstream pressure of 10 kPa. When combined with the 100% opening velocity cloud diagram, the fluid enters the valve body from the upstream side and passes through the valve, forming a jet convergence at the center of the pipeline through the squirrel cage overflow groove. As a result, a high-speed flow area is established near the downstream end of the overflow trough, while a localized low-pressure area forms adjacent to the high-speed jet, particularly near the end of the squirrel cage close to the pipeline wall.

The figure demonstrates that the low-pressure area of the piston cage structure with an 8 mm groove width is the most significant, while the low-pressure area of the piston cage structure with a 12 mm groove width is the least pronounced. This localized low-pressure zone promotes the rapid formation of bubbles in the fluid, leading to more severe cavitation in the piston flow control valve with an 8 mm groove width.

Simulation Analysis of 8 mm, 10 mm and 12 mm Slot Widths at 50% Opening. The simulation results for a 50% opening of the plunger valve with slot widths of 8 mm, 10 mm, and 12 mm are analyzed. The boundary conditions used for the simulation are an upstream pressure of 210 kPa and a downstream pressure of 10 kPa. The velocity and pressure cloud diagrams of the piston flow control valve featuring a squirrel cage structure with groove widths of 8 mm, 10 mm, and 12 mm are presented in Fig. 3.

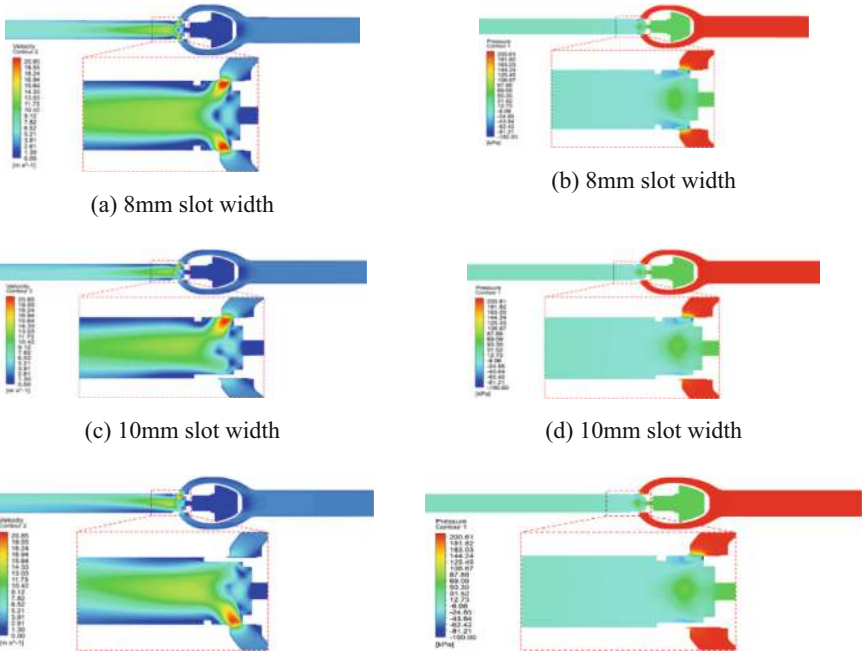

(a) 8mm slot width (b) 8mm slot width

(c) 10mm slot width (d) 10mm slot width

(e) 12mm slot width (f) 12mm slot width

Fig. 3. 50% opening velocity cloud and pressure cloud of different structures of slot cage.

From Fig. 3, it is evident that the internal fluid velocity distribution across the three slot cage structures is fundamentally similar at 50% opening. The fluid enters the valve body from the upstream side and passes through, forming a jet convergence at the center of the pipeline. Unlike the 100% opening scenario, the 50% opening overflow slot is closer to the slot path, which results in a relatively larger high-speed flow area. Additionally, along the longitudinal direction of the slot, the flow at 50% opening is more uniform compared to the 100% opening, with the velocity appearing more stable and higher overall.

A low-flow area is generated at the end of the slot cage (non-overflow notch), and a relatively smaller low-flow area is also created at the end of the overflow slot. Although the internal fluid velocity distribution across the three structures remains fundamentally similar to that of the 100% opening, there are noticeable differences in the low-flow velocity areas indicated by the velocity cloud diagram. From the figure, it can be observed that the high-velocity flow areas for slot widths of 8 mm, 10 mm, and 12 mm decrease sequentially, leading to a relatively larger low-velocity flow area near the end of the slot cage for the 8 mm slot width.

Figure 3 illustrates the pressure cloud diagram for slot widths of 8 mm, 10 mm, and 12 mm at 50% opening, with upstream pressure set at 210 kPa and downstream pressure at 10 kPa. In the velocity cloud diagram at 50% opening, the fluid enters the valve body from the upstream flow, passing through and forming a jet convergence at the center of

the pipeline. As the fluid flows through the slot cage, the overflow area at 50% opening becomes smaller, resulting in a relatively larger jet area.

In the adjacent region of the high-velocity jet, near the downstream end of the slot cage overflow, a local low-pressure area is formed. This low-pressure area increases in size as the flow continues. From the figure, it is observed that the low-pressure area for the 8 mm slot width is the largest, while the 12 mm slot width exhibits the smallest low-pressure area. The presence of this local low-pressure area promotes the rapid growth of bubbles in the water, leading to more severe cavitation in the plunger valve with the 8 mm slot width.

Simulation Analysis of 20% Opening for 8 mm, 10 mm, and 12 mm Slot Widths. The simulation results for a 20% opening of the plunger valve with slot widths of 8 mm, 10 mm, and 12 mm are analyzed under continuous cavitation conditions. For this simulation, upstream pressure is set to 350 kPa and downstream pressure to 10 kPa. The velocity cloud and pressure cloud diagrams for the plunger valve with 8 mm, 10 mm, and 12 mm slot widths are shown in Fig. 4.

At 20% opening, the internal fluid velocity distribution for the three slot cage structures is fundamentally similar. The overflow area is considerably small, resulting in a low overall flow rate. The flow convergence effect is reduced, and the fluid passes through the narrow slots, creating a high-speed jet. As a result, a low-flow area emerges adjacent to the high-speed jet, specifically at the end of the slot cage near the slot and the piston.

Although the internal fluid velocity distribution for the three slot structures remains similar, differences are evident in the low-flow velocity regions in the velocity cloud diagram. The slot cage with an 8 mm slot width has the smallest slots, resulting in a larger number of slots with minimal distance between the flow paths of each slot. Figure 4 illustrates the pressure cloud diagram of the slot cage structures with 8 mm, 10 mm, and 12 mm slot widths under the 20% opening condition (upstream pressure 350 kPa and downstream pressure 10 kPa). In this diagram, the low-pressure area for the 8 mm slot width is the largest, while the 12 mm slot width has the smallest low-pressure area.

This local low-pressure area promotes the rapid growth of bubbles in the fluid, leading to more severe cavitation in the valve with the 8 mm slot width.

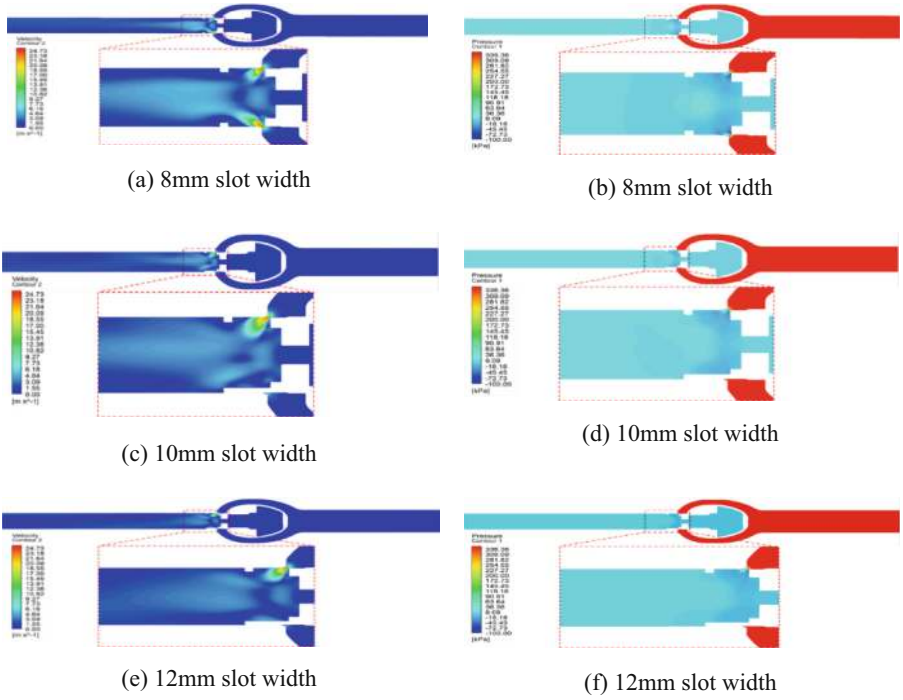

(a) 8mm slot width (b) 8mm slot width

(c) 10mm slot width (d) 10mm slot width

(e) 12mm slot width (f) 12mm slot width

Fig. 4. 50% opening velocity cloud and pressure cloud of different slot cage structures.

3 Influence of Slot Width on the Flow Field of Plunger Valve

This study simulates the flow fields of the plunger valve with slot cage structures, examining 100%, 50%, and 20% openings for slot widths of 8 mm, 10 mm, and 12 mm. By analyzing the velocity and pressure cloud diagrams, the flow field in the valve body of the three slot cage structures is compared under different conditions. The valve structure inherently creates a local low-pressure area near the high-speed jet. The overflow areas of the three cage structures are nearly identical, resulting in similar flow rates through the flow control valve. However, the pressure cloud diagrams reveal distinct differences in the local low-pressure areas generated by the three slot widths.

The 8 mm slot width, being the smallest, results in the largest number of slots for the same overflow area. With minimal distance between the slots, the fluid convergence effect is optimized as it passes through the slot cage. To analyze the impact of slot width on the internal flow field of the valve body, the velocity and pressure cloud diagrams of the YZ plane at the end of the slot cage are intercepted. These are then compared with the corresponding diagrams at 100% opening. The velocity and pressure cloud diagrams for the three structures in the YZ plane at the end of the slot cage are shown in Fig. 5.

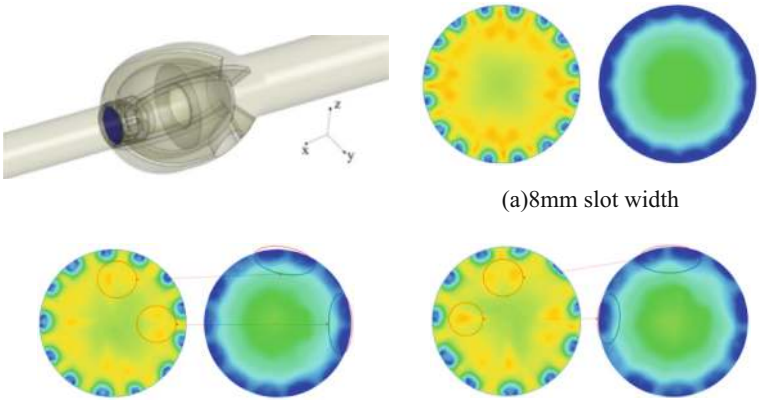

(a)8mm slot width

(b)10mm slot width (c)12mm slot width

Fig. 5. Velocity cloud and pressure cloud of the three slot structures at 100% opening.

As shown in Fig. 6, the fluid convergence effect of the slot cage structure with a slot width of 8 mm is the most pronounced. In this case, the high-velocity flow area forms a near-circular shape in the YZ plane. However, as the slot width increases, the high-velocity flow area becomes more dispersed. Additionally, a local low-pressure area is observed between the high-velocity flow region and the valve outlet wall, indicating that the low-pressure zone created by the 8 mm slot width is more likely to induce cavitation. This observation aligns with our previous experimental conclusions, which suggest that the cavitation resistance of the plunger valve improves with groove widths of 8 mm, 10 mm, and 12 mm.

Figure 6 illustrates the isosurface diagram of the gas phase volume fraction at 10% for the slot cage structure with slot widths of 8 mm, 10 mm, and 12 mm at 100% opening.

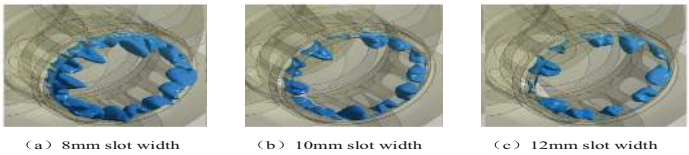

Fig. 6. Isosurface of the gas phase volume coefficient of 10% at 100% opening of three rat cage structures.

4 Conclusion

This study simulated the flow characteristics of a plunger valve with slot widths of 8 mm, 10 mm, and 12 mm under openings of 100%, 50%, and 20%. Corresponding pressure differentials were applied for each opening. Analysis of pressure, velocity, and gas content cloud diagrams revealed that a smaller slot width (e.g., 8 mm) results in more slots and narrower spacing, enhancing flow convergence but also causing more

pronounced local low-pressure zones near high-velocity jets. These low-pressure regions increase cavitation risk.

Comparative results show that anti-cavitation performance improves as slot width increases, with the 12 mm slot exhibiting the best resistance to cavitation, followed by 10 mm and 8 mm. It is recommended to increase slot width appropriately within design requirements to enhance cavitation resistance. Additionally, operating at smaller openings helps suppress cavitation under stable pressure conditions.

This study focused on a DN100 valve with slot widths between 8–12 mm and an overflow area of 60%. Further research is needed to evaluate valves with smaller or larger slot geometries and different sizes, as well as to predict cavitation numbers across various valve dimensions.

References

1. Li, Y.H., Liao, Z.F., Jiang, J.: Flow characteristics analysis of large-diameter flow and pressure regulating valve with piston sleeve. Hydraul. Eng. **50**(4), 516–523 (2019). https://doi.org/10.13243/j.cnki.slxb.20180950
2. Tang, Z.R., Wang, J.X., Jiang, J., et al.: An analysis of flow characteristics of flow and pressure regulating valve with piston sleeves. China Rural Water Hydropower. **3**, 148–152 (2021). https://doi.org/10.3969/j.issn.1007-2284.2021.03.029
3. Catana, I., Magheti, I., Baran, G.: Controlling the cavitation phenomenon of evolution on a butterfly valve. Iop Conference. **12**, 012100 (2010). https://doi.org/10.1088/1755-1315/12/1/012100
4. Zheng, Z.L., Chen, X.G., Tan, S.Y., et al.: Numerical prediction and analysis on cavitation noise of control valve based on fluid-acoustic coupling method. Xihua Univ. (Nat. Sci. Ed.). **37**(6), 42–47 (2018). https://doi.org/10.3969/j.issn.1673-159X.2018.06.008
5. Chen, X.G., Zhang, X.H., Wang, S.P., et al.: Numerical analysis of cavitation noise of control valves. Noise Vib. Control. **38**(6), 52–57 (2018). https://doi.org/10.3969/j.issn.1006-1355.2018.06.010
6. Wang, S.P.: Numerical simulation of control valve cavitation and noise. Dissertation Msc, Lanzhou: Lanzhou University of Technology (2018)
7. Picinali, L., Janus, T., Ulanicki, B.: Measurements and analysis of cavitation in a pressure reducing valve during operation – a case study. Procedia Eng. **119**, 270–279 (2015). https://doi.org/10.1016/j.proeng.2015.08.886
8. Ceccio, S.L., Iyer, C.O.: The influence of developed cavitation on the flow of a turbulent shear layer. Phys. Fluids. **14**(10), 3414–3431 (2002). https://doi.org/10.1063/1.1501541
9. Kubota, A., Kato, H., Yamaguchi, H., et al.: Unsteady structure measurement of cloud cavitation on a foil section using conditional sampling tech. ASME J. Fluid Eng. **111**(2), 204 (1989). https://doi.org/10.1115/1.3243624
10. Van Doorne, C.W., Foeth, E.J.: Time resolved piv and flow visualization of 3d sheet cavitation. Exp. Fluids. **40**(4), 503–513 (2006). https://doi.org/10.1007/s00348-005-0082-9
11. Brennen, C.E.: Fission of collapsing cavitation bubbles. J. Fluid Mech. **472**, 153–166 (2002). https://doi.org/10.1017/S0022112002002268

Study on the Temperature Field Change of Frozen Soil Subgrade Treated with Foamed Mixture Soil

Qiang Tang[1], Xintong Song[2(✉)], Yuanxiang Wang[3], Qindong Li[2], and Yin Cheng[2]

[1] Xinjiang Road and Bridge Construction Group Co., Ltd., Urumqi 830000, China
[2] Engineering Technology and Materials Research Center, China Academy of Transportation Science, Beijing 100029, China
17801123657@163.com
[3] Xinjiang Jiaotou Duku Expressway Investment Development Co., Ltd., Urumqi 830000, China

Abstract. To investigate the effect of foamed mixture soil subgrade on the temperature field change of frozen soil foundation in the perennial permafrost area, the time-varying law, monthly average temperature and temperature decreasing rate distribution in all depths are studied based on the long-term temperature monitoring data of a highway in Xinjiang. The treatment effect of frozen soil foundation with foamed mixture soil are further analyzed. The results show that: the time-varying law of temperature within the road structure is consistent with the change of atmospheric temperature, and there is an obvious time delay. While the depth enhances, the change range of temperature declines, the time delay becomes more obvious. Comparing with the original subgrade, the foamed mixture soil subgrade is conducive to weakening the permafrost foundation temperature affected by the change of atmospheric temperature. This phenomenon can be specifically proven by the smaller temperature decreasing rate in summer, which indicates that the heat in foamed mixture soil subgrade is consumed more. While in winter, the temperature decreasing rate of the subgrade is more than that of the original subgrade, and at this time, the foamed mixture soil subgrade can effectively block heat conduction. Besides, the analysis of the temperature field of its road structure shows that the isotherms of the pavement layer are dense, indicating a wide range of temperature distribution and large variation, while the isotherms of the subgrade and frozen soil subgrade are sparse, indicating small temperature changes and uniform distribution.

Keywords: Frozen Soil · Foamed Mixture Soil · Temperature Field · On-Site Monitoring · Data Analysis

1 Introduction

Permafrost is a mixture of minerals, organic matter and water, in which the presence of water makes it very sensitive to temperature changes [1]. The rising temperature will cause the melting of the solidified water in permafrost, lead to the decrease of the

© The Author(s), under exclusive license to Springer Nature Switzerland AG 2027
G. Feng et al. (Eds.): ICCE 2025, SUCI, pp. 491–503, 2027.
https://doi.org/10.1007/978-3-032-32237-1_35

bearing capacity of permafrost, and even cause the heat thaw subsidence, subgrade slurry, landslide and other diseases [2–4]. China is the third largest permafrost distribution country in the world, the area of permafrost region accounts for 70% of the total area of the country. At present, the treatment of subgrade in permafrost region mainly adopts the method of keeping freezing, i.e., permafrost subgrade is kept frozen in the construction process and the whole period of operation [5].

Temperature is the main index to determine whether the frozen subgrade is stable or not, and a large number of scholars evaluate the stability of subgrade by simulating the change of temperature field of subgrade in permafrost area [6–11]. Fu et al. [9] studied the change of temperature field in different permafrost conditions and engineering measures. The analysis results showed that after constructing the subgrade in the high-latitude perennial permafrost area, it would cause the upper limit of perennial permafrost to move down significantly, thus formed a thicker weak layer under the subgrade, which in turn triggered the subsidence of the subgrade. And gravel or block stone could be used to alleviate the deformation of the subgrade due to the subsidence of the lower layer soil. Based on the long-term foundation temperature data, Fan et al. [10] analysed the mechanism of the long-term behaviour of the low- temperature perennial permafrost. Their results showed that the foundation temperature increase at the foot of the subgrade slope was small due to the cooling effect of the block subgrade, and showed an asymmetric warming trend between the cold season and the warm season. Based on ABAQUS finite element software, Zhang and Jiang [11] analysed the temperature field of airport runway foundation without heat insulation layer, with XPS material heat insulation layer and EPS material heat insulation layer comparatively. The results showed that the outside temperature had drastically influence on the depth of 0~8 m foundation temperature. In the depth of 10m or deeper, the outside temperature had no effect on the foundation temperature. According to the runway foundation maximum melting depth, runway paved with XPS material heat insulation layer was the smallest, and the runway without heat insulation layer was the biggest. It can be seen that thermal insulation materials are beneficial to improve the thermal stability of frozen soil foundations.

In recent years, great attention has been paid to the use of new thermal insulation materials as a kind of thermal insulation method for projects in permafrost areas. The foamed mixture soil is a commonly used material, which is made of cement and/or other cementitious materials, water, raw materials, soil and stabilized foamed group in a certain proportion. Foamed mixture soil has the good properties of low thermal conductivity, good thermal insulation, lightweight, high strength and other characteristics [12]. Lin et al. [13] indicated that foamed mixture soil was able to prevent seasons freezing of the highway and the thawing and sinking of the permafrost foundations relying on a test section of a primary highway in the north of China. He analysed the temperature field of foamed concrete insulation subgrade using ABAQUS finite element simulation, and concluded that the freezing range decreased with the increasing thickness of foamed concrete insulation layer in pavement. Li and Cheng [14] used ABAQUS finite element analysis software to establish the temperature field model of foamed concrete insulation subgrade, and studied the thermal insulation effect of foamed concrete insulation layer on the railway subgrade in seasonal permafrost area. Simulation results showed that foamed concrete had obvious thermal insulation effect. When the laying length of the

insulation layer extended from the shoulder to 4.0m, the thermal insulation effect was the best.

The above research proves the thermal insulation effect of foamed mixture soil subgrade on permafrost foundation based on the change law of subgrade temperature field. Although the research results of the thermal condition of subgrade structure in permafrost area provides a lot of information, but most of these studies are based on short-term data or numerical modelling simulation. And there are still fewer studies related to the change of the temperature field of the subgrade in permafrost area under the state of long-term operation, and the long-term thermal insulation effect of foamed mixture soil subgrade is not clear. This study is based on a foamed mixture soli subgrade construction project in Xinjiang permafrost area. The long-term temperature monitoring data of the road is obtained through the buried sensors. The temperature field and the varying law of the temperature are analysed and explored within different foamed mixture soil subgrades. The research results provide scientific basis and guidance for the maintenance and reinforcement of subgrade in permafrost areas.

2 Methodology

2.1 Overview of Monitoring Area

The on-site monitoring was carried out on the basis of a highway construction project in Xinjiang, which was located at an altitude of 5600–5700 m, and was a section of ice-saturated permafrost foundation, with a freezing depth of 1.0 m. The hot thawing and sliding phenomenon had already appeared, i.e., under the action of permafrost thawing and snowmelt, the sliding material was often in the form of "rheoplastic", sliding to the foot of the slope and pavement and the road surface (Fig. 1).

Fig. 1. Original road condition of the project section.

In order to solve this problem, different thicknesses of foamed mixture soil insulation subgrade were constructed on site. Monitoring components were buried to monitor the internal temperature field distribution of the road structure, and the effect of foamed mixture soil treatment on permafrost foundation was evaluated by comparing and analysing the temperature field with that of the original subgrade.

2.2 Monitoring Equipment Deployment

In addition to the control section featuring the original subgrade structure (K36+515, comprised of a conventional asphalt pavement over a schist subgrade), a series of dedicated on-site test sections were constructed to evaluate the thermal performance of foamed mixture soil as an engineered fill material. These test sections, situated at chainages K36+845, K36+525, K37+095, and K36+710, were each filled with a distinct thickness of foamed mixture soil. The designed thicknesses for these sections were 60 cm, 90 cm, 120 cm, and 150 cm, respectively, allowing for a systematic investigation into the influence of insulation layer thickness on the subgrade's thermal regime.

To provide a detailed examination, the road structure at the test section with a 120 cm thickness of foamed mixture soil (K37+095) is described as a representative example. Its structural profile, from top to bottom, consisted of a 5 cm asphalt surface layer, underlain by a 25 cm base course, followed by a 30 cm subbase layer, and finally the 120 cm core layer of foamed mixture soil subgrade resting upon the natural foundation. To meticulously investigate the law governing temperature variation throughout this multi-layered road structure, a comprehensive array of temperature sensors was strategically deployed at critical interfaces and within key layers. Sensor positions included the interface between the asphalt surface layer and the base course, the interface between the base course and the subbase, the interface between the subbase and the foamed mixture soil subgrade, at a point within the interior of the foamed mixture soil subgrade layer, at the critical interface between the bottom of the subgrade and the top of the underlying frozen soil foundation, and finally, at a designated depth within the interior of the frozen soil foundation. To ensure continuous and reliable data collection across the entire test site, an automated acquisition system equipped with wireless transmission capability was employed, enabling real-time remote monitoring. The specific spatial arrangement and precise locations of all these sensors within the roadbed cross-section are graphically detailed in Fig. 2.

2.3 Data Analysis Methods

Calculation of Average Temperature. For analyzing the temperature field of the foamed mixture soil subgrade, the monthly average temperature data over a 12-month period from May 2023 to April 2024 are selected. The monthly average temperature at various subgrade depths is calculated by summing the daily temperatures for each day of the month and then dividing the total by the number of days in that month. This set of monthly average values across different depths provides a basis for examining the distribution and variation characteristics of internal subgrade temperatures with seasonal changes and depth. The analysis aims to evaluate the thermal stability and long-term performance of foamed mixture soil as a subgrade material.

Calculation of Temperature Decreasing Rate. To provide a clearer and more intuitive visualization of how temperature varies with depth across each structural layer of the road, a quantitative measure of the temperature decrease rate is calculated. Specifically, the temperature difference between two adjacent structural layers is determined, and this value is then divided by the corresponding difference in depth between those layers. This calculation yields the rate at which temperature declines per unit depth, effectively

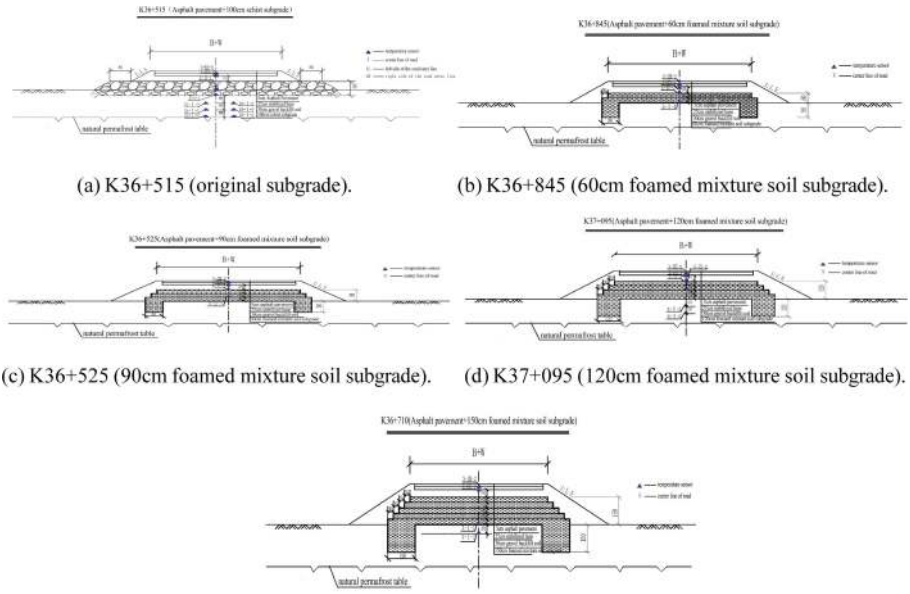

(a) K36+515 (original subgrade). (b) K36+845 (60cm foamed mixture soil subgrade).

(c) K36+525 (90cm foamed mixture soil subgrade). (d) K37+095 (120cm foamed mixture soil subgrade).

(e) K36+710 (150cm foamed mixture soil subgrade).

Fig. 2. Layout of monitoring section sensors.

representing the thermal gradient within the road structure. This approach allows for a precise, layer-by-layer analysis of the temperature reduction trend, facilitating direct comparison between different material sections and helping to identify zones where insulation or thermal properties change significantly.

Drawing of Subgrade Temperature Field. The temperature field of the foamed mixture soil subgrade is visualized and analyzed using Origin software. Through this software, detailed two-dimensional graphical representations of the subgrade's thermal distribution at various depths and over time are generated. By systematically adjusting the relevant computational and graphical parameters, the annual evolution of the temperature field across all seasons can be clearly depicted. The resulting comprehensive visualizations effectively capture the dynamic spatial and temporal variations in temperature throughout the entire year, enabling a thorough examination of the material's thermal behavior and providing critical insights into its insulating properties under changing environmental conditions.

3 Time-Varying Law of Temperature

The temperature at different depths is taken for monthly homogenization, and the annual temperature variation law can be obtained, as shown in Fig. 3. The temperature change at different depths is consistent with the variation of atmospheric temperature. The highest temperature occurs from August to October, and the lowest temperature occurs from

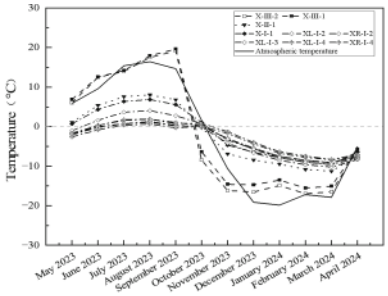

(a) K36+515 (original subgrade)

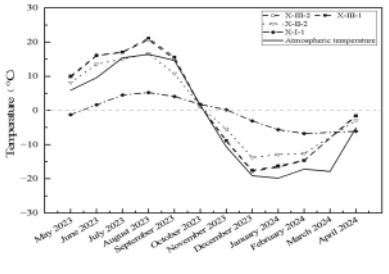

(b) K36+845 (60cm foamed mixture soil subgrade)

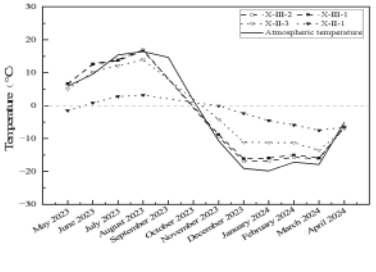

(c) K36+525 (90cm foamed mixture soil subgrade)

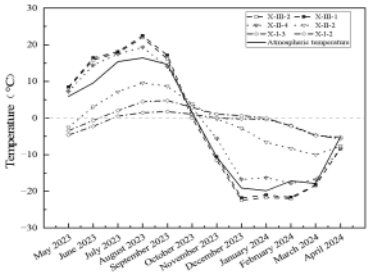

(d) K37+095 (120cm foamed mixture soil subgrade).

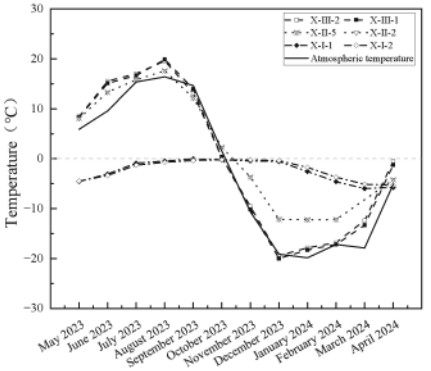

(e) K36+710 (150cm foamed mixture soil subgrade)

Fig. 3. Temperature variation curve of road structure throughout one year.

December to April. Furthermore, the amplitude of temperature change is not uniform throughout the layered structure. The road surface experiences the most pronounced and immediate temperature fluctuations, directly exposed to ambient conditions. The subgrade layer beneath it shows a moderated but still significant thermal response. In contrast, the deeper frozen soil foundation exhibits a notably gentler temperature variation, and its thermal response is characterized by a distinct temporal delay relative to

surface changes. Compared with the original subgrade, the foamed mixture soil subgrade demonstrates a beneficial insulating effect. It actively weakens the transmission and influence of atmospheric temperature changes on the underlying permafrost foundation. Moreover, the analysis confirms a direct relationship between the thickness of the foamed mixture soil layer and its mitigating effect: a larger thickness corresponds to a measurably smaller temperature fluctuation within the protected foundation layers, thereby enhancing long-term thermal stability.

In order to further investigate the influence of different subgrade thickness on the frozen soil foundation temperature, the monthly average temperature of the frozen soil foundation is selected to explore the change rule with time, as shown in Fig. 4.

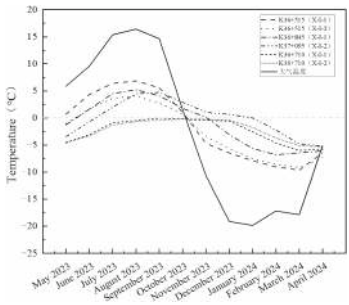

Fig. 4. Time-varying temperature curve of frozen soil foundation.

As demonstrated by the observational data, the annual temperature variation of the frozen soil foundation is confined to a range between a maximum of approximately 6.86 °C and a minimum of around −9.63 °C. This quantified thermal regime clearly indicates the active layer's dynamic response to seasonal climatic cycles. A primary factor influencing this thermal behavior is the thickness of the overlying foamed mixture soil subgrade, which exerts a significant controlling effect on the magnitude of temperature fluctuation experienced at the foundation level. The analysis reveals a distinct inverse relationship. As the thickness of the insulating foamed mixture soil layer increases, the corresponding amplitude of temperature change within the underlying frozen foundation becomes progressively smaller. Furthermore, the depth within the frozen foundation is a crucial determinant of its thermal stability. The data indicates that when the depth of measurement or observation reaches 0.5 m or greater below the interface, the temperature of the frozen foundation can be consistently maintained below the freezing point of 0 °C. This ensures the preserved frozen state of the soil, which is vital for the structural integrity of the roadway in permafrost regions. Therefore, the synergistic combination of a sufficiently thick foamed mixture soil subgrade and an adequate depth into the foundation works to create a stable thermal environment, effectively decoupling the sensitive frozen ground from the more extreme temperature variations at the surface and within the upper pavement layers.

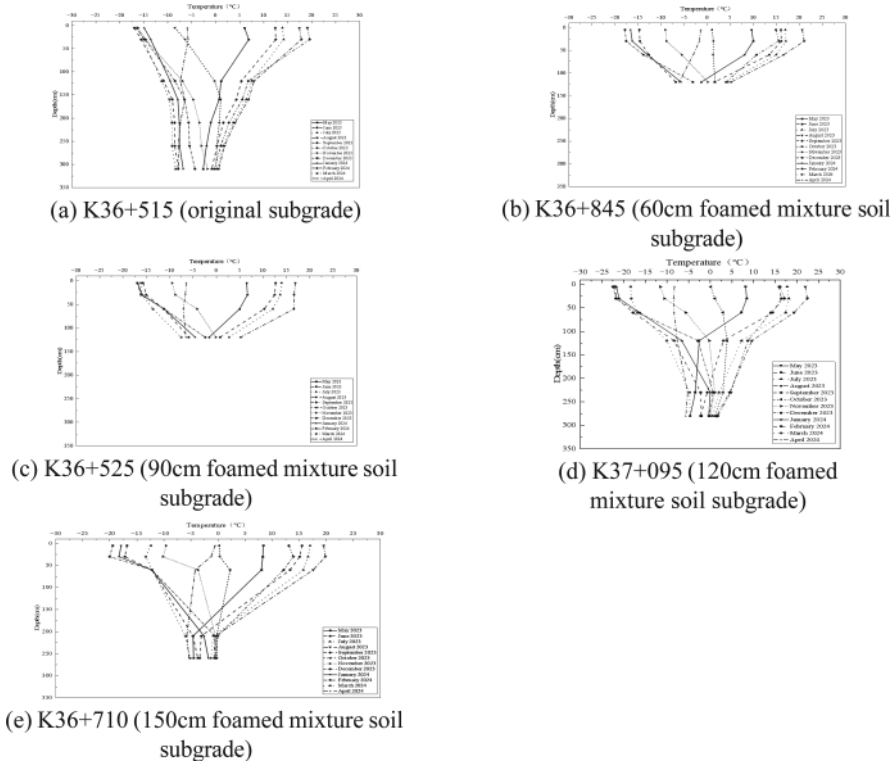

(a) K36+515 (original subgrade)

(b) K36+845 (60cm foamed mixture soil subgrade)

(c) K36+525 (90cm foamed mixture soil subgrade)

(d) K37+095 (120cm foamed mixture soil subgrade)

(e) K36+710 (150cm foamed mixture soil subgrade)

Fig. 5. Temperature distribution at different depths.

4 The Variation Law of Temperature with Depth

Figure 5 illustrates the detailed distribution of temperature relative to depth within the road structure. As the depth increases, the magnitude of temperature fluctuation diminishes significantly, indicating a dampening effect exerted by the overlying materials on surface thermal variations. The seasonal dynamics of heat transfer are distinctly revealed. From May through September, during the warmer months, temperature consistently decreases with increasing depth, signifying a downward conduction of heat from the warmer surface. Conversely, from October to April, encompassing the colder period, the trend reverses, and temperature increases with depth, reflecting the relative warmth of the deeper soil layers compared to the frigid surface and the upward migration of geothermal heat.

The thermal insulation properties of the foamed mixture soil layer play a pivotal role in this system. Its presence significantly modulates the thermal impact on the overlying pavement layer. Specifically, a thicker layer of foamed mixture soil subgrade enhances its insulating capacity, which paradoxically results in a larger temperature range experienced by the pavement layer directly above it. This occurs because the insulating layer effectively decouples the pavement from the stabilizing thermal mass below, leaving it more exposed to and responsive to direct atmospheric temperature swings.

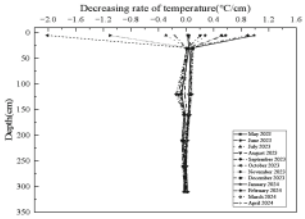

(a) K36+515 (original subgrade)

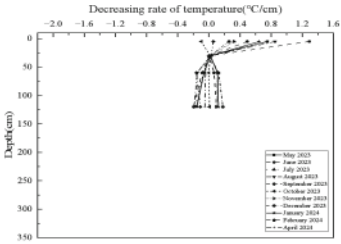

(b) K36+845 (60cm foamed mixture soil subgrade)

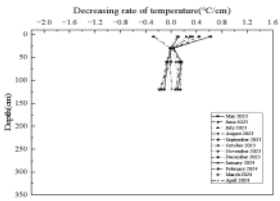

(c) K36+525 (90cm foamed mixture soil subgrade)

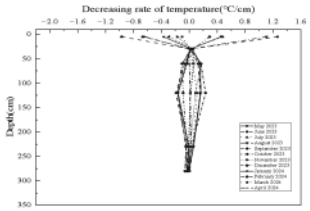

(d) K37+095 (120cm foamed mixture soil subgrade)

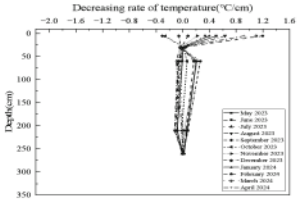

(e) K36+710 (150cm foamed mixture soil subgrade).

Fig. 6. Temperature decreasing rate distribution at different depths.

Meanwhile, the underlying frozen soil foundation maintains a characteristically low temperature with a very narrow range of variation. This stable material acts as a significant thermal reservoir. During the summer, it acts as a heat sink, absorbing thermal energy migrating downward, which results in a net heat loss from the overlying structure. In winter, it conversely helps preserve heat within the system by reducing the rate of heat loss from the deeper layers to the cold surface. Consequently, the thermal insulation performance of the entire road structure is highly dependent on subgrade thickness; a thicker subgrade, particularly of the insulating foamed mixture soil, makes this regulation of heat flow more pronounced and effective.

By calculating the decreasing rate of temperature with depth, the insulation effect of the foamed mixture soil subgrade is further quantified and analyzed. Figure 6 displays the distribution curve of temperature decreasing rate with depth. It can be seen that the temperature decreasing rate at the interface between the base and the subbase, as well as at the interface between the subgrade and the frozen soil foundation in different months, is close to 0, indicating that the temperature has not been lost and completely entered the lower structure during conduction process. The temperature decreasing rate inside the

subgrade in summer is mostly negative, while in winter it is mostly positive, reflecting the direction of heat conduction. That is, in summer, it is conducted from the road surface to the frozen soil foundation, and in winter, it is transmitted from the frozen soil foundation to the road surface. The temperature decreasing rate in October and April is close to 0, indicating that the temperature distribution is uniform with depth. Compared with the original subgrade, the temperature decreasing rate of foamed mixture soil subgrade is smaller in summer, suggesting that more heat is consumed at this time. The temperature decreasing rate is greater in winter, meaning that the foamed mixture soil subgrade can effectively block heat conduction.

5 Temperature Field Characterization Analysis

Figure 7 presents the temperature isotherms derived from different monitoring sections of the road structure, providing a comparative visual analysis of thermal distribution. A key observation from the figure is the distinct thermal performance of the pavement surface constructed with foamed mixture soil when compared to the original subgrade. Specifically, due to the material's thermal insulation properties, the surface over the foamed mixture soil exhibits higher temperatures during the summer months and lower temperatures during the winter months. This phenomenon can be attributed to the material's capacity to retard heat transfer, creating a thermal lag and a moderated thermal regime at the surface relative to ambient extremes.

Analyzing the period from May 2023 to April 2024, the temporal evolution of the temperature-depth isotherms reveals a dynamic, cyclical pattern characterized by alternating intervals of dense and sparse contour lines. The isotherms appear most concentrated from August to September and from December to March, corresponding to peak winter cold penetration, indicating steeper thermal gradients. In contrast, the transitional periods of October and April exhibit more uniform and widely spaced isotherms, reflecting a state of reduced thermal gradient and more stable, homogeneous temperature distribution with depth.

The density of these isothermal lines directly correlates with the rate of temperature change. A higher density signifies a rapid temperature variation over a short depth interval, whereas sparser lines indicate a more gradual change. The visualization clearly demonstrates that as depth increases, the isotherms invariably become more dispersed. This graphical trend confirms the attenuation of surface temperature fluctuations with depth, leading to a smaller range of temperature changes and a progressively more uniform thermal distribution within the deeper layers of the road structure. Furthermore, a direct comparison between the two subgrade types elucidates their differing thermal behaviors. For the original roadbed, the temperature distribution with depth is relatively uniform, but the isotherms within its structure do not show the same pronounced decoupling effect. For the foamed mixture soil subgrade, however, the isotherms within the subgrade layer and the underlying frozen soil foundation are notably sparse. This sparsity is a critical indicator, signifying that temperature changes in these zones are minimal and the distribution is highly uniform. It provides graphical evidence that the foamed mixture soil effectively dampens thermal waves, protecting the underlying foundation from significant temperature shifts and thereby enhancing the overall thermal stability of the road system.

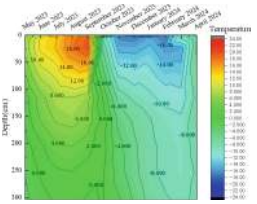

(a) K36+515 (original subgrade).

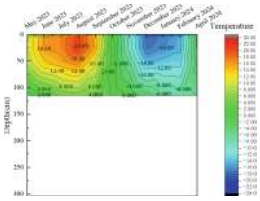

(b) K36+845 (60cm foamed mixture soil subgrade).

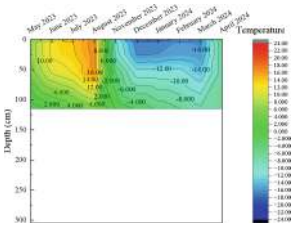

(c) K36+525 (90cm foamed mixture soil subgrade).

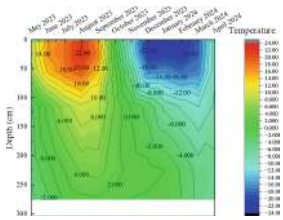

(d) K37+095 (120cm foamed mixture soil subgrade).

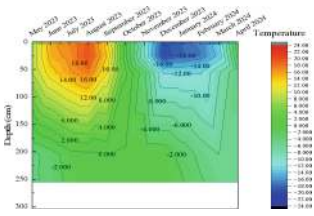

(e) K36+710 (150cm foamed mixture soil subgrade)

Fig. 7. Temperature field of road structure.

6 Conclusion

The temperature variation law, temperature distribution, temperature decreasing rate, and temperature field inside the foamed mixture soil subgrade were obtained based on actual engineering and on-site temperature monitoring data in this study. By comparing the temperature changes of the original subgrade with different thicknesses of foamed mixture soil subgrade, the treatment effect of foamed mixture soil on frozen soil foundation were evaluated. The main conclusions are as follows:

(1) The temperature variation within the road structure is consistent with the atmospheric temperature variation, with higher temperatures in summer and lower temperatures in winter. The temperature change amplitude of the road surface is the largest, followed by the subgrade structure layer. The annual temperature of the frozen soil foundation ranges from 6.86 °C to −9.63 °C, and the temperature change is gentle and has a certain delay. While the depth of frozen foundation reaches 0.5 m and above, the temperature of frozen foundation can be maintained below 0 °C and keep frozen.

(2) The temperature distribution at different depths within the road structure indicates that the greater depth makes the smaller change in temperature and the more significant time delay effect. Due to the thermal insulation performance of foamed mixture soil, temperature changes have a significant impact on the temperature of the pavement layer. This is reflected in the fact that the thickness of the foamed mixture soil subgrade is about large, and the range of temperature changes in the pavement layer is larger, resulting in more heat loss during the conduction process of the foamed mixture soil subgrade.
(3) According to the calculation results, the temperature decreasing rate between the subbase layer and the subgrade, as well as between the subgrade and the frozen soil foundation, is close to 0 in different months, indicating that the temperature entered the lower structure completely while conducting through this layer. The temperature decreasing rate of the foamed mixture soil subgrade is smaller in summer, and heat is consumed. In winter, the temperature decreasing rate is greater, and the foamed mixture soil subgrade effectively blocks heat conduction. This proves the excellent thermal insulation performance of the foamed mixture soil subgrade. In addition, as the thickness of the foamed mixture soil subgrade increases, the conduction loss of heat is greater, and the frozen soil subgrade is less affected by temperature changes.
(4) For the original roadbed, the temperature field is relatively evenly distributed with depth. For the foamed subgrade soil subgrade, the isotherms of the pavement layer are dense, stating a wide range of temperature distribution and large changes, while the isotherms of the subgrade and frozen soil foundation are sparse, indicating small temperature changes and uniform distribution.

Acknowledgments. This work was supported by the National Key Research and Development Program of China (Grant numbers, 2024YFB2605301).

References

1. Mao, X.S., Wang, L.Y., Da, W.Z.R., et al.: Study on frost heaving and grout boiling of roadbeds caused by water and heat changes in seasonal frozen areas. China Foreign Highway. **37**(1), 5 (2017). https://doi.org/10.14048/j.issn.1671-2579.2017.01.001
2. Zhang, Y.Z., Jia, M.T., Zhu, D.P., et al.: Monitoring and analysis of the thermal condition of insulation protection roadbed in high-temperature unstable permafrost region. Glaciol. Geocryol. **46**(4), 1214–1224 (2024). https://doi.org/10.7522/j.issn.1000-0240.2024.0095
3. Wang, J., Zhao, J.Y., Chen, L., et al.: Observation and prediction of long-term thermal state of rock embankment in high temperature frozen soil area. China Railway Sci. **44**(6), 34–45 (2023). https://doi.org/10.3969/j.issn.1001-4632.2023.06.04
4. Bao, W.X., Liu, Y.L., Mao, X.S., et al.: Characteristics of subgrade temperature field of gravel road in high altitude permafrost region. Traffic. Transp. Eng. **23**(4), 60–74 (2023). https://doi.org/10.19818/j.cnki.1671-1637.2023.04.004
5. Xu, Y.Z., Shen, M.D., Zhou, Z.W., et al.: Long-term thermal stability study of the typical embankment along the Qinghai-Tibet Railway in warm permafrost regions. Glaciol. Geocryol. **44**(6), 1784–1795 (2022). https://doi.org/10.7522/j.issn.1000-0240.2022.0155

6. Duan, F., Quan, L., Wang, H., et al.: Effects of cyclical climate change on water temperature characteristics of permafrost slopes. Appl. Sci. **15**(3403), 1–16 (2025). https://doi.org/10.3390/app15063403
7. Cai, W., Zhu, C., Lein, W.: Temperature- and stress-dependent electrical responses of frozen soils. Acta Geotech. **20**, 1–9 (2025). https://doi.org/10.1007/s11440-025-02604-z
8. Jia, J., He, Z., Tenorio, O.V.: A hydrothermal coupling model for permafrost subgrade considering temperature gradient and its application. Sci. Rep. **15**, 1816 (2025). https://doi.org/10.1038/s41598-024-84767-5
9. Fu, J., Li, J., Tang, X.X.: Research on the temperature field of roadbeds in high latitude permafrost regions. China Foreign Highway. **34**(2), 6 (2014). https://doi.org/10.3969/j.issn.1671-2579.2014.02.012
10. Fan, X.W., Lin, Z.J., Luo, J., et al.: Long-term effects of embankment engineering behaviors on cold permafrost in high-altitude permafrost regions. Glaciol. Geocryol. **43**(5), 1323–1333 (2021). https://doi.org/10.7522/j.issn.1000-0240.2021.0086
11. Zhang, K., Jiang, D.J.: Influence of thermal insulation material on temperature field of permafrost foundation of airport runway. Water Resour. Archit. Eng. **21**(3), 91–98 (2023). https://doi.org/10.3969/j.issn.1672-1144.2023.03.013
12. He, M.W.: Research on application of foamed lightweight concrete thermal insulation layer in highway subgrade engineering in seasonal frozen soil area. Constr. Mach. 24–29 (2022). https://doi.org/10.14189/j.cnki.cm1981.2022.12.023
13. Lin, L.B., Liu, H.B., Han, S., et al.: Experimental research on foamed cement banking for frozen soil foundation protection. Highway Transp. Res. Dev. **26**(6), 55–58 (2009). https://doi.org/10.3969/j.issn.1002-0268.2009.06.011
14. Li, D., Cheng, J.: On the numerical simulation of the temperature field of a foamed concrete insulation board subgrade in seasonally frozen regions. Traffic Eng. Technol. Natl. Def. **14**(3), 4 (2016). https://doi.org/10.13219/j.gjgyat.2016.03.009

Dynamic Assessment and Optimization of Daily Operational Resilience for the Urban Roadway Tunnel System

Deyi Liu[1], Jiang Liu[1], Weiyu Jiang[2], Yachao Li[1], Yuehui Wang[1], Huijun Lan[2(✉)], and Xiaodong Pan[2]

[1] China Railway Tunnel Stock Co., Ltd., Zhengzhou 450000, China
[2] College of Civil Engineering, Zhejiang University of Technology, Hangzhou 310014, China
2112006012@zjut.edu.cn

Abstract. To enhance the capacity of urban roadway tunnel systems in preventing daily operational risks, this study introduces the concept of daily operational resilience, grounded in system resilience theory. The existing framework for evaluating tunnel system resilience has been refined. This study conducts a daily operational resilience assessment of urban roadway tunnel systems based on a multi-state Bayesian network Firstly, the D-TOSE model and TOPSIS method are used to identify 56 factors influencing daily operational resilience. Then, the node probability tables are obtained by expert questionnaires, the Noisy-Max model, and the FCEM method. Subsequently, a dynamic Bayesian network model is constructed using a transition matrix. And critical importance analysis is conducted to offer decision-makers dynamic operational optimization strategies. The model is applied to the tunnel W. The evaluation results show that the daily operational resilience of the tunnel system is projected to decrease from 0.802 to 0.761 over the next decade, with varying focus areas for optimization strategies at different periods. As the service time increases, the emphasis on optimizing the daily operational resilience of the tunnel system should gradually shift from resource allocation capabilities to personnel operational factors. Moreover, this evaluation model could provide a reference for daily operational resilience assessment.

Keywords: Urban Roadway Tunnel System · Daily Operational Resilience · Dynamic Bayesian Network · Operation and Maintenance

1 Introduction

Recent rapid development in road infrastructure has greatly enhanced the engineering value for urban roadway tunnel systems. These tunnels now serve as vital components in the broader transportation network. Roadway tunnels are critical nodes in urban traffic systems and effectively improve traffic flow while reducing congestion. However, the expansion of tunnel operations introduces increasingly prominent safety risks. Operational risks in urban roadway tunnels are primarily categorized as “low-frequency,

© The Author(s), under exclusive license to Springer Nature Switzerland AG 2027
G. Feng et al. (Eds.): ICCE 2025, SUCI, pp. 504–526, 2027.
https://doi.org/10.1007/978-3-032-32237-1_36

high-consequence" events (e.g., floods, fires, earthquakes) and "high-frequency, low-impact" events (e.g., structural defects, equipment failures, human errors). These events occur infrequently yet are highly sudden and destructive, and they present significant challenges to post-disaster rescue and repair efforts [1]. Although individual occurrences of the latter cause limited damage, their high frequency results in substantial cumulative effects over time. Consequently, the establishment of a scientific risk assessment framework and the optimization of tunnel service performance are crucial research objectives in tunnel engineering.

Various safety assessment methods exist for tunnel operational safety. Ren Gaofeng [2] and colleagues established a fuzzy comprehensive evaluation model. This model employs real-time structural health monitoring system data from shield tunnels to assess safety conditions. Song Jie [3] and coworkers proposed an operational safety evaluation method for roadway tunnel groups. Their approach integrates a fuzzy comprehensive evaluation model with a dual dynamic weight calculation model based on the factor-time variable weight method. This combination effectively reflects the time-varying characteristics of evaluation indicators. Zhou Bing [4] and his team developed an operational safety risk assessment system for urban traffic tunnels. This system successfully merges overall and specialized assessments. It constructs a three-layer index system comprising the target layer, criterion layer, and indicator layer, alongside corresponding algorithms. The framework facilitates dynamic risk assessment and management. Xiao Shan [5] constructed a sectional evaluation index system for tunnels. Her system incorporates tunnel condition, traffic characteristics, operational environment, and operational management aspects. She also established an operational safety risk assessment model for long roadway tunnels. This model combines the triangular fuzzy analytic hierarchy process (FAHP) with the set pair analysis (SPA) method. Compared to single-method approaches, integrated methods combining analytic hierarchy process (AHP) and fuzzy comprehensive evaluation demonstrate superior accuracy and reliability [6–9]. The AHP provides a structured decision-making framework. Fuzzy comprehensive evaluation effectively integrates diverse uncertain information. Their combination enables more comprehensive risk assessment and management for tunnel operational safety. Wu Xianguo [10] and associates introduced the cloud model to address uncertainty. They discussed the randomness and fuzziness of uncertain information. They further proposed a safety risk level evaluation method based on two-dimensional and multi-dimensional cloud inference.

Resilience theory examines system disaster-bearing and recovery capabilities, now widely applied across ecology, economics, and engineering disciplines. Holling [11] pioneered its application in ecosystem research by exploring resilience-system relationships. Recently, this theory has offered new infrastructure disaster management perspectives. Its framework assesses systems across four dimensions—absorption, resistance, recovery, and adaptation—during pre-disaster, disaster, and post-disaster phases, enhancing scientific rigor and effectiveness. Chen et al. [12] established a Bayesian network (BN) model for Suzhou Metro resilience evaluation, collecting data via construction logs, questionnaires, and expert consultations. Lin Xingtao et al. [13] analyzed resilience performance curves to quantify repair decision time and repair cost relationships. Yin et al. [14] developed a BN-based model using historical data to assess Beijing subway system resilience.

Yin Ziwei [15] evaluated metro tunnel systems operational resilience through tunnel performance curve establishment and dynamic Bayesian network construction; Kammouh et al. [16] employed dynamic Bayesian networks (DBN) for simulating dynamic engineering systems resilience. Fan Yanyan et al. [17] constructed a plateau railway tunnel safety evaluation system pairing combination weighting and Euclidean distance. Bi Wei [18] utilized a DBN model for urban metro station fire resilience evaluation. Weng Yuan et al. [19] proposed a tunnel engineering resilience assessment model integrating the Decision Making Trial and Evaluation Laboratory (DEMATEL) method and BN.

Existing studies exhibit several limitations. Traditional risk assessment methods predominantly focus on post-disaster scenarios, lacking comprehensive lifecycle perspectives. BN models typically simplify node states to just two conditions, which cannot accurately reflect actual tunnels' complex operational conditions. Research on tunnel operation and maintenance dynamics remains insufficient.

This study enhances the resilience assessment framework proposed by Bi Wei et al. [18] to address the aforementioned challenges, introducing the concept of daily operational resilience. This approach substitutes BN with DBN and defines discrete state spaces of 3–5 levels based on influencing factor characteristics, thereby improving adaptability to practical scenarios. The research systematically identifies influencing factors of daily resilience across four phases: prevention and absorption before risks occur, resistance during risk events, and recovery and adaptation post-event. This framework supports the construction of a BN model for the daily operational resilience of tunnel systems. Based on influencing factor types, the study develops transition matrices for the DBN model. Using Hangzhou's tunnel W as a case study, the research derives node probability tables for the DBN model from expert questionnaires and historical statistics. This approach evaluates the tunnel system daily resilience. The study refines node states into two to five distinct conditions according to different influencing factors' actual states. This refinement overcomes the limitation of existing studies in describing actual factor states. It enhances scenario simulation realism and improves resilience assessment accuracy. Versus traditional BN models' static evaluations, the developed DBN model predicts urban roadway tunnels daily resilience changes over the next decade. The model also performs key importance analysis on root nodes by influencing factor type. These analyses support proposing dynamic operation and maintenance strategies to enhance urban roadway tunnel systems daily resilience.

2 Assessing Daily Operational Resilience of Urban Roadway Tunnel Systems Using Dynamic Bayesian Networks

The daily operational resilience of urban roadway tunnel systems reflects their comprehensive capability to withstand common risk disturbances. This resilience includes absorbing and resisting operational performance impacts, rapidly restoring functionality, and adaptively adjusting operations. Enhancing resilience significantly reduces system failure probability and effectively controls operational performance losses. It further mitigates accident-related economic and social impacts while accelerating tunnel performance recovery.

2.1 Identifying and Prioritizing Influencing Factors for Urban Roadway Tunnel Systems Daily Operational Resilience

This study systematically identifies urban roadway tunnel systems daily operational resilience based on routine hazard lifecycle scenarios. A resilience cognition framework establishes key influencing factors for operation and maintenance personnel and decision-makers. The methodology adopts the D-TOSE model proposed by Tang et al. [20] and an enhanced Technique for Order Preference by Similarity to Ideal Solution (TOPSIS). This combined approach identifies indicators and influencing factors of daily disaster resilience while quantifying each factor's contribution to pinpoint critical elements.

Key influencing factors were screened through distribution of Questionnaire A ("Questionnaire for Identifying Influencing Factors of Daily Operational Resilience in Urban Roadway Tunnel Systems") to 13 experts. Among 12 returned questionnaires, two were excluded due to insufficient scoring time or incomplete attention-test questions, yielding 10 valid responses (83.3% valid response rate).

Using the D-TOSE model, 56 daily operational resilience influencing factors were preliminarily identified. Table 1 details these factors' correspondence with system resilience 4R attributes. Based on the 10 valid questionnaires, each factor's importance, discrimination, and impact indices were determined, with Table 2 presenting detailed results. All 56 factors exceeded calculated thresholds (degree of importance $I_0 = 2.338$, degree of differentiation $D_0 = 0.015$, degree of contribution $C_0 = 0.009$), confirming their retention as key influencing factors for urban roadway tunnel systems.

Table 1. Preliminary identification of influencing factors.

Resilience Characterization	Identification Dimension	Influencing Factor	Code	Manifestation	Source
Absorption Capacity	T (R1)	Traffic Accidents	$AbsT_1$	Traffic accident occurrence status	[9]
		Weather Conditions	$AbsT_2$	Presence of adverse weather conditions	[9]
		Operational Status of Power Supply System	$AbsT_3$	Equipment availability rate: ≥98% / 93%–98% / 85%–93% / ≤85%	[21]
		Operational Status of Lighting System	$AbsT_4$	Equipment availability rate: ≥95% / 86%–95% / 74%–86% / ≤74%	[21]
		Operational Status of Ventilation System	$AbsT_5$	Equipment availability rate: ≥98% / 91%–98% / 82%–91% / ≤82%	[21]
		Operational Status of fire Protection System	$AbsT_6$	Firefighting equipment availability: 100% / 95%–100% / 89%–95% / ≤89%	[21]

(*continued*)

Table 1. (*continued*)

Resilience Characterization	Identification Dimension	Influencing Factor	Code	Manifestation	Source
		Operational Status of Monitoring and Communication System	$AbsT_7$	Equipment availability rate: ≥98% / 91%–98% / 81%–91% / <81%	[21]
		Operational Status of Electromechanical System	$AbsT_8$	Operational state index determined by weighted AbsT3-AbsT7	[21]
		Structural Integrity Degradation of Main Tunnel	$AbsT_9$	Material degradation levels: No degradation / Minor degradation / Moderate degradation / Severe degradation / Critical degradation (evident damage)	[21]
		Main tunnel structure leakage status	$AbsT_{10}$	Leakage levels: None / Seepage (no traffic impact) / Dripping (potential safety risk) / Flowing water (impaired safety) / Water gushing (severe hazard)	[21]
		Main tunnel structural safety	$AbsT_{11}$	Structural safety index weighted by AbsT9-AbsT10	[21]
		Portal condition	$AbsT_{12}$	Portal integrity: Intact / Minor cracks / Cracking with drainage damage / Severe cracking with drainage failure / Partial collapse	[21]
		Portal entrance condition	$AbsT_{13}$	Entrance condition: Intact / Surface cracks / Local cracking with seepage / Structural cracking / Large-scale cracking	[21]
		Ceiling systems with embedded parts	$AbsT_{14}$	Ceiling systems: Intact / Slight deformation / Damaged with corrosion / Severe deformation / Critical damage	[21]
		Interior finish condition	$AbsT_{15}$	Interior finish: Intact (0% damage) / ≤10% damage (no impact) / 10–20% damage (safety concern) / >20% damage (severe hazard)	[21]
		Traffic markings and signs	$AbsT_{16}$	Traffic markings: Intact / ≤10% soiling / 10–20% damage (potential risk) / >20% damage (safety impairment)	[21]

(*continued*)

Table 1. (*continued*)

Resilience Characterization	Identification Dimension	Influencing Factor	Code	Manifestation	Source
		Operational Status of Drainage Facilities	$AbsT_{17}$	Drainage functionality: Intact / Minor structural damage / Siltation with structural damage / Severe siltation with structural impairment / Complete blockage with critical damage	[21]
		Pavement condition	$AbsT_{18}$	Pavement condition: Intact / Dampness with minor cracks / Local subsidence / Extensive subsidence or potholes / Flooding or icing	[21]
		Maintenance walkway status	$AbsT_{19}$	Maintenance walkway status: Fully functional / Minor component damage / Partial functional impairment (safety concern) / Severe damage or missing components (traffic hazard)	[21]
		Ancillary tunnel structural safety	$AbsT_{20}$	Compliant with the Technical Specifications for Maintenance of Highway Tunnels (JTG H12-2015)	[21]
		Tunnel structural integrity	$AbsT_{21}$	Compliant with the Technical Specifications for Maintenance of Highway Tunnels (JTG H12-2015)	[21]
	O (R1)	Emergency safety training	$AbsO_1$	Safety training implementation: Regular drills & assessments / Sporadic implementation / Not implemented	[9]
		Electromechanical facility maintenance protocols	$AbsO_2$	Electromechanical maintenance: Periodic inspection protocols / Irregular implementation / No maintenance (equipment risk)	[21]
		Civil structure inspection standards	$AbsO_3$	Civil structure inspections: Scheduled maintenance / Occasional checks / No inspections (structural risk)	[21]

(*continued*)

Table 1. (*continued*)

Resilience Characterization	Identification Dimension	Influencing Factor	Code	Manifestation	Source
		Patrol operation safety compliance	$AbsO_4$	Patrol operation compliance: Full PPE & procedure adherence / Partial compliance / Non-compliance (e.g., PPE violations)	[21]
	S(R1)	Driver safety awareness	$AbsS_1$	Driver safety performance: Full compliance / Partial compliance / Non-compliance (risky behaviors)	[4]
		Public safety awareness	$AbsS_2$	Public safety awareness: Full knowledge of tunnel protocols / Partial awareness / No awareness (e.g., window closure rules)	[22]
	E (R2, R3)	Preventive risk resource allocation capacity	$AbsE_1$	Risk resource allocation: Adequate resources (effective prevention) / Insufficient allocation (prevention failure) / Mismanaged resources (systemic failure)	[18]
Resistance Capability	T (R2, R4)	Operational Status of Tunnel·Monitoring and·Early Warning·System	$ResT_1$	Tunnel Monitoring System Functionality: Fully operational (timely hazard detection & alert) / Partial failure (delayed incident response) / Complete failure (zero warning capability)	[21]
		Emergency facilities	$ResT_2$	Emergency lighting functionality: Fully operational (no consequence escalation) / Partial failure (delayed evacuation) / Complete failure (severe consequence exacerbation)	[23]
		Tunnel evacuation design	$ResT_3$	Evacuation exit compliance: Meets all requirements / Partial non-compliance / Total non-compliance	[23]

(*continued*)

Table 1. (*continued*)

Resilience Characterization	Identification Dimension	Influencing Factor	Code	Manifestation	Source
		Flood resilience design	$ResT_4$	Flood defense compliance: Pump capacity & drainage meet standards / Partial deficiency / Systemic failure	[23]
		Seismic-resistant design	$ResT_5$	Seismic design verification: Structural integrity confirmed / Partial non-conformance / Design failure	[23]
		Fire-resistant structural design	$ResT_6$	Fire resistance compliance: Full code compliance / Partial deficiency / Non-compliant	[23]
		Operational Status of Fire suppression equipment	$ResT_7$	Fire suppression status: Immediate extinguishment capability / Partial failure / Total failure	[23]
		Operational Status of ventilation and smoke control system	$ResT_8$	Ventilation system: Optimal smoke control / Partial malfunction (rescue impairment) / Complete failure (severe impact)	[23]
	O (R4)	Operation staff safety awareness	$ResO_1$	Patrol efficacy: All staff effective / Partial staff deficiency / Total patrol failure	[22]
		Emergency response plans	$ResO_2$	Emergency plan status: Comprehensive & updated protocols / Partial plan deficiencies / Obsolete plans	[22]
		Emergency organization structure	$ResO_3$	Organization efficacy: Optimal command structure / Partial coordination failure / Severe breakdown	[18]
		Emergency personnel competency	$ResO_4$	Personnel performance: 100% task efficiency / Partial operational failure / Critical mission failure	[18]

(*continued*)

Table 1. (*continued*)

Resilience Characterization	Identification Dimension	Influencing Factor	Code	Manifestation	Source
		Emergency management operations	$ResO_5$	Emergency management efficacy: Fully executed / Partially effective / Complete failure	[18]
		Unobstructed evacuation routes	$ResO_6$	Evacuation route status: Unobstructed (no consequence) / Partial blockage (increased casualties) / Total blockage (catastrophic impact)	[23]
		Response team arrival time	$ResO_7$	Response time: <5 min / 5–15 min / >15 min	[22]
	S (R4)	Public escape skills	$ResS_1$	Public evacuation capability: Proficient skills / Partial deficiency / No capability	[22]
		Public safety awareness	$ResS_2$	Public first-aid knowledge: Full awareness / Partial unawareness / No knowledge	[22]
		City fire response network	$ResS_3$	Fire rescue response: Timely intervention / Partial delay / Total failure	[18]
	E (R2, R3)	Risk resistance resource allocation	$ResE_1$	Emergency resource allocation: Optimal deployment / Partial adequacy / Inadequate distribution	[18]
Restoration Capacity	O (R3, R4)	On-site specialist rescue teams	$RecO_1$	On-site rescue efficacy: Timely hazard clearance / Delayed clearance	[18]
		Facility repair & replenishment	$RecO_2$	Post-incident equipment recovery: Immediate restoration / Delayed restoration	[18]
		Operational recovery actions	$RecO_3$	Recovery efficiency: High / Low / Critical low	[18]
	E (R2, R3)	Recovery resource allocation	$RecE_1$	Recovery resource allocation: Optimal / Partial adequacy / Inadequate	[18]
Adaptive Capacity	O (R3)	Accident cause investigation	$AdaO_1$	Accident investigation: Effective hazard elimination / Ineffective elimination	[18]

(*continued*)

Table 1. (*continued*)

Resilience Characterization	Identification Dimension	Influencing Factor	Code	Manifestation	Source
		Incident experience documentation	$AdaO_2$	Lessons learned: Full implementation / Partial adoption / No adoption	[18]
		Rectification implementation & oversight	$AdaO_3$	Rectification oversight: Effective execution / Suboptimal execution / No execution	[18]
		Records archiving	$AdaO_4$	Records management: Complete archival / Partial archival / No archival	[18]
	E (R2, R3)	Corrective resource allocation capacity	$AdaE_1$	Rectification effectiveness: Significant value / Partial value / No value	[18]

(1) T, O, S, E denote Technical, Organizational, Social, and Economic dimensions respectively;
(2) R1, R2, R3, R4 represent Robustness, Redundancy, Resourcefulness, and Rapidity respectively

Table 2. Importance, distinctiveness, and impact of influencing factors.

No.	Node	Degree of Importance (I)	Degree of Differentiation (D)	Degree of Contribution (C)	Removal Decision
1	$AbsT_1$	3.133	0.0314	0.0249	No
2	$AbsT_2$	2.093	0.0677	0.0358	No
3	$AbsT_3$	3.123	0.0206	0.0162	No
4	$AbsT_4$	2.939	0.0209	0.0155	No
5	$AbsT_5$	2.506	0.0163	0.0103	No
6	$AbsT_6$	2.724	0.0207	0.0143	No
7	$AbsT_7$	2.691	0.0160	0.0109	No
8	$AbsT_8$	3.064	0.0180	0.0139	No
9	$AbsT_9$	2.956	0.0256	0.0191	No
10	$AbsT_{10}$	2.994	0.0301	0.0228	No
11	$AbsT_{11}$	3.28	0.0192	0.0159	No
12	$AbsT_{12}$	2.862	0.0230	0.0166	No
13	$AbsT_{13}$	2.942	0.0186	0.0139	No
14	$AbsT_{14}$	2.833	0.0176	0.0126	No

(*continued*)

Table 2. (*continued*)

No.	Node	Degree of Importance (I)	Degree of Differentiation (D)	Degree of Contribution (C)	Removal Decision
15	$AbsT_{15}$	2.708	0.0795	0.0544	No
16	$AbsT_{16}$	2.857	0.0518	0.0374	No
17	$AbsT_{17}$	2.798	0.0167	0.0118	No
18	$AbsT_{18}$	2.659	0.0195	0.0131	No
19	$AbsT_{19}$	2.697	0.0185	0.0126	No
20	$AbsT_{20}$	2.991	0.0188	0.0142	No
21	$AbsT_{21}$	3.095	0.0273	0.0214	No
22	$AbsO_1$	2.981	0.0292	0.022	No
23	$AbsO_2$	3.093	0.0245	0.0191	No
24	$AbsO_3$	3.278	0.0220	0.0183	No
25	$AbsO_4$	2.884	0.0235	0.0172	No
26	$AbsS_1$	3.014	0.0196	0.0149	No
27	$AbsS_2$	2.66	0.0184	0.0124	No
28	$AbsE_1$	3.095	0.0171	0.0134	No
29	$ResT_1$	2.977	0.0214	0.0161	No

2.2 Measurement of Daily Operational Resilience for Urban Roadway Tunnel Systems

This study employs a dynamic Bayesian network (DBN) approach to quantify the daily operational resilience of urban roadway tunnel systems, accurately characterizing the complex causal relationships between resilience and its influencing factors. Based on an improved version of Bi Wei's method [18], this research integrates questionnaire surveys with historical statistics to determine prior and conditional probabilities for network nodes. It further defines probability distribution functions for state transitions across various influencing factors, establishing a comprehensive DBN model. This model incorporates time-varying factor characteristics—including performance degradation and enhancement processes—into optimization strategy analysis, providing decision-makers with a scientific basis for prioritizing operational and maintenance strategies.

Fundamental Theory of Dynamic Bayesian Networks. Bayesian networks (BN) model complex systems using graph and probability theory, depicting systems via directed acyclic graphs where nodes and directed arcs capture causal relationships. A BN model contains n variables X_1, X_2, X_3, …, X_n. Bayesian theory determines their joint probability distribution, expressed as Equation:

$$P(X_1, X_2, X_3, \ldots, X_n) = \prod_{i=1}^{n} P(X_i|pa(X_i)) \tag{1}$$

$pa\ (X_i)$ represents the parent nodes of variable X_i.

This study employs dynamic DBN that extend standard BN to discrete time sequences [15] through variable connections across time steps to model probability temporal evolution, considering these networks unrolled over time periods 0, 1, …, t under three fundamental assumptions in practical engineering applications:

(1) Temporal Invariance: Conditional probabilities remain invariant across all time steps t.
(2) Markov Property: The urban roadway tunnel system state at time $t + 1$depends solely on its state at time t, formally expressed as $(X^t|X^0, X^1, \cdots, X^{t-1}) = P(X^t|X^{t-1})$
(3) Transition Stability: Conditional probability transitions across consecutive time periods remain stationary, which permits straightforward derivation of transition probabilities $P(X^t|X^{t-1})$ for all t.

Computation of Conditional Probability Tables. Given scarce historical tunnel engineering data and significant individual variations among tunnels, this study integrates expert questionnaires with historical statistics. The Noisy-Max model [24] and Fuzzy Comprehensive Evaluation Method (FCEM) [24] are employed to process questionnaire data, constructing conditional probability tables—including prior and conditional probabilities—for BN nodes. In DBN modeling, child nodes frequently have multistate parents. Direct computation of multistate joint probabilities would impose excessive demands on expert input and computational resources. The Noisy-Max model addresses this challenge by assuming parent node independence, simplifying conditional probability calculations to individual parent impact assessments [25]. This approach maintains Bayesian inference accuracy while eliminating complex joint probability computations, requiring experts to evaluate only single-parent influences without considering combinatorial effects. Concurrently, FCEM converts qualitative expert judgments into quantitative assessments, effectively reducing evaluation subjectivity.

Transition Matrix in DBN Models. DBN models transfer three root node types affecting urban tunnel systems daily operational resilience from period t to $\boldsymbol{t + \Delta t}$, comprising thirty-four factors categorized as:

(1) Equipment and facility factors: $AbsT_8$, $AbsT_{21}$, $ResT_1$, $ResT_2$, $ResT_3$, $ResT_4$, $ResT_5$, $ResT_6$, $ResT_7$, $ResT_8$, $ResS_3$.
(2) Personnel operational factors: $AbsT_1$, $AbsO_2$, $AbsO_3$, $AbsO_4$, $AbsS_1$, $AbsS_2$, $ResO_1$, $ResO_6$, $ResO_7$, $ResS_1$, $ResS_2$, $RecO_1$, $RecO_2$, $RecO_3$.
(3) Organizational management factors: $AbsO_1$, $AbsE_1$, $ResO_2$, $ResO_3$, $ResO_4$, $ResE_1$, $RecE_1$, $AdaO_1$, $AdaE_1$.

Figure 1(a)–(f) presents Dynamic Bayesian Network transition schematics for these resilience factors: (a) equipment and facility factor $AbsT_{21}$; (b) equipment and facility factor $AbsT_8$; (c) equipment and facility non-root nodes; (d) personnel operational non-root nodes; (e) personnel operational factor $AbsT_1$; (f) organizational management factors. The state transition assumptions governing all influencing factors are as follows:

(1) Equipment and facility factors exhibit distinct state configurations: $AbsT_{21}$ occupies five states (Class 1-State 0 to Class 5-State 4), $AbsT_8$ assumes four states

(Class 1-State 0 to Class 4-State 3), while other nodes operate under three states—normal operation (State 0), partial failure (State 1), and complete failure (State 2). Aging mechanisms progress with cumulative operational events, necessitating regular maintenance, where failure and repair rates obey exponential distributions [26].

(2) Personnel operational factors assign $AbsT_1$ a binary state model: safe driving without accidents (State 0) versus unsafe driving with collisions (State 1). Other personnel nodes transition among three states: standard compliance (State 0), partial compliance (State 1), and non-compliance (State 2), with operational failure rates conforming to Poisson distributions [27].

(3) Organizational management factors evolve through three states: rational decision-making (State 0), partially rational decisions (State 1), and irrational decisions (State 2). Management experience intensifies with operational tenure, quantified by organizational experience enhancement coefficient ν [28].

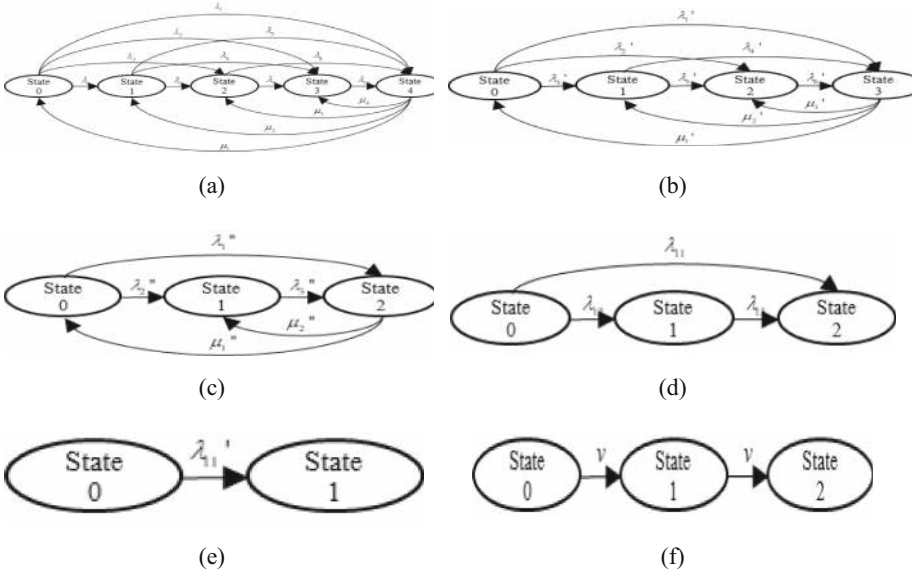

Fig. 1. DBN transition diagram.

All root nodes in the multi-state dynamic Bayesian network (M-DBN) model undergo state transitions governed by hidden Markov processes, with transition probability matrices for the three categories detailed in Tables 3, 4 and 5.

Table 3. State transition matrices for equipment and facility factors nodes.

t	$(t+\Delta t)$				
Equipment and facility factors					
$AbsT_{21}$	State 0	State 1	State 2	State 3	State 4
State 0	$e^{-(\lambda_1+\lambda_2+\lambda_3+\lambda_4)\Delta t}$	$\frac{\lambda_4\left(1-e^{-(\lambda_1+\lambda_2+\lambda_3+\lambda_4)\Delta t}\right)}{\lambda_1+\lambda_2+\lambda_3+\lambda_4}$	$\frac{\lambda_3\left(1-e^{-(\lambda_1+\lambda_2+\lambda_3+\lambda_4)\Delta t}\right)}{\lambda_1+\lambda_2+\lambda_3+\lambda_4}$	$\frac{\lambda_2\left(1-e^{-(\lambda_1+\lambda_2+\lambda_3+\lambda_4)\Delta t}\right)}{\lambda_1+\lambda_2+\lambda_3+\lambda_4}$	$\frac{\lambda_1\left(1-e^{-(\lambda_1+\lambda_2+\lambda_3+\lambda_4)\Delta t}\right)}{\lambda_1+\lambda_2+\lambda_3+\lambda_4}$
State 1	0	$e^{-(\lambda_5+\lambda_6+\lambda_7)\Delta t}$	$\frac{\lambda_7\left(1-e^{-(\lambda_5+\lambda_6+\lambda_7)\Delta t}\right)}{\lambda_5+\lambda_6+\lambda_7}$	$\frac{\lambda_6\left(1-e^{-(\lambda_5+\lambda_6+\lambda_7)\Delta t}\right)}{\lambda_5+\lambda_6+\lambda_7}$	$\frac{\lambda_5\left(1-e^{-(\lambda_5+\lambda_6+\lambda_7)\Delta t}\right)}{\lambda_5+\lambda_6+\lambda_7}$
State 2	0	0	$e^{-(\lambda_8+\lambda_9)\Delta t}$	$\frac{\lambda_9\left(1-e^{-(\lambda_8+\lambda_9)\Delta t}\right)}{\lambda_8+\lambda_9}$	$\frac{\lambda_8\left(1-e^{-(\lambda_8+\lambda_9)\Delta t}\right)}{\lambda_8+\lambda_9}$
State 3	0	0	0	$e^{-\lambda_{10}\Delta t}$	$1-e^{-\lambda_{10}\Delta t}$
State 4	$\frac{\mu_1\left(1-e^{-(\mu_1+\mu_2+\mu_3+\mu_4)\Delta t}\right)}{\mu_1+\mu_2+\mu_3+\mu_4}$	$\frac{\mu_2\left(1-e^{-(\mu_1+\mu_2+\mu_3+\mu_4)\Delta t}\right)}{\mu_1+\mu_2+\mu_3+\mu_4}$	$\frac{\mu_3\left(1-e^{-(\mu_1+\mu_2+\mu_3+\mu_4)\Delta t}\right)}{\mu_1+\mu_2+\mu_3+\mu_4}$	$\frac{\mu_4\left(1-e^{-(\mu_1+\mu_2+\mu_3+\mu_4)\Delta t}\right)}{\mu_1+\mu_2+\mu_3+\mu_4}$	$e^{-(\mu_1+\mu_2+\mu_3+\mu_4)\Delta t}$
$AbsT_8$	State 0	State 1	State 2	State 3	
State 0	$e^{-(\lambda_1{}'+\lambda_2{}'+\lambda_3{}')\Delta t}$	$\frac{\lambda_3{}'\left(1-e^{-(\lambda_1{}'+\lambda_2{}'+\lambda_3{}')\Delta t}\right)}{\lambda_1{}'+\lambda_2{}'+\lambda_3{}'}$	$\frac{\lambda_2{}'\left(1-e^{-(\lambda_1{}'+\lambda_2{}'+\lambda_3{}')\Delta t}\right)}{\lambda_1{}'+\lambda_2{}'+\lambda_3{}'}$	$\frac{\lambda_1{}'\left(1-e^{-(\lambda_1{}'+\lambda_2{}'+\lambda_3{}')\Delta t}\right)}{\lambda_1{}'+\lambda_2{}'+\lambda_3{}'}$	
State 1	0	$e^{-(\lambda_4{}'+\lambda_5{}')\Delta t}$	$\frac{\lambda_5{}'\left(1-e^{-(\lambda_4{}'+\lambda_5{}')\Delta t}\right)}{\lambda_4{}'+\lambda_5{}'}$	$\frac{\lambda_4{}'\left(1-e^{-(\lambda_4{}'+\lambda_5{}')\Delta t}\right)}{\lambda_4{}'+\lambda_5{}'}$	
State 2	0	0	$e^{-\lambda_6{}'\Delta t}$	$1-e^{-\lambda_6{}'\Delta t}$	
State 3	$\frac{\mu_1{}'\left(1-e^{-(\mu_1{}'+\mu_2{}'+\mu_3{}')\Delta t}\right)}{\mu_1{}'+\mu_2{}'+\mu_3{}'}$	$\frac{\mu_2{}'\left(1-e^{-(\mu_1{}'+\mu_2{}'+\mu_3{}')\Delta t}\right)}{\mu_1{}'+\mu_2{}'+\mu_3{}'}$	$\frac{\mu_3{}'\left(1-e^{-(\mu_1{}'+\mu_2{}'+\mu_3{}')\Delta t}\right)}{\mu_1{}'+\mu_2{}'+\mu_3{}'}$	$e^{-(\mu_1{}'+\mu_2{}'+\mu_3{}')\Delta t}$	
Non-root nodes	State 0	State 1	State 2		

(*continued*)

Table 3. (*continued*)

t	$(t+\Delta t)$				
Equipment and facility factors					
$AbsT_{21}$	State 0	State 1	State 2	State 3	State 4
State 0	$e^{-(\lambda_1'' + \lambda_2'')\Delta t}$	$\frac{\lambda_2''\left(1-e^{-(\lambda_1'' + \lambda_2'')\Delta t}\right)}{\lambda_1'' + \lambda_2''}$	$\frac{\lambda_1''\left(1-e^{-(\lambda_1'' + \lambda_2'')\Delta t}\right)}{\lambda_1'' + \lambda_2''}$		
State 1	0	$e^{-\lambda_3''\Delta t}$	$1 - e^{-\lambda_3''\Delta t}$		
State 2	$\frac{\mu_1''\left(1-e^{-(\mu_1'' + \mu_2'')\Delta t}\right)}{\mu_1'' + \mu_2''}$	$\frac{\mu_2''\left(1-e^{-(\mu_1'' + \mu_2'')\Delta t}\right)}{\mu_1'' + \mu_2''}$	$e^{-(\mu_1'' + \mu_2'')\Delta t}$		

Table 4. State transition matrix for personnel operational factors nodes.

t	$(t+\Delta t)$		
Personnel operational factors			
Non-root nodes	State 0	State 1	State 2
State 0	$1-\lambda_{11}\Delta te^{-\lambda_{11}\Delta t}-\lambda_{12}\Delta te^{-\lambda_{12}\Delta t}$	$\lambda_{12}\Delta te^{-\lambda_{12}\Delta t}$	$\lambda_{11}\Delta te^{-\lambda_{11}\Delta t}$
State 1	$e^{-\lambda_{12}\Delta t}$	$1-e^{-\lambda_{12}\Delta t}-\lambda_{13}\Delta te^{-\lambda_{13}\Delta t}$	$\lambda_{13}\Delta te^{-\lambda_{13}\Delta t}$
State 2	$e^{-\lambda_{11}\Delta t}$	$\lambda_{13}\Delta te^{-\lambda_{13}\Delta t}$	$1-e^{-\lambda_{11}\Delta t}-\lambda_{13}\Delta te^{-\lambda_{13}\Delta t}$
AbsT1	State 0	State 1	
State 0	$1-\lambda_{11}{}'\Delta te^{-\lambda_{11}{}'\Delta t}$	$\lambda_{11}{}'\Delta te^{-\lambda_{11}{}'\Delta t}$	
State 1	$e^{-\lambda_{11}{}'\Delta t}$	$1-e^{-\lambda_{11}{}'\Delta t}$	

Table 5. State transition matrix for organizational management factors nodes.

t	$(t+\Delta t)$		
Organizational management factors	State 0	State 1	State 2
State 0	1	0	0
State 1	v	1 − v	0
State 2	0	v	1 − v

Notes: According to [20, 27, 28] (1) $\Delta t = 1$ means the transition time slice is 1 year. (2) $\lambda_2 = \lambda_5$, $\lambda_3 = \lambda_6 = \lambda_8$, $\lambda_4 = \lambda_7 = \lambda_9 = \lambda_{10}$, $\lambda = \lambda_1 + \lambda_2 + \lambda_3 + \lambda_4$, $\lambda_1 : \lambda_2 : \lambda_3 : \lambda_4 = 1{:}7{:}3{:}2$, $\lambda = 12/365$, where λ satisfies denotes the monthly failure rate of equipment and facilities. Then $\lambda_1 = 0.00253$, $\lambda_2 = \lambda_5$=0.01770, $\lambda_3 = \lambda_6 = \lambda_8$=0.00759, $\lambda_4 = \lambda_7 = \lambda_9 = \lambda_{10}$=0.00506. $\mu = \mu_1 + \mu_2 + \mu_3 + \mu_4$, $\mu_1 : \mu_2 : \mu_3 : \mu_4$=6:2:1:1, μ =10%, where μ implies that the repair of equipment and facilities can result in a 10% reduction in the failure probability of associated influential factors. Then $\mu_1 = 0.06, \mu_2 = 0.02, \mu_3 = 0.01, \mu_4$ 0.01. $\lambda_2{}' = \lambda_4{}', \lambda_3{}' = \lambda_5{}' = \lambda_6{}', \lambda_1{}' + \lambda_2{}' + \lambda_3{}' = \lambda', \lambda_1{}' : \lambda_2{}' : \lambda_3{}' = 1{:}6{:}3$, $\lambda' = 12/365$, then $\lambda_1{}' = 0.00329$, $\lambda_2{}' = \lambda_4{}'$=0.01973, $\lambda_3{}' = \lambda_5{}' = \lambda_6{}'$=0.0986. $\mu' = \mu_1{}' + \mu_2{}' + \mu_3{}', \mu_1{}' : \mu_2{}' : \mu_3{}' = 7{:}2{:}1$, $\mu' = 10\%$, then $\mu_1{}' = 0.07, \mu_2{}' = 0.02, \mu_3{}' = 0.01$. $\lambda_1{}'' = \lambda_3{}'', \lambda'' = \lambda_1{}'' + \lambda_2{}'', \lambda_1{}'' : \lambda_2{}'' = 3:7, \lambda'' = 12/365$, then $\lambda_1{}'' = \lambda_3{}'' = 0.00986, \lambda_2{}'' = 0.02301$. $\mu'' = \mu_1{}'' + \mu_2{}'', \mu_1{}'' : \mu_2{}'' = 7{:}3, \mu'' = 10\%$, then $\mu_1{}'' = 0.07, \mu_2{}'' = 0.03$. (3) $\lambda_{11} = \lambda_{13}, \lambda' = \lambda_{11} + \lambda_{12}, \lambda_{11} : \lambda_{12} = 3{:}7, \lambda' = 12$, where λ' denotes a monthly human error occurrence, then $\lambda_{11} = \lambda_{13} = 3.6, \lambda_{12} = 8.4$. (4) $v = 0.1$ denotes a 10% growth rate in organizational management experience.

2.3 Dynamic Optimization Strategies for Daily Operational Resilience Based on Critical Importance Analysis

This study applies Critical Importance (CI) analysis within the DBN framework to determine resilience factors optimization priorities across time periods and formulate dynamic operational resilience strategies. CI quantifies root-to-leaf node failure probability change rate ratios, demonstrating higher optimizability for root nodes with elevated failure probabilities versus lower probability nodes [29, 30]. The root node possesses three discrete states: 2 (complete failure), 1 (partial failure), and 0 (reliable state). Equation (2) determines its Condition Index (CI) for any specific operational period.

$$CI_i = \frac{P(Xr_i = 2) * [P(R = 2|Xr_i = 2) - P(R = 2|Xr_i = 1) - P(R = 2|Xr_i = 0)]}{P(R = 2)} \tag{2}$$

Here, Xr_i represents the root node. $P(R = 2|)$ denotes the conditional probability of the child node, and $P(R = 2)$ signifies its unconditional failure probability.

3 Case Study

3.1 Project Overview: Tunnel W System

Tunnel W faces problems of foundation settlement, sliding, and insufficient bearing capacity due to its location in deep soft silt strata. Complex hydrogeological conditions with dense river networks further create groundwater environments causing concrete structure corrosion. Safe tunnel operation relies critically on electromechanical equipment reliability and personnel adherence to standardized O&M procedures. Although individual equipment failures or human errors during maintenance exhibit low probability, their cumulative effects significantly elevate operational safety risks. Addressing these challenges, this study develops a daily operational resilience assessment and optimization framework for the tunnel W system, demonstrating significant practical value for incident risk and loss mitigation.

3.2 Daily Operational Resilience Assessment of the Tunnel W System

Calculation of Node Probability Tables. This research establishes the node probabilities by employing a multi-source data fusion approach. The prior probabilities for nodes $AbsT_1$, $AbsT_2$, $AbsT_8$, $AbsT_{21}$, and their parent nodes derive from historical statistics and literature. The remaining probabilities were acquired through an expert questionnaire survey. This research developed the "Questionnaire on Causal Relationships Among Factors Influencing Daily Operational Resilience of the Road Tunnel W" (Questionnaire B) for systematic analysis of causal relationships among influencing factors. The survey results facilitated the development of the node probability tables. For reliable professional assessment, the study selected ten respondents from Questionnaire A participants possessing extensive practical experience as the target group for Questionnaire B distribution. The primary objective focused on enhancing research quality

via in-depth expert evaluation rather than increasing sample size. All selected respondents participated in the systematic assessment of causal relationships between nodes for the DBN model. The study achieved a 100% valid response rate by collecting all ten distributed questionnaires, ensuring complete data integrity.

Statistical data indicate that national and Zhejiang provincial motor vehicle accident rates remained under 0.15% during 2010–2022. Figure 2 reveals Zhejiang's accident rate slightly exceeded the national average between 2016 and 2022 but remained low. Based on historical trend analysis, this study conservatively estimates future traffic accident probabilities in Zhejiang will remain below 0.15%. Therefore, the traffic accident node ($AbsT_1$) receives a probability of 0.15%, indicating its probability for being in failure state (State 1) equals 0.0015.

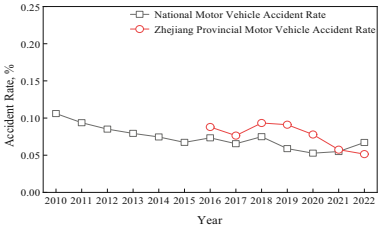

Fig. 2. Motor vehicle accident rates in China and Zhejiang province from 2010 to 2022.

Figure 3 indicates that Hangzhou experienced 1,752 days of adverse weather (rain or snow) between January 2011 and June 2024, which accounts for 37.5% of the total period. Consequently, this study defines the adverse weather probability for Hangzhou as 37.5%, denoting the probability that weather conditions ($AbsT_2$) reach failure state (State 1).

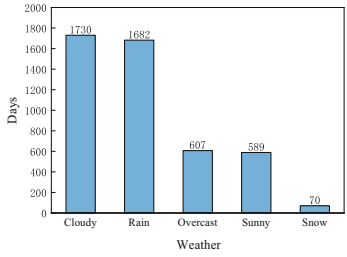

Fig. 3. Weather statistics for Hangzhou from January 1, 2011 to June 30, 2024.

The states of nodes for tunnel electromechanical system safety ($AbsT_8$) and tunnel structural safety ($AbsT_{21}$) depend on the technical conditions of their respective sub-nodes ($AbsT_3$–$AbsT_7$ and $AbsT_9$–$AbsT_{20}$) [21]. These sub-node conditions derive from daily inspections, monitoring, and periodic testing. Since the tunnel remains in its initial service period, this study considers both $AbsT_8$ and $AbsT_{21}$ optimal. Future updates

might integrate actual tunnel condition data for node states. Probability tables for nodes beyond $AbsT_1$, $AbsT_2$, $AbsT_8$, and $AbsT_{21}$ can be derived using Sect. 2.2.

Developing a DBN Model for Daily Operational Resilience Assessment. As shown in Fig. 4, this study establishes a 54-node DBN model incorporating five evaluation metrics, ten scenario state variables, and thirty-nine influencing factors. $AbsT_8$ and $AbsT_{21}$ node states are excluded from the model since they are assessed according to historical tunnel technical conditions of 17 sub-nodes ($AbsT_3$–$AbsT_7$ and $AbsT_9$–$AbsT_{20}$) based on the Technical Specifications of Maintenance for Roadway Tunnel (JTGH12-2015) [21].

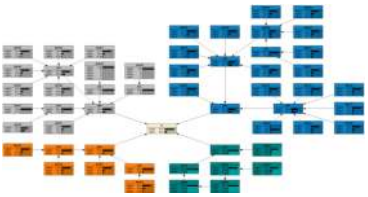

Fig. 4. The DBN Model for Daily Operational Resilience of the Tunnel W System.

Results of Daily Operational Resilience Assessment. This study develops an 11 times DBN model to simulate the decade-long operational evolution of the tunnel W system. Figure 5 demonstrates significant divergence in daily resilience metrics under conventional maintenance lacking scientific operation strategies: The resilience value decreases from 0.802 to 0.762, absorption capacity plummets from 0.744 to 0.620, resistance capability drops from 0.626 to 0.515, and recovery performance declines from 0.875 to 0.847. Conversely, adaptation capacity rises from 0.923 to 0.963. Continuous degradation affects all metrics except adaptation, primarily from equipment aging, human errors, and insufficient organizational learning. Results indicate accumulated management experience cannot offset infrastructure deterioration effects. To counteract this trend, lifecycle operation strategies should focus on equipment monitoring, personnel training, and systematic knowledge transfer for enhanced urban highway tunnel resilience.

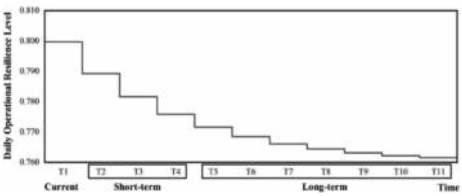

Fig. 5. Predicted resilience curve for the \Tunnel W system over the next ten years.

3.3 Optimization Strategies for Daily Operational Resilience of the Tunnel W System

Critical Importance Analysis. This study applies Sect. 2.3. Dynamic Optimization Strategies for Daily Operational Resilience Based on Critical Importance Analysis's computational methodology to evaluate annual critical importance (CI) for 34 root nodes, enabling formulation of dynamic resilience enhancement strategies. CI values categorize optimization priorities into three tiers: Level 1 ($CI_i > 0.30$), Level 2 ($0.15 < CI_i \leq 0.30$), and Level 3 ($CI_i \leq 0.15$).

Figure 6 reveals minimal CI fluctuations for most facility and equipment factors, which consistently rank as Tier 3 priorities. $AbsT_{21}$ exhibits notable CI variation, with values rising from 0 at T1 to 0.1323 by T11.

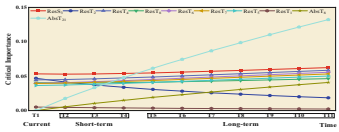

Fig. 6. Evolving optimization priorities for facility and equipment factors in the W tunnel system.

As Fig. 7 indicates, most facility and equipment factors exhibit rising critical importance trends except $ResO_7$, with progressive priority elevation from Tier 3 to Tier 2 occurring over time. At T1, all facility factors hold Tier 3 priority. During T2-T4, $RecO_3$, $AbsO_2$, and $AbsS_2$ become elevated to Tier 2. The T5-T11 period sees four additional factors reaching Tier 2 status: $AbsO_3$, $ResO_6$, $AbsS_1$, and $AbsO_4$.

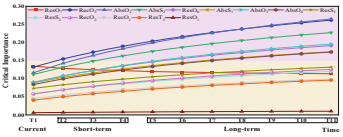

Fig. 7. Evolving optimization priorities for human operational factors in the tunnel W system.

Figure 8 reveals declining critical importance trends among organizational management factors, particularly pronounced for $AbsE_1$ and $RecE_1$. At T1, $AbsE_1$ and $RecE_1$ hold Tier 1 optimization priority versus $AdaE_1$'s Tier 2 ranking. Between T2 and T4, $AbsE_1$ and $RecE_1$ retain Tier 1 status while $AdaE_1$ declines to Tier 3. From T5 to T11, both $AbsE_1$ and $RecE_1$ decrease to Tier 2 as other nodes persist at Tier 3.

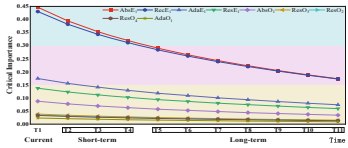

Fig. 8. Evolving optimization priorities for organizational management factors in the tunnel W system.

Optimizing Daily Operational Resilience: Dynamic Strategies. At T1, decision-makers should allocate maximum resources to optimize $AbsE_1$, $RecE_1$, and $AdaE_1$, thus improving tunnel absorption, recovery, and adaptation capacities.

During short-term phase T2–T4, prioritization targets Tier 1 factors ($AbsE_1$, $RecE_1$) and Tier 2 factors ($RecO_3$, $AbsO_2$, $AbsS_2$). Implementation requires:

(1) Enhanced human/financial resource allocation for safety training and maintenance teams;
(2) Optimized post-disaster resource deployment for accelerated operational recovery;
(3) Streamlined operational restoration procedures to enable rapid tunnel reopening;
(4) Strengthened electromechanical maintenance and safety inspection regimes;
(5) Expanded public risk awareness programs to reduce traffic accident likelihood.

Throughout long-term operations (T4–T11), resource allocation capabilities decline in critical importance while human operational factors become prominent. This shift reflects diminishing marginal returns beyond T8 for resource optimization. Optimization focus must transition toward personnel factors since $AbsO_2$, $RecO_3$, $AbsS_2$, $AbsO_3$, and $ResO_6$ sequentially exceed $AbsE_1$/$RecE_1$ in significance. Key strategies should include:

(1) Rigorous enforcement of electromechanical maintenance and safety protocols;
(2) Accelerated operational restoration workflows;
(3) Expanded public safety education initiatives;
(4) Improved civil maintenance crew performance and hazard response timeliness;
(5) Guaranteed unimpeded evacuation/rescue route accessibility.

4 Conclusions

This study successfully establishes a daily operational resilience assessment framework specifically designed for urban roadway tunnel systems to facilitate long-term, efficient, and resilience-oriented operations. Framework development identified 56 critical resilience-influencing factors across technical, organizational, social, and economic dimensions, forming the methodology's foundation.

Application to the Tunnel W case revealed a notable resilience decline from 0.802 to 0.762. This deterioration primarily resulted from inadequate systematic management during prolonged operations, exacerbated by equipment aging and inherent human error randomness despite accumulated organizational experience.

Optimization strategies require immediate focus on enhanced resource allocation to bolster resilience. Long-term sustainability demands progressive evolution toward prioritizing electromechanical maintenance, safety inspections, robust operational recovery, and public risk awareness enhancement. Critical attention should target civil structural maintenance, safety checks, and optimal evacuation route accessibility.

The Bayesian network probability tables utilized combined historical data and expert elicitation. Future research must reduce reliance on expert judgment to decrease subjectivity, thereby enhancing assessment accuracy and robustness for more reliable urban tunnel resilience evaluations.

References

1. Zheng, G., Cheng, X., Zhou, H., et al.: Resilient evaluation and control in geotechnical and underground engineering. China Civ. Eng. **55**(7), 1–38 (2022). https://doi.org/10.15951/j.tmgcxb.2022.07.0419
2. Ren, G.F., Chen, S., Zhou, C., et al.: Research on health and safety assessment method of shield tunnel structure during operational period. Wuhan Univ. Technol. (Inf. Manag. Eng.). **45**(4), 520–526 (2023). https://doi.org/10.3963/j.issn.2095-3852.2023.04.004
3. Song, J., Liu, S., Bi, Y., et al.: Dynamic safety evaluation and management of highway tunnel group in operation period based on factor-time variable weight model. Sci. Technol. Eng. **20**(23), 9634–9639 (2020). https://doi.org/10.3969/j.issn.1671-1815.2020.23.056
4. Zhou, B., Wang, C., Liu, F., et al.: Study on risk assessment model and management system for urban traffic tunnel operation safety. Highway Transp. Res. Dev. **38**(1), 97–103 (2021). https://doi.org/10.3969/j.issn.1002-0268.2021.01.012
5. Xiao, S.: Research on operational safety risk assessment and control technology of expressway long tunnel. Master's Degree, Chang'an University, Xi'an (2021). https://doi.org/10.26976/d.cnki.gchau.2020.002113
6. Gong, H.J., Wei, X.: Study on comprehensive evaluation of operation safety of expressway tunnel. Highway Transp. Res. Dev. **27**(8), 127–130, 135 (2010). https://doi.org/10.3969/j.issn.1002-0268.2010.08.024
7. Lin, P.D., Zhang, D., Yan, J., et al.: Study on assessment method for structural safety of operating shield-bored tunnels. Tunnel Constr. **35**(S2), 43–49 (2015). https://doi.org/10.3973/j.issn.1672-741X.2015.S2.009
8. Luo, Y., Li, Y., Yuan, J., et al.: Research on risk assessment of operational safety for highway tunnels. Mod. Tunneling Technol. **53**(6), 25–30 (2016). https://doi.org/10.13807/j.cnki.mtt.2016.06.004
9. Wang, Z.J., Wang, R., Shu, Y., et al.: Research on risk assessment of operational safety for long tunnels and tunnel groups on highways. Mod. Tunneling Technol. **56**(S2), 36–43 (2019). https://doi.org/10.13807/j.cnki.mtt.2019.S2.006
10. Wu, X.G., Qin, Y., Shen, M., et al.: Research on health and safety risk assessment of operational tunnels based on cloud reasoning. China Saf. Sci. J. **27**(2), 133–138 (2017). https://doi.org/10.16265/j.cnki.issn1003-3033.2017.02.024
11. Holling, C.S.: Resilience and stability of ecological systems. Annu. Rev. Ecol. Syst., 1–23 (1973). https://doi.org/10.1146/annurev.es.04.110173.000245
12. Chen, Q., Huang, Q., Chen, Z., et al.: Quantitative evaluation of resilience of metro engineering system based on Bayesian networks. China Saf. Sci. J. **28**(11), 98–103 (2018). https://doi.org/10.16265/j.cnki.issn1003-3033.2018.11.01
13. Lin, X.T., Chen, X., Su, D., et al.: Evaluation method for resilience of shield tunnel linings considering multiple disturbances and its application. Chin. J. Geotech. Eng. **44**(4), 591–601 (2022). https://doi.org/10.11779/CJGE202204001
14. Yin, J.T., Ren, X.L., Liu, R.H., et al.: Quantitative analysis for resilience-based urban rail systems: a hybrid knowledge-based and data-driven approach. Reliab. Eng. Syst. Saf. **219**, 108183 (2022). https://doi.org/10.1016/j.ress.2021.108183
15. Yin, Z.W.: Research on operation resilience assessment of subway tunnel system based on dynamic Bayesian network (dbn). Master's Degree, Huazhong University of Science and Technology, Wuhan (2020). https://doi.org/10.27157/d.cnki.ghzku.2020.000917
16. Kammouh, O., Gardoni, P., Cimellaro, G.P.: Probabilistic framework to evaluate the resilience of engineering systems using Bayesian and dynamic Bayesian networks. Reliab. Eng. Syst. Saf. **198**, 106813 (2020). https://doi.org/10.1016/j.ress.2020.106813

17. Fan, Y.Y., Han, S., Jiang, X., et al.: Highland railway operational safety system resilience evaluation based on combined weighting-Euclid distance. J. Railway Sci. Eng. **20**(9), 3536–3546 (2023). https://doi.org/10.19713/j.cnki.43-1423/u.t20221861
18. Bi, W.: Resilience identification and assessment of urban subway station systems to fire disasters. Master's Degree, Southeast University, Nanjing (2020). https://doi.org/10.27014/d.cnki.gdnau.2020.000847
19. Weng, Y., Li, A., Zhao, T., et al.: Research on factors influencing the resilience of the tunnel system and related evaluation. Mod. Tunneling Technol. **60**(5), 40–47 (2023). https://doi.org/10.13807/j.cnki.mtt.2023.05.005
20. Tang, Y., Bi, W., Vargal, L., et al.: An integrated framework for managing fire resilience of metro station system: identification, assessment, and optimization. Int. J. Disaster Risk Reduct. **77**, 103037 (2022). https://doi.org/10.1016/j.ijdrr.2022.103037
21. Jtg H12-2015: Technical Specifications of Maintenance for Highway Tunnel. China Communication Press, Beijing (2015)
22. Xi, Y.J.: Research on Sensitivity of Operation Safety Indicators and Prevention and Control Strategies for Highway Tunnels. Master's Degree, Chongqing Jiaotong University, Chongqing (2023). https://doi.org/10.27671/d.cnki.gcjtc.2023.000734.
23. Jtg 3370.1-2018: Design Specifications for Highway Tunnels: Part 1 Civil Engineering Works. China Communication Press, Beijing (2015)
24. Kang, N.: Study on comprehensive model for fire risk assessment in road tunnel operation. Doctoral Dissertation, China University of Mining & Technology-Beijing, Beijing (2020). https://doi.org/10.27624/d.cnki.gzkbu.2019.000070
25. Li, M.: Study on the risk assessment method of railway tunnel complex system based on Bayes and complex network. Master's Degree, Shijiazhuang Tiedao University, Shijiazhuang (2020). https://doi.org/10.27334/d.cnki.gstdy.2020.000043
26. Liu, X.R.: Fault tree and Bayesian network model for fatal and injury crashes on mountainous freeways. Master's Degree, Harbin Institute of Technology, Harbin (2020). https://doi.org/10.27061/d.cnki.ghgdu.2019.004106
27. Cai, B., Liu, Y., Fan, Q., et al.: Performance evaluation of subsea bop control systems using dynamic Bayesian networks with imperfect repair and preventive maintenance. Eng. Appl. Artif. Intell. **26**(10), 2661–2672 (2013). https://doi.org/10.1016/j.engappai.2013.08.011
28. Li, Y.L.: Probability Analysis of Offshore Fire Based on Dynamic Bayesian Network. China University of Petroleum (East China), Qingdao (2018)
29. Zhou, Q.: Study on reliability analysis and maintenance mode decision of metro train bogie system. Jiaotong University, Beijing, Master's Degree (2020)
30. Guo, S.W.: Reliability analysis of compressor unit based on dynamic Bayesian network. University of Electronic Science and Technology of China, Chengdu, Master's Degree (2024). https://doi.org/10.27005/d.cnki.gdzku.2023.004258

Research on the Impact of Unfavorable Topography on the Seismic Safety of Gravity Dams with Deep Anti-sliding Stability

Dudu Su[1], Chunli Yan[2(✉)], Songtao Zhao[1], Jin Tu[2], and Hui Liang[2]

[1] Gansu Water Resources and Hydropower Survey Design and Research Institute Limited Liability Company, Lanzhou 730000, China
[2] China Institute of Water Resources and Hydropower Research, Beijing 100038, China
yancl@iwhr.com

Abstract. The topography conditions and weak interlayers of the bedrock may impact the seismic safety of the dam-foundation system to varying degrees. This paper takes a gravity dam with deep anti-sliding stability issues as an example to investigate whether the unfavorable topography of the downstream bedrock is considered. The impacts of unfavorable topography on the seismic safety of the dam-foundation system are compared and analyzed using the overload analysis method and strong analysis storage method from the sliding failure process of the different sliding surfaces, the maximum compressive stress on the downstream of the bedrock slider, and the maximum residual slippage. The sliding yield zone penetration is taken as the evaluation criterion to evaluate the ultimate seismic capacity of the dam-foundation system. The results indicate that when unfavorable topography is considered, the overload coefficient or strong storage coefficient corresponding to the complete sliding of sliding surfaces is smaller, the maximum compressive stress on the bedrock slider downstream increases, and the maximum residual sliding slippage is larger. Therefore, the influence of downstream unfavorable topography should be considered from a safety perspective.

Keywords: Unfavorable Topography · Deep Anti-Sliding Stability · Gravity Dams · Overload Analysis · Strong Storage Analysis

1 Introduction

In actually, various unfavorable weak layers may exist within the bedrock. If their orientation is conducive to the sliding of the dam body, it will easily pose a significant threat to the anti-sliding stability of the dam-foundation system [1–3]. According to incomplete statistics, as of 1979, 92 large and medium-sized dams in China had been built, under construction, and in design contained weak interlayers. Therefore, the deep anti-sliding stability has always been a critical issue in dam design [4–6]. Chen et al. [7] study the deep anti-sliding stability problem under natural bedrock conditions through model tests, revealing the mechanisms influencing dam-foundation system stability and proposing corresponding reinforcement measures. Zhou et al. [8] introduce three different types of

© The Author(s), under exclusive license to Springer Nature Switzerland AG 2027
G. Feng et al. (Eds.): ICCE 2025, SUCI, pp. 527–539, 2027.
https://doi.org/10.1007/978-3-032-32237-1_37

deep sliding failure in gravity dams and point out the unclear and unreasonable aspects in limit state design formulation for sliding stability along double inclined planes within the Code for Design of Concrete Gravity Dams (DL5108-1999) [9], subsequently proposing a more rational design formulation. Peng et al [10] evaluate the advantages and disadvantages of various deep sliding stability analysis methods, and discuss the potential future developments for these methods. Wang et al. [11] employ the overloading-strength reduction method to investigate the deep sliding stability of gravity dams containing multiple weak interlayers within the bedrock. Moreover, different topographical conditions may differently influence the deep anti-sliding stability of the dam-foundation system. Thus, it is necessary to investigate the impact of unfavorable topography on the seismic safety of gravity dams with deep anti-sliding stability issues.

This paper takes a gravity dam with deep anti-sliding stability issues as an example to investigate whether the unfavorable topography of the downstream bedrock is considered. Two three-dimensional finite element models of the dam-foundation system with and without considering the unfavorable topography are developed. Nonlinear dynamic response analyses of the dam-foundation system are performed for different models using the overload method and strong storage method, respectively. Then, the sliding failure process of the different sliding surfaces, the maximum compressive stress on the downstream of the bedrock slider, and the maximum residual slippage are compared and analyzed, and the ultimate seismic capacity of the dam-foundation system is evaluated.

2 Calculation Models and Conditions

2.1 Calculation Models

Finite Element Model of the Dam-Foundation System without Considering Unfavorable Topography. This study takes a gravity dam with deep anti-sliding stability issues as an example. A 3D finite element mesh of the dam-foundation system containing multiple faults and fractures is generated according to the topographical and geological characteristics of the dam site, as illustrated in Fig. 1. The dam element size is approximately 5 m, and the upstream, downstream, and depth extents of the foundation are taken as approximately twice the dam height. Figure 2 shows the diagram of faults and fractures distribution. Figure 3 shows the diagram of faults and fractures contact surfaces.

Finite Element Model of the Dam-Foundation System Considering Unfavorable Topography According to the on-site excavation, it is found that the bedrock at the downstream side of the gravity dam is thin. Therefore, the finite element mesh model of the downstream bedrock is modified from the original model (which neglected unfavorable topography) to ensure the safety of the dam-foundation system. The downstream bedrock is simulated as a free surface in the finite element analysis. The modified finite element mesh model of the dam-foundation system is shown in Fig. 4.

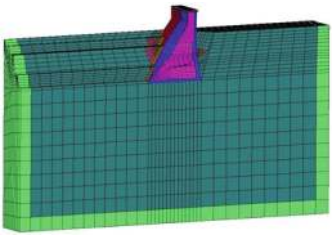

Fig. 1. Finite element mesh model of the dam-foundation system without considering the unfavorable topography.

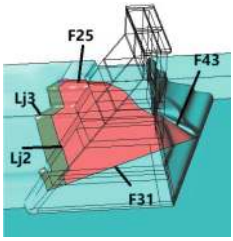

Fig. 2. Diagram of faults and fractures distribution.

Fig. 3. Diagram of faults and fractures contact surfaces.

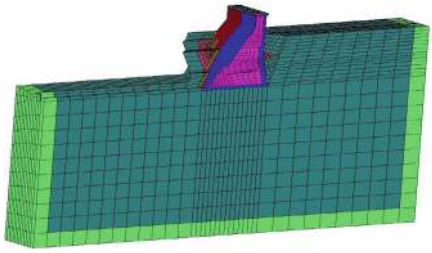

Fig. 4. Finite element mesh model of the dam-foundation system considering unfavorable topography.

2.2 Calculation Conditions

The contact surface parameters in the model are as follows: the friction coefficient of contraction joints, interface of the dam-foundation, F31, F43, F25, Lj2 and Lj3, are 0.8, 1.03, 0.4, 0.5, 0.5, 0.8 and 0.8 respectively; and the cohesion are 0 MPa, 0.72 MPa, 0.065 MPa, 0.09 MPa, 0.09 MPa, 0.405 MPa and 0.405 MPa respectively. The contact surfaces are simulated using the dynamic contact force model based on the Lagrange multiplier method.

Static and dynamic loads: the self-weight of the dam, upstream and downstream water pressure, sediment pressure, uplift pressure, and seismic load. The density of the dam and foundation is 2400 kg/m^3 and 2670 kg/m^3, respectively; The water level of upstream and downstream is 1432 m and 1365.16 m, respectively; The elevation of sediment is 1383.5 m; The bulk density of sediment is 8.0 kN/m^3, and the internal friction angle is 13°. The uplift pressure head of the interface of the dam-foundation is determined according to the *S*tandard for Load on Hydraulic Structures (GB/T 51394-2020) [12]. The uplift pressure head of faults and fractures is the sum of the dam-foundation uplift pressure head and the elevation difference between the fault/fracture and the dam-foundation interface. The radiation damping effect of the foundation is simulated using a viscoelastic artificial boundary. Displacement and velocity time history are converted into equivalent nodal

loads applied on the artificial boundary to complete the seismic input. Artificial earthquake acceleration time history curves are shown in Fig. 5. Dam-reservoir interaction is simulated using the Westergaard added-mass approach [13].

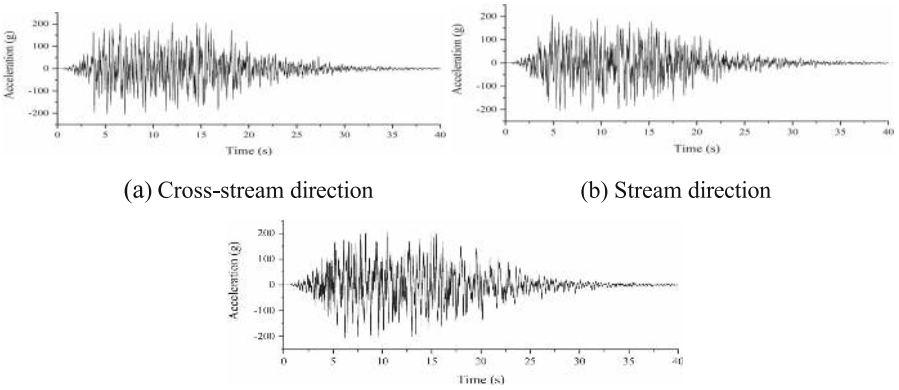

(a) Cross-stream direction (b) Stream direction

(c) Vertical direction

Fig. 5. Artificial earthquake acceleration time history curves.

3 Analysis Results and Discussion

3.1 Overload Analysis

The overload analysis method is used to carry out the nonlinear dynamic response analysis in this section by taking the ground motion amplification of 2.0, 3.0, 4.0, and 4.5 times as the input. The sliding yield zone penetration is taken as the evaluation criterion for the dam-foundation system reaching its ultimate state, which is used to determine the minimum overload coefficient corresponding to the failure of the dam-foundation system.

Table 1 presents the overload coefficients corresponding to complete sliding of different sliding surfaces under different topographic conditions. Figures 6 and 7 show the residual slippage of the dam-foundation interface-fault-fracture under design earthquake without and with considering unfavorable topographies, respectively. Figures 8 and 9 show the minimum principal stress of bedrock under the design earthquake without and with considering unfavorable topography, respectively. From figures and tables, under the design seismic conditions, without considering the influence of unfavorable topography, contact surfaces F25, F43, F31, Lj2, Lj3, and the interface of the dam-foundation do not undergo complete sliding. The maximum compressive stress on the downstream side of the slider is generally below 0.5 MPa. When unfavorable topography effects are accounted for, only F43 experiences complete sliding, while other sliding surfaces do not experience complete sliding. The sliding failure range of the sliding surface, the maximum residual sliding displacement, and the maximum compressive stress

on the downstream side of the bedrock slider increase compared with the results of without considering unfavorable topography. The maximum compressive stress reaches approximately 1 MPa. This shows that the gravity dam does not form a sliding yield zone penetration channel under the design earthquake, with or without considering the unfavorable topography, which meets the requirements of deep anti-sliding stability. In addition, based on the saturated compressive strength of 45 MPa for Class III2 rock mass, the rock compressive strength calculated as one-fifteenth of this value is 3 MPa. If the enlarged coefficient of dynamic solution is 1.5, the compressive strength is 4.5 MPa, indicating that the bearing capacity of rock still has a significant safety margin.

Table 1. Overload coefficients corresponding to complete sliding of different sliding surfaces under different topographic conditions.

Overload coefficient	Without unfavorable topography effects						With unfavorable topography effects					
	F 43	F 25	F 31	Lj 2	Lj 3	Interface of dam-foundation	F 43	F 25	F 31	Lj 2	Lj 3	Interface of dam-foundation
1.0							⊗					
2.0	⊗						⊗					
3.0	⊗	⊗					⊗	⊗	⊗			
4.0	⊗	⊗	⊗				⊗	⊗	⊗			
4.5	⊗	⊗	⊗	⊗			⊗	⊗	⊗	⊗		

Note: ⊗ indicates that the corresponding sliding surface has complete sliding.

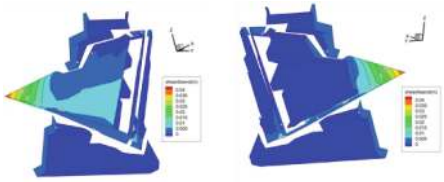

Fig. 6. Residual slippage of the dam foundation interface-fault-fracture under design earthquake without considering unfavorable topography.

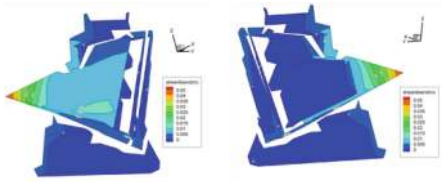

Fig. 7. Residual slippage of the dam-foundation interface-fault-fracture under design earthquake considering unfavorable topography.

Figures 10, 11, 12, 13 and Figs. 14, 15, 16, 17 show the residual slippage of the dam-foundation interface-fault-fracture under 2.0, 3.0, 4.0, and 4.5 times the design earthquake with and without considering unfavorable topography. Under overload conditions, without considering the influence of unfavorable topography, sliding surfaces F43, F25, F31, and Lj2 slide completely when the overload coefficient is 2.0, 3.0, 4.0, and 4.5, respectively. When considering unfavorable topography, sliding surfaces F43, F25, F31, and Lj2 slide completely when the overload coefficient is 1.0, 3.0, 3.0, and 4.5,

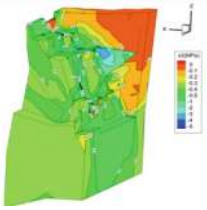

Fig. 8. Minimum principal stress of bedrock under design earthquake without considering unfavorable topography.

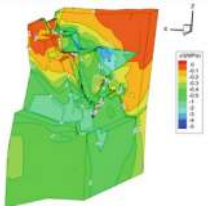

Fig. 9. Minimum principal stress of bedrock under design earthquake considering unfavorable topography.

respectively. When the overload coefficient is 4.0, a complete sliding yield zone penetration channel is not formed with or without considering the influence of unfavorable topography. The maximum compressive stress on the downstream side of the bedrock slider is approximately 1.5 MPa (as shown in Fig. 18) and below 4.0 MPa (as shown in Fig. 19), respectively. However, localized compressive stress values exceeding 4.5 MPa appear in stress concentration zones at the bedrock slope toe within the model. This is primarily attributed to assumptions regarding the shape of the free face. Nevertheless, even if local minimal yielding occurs in the bedrock, there remains a considerable distance before a yield zone penetrates the free face. When the overload coefficient is 4.5, the F25, Lj2, and the dam-foundation interface on the downstream side of the Lj2, F43, and the dam-foundation interface on the upstream side of the F43, F31, and the dam-foundation interface on the upstream side of the F31 form a complete sliding channel under the two topography conditions. Thus, the overload coefficient of 4.0 can be taken as the ultimate seismic capacity of the dam-foundation systems.

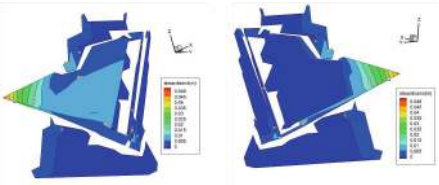

Fig. 10. Residual slippage of the dam-foundation interface-fault-fracture under 2.0 times design earthquake without considering unfavorable topography.

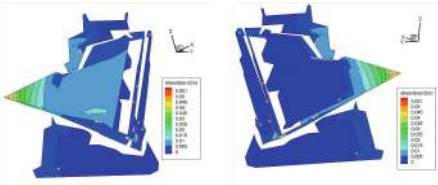

Fig. 11. Residual slippage of the dam-foundation interface-fault-fracture under 3.0 times design earthquake without considering unfavorable topography.

From the above analysis result, considering the unfavorable topography, the overload coefficient corresponding to complete sliding on the sliding surface F43 and F31 becomes smaller, the maximum compressive stress at the downstream side of the bedrock slider increases, and the residual sliding displacements under different overload coefficients are consistently larger (as shown in Fig. 20). This show that although the overload coefficient of ultimate seismic capacity remains the same under these two topography conditions, from the perspectives of overload coefficients corresponding to complete sliding on

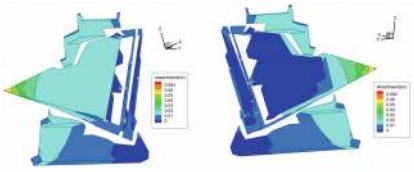

Fig. 12. Residual slippage of the dam-foundation interface-fault-fracture under 4.0 times design earthquake without considering unfavorable topography.

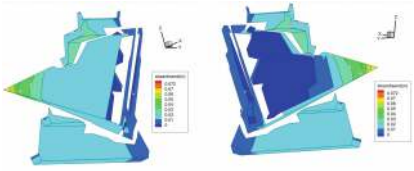

Fig. 13. Residual slippage of the dam-foundation interface-fault-fracture under 4.5 times design earthquake without considering unfavorable topography.

Fig. 14. Residual slippage of the dam-foundation interface-fault-fracture under 2.0 times design earthquake considering unfavorable topography.

Fig. 15. Residual slippage of the dam-foundation interface-fault-fracture under 3.0 times design earthquake considering unfavorable topography.

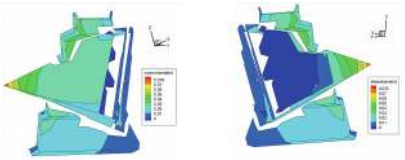

Fig. 16. Residual slippage of the dam-foundation interface-fault-fracture under 4.0 times design earthquake considering unfavorable topography.

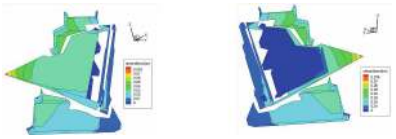

Fig. 17. Residual slippage of the dam-foundation interface-fault-fracture under 4.5 times design earthquake considering unfavorable topography.

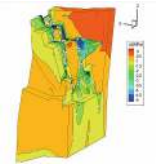

Fig. 18. Minimum principal stress of bedrock under 4.0 times design earthquake without considering unfavorable topography.

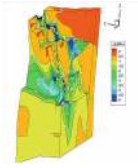

Fig. 19. Minimum principal stress of bedrock under 4.0 times design earthquake considering unfavorable topography.

different sliding surfaces, the maximum compressive stress on the downstream side of the bedrock slider, and the maximum residual sliding displacement, it is advisable to account for the influence of unfavorable topography.

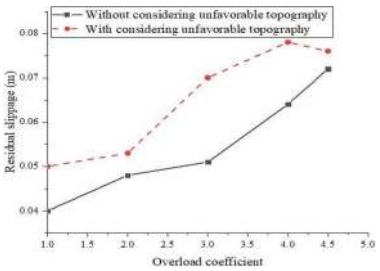

Fig. 20. Residual slippage of the dam-foundation interface-fault-fracture under different overload coefficients without considering and considering unfavorable topography.

3.2 Strong Storage Analysis

The strong storage analysis method is used to carry out the nonlinear dynamic response analysis in this section. The shear strength parameters of sliding surfaces are progressively reduced by coefficients of 2.0, 3.0, 4.0, 5.0, and 6.0 times as the input. The sliding yield zone penetration is taken as the evaluation criterion for the dam-foundation system reaching its ultimate state, which is used to determine the minimum strong storage coefficient corresponding to the failure of the dam-foundation system.

Table 2 shows strong storage coefficients corresponding to complete sliding of different sliding surfaces under different topographic conditions. Figures 21, 22, 23, 24, 25 and Figs. 26, 27, 28, 29, 30 show residual slippage of the dam-foundation interface-fault-fracture under 2.0, 3.0, 4.0, 5.0, and 6.0 times strong storage coefficient without and with considering unfavorable topography.

From figures and tables, without considering the influence of unfavorable topography, sliding surfaces F25, F43, F31, Lj3, and the interface of dam-foundation occur complete sliding at the strong storage coefficient of 2.0, 2.0, 2.0, 6.0, and 4.0, respectively. When the strong storage coefficient is 5.0, a complete sliding penetration channel is not formed. The maximum compressive stress on the downstream side of bedrock slider is below 1.0 MPa expect for localized stress concentration at the bedrock toe, not exceeding the bearing capacity of bedrock, as shown in Fig. 31.

When the strong strong coefficient is 6.0, the sliding surfaces F43, F25, F31, Lj3, and the interface of the dam-foundation form a complete sliding penetration channel. Thus, the strong storage coefficient of 5.0 can be taken as the current strong storage safety coefficient.

Considering the influence of unfavorable topography, sliding surfaces F25, F43, F31, Lj3, and the interface of dam-foundation occur complete sliding at the strong storage coefficient of 2.0, 2.0, 2.0, 5.0, and 4.0, respectively. When the strong coefficient is 4.0, a complete sliding penetration channel is not formed. The maximum compressive stress on the downstream side of bedrock slider is below 2.5 MPa expect for localized stress concentration at the bedrock toe, not exceeding the bearing capacity of bedrock, as shown in Fig. 32. When the strong strong coefficient is 5.0, the sliding surfaces F43, F25, F31, Lj3, and the interface of the dam-foundation form a complete sliding penetration channel. Thus, the strong storage coefficient of 4.0 can be taken as the current strong storage safety coefficient.

Table 2. Strong storage coefficients corresponding to complete sliding of different sliding surfaces under different topographic conditions.

	Without unfavorable topography effects						With unfavorable topography effects					
Strong storage coefficients	F43	F25	F31	Lj2	Lj3	Interface of dam-foundation	F43	F25	F31	Lj2	Lj3	Interface of dam-foundation
2.0	⊗	⊗	⊗				⊗	⊗	⊗			
3.0	⊗	⊗	⊗				⊗	⊗	⊗			
4.0	⊗	⊗	⊗			⊗	⊗	⊗	⊗			⊗
5.0	⊗	⊗	⊗			⊗	⊗	⊗	⊗		⊗	⊗
6.0	⊗	⊗	⊗		⊗	⊗	⊗	⊗	⊗		⊗	⊗

Note: ⊗ indicates that the corresponding sliding surface has complete sliding.

From the above analysis result, when considering the unfavorable topography, the strong storage coefficient corresponding to complete sliding on the sliding surface Lj3 become smaller, the maximum compressive stress at the downstream side of the bedrock slider increases, and the residual sliding displacements under different strong storage coefficients are consistently larger, as shown in Fig. 33. Thus, from the perspectives of strong storage coefficients corresponding to complete sliding on different sliding surfaces, the maximum compressive stress on the downstream side of the bedrock slider, and the maximum residual sliding displacement, it is advisable to account for the influence of unfavorable topography.

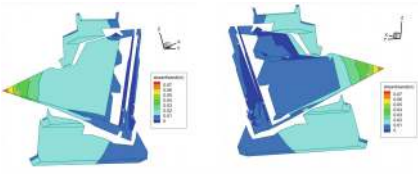

Fig. 21. Residual slippage of the dam-foundation interface-fault-fracture under 2.0 times strong storage coefficient without considering unfavorable topography.

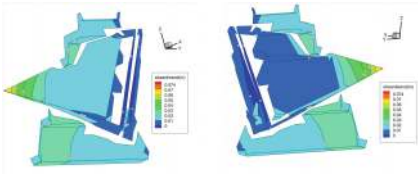

Fig. 22. Residual slippage of the dam-foundation interface-fault-fracture under 3.0 times strong storage coefficient without considering unfavorable topography.

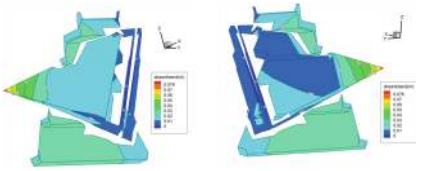

Fig. 23. Residual slippage of the dam-foundation interface-fault-fracture under 4.0 times strong storage coefficient without considering unfavorable topography.

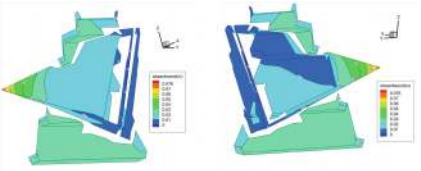

Fig. 24. Residual slippage of the dam-foundation interface-fault-fracture under 5.0 times strong storage coefficient without considering unfavorable topography.

Fig. 25. Residual slippage of the dam-foundation interface-fault-fracture under 6.0 times strong storage coefficient without considering unfavorable topography.

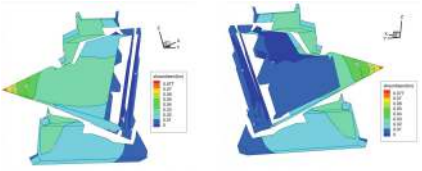

Fig. 26. Residual slippage of the dam-foundation interface-fault-fracture under 2.0 times strong storage coefficient considering unfavorable topography.

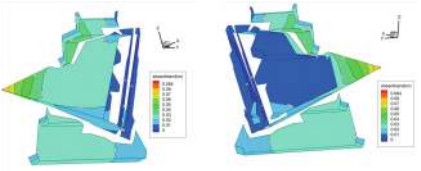

Fig. 27. Residual slippage of the dam-foundation interface-fault-fracture under 3.0 times strong storage coefficient considering unfavorable topography.

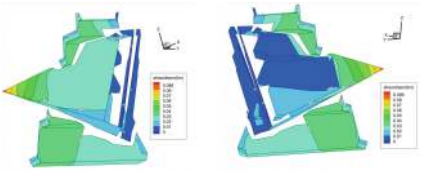

Fig. 28. Residual slippage of the dam-foundation interface-fault-fracture under 4.0 times strong storage coefficient considering unfavorable topography.

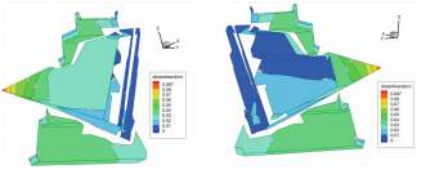

Fig. 29. Residual slippage of the dam-foundation interface-fault-fracture under 5.0 times strong storage coefficient considering unfavorable topography.

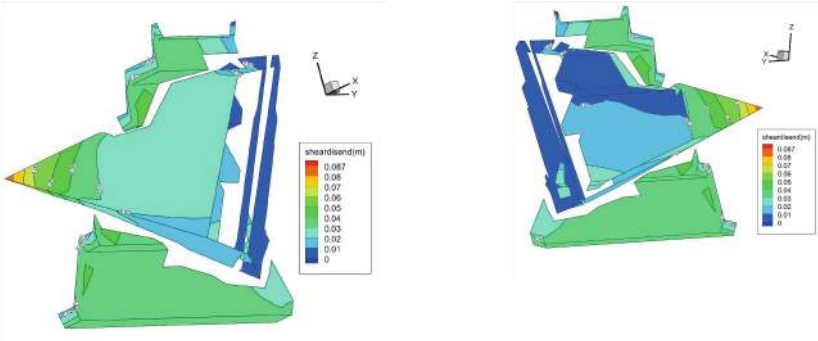

Fig. 30. Residual slippage of the dam-foundation interface-fault-fracture under 6.0 times strong storage coefficient considering unfavorable topography.

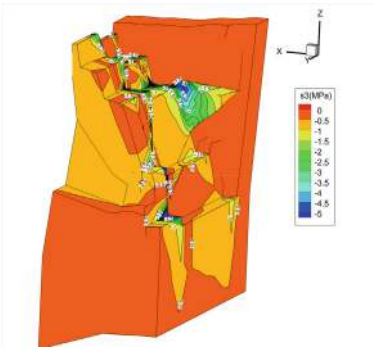

Fig. 31. Minimum principal stress of bedrock under 5.0 times design earthquake without considering unfavorable topography.

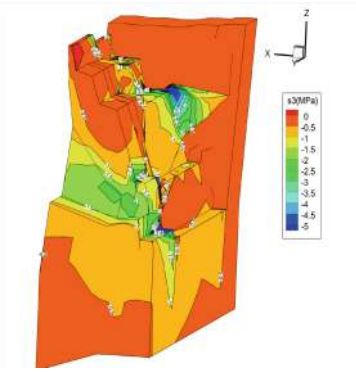

Fig. 32. Minimum principal stress of bedrock under 4.0 times design earthquake considering unfavorable topography.

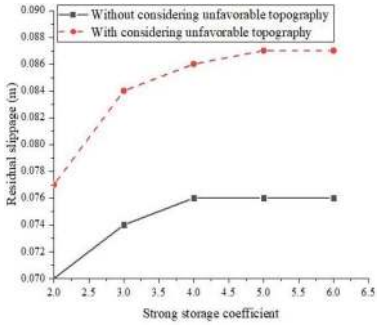

Fig. 33. Maximum residual slippage of the dam-foundation interface-fault-fracture under different strong storage coefficients without considering and considering unfavorable topography.

4 Result

In this paper, the deep anti-sliding stability of a gravity dam is studied, and the effects of unfavorable topography on the sliding failure process of the different sliding surfaces, the maximum compressive stress on the downstream of the bedrock slider, and the maximum residual slippage are compared and analyzed, and the ultimate seismic capacity of the dam-foundation system are evaluated. The principal conclusions are as follows:

(1) Based on the overload analysis method, the yield zone penetration is taken as the evaluation criterion for the dam-foundation system to reach the limit state, and the overload coefficient of 4.0 can be taken conservatively as the ultimate seismic capacity of the dam-foundation system without and with considering unfavorable topography.
(2) Based on the strong storage analysis method, the yield zone penetration is taken as the evaluation criterion for the dam-foundation system to reach the limit state, and the strong storage coefficient of 5.0 can be taken conservatively as the ultimate seismic capacity of the dam-foundation system without and with considering unfavorable topography.
(3) Under the given conditions of sliding surfaces combination, the gravity dam meets the deep anti-sliding stability requirements under the design earthquake, and has a large safety margin without and with considering unfavorable topography.
(4) The overload safety coefficients without and with considering the influence of unfavorable topography are the same, and the strong storage safety coefficients are not much different. However, considering the influence of unfavorable topography, the overload coefficient or strong storage coefficient corresponding to complete sliding on the sliding surfaces becomes smaller, the maximum compressive stress at the downstream side of the bedrock slider increases, and the residual sliding displacements under different strong storage coefficients are consistently larger. Thus, it is advisable to account for the influence of unfavorable topography from the perspective of safety.

References

1. Pan, J.: Gravity Dam Design. Water Resources and Electric Power Press, Beijing (1987). ISBN: 978-7-5123-8351-7
2. Chen, H.: Research on Seismic of Concrete High Dam. Higher Education Press, Beijing (2011). ISBN: 9787040333909
3. Yu, S., Chen, Z.Y., Jia, Z.X.: Analysis on the deep anti-sliding stability of Xiangjiaba dam foundation by using fluid-structure interaction analysis. J. China Inst. Water Resour. Hydropower Res. **8**(1), 11–17 (2010). https://doi.org/10.3969/j.issn.1672-3031.2010.01.002
4. Pan, J.: Anti-Sliding Stability and Landslide Analysis of Buildings. Beijing Electric Power Press (1980). ISBN: 15047.4020
5. Zhou, Q.: Deep anti-sliding stability of gravity dams. Tianjin University (2001). https://doi.org/10.7666/d.Y397702
6. Pang, J.R.: The comprehensive method above overloading and strength reducing for finite element analysis of the deep stability of gravity dam. Taiyuan University of Technology (2015). https://doi.org/10.7666/d.Y2797855

7. Chen, J.Y., Zhang, L., Chen, Y.: Failure model test on deep anti-sliding stability of Wudu Rcc gravity dam. Rock Mech. Eng. **26**(10), 2097–2103 (2007). https://doi.org/10.3321/j.issn:1000-6915.2007.10.020
8. Zhou, Z., Zhou, F., Pan, J.X., et al.: Study on stability against deep sliding of gravity dam. Rock Soil Mech. **29**(6), 1719–1722 (2008). https://doi.org/10.3969/j.issn.1000-7598.2008.06.055
9. State Grid Corp China East China Surv Des Res Inst: Dl5108-1999 Design Specification for Concrete Gravity Dams. China Electric Power Press, Beijing (2000)
10. Peng, W.M., Zhang, L.M., Chen, Q.: Review of deep anti-sliding stability analysis methods for gravity dams. Hydropower Stn. Des. **26**(3), 52–54 (2010). https://doi.org/10.3969/j.issn.1003-9805.2010.03.014
11. Wang, Z.P., Sun, J.S., Zhao, D.: Study on anti-sliding stability of deep layer under gravity dam with complex foundation based on catastrophe theory. Yangtze River Sci. Res. Inst. **33**(7), 132–136 (2016). https://doi.org/10.11988/ckyyb.20150458
12. China Electric Power Enterp Fed, Minist Water Resour P R C: Gb/t 51394-2020 standard for load on hydraulic structures. China Planning Publishing House, Beijing (2020)
13. Westergaard, H.M.: Water pressure on dams during earthquakes. Trans. Asce. **98**, 418–432 (1933). https://doi.org/10.1061/TACEAT.0004496

Application of Composite Reinforcement Technology with High-Precision Large-Diameter Pipe Roof and Sleeve Valve Pipe in Urban Ultra-Shallow Buried Backfill Soil Tunneling by Underground Excavation

Bo Deng[1], Wentao Liu[2], Yunhao Gou[2], Longquan Zhao[3](✉), and Rui Su[3]

[1] Chongqing Transportation Construction Management Co., Ltd., Chongqing 400043, China
[2] No. Three Engineering Co., Ltd. of CCCC First Highway Engineering Co., Ltd., Beijing 101102, China
[3] School of Civil Engineering, Chongqing Jiaotong University, Chongqing 400074, China
1486938162@qq.com

Abstract. Traditional pre-support methods in urban ultra-shallow buried tunnels often face challenges such as poor grout diffusion, significant ground disturbance, and water ingress, which complicate the stringent control of surface settlement. This study investigates an effective pre-reinforcement technique to address these issues. Using the Chongqing Rail Transit Line 18 project as a case study, we developed and implemented a composite reinforcement method combining high-precision large pipe-roofing with improved sleeve-valve grouting. First, we explain the synergistic mechanism of this technique, which integrates structural support with ground improvement. Second, we detail the key construction procedures: precise spatial trajectory simulation of the pipe roof using Revit, real-time drilling elevation monitoring based on the principle of connected vessels, and a dynamic deviation correction system employing a custom-designed guide drill bit. Finally, FLAC3D numerical simulations were conducted to compare the vertical displacement fields of the surrounding rock induced by tunnel excavation, with and without the composite reinforcement. The numerical simulation results show that the composite reinforcement technology reduces the vault settlement from 23.5 mm to 18.3 mm, with a decrease of 22%. The displacement field distribution tends to be continuous and uniform, and the stress state of surrounding rock is significantly improved. The tensile stress decreases by more than 36.4%, effectively forming a pre-loaded arch structure. This high-precision composite reinforcement technique effectively suppresses deformation, improves stress distribution, and mitigates risks like water leakage, borehole collapse, and face instability. It offers a reliable technical reference and practical example for similar complex urban tunnel projects.

Keywords: Shallow-Buried Tunnel · Large-Diameter Pipe Roof · Sleeve Valve Pipe Grouting · Numerical Simulation · Composite Reinforcement

© The Author(s), under exclusive license to Springer Nature Switzerland AG 2027
G. Feng et al. (Eds.): ICCE 2025, SUCI, pp. 540–555, 2027.
https://doi.org/10.1007/978-3-032-32237-1_38

1 Introduction

With the advancement of urbanization and the continuous growth of transportation demands within cities, underground transportation projects such as rail transit and utility tunnels are increasingly prevalent. Rail transit construction, often located in urban core areas, faces significant challenges due to the complex and variable underground structures, dense building clusters, and busy surface traffic, which impose stringent requirements on tunnel construction methods. Constructing in backfill soil layers, ultra-shallow-cover cut-and-cover tunnels are highly susceptible to engineering disasters such as tunnel collapses and ground surface subsidence due to their thin overburden and poor self-stabilizing capacity of the strata [1–4]. Therefore, the adoption of efficient and precise ground pre-reinforcement techniques to address leakage and collapse issues in conventional tunnel advance support has become a critical technical bottleneck constraining the safe construction of urban cut-and-cover tunnels.

In recent years, the conventional advance support for conventional tunnel excavation has typically employed a combination of large pipe arches and small-diameter grouting pipes for reinforcement. The grouting through the small pipes permeates the strata to consolidate the ground, forming a protective shell arch around the excavation face. While large pipe arches provide direct support through their steel pipe framework, enhancing the shear strength of the surrounding rock near the pipes and integrating the pipes with the rock mass to form a combined arch system [5–7]. Research on advance support for shield-driven tunnels has centered on this reinforcement technique. For instance, Jiang Huiyuan [8] analyzed the relevant definitions of advance small-diameter pipe technology and its connection to shallow-buried shield-driven tunnel construction methods, while also studying the specific application of advance small-diameter pipe support during shallow-buried tunnel excavation. Jiang Hao et al [9]. Used a shallow-excavation tunnel project for an underground utility tunnel as a case study, illustrating the application of small-pipe advance support technology in controlling ground settlement and structural deformation. Chen Muzhen et al [10]. Improved upon traditional large pipe arch construction techniques. They employed a composite reinforcement method combining large pipe arches with modified sleeve valves to construct urban shallow-buried tunnels under the protection of the reinforced arch ring formed.

In traditional tunnel construction techniques, common issues include pipe arch collapse [11, 12], poor grout diffusion effectiveness [13], damage to shallow surrounding rock [14], and water and sand surges at the excavation face [15]. To address these challenges, this paper presents and applies a composite reinforcement advance support technique developed for the Chongqing Rail Transit Line 18 project in shallow-buried backfilled soil strata. The technique primarily involves high-precision large-diameter pipe arch drilling with pipe following and surface sleeve valve grouting. Through innovative improvements in drill bit design, pipe arch construction, sleeve valve pipe layout, and grouting techniques, this method effectively enhances the self-stabilizing capacity of the surrounding rock. It ensures the safety and controllability of the tunnel excavation process, successfully resolving common issues such as leakage and hole collapse in traditional advance support systems. This technique holds significant technical guidance and promotional value for tunnel construction in similar geological conditions.

2 Project Overview

The cut-and-cover section between Chongqing Station and Caiyuan Road Station on the Chongqing Rail Transit Line 18 North Extension Project was constructed using the mining method. This tunnel is an ultra-shallow-cover tunnel with a burial depth ranging from approximately 6.80 to 9.50 m. The standard cross-section excavation width is 8.6 to 8.8 m, and the height is 8.7 to 9.03 m. The primary strata traversed include artificial backfill, sandy mudstone, and sandstone. The overlying moderately weathered rock layer ranges from 0 to 9.91 m thick, with backfill extending from 0 to 17 m and sandy mudstone from 4 to 21.9 m. Furthermore, this tunnel section is situated within a gully terrain unit, functioning as a groundwater convergence zone. During the rainy season, significant groundwater accumulation occurs in the gully area. Concurrently, the tunnel's surface is primarily occupied by a major municipal thoroughfare with heavy traffic flow, imposing stringent requirements for surface settlement control. The geological longitudinal profile of the tunnel is shown in Fig. 1.

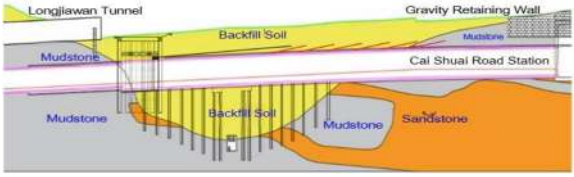

Fig. 1. Geological longitudinal profile of the dark excavation section in the heavy load zone.

3 Composite Reinforcement System Construction Process

3.1 Technical Principles and Components

High-Precision Large Pipe Arch Combined with Sleeve Valve Pipe Reinforcement Technology for Underground Tunneling in Ultra-Shallow Backfill Soil represents a systematic upgrade of traditional large pipe arch construction techniques. This technology employs precise angle simulation and specialized directional drill bits to install large pipe arches in a single pass within a 156° range, forming the primary load-bearing arch shell. Simultaneously, sleeve valves are drilled diagonally from the surface into the area ahead of the tunnel face, with jump grouting performed to permeate and consolidate the surrounding rock. Together, these elements form a three-dimensional reinforcement system that integrates in-tunnel and surface operations, combining pre-support with grouting improvement. This dual-pronged approach provides a robust safety guarantee for tunnel excavation.

Mechanism of Pipe Arch Reinforcement. The reinforcement mechanism of advance pipe arches can be summarized as follows: The beam effect manifests as the pipe arches forming an integral beam structure, supported by the steel frame near the working face and the stable rock and soil mass ahead. This structure bears loose loads within the longitudinal range from the working face extrusion zone to the pre-convergence zone ahead,

effectively constraining surrounding rock deformation and exhibiting a pronounced spatial effect. The arch shell effect refers to the superimposition of individual pipe arch reinforcement units forming an integrated arch shell structure. Together with the steel arch, this creates a high-bearing-capacity arch shell layer that bears the pressure from the overlying rock mass, significantly enhancing tunnel and rock mass stability. The reinforcement effect occurs through grouting into the pipe walls, allowing cement slurry to infiltrate rock fractures. This enhances rock strength and stiffness, suppresses deformation and collapse caused by excavation disturbance and stress redistribution, and reduces the extent of the loosened zone [16].

Mechanism of Sleeve Valve Pipe Reinforcement. Sleeve-valve pipe grouting reinforcement involves using a high-pressure grouting pump to inject grout through the outer grouting pipe into the inner grouting pipe. Under internal pressure, the grout flows through reserved overflow holes, simultaneously rupturing the rubber rings encasing the borehole section and crushing the shell material. It then permeates into the rock and soil mass requiring reinforcement, achieving filling, permeation, and compaction effects. For tunnels, segmental grouting using retractable sleeve valves reinforces the tunnel borehole strata. Tunnel excavation commences only after all advance-level drill holes and inspection borehole cores meet density and strength requirements [17].

Composite Reinforcement Technology Combining Large Pipe Arch and Sleeve Valve Pipe. This technology combines the structural support advantages of large pipe arches with the rock mass improvement benefits of sleeve valves. The large pipe arch serves as the primary load-bearing skeleton, providing immediate, rigid pre-support; while sleeve valve grouting proactively enhances the stress environment of the main pipe arch and the mechanical properties of the underlying rock mass. The spatiotemporal integration of these two elements collectively forms a highly cohesive, high-load-bearing pre-loaded arch, significantly improving the self-stabilization capacity in shallow-buried soft rock formations. This technology is primarily applicable to urban dense areas, ultra-shallow-buried tunnels, and shield tunneling projects with stringent settlement control requirements, serving as a key solution for addressing challenges in such engineering contexts.

Based on the differing mechanisms of action for pipe arches, sleeve valves, and composite reinforcement techniques, this paper summarizes their respective advantages, disadvantages, and applicable conditions in Table 1.

Table 1. Comparison of pipe arch, sleeve valve pipe, and composite reinforcement technologies.

	Mechanism of Action	Advantages	Disadvantages	Applicable Conditions
Pipe Arch	Form beam or arch shell structures to bear longitudinal loads and suppress surrounding rock deformation.	High load-bearing capacity, mature construction techniques, and provides rigid support.	Prone to leakage and hole collapse, low grouting pressure (approximately 0.5 MPa), difficult hole formation, and uneven grout dispersion.	Suitable for tunnels in relatively stable strata at greater depths, but less effective in shallow soft rock layers.
Sleeve valve pipe	Grouting strengthens the surrounding rock, enhancing its strength and stiffness while reducing the loose zone.	Grouting delivers excellent results, enhancing rock mass density while offering flexible operation.	Horizontal borehole formation is challenging, grouting pressure is limited (0.2–0.5 MPa), prone to clogging, and lacks structural support.	Suitable for areas with highly fractured rock mass, but must be used in conjunction with other support systems.
Composite Reinforcement Technology Using Pipe Arches and Sleeve Valves	The combination of pipe arches and sleeve valves forms an integrated arch shell layer, providing structural support and grout reinforcement.	High efficiency in single-pass construction, high grouting pressure (1.5–2 MPa), effectively addressing borehole collapse and water inflow, with comprehensive support.	The process is complex, costly, and requires specialized equipment.	Particularly suitable for shallow burial, sand layers, or soft rock formations, as well as tunnel projects in densely populated urban areas.

3.2 High-Precision Guidance and Correction System

The precision of pipe arch construction is critical to ensuring effective support. This project employs an asymmetric correction system based on the wedge plate principle, as shown in Fig. 2. The guidance and correction drill bit is mounted at the front end

of the drill rod. By dynamically adjusting the orientation of the wedge plate relative to the outer casing, it alters the direction of forces acting on the drill bit in real time. This enables precise control of the drilling trajectory, ensuring the pipe arch is laid along the designed path.

Fig. 2. Schematic diagram of guided drift correction drill bit.

3.3 Pipe Arch Construction Process and Key Technologies

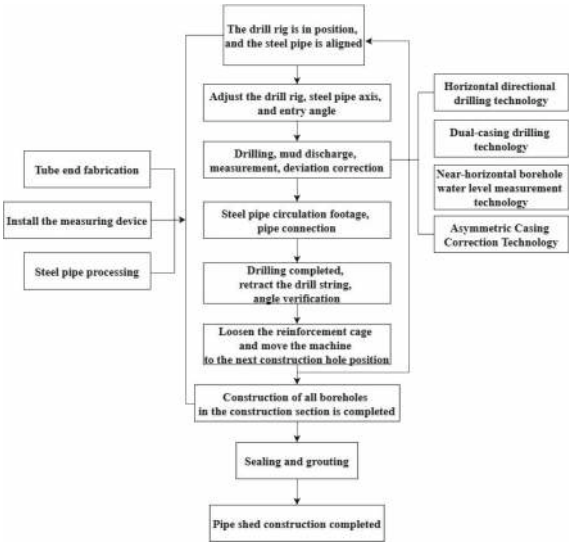

Fig. 3. Pipe arch construction flowchart.

The pipe arch uses Φ108 steel pipes, with Φ89 drill pipes for pipe-following drilling. The core construction process includes: surveying and positioning → rig positioning → directional drilling → pipe-following connection → drilling to design depth → grouting. The specific process is shown in Fig. 3.

Precise Control Technology for Spatial Trajectories. To address the tunnel's alignment characteristics—a 2% upward gradient and an 800-m curve with a small radius—this study employed BIM (Revit) software to conduct precise three-dimensional simulations of each pipe arch's spatial trajectory (Fig. 4). This enabled the pre-calculation

of optimal installation angles and orientations, ensuring the overall support stiffness and optimal spatial positioning of the pipe arch cluster from the outset.

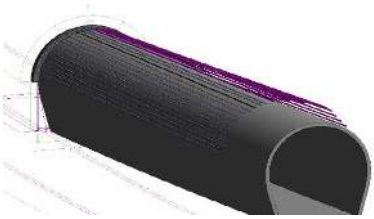

Fig. 4. Simulation rendering of pipe arch.

Real-time Monitoring Technology for Drilling Elevation. During the drilling process, a simple monitoring device based on the principle of communicating vessels was employed to measure the drill bit elevation in real time (Fig. 5). This method stabilizes the inlet liquid level by closing the inlet valve, at which point the inlet liquid level corresponds to the real-time height of the drill bit ahead of the working face. This achieves visual, high-precision monitoring of the drill bit elevation without cumulative error.

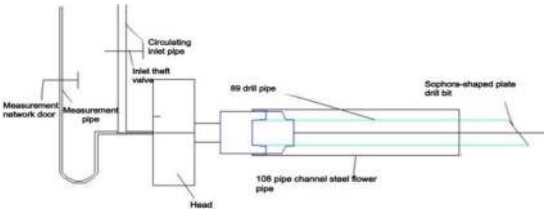

Fig. 5. Schematic diagram of monitoring device.

Dynamic Correction Control Technology. During construction, sensors embedded within the directional drill head transmit real-time inclination and azimuth angle (indicated in clockwise direction) to an external display (Fig. 6). Should the trajectory deviate, adjustments to the guide plate in the corresponding direction can be made to correct the thrust path.

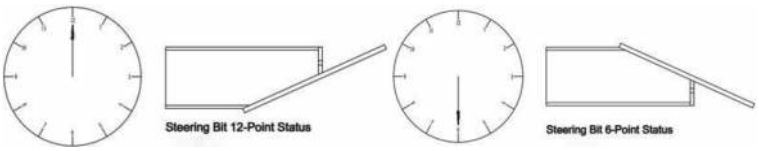

Fig. 6. Correction diagram.

Large-Diameter Pipe Arch High-Pressure Grouting Technology. The effectiveness of grouting hinges on proper sealing at the borehole opening. To address this, no grouting holes are installed within the outermost 2 m of the steel pipe. Instead, a perforated steel plate with a thickness of 3–5 mm is welded over the opening to seal it.

For the circumferential gap between the steel pipe and the borehole wall, a custom-made tool is used to pack in at least 1 m of early-strength cement mortar, ensuring a tight seal. This guarantees the establishment of effective grouting pressure during the grouting process.

3.4 Key Points for Sleeve Valve Pipe Grouting Construction

The sleeve valve pipe uses Φ48 mm × 4 mm PVC plastic pipe. Grouting employs a retreating segmented grouting process, following the principle of "periphery first, interior later." Interval grouting is applied to prevent grout migration. When groundwater flow is present, grouting commences from the end with the higher water head. Grout pressure must be applied slowly and uniformly. After reaching the design value, maintain pressure for 2–3 min. The grouting hole layout is shown in Fig. 7.

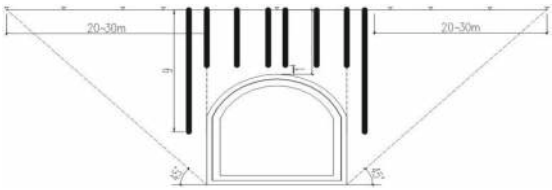

Fig. 7. Schematic cross-section of grouting hole layout.

4 Numerical Simulation Analysis

To quantitatively evaluate the mechanism and effectiveness of the composite reinforcement system combining large pipe arches and sleeve valves in controlling rock mass deformation in ultra-shallow tunnels, this study employed FLAC3D to establish a three-dimensional numerical model. The tunnel excavation process was simulated, and comparative analysis was conducted to reveal the mechanical behavior of the composite reinforcement technology. Figure 8 and Fig. 9 illustrate the advance support scheme and the composite reinforcement structure, respectively.

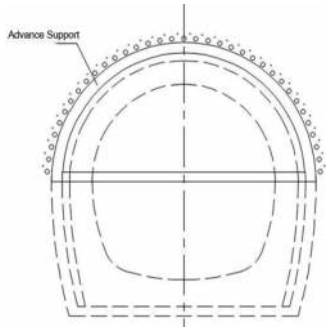

Fig. 8. Advance support diagram.

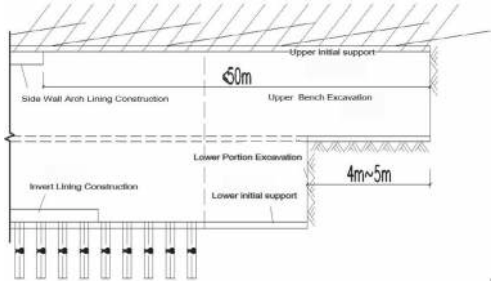

Fig. 9. Composite reinforcement structure diagram of pipe arch and sleeve valve pipe.

4.1 Model Development and Parameters

Given the shallow burial depth and complex geological conditions of the tunnel, the model dimensions must be determined to fully eliminate boundary effects. This study established a model with dimensions of 80 × 30 × 80 (length × width × height). The upper surface of the model was defined as a free boundary, while the bottom was constrained for triaxial displacement. Normal displacement constraints were applied to all four lateral sides.

The rock mass is modeled using an idealized elastic-plastic constitutive model and follows the Mohr-Coulomb yield criterion. Large pipe arches are modeled using beam structural elements to reflect their beam-like support effect. The grouting reinforcement zone of sleeve valves is equivalently simulated by enhancing the mechanical parameters of the corresponding surrounding rock area, a common practice considering their compaction and permeability effects. Key physical and mechanical parameters for various materials are primarily determined based on actual field geological reports and engineering analogies, as detailed in Table 2.

Table 2. Soil and material properties.

Name	Modulus of elasticity (Gpa)	Poisson ratio	Bulk density (kN/m^3)
sandy mudstone	103.0	0.30	24.0
Large Pipe Arch	200.0	0.25	78.5
Sleeve valve pipe	2.5	0.35	13.0
Grout Injection reinforcement	1.0	0.30	22.0

The model employs a tetrahedral-dominated mesh with locally refined meshes around the tunnel periphery and reinforcement zones to ensure computational accuracy, as shown in Fig. 10 . The simulation process follows the actual construction sequence: ground stress equilibrium analysis, composite reinforcement structure installation, and finally tunnel sectional excavation.

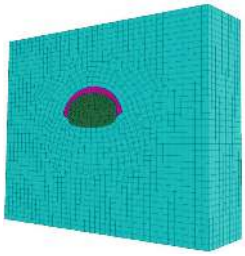

Fig. 10. FLAC3D model diagram.

4.2 Calculation Results and Analysis

Comparative Analysis of Surrounding Rock Displacement. Based on the established computational model, vertical displacement contour maps of the surrounding rock during tunnel excavation were extracted. A comparative analysis was conducted on the deformation responses under two scenarios: with and without the combined reinforcement technique of large pipe arches and sleeve valves. The results are shown in Fig. 11.

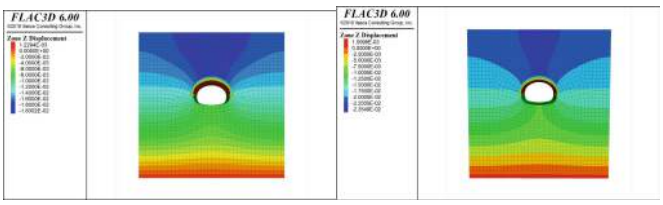

(a) Composite reinforcement support (b) No composite reinforcement support

Fig. 11. Analysis of vertical displacement of surrounding rock during excavation process.

Vertical displacement simulation results indicate that the excavation unloading effect causes stress redistribution in the surrounding rock, leading to significant vertical displacement. Without any reinforcement measures (Fig. 11 (b)), the crown settlement reached 23.5 mm, with an uneven displacement field distribution and discontinuous settlement patterns, indicating that the surrounding rock had undergone unstable large deformation. In contrast, after applying composite reinforcement technology (Fig. 11 (a)), rock mass displacement was effectively controlled. The displacement field exhibited continuous and uniform contour distribution without noticeable abrupt changes or concentrated phenomena, with maximum crown settlement reduced to 18.3 mm. Compared to the unreinforced condition, settlement decreased by 5.2 mm—a 22% reduction—demonstrating the technology's significant effectiveness in deformation control.

The deformation mechanisms differ between large pipe arch and sleeve valve pipe composite reinforcement support systems. Without reinforcement, rapid stress release occurs in the surrounding rock after excavation unloading. The poor self-stabilization capacity of overlying backfill soil in shallow-buried tunnels accelerates crown settlement. After reinforcement, the large pipe arch forms a "pre-supported arch" through its beam effect, constraining displacement of the overlying soil. Grouting through sleeve valves enhances the stiffness of the surrounding rock mass. Together, these elements transfer loads to the deep stable rock layers, thereby limiting structural displacement.

Comparative Analysis of Surrounding Rock Stresses. To further elucidate the influence of composite reinforcement systems on the stress state of surrounding rock, a comparative analysis of stress distribution characteristics under two operating conditions was conducted. The results for the minimum principal stress are shown in Fig. 12.

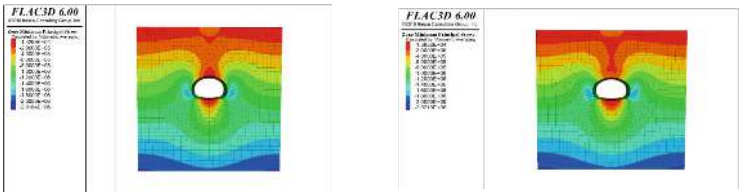

(a) Composite reinforcement support (b) No composite reinforcement support

Fig. 12. Analysis of minimum principal stress in surrounding rock during excavation process.

Simulation results for the minimum stress in the surrounding rock indicate that stress distribution curves in both scenarios exhibit a gradual increase from the tunnel periphery toward the rock mass interior, consistent with typical excavation unloading characteristics. However, comparative analysis reveals that without reinforcement measures (Fig. 12(b)), compressive stress concentration at critical locations such as the arch toe and sidewalls is significantly higher than in the scenario employing composite reinforcement technology (Fig. 12(a)). This discrepancy arises because the large pipe arches in the composite reinforcement technology function as beams and arches, proactively assuming part of the load originally borne by the surrounding rock. This creates a "load-sharing" mechanism that effectively alleviates stress concentration and improves

the stress state of the surrounding rock. In contrast, under the unsupported condition, the surrounding rock must independently bear the entire load, leading to more severe compressive stress concentration and increasing the risk of localized failure.

The comparison of maximum principal stresses with and without composite reinforcement technology is shown in Fig. 13.

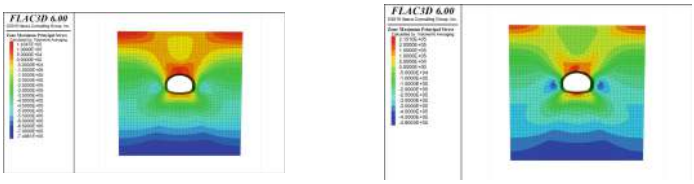

(a) Composite reinforcement support (b) No composite reinforcement support

Fig. 13. Analysis of maximum principal stress in surrounding rock during excavation process.

Simulation results for maximum rock stress indicate that after composite reinforcement support (Fig. 13 (a)), the maximum tensile stress is 0.14 MPa, compared to 0.22 MPa without reinforcement (Fig. 13(b)), representing a reduction of 36.4%. This demonstrates that the composite reinforcement system provides bending resistance through the beam effect of large pipe arches. Combined with the integrity enhancement of the surrounding rock via sleeve valve grouting, it effectively counters the tensile tendencies induced by excavation, essentially eliminating tensile stress zones. This mechanism prevents instability caused by tensile cracking. Furthermore, the maximum compressive stress under composite reinforcement was 0.75 MPa, compared to 0.48 MPa without reinforcement. This further demonstrates that the support system alleviates compressive stress concentration within the rock mass by sharing the load, consistent with the conclusions from the minimum principal stress analysis.

Stress analysis of the surrounding rock indicates that composite reinforcement technology fundamentally improves the tensile-compressive state of the rock mass. Following composite reinforcement, the synergistic effect of the powerful bending resistance provided by the large pipe arch through its "beam-arch effect" and the enhanced integrity of the rock mass via sleeve valve grouting significantly alleviates stress concentration in critical areas and the tensile-compressive tendencies induced by excavation unloading. This results in a more gradual stress distribution curve and a more uniform stress state within the rock mass. This system not only bears and redistributes rock mass loads but also shifts stress concentration points from the weak rock mass itself to the higher-strength reinforcement system. This achieves active optimization of the stress state in the rock mass of ultra-shallow backfilled tunnels.

In summary, this remarkable control effect is mechanically substantiated: the large pipe arch, functioning as a rigid skeleton, significantly enhances the support system's bending resistance through its high elastic modulus, thereby suppressing arch deflection. Through its beam effect and shell effect, it forms the primary load-bearing framework. Meanwhile, the sleeve valve grouting enhances the mechanical properties of the core rock and soil through a strengthening effect. By filling fractures and exerting a compaction effect, it transforms loose backfill into a continuous medium, reducing the magnitude

of stress release. Working synergistically, they collectively form an effective pre-loaded arch. This composite arch shell not only significantly suppresses surrounding rock deformation but also optimizes the distribution pattern of the displacement field, controlling the extent of the plastic zone within manageable limits. This substantially enhances the stability and safety during excavation of ultra-shallow tunnels.

4.3 Model Feasibility Verification

To validate the reliability of the numerical model, field monitoring data of crown settlement (GDC02) from the same soil layer were compared with simulation results. The settlement comparison diagram (Fig. 14) clearly demonstrates that the FLAC3D numerical simulation results closely match the field measurement data in terms of settlement development patterns, confirming the model's reliability. Both data sets exhibit identical three-stage characteristics: settlement initiation as the excavation face approaches the monitoring section, rapid settlement progression followed by gradual convergence within approximately 25 m beyond the face, and subsequent stabilization. Although simulated values systematically exceed measured values throughout the process (maximum deviation ~2 mm), this discrepancy remains within reasonable limits. It reflects the numerical model's idealized treatment of material parameters or soil-structure interactions.

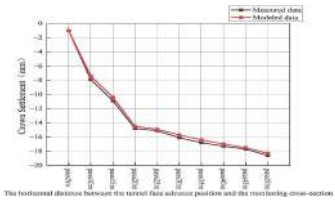

Fig. 14. Comparison of actual tunnel crown settlement and numerical simulation.

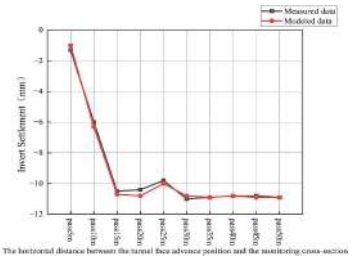

Fig. 15. Comparison of actual tunnel arch foot settlement and numerical simulation.

By comparing the arch foot settlement data obtained from FLAC3D numerical simulations with actual engineering monitoring results, the validity of the established numerical model is further substantiated. Both sets of data exhibit a highly consistent overall

trend in settlement progression with excavation advancement. They clearly reveal that settlement primarily occurs during the disturbance phase preceding the passage of the excavation face through the monitored section, followed by a phase of rapid deformation after passage, ultimately entering a slow convergence pattern (Fig. 15). This comparison not only validates the reliability of numerical simulation as an effective analytical tool but also mechanically substantiates the exceptional efficacy of the high-precision large pipe arch combined with sleeve valve pipe reinforcement technology. This technique synergistically forms a pre-loaded arch, thereby transforming the large, non-uniform deformation inherent in shallow-cover backfilled tunnels into controllable, continuous deformation.

5 Conclusion

Through comprehensive analysis of engineering practice and numerical simulation, this study proposes a high-precision composite reinforcement technique combining large pipe arches and sleeve valve pipes for ultra-shallow buried cut-and-cover tunnels. The following key conclusions are drawn:

1) The composite reinforcement system developed in this study forms an effective pre-loaded arch through the synergistic mechanism of structural support provided by large pipe arches and rock mass improvement achieved by grouting via sleeve valves. Combining comprehensive control measures—including millimeter-level precision placement of pipe arches via BIM-based spatial trajectory simulation, real-time elevation monitoring based on the communicating vessels principle, and dynamic deviation correction of directional drill bits—this system establishes a coordinated three-dimensional reinforcement model linking subterranean and surface operations.
2) The independently developed high-precision guidance and alignment system effectively addresses the challenge of low boring accuracy encountered by traditional methods in complex linear tunnels. This system ensures the spatial design configuration of the pipe arch, thereby guaranteeing the overall rigidity and load-bearing capacity of the pre-support structure. It provides core technological support for safe excavation.
3) Numerical simulation results comprehensively validated the integrated support effectiveness of this composite reinforcement technology. Analysis indicates: Regarding deformation control, the composite reinforcement technology reduced crown settlement by 22%, produced a more continuous and uniform displacement field distribution, and effectively suppressed inconsistent deformation of the surrounding rock. Regarding stress optimization, this technology decreased tensile stress levels in the surrounding rock by 36.4%, while significantly alleviating compressive stress concentration at critical locations, forming a more rational stress distribution pattern. Furthermore, experimental comparisons with actual monitoring data validated the reliability of the numerical simulation model. From both mechanical and displacement perspectives, this confirms the superior applicability of the high-precision large-diameter pipe arch combined with sleeve valve pipe reinforcement technology for ultra-shallow backfilled soil tunnels.

This result confirms the synergistic mechanism between the beam effect of large-diameter pipe arches and the reinforcement effect of sleeve grouting. Through the dual actions of load sharing and rock mass improvement, it achieves an ideal support state characterized by controllable deformation and uniform stress distribution. This research provides a reliable technical solution and practical reference for urban tunnel construction in similar complex geological conditions.

References

1. Zhang, D.H., Wang, M.S.: Safety analysis of urban subway tunnel by shallow excavation technique and measures for disaster prevention J. China Saf. Sci. J. (08), 53–55+1 (2003). https://doi.org/10.16265/j.cnki.issn1003-3033.2003.08.013
2. Pu, Z.H.: Analysis of the impact of shallow-buried tunneling construction reinforcement measures on geological formations and utility lines. J. Sci. Technol. Innovation **12**, 127–130 (2025). https://doi.org/10.15913/j.cnki.kjycx.2025.12.033
3. Yan, D.M.: Research on key construction technologies for shallow-buried excavation tunnel through abandoned soil stratum. J. Archit. Technol. **56**(21), 2646–2650 (2025). https://doi.org/10.13731/j.jzjs.2025.21.2646
4. Lü, X.X., Liu, A.W., Xuan, L., et al.: Research on rapid tunnel entrance construction technology for urban shallow-buried mined tunnels using oblique trenching method. J. Modern Tunn. Technol. **62**(S1), 376–384 (2025)
5. Song, Z.P., Pei, J.F., Pan, H.W., et al.: Analysis on the support effect of advance large pipe umbrella at portal section of shallow tunnel under unsymmetrical load. J. Modern Tunn. Technol. **59**(6), 86–96 (2022). https://doi.org/10.13807/j.cnki.mtt.2022.06.010
6. Zeng, R.Z., Zhan, T., Yang, C.Z.: Parameters for pipe roof support of shallow bored tunnels. J. Modern Tunn. Technol. **55**(01), 210–215 (2018). https://doi.org/10.13807/j.cnki.mtt.2018.01.028
7. Ji, Y.P., Fang, L.G., Tang, H.T., et al.: Study on forces on pipe umbrella support in the whole process of tunnel excavation. J. Modern Tunn. Technol. **60**(3), 123–138 (2023). https://doi.org/10.13807/j.cnki.mtt.2023.03.013
8. Jiang, H.Y.: Application and analysis of small duct advance support technology in shallow tunnel excavation construction J. Constr. Design Eng. (16), 125–127 (2022). https://doi.org/10.13616/j.cnki.gcjsysj.2022.08.238
9. Jiang, H., Jiang, H.: Application of small duct advanced supporting technology in tunnel shallow-buried excavation method. J. Low Temp. Archit. Technol. **41**(03), 86–88 (2019). https://doi.org/10.13905/j.cnki.dwjz.2019.03.023
10. Chen, M.Z., Li, D., Qin, J.X., et al.: A composite reinforcement technology of leading steel tube shed and sleeve valve tube applied to shallow and undercut pipeline construction in urban area. J. Building Constr. **32**(08), 856–858 (2010). https://doi.org/10.3969/j.issn.1004-1001.2010.08.047
11. Liu, J.Y.: Application of self-advancing anchor rods in coordination with advanced small pipes in treatment of large landslide in tunnels. J. Technol. Highway Transp. **04**, 105–108 (2010). https://doi.org/10.3969/j.issn.1009-6477.2010.04.029
12. Liu, J.: Study on stability analysis of surrounding rock and optimization of pipe roof support in mountain tunnel. J. Constr. Technol. **54**(04), 67–73 (2025). https://doi.org/10.7672/sgjs2025040067
13. Tan, Z.Z.: Full-sleeve follow-up construction method for advanced large pipe shed in tunnels. J. Western China Commun. Sci. Technol. **05**, 135–137 (2024). https://doi.org/10.13282/j.cnki.wccst.2024.05.043

14. Guo, L.M.: Mechanisms and support system of shallow layer damage in tunnels in mountainous areas. J. Railway Constr. Technol. **05**, 79–82 (2024). https://doi.org/10.3969/j.issn.1009-4539.2024.05.020
15. He, Z.N.: Analysis of geological problems of railway tunnels: case study of typical tunnels. J. Tunnel Constr. **36**(06), 636–665 (2016). https://doi.org/10.3973/j.issn.1672-741X.2016.06.002
16. Yao, Z.X., He, J.W., Zheng, G.W., et al.: Analysis of the load bearing mechanism and mechanical properties of the advanced pipe roof and discussion on its engineering application. J. Modern Tunn. Technol. **62**(2), 60–70 (2025). https://doi.org/10.13807/j.cnki.mtt.2025.02.006
17. Wang, C.: Application of sleeve valve pipe grouting technology in unbalanced pressure tunnels. J. Value Eng. **43**(30), 65–67 (2024)

Application of Integrated Grouting at Tunnel Arch Foot and Face in Ultra-Shallow Buried Backfill Tunneling

Wentao Liu[1], Yunpeng Han[1], Wenjing Duan[1], Yuxuan He[2(✉)], and Rui Su[2]

[1] No. Three Engineering Co., Ltd. of CCCC First Highway Engineering Co., Ltd., Beijing 100102, China
[2] School of Civil Engineering, Chongqing Jiaotong University, Chongqing 400074, China
heyuxuan11112024@163.com

Abstract. Addressing the critical challenges of face instability and ground settlement control during tunnel excavation in mixed soil-rock backfill strata within urban core areas, this study investigates the tunnel section between Chongqing Railway Station and Caiyuanlu Station on Chongqing Rail Transit Line 18 Northern Extension. Characterized by a minimal overburden depth of 6.8 m, the tunnel traverses heterogeneous backfill zones featuring poor self-stabilization capacity, variable soil composition, and large-diameter boulders, posing significant construction risks. To mitigate these risks, a comprehensive reinforcement scheme integrating arch foot and tunnel face grouting was proposed and implemented. A numerical model simulating the construction process was established using MIDAS GTS to systematically evaluate the effectiveness of this approach, with validation through field monitoring data including ground surface settlement and crown settlement. Results demonstrate that the composite grouting technique restricts maximum vertical ground displacement to 5.39 mm—significantly below the 40 mm control threshold. Monitoring data align closely with simulation predictions, while actual stabilization time slightly outperformed model forecasts, confirming the technique's reliability and applicability. This solution substantially enhances face and crown stability, effectively averts collapse risks, ensures construction safety, accelerates excavation progress, and facilitates subsequent secondary lining construction, thereby improving long-term structural safety and stability. The study provides valuable insights for urban shallow-buried tunnel projects in analogous complex geological conditions.

Keywords: Ultra-Shallow Buried Tunnels · Composite Grouting · MIDAS-GTS · Mixed Soil-Rock Backfill Zones · Deformation Control

1 Introduction

In recent years, with the acceleration of urbanization, the development of underground space resources has gradually become a key focus in urban development. Underground construction projects such as tunnels and integrated utility corridors are increasing,

© The Author(s), under exclusive license to Springer Nature Switzerland AG 2027
G. Feng et al. (Eds.): ICCE 2025, SUCI, pp. 556–565, 2027.
https://doi.org/10.1007/978-3-032-32237-1_39

significantly raising the difficulty of construction safety management [1–3]. The high-risk accidents in tunnel construction primarily include roof collapse [4, 5], water inrush and mud outbursts [6, 7], toxic gas leaks [8, 9] and surrounding rock instability leading to collapses. Among these, collapses, due to their high frequency, have become the most representative and typical disaster. Therefore, dense construction areas and surface traffic loads impose high demands on controlling surface settlement and improving the stability of the soil in front of the tunnel face during the construction of shallow-buried tunnels. Current research suggests that the use of advanced support systems and secondary lining construction techniques can address the issues of excessive crown settlement and large ground settlement in urban shallow-buried tunnels [10–12]. In addition to applying shallow-buried tunnel construction techniques, some researchers have implemented dual-layer advanced support measures, such as "advanced pipe sheds + advanced small conduits," to enhance ground settlement control [13, 14]. Beyond methods for controlling surface settlement, measures to prevent tunnel face instability include proactive predictions of surrounding rock dynamics, timely reinforcement of the initial support structure, and strict adherence to a three-step construction process during excavation. Furthermore, the exposure time of the tunnel face should be minimized as much as possible [15, 16]. However, challenges remain when excavating in mixed soil-rock backfill zones, where issues like uneven soil, large boulders, and poor self-stabilization persist. This increases the risk of grout loss, slurry leakage, and even tunnel face collapse during construction. Therefore, it is essential to further study grouting methods for tunnel excavation to mitigate surface settlement caused by excavation and enhance the stability of the soil ahead of the tunnel face, thereby preventing face collapse and ensuring construction safety.

Given the current state of development, no effective method has yet been established that simultaneously addresses both the prevention of tunnel face collapse and the control of surface settlement. This study, based on the fundamental principles of shallow-buried tunnel excavation, investigates the characteristics of the tunnel section between Chongqing Railway Station and Caiyuanlu Station on the Chongqing Rail Transit Line 18 Northern Extension. A combined grouting method for the tunnel arch foot and face was applied. After each face excavation, C25 shotcrete was sprayed for reinforcement. T76 pipe sheds with large lock feet were installed on both sides of the initial tunnel support, and welded to the initial support arch while simultaneously securing the angle, followed by injection of M30 cement mortar for reinforcement. Additionally, 16 φ42 × 3.5 lock-foot anchor pipes were installed for each arch frame, with "L-shaped" steel bars welded at the rear to enhance the stability of the structure. This study enhanced the stability of the soil in front of the tunnel face and mitigated surface settlement, providing theoretical support and practical references for similar projects in the future.

2 Project Analysis

2.1 Project Overview

The tunnel section between Chongqing Railway Station and Caiyuanlu Station on the Northern Extension of Chongqing Rail Transit Line 18 is situated beneath the central greenbelt and municipal road of Caiyuanlu. The tunnel structure passes through a backfill

soil zone and crosses over a drainage culvert, with the geological profile illustrated in Fig. 1.

This section of the tunnel is relatively shallow, with burial depths ranging from 6.80 to 9.50 m. The surrounding rock consists mainly of artificial fill and highly weathered rock, with a basic rock mass quality rating of V. As a shallow-buried tunnel, it was constructed using the mining method. The standard cross-sectional excavation width is between 8.6 m and 8.8 m, with a height ranging from 8.7 m to 9.03 m. The left line backfill section extends 62 m, while the right line spans 55.5 m. A 40-m-long advanced large pipe shed was installed for preliminary support at the tunnel entrance, and advanced small conduits of lengths 3 m and 4.5 m were arranged in the backfill soil section.

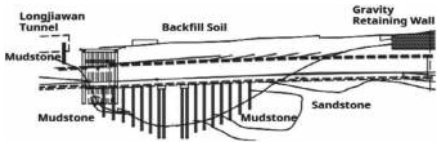

Fig. 1. Longitudinal geological profile of the tunnel section.

2.2 Analysis of Key Construction Challenges

This construction faces two major challenges. The first is the poor self-stabilization capacity of the tunnel face in the backfill soil zone. The backfill soil in this section consists of sandstone, mudstone fragments, cohesive soil, and small amounts of construction and household waste. The size of the fragmented stones ranges from 20 mm to 200 mm, with a skeleton particle content of 30% to 50%, and the overall structure is loose to slightly dense. Traditional advanced small conduit and T76 pipe shed radial grouting techniques are prone to grout loss and irregular diffusion paths in this type of soil, which makes it difficult to ensure effective grouting reinforcement. During excavation, the tunnel face is susceptible to block collapse, which could even lead to crown collapse, posing a significant risk to construction safety. Additionally, the tunnel in this section is primarily located directly beneath the main urban road, Caiyuanlu, with a minimal burial depth of approximately 6.8 m, classifying it as an ultra-shallow-buried tunnel. During the installation of a 12-m-long T76 pipe shed, significant disturbance to the soil above the crown occurred, resulting in a sharp increase in surface settlement rate. This not only poses a serious risk to the construction safety of the tunnel itself but also creates a potential threat to the operational safety of the municipal road above.

3 Tunnel Combined Grouting Calculation Model

3.1 Based on the Construction Plan

(1) After each excavation cycle, a 15 cm thick C25 shotcrete layer is immediately applied to seal the tunnel face, preventing surface soil from falling off. Then, three rows of Φ42 × 3.5 mm advanced small conduits are installed along the excavation profile at 0.3-m intervals, each with a length of 6 m. Axial grouting is carried out at the tunnel face, effectively forming a pre-support reinforcement zone ahead of the excavation.
(2) To control the overall settlement of the tunnel, T76 pipe sheds are symmetrically installed every 5 m on both sides of the tunnel in the initial support section, forming large lock-foot structures. In each cycle, two steel pipes, each 6 m in length, are installed at both arch feet, driven into the surrounding rock at a 30° angle. These pipes are then securely welded to the initial support arch. Finally, M30 cement mortar is injected to form a robust arch foot support, effectively preventing structural settlement.

3.2 Modeling and Analysis

This study uses the large-scale general finite element software MIDAS GTS to establish a three-dimensional numerical model for simulating the tunnel excavation and support process. The model employs the Mohr-Coulomb yield criterion to characterize the elasto-plastic behavior of the geotechnical materials, and the element birth-and-death method is used to accurately analyze the stress conditions during the excavation of the soil layers. To ensure computational accuracy and efficiency, the model dimensions are set to 180 m × 110 m × 90 m, as shown in Fig. 2.

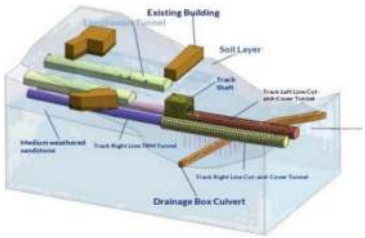

Fig. 2. Tunnel section model.

Boundary Constraints and Calculation Parameters. The boundary conditions for the model are set as follows: vertical (Z-direction) displacement is constrained at all nodes along the bottom boundary, and horizontal (X and Y directions) displacement is constrained at all nodes along the lateral boundaries. The ground surface is treated as a free surface.

The geotechnical parameters used in the calculations are primarily based on the engineering geological survey report and the "Geotechnical Mechanics Parameters Table for the Chongqing-Caiyuanlu Section Tunnel." To conservatively account for the spatial

variability of geotechnical parameters and the adverse effects of joint fractures, a reduction factor of 0.8 was applied to critical parameters such as the elastic modulus, cohesion, and internal friction angle of the rock layers. The specific material parameters are listed in Table 1.

Table 1. Material simulation data.

Material Properties	Thickness (m)	Natural Unit Weight (kN/m^3)	Elastic Modulus (GPa)	Poisson's Ratio	Cohesion (GPa)	Internal Friction Angle (°)	Tensile Strength (kPa)	Compressive Strength (MPa)
Backfill Soil	6.8	20.0	0.02	0.4	/	28	/	/
Moderately Weathered	8.7	25.5	0.816	0.38	0.32	26	150	9.2
Mudstone Moderately Weathered	9.03	24.9	3.264	0.13	1.04	32.4	410	31.6
Sandstone								
Concrete C30	0.15	25	30	0.2	/	/	1430	14.3
Steel Arch Frame	0.013	76.98	200	0.3	/	/	/	345
T76 Steel Pipe	0.008	78.50	200	0.3	/	/	/	235

Analysis of Calculation Results. To visually illustrate the response of the soil layers after tunnel excavation and support, Figs. 3 and 4 present the vertical displacement contour plots after construction.

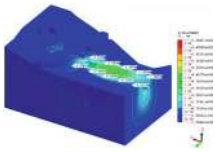

Fig. 3. Vertical displacement contour of theleft line tunnel excavation phase.

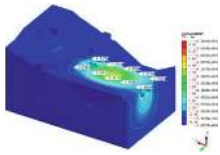

Fig. 4. Vertical displacement contour of the right line tunnel excavation phase.

The numerical results show that, after implementing the combined grouting method at the tunnel arch foot and face, the maximum vertical displacement at the surface is approximately 5.39 mm, well below the 40 mm control standard. These findings preliminarily confirm that the proposed method effectively mitigates soil deformation, significantly reducing the risks of surface collapse and the cracking of surrounding structures.

The displacement contour plots show that the majority of displacement responses within the tunnel influence zone are at relatively low levels, with most values concentrated between 0.0001 mm and 0.01 mm, which aligns with the calculated maximum surface displacement of 5.39 mm. This distribution pattern indicates that the combined grouting method effectively controls the overall displacement field, with continuous and uniform spatial displacement distribution, and no local anomalies. This further supports the effectiveness of the reinforcement scheme in controlling deformation, ensuring construction safety, and stabilizing the surrounding environment. As the soil deformation was effectively controlled, the construction process was not interrupted due to excessive settlement, creating favorable conditions for continuous operations and project schedule compression.

4 Field Implementation and Monitoring

4.1 Field Implementation

To validate the reliability of the numerical simulation results and evaluate the actual effectiveness of the combined grouting scheme, systematic reinforcement operations were carried out on-site, strictly following the process parameters defined in the simulation. The procedure included axial grouting reinforcement at the tunnel face (shotcrete sealing + advanced small conduit grouting), installation of T76 pipe sheds with large lock feet, and reinforcement of lock-foot anchor rods through welding. Each process step was inspected for quality before advancing to the next cycle. The detailed process is illustrated in Fig. 5.

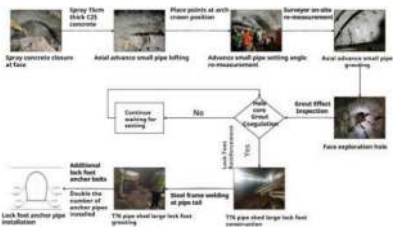

Fig. 5. On-site implementation flowchart.

4.2 Monitoring and Measurement

Monitoring Point Installation. The monitoring system layout follows the same principles as the simulation measurement points, as shown in Fig. 6. It includes: a monitoring section set every 10 m along the tunnel's longitudinal direction, with 10 surface monitoring points arranged at 5-m intervals to collect surface settlement data. Additionally, synchronized monitoring sections are placed behind the tunnel face to collect crown settlement data.

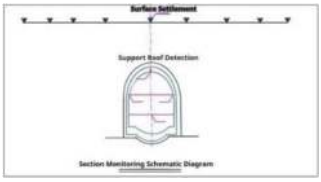

Fig. 6. Monitoring section diagram.

Comparison and Verification of Measured Data with Simulation Results.

(1) Verification of arch settlement: The crown settlement verification was conducted at Section 02, ZK6+571, with a comparison between the measured values after the combined grouting and the simulation results, as shown in Fig. 7.

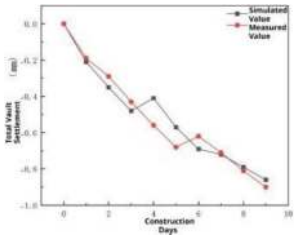

Fig. 7. Comparison of crown settlement.

As shown in Fig. 7, with the increase in construction days, the tunnel crown settlement rate gradually converges, ultimately stabilizing at −0.09 mm/day, which is below the 0.2 mm/day control standard. The numerical simulation results are consistent with the trend of the measured data, validating the model's effectiveness. The localized rebound phenomenon observed in the figure is primarily caused by the slight bulging effect of the surrounding rock under the grout pressure. The rebound response in the simulation occurs slightly earlier than in the actual monitoring data, mainly due to the difficulty of fully replicating the time effects of grout infiltration and consolidation in the actual soil layers, causing the simulation of grout response to be slightly ahead of the real process.

(2) Ground subsidence verification: Surface settlement verification was conducted at Section 02, ZK6+581, with a comparison between the measured values after the combined grouting and the simulation results, as shown in Fig. 8.

As shown in Fig. 8, as construction progresses, the surface settlement rate gradually converges and ultimately stabilizes. The final measured settlement value is 5.67 mm, slightly higher than the simulated value of 5.39 mm. This deviation is mainly due to the higher heterogeneity of the actual soil layers and the complexity of the geological structure compared to the idealized numerical model. Although there is a small absolute deviation, the measured and simulated data show good consistency in terms of settlement development trends, stabilization time, and overall control effectiveness, validating the

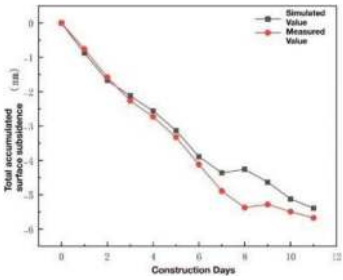

Fig. 8. Comparison of surface settlement.

accuracy of the numerical model and the reliability of the composite reinforcement system in the actual project.

Comparison of Data Before and After Optimization. Based on data from three typical monitoring sections, ZK6+591, ZK6+601, and ZK6+611, this study compares the surface settlement evolution characteristics before and after the implementation of the combined grouting technique, using a 15-m excavation depth as the boundary. The results are shown in Fig. 9.

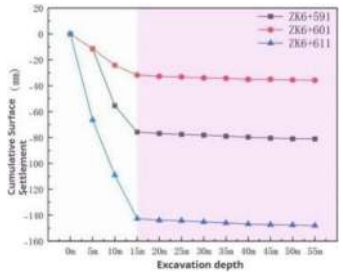

Fig. 9. Comparison before and after optimization.

As shown in Fig. 9, during the not grouted phase with an excavation depth of less than 15 m, surface settlement progressed significantly, with an average settlement of 27.8 mm for every 5 m of excavation. This indicates a severe lack of self-stabilization in the surrounding rock, which poses a significant threat to the tunnel structure and the safety of the road above. After the implementation of the combined grouting method at a depth of 15 m, surface settlement was effectively controlled. For instance, at section ZK6+611, the cumulative settlement before grouting was −142.63 mm; by the time the excavation reached 55 m, the cumulative settlement was −148.01 mm, meaning that the additional settlement during the subsequent 40 m of excavation was only 5.38 mm. The settlement rate significantly decreased, meeting the control requirements. These results demonstrate that the combined grouting method, through consolidation and reinforcement of the soil ahead of the tunnel face, effectively enhances the self-bearing capacity of

the surrounding rock, significantly reducing surface settlement caused by tunnel excavation, and improving the controllability and environmental safety of shallow-buried tunnel construction.

5 Conclusion

This study takes the tunnel excavation of the Chongqing Rail Transit Line 18 Northern Extension, between Chongqing Railway Station and CaiYuanlu Station, as a case study. It investigates the construction of ultra-shallow buried tunnels in backfill soil zones using a combined grouting method at the tunnel arch foot and face, and the following conclusions are drawn:

(1) To address the technical challenges in loose backfill soil layers, where traditional grouting methods often result in grout loss and insufficient reinforcement, this study introduces and applies a combined grouting technique. This method integrates axial grouting through advanced small conduits at the tunnel face with T76 pipe sheds and large lock feet at the tunnel arch foot. By combining proactive pre-support ahead of the tunnel face and strong lock feet behind the formed tunnel section, a three-dimensional reinforcement system is established, significantly improving the mechanical properties of the soil ahead of the excavation face and above the crown.
(2) The numerical simulation results confirm the effectiveness of the combined grouting method in controlling soil deformation. The numerical model developed using MIDAS GTS indicates that, after implementing this method, the maximum vertical displacement at the surface is limited to 5.39 mm, well below the 40 mm control threshold. The displacement contour plots further demonstrate that the soil deformation is continuous, smooth, and free of abrupt changes. This distribution pattern, supported by the underlying mechanical mechanisms, validates that the combined grouting technique effectively restrains soil displacement and optimizes the stress path, providing essential theoretical and data support for the successful decision-making and optimization of the method.
(3) The field monitoring data closely match the numerical simulation results, showing good consistency in their developmental trends. Notably, the actual time for the surrounding rock to reach basic stability is even slightly shorter than predicted by the model. This indicates that the actual reinforcement effect and long-term stability of the combined grouting method in complex strata exceed theoretical expectations, confirming the excellent adaptability and reliability of the combined grouting technique in complex geological conditions.
(4) A comparison of data before and after optimization demonstrates that the combined grouting technique effectively reduced the surface settlement rate from 7.5 mm/day to within the safe standard, fundamentally resolving the critical issue of construction interruptions due to uncontrolled deformation. This technique has successfully ensured the safe tunneling of the tunnel beneath the urban main road, and its effectiveness in controlling deformation has provided essential technical support for continuous and efficient construction. It emphasizes the method's core application and its significant potential for widespread adoption in tunnel projects within complex urban environments.

References

1. He, G., Yang, J.H., Chen, Q.: Inquiring into vault and surface subsidence control in excavation of tunnel with shallowly-buried back filling soil. Mining Safety Environ. Protect. **33**(B06), 105–107 (2006). https://doi.org/10.3969/j.issn.1008-4495.2006.z1.048
2. Jao, G.I.: Discussion on construction control techniques for metro tunnels passing under backfilled soil. Build. Mater. Decoration. **000**(011), 69–70 (2018). https://doi.org/10.3969/j.issn.1674-3024
3. Tian, X.J., Hu, L.C.: Construction techniques for excavation of shallow-buried tunnel in backfill soil. China Water Transport. **07**, 239–240 (2012). https://doi.org/10.3969/j.issn.1006-7973-C.2012.07.114
4. Liu, Z.: Cause analysis and construction preventive measures for tunnel collapse and roof fall accidents. Commun. Sci. Technol. Heilongjiang. **36**(07), 132 (2013). https://doi.org/10.3969/j.issn.1008-3383.2013.07.115
5. Xu, G.W., Ma, Y.F.: Cause analysis and treatment of roof fall accidents in the Jiahuan North connecting line tunnel. China Homes. **11**, 137–138 (2011). https://doi.org/10.3969/j.issn.1674-3954.2011.11.511
6. Li, G.F., Chen, J.W., Wang, A.M., et al.: Prevention and treatment technology for mud and water inrush in mountainous highway tunnels. Value Eng. **44**(11), 69–73 (2025). https://doi.org/10.3969/j.issn.1006-4311.2025.11.021
7. Meng, Y.S.: Handling and preventive measures for water and mud inrush disasters in tunnels. Guangdong Highway Commun. **50**(06), 49–53 (2024). https://doi.org/10.19776/j.gdgljt.2024-06-0049-05
8. Gao, J.F., Gu, B.Q.: The numerical simulation of hazardous heavy material leakage and dispersion in a tunnel. Indus. Safety Environ. Protect. **41**(04), 1–3 (2015). https://doi.org/10.3969/j.issn.1001-425X.2015.04.001
9. Huang, Y.Z.: Research of measures for gas-leakage prevention of concrete. Fujian Constr. Sci. Technol. **04**, 50–52 (2008)
10. Zhou, Y.X., Zhou, Y.J., Pei, T.: Construction technique management for shallow-buried tunnel excavation. Wisdom China. **03**, 121–122 (2025)
11. Wang, Z.W.: Application of advanced support technology in highway tunnel construction. Create Living. (01), 82–84 (2025). https://doi.org/10.3969/j.issn.2095-4085.2025.01.029
12. Wang, D.C.: Quality control and process optimization in tunnel construction: a case study of tunnel secondary lining construction. China Brand and Anti-counterfeiting, (04), 116–118 (2025)
13. Zhang, H.D.: Study on shallow-buried tunnel construction technology and ground settlement control measures. J. Transport Bus. China. **35**, 105–107 (2024). https://doi.org/10.3969/j.issn.1673-3681.2024.35.035
14. Gao, Z.: Monitoring of ground pressure in advanced pipe shed support and optimization of support parameters. J. Mining Technol. **22**(04), 67–70 (2022). https://doi.org/10.3969/j.issn.1671-2900.2022.04.016
15. Rao, P.B.: Analysis and control of the cause of the collapse of the palm surface of shallow buried tunnel. J. Jiangxi Building Mater. **01**, 77–79 (2020). https://doi.org/10.3969/j.issn.1006-2890.2020.01.041
16. Li, Z.: Research on mechanical characteristics of three step construction method for double hole tunnel with extra large cross section. J. Constr. Mechaniz. **45**(12), 36–40 (2024). https://doi.org/10.3969/j.issn.1001-1366.2024.12.006

Research on Optimization of Tunnel Rock Mass Support Parameters and Deformation Control Based on Orthogonal Experiments

Zhenguo Liu[1], Fangjie Jiang[2], Wei Li[1], Jinhui Duan[3(✉)], and Rui Su[3]

[1] Three Engineering Co., Ltd. of CCCC First Highway Engineering Co., Ltd., Beijing 100102, China
[2] Chongqing Transportation Construction Management Co., Ltd., Chongqing 400043, China
[3] School of Civil Engineering, Chongqing Jiaotong University, Chongqing 400074, China
2390738887@qq.com

Abstract.. Currently, systematic research remains lacking on balancing deformation control, rock mass stress optimization, and structural load safety in the design of support parameters for Grade V rock mass tunnels. Based on the engineering geological conditions of the Chongcai section of Chongqing Rail Transit Line 18, a strata-structure coupled model was established using FLAC3D software. Orthogonal experiments were conducted with steel arch spacing, anchor spacing, and secondary lining concrete grade as factors. Range analysis was performed using crown displacement, rock stress, support structure stress, and cost-effectiveness as indicators, with multi-objective trade-offs evaluated among these factors. Results indicate: 1) When displacement control is the objective, optimal parameters are anchor spacing of 0.3 m, steel arch spacing of 0.8 m, and concrete grade C25, limiting crown displacement to 3.34 mm; 2) For rock stress optimization, the combination of 0.7 m anchor spacing, 0.5 m steel arch spacing, and C25/C30 concrete effectively reduces stress concentration; 3) For support structure safety optimization, the combination of 0.5 m anchor spacing, 0.5 m steel arch spacing, and C30 concrete reduces maximum tensile stress to 539.5 kPa. 4) When targeting cost-effectiveness, the combination achieving the theoretically lowest cost objective is anchor spacing of 0.7 m, steel arch spacing of 1.5 m, and secondary lining concrete C25. Based on comprehensive safety and economic analysis, the recommended optimized solution is anchor spacing of 0.5 m, steel arch spacing of 0.8 m, and secondary lining concrete grade C25. This approach balances structural safety and cost-effectiveness while ensuring deformation control. The research findings provide theoretical basis and engineering reference for similar soft rock tunnel support parameter design.

Keywords: Tunnel Surrounding Rock · Support Parameter Optimization · Orthogonal Experiments · FLAC3D · Deformation Control

© The Author(s), under exclusive license to Springer Nature Switzerland AG 2027
G. Feng et al. (Eds.): ICCE 2025, SUCI, pp. 566–577, 2027.
https://doi.org/10.1007/978-3-032-32237-1_40

1 Introduction

With the expansion of urban rail transit networks towards city centers, tunnel construction faces increasingly complex geological and environmental challenges. In soft strata such as Grade V rock mass, ensuring safety and long-term stability is crucial [1–2]. Support systems must not only control deformation, prevent collapse, and optimize stress fields, but also consider the coupled interaction between support and surrounding rock [3]. However, current design methods relying on engineering analogy or single indicators often fail to address multi-factor coupling effects, limiting reliability under complex conditions [4–5].

Extensive research exists on tunnel support parameter optimization, yet current approaches have limitations: some studies only apply orthogonal experimental analysis to bolt parameters [6]; certain models lack in-depth FLAC3D numerical verification [7]; many focus on single support components without systematic coupling analysis of steel arches and bolts [8–9]; and some methods inadequately integrate intelligent algorithms with ground response, reducing engineering applicability [10–11].

Therefore, this study establishes a FLAC3D 3D model for a Grade V rock mass tunnel on Chongqing Rail Transit Line 18. Using orthogonal experiments, it systematically analyzes the effects of steel arch spacing, anchor spacing, and secondary lining concrete grade on crown displacement, rock mass stress, support structure stress, and cost-efficiency. Range analysis identifies the relative importance of each factor and their optimal combinations. A comprehensive multi-objective solution is proposed, offering theoretical and decision-making support for similar projects.

2 Project Overview

The Chongqing–Caiyuan Road section of Chongqing Rail Transit Line 18 North Extension (referred to as the "Caiyuan Section") is located beneath the exit of Longjiawan Tunnel on Caiyuan Road in Yuzhong District. It is a double-track urban underground rail transit tunnel. The left line is approximately 1,775.2 m long and the right line about 1,778.3 m. Construction uses cut-and-cover method with a dual-track single-bore structure; the typical cross-section follows Profile A, as shown in Fig. 1.

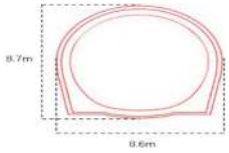

Fig. 1. Cross-section of Tunnel A.

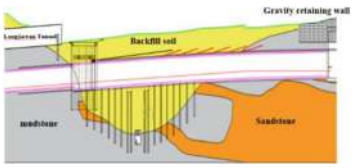

Fig. 2. Geological longitudinal profile of the dark excavation section in the heavy load.

To investigate the mechanical response of tunnel structures beneath Grade V rock in complex urban environments, this study selected the right-line tunnel as its research

subject. This tunnel section features relatively uniform burial depth and typical geological conditions, with rock mass predominantly classified as Grade V. Characterized by fractured rock and poor self-stabilization capacity, it offers excellent representativeness.

The project's original topography belongs to a tectonically eroded hilly area. Long-term human activity has transformed it into predominantly strip-like flat land, with locally preserved high, steep slopes. The excavation strata primarily consist of interbedded moderately weathered sandstone and sandy mudstone, classified as soft rock. The geological longitudinal profile of the tunnel is shown in Fig. 2.

3 Finite Difference Model Development

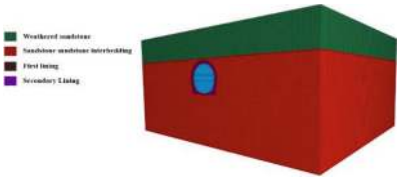

Fig. 3. Tunnel excavation numerical model.

Table 1. Parameters of grade v rock mass and support structure materials.

Material Type	Modulus of Elasticity (GPa)	Poisson's Ratio	Cohesion (MPa)	Internal Friction Angle (°)	Specific Gravity (kN/m³)	Thickness (m)
Moderately Weathered Sandstone	2.5	0.28	1.5	35	24.5	25
Sand-Silt Interbedded	1.0	0.38	0.15	22	22.0	75
Advance Pipe Arch	200	0.30	—	—	78.5	—
Steel Arch Frame	210	0.30	—	—	78.0	—
C25 Shotcrete	28	0.20	—	—	25.0	—

Based on the geological and support design of the Chongqing- Caiyuan tunnel section on Metro Line 18, a FLAC3D soil- structure interaction model was established. The model dimensions are 120 m × 100 m × 100 m (length × width × height), treated as a plane- strain problem (Fig. 3). Boundary conditions include fixed vertical displacement at the base, normal displacement constraints on the four sides, and a free ground surface.

Stratigraphy, based on survey data, consists mainly of interbedded moderately weathered sandstone and sandy mudstone, representing typical Grade V soft rock.

Material behavior was simulated using the homogeneous, isotropic Mohr- Coulomb elastic- plastic model. Parameters for the surrounding rock and support materials are given in Table 1.

4 Orthogonal Test Design and Analysis of Support Parameters

4.1 Orthogonal Experimental Design

Anchor Bolt Spacing. Anchoring enhances rock mass integrity through its synergistic "point-line-surface" effect, playing a key role in controlling deformation and improving stability. As a core design parameter, bolt spacing must balance support effectiveness, economy, and constructability. According to current standards such as the Highway Tunnel Construction Technical Specifications [12] and Railway Tunnel Design Specifications [13], typical bolt spacings are 1.0–1.5 m for Grade III rock, 0.8–1.2 m for Grade IV rock, and a denser 0.6–1.0 m for Grade V rock.

Guided by these empirical recommendations, this study sets anchor spacing as an experimental variable at three levels: 0.3 m, 0.5 m, and 0.7 m. Numerical simulations are used to examine the influence of different spacings on rock mass deformation and support stress distribution, thereby revealing parameter sensitivity and providing a basis for optimization. The cross-sectional layout of anchors and steel arches is shown in Fig. 4.

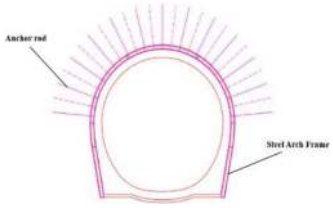

Fig. 4. Anchor bolt arrangement cross-section.

Spacing Between Steel Arches. In soft rock tunnels, steel arches provide essential rigid support due to the poor self-stabilizing capacity of the surrounding rock. Their spacing must balance stiffness and economy. Empirically, spacing is often set at 1.0–1.5 m for Grade III, 0.8–1.0 m for Grade IV, and 0.5–0.8 m for Grade V rock [6]. While empirical values offer guidance, numerical optimization is valuable under complex conditions.

In this study, steel arch spacing is taken as an orthogonal test factor with three levels: 0.5 m, 0.8 m, and 1.5 m. Numerical simulations of rock displacement and arch stress under different spacings reveal their influence on tunnel stability, supporting parameter optimization.

Concrete Grade. The secondary lining serves as the permanent structural support in tunnels, crucial for long-term stability and operational safety. Its concrete grade, selected

based on rock class, directly influences safety and cost-effectiveness: typically C25–C30 for Grade III, C25 for Grade IV, and not less than C25 (often C30) for Grade V.

In the numerical simulations, concrete grade (C25, C30, C35) is treated as a key parameter, representing conventional to high-strength lining schemes. By adjusting related mechanical properties, this study systematically evaluates the effect of different grades on rock deformation, lining internal forces, and long-term stability, providing quantitative evidence for design optimization.

To systematically investigate the influence of support parameters on tunnel stability and determine optimal combinations, three key factors were selected: steel arch spacing (A), anchor spacing (B), and secondary lining concrete grade (C). Each factor was assigned three levels (Table 2), and simulations were arranged using an $L_9(3^3)$ orthogonal array (Table 3).

Table 2. Factor level table.

Factor	Level 1	Level 2	Level 3
Steel Arch Spacing (m)	0.5	0.8	1.5
Anchor Bolt Spacing (m)	0.3	0.5	0.7
Concrete Grade	C25	C30	C35

Table 3. Orthogonal test Table ($L9(3^3)$).

Test No.	Steel Arch Spacing (m)	Anchor Spacing (m)	Concrete Grade
1	0.5	0.3	C25
2	0.5	0.5	C30
3	0.5	0.7	C35
4	0.8	0.3	C30
5	0.8	0.5	C35
6	0.8	0.7	C25
7	1.5	0.3	C35
8	1.5	0.5	C25
9	1.5	0.7	C30

4.2 Analysis Based on Safety Numerical Simulation Results

Range Analysis Method. Range analysis is a classic and intuitive method for processing orthogonal test results. Its core principle is to calculate and compare the range of average values for each factor level, thereby assessing the significance of each factor's influence and determining the optimal parameter combination. The analysis proceeds at two main levels: first, by comparing the average results of a factor across its levels, the optimal level

for a given objective can be identified; second, by computing the range of these averages, the relative importance of each factor can be ranked—a larger range indicates greater influence on the results. This study applies range analysis to systematically evaluate the impact of three key parameters—steel arch spacing, anchor spacing, and secondary lining concrete grade—on tunnel stability and economic efficiency, aiming to identify the optimal support combination under multiple objectives.

Analysis of Control Performance Based on Arch Displacement. Tunnel crown settlement serves as the most intuitive indicator for assessing rock mass stability. Through range analysis of all nine test results, a systematic investigation was conducted on the combined effects of three factors: steel arch spacing (A), anchor spacing (B), and secondary lining concrete grade (C). The relative influence of each factor was determined by calculating the mean value (K) and range (R) of corresponding indicators at different levels through range analysis. The results are presented in Table 4.

Table 4. Range analysis results.

Factor	Level 1 Mean(K1)/mm	Level 2 Mean(K2)/mm	Level 3 Mean(K3)/mm	Range(R)/mm	Factor Priority	Optima 1 Level
A: Steel Arch Spacing	3.6638	3.3413	3.5100	0.3225	2	A2(0.8 m)
B: Anchor Spacing	3.3414	3.5811	3.5926	0.2512	1	B1(0.3 m)
C: Concrete Grade	3.4265	3.5950	3.4936	0.1685	3	C1(C25)

Based on the range analysis results, the order of influence of the three factors on crown displacement is: B (anchor bolt spacing) > A (steel arch spacing) > C (concrete grade). To minimize crown displacement, the optimal parameter combination is A2B1C1, i.e., steel arch spacing of 0.8 m, anchor bolt spacing of 0.3 m, and secondary lining concrete grade C25. This scheme controls crown displacement to approximately 3.844 mm, as shown in Fig. 5.

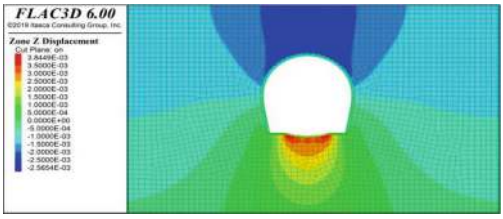

Fig. 5. Displacement contour map of the arch under the optimal combination (A2B1C1).

Analysis of the Effectiveness of Controlling Based on the Minimum Principal Stress of the Surrounding Rock Mass. The minimum principal stress of the surrounding rock reflects the degree of compressive stress concentration. Excessively high values can lead to shear failure of the rock mass. Experimental results were used to simulate the minimum principal stress values. A range analysis was performed on the data to calculate the average value (K value) and range (R value) of the minimum principal stress extremes at different levels for each factor. The results are shown in Table 5.

Table 5. Analysis results of minimum principal stress range.

Factor	Level 1 Mean (K1)/mm	Level 2 Mean (K2)/mm	Level 3 Mean (K3)/mm	Range (R)/mm	Factor Priority	Optimal Level
A: Steel Arch Spacing	-16,629	-16,667	-16,767	138	3	A1(0.5m)
B: Anchor Spacing	-17,000	-16,800	-16,262	738	1	B3(0.7m)
C: Concrete Grade	-16,567	-16,567	-16,929	362	2	C1/C2(C25/C30)

Based on the range analysis results, the order of influence of each factor on the minimum principal stress value of the surrounding rock is: B (bolt spacing) > C (concrete grade) > A (steel arch spacing). Bolt spacing is the decisive factor controlling the stress state of the surrounding rock, with its range significantly greater than that of other factors. Following the principle of optimizing stress concentration to minimize the absolute value of the minimum principal stress, the optimal combinations are A1B3C1 and A1B3C2. These correspond to steel arch spacing of 0.5 m, anchor bolt spacing of 0.7 m, and secondary lining concrete grade C25 or C30, as illustrated in Figs. 6 and 7.

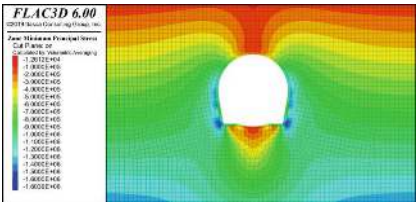

Fig. 6. Contour plot of minimum principal stress in the surrounding rock under the optimal combination (A1B3C1).

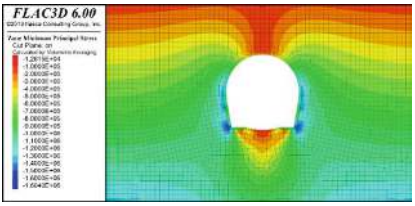

Fig. 7. Contour plot of minimum principal stress in the surrounding rock under the optimal combination (A1B3C2).

Analysis of the Effectiveness of Controlling the Maximum Principal Stress in Support Structures. The maximum principal stress of the support structure is critical

for assessing the risk of lining cracking. Experimental results were obtained through numerical simulation, and the data underwent range analysis. With the objective of minimizing the maximum principal stress, the results are presented in Table 6.

Table 6. Analysis results of maximum principal stress range.

Factor	Level 1 Mean (K1)/pa	Level 2 Mean (K2)/pa	Level 3 Mean (K3)/pa	Range (R)/pa	Factor Priority	Optimal Level
A: Steel Arch Spacing	932.6	1451.1	1242.7	518.5	1	A1(0.5m)
B: Anchor Spacing	1252.1	1043.2	1331.0	287.8	3	B2(0.5m)
C: Concrete Grade	1127.8	1053.3	1445.3	392.0	2	C2(C30)

Based on the range analysis results, the order of influence of each factor on the maximum principal stress of the support structure is: A (steel arch spacing) > C (concrete grade) > B (anchor spacing). Steel arch spacing is the primary factor controlling the tensile stress level in the support structure. Following the principle of minimizing tensile stress within the support structure through optimal parameter combinations, the best combination of factor levels is A1B2C2—i.e., steel arch spacing of 0.5 m, anchor bolt spacing of 0.5 m, and secondary lining concrete grade C30—as shown in Figs. 8 and 9.

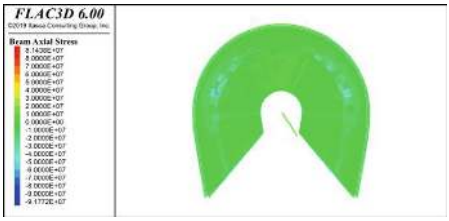

Fig. 8. Maximum principal stress contour map for steel arch support under optimal combination (A1B2C2).

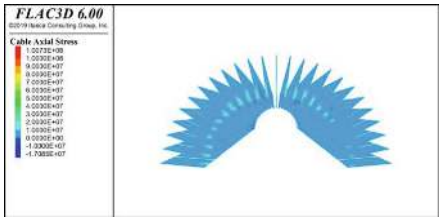

Fig. 9. Maximum principal stress contour map for anchor support under optimal combination (A1B2C2).

4.3 Analysis Based on Economic Indicators

The optimization of support parameters is both a technical and an economic challenge. An effective support scheme must ensure safety while maintaining cost-effectiveness for optimal resource allocation. This study conducts an economic analysis based on current material prices in Chongqing, relevant engineering quotas, and the design principles outlined in the Technical Specifications for Highway Tunnel Construction [12]. It calculates

the costs of the main support components—rock bolts, steel arches, and secondary lining concrete—to assess each parameter level from a purely economic viewpoint, clarify cost sensitivity, and provide an independent economic basis for subsequent multi-objective decision-making.

The comprehensive cost of anchor engineering includes anchor body materials, grouting materials, drilling, and installation labor costs. The total cost is directly proportional to the number of anchors per unit length of tunnel. According to tunnel support design theory, the number of anchors N can be expressed as:

$$N = \frac{L}{A} \times \frac{C}{R} \tag{1}$$

Where L is the tunnel length, A is the circumferential spacing of the bolts, and R is the longitudinal spacing of the bolts. Since rock bolts must be arranged both circumferentially and longitudinally, their total quantity is inversely proportional to the product of spacing and quantity. Consequently, even minor adjustments to bolt spacing can cause significant fluctuations in total costs. In Grade V rock mass, increasing bolt spacing from 0.3 m to 0.5 m can reduce support costs by approximately 30%–40% [14]. Calculations in this study indicate that increasing spacing from 0.3 m to 0.7 m reduces the number of bolts per unit area by approximately 79%, leading to a corresponding substantial decrease in material and construction costs. Therefore, from a purely economic perspective, larger bolt spacing is more economical, with the optimal level being B3 (0.7 m).

As the primary load-bearing component of initial support, the economic assessment of steel arches must account for material, fabrication, and installation costs. Their installation is complex and time-consuming, often affecting project duration and labor costs more than material expenses. Increasing the spacing from

0.5 m to 0.8 m reduces the number of arches by 37.5%, saving structural steel and significantly cutting installation procedures and construction time. Further increasing spacing to 1.5 m minimizes costs, though potential stiffness reduction must be considered. Thus, under purely economic criteria, larger spacing yields greater savings, with level A3 (1.5 m) being optimal.

The economic analysis of secondary-lining concrete grades is more straightforward, with cost differences mainly driven by material unit prices. According to market data and Technical Specifications for Highway Tunnel Construction [12], each grade increase raises the price per cubic meter by about 5–8%. Since lining thickness is constant across all schemes, total material cost is directly proportional to strength grade. Studies indicate that C25 already meets basic support requirements for Grade V rock; raising the grade adds cost with diminishing marginal benefits [8]. C35 incurs the highest cost but offers limited additional control over deformation. Therefore, economically, the lowest grade that satisfies design requirements is optimal, i.e., C1 (C25).

Based on the independent economic analysis above, the theoretically lowest-cost combination is A3B3C1: anchor spacing 0.7 m, steel-arch spacing 1.5 m, and secondary-lining concrete C25.

4.4 Analysis of Support Parameter Combinations Based on Safety and Economy

To systematically evaluate the overall performance of support parameters in balancing safety and economy, this section establishes a comprehensive evaluation index. This index unifies and quantifies four objectives—roof displacement, minimum principal stress of surrounding rock, maximum principal stress of support structure, and economic cost—to achieve normalized processing for multi-objective decision-making. The comprehensive evaluation index is defined as follows:

$$S_i = w_1 \cdot \frac{D_i - D_{min}}{D_{max} - D_{min}} + w_2 \cdot \frac{\sigma_{\min,i} - \sigma_{\min,\max}}{\sigma_{\min,\min} - \sigma_{\min,\max}} + w_3 \cdot \frac{\sigma_{\max,i} - \sigma_{\max,\min}}{\sigma_{\max,\max} - \sigma_{\max,\min}} + w_4 \cdot \frac{c_i - c_{min}}{\sigma_{\max,\min} - c_{min}} \quad (2)$$

Where: S_i denotes the comprehensive score for Test Group D_i;$D_i$represents the crown displacement; $\sigma_{min,\,i}$ and $\sigma_{max,\,i}$ denote the minimum principal stress of the surrounding rock and the maximum principal stress of the support structure,respectively; $^{c\,i}$represents the economic cost; w_1 ~ w_4 denote the weighting coefficients for each indicator, respectively. In this paper, based on the actual project conditions, $w_1 = 0.3$, $w_2 = 0.2$, $w_3 = 0.3$ and $w_4 = 0.2$ are adopted to reflect the emphasis on structural safety and deformation control.

By calculating the comprehensive scores for the nine experimental designs in the orthogonal test, the overall scores for each design are presented in Table 7.

Table 7. Comprehensive evaluation scores for orthogonal test plans.

Test No.	Steel Arch Spacing (m)	Anchor Spacing (m)	Secondary Lining Concrete Grade	Comprehensive Score
1	0.5	0.3	C25	0.62
2	0.5	0.5	C30	0.71
3	0.5	0.7	C35	0.54
4	0.8	0.3	C30	0.71
5	0.8	0.5	C25	0.74
6	0.8	0.7	C35	0.69
7	1.5	0.3	C35	0.48
8	1.5	0.5	C25	0.73
9	1.5	0.7	C30	0.59

As shown in Table 7, after comprehensively balancing safety and economic considerations and analyzing the relative importance of each factor in the range analysis, the recommended design parameters are: anchor spacing of 0.5 m, steel arch spacing of 0.8 m, and secondary lining concrete grade C25. This solution achieves the optimal balance among crown displacement, structural loading, and project cost. It ensures adequate safety reserves while offering favorable economic viability and construction feasibility, making it suitable for promotion and application in similar Grade V rock mass tunnel projects.

5 Conclusion

This study examines the influence of three key support parameters—steel arch spacing, bolt spacing, and secondary lining concrete grade—on the deformation, rock stress, and structural loading of a Grade V rock tunnel section between Chongcai stations on Chongqing Metro Line 18. Using FLAC3D numerical simulation combined with orthogonal experimental design, the factors are systematically analyzed and multi-objective optimization is performed. The established method, based on orthogonal testing and multi-objective decision-making, offers theoretical and practical guidance for similar soft-rock tunnel projects. The main findings are:

1. Range analysis clarified the influence hierarchy of each parameter on different response indicators. For crown-displacement control, anchor spacing was most influential, followed by steel-arch spacing and concrete grade. For minimizing rock principal stress, anchor spacing remained dominant, with concrete grade secondary. For limiting support-structure principal stress, steel-arch spacing had the strongest effect.
2. Safety-oriented optimal combinations were identified: for displacement control, anchor spacing 0.3 m, steel-arch spacing 0.8 m, and C25 lining; for rock-stress optimization, anchor spacing 0.7 m, steel-arch spacing 0.5 m, and C25/C30 lining; for support-structure safety, anchor spacing 0.5 m, steel-arch spacing 0.5 m, and C30 lining. Economically, the lowest-cost combination is anchor spacing 0.7 m, steel-arch spacing 1.5 m, and C25 lining.
3. Balancing displacement control, structural safety, and economy, the recommended support scheme for this project is anchor spacing 0.5 m, steel-arch spacing 0.8 m, and secondary-lining concrete C25. This design significantly reduces material use and cost while keeping crown displacement controllable, achieving an integrated balance of safety and economy.

References

1. Jiang, Y.S., Jiang, H., Wang, J.X.: Pressure distribution and its varying characteristics of steel rib support in grade V surrounding rock of road tunnel. J. Eng. Geol. **20**(3), 453–458 (2012). https://doi.org/10.3969/j.issn.1004-9665.2012.03.022
2. Li, L., Zhang, M.X., Wu, H.M.: Influence of short-distance multi-line overlapped shield tunnelling on deformation of existing tunnels. Chin. J. Geotech. Eng. **36**(6), 1061–1069 (2014). https://doi.org/10.11779/CJGE201406010
3. Yang, C.B., Zhang, S.Y., Xu, J.B.: FLAC3D program and its applications in couple problem between primary support design and rock wall condition in double-arch tunnel. J. Coalfield Geol. Explor. **32**(6), 49–52 (2004) OI: 10.3969/j.issn.1001-1986.2004.05.018
4. Sun, Z.Y., Zhang, D.L., Fang, Q.: Synergistic optimization design method for tunnel support structure system and its application. Chin. J. Geotech. Eng. **43**(8), 1503–1514 (2021). https://doi.org/10.11779/CJGE202103016
5. Zhang C, Du H B and Qin S Y: Research on optimization of initial support parameters for tunnels in weak rock mass based on numerical simulation Western China J. Transport. Sci. Technol., (3): 130–133 (2025). DOI: 10.13282/ j.cnki.wccst.2025.03.037.
6. Jin Y Y: The Analysis on Parameter Optimization of Tunnel Bolt Chongqing Jiaotong University, Master's Thesis (2020).

7. He, C., Zhang, Y.G., Wei, W.L., et al.: Intelligent design and evaluation method of tunnel support system based on machine learning. China J. Highw. Transp. **36**(2), 1–12 (2023). https://doi.org/10.19721/j.cnki.1001-7372.2023.11.003
8. Yang C M: Research on Optimization of Initial Support Parameters for Tunnels in Weak Rock Masses Chongqing Jiaotong University, Master's Thesis (2022).
9. Ma, R.: Study on construction process numerical simulation and supporting parameters optimization of tunnel Central South University. Master's Thesis. (2021)
10. Li, F., Jiang, A., Zheng, S.: Anchoring parameters optimization of tunnel surrounding rock based on particle swarm optimization. J. Geotech. Geol. Eng. **39**(6), 1–11 (2021). https://doi.org/10.1007/s10706-021-01782-3
11. Zhang, T., Zhao, J., Kuang, R.: Stability analysis and support optimization of tunnel surrounding rock with weak interlayer based on catastrophe theory. J. Buildings. **15**(3), 507–507 (2025). https://doi.org/10.3390/buildings15030507
12. Ministry of Transport of the People's Republic of China: Technical specifications for highway tunnel construction: JTG F60–2009 (2009).
13. Ministry of Railway of the People's Republic of China: Railway tunnel design specification: TB 10003–2005 (2005).
14. Li, Y.P., Wang, Z.Y., Han, C.L.: Simulating study on construction process of tunnels with small spacing for different classes of surrounding rocks. J. Rock Soil Mech. **1**, 11-16+28 (2006). https://doi.org/10.3969/j.issn.1000-7598.2006.01.003

Parameter Analysis of Mechanical Performance of UHPC Continuous Bridge Deck Structure for Concrete Beam Bridge

Chaomin Chu[1], Lvshan Huang[2], Qiaosha Chen[2], Liang Xiao[3(✉)], and Runchuan Xu[3]

[1] Ningbo Datong Development Co., Ltd, Ningbo 315100, China
[2] Ningbo Yongtaiwen Transportation Development Co., Ltd, Ningbo 315800, China
[3] College of Civil Engineering, Tongji University, Shanghai 200092, China
1911393@tongji.edu.cn

Abstract. To address the issue of poor crack resistance in conventional continuous bridge deck structure and enhance both the durability and driving comfort of the bridge deck, this study applies Ultra-High Performance Concrete (UHPC) to continuous bridge deck structure. Based on the properties of UHPC material, a novel continuous bridge deck structure is proposed, featuring continuous UHPC bridge deck pavement combined with UHPC bridge deck link slab. To investigate the mechanical behavior of this structure, a refined full-bridge finite element model is established using ANSYS software, enabling a clear understanding of its stress distribution. Building on this, the study analyzes the impact of the isolation section length, thickness of the bridge deck link slab, and length of the bridge deck link slab on the mechanical performance of the UHPC continuous bridge deck structure. The findings reveal that: (1) When the length of the bridge deck link slab is constant, increasing the isolation section length reduces the tensile stress in the bridge deck pavement, with a recommended half isolation length of 0.6 m. (2) As the thickness of the UHPC bridge deck link slab increases, the tensile stress on the top surface of the UHPC bridge deck pavement within the overall model also rises. (3) When the length of the half isolation section is fixed, the length of the bridge deck link slab has minimal effect on the bridge deck's stress, with a recommended half bridge deck link slab length of 0.68 m.

Keywords: Concrete Beam Bridge · Ultra-High Performance Concrete (UHPC) · Continuous Bridge Deck Structure · Parameter Analysis

1 Introduction

With its core strengths of clear structural stress distribution, mature design and construction techniques, and high cost-effectiveness, simply supported beam bridge plays an indispensable foundational role in modern transportation networks. It is not only the preferred bridge type for spanning small to medium-sized rivers, valleys, and interchange nodes in highway and railway systems, forming the capillaries and crucial nodes of the road network, but also, with its standardized prefabrication and rapid assembly

© The Author(s), under exclusive license to Springer Nature Switzerland AG 2027
G. Feng et al. (Eds.): ICCE 2025, SUCI, pp. 578–588, 2027.
https://doi.org/10.1007/978-3-032-32237-1_41

capabilities, significantly support the large-scale and efficient construction of transportation infrastructure. However, its inherent expansion joint devices, while offering notable advantages, also introduces defects that cannot be overlooked. Although these joints effectively accommodate deformations in the beam caused by temperature variations and loads, their physical segmentation directly compromises the overall continuity of the bridge deck, creating structural vulnerabilities. Repeated impacts from vehicles can easily damage the joints themselves and cause cracking in the concrete of the anchorage zones, leading to an uncomfortable bumping sensation and significantly reducing driving comfort and safety. More critically, damaged expansion joints allow erosive substances such as water and deicing salts to penetrate, causing long-term harm to substructures like piers and bearings. This substantially increases maintenance costs and complexity throughout the bridge's lifecycle, posing a key challenge to the durability and service performance of such bridges [1, 2].

To address the aforementioned issues, engineers introduced the concept of bridge deck continuity in the late 1970s [3]. This innovative design represents an optimization and upgrade of the upper bridge deck system, while fully preserving the core advantages of simply supported beam bridge, including clear stress distribution in the lower structure, ease of construction, cost-effectiveness, and strong adaptability to foundation deformation. Its essence lies in connecting the bridge decks or deck pavements of two adjacent spans into a continuous whole at the hinged area of the beam ends, thereby eliminating traditional physical expansion joints. This approach yields multiple significant benefits: Firstly, it eradicates the bumping phenomenon and impact noise caused by expansion joints, ensuring a smooth and comfortable ride for vehicles crossing the bridge. Secondly, the continuous bridge deck effectively resolves the persistent issues of water accumulation and debris buildup at expansion joints, significantly enhancing the bridge deck's waterproof performance and preventing water seepage from corroding substructures such as bearings, piers, and abutments, thus extending the overall service life of the bridge. Finally, it substantially reduces the workload and costs associated with frequent maintenance in the later stages and avoids traffic disruptions caused by expansion joint repairs. The bridge deck continuity technology successfully leverages strengths while mitigating weaknesses, significantly improving driving quality and durability while retaining all the structural advantages of simply supported beam.

Currently, the continuous deck structure is extensively employed in small-span and medium-span reinforced concrete beam bridge across China [4]. The majority of these continuous bridge deck structures falls under the category of continuous bridge deck pavement, which can be further classified into hinged, rigid, and tie-bar types based on their stress mechanism and construction method [5]: (1) The hinged continuous bridge deck is composed of a concrete wearing course, an asphalt concrete overlay, a waterproofing layer, longitudinal and transverse reinforcement mesh, and longitudinal connecting bars. Once the main beam is erected, bind the longitudinal connecting bars to the longitudinal reinforcement of the main beam deck and wrap them with rubber sleeves. Next, install the reinforcement mesh, pour concrete, lay the waterproof layer and asphalt concrete, and create a break joint on the concrete beam slab. The hinged continuous bridge deck structure, featuring a break joint and allowing slight vertical displacement of the connecting reinforcement, prevents the generation of bending moments within the

plate when the main beam bends or the beam end rotates. The axial force transmission is handled by the connecting reinforcement. However, constructing this type of continuous bridge deck structure is complex, and the presence of break joints can lead to water seepage, which in turn may erode the reinforcement. (2) The rigid continuous bridge deck consists of a concrete wearing course, an asphalt concrete overlay, longitudinal and transverse reinforcement mesh, waterproofing membranes, and a soft cushion layer. Upon completion of the main beam erection, apply a layer of asphalt at the reserved notch on the main beam, arrange the reinforcement mesh, and coat it with epoxy resin. Subsequently, construct the concrete pavement layer followed by the asphalt concrete pavement layer in sequence. Additionally, install waterproof coiled materials within the specified range on both sides of the pier centerline, between the cement concrete and asphalt concrete pavement layer. In addition to transferring axial forces induced by braking forces, shrinkage, and creep, the deck slab develops bending moments due to the rotation of the main girder ends, rendering it structurally analogous to a fixed-end beam. (3) The tie-bar continuous bridge deck comprises a concrete wearing course, an asphalt concrete overlay, a waterproofing layer, longitudinal and transverse reinforcement mesh, longitudinal prestressed tie-bars, and oil-impregnated softwood strips. The construction procedure for the continuous structure of tie-bar bridge deck is as follows: First, place an oil-soaked balsa strip both above and below the reserved section of the main beam. Next, bind the thick reinforcement bars with those embedded in the main beam deck, lay down the reinforcement mesh, and then pour cement concrete followed by asphalt concrete for the pavement. Among these steps, the thick steel bars that are bound with the reinforcement in the main beam deck should be coated with epoxy ester acid paint and subsequently wrapped with two layers of glass fiber cloth and polyethylene tape from the inside out, forming what is known as a “tie bar”. The axial tension resulting from factors such as temperature variations, shrinkage, creep, and braking forces is borne by the tie bar and the reinforcement mesh within the structure. The installation of oil wood strip at both ends of the continuous bridge deck structure aims to diminish the bending resistance of the section at these points and reduce the constraining effect between the pavement and the beam, thereby minimizing the bending moment within the continuous slab caused by the rotation at the end of the main beam. Engineering practices have demonstrated that such continuous bridge deck structures are prone to cracking due to the relatively thin pavement structure and limited reinforcement.

To address the cracking distress in continuous bridge deck, researchers both domestically and internationally have proposed improvement measures for traditional continuous bridge deck structure, which can be categorized into two types: enhancing the structural detail and replacing the deck material.

Firstly, regarding structural improvement, Pan et al. [6] proposed an embedded continuous deck structure and conducted analysis using finite element method. The results indicated that the embedded structure significantly reduces combined stresses under the most unfavorable conditions and substantially decreases calculated crack width compared to rigid continuous bridge deck. This suggests that adopting such a detail helps mitigate cracking in continuous bridge deck and prevents or reduces the formation of reflective cracks in the overlying asphalt concrete. Wang et al. [1] introduced an arched continuous deck structure and employed numerical method and model test. Their study

concluded that the arched continuous deck effectively avoids direct action of deformation—such as longitudinal displacement, rotation, and differential settlement of simply-supported bridge—on the continuous deck concrete. It also better distributes wheel load pressures, markedly improving the stress state of the continuous deck concrete and alleviating its primary distresses.

Secondly, concerning material replacement for continuous bridge deck, Lin [7] applied Engineered Cementitious Composite (ECC) to continuous bridge deck structure. Using linear elastic analysis and finite element method, they analyzed the mechanical behavior of ECC link slab and accordingly proposed a design methodology, recommended values for design parameters, and optimized structural scheme, providing theoretical foundation and reference for its application. Qian [8] established a finite element model of an ECC continuous deck structure using ABAQUS software, investigating its mechanical performance, deformation characteristics, and interfacial connection under various conditions. The study also analyzed the influence of key design parameters on the structural behavior. Shao et al. [9] proposed a novel Ultra-High Performance Concrete (UHPC) continuous deck structure for steel simply-supported bridge. Through experimental and numerical investigation, their results demonstrated that the continuous deck structure significantly enhances the rotational stiffness at girder ends, thereby markedly improving ride comfort under normal service conditions by avoiding issues such as bumping at bridge end. Additionally, this structure creates a more favorable stress state for the deck pavement. Zhou et al. [10] introduced a steel-UHPC composite continuous deck structure. Based on finite element method, they analyzed the distress mechanisms of traditional continuous deck structure and compared the displacement and stress response of the new steel-UHPC composite structure with traditional one under design vehicle load and thermal effect.

Currently, research on UHPC continuous bridge deck structure remains insufficient, primarily focusing on the application of UHPC in single structures like bridge deck pavement or bridge deck link slab. Studies on continuous bridge deck structure incorporating both continuous UHPC deck pavement and continuous UHPC deck slab are relatively scarce. This paper applies UHPC to continuous bridge deck structure. To investigate the mechanical performance of this structure, a full-bridge finite element model of the background project is established using numerical analysis method. The study focuses on analyzing the impact of the isolation section length of the bridge deck link slab, the thickness of the bridge deck link slab, and the length of the bridge deck link slab on the mechanical performance of the UHPC continuous bridge deck structure.

2 Introduction to UHPC Bridge Deck Continuous Structure

The schematic diagram of the UHPC bridge deck continuous structure proposed in this paper is illustrated in Fig. 1. This structure is applicable to simply supported T-beam with spans ranging from 25 to 30 m, where continuity of the bridge deck is achieved through UHPC link slab at the beam end joints. Concurrently, the T-beam bridge deck is topped with a 10cm thick C50 concrete pavement followed by a 10cm thick asphalt pavement. A specific thickness of UHPC is employed to replace the conventional C50 concrete pavement on the UHPC link slab, with both the UHPC link slab and UHPC pavement

being poured simultaneously. Additionally, steel plate or rubber are inserted between the UHPC link slab and the main beam to provide isolation. Notably, the UHPC bridge deck link slab is not fully isolated from the normal concrete across its entire section; hence, the length of the isolation section is used to denote the length of the isolated portion between the UHPC link slab and the normal concrete slab. As depicted in Fig. 1, *l1* represents the length of the isolation section of the UHPC bridge deck link slab; *l2* denotes the length of the UHPC bridge deck link slab; *l3* signifies the length of the UHPC bridge deck pavement; and *t1* indicates the thickness of the UHPC bridge deck link slab.

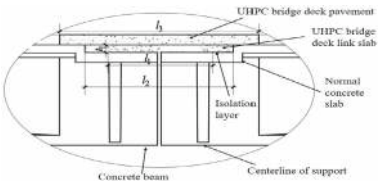

Fig. 1. Schematic diagram of bridge deck continuous structure.

3 Background Engineering

As illustrated in Fig. 2, the background project discussed in this paper involves a prefabricated simply supported T-beam bridge, featuring a span ranging from 25 to 30 m, a bridge width of 20.25 m, and a beam height of 2 m. The top slab has a thickness of 160 mm, the haunch section measures 250 mm in thickness, the web at mid-span is 200 mm thick, while the web at the support points is 500 mm thick. The flange slab is 850 mm wide, the diaphragm ranges from 180 to 200 mm in thickness with a spacing of approximately 7.2 m, and the longitudinal wet joint is 563 mm wide. The bridge is surfaced with a 100 mm-thick C50 concrete pavement followed by a 100 mm-thick asphalt concrete pavement.

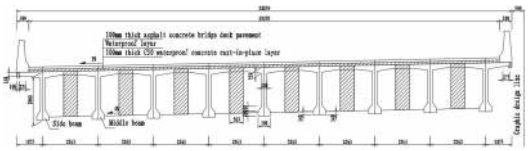

Fig. 2. Midspan cross section of fabricated simply supported T-beam.

4 Finite Element Analysis

4.1 Introduction to the FEM Model

For a 4-span monolithic T-beam with each span measuring 30 m, a refined full-bridge solid finite element model is established using ANSYS software. The constitutive relations for each material are selected in accordance with the relevant specification, with

specific parameters detailed in Table 1. Notably, materials such as C50 concrete and UHPC are treated as elastic.

Table 1. Material property parameters.

Material type	Bulk density (kN/m^3)	Poisson's ratio	Elastic modulus (MPa)	Coefficient of thermal expansion (1/°C)
Main beam C50	26	0.2	34500	1.0 × 10–5
UHPC	28	0.2	42900	1.1 × 10–5
Steel plate	78.5	0.3	206000	–
Rubber plate	13.8	0.4	2	–
Rubber support	20	0.49	350	–

To reduce computational costs, two 30-m span T-beams are selected for analysis based on structural symmetry. Given that the UHPC bridge deck link slab and the UHPC bridge deck pavement are cast simultaneously, it is necessary to consider the mechanical performance of the UHPC bridge deck pavement. Therefore, the pavement layer is incorporated into the solid model. In the conventional section of the bridge deck, the C50 concrete of the bridge deck pavement and the T-beam are simulated using a shared-node approach. In the continuous structural section of the bridge deck, the UHPC link slab and the T-beam are separated by rubber or steel plate, eliminating any mutual bonding between them. The stiffness of the rubber and steel plate is simulated using elastic connection, with the steel plate exhibiting a vertical stiffness of 1.65×10^8 N/mm and a shear stiffness of 6.34×10^5 N/mm, while the rubber plate has a vertical stiffness of 1600 N/mm and a shear stiffness of 800 N/mm.

The main beam, UHPC bridge deck pavement, and UHPC link slab are all modeled using solid elements primarily composed of hexahedron, as shown in the finite element model in Fig. 3.

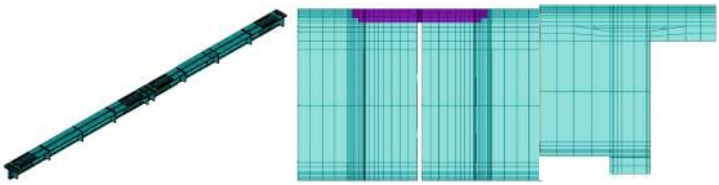

(a) Overall schematic diagram (b) Partial elevation (c) Cross-sectional view

Fig. 3. Schematic diagram of finite element model.

The load cases applied in the finite element model encompass the second-stage dead load, vehicle live load, uniform temperature change, temperature gradient, and foundation displacement. Specifically, the second-stage dead load ranges from 16.263

to 16.569 kN/m; the vehicle load is classified as Highway Grade I and applied according to lane load; the uniform temperature rise is 19 °C, while the uniform temperature drop is −28 °C; for the temperature gradient, the heating base values are T1 = 14.0 °C and T2 = 5.5 °C, whereas the cooling base values are T1 = −7.0 °C and T2 = −2.75 °C; the foundation displacement is set at 5 mm.

The boundary conditions of the finite element model are implemented based on the actual project conditions. An elastic connection is established within the bearing area at the bottom of the T-beam to simulate the bridge bearing. Given that the bearing is a 400 mm × 400 mm rubber bearing, the total vertical stiffness within the bearing area is 887256 kN/m, and the total transverse stiffness is 2113 kN/m.

4.2 FEA Results

Given the large number of structural parameters involved, it is essential to first establish a finite element benchmark model. This model employs an isolation configuration consisting of a 2 mm steel plate, a 4 mm rubber layer, and another 2 mm steel plate. The total length of the isolation section, denoted as *l1*, is 1.2 m; the length of the bridge deck link slab *l2*, measures 1.36 m; and the length of the UHPC bridge deck pavement *l3*, is set at 1.5 m. The thickness of the continuous bridge deck structure is composed of 10 cm for the UHPC bridge deck pavement and 5 cm for the UHPC bridge deck link slab. The stress distribution within the benchmark model is illustrated in Fig. 4.

(a) The overall model (b) The continuous bridge deck structure

Fig. 4. Longitudinal stress contour of benchmark model (unit: MPa).

As shown in Fig. 4, the overall structural stress level of the benchmark model remains relatively low. The maximum tensile stress in the concrete slab is 9.8 MPa, while the maximum compressive stress reaches 20.9 MPa, both occurring at the continuous bridge deck structure. Therefore, using this structure as a reference, a parametric analysis is conducted on the mechanical properties of the UHPC continuous bridge deck structure.

5 Parameter Analysis

Next, this paper conducts a parametric analysis on the mechanical properties of the UHPC bridge deck structure, focusing on three key aspects: the length of the isolation section in the bridge deck link slab, the thickness of the UHPC bridge deck link slab, and the length of the bridge deck link slab.

5.1 Length of Isolation Section of Bridge Deck Link Slab

The isolation length between the UHPC bridge deck link slab and the normal concrete slab significantly affects the stress distribution in the bridge deck pavement. Consequently, a variable parameter analysis is conducted, varying the isolation length of the half bridge deck link slab from 0.1 m to 0.6 m. The maximum longitudinal tensile stress in the continuous bridge deck structure and the maximum longitudinal tensile stress at the interface between the UHPC bridge deck pavement and the normal concrete slab are extracted for each model under different isolation lengths. These results are then plotted, as illustrated in Fig. 5.

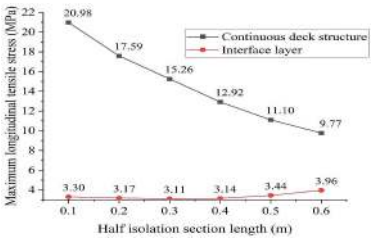

Fig. 5. Variations in structural stress under different isolation lengths of link slab.

As shown in Fig. 5, when the length of the bridge deck link slab remains constant, the tensile stress in the bridge deck pavement decreases as the length of the isolation section increases. When the half length of the isolation section reaches 0.6 m, the maximum longitudinal tensile stress in the bridge deck pavement attains its minimum value, specifically 9.77 MPa. As the length of the isolation section continues to increase, the longitudinal stress at the interface between the UHPC bridge deck pavement and the normal concrete slab first decreases and then increases. When the half length of the isolation section is 0.3 m, the tensile stress reaches an extreme value, with the maximum tensile stress at the interface being 3.11 MPa. Given that the stress values at the interface between the UHPC bridge deck pavement and the normal concrete slab are relatively low, it is recommended to select a half isolation length of 0.6 m.

5.2 Thickness of Bridge Deck Link Slab

The overall thickness of the continuous bridge deck structure comprises the thickness of the UHPC bridge deck pavement and that of the UHPC bridge deck link slab. The UHPC bridge deck pavement has a thickness of 10 cm, while the UHPC bridge deck link slab has thicknesses of 0 cm, 5 cm, 6 cm, 7 cm, 8 cm, 9 cm, 10 cm, 11 cm, and 12 cm, respectively. When the UHPC thickness is 0 cm, normal concrete is utilized in the isolation section instead of UHPC. Given that the stress states of T-beams under frequent combination and local loads differ, the load cases are categorized into frequent combination, local load, and local combination. The local load involves applying a wheel load (70 kN) at the center of the continuous bridge deck section, whereas the local combination entails substituting the lane load in the frequent combination with the local load. The maximum

longitudinal tensile stresses of the continuous bridge deck structure for each model under varying thicknesses of the bridge deck link slab are extracted and plotted in a diagram, as illustrated in Fig. 6.

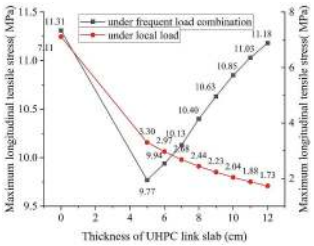

Fig. 6. Variations in structural stress under different thicknesses of bridge deck link slab.

As shown in Fig. 6, under the frequency combination, the tensile stress on the top surface of the UHPC bridge deck pavement in the overall model increases as the thickness of the UHPC link slab increases. Specifically, the maximum tensile stress is 9.77 MPa for a combination of 10 cm UHPC pavement and 5 cm UHPC link slab, and 10.85 MPa for a combination of 10 cm UHPC pavement and 10 cm UHPC link slab. When normal concrete is used in the isolation section instead of UHPC, the maximum tensile stress reaches 11.31 MPa. Furthermore, the maximum tensile stress in the UHPC link slab under local load decreases with an increase in the thickness of the link slab. Considering all these factors, it is recommended to adopt a total thickness configuration of 10 cm UHPC bridge deck pavement plus 5 cm UHPC link slab for the continuous bridge deck structure.

5.3 Length of Bridge Deck Link Slab

The half length of UHPC bridge deck pavement is set at 1 m, The half length of the isolated section of the bridge deck link slab is 0.60 m, and the half length of the bridge deck link slab ranges from 0.68 m to 0.98 m for variable parameter analysis. The maximum longitudinal tensile stress in continuous bridge deck structure and the maximum longitudinal tensile stress in the interface layer of each model under varying lengths of the bridge deck link slab are extracted and plotted, as illustrated in Fig. 7.

As shown in Fig. 7, when the half length of the isolation section is constant, the length of the bridge deck link slab exerts minimal influence on the stress distribution of the bridge deck, with the maximum and minimum longitudinal tensile stresses differing by only approximately 0.1 MPa. Therefore, a half length of 0.68 m is recommended for the bridge deck link slab.

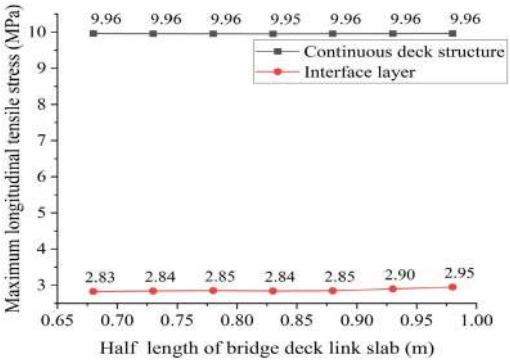

Fig. 7. Variations in structural stress under different lengths of bridge deck link slab.

6 Conclusion

This paper introduces a novel continuous bridge deck structure featuring continuous UHPC bridge deck pavement combined with UHPC bridge deck link slab. To investigate the mechanical properties of this structure, a refined finite element model of the entire bridge for the background project is established using ANSYS software, with a particular focus on analyzing the effects of the isolation section length, thickness, and length of the bridge deck link slab on the mechanical performance of the UHPC continuous bridge deck structure. The key findings are as follows:

(1) When the length of the bridge deck link slab remains constant, the tensile stress in the bridge deck pavement decreases as the isolation section length increases. Specifically, when the half length of isolation section is 0.6 m, the maximum longitudinal tensile stress reaches its minimum value of 9.77 MPa. Therefore, it is recommended that the half length of isolation length be set at 0.6 m.
(2) As the thickness of the UHPC bridge deck link slab increases, the tensile stress on the top surface of the UHPC bridge deck pavement within the overall model also rises. For the continuous bridge deck structure, a combination of 10 cm UHPC bridge deck pavement and 5 cm UHPC bridge deck link slab is recommended.
(3) When the half length of the isolation section is fixed, the length of the bridge deck link slab has minimal impact on the stress distribution of the bridge deck, with the maximum and minimum stress values differing by only approximately 0.1 MPa. Hence, it is advisable to select a half length of 0.68 m for the bridge deck link slab.

The research results can provide reference for the design and construction of similar bridges in the future.

References

1. Wang, G., Xie, X., Wang, C.Q., et al.: Mechanical performance of arch-type continuous slab-deck on simply-supported girder bridge. J. Zhejiang Univ. (Eng. Sci.). **48**(6), 1049–1057 (2014). https://doi.org/10.3785/j.issn.1008-973X.2014.06.012

2. Zhuang, Y.Z., Xu, L., Cheng, J.F., et al.: Theoretical analysis of mechanical properties for continuous deck structure of simply supported beam bridge. China J. Highway Transport. **30**(7), 73–85 (2017). https://doi.org/10.19721/j.cnki.1001-7372.2017.07.010
3. Liu, L.: Study on the continuous deck's behavior of simply supported prestressed concrete beam bridge. Master's Thesis, Southwest Jiaotong University, Chengdu (2014)
4. Lan, X.K.: Research on mechanical behavior and influence factors of continuous slab-deck. Master's Thesis, South China University of Technology, Guangzhou (2016)
5. Liu, X.W.: Analysis of mechanical behavior of rigid connected continuous slab-deck on simply-supported girder. Master's Thesis, South China University of Technology, Guangzhou (2018)
6. Pan, Z.Y., Mao, Z.X., Liu, M., et al.: The finite element analysis and improvement of continuous slab-deck of simple supported beam bridge. J. Highway Transp. Res. Dev. **27**(4), 89–94 (2010). https://doi.org/10.3969/j.issn.1002-0268.2010.04.017
7. Lin, X.: Study on ECC link slabs of simply supported girder bridges. Master's Thesis, Southeast University, Nanjing (2017)
8. Qian, Z.X.: Optimal design and mechanical Properties of bridge continuous Decks based on engineered Cementitious composites (ECC). Master's Thesis, Southeast University, Nanjing (2021)
9. Zhou, S.M., Cui, B., Guo, F.K.: Performance of novel steel-UHPC composite continuous slab-deck structure. J. Highway Transp. Res. Dev. **42**(1), 156–165 (2025). https://doi.org/10.3969/j.issn.1002-0268.2025.01.017
10. Shao, X.D., Zhou, Y.D., Cao, J.H., et al.: Experimental study on flexural behavior of novel continuous deck structure in steel simply-supported beams. China Civil Eng. J. **52**(12), 80–92 (2019). https://doi.org/10.15951/j.tmgcxb.2019.12.008

Performance Analysis of Steel-Concrete Composite Bridge with Thin Steel Bottom Formwork Deck

Yangfu Xu[1,2], Qing Zhang[1,3(✉)], Yuhan Liu[4], and Liang Xiao[4]

[1] Jiangxi Ganyue Expressway Co., Ltd., Nanchang 330025, Jiangxi, China
1911393@tongji.edu.cn
[2] Nanchang West Management Center Maintenance Office, Nanchang 330025, Jiangxi, China
[3] Jiangxi Changtong Expressway Co., Ltd., Nanchang 330025, Jiangxi, China
[4] College of Civil Engineering, Tongji University, Shanghai 200092, China

Abstract. To minimize potential safety hazards posed by construction activities beneath bridges, an increasing number of cross-line steel-concrete composite beam bridges are adopting a bridge deck structure with thin steel bottom formwork. To further elucidate the impact of steel bottom formwork on the overall mechanical performance of steel-concrete composite bridge, this paper establishes a shell-solid finite element model of a background engineering project. This model meticulously calculates the overall stress of this composite bridge throughout various stages, from construction to bridge completion. It emphatically analyzes and compares the stress distribution of steel beam in composite bridge with steel bottom formwork and conventional composite bridge. The findings reveal that the presence of steel bottom formwork leads to a certain increase in steel beam stress during the construction stage, yet the magnitude of stress variation does not exceed 3 MPa. During the concrete pouring and pavement construction stages, the stress in the steel beam of composite bridge with thin steel bottom formwork closely approximates that of conventional composite bridge, with a stress difference not surpassing 2 MPa. Under diverse working condition combinations, the stress difference between steel main beams of composite bridge with thin steel bottom formwork and conventional composite bridge remains below 5 MPa, which is essentially negligible compared to the design strength value of steel. Consequently, the influence of the steel bottom formwork can be disregarded in the overall structural calculation and analysis. Instead, the calculation and analysis can be conducted based on the conventional steel-concrete composite beam bridge.

Keywords: Steel-Concrete Composite Beam Bridge · Thin Steel Bottom Formwork Deck · Finite Element Analysis · Overall Mechanical Performance

1 Introduction

The steel-concrete composite girder bridge represents another bridge structure form that has been embraced and rapidly developed by the engineering community, following the advent of steel bridges and reinforced concrete bridges. This type of bridge is a modern

© The Author(s), under exclusive license to Springer Nature Switzerland AG 2027
G. Feng et al. (Eds.): ICCE 2025, SUCI, pp. 589–600, 2027.
https://doi.org/10.1007/978-3-032-32237-1_42

bridge design that organically integrates steel and concrete through shear connectors (such as studs and perfobond connectors) into a unified, load-sharing system. The core design philosophy involves strategically placing steel in the tensile zone at the lower edge of the beam to leverage its high tensile strength, while utilizing concrete in the compressive zone at the upper edge to capitalize on its superior compressive properties. This scientific material allocation and structural integration endow the system with outstanding overall performance [1–3]: Firstly, the structure exhibits significantly higher overall stiffness and load-bearing capacity compared to pure steel or concrete structures under equivalent conditions, making it particularly suitable for long-span or heavy-load bridges. Secondly, the ductility of steel, combined with the restraining effect of concrete, grants the bridge exceptional seismic resistance and fatigue durability. Additionally, the structure lends itself well to a construction approach that combines industrial prefabrication with rapid on-site assembly, effectively shortening the construction timeline and minimizing disruptions to the surrounding environment and traffic flow. Therefore, steel-concrete composite bridge has emerged as a highly competitive and preferred option in modern bridge engineering, especially for urban interchanges, high-speed railways, and long-span bridge projects, while balancing economic efficiency and safety considerations.

Currently, the predominant forms of composite structure bridges spanning across lines are steel plate composite beam and steel box composite beam, as depicted in Fig. 1. The steel plate composite beam [2] comprises several I-shaped steel girders connected via a transverse connection system and forms a unified load-bearing structure with the concrete bridge deck through shear connectors. Stiffeners are installed at specific locations between the steel longitudinal beams to ensure the structural stability of the steel framework. Owing to its relatively simple structure and the lightweight nature of each I-beam, the I-beam concrete composite beam offers great convenience in erection and hoisting, boasts significant bending stiffness, and finds widespread application in engineering projects. The steel box composite beam [3], on the other hand, is a bridge structure that integrates a box-shaped steel main beam with a concrete bridge deck through shear connectors, creating a unified load- bearing system. Compared to I-shaped composite beam bridge with open sections, the steel box composite beam exhibits superior torsional stiffness, enhanced load-bearing capacity, and greater spanning capability, making it the preferred choice for bridges that cross traffic routes. Research on these composite beam structures primarily focuses on those with spans ranging from 30 to 40 m, with relatively less research conducted on spans of 50 to 60 m, mainly due to the increased steel consumption associated with greater steel beam heights and plate thicknesses.

With the rapid development of expressway construction in China, the road network is becoming increasingly dense, leading to a growing number of new bridges needing to cross over existing expressways [4]. Current bridge constructions across traffic lines often necessitate the complete or partial closure of existing traffic roads, causing inconvenience to citizens, increasing potential safety hazards, and negatively affecting the construction image. Notably, the economic losses incurred by closing existing traffic can significantly outweigh the direct costs of bridge construction. Therefore, the fundamental objective of

new bridge constructions across traffic lines is to avoid interfering with existing highway traffic.

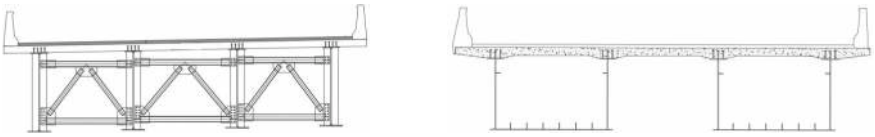

(a) Steel-plate composite beam (b) Steel-concrete composite box beam

Fig. 1. Main forms of steel-concrete composite beam.

To address this issue, this paper proposes a novel cross-section form of steel- concrete composite beam bridge without traffic interference, based on a specific new highway crossing project. This involves installing steel formworks on the outside of the concrete bridge deck and concrete barrier. Stiffeners are placed on the upper surface of the steel bottom formwork and embedded within the concrete bridge deck, while stiffeners are positioned inside the steel side plate of the barrier and embedded in the concrete barrier. Both the formwork and stiffener components have a thickness of 3 mm, as illustrated in Fig. 2. This innovative composite beam section form creates a comprehensive protective layer on the bottom and side of the concrete, ensuring no mortar leakage under the bridge during concrete pouring. It also meets the requirements of not closing highways, not leaking mortar, and not requiring protective sheds during bridge construction.

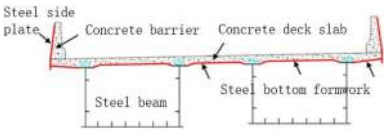

Fig. 2. Sectional configuration of an innovative steel-concrete composite bridge over existing lines.

Currently, strictly speaking, the research on composite beam bridge with steel bottom formwork pertains to the study of the mechanical properties of steel plate- concrete composite bridge deck, implying the presence of connectors between steel plate and concrete slab. The key contents of this research primarily encompass: the interfacial load-transfer mechanism, particularly focusing on the load–slip relationship and fatigue performance of shear connectors; the global and local structural responses, including static load-bearing capacity, buckling stability, and stress distribution under dynamic impact loading; as well as the long-term performance evolution, specifically addressing the durability degradation behavior under the coupled effects of environmental exposure and repeated loading. These investigations aim to establish a scientific basis for the design theory and safety assessment of steel–concrete composite bridge deck. It is worth noting that this field has already attracted considerable attention from numerous scholars, who have conducted extensive studies on various aspects of the aforementioned topics, thereby laying a substantial theoretical and experimental foundation for

further advancements. For instance, Zhan Yulin et al. [5] conducted experiments on steel-concrete composite bridge decks in the positive bending moment region and discovered that this bridge deck exhibits significant stiffness and high load-bearing capacity. Yang Yong et al. [6] performed two-point symmetrical concentrated loading static test on six steel plate- concrete composite bridge deck specimens, with a particular focus on examining how key factors—such as the arrangement of transverse through reinforcement in the perfobond connectors, the nominal shear span ratio, and the spacing between perforated steel plates—influence the mechanical behavior of the composite bridge decks. The test results indicate that these composite bridge decks typically undergo flexural failure, and the flexural capacity can be calculated using the plane section assumption. Through static tests on four steel plate-concrete composite bridge deck specimens, Huo Xudong et al. [7] discovered that the composite bridge deck with perforated steel plate connector functioned effectively under static load, with no interfacial slip observed. Yang Yong et al. [8] conducted fatigue performance and ultimate bearing capacity tests on composite bridge with steel plate-concrete composite bridge deck. Zhang Xieli et al. [9, 10] performed loading test on profiled steel sheet-concrete composite bridge deck, measuring its ultimate bearing capacity and fatigue performance. They also calculated these results using plastic theory, which aligned well with the experimental findings.

However, research on composite beam bridge with steel bottom formwork, which lack connections between the steel plate and concrete slab, remains scarce. To investigate the similarities and differences in mechanical performance between this new type of composite beam bridge and conventional ones, especially to clarify the influence of a 3 mm thick steel bottom formwork on the structural mechanical properties, this paper constructs refined shell-solid finite element models. These models are used to analyze how the presence or absence of steel bottom formwork in the bridge deck affects the overall mechanical performance of the steel beam. The findings of this study can serve as a reference for the design and construction of similar bridges in the future.

2 Background Engineering

This paper conducts research based on the background engineering of the first span of an overpass bridge. This bridge is a steel-concrete composite trough bridge with a total length of 140 m, featuring a span arrangement of 40 m + 60 m + 40 m. Its elevation is depicted in Fig. 3. The cross-section is illustrated in Fig. 4. It employs two straight web trough girders, with a web spacing of 3.4 m, a beam height of 2.5 m, a deck thickness of 240 mm, a haunch thickness of 320 mm, and a steel beam height of 2.18 m. The top flange of the steel beam has a width ranging from 500 to 750 mm and a thickness of 20 to 28 mm. The web plate has a thickness ranging from 12 to 16 mm. The bottom flange has a width of 3700 mm and a thickness ranging from 12 to 24 mm.

The concrete bridge deck is connected to the steel main beam using shear studs, while the transverse connection between the steel main beams is reinforced with crossbeams. Inside the box, a truss-type crossbeam is installed every 5 m, utilizing 140 × 140 × 14 angle steel of Q235C grade. Outside the box, a solid-web type crossbeam is placed every 10 m, with a web thickness of 12 mm; at the supports, a solid-web type crossbeam is also installed, featuring a web thickness of 16 mm. The steel main beam is welded to

the solid-web type crossbeam, bolted to the truss-type crossbeam, and the longitudinal segments of the steel main beam are connected through welding.

For the cast-in-place bridge deck slab, the transverse measurement at the midspan of the steel main girder is 240 mm, while the top plate of the steel girder measures 320 mm. The cantilevered section ranges in thickness from 233 mm to 320 mm. The steel structure is connected to the concrete bridge deck slab using shear studs. In the positive bending moment zone at the midspan, the longitudinal reinforcement bars in both the upper and lower layers of the bridge deck slab have a diameter of 20 mm and are spaced 100 mm apart. Conversely, in the negative bending moment zone at the support points, the longitudinal reinforcement bars in both layers have a diameter of 25 mm, the transverse reinforcement bars have a diameter of 16 mm, and both are spaced 100 mm apart.

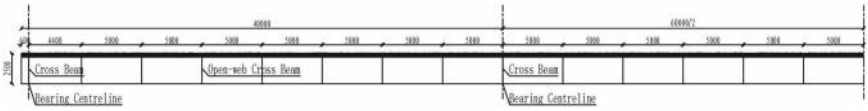

Fig. 3. Elevation (Unit: mm).

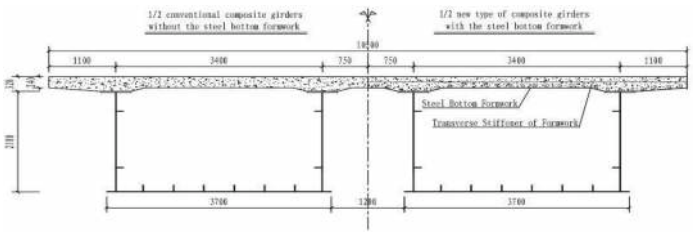

Fig. 4. Cross-section (Unit: mm).

3 Introduction to the Finite Element Model

3.1 Conventional and New Composite Bridge Models

ANSYS software is utilized to create shell-solid finite element models of both the original and the new composite bridges for comparative analysis. Apart from the presence or absence of steel formwork, the two structural models remain identical. Since the barrier and its formwork do not contribute to the main structure's stress, they are excluded from the model. Concrete is represented using the solid element SOLID95, while steel structures are modeled with the shell element SHELL181. The grid size is set at 125 mm. No consideration is given to the relative slip between the steel and concrete interfaces, and a rigid connection is assumed between the steel top flange and the concrete bridge deck.

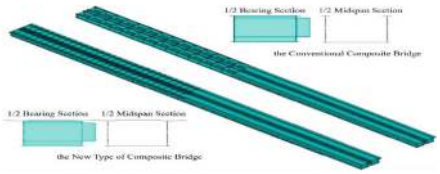

Fig. 5. Finite element models and cross-sections: conventional (top) vs. new (bottom) composite bridges.

The stress analysis of composite bridge must consider the stages from construction to bridge operation. During the construction phase, the model consists solely of the top flange, bottom flange, web plate, and diaphragm of the steel beam. The wet weight resulting from concrete pouring is applied to the top flange of the steel beam in the form of a uniformly distributed load. Once the concrete hardens, it forms a composite section with the steel beam, jointly bearing the load. The model then comprises the concrete slab, top flange, bottom flange, web plate, and diaphragm of the steel beam. The section forms of the two finite element models are illustrated in Fig. 5.

3.2 Boundary Conditions of the Model

The bridge is a three-span continuous beam bridge with 16 bearings, and the direction of constraints is shown in Fig. 6. In the model, the X direction represents the longitudinal direction, the Y direction represents the vertical direction, and the Z direction represents the transverse direction. Each bearing is provided with vertical constraints. Longitudinal bridge direction constraints are set on the bearings of the second pier, while transverse bridge direction constraints are set on the bearings of the third row. The remaining bearings are bidirectional movable bearings.

Fig. 6. Schematic diagram of the model boundary conditions (Unit: mm).

3.3 Load Cases

Phase I Dead Load. Erection stage of steel beam: gravity acceleration is used for simulation. The dead weight of steel structure is calculated based on a unit weight of 78.5 kN/m^3.

Concrete pouring load: The wet weight of bridge deck concrete is calculated based on a unit weight of 24 kN/m^3, which is then converted into a uniformly distributed node force. This force is applied on the top of the steel structure during the pouring stage and is automatically incorporated by the software after hardening.

Phase II Dead Load. In this case, a 10 cm asphalt deck pavement is considered. the concrete deck and steel beam share the stress, with a uniformly applied load of 24 kN/m^3.

Vehicle Load. Vehicle load is defined in accordance with the General Code for Design of Highway Bridges and Culverts (JTG D60–2015). The lane load is 10.5 kN/m, and the vehicle load adopts the standard value. Three most unfavorable live load conditions are considered: the most unfavorable at the midspan of the central span, the most unfavorable at the midspan of the side span, and the most unfavorable at the central support.

Basic Combination. The basic combination is defined in accordance with the General Code for Design of Highway Bridges and Culverts (JTG D60–2015).

4 Comparative Analysis of Finite Element Results

According to the calculation results from ANSYS software, the stresses of the two models under dead load, live load, and basic combinations are extracted. For the steel beam, the longitudinal stress of the top and bottom flanges, shear stress of the web plate, and longitudinal stress of the concrete bridge deck are examined. Tensile stress is considered positive, while compressive stress is negative.

Table 1. Comparison of Maximum Stress in Each Component at Different Stages under Dead Load (Unit: MPa).

Construction Stages	Plate Components	Conventional Model ①		New Model ②		(②-①)/①	
		Tensile Stress	Compressive Stress	Tensile Stress	Compressive Stress		
	Longitudinal stress of bridge deck	1.78	-0.83	1.76	-0.80	-1.12%	-3.61%

The comparison results of the maximum stress in each structural component under dead load during various construction stages are presented in Table 1. The stress contour for the steel beam erection stage is illustrated in Fig. 7. During the steel beam erection phase, the presence of steel formwork increases the overall stress of steel beam by approximately 10%. In the concrete pouring stage, the tensile stress on the steel beam top flange of the new composite bridge decreases by 3%, but the compressive stress on the top flange, bottom flange stress, and web shear stress all increase. In Phase II deck pavement stage, the stress of each component of the new composite bridge is slightly lower than that of the conventional bridge. It is evident that, compared with the conventional bridge, the stress of the steel beam of the new composite bridge increases significantly only during the steel beam erection stage, with the stress value changing by no more than 3 MPa. The stress of the steel beam decreases slightly during the

concrete pouring and phase II pavement stages, and there is a slight improvement in the longitudinal stress of the bridge deck, with the stress change remaining within 2 MPa, indicating a minor overall change.

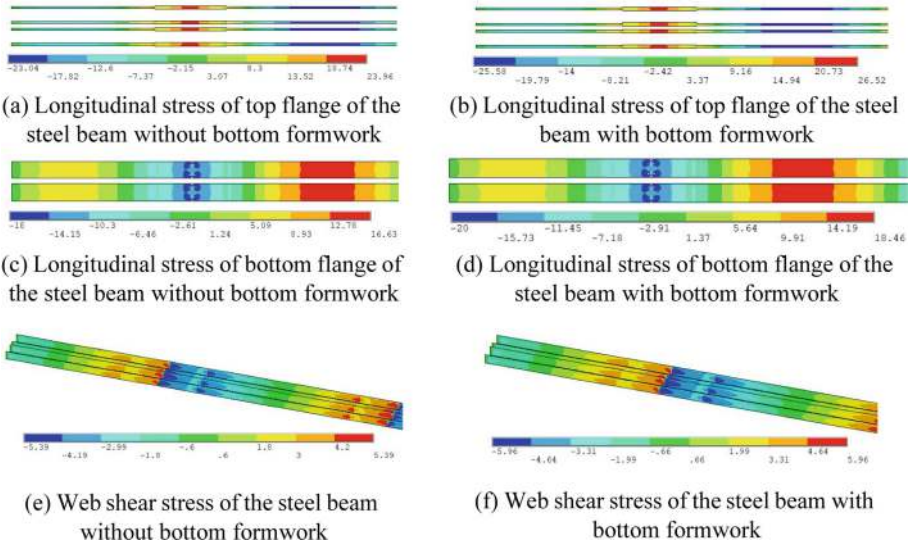

Fig. 7. Stress contour of the half model under steel beam self-weight (Unit: MPa).

The stress contour of the half model under the most unfavorable live load at midspan of central span is shown in Fig. 8. Under the most unfavorable live load in the middle span, the top flanges of the two kinds of steel beam are tensioned near the middle support and compressed at other parts. The maximum tensile stresses of the steel top flange of bridge without bottom formwork and with bottom formwork are 8.12 MPa and 7.58 MPa, respectively, and the maximum compressive stresses of the top flange are 8.85 MPa and 8.13 MPa, respectively. The maximum tensile stresses of the steel bottom flange of bridge without and with bottom formwork are 40.37 MPa and 40.37 MPa, respectively, and the maximum compressive stresses of the bottom flange are 24.50 MPa and 25.07 MPa, respectively. The maximum shear stresses of steel web of bridge without and with bottom formwork are 7.71 MPa and 7.63 MPa, respectively. It can be seen that under the most unfavorable load of the midspan, whether there is steel bottom formwork or not, the stress difference in the main plates of the steel beam is minimal.

The comparison of maximum stress results for each structural component under three live load conditions is presented in Table 2. It is evident that under each live load condition, the longitudinal stress of the top flange of the steel beam can be reduced by approximately 6% to 8%. However, this has minimal impact on the stress of the bottom flange, and there is also a slight decrease in the shear stress of the web and the longitudinal stress of the bridge deck. The stress variations under live load are all within 1 MPa, which can be essentially ignored.

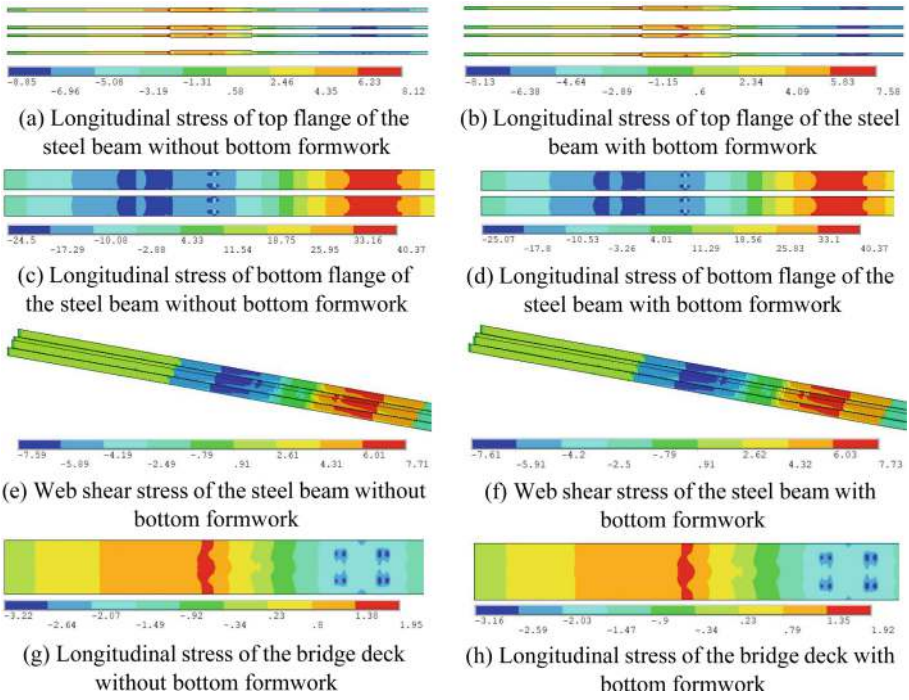

Fig. 8. Stress contour of the half model under the most unfavorable live load at midspan of central span (Unit: MPa).

Under the three basic combinations, the comparison of the maximum stress results of each structural component is presented in Table 3. Under these basic combinations, the tensile stress of the steel beam top flange decreases by approximately 6% to 7%, while the compressive stress increases by about 4% to 5%. The stress on the steel beam bottom flange also rises, with an increase of 2% to 3% for Combination 1 and 3% to 4% for Combination 3. The shear stress in the web plate also increases by about 4% to 5%. Nevertheless, the longitudinal stress level of the bridge deck slab decreases under all three basic combinations, indicating that the presence of the steel bottom formwork benefits the stress distribution of the concrete bridge deck.

Table 2. Comparison of maximum stress in each structural component under live load (Unit: MPa)

Live Load Cases	Plate Components	Conventional Model ①		New Model ②		(②-①)/①	
		Tensile Stress	Compressive Stress	Tensile Stress	Compressive Stress		
The most unfavorable condition at the midspan of the central span	Longitudinal stress of top flange	8.12	-8.85	7.58	-8.13	-6.65%	-8.14%
	Longitudinal stress of bottom flange	40.37	-24.5	40.37	-25.07	0.00%	2.33%
	Web shear stress	7.71		7.73		0.26%	
	Longitudinal stress of bridge deck	1.95	-3.22	1.92	-3.16	-1.54%	-1.86%
The most unfavorable condition at midspan of the side span	Longitudinal stress of top flange	4.19	-7.03	3.91	-6.44	-6.68%	-8.39%
	Longitudinal stress of bottom flange	32.45	-14.12	32.48	-14.10	0.09%	-0.14%
	Web shear stress	7.19		7.19		0.00%	
	Longitudinal stress of bridge deck	1.15	-2.84	1.13	-2.8	-1.74%	-1.41%
The most unfavorable condition at the central support	Longitudinal stress of top flange	8.24	-3.76	7.71	-3.58	-6.43%	-4.79%
	Longitudinal stress of bottom flange	16.19	-26.00	15.66	-26.63	-3.27%	2.43%
	Web shear stress	7.57		7.55		-0.26%	
	Longitudinal stress of bridge deck	2.2	-0.87	2.18	-0.84	-0.91%	-3.45%

Table 3. Comparison of maximum stress in each structural component under different load combinations (Unit: MPa).

Load Combinations	Plate Components	Conventional Model ①		New Model ②		(②-①)/①	
		Tensile Stress	Compressive Stress	Tensile Stress	Compressive Stress		
Basic combination 1	Longitudinal stress of top flange	124.26	-119.78	115.61	-125.11	-6.96%	4.45%
	Longitudinal stress of bottom flange	154.75	-179.05	158.26	-182.87	2.27%	1.80%
	Web shear stress	39.04		41.29		5.76%	
Basic combination 2	Longitudinal stress of bridge deck	4.94	-5.73	4.86	-5.61	-1.62%	-2.09%
	Longitudinal stress of top flange	119.06	-105.92	111.12	-112.24	-6.67%	5.97%
	Longitudinal stress of bottom flange	88.86	-160.35	88.96	-163.49	0.11%	1.96%
	Web shear stress	36.23		37.72		4.11%	
Basic combination 3	Longitudinal stress of bridge deck	3.72	-4.57	3.67	-4.49	-1.34%	-1.75%
	Longitudinal stress of top flange	123.14	-112.46	114.79	-118.51	-6.78%	5.38%
	Longitudinal stress of bottom flange	119.16	-180.49	123.29	-183.58	3.47%	1.71%
	Web shear stress	41.83		41.99		0.38%	
	Longitudinal stress of bridge deck	5.42	-2.27	5.36	-2.2	-1.11%	-3.08%

5 Conclusions

Based on a practical engineering of overpass steel-concrete composite beam bridge, focusing on steel-concrete composite bridge with and without steel bottom formwork, this paper establishes shell-solid finite element models and analyzes the overall stress during each construction stage, drawing the following main conclusions:

1. The presence of steel bottom formwork increases the stress of steel beam components during the steel beam erection stage, but the increase is no more than 3 MPa. During the concrete pouring and pavement construction stages, the stress of the new composite bridge slightly decreases, with the stress difference not exceeding 2 MPa.
2. Under live load and load combination conditions, the steel bottom formwork generally reduces structural stress. However, the longitudinal stress of the bottom flange and the shear stress of the web plate increase, with both stress differences not exceeding 5 MPa. Nevertheless, it improves the longitudinal stress condition of the concrete bridge deck.
3. Overall, the addition of steel bottom formwork enhances the structural stress performance, particularly improving the stress state of the bridge deck. Although some components experience increased stress during construction, the increase is minor and significantly lower than the serviceability limit state. Therefore, the impact of the steel bottom formwork can be disregarded, allowing for overall calculation and analysis based on conventional steel-concrete composite beam bridge.

The research results can provide reference for the design and construction of similar bridges in the future.

References

1. Nie, J.G., Tao, M.X., Wu, L.L., et al.: Advances of research on steel-concrete composite bridges. China Civil Eng. J. **45**(6), 110–122 (2012). https://doi.org/10.15951/j.tmgcxb.2012.06.003
2. Chen, B.C., Mu, T.M., Chen, Y.Y., et al.: State-of-the-art of research and engineering application of steel-concrete composite bridges in China. J. Build. Struct. **34**(1), 1–10 (2013). https://doi.org/10.14006/j.jzjgxb.2013.s1.006
3. Xiang, Y.Q., Zhu, S., Zhao, Y.: Research and Development on accelerated bridge construction technology. China J. Highway Transport. **31**(12), 1–27 (2018). https://doi.org/10.3969/j.issn.1001-7372.2018.12.001
4. Nie, J.G., Wang, Y.H.: Analysis of ultimate capacity of continuous profiled steel sheet- concrete composite slab based on partial connection model. J. Build. Struct. **40**(1), 1–5 (2010). https://doi.org/10.19701/j.jzjg.2010.01.001
5. Zhan, Y.L., Zhao, R.D., Mao, X.M., et al.: Experiment of mechanical behavior of steel and concrete composite deck slab under positive bending moment. J. Bridge Construct. **5**, 5–8 (2006). https://doi.org/10.3969/j.issn.1003-4722.2007.01.002
6. Yang, Y., Zhu, G., Zhou, P.J., et al.: Experimental study on the mechanical behavior and design method of plain steel-plate and concrete composite bridge decks. China Civil Eng. J. **42**(12), 135–141 (2009). https://doi.org/10.15951/j.tmgcxb.2009.12.001
7. Huo X D: Experiment on Static and Fatigue Behavior of Steel Plate-Concrete Composite Bridge Decks Xi'an University of Architecture and Technology, Xi'an, Master's Thesis (2011).
8. Yang, Y., Zhou, X.W., Xue, J.Y., et al.: Experiment study on fatigue behavior of composite girders with steel plate-concrete composite bridge decks. China Civil Eng. J. **45**(6), 123–131 (2012). https://doi.org/10.15951/j.tmgcxb.2012.06.004
9. Zhang, X.L., Wu, C., Su, Q.T.: Experiment on load capacity of profiled steel sheeting- concrete composite bridge decks. J. Jilin Univ. (Eng. Technol. Ed.). **54**(10), 2870–2883 (2024). https://doi.org/10.13229/j.cnki.jdxbgxb.20221556
10. Zhang, X.L., Wu, C., Su, Q.T.: Experimental study of the fatigue behavior of profiled steel sheeting-concrete composite bridge decks with perfobond connectors. J. Tongji Univ. (Nat. Sci.). **51**(9), 1395–1406 (2023). https://doi.org/10.11908/j.issn.0253-374x.22417

Innovative Tool-Type Single-Sided Formwork System for in-Situ Construction of Underground Concrete Walls: Finite Element Analysis and Experimental Validation

Wei Liu[1(✉)], Lin He[2], Jikai Liu[1], Guanjie Li[1], Hui Zhang[1], Chengqiang Zhao[1], and Xiangle Kong[1]

[1] China Construction Engineering (Macao) Co., Ltd., Macao 999078, China
liuweihd@cohl.com

[2] School of Civil Engineering and Transportation, Guangzhou University, Guangzhou 510006, Guangdong, China

Abstract. In response to the critical challenges of constrained structural boundaries and limited construction space in the development of urban underground spaces, this paper innovatively proposes and systematically investigates a tool-type one-sided formwork support system. Integrating finite element (FE) numerical simulation and full-scale model testing, this study comprehensively evaluates the system's mechanical performance and deformation patterns under various working conditions, including different story heights (2.44 m ~ 3.2 m), wall thicknesses (250 mm ~ 400 mm), and materials (conventional steel-wood combination vs. aluminum alloy). The results demonstrate that the formwork system satisfies the code-specified deformation limits within conventional story height and wall thickness ranges, showing good adaptability. The standard components exhibit reliable load-bearing capacity, although the stiffness of the additional height layers requires enhancement. The use of aluminum alloy components achieves a weight reduction of approximately one-third, indicating significant lightweight potential; however, local stress in the support frame slightly exceeds the design strength, necessitating sectional optimization. The full-scale test validates the accuracy of the numerical model, confirming that the system offers excellent constructability, characterized by tool-based, standardized, and rapid assembly/dismantling, while ensuring construction quality and safety. This research provides a solid theoretical foundation and practical support for the optimized design, safe application, and standardized promotion of the one-sided formwork system.

Keywords: Single-Sided Formwork · Finite Element Analysis · Full-Scaletest · Tool-Type System · Lightweight Design

1 Introduction

With the rapid advancement of global urbanization and the increasing scarcity of land resources, the density of urban buildings has continued to rise, leading to increasingly constrained building boundaries and underground development spaces [1, 2]. Against

© The Author(s), under exclusive license to Springer Nature Switzerland AG 2027
G. Feng et al. (Eds.): ICCE 2025, SUCI, pp. 601–613, 2027.
https://doi.org/10.1007/978-3-032-32237-1_43

this backdrop, large-scale underground projects—such as deep basements of high-rise buildings, metro interchange hubs, urban utility tunnels, underground commercial complexes, and deep shafts—have reached unprecedented scales and levels of complexity. In most of these projects, the main structural components are constructed using cast-in-place concrete technology, where construction quality, efficiency, and cost control largely depend on the formwork support system adopted. The formwork system not only determines the geometric accuracy and surface quality of the concrete structure but also serves as a critical temporary structure that resists the lateral pressure exerted by freshly poured concrete. Its reliability is thus directly related to both construction safety and project progress [3–5].

Traditional double-sided formwork systems require the installation of formwork panels on both sides of the wall and sufficient working space (commonly referred to as "haunches" or "fat slots") for construction operations [6]. In deep excavations where building boundaries are adjacent to existing structures or where the available space is extremely limited, the application of such systems becomes severely restricted. These systems often lead to excessive earth excavation, difficulties in controlling backfill quality, and long-term leakage risks if the backfilled area is not properly treated. To address these challenges, single-sided formwork systems, which enable formwork installation and concrete pouring to be completed from only one side of the structure, have emerged as a technically superior alternative [7–9]. Through an ingenious mechanical load transfer mechanism, the lateral pressure of fresh concrete is effectively transmitted to the completed base slab, floor slab, or pre-installed ground anchor system, thereby resolving the spatial constraints inherent to double-sided formwork. Furthermore, since single-sided systems eliminate the need for through-wall tie rods, they fundamentally enhance the integrity and watertightness of underground exterior walls. Consequently, this technology has become an indispensable component in the modern, intensive construction of underground engineering projects [10–12].

Despite the promising application prospects of single-sided formwork systems, their lightweight, tool-based, and high-quality development still faces multiple challenges: firstly, insufficient standardization in design, with inconsistent component specifications and incompatible connection interfaces, hinders interchangeability and efficient reuse; secondly, a contradiction exists between the reliability and simplicity of connection nodes, making it difficult to balance high load-bearing capacity with high-efficiency assembly; thirdly, there is a lack of refined design methods, with heavy reliance on empirical knowledge and simplified calculations, failing to establish a systematic design framework based on accurate mechanical models and optimization algorithms; fourthly, the system's adaptability to diverse engineering scenarios is inadequate, as it is challenging to flexibly adapt limited standard components to different wall heights and thicknesses; fifthly, the application of new lightweight materials is progressing slowly, as their high initial cost requires full lifecycle assessment and necessitates the development of compatible connection technologies.

In light of these issues, this study aims to address the above-mentioned key challenges by conducting a comprehensive performance investigation and optimization of a newly developed tool-type single-sided formwork support system designed by the research team. Finite element (FE) numerical simulation serves as the primary research approach,

through which a high-fidelity mechanical model of the proposed formwork system is established. The analysis focuses on its structural response under three representative variable working conditions: Adaptability to different story heights, including deformation patterns and overall stability; Mechanical performance and economic comparison between different construction materials (e.g., conventional Q235 steel and high-strength aluminum alloy); and Load-bearing effectiveness and force transfer mechanisms under different formwork width configurations.

Based on the FE results, full-scale or reduced-scale experimental tests are conducted to validate the numerical findings, ensuring the accuracy and reliability of the theoretical model. Ultimately, this research seeks to provide a robust theoretical foundation and empirical data to support the optimized design, safe application, and standardized promotion of the proposed tool-type single-sided formwork system, thereby contributing to the advancement of green, efficient, and industrialized underground construction technologies in China.

2 The Innovative SSFS and its Finite Element Model

The research team has developed a tool-type single-sided formwork support system, as illustrated in Fig. 1. This system is assembled by connecting several standardized unit formwork panels, each measuring 2440 mm in height and 1220 mm in width. Each unit consists of two main components: a panel system and a triangular support system. The panel system comprises the formwork panel, vertical ribs, and horizontal ribs. The panel is a standard-sized (2440 × 1220 × 16.5 mm) film-faced composite wood panel, requiring no additional cutting. The vertical ribs are designed as hollow rectangular sects. (40 × 25 × 1.2 mm) spaced at 250 + 240 × 3 + 250 mm. The horizontal ribs are hollow rectangular sects. (60 × 60 × 4.0 mm) spaced at 585 + 660 + 610 + 585 mm. Serving as the direct contact surface for cast-in-place concrete, the panel system ensures the quality of the concrete's final shape. The composite wood panel has an elastic modulus of 9200 MPa, a density of 500 kg/m^3, and a design strength of 13 MPa.

The triangular support system incorporates two identical L-shaped support structures per unit. Each L-shaped structure consists of a vertical member, a horizontal member, a diagonal brace, and embedded bolts. The vertical and horizontal members are perpendicular to each other, connected by the diagonal brace, which forms angles of approximately 43°, 53°, and 53° with the vertical member. The main embedded bolt has a diameter of 18 mm and is anchored 600 mm into the foundation. Furthermore, additional vertical anchor bolts are installed at positions 755 mm and 1410 mm from the main bolt along the horizontal member to ensure a stable connection with the ground and prevent sliding. All structural members except the wood panel are made of Q235 steel, with an elastic modulus of 205,000 MPa, a density of 7850 kg/m^3, and a design strength of 205 MPa.

Previous research and engineering applications have demonstrated that this formwork system possesses excellent stiffness and stability, along with superior constructability. On-site installation and dismantling can be efficiently performed by just two workers, highlighting its simplicity and high efficiency. To further explore the performance potential of this support system, finite element analysis will be employed as the primary method to investigate its behavior under various extreme application scenarios. This

includes determining the maximum applicable story height, the maximum applicable wall thickness, and evaluating its performance when utilizing new materials.

(a) Schematic diagram (b) ANSYS finite element model

Fig. 1. Diagram of the tool-type single-sided formwork system.

3 Finite Element Analysis for Different Scenarios

3.1 Under Different Story Heights

According to current code requirements, the story height of basements shall not be less than 2.2 m. In practice, basement story heights typically range from 2.6 m to 3.2 m. This study employs ANSYS finite element software for simulation analysis. The panel portion is modeled using the shell element SHELL181, while the members are modeled with the beam element BEAM188. The ground anchor bolt locations are treated as fixed supports, and other connections are simulated either through shared nodes or by coupling two nodes. In actual conditions, the top of the formwork is reinforced and connected to the floor slab formwork using timber battens. However, as the connection strength is often insufficient in most cases, and to investigate the deformation under the most critical scenario, no constraints are applied at the top in the simulation, resulting in a model with relatively weaker constraints compared to reality. To analyze the deformation and mechanical performance of the system one-sided formwork, analysis scenarios were established for story heights of 2.44 m, 2.8 m, 3.0 m, and 3.2 m. Among these, the scenarios of 2.44 m, 2.8 m, and 3.0 m employ standard formwork components of 2.44 m height with corresponding additional height layers. The deformation nephograms are shown in Fig. 2. In accordance with the deformation limits specified in the Technical Code for Safety of Construction Templates (JGJ 162–2008), for formwork with concealed structural surfaces, the maximum deformation shall not exceed L/250 of the calculated span. In this study, the minimum calculated span of 2.44 m is adopted, resulting in a deformation limit of 9.76 mm.

Among these, the maximum deformation of the standard 2.44 m formwork component is 2.05 mm, primarily concentrated at the top center. When the standard 2.44 m formwork component is extended by a 0.36 m additional height layer to reach 2.8 m, the maximum deformation increases to 3.96 mm, mainly occurring at the top of the additional height layer. Although the height increases by only 14.8%, the deformation

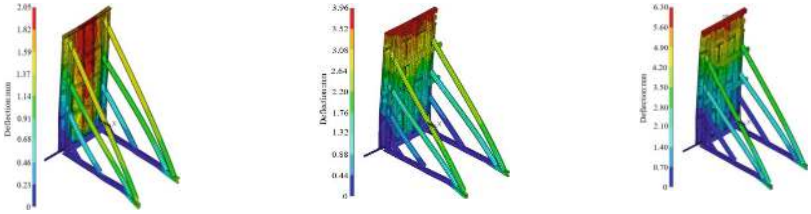

(a) Height of 2.44 m (b) Height of 2.80 m (c) Height of 3.00 m

Fig. 2. Deformation nephograms of the system with added layers under different heights.

increases significantly by 93.2%. For the 3.0 m configuration, the maximum deformation reaches 6.30 mm. Compared to the 2.8 m case, the height increases by only 7.1%, while the deformation increases by 59.1%.In summary, the additional height layer is a temporary structure connected only by timber battens and exhibits relatively lower strength compared to the standard formwork components. If the story height continues to increase, the deformation shows a multiplied growth trend. Furthermore, by proportionally scaling up the standard formwork height to 2.8 m and adding a 0.4 m additional height layer to reach 3.2 m, the specific deformation behavior is shown in Fig. 3.

(a) Height: 2.80 m (b) Height: 3.20 m

Fig. 3. Deformation nephograms of the system with scaled spacings at different heights.

As can be seen from the figure above, when facing the same story height of 2.8 m, the deformation of the 2.8 m standard formwork component is reduced by 0.75 mm compared to that of the 2.44 m standard formwork component with an additional height layer. Furthermore, when the height is increased to 3.2 m by adding another height layer, the maximum deformation reaches 6.13 mm, which is still smaller than the deformation of the 2.44 m standard component extended to 3.0 m with an additional height layer. However, compared to its standard component height, an increase of only 0.4 m results in a doubling of the deformation. This may be attributed to the relatively weak constraints of the additional height layer, but it also indirectly demonstrates the reliability of the mechanical performance of the standard components of this tool-type one-sided formwork. Subsequent structural reinforcement of the additional height layer can be achieved by methods such as adding lateral bracing. The deformations in all the above working conditions remain within the limits specified by the code. Further analysis was conducted on the stress distribution of the components. Taking the 2.44 m standard

component as an example, the structure was divided into three parts based on material properties and components: the face panel, the support frame, and the diagonal bracing. The stress nephograms are shown in Fig. 4.

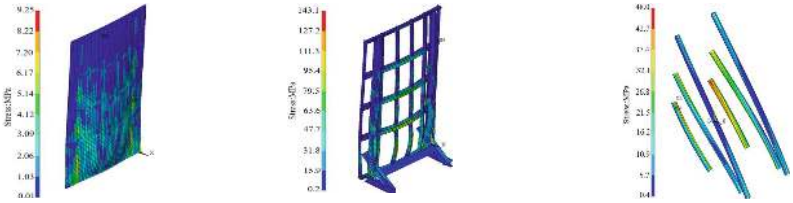

Face panel Support frame Diagonal bracing

Fig. 4. Stress nephogram of the standard system of 2.44 m in height.

The figure clearly illustrates the stress response characteristics of the tool-type one-sided formwork system under concrete lateral pressure. From the stress distribution of the face panel, the maximum stress value is 9.25 MPa, occurring in the lower-left and lower-right regions of the panel, exhibiting typical compressive distribution characteristics. The gradual variation in the stress gradient indicates a relatively uniform stiffness distribution in the panel system. The maximum stress in the support frame is 143.1 MPa, appearing at the flange of the channel steel vertical member. Areas of higher stress are mainly concentrated at the joints between the vertical and horizontal members. As critical nodes in the primary load path, stress concentration in these regions is within expected limits. The maximum stress in the diagonal bracing is 48.0 MPa. The stress variation increases progressively from high to low, with a relatively uniform distribution along the axial direction of the member, validating the effectiveness of its force-transfer mechanism as a two-force member. The stress conditions for the remaining working conditions are presented in Table 1 below. The stress levels in all systems are well below the design strength of 205 MPa for Q235 steel and the design strength of 13 MPa for the film-faced wood panel.

Table 1. Maximum stress of components under different story height conditions (Unit: MPa).

Story Height(m)	Face Panel	Location	Support Frame	Location	Diagonal Bracing	Location
2.44 + 0.36	10.2	Lower-left / Lower-right	161.0	Flange of the Vertical Member	74.9	Connection Zone of the Diagonal Bracing
2.44 + 0.56	11		169.1		94.9	
2.80	11.9		168.4		62.1	
2.80 + 0.40	12.7		174.3		99.8	

3.2 Under Different Wall Thicknesses

Table 2. Data for working conditions with different wall thicknesses.

Wall Thickness	S' k(kN/m^2)	Maximal Deformation (mm)	Sk(kN/m^2)	Maximal Stress (MPa)
250mm	35.34	2.05	49.67	143
300mm	32.44	1.88	45.75	131
350mm	29.84	1.73	42.24	121
400mm	28.10	1.63	39.90	114

In general, the thickness of basement retaining walls ranges from 200 to 400 mm. Different concrete thicknesses affect the initial setting time (t_0) and the pouring rate (V) of the concrete [12]. For the same height, thicker concrete leads to higher temperatures and accelerated hydration heat release, thereby reducing the initial setting time. However, due to the lack of experimental data for validation, the initial setting time in this study is determined according to the code specification. The pouring rate is measured in meters per hour (m/h). Assuming a constant pumping speed of the concrete truck, the increase in thickness results in a larger volume of concrete required, which reduces the concrete pouring height achieved per hour. Consequently, the overall lateral pressure imposed on the formwork is reduced. To analyze the deformation and mechanical behavior of the 2.44 m high tool-type one-sided formwork, scenarios with wall thicknesses of 250 mm, 300 mm, 350 mm, and 400 mm were established. The calculation results are presented in Table 2.

3.3 Scenarios with Different Novel Materials

Aluminum alloy is increasingly used to replace wood and steel in construction applications. Although pure aluminum exhibits low stiffness and high plasticity, alloying can significantly enhance its mechanical properties. In this study, the original steel-wood composite SFSS is redesigned by replacing the face panel, support frame, and diagonal bracing with aluminum alloy 5083. Using the standard 2.44 m in height formwork component as the example, the deformation and mechanical performance of the aluminum-alloy version are analyzed to assess its feasibility as a new material alternative. The performance comparison of different components is presented in Table 3.

Based on equivalent mass conversion, the 16.5 mm wood face panel was replaced with a 3.2 mm aluminum alloy plate, increasing overall deformation by 1.79 mm as shown in Fig. 5(a). Replacing the steel support frame with aluminum alloy reduced its weight by 28.6 kg, only one-third of the original, while deformation rose by 1.88 mm as shown in Fig. 5(b). The diagonal bracing, already lightweight, saw a 7.36 kg reduction and a 1.03 mm deformation increase as shown in Fig. 5(c). Stress analysis of the aluminum alloy components was also conducted. According to aluminum structural design codes, the design strength of 5083 aluminum alloy is 90 MPa with a yield strength of 240 MPa. In general, all schemes comply with the design requirement.

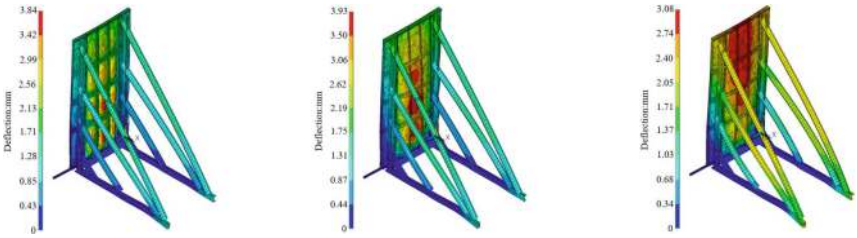

(a) Aluminum alloy face panel (b) Aluminum alloy support frame (c) Aluminum alloy diagonal bracing

Fig. 5. Deformation nephograms of the 2.44 m standard component with different material configurations.

Table 3. Performance comparison of different components.

Component	Original Material		New Material		Weight Comparison	Deformation Comparison
	Modulus (MPa)	Density (kg/m^3)	Modulus (MPa)	Density (kg/m^3)		
Face Panel	9200	500	60000	2600	0	+1.79mm
Support Frame	205000	7850			-28.6kg	+1.88mm
Diagonal Bracing	205000	7850			-7.36kg	+1.03mm

4 Full-Scale Model Test Validation

Based on the aforementioned finite element analysis, a systematic investigation has been carried out to reveal the mechanical behavior and deformation patterns of the tool-type one-sided formwork system under varying story heights, wall thicknesses, and material types, providing theoretical insights into its load-bearing mechanism and potential optimization directions. However, the accuracy and reliability of the numerical simulation results still require validation through physical testing. Therefore, based on the analytical conclusions drawn in Chapter 3, this chapter designs and carries out a full-scale model test. The test aims to realistically simulate the actual working state of the formwork under concrete lateral pressure. By accurately measuring displacements and strains at critical locations, a comparative analysis with the finite element calculation results will be conducted to verify the correctness of the numerical model and to provide solid practical support for the engineering application of this system. The specific test parameters are listed in Table 4.

Table 4. Parameters of test specimens.

Component Name	Material Type	Dimensions	Remarks
Face Panel	Plywood	1.22×2.44×0.024m	Width × Height × Thick
Height Extension Panel	Plywood	1.22×0.3×0.024m	Width × Height × Thick
Vertical Rib	Aluminum Alloy	4×2.5×0.12cm	Length × Width × Thick
Horizontal Rib	Aluminum Alloy	6×6×0.4cm	Length × Width × Thick
Tubular Diagonal Brace	Q235 Steel	48mm/45mm	Outer / Inner Diameter
Vertical Rib Spacing	/	25+24×3+25cm	/
Horizontal Rib Spacing	/	70+54.5+55.5+64cm	Bottom to Top
Diagonal Brace Spacing	/	95+60+80cm	Bottom to Top

Based on the preceding analysis, the use of aluminum alloy for the support frame can maximize the reduction of the maximum unit weight of the formwork. However, for the face panel, which has a relatively large volume, an aluminum alloy of the same mass does not perform as effectively as plywood. The diagonal bracing, being critical for preventing formwork overturning, remains constructed with higher-stiffness Q235 steel. Additionally, increasing the panel thickness to 24 mm aims to enhance the deformation resistance of both the face panel component and the height extension sections.

To comprehensively evaluate the structural performance of the optimized single-sided formwork, the research team conducted a full-scale field test. The test setup consisted of three formwork units, with the central unit serving as the primary monitoring target, as shown in Fig. 6. The measurement system employed an independent steel truss to secure monitoring equipment, ensuring complete separation from the formwork system. Concrete was poured from the top using pump technology, with slump and temperature tested before each truckload. The pouring rate was appropriately increased to adequately excite the structural response. All necessary testing tools were prepared during the test setup phase, and the data acquisition system was verified to be operating stably. After concrete placement, its workability was immediately tested, and theoretical lateral pressure was calculated as the analysis baseline. During pouring, layered placement was implemented with data recorded at every 0.6-m interval, while displacement and strain measurements were simultaneously collected. Data acquisition utilized two methods: a laser deflection tester for non-contact measurement with ±0.01 mm accuracy, and traditional displacement meters fixed by independent supports for real-time data transmission. Stress data were collected using a TDS-540 acquisition instrument with strain gauges at 1 Hz sampling frequency, effectively meeting field testing requirements. The test provided reliable validation for numerical models by comparing measured data with theoretical predictions, comprehensively evaluating the formwork system's deformation behavior and construction quality.

(a) The overall structure

(b) Displacement transducers

(c) Measurement points

Fig. 6. Photo of the full-scale field test setup.

The measured maximum stress values (after stabilization) from the test were compared with the theoretical maximum stress values, as shown in the Table 5. The specific locations of all measurement points are indicated in Fig. 7. The variation trends of both sets of data are generally consistent, showing a distribution characteristic of increasing from top to bottom; however, the measured values are generally higher than the theoretical values. At the mid-height of the formwork, the difference between the measured and theoretical maximum values is most significant, reaching 121.71%. This deviation can be attributed to the influence of environmental factors such as temperature during field testing, as well as the potential damage to the strain gauge at measurement point 04 during the experiment, which may have caused abnormally high readings. With reference to the material parameters of Q235 steel, whose design values for tensile, compressive, and flexural strength are 215 MPa, the test results still meet the design requirements.

The comparison between the measured displacement values (after stabilization) obtained from the test and the theoretical values is presented in the Table 5. Both sets of data show generally consistent trends, characterized by a gradual decrease from top to bottom. The maximum measured displacement is relatively close to the theoretical value; however, the rate of decrease in the measured values is less pronounced than in the theoretical results, indicating overall larger deformations. This discrepancy is primarily attributed to the stronger boundary constraints at the base of the theoretical model compared to the actual conditions, as well as the non-uniformity in the concrete pouring rate. According to the requirements of the Technical Code for Safety of Construction Templates, for formwork with concealed structural surfaces, the deformation limit is specified as L/250 of the member's calculated span, i.e., 2.74 m/250 = 10.96 mm. The test results satisfy this provision. Furthermore, in accordance with the Code for Construction Quality Acceptance of Concrete Structures, the vertical flatness limit for concrete exterior walls with a story height less than 6 m is 10 mm. The test results also comply with this construction acceptance requirement.

Stress measurement point

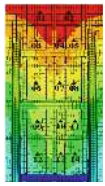

Displacement measurement point

Fig. 7. Layout of stress and displacement measurement points.

Table 5. Comparison of measured and theoretical stresses and displacements.

Maximal StressMaximal Displacement						
Measur ement Point	Theoret ical (MPa)	Measur ed. (MPa)	Relative Error	Laser Deflectio n Tester (mm)	Displacement Transducer (mm)	Theoretic al (mm)
01	19.6	17.8	−9.18%	/	6.55	6.23
02	40.2	38.6	−3.98%	6.34	5.94	6.19
03	25.4	20.3	−20.08%	5.98	5.76	5.83
04	62.3	47.1	−24.40%	/	6.31	6.10
06	42.1	33.2	−21.14%	5.89	6.12	5.78
08	39.8	34.5	−13.32%	4.56	/	4.89
09	55.7	44.4	−20.29%	/	5.11	5.08
10	61.8	49.9	−19.26%	4.87	5.06	4.81
11	48.9	38.5	−21.27%	/	3.93	3.69
12	54.6	45.6	−16.48%	/	4.82	4.05
13	50.7	39.3	−22.49%	3.95	/	2.87
14	61.5	54.1	−12.03%			
15	69.7	52.6	−24.53%			
16	49.5	58.1	17.37%			
17	70.9	65.8	−7.19%			
19	80.6	56.8	−29.53%			
20	86.4	58.4	−32.41%			
21	5.6	4.8	−14.29%			

Note: /indicate the measurement point is masked by other objects during measurement.

5 Conclusion

Based on systematic finite element analysis and validation via a full-scale model test, the following main conclusions are drawn:

1. Adaptability to Story Height: The proposed tool-type one-sided formwork system satisfies the code-specified deformation limits within the story height range of 2.44 m to 3.2 m, demonstrating its reliability for conventional basement scenarios. However, the significant increase in deformation with the use of additional height layers identifies these temporary structures as the critical stiffness weak point, necessitating subsequent local reinforcement, such as adding lateral bracing.
2. Adaptability to Wall Thickness: Under varying wall thickness conditions (250 mm to 400 mm), the lateral concrete pressure decreases slightly with increasing wall thickness, leading to corresponding reductions in system deformation and stress. This indicates the system possesses good adaptability and an adequate safety margin across common wall thickness ranges.
3. Potential of New Material Application: Substituting steel components with 5083 aluminum alloy significantly reduces the system weight (by approximately one-third), confirming substantial potential for lightweight applications. However, the material substitution also reduces overall stiffness and increases deformation, with local stress in the aluminum alloy support frame slightly exceeding the design strength. Consequently, the application of new materials must be coupled with sectional optimization to balance weight reduction and performance assurance.
4. Experimental Validation and Model Reliability: The measured data from the full-scale test showed a highly consistent trend with the FE simulation results, successfully validating the established numerical model's accuracy and reliability. Although deviations occurred at some measurement points due to environmental interference or potential instrument damage, the overall test results confirm the system's safety and feasibility under practical construction conditions.

   In summary, the tool-type one-sided formwork system performs reliably within conventional engineering parameters and shows significant potential through new material applications. Future work should focus on the structural optimization of the additional height layers and the refined design of aluminum alloy components to further enhance the system's comprehensive performance and economy, thereby promoting its standardized and industrialized application.

References

1. Sterling, R., et al.: Sustainability issues for underground space in urban areas. Proc. Inst. Civ. Eng-U. **165**(4), 241–254 (2012). https://doi.org/10.1680/udap.10.00020
2. Broere, W.: Urban underground space: solving the problems of today's cities. Tunn. Undergr. Sp. Tech. **55**, 245–248 (2016). https://doi.org/10.1016/j.tust.2015.11.012
3. De Sutter, S.; Remy, O.; Tysmans, T.; Wastiels, J. Development and experimental validation of a lightweight stay-in-place composite formwork for concrete beams. Constr. Build. Mater. 63, 33–39 (2014). DOI: 10.1016/ j.conbuildmat.2014.03.032.

4. Turkoglu, H. Analysis of formwork system selection criteria for building construction projects: a comparative study. Buildings, 11(12). 618 (2021). DOI: 10.3390/ buildings14072116.
5. Abbasa, Z.H., Hassana, M.S., Gorgisb, I.N.: Stay in place formwork, encased reinforced concrete column: a. Eng. Technol. J. **41**(11), 1355–1378 (2023). https://doi.org/10.30684/etj.2023.139421.1428
6. Zhou, Y., He, Z.: Construction technology of unilateral formwork support by pulling planting bar for super tall exterior wall of basement. Construct. Technol. **43**(23), 34-35+72 (2014). https://doi.org/10.7672/sgjs2014230034
7. Hao, J.B., Wang, Z., Zhang, S.Y., Fang, Y.S., Li, G.X., Xu, J.: Design and application of prefabricated triangle truss self-stabilized single sided formwork in CBD project in Egypt. Construct. Technol. **49**(21), 94–97 (2020). https://doi.org/10.7672/sgjs2020210094
8. Kang, Q.Q.; Li, Z.P.; Lu, D.Q.; Mao, L. Construction of basement single wall formwork in Silverstone Square. Sichuan Archit., 30(6): 206–207(2010). DOI: 10.3969/ j.issn.1007–8983.2010.06.084.
9. Zhang, Y.L., Li, K.J., Wang, H., Liu, J.P., Li, G.: General construction technique of Tianjin Jinde garden underground engineering. Archit. Technol. **43**(3), 198–203 (2012). https://doi.org/10.3969/j.issn.1000-4726.2012.03.001
10. Tao, Y.H. Study on unilateral formwork with steel pipe fastener and diagonal bracing system. Build. Construct., 38(5): 596–599 (2016). DOI: 10.14144/ j.cnki.jzsg.2016.05.028.
11. Huang, H.L., Wang, Y., Chen, L., Chen, S.: Construction technology of one side formwork support for basement of Jinshuibei central building. Construct. Technol. **46**(s1), 414–417 (2017). https://doi.org/10.7672/sgjs2018S1303
12. Liu, W., He, L., Liu, J., et al.: Design optimization of an innovative instrumental single-sided formwork supporting system for retaining walls using physics-constrained generative adversarial network. Buildings. **15**(1), 132 (2025). https://doi.org/10.3390/buildings15010132

Author Index

C
Cai, Can 464
Cao, Hongfei 186
Chang, Jingyuan 132
Chang, Zhengbai 478
Chen, Hao 464
Chen, Huan-yong 147
Chen, Qiaosha 578
Chen, Shilei 120
Chen, Yuan-xi 147
Chen, Zhiqing 132
Cheng, Heng 451
Cheng, Shengming 323
Cheng, Yin 491
Cheng, Zhibao 340
Chu, Chaomin 578

D
Dai, Baoqian 350
Deng, Bo 540
Deng, Wei 1, 147
Deng, Zhongjun 421
Dili, A. 478
Ding, Wen 295
Ding, Xi 407
Du, Ruilin 159
Duan, Jinhui 566
Duan, Wei 172
Duan, Wenjing 556

F
Fan, Feilong 407
Fang, Minjin 222
Fang, Zhen 340
Feng, Haoyuan 31
Feng, Wenhui 186
Fu, Shenghang 1

G
Gao, Chao 464
Gao, Junze 172
Gou, Yunhao 540
Guo, Haifeng 295
Guo, Haoran 280
Guo, Hongbo 295
Guo, Minghui 309
Guo, Peng 203
Guo, Wenguang 438
Guo, Yingfu 407

H
Han, Pan 79
Han, Yiming 44
Han, Yunpeng 556
He, Huaijian 159
He, Lin 601
He, Yubin 309
He, Yuxuan 556
Hong, Ning 378
Hou, Chunyao 234
Hu, Aiguo 464
Hu, Shiruo 309
Huang, Fenglei 251
Huang, Heming 251
Huang, Lvshan 578

J
Jang, Jin 478
Ji, Shaohua 203
Jiang, Chenfang 451
Jiang, Fangjie 566
Jiang, Feng 147
Jiang, Weiyu 504
Jiang, Yanfang 464
Jin, Rui 222

© The Editor(s) (if applicable) and The Author(s), under exclusive license to Springer Nature Switzerland AG 2027
G. Feng et al. (Eds.): ICCE 2025, SUCI, pp. 615–617, 2027.
https://doi.org/10.1007/978-3-032-32237-1

K
Kong, Xiangle 601

L
Lan, Huijun 504
Li, Bin 366
Li, Dongxue 350
Li, Fei 186
Li, Guanjie 601
Li, Peng 172
Li, Qindong 491
Li, Ruixin 92
Li, Sheng 366
Li, Wei 159, 566
Li, Xueming 407
Li, Yachao 504
Li, Yangyang 464
Li, Yingjia 309
Li, Yuke 438
Li, Zhe 44
Li, Zhengkai 132
Li, Zongqi 421
Liang, Hui 234, 527
Lin, Ende 44
Lin, Hai 44
Lin, Junjie 16
Lin, Xiushan 350
Liu, Deyi 504
Liu, Dingxiao 309
Liu, Guili 393
Liu, Haifeng 159
Liu, Jiang 504
Liu, Jikai 601
Liu, Wei 601
Liu, Wentao 540, 556
Liu, Xiang 64
Liu, Xiaoqiang 222
Liu, Xubo 64
Liu, Xuecong 234
Liu, Ying 106
Liu, Yuhan 589
Liu, Zhenguo 566
Lu, Yulong 186
Luo, Wei 309
Lv, Lei 393

M
Ma, Jinyu 340
Ma, Ruilong 251
Ma, Xiaofei 393
Mao, Yanpian 451
Mao, Yu 16
Mi, Jia 407
Mo, Yang 159
Mou, You 451

N
Nian, Zhiwei 438

O
Ouyang, Jinhui 234

P
Pai, Lifang 366
Pan, Jun 64
Pan, Xiaodong 504
Pei, Jiangrong 421

Q
Qi, Zhiyong 451
Qiao, Fangbo 186
Qin, Ken 79
Qiu, Qingying 120
Qiu, Yanliang 172
Qu, Ru 159

R
Rao, Dengyu 132

S
Shen, Chuanqi 421
Shen, Jun 438
Shen, Tongke 172
Shi, Kaite 44
Shu, Ziyan 251
Si, Shuhao 323
Song, Xintong 438, 491
Su, Dudu 527
Su, Rui 540, 556, 566
Sun, Yong 172

T
Tan, Dawen 234
Tang, Qiang 491
Tang, Xianglong 92
Tie, Ruian 323
Tu, Jin 527

W
Wang, Bin 64
Wang, Chuantong 1
Wang, Fan 464
Wang, Haoyu 295
Wang, Jin-liang 147
Wang, Juke 393
Wang, Jun 203
Wang, Lingfeng 323
Wang, Lizhi 309
Wang, Miao 31
Wang, Nannan 31
Wang, Qilin 159
Wang, Qingpeng 1
Wang, Ronghui 478
Wang, Xiaoyu 295
Wang, Xinjie 251
Wang, Xinyi 31
Wang, Xuepan 478
Wang, Xueqi 438
Wang, Yaping 16
Wang, Yingqi 295
Wang, Yuanxiang 491
Wang, Yuehui 504
Wang, Zheshi 132
Wei, Huaizhou 464
Wei, Xuefeng 172
Wu, Qidong 366

X
Xiang, Binhui 106
Xiao, Liang 578, 589
Xiao, Yan 64
Xu, Guowen 203
Xu, Hongtao 323
Xu, Lizhi 44
Xu, Runchuan 578
Xu, Yangfu 589
Xu, Yin 280

Y
Yan, Chunli 527
Yan, Jinpeng 464
Yang, Jing 280
Yang, Lingling 186
Yang, Moxuan 64
Ye, Qinglan 378
Yu, Xinpeng 309
Yuan, Jin 451

Z
Zhai, Shun 159
Zhang, Haihong 16
Zhang, Hui 601
Zhang, Jianpeng 31
Zhang, Jin 350
Zhang, Jun 44
Zhang, Kunfeng 407
Zhang, Qing 589
Zhang, Shuangcheng 323
Zhang, Wenjing 16
Zhang, Xiaopeng 16
Zhao, Chengqiang 601
Zhao, Jianshi 309
Zhao, Longquan 540
Zhao, Ping 407
Zhao, Songtao 527
Zhao, Zilong 393
Zheng, Kaiyuan 44
Zheng, Qiao 222
Zhong, Xingjie 31
Zhou, Rui 350
Zhu, Baoguo 31
Zhu, Binglong 266
Zhu, Jianyong 366
Zhu, Jianyun 366
Zong, Yiyang 323